

Copy No.

MSC-A-R-66-3



POSTLAUNCH REPORT FOR APOLLO MISSION A-004

(Spacecraft 002)

(NASA-TM-X-69864) POSTLAUNCH REPORT FOR  
APOLLO MISSION A-004 (SPACECRAFT 002)  
(NASA) 377 F

N74-71225

Unclas  
00/99 16635

NATIONAL AERONAUTICS AND SPACE ADMINISTRATION

MANNED SPACECRAFT CENTER

HOUSTON, TEXAS

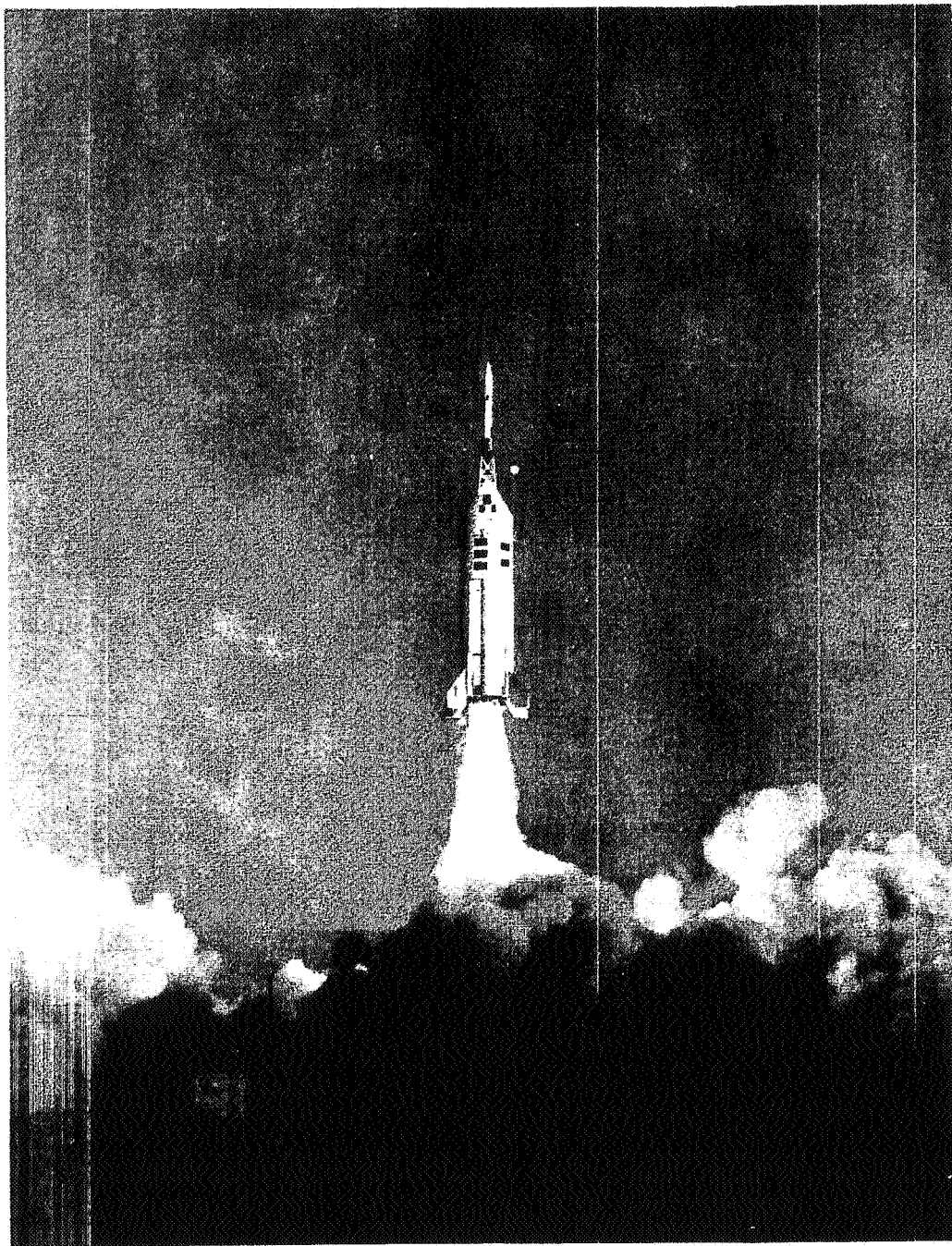
April 15, 1966

REPRODUCED BY  
NATIONAL TECHNICAL  
INFORMATION SERVICE  
U.S. DEPARTMENT OF COMMERCE  
SPRINGFIELD, VA. 22161

# APOLLO SPACECRAFT FLIGHT HISTORY

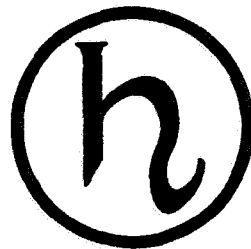
Mission	Spacecraft	Description	Launch date	Launch site
PA-1	BP-6	First pad abort	Nov. 7, 1963	White Sands Missile Range, N. Mex.
A-001	BP-12	Transonic abort	May 13, 1964	White Sands Missile Range, N. Mex.
AS-101	BP-13	Nominal launch and exit environment	May 28, 1964	Cape Kennedy, Fla.
AS-102	BP-15	Nominal launch and exit environment	Sept. 18, 1964	Cape Kennedy, Fla.
A-002	BP-23	Maximum dynamic pressure abort	Dec. 8, 1964	White Sands Missile Range, N. Mex.
AS-103	BP-16	Micrometeoroid experiment	Feb. 16, 1965	Cape Kennedy, Fla.
A-003	BP-22	Low-altitude abort (planned high- altitude abort)	May 19, 1965	White Sands Missile Range, N. Mex.
AS-104	BP-26	Micrometeoroid experiment and service module RCS launch environment	May 25, 1965	Cape Kennedy, Fla.
PA-2	BP-23A	Second pad abort	June 29, 1965	White Sands Missile Range, N. Mex.
AS-105	BP-9A	Micrometeoroid experiment and service module RCS launch environment	July 30, 1965	Cape Kennedy, Fla.
A-004	SC-002	Power-on tumbling boundary abort	Jan. 20, 1966	White Sands Missile Range, N. Mex.

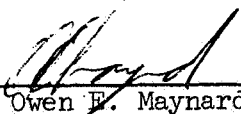
NASA-S-66-3657 APR 15



Lift-off, Apollo Mission A-004.

POSTLAUNCH REPORT FOR APOLLO MISSION A-004  
(SPACECRAFT 002)



  
Owen E. Maynard, Chief  
Mission Operations Division

NATIONAL AERONAUTICS AND SPACE ADMINISTRATION

MANNED SPACECRAFT CENTER

HOUSTON, TEXAS

April 15, 1966



NOTICE

Unless otherwise specified, zero time (T-0) for all data in this report is referenced to 4-inch motion of the test vehicle.

# CONTENTS

Section		Page
	TABLES . . . . .	v
	FIGURES . . . . .	vii
	ABBREVIATIONS AND SYMBOLS	
	Abbreviations . . . . .	xxii
	Symbols . . . . .	xxiv
1.0	MISSION SUMMARY . . . . .	1-1
2.0	INTRODUCTION . . . . .	2-1
3.0	TEST VEHICLE DESCRIPTION . . . . .	3-1
	3.1 Spacecraft . . . . .	3-1
	3.2 Launch Vehicle . . . . .	3-8
	3.3 Mass Characteristics . . . . .	3-10
4.0	MISSION TRAJECTORY ANALYSIS . . . . .	4-1
	4.1 Real-Time Flight Dynamics Control . . . . .	4-1
	4.2 Comparison of Flight with Preflight and Postflight Simulations . . . . .	4-6
5.0	SPACECRAFT PERFORMANCE . . . . .	5-1
	5.1 Aerodynamics . . . . .	5-4
	5.2 Structural Loads . . . . .	5-8
	5.3 Structural Dynamics . . . . .	5-32
	5.4 Boost Protective Cover . . . . .	5-96
	5.5 Mechanical Subsystems . . . . .	5-101
	5.6 Launch-Escape Propulsion Subsystem . . . . .	5-117
	5.7 Pyrotechnic Devices . . . . .	5-121
	5.8 Earth Landing and Impact Attenuation . . . . .	5-129
	5.9 Crew Station Acoustics . . . . .	5-150
	5.10 Sequential Subsystem . . . . .	5-156
	5.11 Electrical Power Subsystem . . . . .	5-159
	5.12 Spacecraft Instrumentation and Communication Subsystem . . . . .	5-168
	5.13 Environmental Control Subsystem Cabin Pressure Relief Valve . . . . .	5-176
	5.14 Crew Windows . . . . .	5-180

Section		Page
6.0	LAUNCH VEHICLE PERFORMANCE . . . . .	6-1
6.1	Propulsion . . . . .	6-1
6.2	Launch Vehicle Pyrotechnic Devices . . . . .	6-6
6.3	Attitude Control Subsystem . . . . .	6-7
6.4	Launch vehicle Aerodynamics . . . . .	6-20
6.5	Launch Vehicle Structures . . . . .	6-22
6.6	Launch Vehicle Electrical Power Subsystem . . . . .	6-23
6.7	Launch Vehicle Instrumentation Subsystem . . . . .	6-24
6.8	Radio-Frequency Command Subsystem . . . . .	6-27
6.9	Range Safety Subsystem . . . . .	6-29
6.10	Launch Vehicle Ignition . . . . .	6-31
7.0	RECOVERY OPERATIONS . . . . .	7-1
7.1	Command Module . . . . .	7-3
7.2	Launch-Escape Subsystem . . . . .	7-8
7.3	Service Module . . . . .	7-10
7.4	Launch Vehicle . . . . .	7-11
8.0	POSTFLIGHT TESTING AND ANOMALY SUMMARY . . . . .	8-1
8.1	Postflight Testing . . . . .	8-1
8.2	Summary of Malfunctions and Deviations . . . . .	8-2
9.0	CONCLUDING REMARKS . . . . .	9-1
10.0	APPENDIX A . . . . .	10-1
10.1	Test Vehicle History . . . . .	10-1
10.2	Launch Procedure . . . . .	10-9
10.3	Real-Time Data System . . . . .	10-16
10.4	Range Operations . . . . .	10-18
10.5	Weather Conditions . . . . .	10-32
11.0	APPENDIX B . . . . .	11-1
11.1	Mission A-004 Test Objectives . . . . .	11-1
11.2	Test Vehicle Measurements . . . . .	11-3
12.0	REFERENCES . . . . .	12-1

# TABLES

Table		Page
3.3-I	MASS PROPERTIES FOR MISSION A-004 . . . . .	3-11
4.2-I	MISSION A-004 TRAJECTORY PARAMETERS . . . . .	4-8
5.2-I	LAUNCH-ESCAPE SUBSYSTEM TOWER LEG LOADS, MISSION A-004 . . . . .	5-15
5.2-II	COMMAND MODULE SUBSTRUCTURE STRESSES, MISSION A-004 . . . . .	5-16
5.2-III	SERVICE MODULE RADIAL BEAM TRUSS AND TENSION TIE STRESSES DURING MISSION A-004 . . . . .	5-19
5.2-IV	MISSION A-004 FLIGHT TRAJECTORY PARAMETERS FOR INTERFACE LOAD CONDITIONS . . . . .	5-20
5.2-V	COMPARISON OF LES-CM INTERFACE LOADS . . . . .	5-21
5.2-VI	COMPARISON OF CM-SM INTERFACE LOADS FROM STRAIN DATA AND FLIGHT PARAMETERS . . . . .	5-22
5.3-I	LOCATIONS OF STRAIN GAGES ON WEBS OF SERVICE MODULE RADIAL BEAMS . . . . .	5-41
5.6-I	MOTOR PERFORMANCE SUMMARY . . . . .	5-118
5.7-I	PYROTECHNIC DEVICES FOR MISSION A-004 (SC-002) . . . .	5-123
5.8-I	EARTH LANDING SUBSYSTEM EVENTS FOR MISSION A-004 . . .	5-133
5.8-II	APOLLO MISSION A-004 FIELD MEASUREMENTS OF IMPACT STRUT STROKES . . . . .	5-134
5.14-I	ELEMENTS FOUND IN LES ENGINE DEPOSITS ON THE SC-002 LEFT-HAND RENDEZVOUS WINDOW . . . . .	5-182
10.1-I	OPERATIONAL CHECKOUT PROCEDURES FOR MISSION A-004 . .	10-3
10.1-II	PROBLEM HISTORY OF LAUNCH VEHICLE . . . . .	10-6
10.2-I	MAJOR TASKS OF SC-002 SPACECRAFT CLOSE-OUT . . . . .	10-11

Table		Page
10.4-I	RANGE EVALUATION OF FILM COPIED FOR MSC . . . . .	10-21
10.4-II	RANGE EVALUATION OF FILM NOT COPIED FOR MSC . . . . .	10-24
10.4-III	FILM EVALUATION OF BEST MOTION PICTURE COVERAGE FOR EVENTS . . . . .	10-28
11.2-I	TEST VEHICLE MEASUREMENT LIST . . . . .	11-4
11.2-II	LAUNCH VEHICLE MEASUREMENT LIST, AIRBORNE . . . . .	11-15
11.2-III	LAUNCH VEHICLE MEASUREMENT LIST, LANDLINE . . . . .	11-17

## FIGURES

Figure		Page
	Lift-off, Apollo Mission A-004 . . . . .	i
2.0-1	Test vehicle for Apollo Mission A-004 prior to launch (11-30-65) . . . . .	2-2
2.0-2	Sequence of major events, Apollo Mission A-004 . . .	2-3
3.1-1	Test vehicle configuration, Apollo Mission A-004 . .	3-2
3.1-2	Launch-escape vehicle reference stations and center- of-gravity locations, Apollo Mission A-004 . . . .	3-3
3.1-3	Launch-escape vehicle center-of-gravity and thrust vector location, Apollo Mission A-004 . . . . .	3-4
3.1-4	Spacecraft axis system for orientation and motion, Apollo Mission A-004 . . . . .	3-5
3.1-5	Paint patterns, Apollo Mission A-004	
	(a) Command module and boost protective cover . . .	3-6
	(b) Launch-escape motor . . . . .	3-7
	(c) Service module . . . . .	3-7
3.2-1	Little Joe II launch vehicle 12-51-3, Apollo Mission A-004 . . . . .	3-9
3.3-1	Apollo Mission A-004 time history of launch-escape vehicle weight . . . . .	3-12
3.3-2	Apollo Mission A-004 time history of launch-escape vehicle center-of-gravity $X_A$ station location . . .	3-13
3.3-3	Apollo Mission A-004 time history of launch-escape vehicle center-of-gravity Y-axis location . . . . .	3-14
3.3-4	Apollo Mission A-004 time history of launch-escape vehicle center-of-gravity Z-axis location . . . . .	3-15
3.3-5	Apollo Mission A-004 time history of launch-escape vehicle roll moment of inertia . . . . .	3-16

Figure		Page
3.3-6	Apollo Mission A-004 time history of launch-escape vehicle pitch and yaw moments of inertia . . . . .	3-17
4.1-1	Apollo Mission A-004 RTDS plotboard displays	
	(a) Plotboard A . . . . .	4-2
	(b) Plotboard B . . . . .	4-3
	(c) Plotboard C . . . . .	4-4
	(d) Plotboard D . . . . .	4-5
4.2-1	Apollo Mission A-004 RTDS plotboard B with T-2 hour weather . . . . .	4-11
4.2-2	Altitude plotted against time, Apollo Mission A-004 . . . . .	4-12
4.2-3	Mach number plotted against time, Apollo Mission A-004 . . . . .	4-13
4.2-4	Dynamic pressure plotted against time, Apollo Mission A-004 . . . . .	4-14
4.2-5	Tangential velocity plotted against time, Apollo Mission A-004 . . . . .	4-15
4.2-6	Flight-path angle plotted against time, Apollo Mission A-004 . . . . .	4-16
4.2-7	Altitude plotted against total range, Apollo Mission A-004 . . . . .	4-17
4.2-8	Ground track, Apollo Mission A-004 . . . . .	4-18
5.0-1	WSMR abort points in relation to Saturn boost flight envelope . . . . .	5-2
5.0-2	Test region and abort points, Apollo Mission A-004 . . . . .	5-3
5.1-1	Comparison of actual and predicted launch-escape vehicle spacecraft rotational rates for Apollo Mission A-004 . . . . .	5-6
5.1-2	Comparison of actual and predicted angular rate envelope, Apollo Mission A-004 . . . . .	5-7

Figure		Page
5.2-1	Launch-escape subsystem structure, Apollo Mission A-004 . . . . .	5-23
5.2-2	Command module structure, Apollo Mission A-004 . . .	5-24
5.2-3	Service module construction, Apollo Mission A-004 . .	5-25
5.2-4	Quad D prototype SM RCS engine chamber and nozzle extension, Apollo Mission A-004 . . . . .	5-26
5.2-5	LES-CM interface total bending moment calculated from tower leg strain gage data, Apollo Mission A-004 . . . . .	5-27
5.2-6	LES-CM interface total axial force calculated from tower leg strain gage data, Apollo Mission A-004 . . . . .	5-28
5.2-7	Maximum conical surface plume impingement pressure and aft equipment compartment pressure measured on CM, Apollo Mission A-004 . . . . .	5-29
5.2-8	Conical surface plume impingement pressures on Mission A-004	
	(a) Upwind surface in pitch plane . . . . .	5-30
	(b) Yaw plane surface . . . . .	5-30
	(c) Downwind surface in pitch plane . . . . .	5-30
5.2-9	CM-SM interface (station X <sub>A</sub> 1010) Block I limit design load capabilities envelope and maximum load conditions, Apollo Mission A-004 . . . . .	5-31
5.3-1	rms time history of CM X-axis acceleration, Apollo Mission A-004 . . . . .	5-42
5.3-2	X-axis acceleration spectral density during staging, Apollo Mission A-004 . . . . .	5-43
5.3-3	Z-axis acceleration spectral density at T+51.5 second, Apollo Mission A-004 . . . . .	5-44
5.3-4	rms time history of Z-axis tower acceleration, Apollo Mission A-004	
	(a) -10 to 130 seconds . . . . .	5-45



Figure		Page
5.3-4	Continued	
	(b) 130 to 270 seconds . . . . .	5-46
5.3-5	Z-axis acceleration spectral density at lift-off, Apollo Mission A-004 . . . . .	5-47
5.3-6	Effect of RCS protuberance of SM fluctuating pressure levels as shown by wind tunnel data . . .	5-48
5.3-7	Comparison of SC-002 and BP-13 fluctuating pressure in vicinity of RCS engines on Apollo Missions A-004 and A-101 . . . . .	5-49
5.3-8	Comparison of SC-002 and BP-15 fluctuating pressure environments on Apollo Missions A-004 and A-102 . . . . .	5-50
5.3-9	Service module fluctuating pressure time history for RCS panel, Apollo Mission A-004 . . . . .	5-51
5.3-10	Service module shell fluctuating pressure time history, Apollo Mission A-004 . . . . .	5-52
5.3-11	Comparison of overall sound pressure levels (dB) on the service module, Apollo Mission A-004 . . . .	5-53
5.3-12	Comparison of angle of attack for Apollo Missions A-004 (SC-002), A-101 (BP-13), and A-102 (BP-15). .	5-54
5.3-13	Comparison of pressure spectral density for similar locations on the SM for Apollo Missions A-004 (SC-002) and A-102 (BP-15) . . . . .	5-55
5.3-14	SM RCS panel fluctuating pressure spectral density during transonic flight, Apollo Mission A-004 . . .	5-56
5.3-15	SM fluctuating pressure spectral density during transonic flight, Apollo Mission A-004 . . . . .	5-57
5.3-16	rms time history of CSM fairing vibration, Apollo Mission A-004 . . . . .	5-58

Figure		Page
5.3-17	rms time history of SM vibration, Apollo Mission A-004	
(a)	Measurement SA0944D . . . . .	5-59
(b)	Measurement SA0945D . . . . .	5-59
(c)	Measurement SA0947D . . . . .	5-60
(d)	Measurement SA0950D . . . . .	5-60
(e)	Measurement SA0946D . . . . .	5-61
(f)	Measurement SA0948D . . . . .	5-62
(g)	Measurement SA0949D . . . . .	5-63
(h)	Measurement SA0952D . . . . .	5-64
5.3-18	CSM fairing acceleration spectral density during transonic flight, Apollo Mission A-004 . . . . .	5-65
5.3-19	SM shell acceleration spectral density during transonic flight, Apollo Mission A-004	
(a)	Measurement SA0944D . . . . .	5-66
(b)	Measurement SA0945D . . . . .	5-67
(c)	Measurement SA0946D . . . . .	5-68
(d)	Measurement SA0947D . . . . .	5-69
(e)	Measurement SA0948D . . . . .	5-70
(f)	Measurement SA0949D . . . . .	5-71
(g)	Measurement SA0950D . . . . .	5-72
(h)	Measurement SA0952D . . . . .	5-73
5.3-20	SM shell acceleration spectral density at lift-off, Apollo Mission A-004 . . . . .	5-74
5.3-21	rms time history of radial beam circumferential vibration, Apollo Mission A-004 . . . . .	5-75
5.3-22	Radial beam acceleration spectral density during transonic flight, Apollo Mission A-004 . . . . .	5-76
5.3-23	Radial beam acceleration spectral density during supersonic flight, Apollo Mission A-004 . . . . .	5-77
5.3-24	rms time history of aft bulkhead vibration, Apollo Mission A-004 . . . . .	5-78
5.3-25	Aft bulkhead acceleration spectral density, Apollo Mission A-004 . . . . .	5-79

Figure		Page
5.3-26	rms time history of forward bulkhead vibration, Apollo Mission A-004 . . . . .	5-80
5.3-27	Forward bulkhead acceleration spectral density, Apollo Mission A-004	
	(a) Lift-off . . . . .	5-81
	(b) During transonic flight . . . . .	5-82
5.3-28	rms time history of $H_2$ tank shelf vibration, tank shelf vibration, Apollo Mission A-004 . . . .	5-83
5.3-29	$H_2$ tank shelf acceleration spectral density, Apollo Mission A-004	
	(a) Lift-off . . . . .	5-84
	(b) During transonic flight . . . . .	5-85
5.3-30	Location of SM RCS quad D, Apollo Mission A-004 . . .	5-86
5.3-31	Location of accelerometers on SM RCS panel and propellant tank bracket, Apollo Mission A-004 . . .	5-87
5.3-32	X-axis vibration measured on the oxidizer tank support bracket of quad D, SM RCS, Apollo Mission A-004 . . . . .	5-88
5.3-33	Digital power spectral density of X-axis vibration measured from T+33.008 to T+36.014 seconds on the oxidizer tank support bracket of quad D, SM RCS, Apollo Mission A-004 . . . . .	5-89
5.3-34	Radial vibration measured in the counterclockwise roll engine nozzle of quad D, SM RCS, Apollo Mission A-004 . . . . .	5-90
5.3-35	Digital power spectral density of radial vibration measured from T+50.014 to T+53.010 seconds in the counterclockwise roll engine nozzle of quad D, SM RCS, Apollo Mission A-004 . . . . .	5-91
5.3-36	Location of radial beams in service module for Apollo Mission A-004 . . . . .	5-92

Figure		Page
5.3-37	Comparison of rms strain history from typical radial beam web panel on SC-002 (Apollo Mission A-004) with strain from ground acoustic test of SC-007 . . . . .	5-93
5.3-38	Comparison between BP-13 measured and SC-002 calculated CM external acoustic environment on Apollo Missions A-101 and A-004 . . . . .	5-94
5.3-39	rms time history of CM heat shield vibration, Apollo Mission A-004 . . . . .	5-95
5.4-1	Boost protective cover assembly and details, Apollo Mission A-004 . . . . .	5-99
5.4-2	Mission A-004 soft boost protective cover static pressures	
	(a) T+25 seconds . . . . .	5-100
	(b) T+36 seconds . . . . .	5-100
	(c) T+73 seconds . . . . .	5-100
5.5-1	Canard deployment time history, Apollo Mission A-004 . . . . .	5-105
5.5-2	Canard +Y link load time history during deployment, Apollo Mission A-004 . . . . .	5-106
5.5-3	Canard -Y link load time history during deployment, Apollo Mission A-004 . . . . .	5-107
5.5-4	Canard +Y link load time history, Apollo Mission A-004 . . . . .	5-108
5.5-5	Canard -Y link load time history, Apollo Mission A-004 . . . . .	5-109
5.5-6	Uprighting system canisters and VHF recovery aids, Apollo Mission A-004 . . . . .	5-110
5.5-7	Uprighting system canisters and recovery aids, Apollo Mission A-004 . . . . .	5-111
5.5-8	Sea dye canister and flashing light recovery aids, Apollo Mission A-004 . . . . .	5-112

Figure		Page
5.5-9	Inner surface of side ablative hatch and latching mechanism, Apollo Mission A-004 . . . . .	5-113
5.5-10	Latched side pressure hatch at recovery, Apollo Mission A-004 . . . . .	5-114
5.5-11	Unlatched side pressure hatch after recovery, Apollo Mission A-004 . . . . .	5-115
5.5-12	Side pressure hatch postflight inspection, Apollo Mission A-004 . . . . .	5-116
5.6-1	Launch-escape motor vacuum thrust time history, Apollo Mission A-004 . . . . .	5-119
5.6-2	Pitch-control motor vacuum thrust time history, Apollo Mission A-004 . . . . .	5-120
5.7-1	CM-SM umbilical disconnect, Apollo Mission A-004 . .	5-126
5.7-2	CM-SM umbilical separation system components on Apollo Mission A-004 . . . . .	5-127
5.7-3	Apollo electrical circuit interrupter . . . . .	5-128
5.8-1	Drogue parachute subsystem (Block I), Apollo Mission A-004 . . . . .	5-135
5.8-2	Pilot parachute subsystem (Block I) except for metal cover, Apollo Mission A-004 . . . . .	5-136
5.8-3	Vehicle harness attach fitting and vehicle harness disconnect, Apollo Mission A-004 . . . . .	5-137
5.8-4	Main parachute harness showing disconnect cut on Apollo Mission A-004 . . . . .	5-138
5.8-5	No. 2 main parachute attach fitting and disconnect, Apollo Mission A-004 . . . . .	5-139
5.8-6	Parachute (-Z) quadrant showing drogue mortar no. 1, Apollo Mission A-004 . . . . .	5-140
5.8-7	Parachute (-Z) quadrant showing drogue mortar no. 2, Apollo Mission A-004 . . . . .	5-141

Figure		Page
5.8-8	Main parachute (+Y) quadrant, Apollo Mission A-004 . . . . .	5-142
5.8-9	Main parachute (+Z) quadrant, Apollo Mission A-004 . . . . .	5-143
5.8-10	Main parachute (-Y) quadrant, Apollo Mission A-004 . . . . .	5-144
5.8-11	Split retention strip (+Z) quadrant, Apollo Mission A-004 . . . . .	5-145
5.8-12	Command module attenuation subsystem, Apollo Mission A-004	
	(a) External configuration . . . . .	5-146
	(b) Internal configuration . . . . .	5-147
5.8-13	Impact attenuation struts, Apollo Mission A-004 predicted load-stroke curves	
	(a) X-X foot strut . . . . .	5-148
	(b) X-X head strut . . . . .	5-148
	(c) Z-Z strut . . . . .	5-149
	(d) Y-Y strut . . . . .	5-149
5.9-1	Microphone mountings on equipment platform at the crew station, Apollo Mission A-004 . . . . .	5-152
5.9-2	Overall sound pressure level time history of crew station acoustics CK0035Y, Apollo Mission A-004 . .	5-153
5.9-3	Spectrum sound pressure levels (SPL per cycle) for CK0035Y at T+38.8 (Mach 1), T+41.5 (max q), and T+73.3 (prior to abort) for Apollo Mission A-004 . . . . .	5-154
5.9-4	Spectrum sound pressure levels (SPL per cycle) for CK0035Y at T+74.3, 75.6, 76.6, and 78.8 sec during abort for Apollo Mission A-004 . . . . .	5-155
5.10-1	Relation of events controlled by sequential subsystem, Apollo Mission A-004 . . . . .	5-157

Figure		Page
5.10-2	Blown fuses and fusistor locations in mission sequencer and ELS sequence controller for Apollo Mission A-004 . . . . .	5-158
5.11-1	Electrical power subsystem block diagram, Apollo Mission A-004 . . . . .	5-161
5.11-2	Time histories of dc current and main bus voltage, Apollo Mission A-004 . . . . .	5-162
5.11-3	Time histories of logic bus A and B voltage, Apollo Mission A-004 . . . . .	5-163
5.11-4	Time histories of pyro bus A and B voltages, Apollo Mission A-004	
	(a) -20 to 260 seconds . . . . .	5-164
	(b) 260 to 460 seconds . . . . .	5-165
5.11-5	Pyro bus A voltage, Apollo Mission A-004 . . . . .	5-166
5.11-6	Pyro bus B voltage, Apollo Mission A-004 . . . . .	5-167
5.12-1	Telemetry subsystem block diagram, Apollo Mission A-004 . . . . .	5-171
5.12-2	Onboard tape recorder F block diagram, Apollo Mission A-004 . . . . .	5-172
5.12-3	Onboard tape recorder H block diagram, Apollo Mission A-004 . . . . .	5-173
5.12-4	Scimitar antenna damage, Apollo Mission A-004 . . . . .	5-174
5.12-5	Tower and CM camera installation, Apollo Mission A-004 . . . . .	5-175
5.13-1	ECS cabin pressure relief valve, Apollo Mission A-004 . . . . .	5-178
5.13-2	SC-002 command module interior pressure profiles, Apollo Mission A-004 . . . . .	5-179
5.14-1	Command module after landing showing general condition of windows, Apollo Mission A-004 . . . . .	5-183

Figure		Page
5.14-2	Left and right rendezvous and docking windows after landing, Apollo Mission A-004 . . . . .	5-184
5.14-3	Left and right crew windows after landing, Apollo Mission A-004 . . . . .	5-185
6.1-1	First-stage Algol motor no. 2 flight thrust time history, Apollo Mission A-004 . . . . .	6-2
6.1-2	First-stage Algol motor no. 5 flight thrust time history, Apollo Mission A-004 . . . . .	6-3
6.1-3	Second-stage Algol motor no. 1 thrust time history, Apollo Mission A-004 . . . . .	6-4
6.1-4	Second-stage Algol motor no. 4 thrust time history, Apollo Mission A-004 . . . . .	6-5
6.3-1	Launch-vehicle attitude control subsystem block diagram, Apollo Mission A-004 . . . . .	6-9
6.3-2	Launch-vehicle pitch attitude plotted against time, Apollo Mission A-004 . . . . .	6-10
6.3-3	Time history of launch-vehicle pitch rate, Apollo Mission A-004 . . . . .	6-11
6.3-4	Time history of launch-vehicle yaw and roll rates, Apollo Mission A-004 . . . . .	6-12
6.3-5	Time history of launch-vehicle roll and yaw attitudes, Apollo Mission A-004 . . . . .	6-13
6.3-6	Time history of launch-vehicle sum of pitch attitude gyro plus pitch programer, Apollo Mission A-004 . . . . .	6-14
6.3-7	Time history of position of launch-vehicle elevons no. 1 and 4, Apollo Mission A-004 . . . . .	6-15
6.3-8	Time history of position of launch-vehicle elevons no. 2 and 3, Apollo Mission A-004 . . . . .	6-16
6.3-9	Time history of launch-vehicle hydraulic pressures, Apollo Mission A-004	
(a)	Elevon no. 1 . . . . .	6-17



Figure		Page
6.3-9	Continued	
	(b) Elevon no. 2 . . . . .	6-17
	(c) Elevon no. 3 . . . . .	6-18
	(d) Elevon no. 4 . . . . .	6-18
6.3-10	Time history of launch-vehicle electrical power, Apollo Mission A-004 . . . . .	6-19
6.4-1	Comparison of estimated power-on drag with two Algol motors with actual drag coefficients for various Mach numbers, Apollo Mission A-004 . . . .	6-21
6.7-1	Launch-vehicle instrumentation subsystem, Apollo Mission A-004 . . . . .	6-25
6.7-2	Launch-vehicle landline instrumentation block diagram, Apollo Mission A-004 . . . . .	6-26
6.8-1	Launch-vehicle RF command subsystem block diagram, Apollo Mission A-004 . . . . .	6-28
6.9-1	Range safety subsystem, Apollo Mission A-004 . . . .	6-30
6.10-1	Apollo Mission A-004 launch-vehicle ignition subsystem. Typical for each motor .	
	(a) First stage ignition system . . . . .	6-32
	(b) Second stage ignition system . . . . .	6-33
7.0-1	Location of recovered components, Apollo Mission A-004 . . . . .	7-2
7.1-1	Apollo Mission A-004 command module after landing, showing cork ablator broken from impact . . . . .	7-5
7.1-2	Lifting Apollo Mission A-004 command module by the recovery loop . . . . .	7-6
7.1-3	Lifting Apollo Mission A-004 command module by alternate three-point sling . . . . .	7-7
7.2-1	Apollo Mission A-004 LES impact area . . . . .	7-9
7.4-1	Apollo Mission A-004 Little Joe II launch vehicle impact area . . . . .	7-12

Figure		Page
10.2-1	Final preparation and countdown schedule, Apollo Mission A-004 . . . . .	10-12
10.2-2	Final preparation and countdown schedule of operation no. 1, Apollo Mission A-004 . . . . .	10-13
10.2-3	Final preparation and countdown schedule of operation no. 2, Apollo Mission A-004 . . . . .	10-14
10.2-4	Final preparation and countdown schedule of operation no. 3, Apollo Mission A-004 . . . . .	10-15
10.4-1	Telemetry, meteorological, and radar station locations, Apollo Mission A-004 . . . . .	10-30
10.4-2	Camera locations, Apollo Mission A-004 . . . . .	10-31
10.5-1	Apollo Mission A-004 atmospheric pressure compared with WSMR December standard. (From Small Missile Range rawinsonde at 8:20 a.m. m.s.t. January 20). . .	10-33
10.5-2	Apollo Mission A-004 atmospheric temperature compared with WSMR December standard. (From Small Missile Range rawinsonde at 8:20 a.m. m.s.t. January 20). . .	10-34
10.5-3	Apollo Mission A-004 atmospheric humidity compared with WSMR December standard. (From Small Missile Range rawinsonde at 8:20 a.m. m.s.t. January 20). . .	10-35
10.5-4	Apollo Mission A-004 atmospheric density compared with WSMR December standard. (From Small Missile Range rawinsonde at 8:20 a.m. m.s.t. January 20). . .	10-36
10.5-5	Apollo Mission A-004 launch time wind direction, SMR Ascension 16. (From Small Missile Range rawinsonde at 8:20 a.m. m.s.t. January 20). . . . .	10-37
10.5-6	Apollo Mission A-004 launch time wind magnitude, SMR Ascension 16. (From Small Missile Range rawinsonde at 8:20 a.m. m.s.t. January 20). . . . .	10-38
11.2-1	LES motor and Q-ball measurement locations, Apollo Mission A-004 . . . . .	11-18
11.2-2	Apollo Mission A-004 canard strain and deployment instrumentation . . . . .	11-19

Figure		Page
11.2-3	Launch-escape tower measurement locations, Apollo Mission A-004 . . . . .	11-20
11.2-4	Conical surface pressures, Apollo Mission A-004. (Location of BPC surface and BPC-CM interface pressure measurements) . . . . .	11-21
11.2-5	Command module structural measurement locations, Apollo Mission A-004 . . . . .	11-22
11.2-6	Forward sidewall longeron 4 command module inner structure - forward sidewall, Apollo Mission A-004 . . . . .	11-23
11.2-7	Strain gage locations on longeron 8 command module, Apollo Mission A-004 . . . . .	11-24
11.2-8	Strain gage locations on longeron 2 command module, Apollo Mission A-004 . . . . .	11-25
11.2-9	Strain gage locations on right-hand beam of main hatch, Apollo Mission A-004 . . . . .	11-26
11.2-10	Command module heat flux measurement locations, Apollo Mission A-004 . . . . .	11-27
11.2-11	Temperature and strain measurements on main heat shield, Apollo Mission A-004 . . . . .	11-28
11.2-12	Base pressure measurement locations, Apollo Mission A-004 . . . . .	11-29
11.2-13	Strain gage locations on CM-SM tension-tie bolts 2, 4, and 6, Apollo Mission A-004 . . . . .	11-30
11.2-14	Strain gage locations CM-SM compression structure, Apollo Mission A-004 . . . . .	11-31
11.2-15	Strain gage locations, beam 2, service module, Apollo Mission A-004 . . . . .	11-32
11.2-16	Strain gage location, beam 4, service module, Apollo Mission A-004 . . . . .	11-33

Figure		Page
11.2-17	Strain gage and vibration measurement location, beam 5, service module, Apollo Mission A-004 . . .	11-34
11.2-18	Vibration measurements, service module, Apollo Mission A-004 . . . . .	11-35
11.2-19	Service module vibration and fluctuating pressure measurement locations, Apollo Mission A-004 . . . .	11-36
11.2-20	Service module temperature and strain gage locations, Apollo Mission A-004 . . . . .	11-37

## ABBREVIATIONS AND SYMBOLS

### Abbreviations

ASD	Apollo standard detonator
BP	Boilerplate
BPC	boost protective cover
CARR	customer acceptance readiness review
CATS	Computer Augmented Trajectory Simulator
CM	command module
ECS	environmental control subsystem
EDS	emergency detection subsystem
ELS	earth landing subsystem
ELSSC	earth landing subsystem sequence controller
EPS	electrical power subsystem
FM	frequency modulation
FRR	Flight Readiness Review
GSE	ground support equipment
LC	Launch Complex
LES	launch-escape subsystem
LEV	launch-escape vehicle
LJ II	Little Joe II
LV	launch vehicle
MAE	measurement acceptance evaluation
MDF	mild detonator fuse

MSC	Manned Spacecraft Center
m.s.l.	mean sea level
m.s.t.	mountain standard time
OCP	operational checkout procedure
PA	pad abort
PAT	pre-delivery acceptance test
PCM	pulse code modulation
PDM	pulse duration modulation
RCS	reaction control subsystem
RF	radio frequency
rms	root mean square
RTDS	real-time data system
SC	spacecraft
SM	service module
SMR	Small Missile Range
SPL	sound pressure level
SPS	secondary propulsion subsystem
VAB	Vehicle Assembly Building
VHF	very high frequency
WSMR	White Sands Missile Range
WSTF	White Sands Test Facility

## Symbols

$g$	gravitational constant
$I_{xx}$	moment of inertia about X-axis
$I_{yy}$	moment of inertia about Y-axis
$I_{zz}$	moment of inertia about Z-axis
$M$	Mach number
$q$	dynamic pressure, $\text{lb/ft}^2$
$T$	elapsed time from lift-off, sec
$X$	longitudinal axis
$X_A$	longitudinal location, referenced to overall spacecraft, in.
$X_C$	longitudinal location, referenced to command module, in.
$X_L$	longitudinal location, referenced to launch-escape subsystem, in.
$Y$	axis normal to the X and Z axes
$Z$	axis normal to the X and Y axis
$\alpha$	angle of attack, deg

## 1.0 MISSION SUMMARY

Apollo spacecraft 002 was launched on January 20, 1966, from the White Sands Missile Range, New Mexico, at 8:17 a.m. m.s.t. after several postponements because of launch vehicle technical difficulties and delays because of adverse weather conditions. The mission was completed successfully.

Apollo spacecraft 002 was of a Block I type configuration. Among the differences between the spacecraft 002 configuration and Block I were the change in location of the center of gravity of the launch-escape vehicle and the change in the thrust vector of the launch-escape subsystem. These changes were made to assure the attaining of the required condition of power-on tumbling after abort initiation.

The Little Joe II two-stage, fin-stabilized, autopilot-controlled launch vehicle performed satisfactorily. First- and second-stage ignition occurred as planned. This was the first completed mission of a two-stage Little Joe II launch vehicle, and the first second-stage application of Algol motors.

The pitch-up maneuver was initiated at T+70.8 seconds when the test region of altitude and velocity was indicated by the real-time data system. At T+73.7 seconds, the planned abort was automatically initiated.

Dynamic loads and structural response data for the service module structure were obtained during the launch phase and the pitch-up maneuver.

Command module - service module separation at abort initiation was satisfactory although the main heat shield suffered limited blast damage from the pyrotechnic cutting of the tension ties. The launch-escape and pitch-control motors performed as required. The boost protective cover remained intact through the launch phase and pitch-up maneuver as required, with the soft cover breaking up during the first tumble after abort initiation, as expected.

The power-on tumbling boundary abort demonstrated the satisfactory performance of the launch-escape vehicle and also the structural integrity of the launch-escape vehicle airframe structure.

At T+74.7 seconds, the single active scimitar antenna failed, and transmission of telemetry signals from the spacecraft ceased for the rest of the mission.

An onboard camera, photographing the condition of the left side rendezvous window from within the command module, operated as planned



from T+70 seconds to T+240 seconds. Film coverage indicated the time at which deposits on the window occurred.

The maximum differential pressure of 7.1 psid, indicated by measurements across the command module exterior wall structure ( $11.1 \pm 1.5$  psid was desired), was attained at T+75.2 seconds during the first tumble and launch-escape motor burn. Maximum plume impingement pressure on the command module was about 80 percent of predicted values, and the aft compartment pressure was about 1.5 psi higher than predicted. Cabin pressure measurements during the flight and postflight testing and inspection results indicated that excessive leakage past the inner hatch seal had occurred during the flight because of the manner in which the hatch was installed before launch.

During the power-on abort phase, pitch and yaw rates reached peak values of 160 deg/sec and roll rates, a peak value of -70 deg/sec.

After launch-escape motor burnout, tumbling continued until canard deployment occurred at T+84.8 seconds. After the canards had deployed, the launch-escape vehicle quickly stabilized to a main heat shield forward attitude. Both the high tumbling rates and quick stabilization of the launch-escape vehicle were partially a result of the mass characteristics peculiar to spacecraft 002.

The sequential subsystem performed as planned. The launch-escape subsystem was jettisoned at T+193.7 seconds and approximately 23 000 ft m.s.l., drogue mortars were fired at T+195.8 seconds, drogue risers were disconnected and main parachute pilot mortars were fired at T+237.6 seconds and 10 450 ft m.s.l.

At T+209.5 seconds onboard recorder F jammed, but onboard recorder H continued to record flight data for the duration of the mission.

Descent of the command module on the main parachutes was steady, and the rate of descent was within nominal limits at the time of landing. The main parachutes were disconnected from the command module at touchdown by the inertial switch disconnect.

The recovered command module was inspected at the field facility, and postflight tests were conducted at the contractor's Downey facility on the scimitar antenna, cabin pressure relief valve, questionable instrumentation, pyro buses A and B and sequencer, and on the crew windows. In addition, command module cabin leak tests were completed.

The test objectives were accomplished.

## 2.0 INTRODUCTION

Apollo Mission A-004 was the first flight with a production type Apollo spacecraft structure, the last of the six unmanned flight abort tests to be launched at the White Sands Missile Range, New Mexico, and the eleventh flight test with an unmanned Apollo spacecraft. (See table on inside front cover.) The test vehicle, consisting of Block I type spacecraft 002 (SC-002) and Little Joe II (LJ II) launch vehicle 12-51-3, was launched from Launch Complex 36 at White Sands Missile Range on January 20, 1966, at 8:17:00.776 a.m. m.s.t. Launch, abort, and recovery were successfully accomplished. Figure 2.0-1 shows the test vehicle at Launch Complex 36. The flight sequence of major events is given in figure 2.0-2.

The first-order test objectives for Mission A-004 were as follows:

- (a) Demonstrate satisfactory launch-escape vehicle (LEV) performance for an abort in the power-on tumbling boundary region.
- (b) Demonstrate the structural integrity of the LEV airframe structure for an abort in the power-on tumbling boundary region.

All test objectives for the mission are listed in section 11.1.

The test region was defined by the altitude and velocity at which the combination of aerodynamic loading and launch-escape-motor plume impingement loading would be sufficient to load the command module structure to its design limit.

This report includes an evaluation of the mission and an analysis of the spacecraft and launch vehicle performance on the basis of the flight-test data and results of completed postflight tests. Although the publication of this report is subsequent to the flight of Apollo Mission AS-201 (first flight test of an Apollo Block I type spacecraft with a Saturn IB launch vehicle, February 26, 1966), the analysis of the Mission A-004 flight data was completed prior to Mission AS-201 and the results applied to pertinent prelaunch preparations.

In addition to the analysis and pertinent plotted data included in this report, the complete plotted flight data are contained in a companion volume, "Flight Data Report for Apollo Mission A-004 (SC-002)" (ref. 1).

Unless otherwise specified, zero time (T-0) for all data in this report is referenced to 4-inch motion of the test vehicle.

NASA-S-66-3661 APR 15

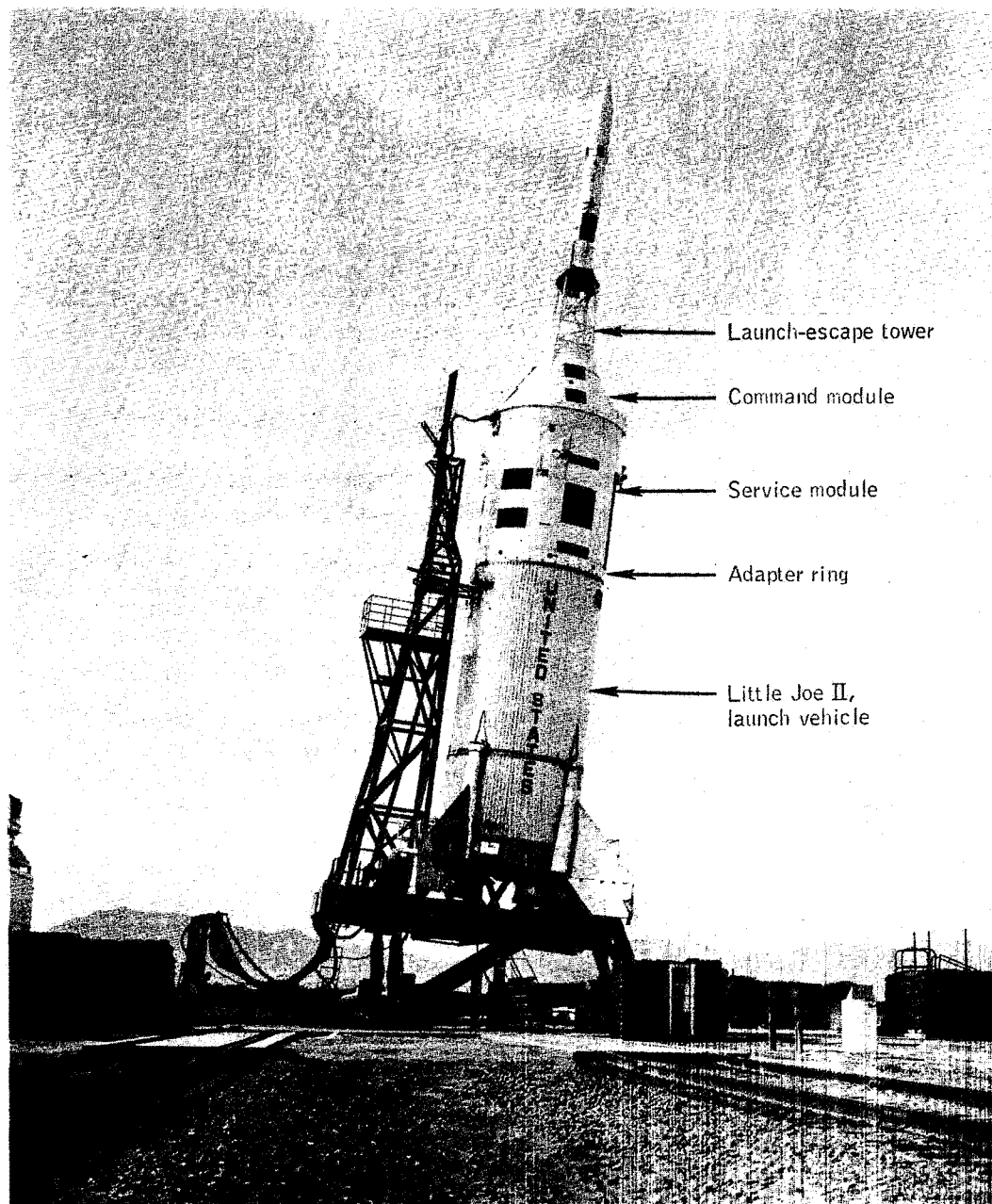


Figure 2.0-1.- Test vehicle for Apollo Mission A-004 prior to launch (11-30-65).

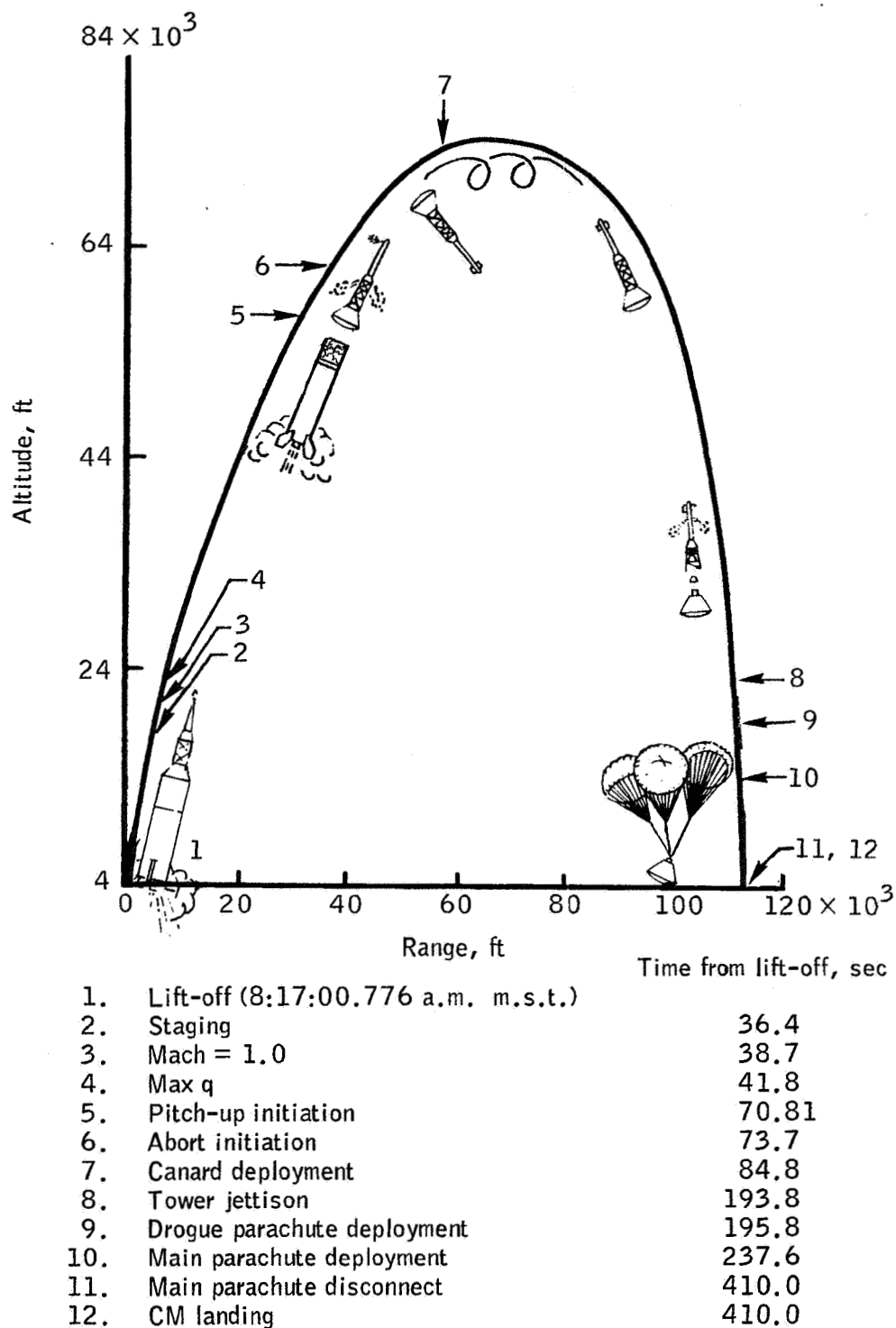


Figure 2.0-2.- Sequence of major events, Apollo Mission A-004.

### 3.0 TEST VEHICLE DESCRIPTION

#### 3.1 Spacecraft

The unmanned spacecraft (SC-002) flown on Apollo Mission A-004 consisted of a modified Block I command module (CM), modified Block I service module (SM), and modified Block I launch-escape subsystem (LES). (See refs. 2 and 3.) Among other differences from the Block I configuration, the center of gravity of the launch-escape vehicle (LEV), and the thrust vector of the launch-escape subsystem were changed to assure the attainment of the required condition of power-on tumbling after abort initiation. (See sections 3.3 and 5.0.) The spacecraft was mated to the Little Joe II (LJ II) launch vehicle by means of an aluminum adapter ring.

The test vehicle configuration is shown in figure 3.1-1; figure 3.1-2 shows the LEV configuration; and the locations of LEV centers of gravity and LES thrust vector are shown in figures 3.1-2 and 3.1-3 and in table 3.3-I.

Spacecraft 002 approached the production spacecraft Block I configuration that will be used for future manned flight, and was approximately the same in external size, shape, and gross weight as the Apollo Mission A-003 boilerplate configuration (ref. 4). Production, prototype, and interim design subsystems were included in the configuration to be compatible with the operational requirements for flight tests at the White Sands Missile Range (WSMR). These subsystems and their associated mission performance are described in detail in sections 5.2 to 5.14 of this report.

Spacecraft body axes are indicated in figure 3.1-4. (Also see ref. 5.)

To assist in photographic identification of spacecraft attitudes and motion during flight, the exterior surfaces of the CM and boost protective cover (BPC), the launch-escape motor, and the SM were painted as shown in figure 3.1-5.

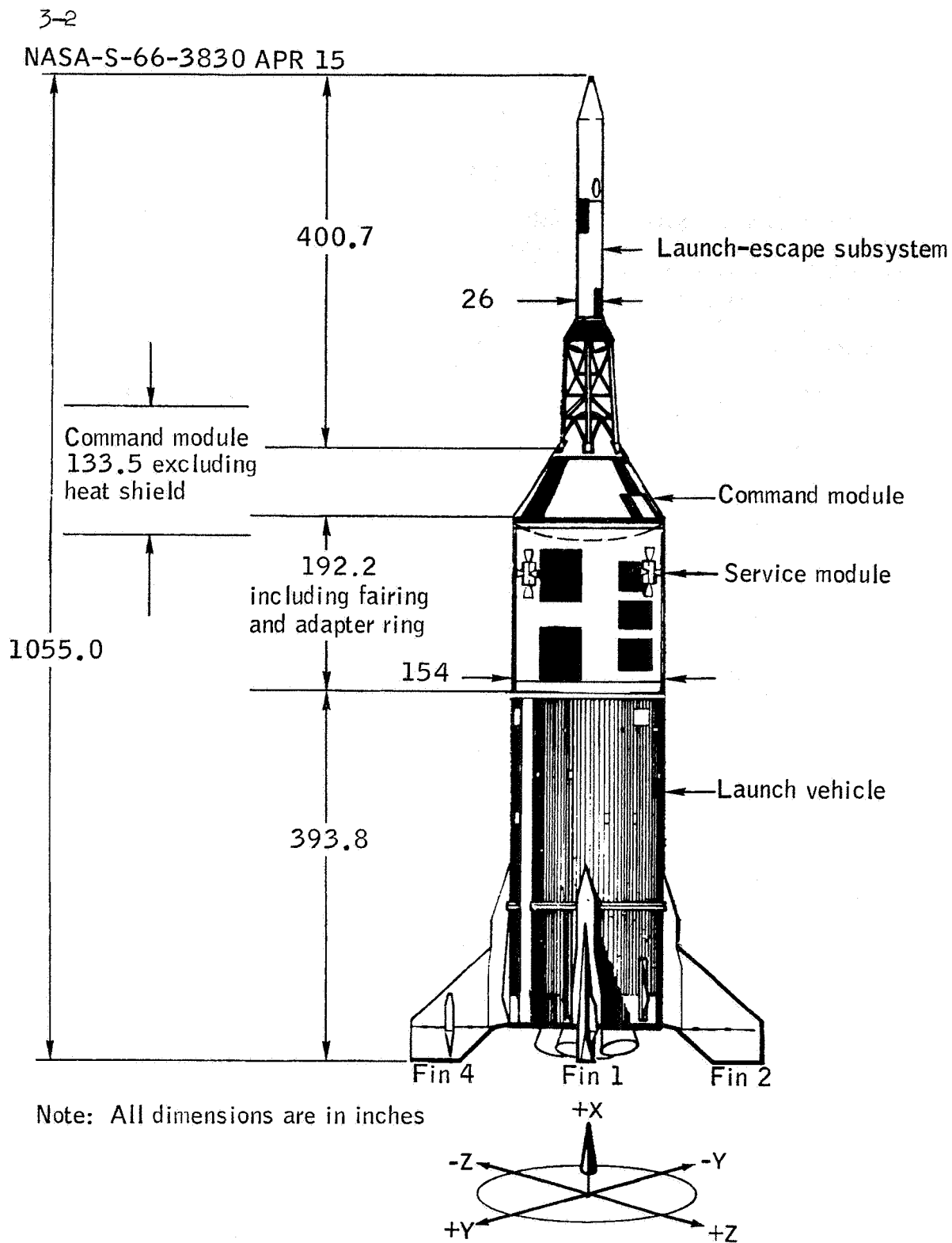


Figure 3.1-1.- Test vehicle configuration, Apollo Mission A-004.  
(Also see figure 3.2-1 and 5.2-1 to 5.2-3).

NASA-S-66-3669 APR 15

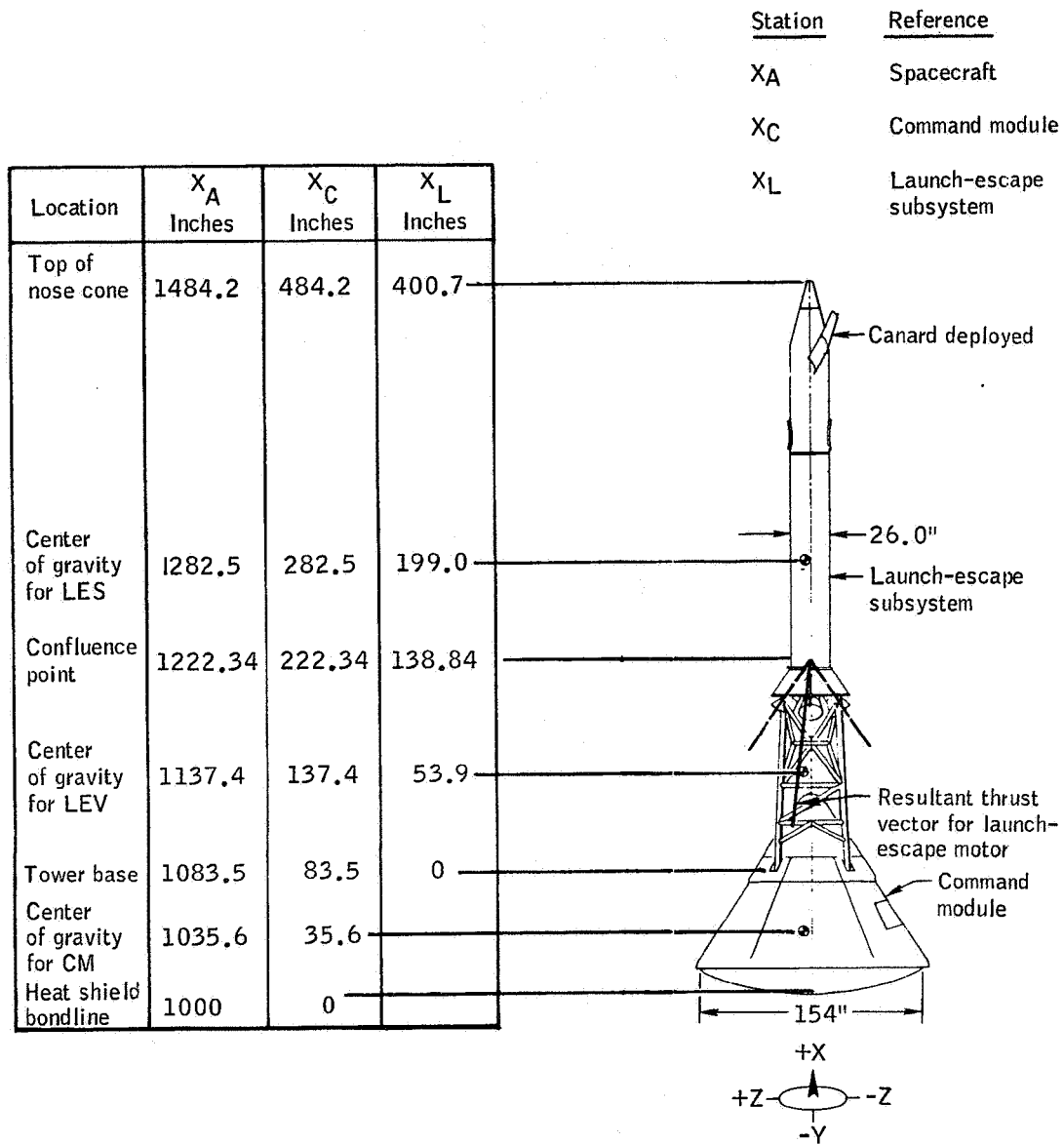


Figure 3.1-2.- Launch-escape vehicle reference stations and center-of-gravity locations, Apollo Mission A-004.

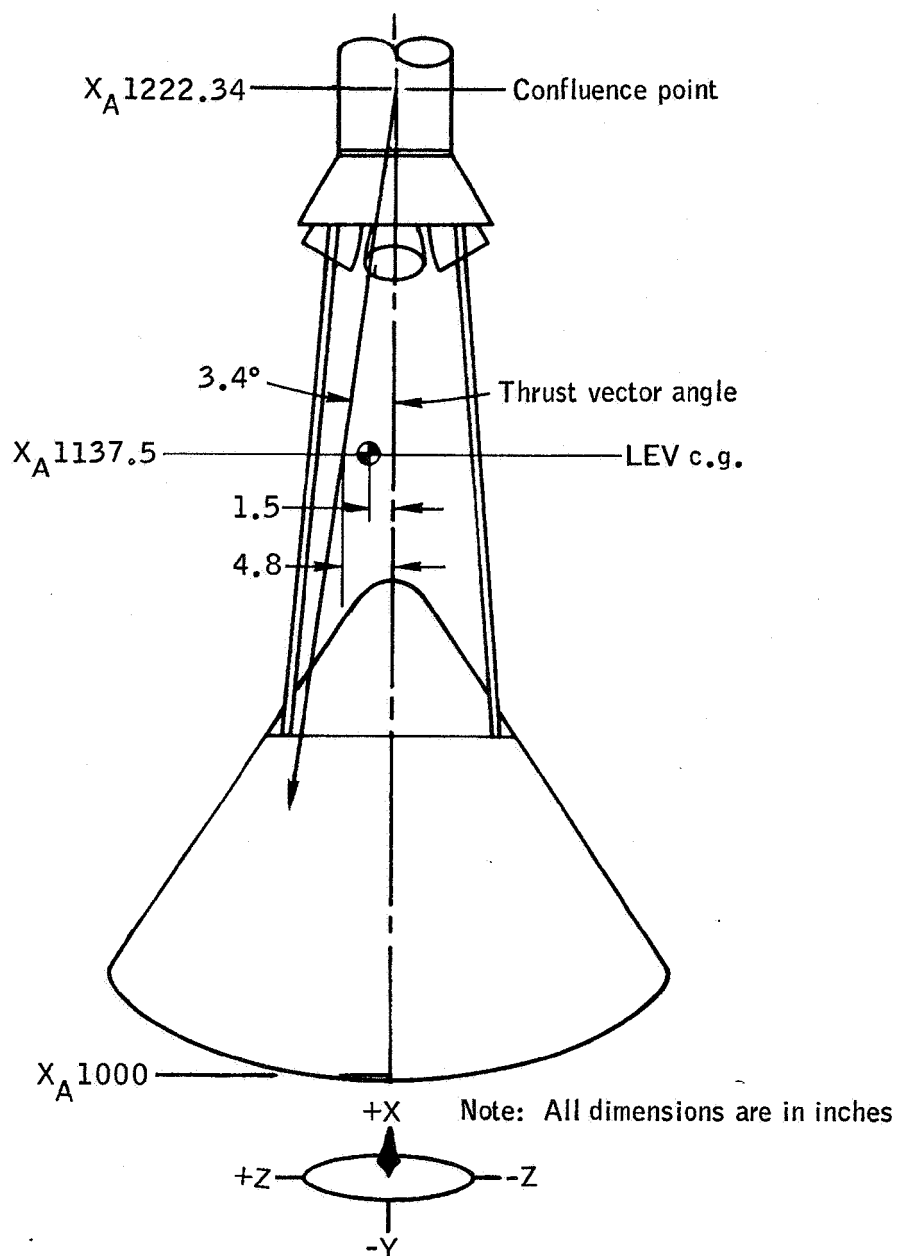
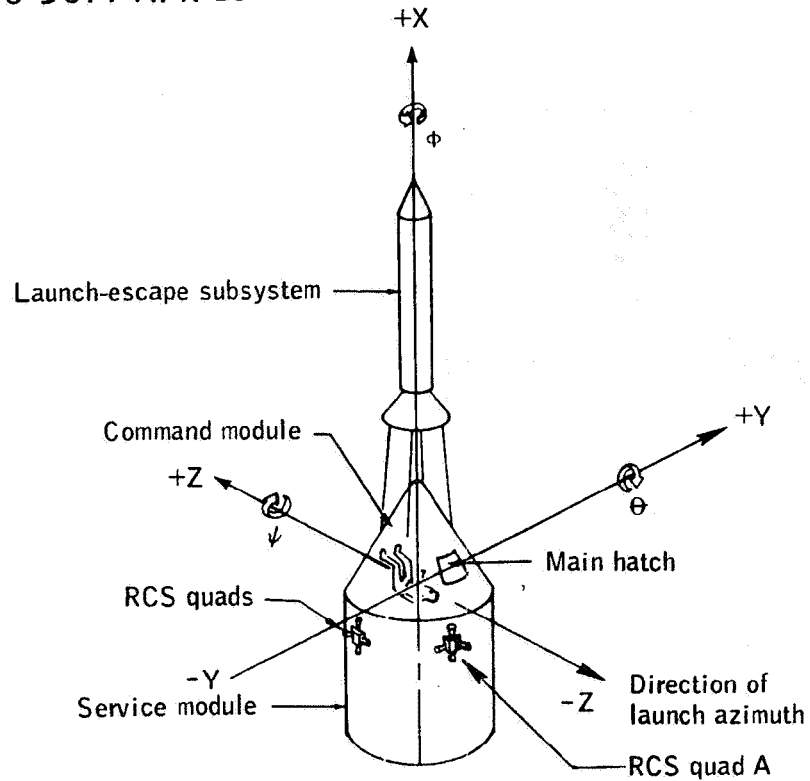


Figure 3.1-3.- Launch-escape vehicle center-of-gravity and thrust vector location, Apollo Mission A-004.



NASA-S-66-3677 APR 15



Direction	Axis	Moment	Positive direction	Spacecraft maneuver & symbol	Linear velocity	Angular velocity
Longitudinal	X	L	Y to Z	Roll $\phi$	u	p
Lateral	Y	M	Z to X	Pitch $\theta$	v	q
Vertical	Z	N	X to Y	Yaw $\psi$	w	r

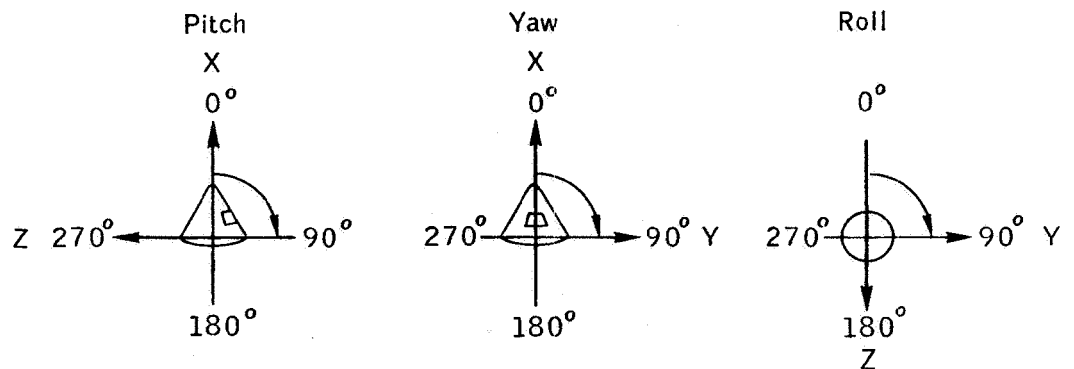
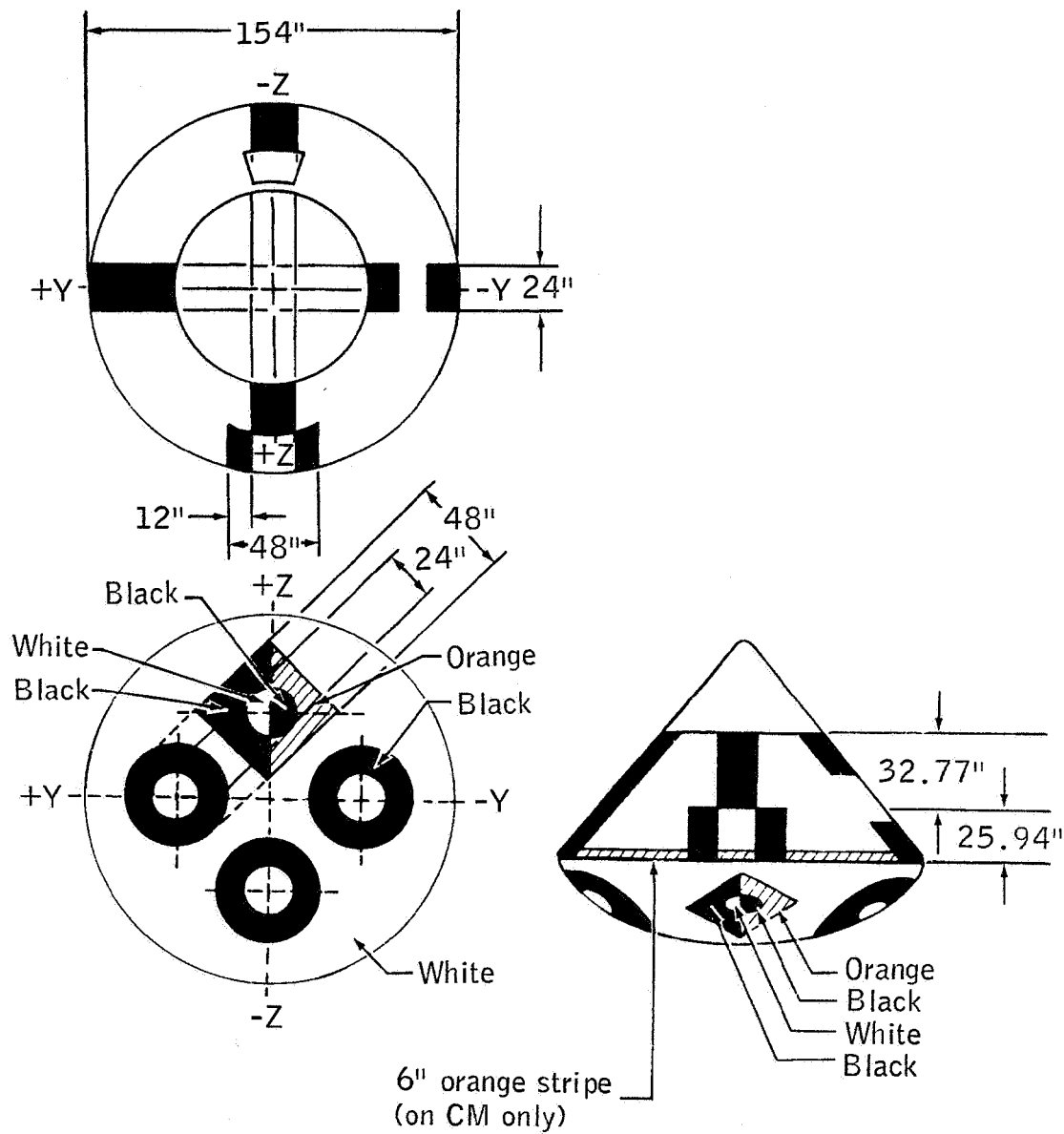


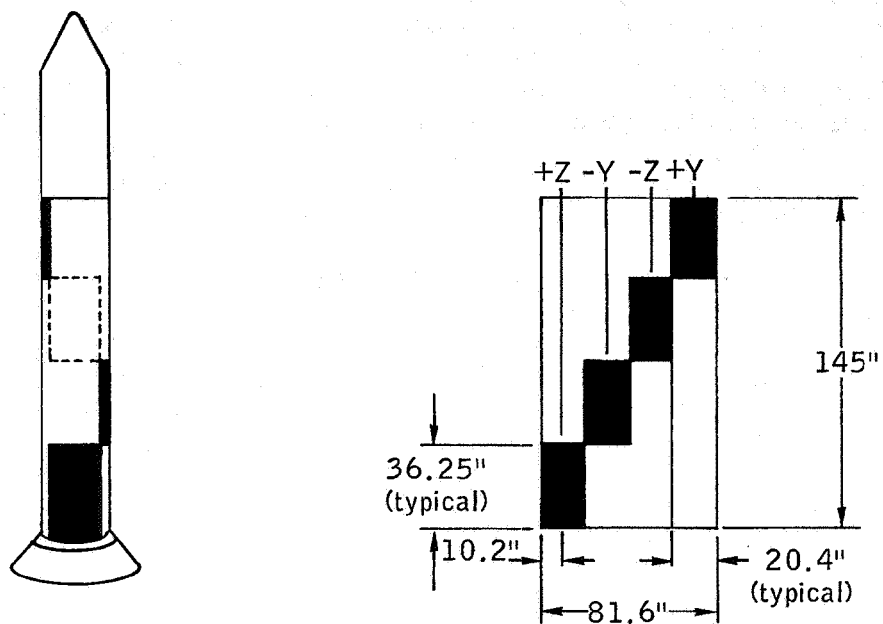
Figure 3.1-4.- Spacecraft axis system for orientation and motion, Apollo Mission A-004.



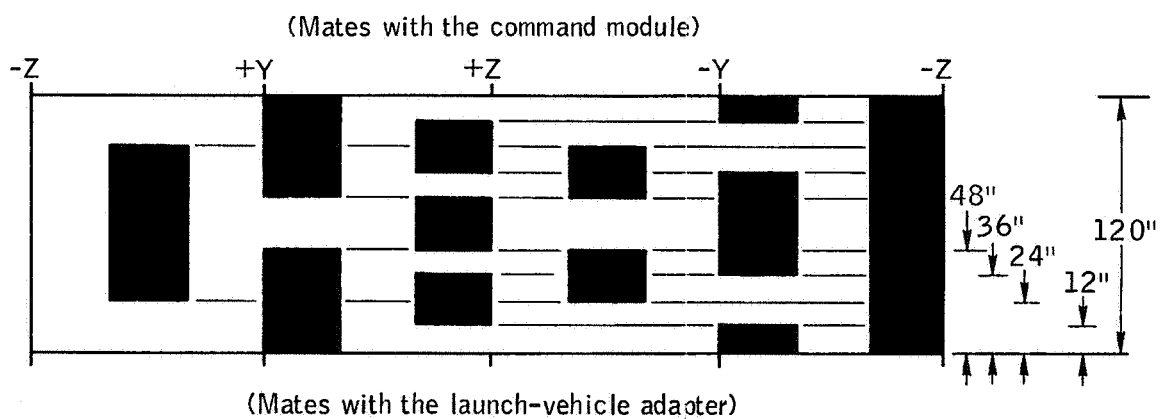
(a) Command module and boost protective cover.

Figure 3.1-5.- Paint patterns, Apollo Mission A-004.

NASA-S-66-3685 APR 15



(b) Launch-escape motor.



(c) Service module.

Figure 3.1-5.- Concluded.

### 3.2 Launch Vehicle

Little Joe II launch vehicle 12-51-3 was the fourth in a series of LJ II launch vehicles utilized to boost an Apollo spacecraft for an abort test at White Sands Missile Range. The launch vehicle was a fin-stabilized, autopilot-controlled airframe which used solid-fuel rocket motors for propulsion power. (See fig. 3.2-1.) This launch vehicle was similar to that used for Mission A-003 (ref. 4). Reference 6 contains a description and specifications for the launch vehicle, including the differences between vehicle 12-51-3 and 12-51-2.

The launch vehicle airframe consisted of cylindrical forebody and afterbody shells, and four fins with autopilot-controlled elevons. A reaction control subsystem included on LJ II 12-51-2 for Mission A-003 was omitted for this mission. Four Algol ID Mod I motors and five Recruit TE-29 motors were mounted on the thrust bulkhead, the main structural member of the vehicle.

The launch vehicle subsystems and their associated mission performance are described in detail in section 6.0 of this report.

NASA-S-66-3689 APR 15

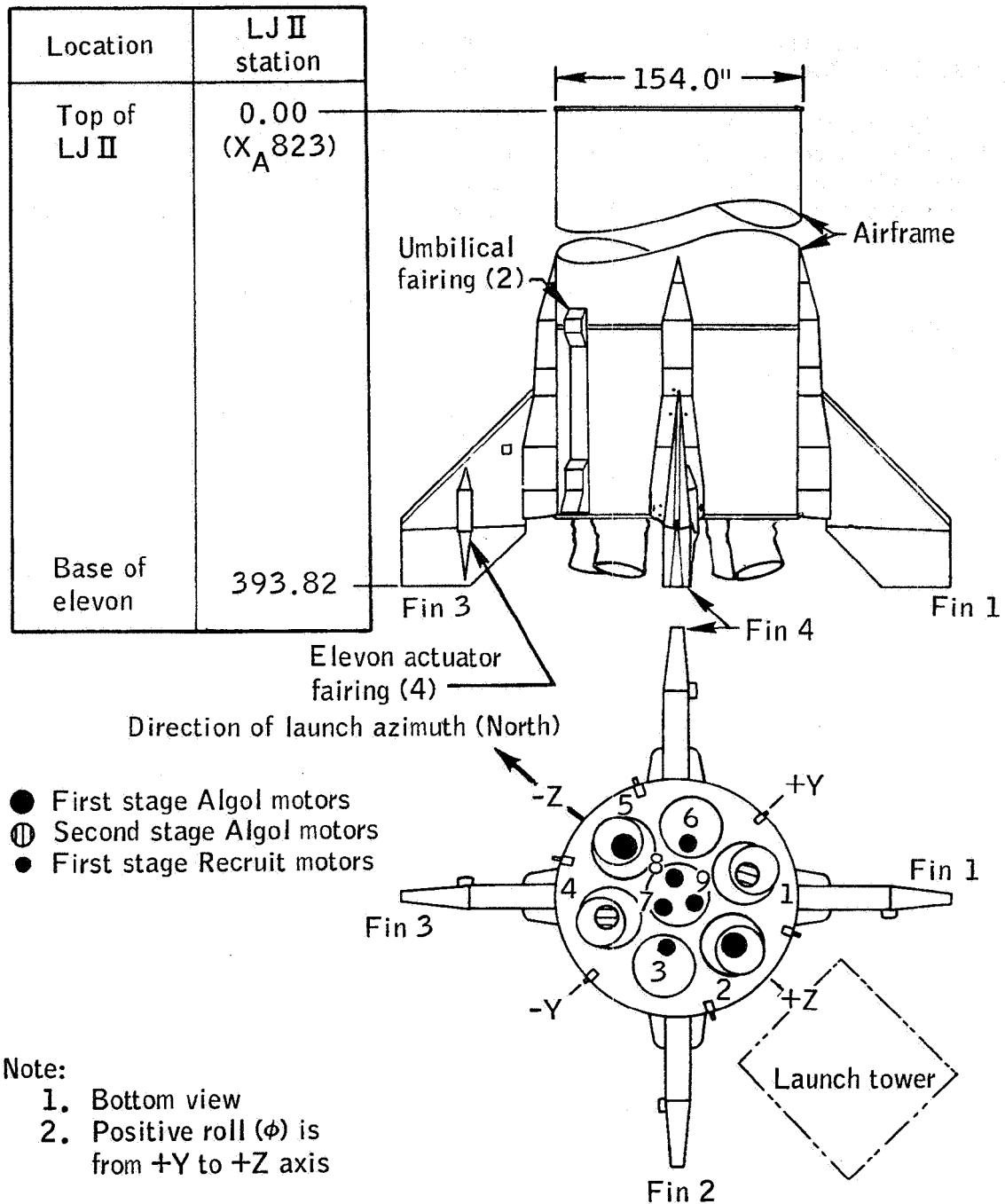


Figure 3.2-1.- Little Joe II launch vehicle 12-51-3, Apollo Mission A-004.

### 3.3 Mass Characteristics

The mass properties calculated from actual measurements and the predicted values are shown in table 3.3-I.

For Mission A-004 the launch-escape system was unballasted and the CM was ballasted to achieve the desired center of gravity of the launch-escape vehicle at launch-escape motor burnout. Primarily as a result of the additional ballast, the command module for Mission A-004 exceeded the Block I control weight by 107 pounds at launch.

Figures 3.3-1 to 3.3-6 illustrate the changes in mass properties with burning time for the launch-escape vehicle. Predicted calculations did not include removal of the soft boost protective cover. Actual values shown are based on the fact that the entire soft portion of the boost protective cover was lost at 1.7 seconds after launch-escape-motor ignition since the actual time for break-up of this portion cannot be determined accurately from the available data.

The mass characteristics for the launch vehicle show minor changes from those predicted. The Y and Z coordinates are zero and remain constant throughout the flight. The remaining mass properties for the launch phase are shown in reference 1.

TABLE 3.3-I. - MASS PROPERTIES FOR MISSION A-004

	Weight, lb	Center of gravity, in.			Moment of inertia, slug-ft <sup>2</sup> (a)		
		X	Y	Z	I <sub>xx</sub>	I <sub>yy</sub>	I <sub>zz</sub>
Test vehicle at launch (actual)	139 875	706.7	0	0	81 421	1 431 700	1 423 500
Launch payload (actual)	32 680	1022.8	0.0	-0.1	16 498	224 634	224 077
Launch-escape vehicle (actual)	18 906	1137.4	0.3	1.5	5 976	85 045	84 894
Launch-escape vehicle at burn-out (without soft BPC)	15 275	1107.1	0.5	2.3	5 537	62 542	62 407
CM prior to drogue parachute deployment (predicted)	<sup>b</sup> 10 695	1033.2	1.1	3.9	5 223	4 370	4 255
CM at landing (predicted)	<sup>b</sup> 10 286	1030.9	1.1	3.3	5 173	4 047	3 917

<sup>a</sup>All moment-of-inertia data are calculated based on weights shown.

<sup>b</sup>Based on measured weights at launch.

NASA-S-66-3693 APR 15

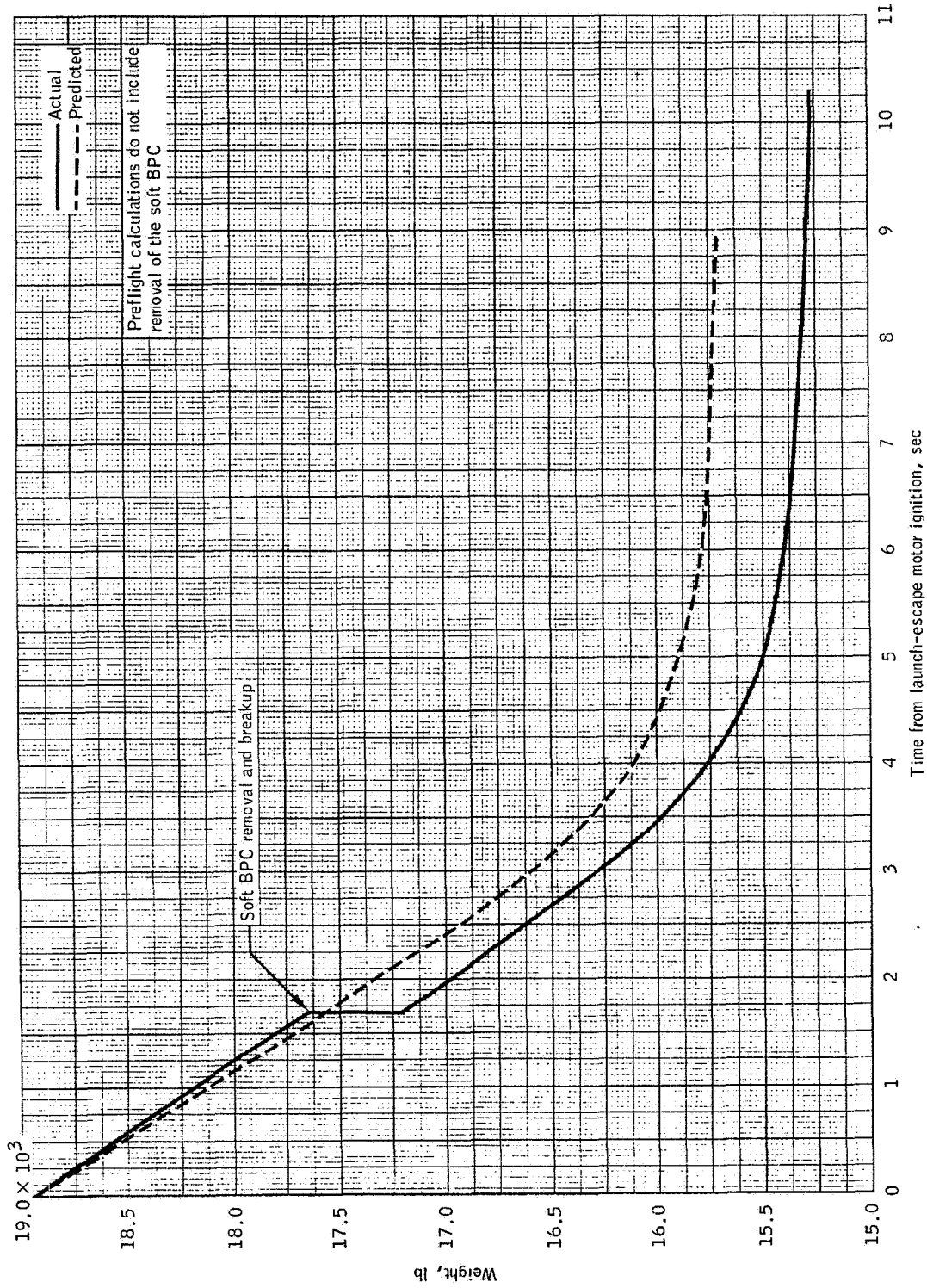


Figure 3.3-1.- Apollo Mission A-004 time history of launch-escape vehicle weight.



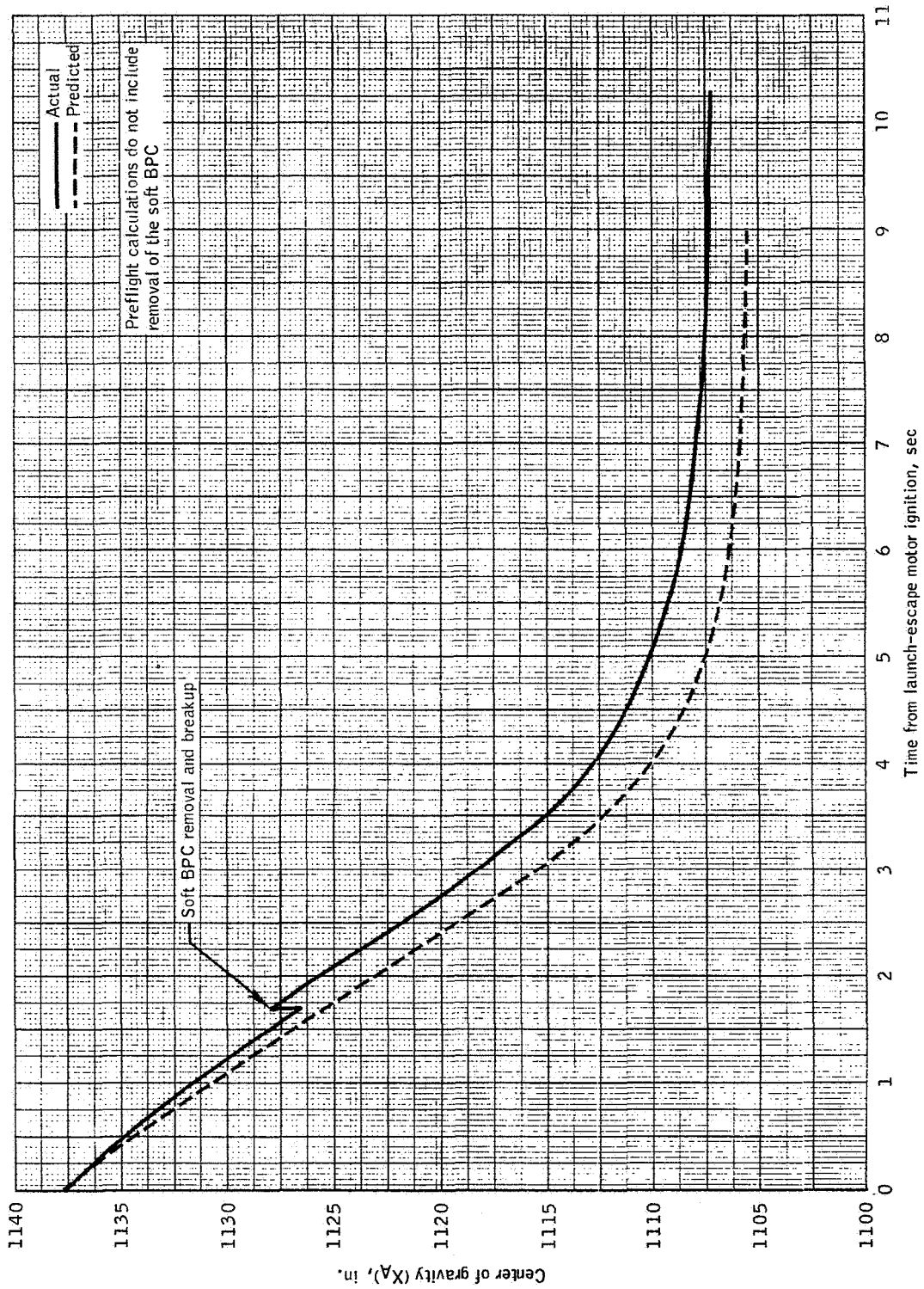


Figure 3.3-2.- Apollo Mission A-004 time history of launch-escape vehicle center-of-gravity  $X_A$  station location.

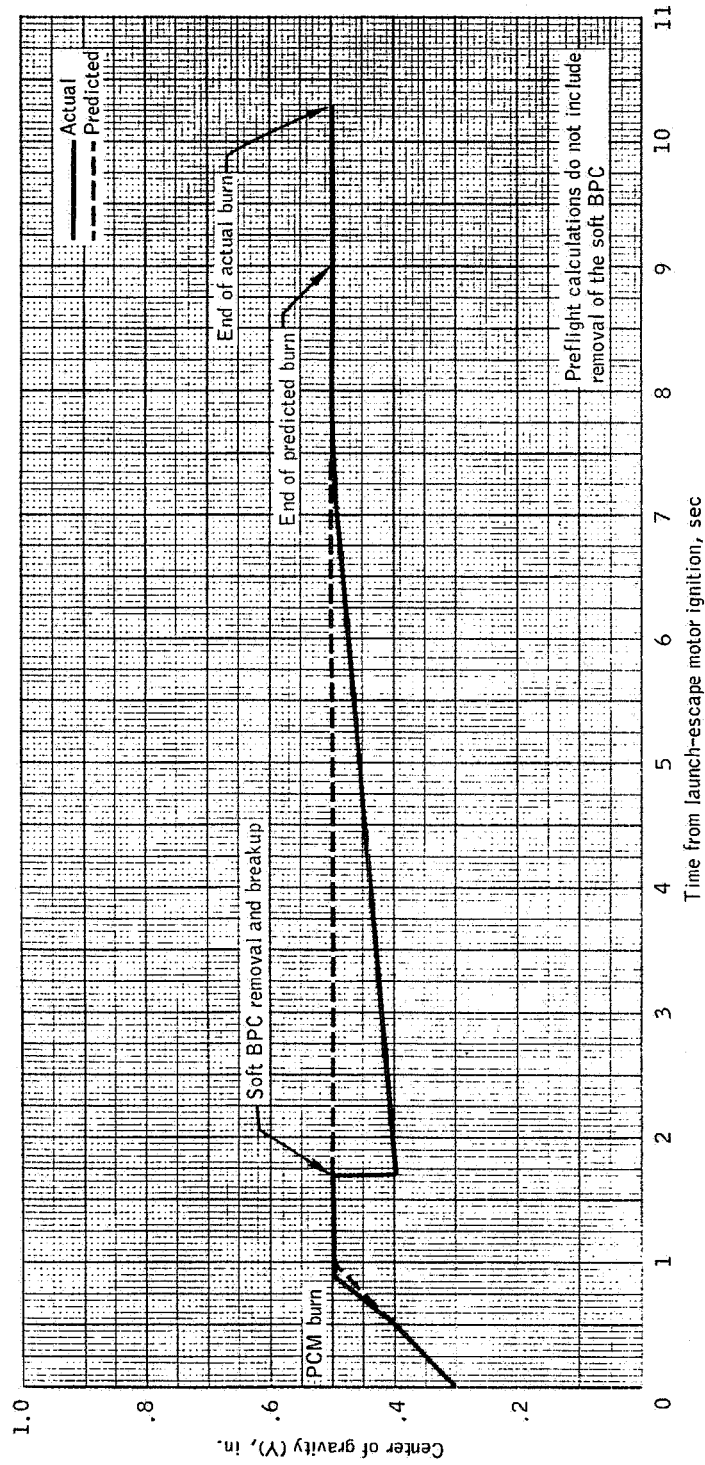


Figure 3.3-3.- Apollo Mission A-004 time history of launch-escape vehicle center-of-gravity Y-axis location.

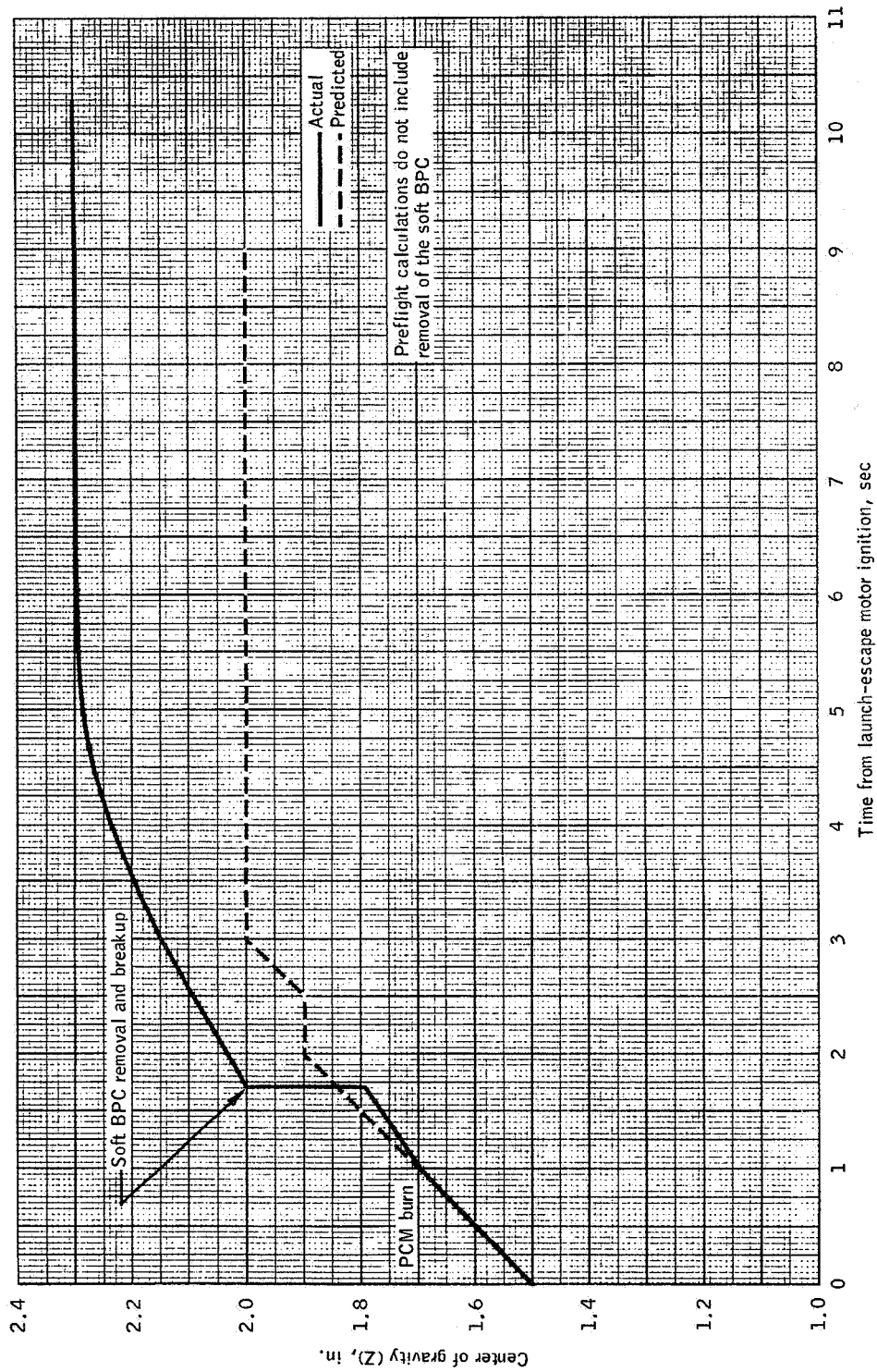


Figure 3.3-4.- Apollo Mission A-004 time history of launch-escape vehicle center-of-gravity Z-axis location.

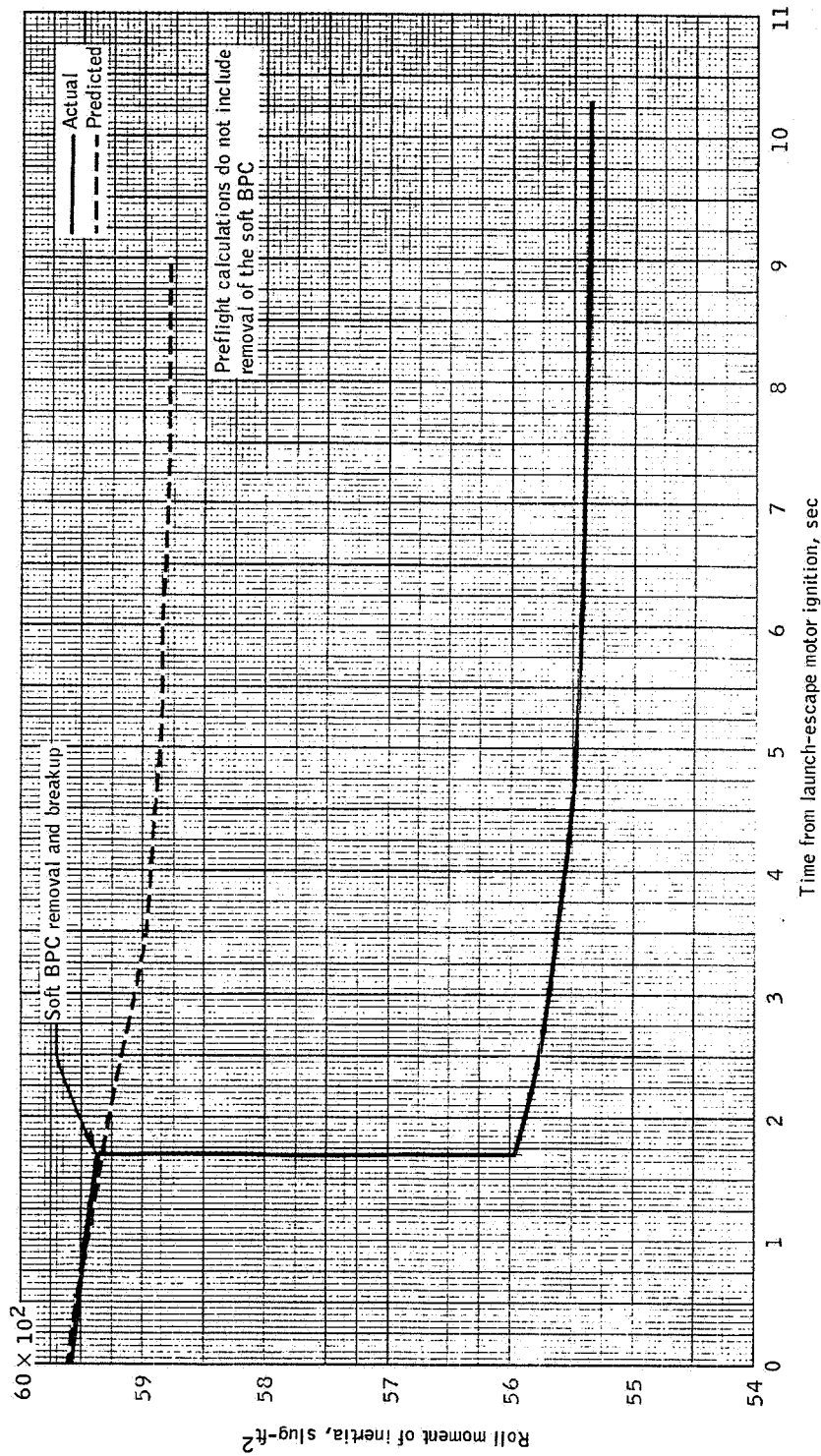


Figure 3.3-5.- Apollo Mission A-004 time history of launch-escape vehicle roll moment of inertia.

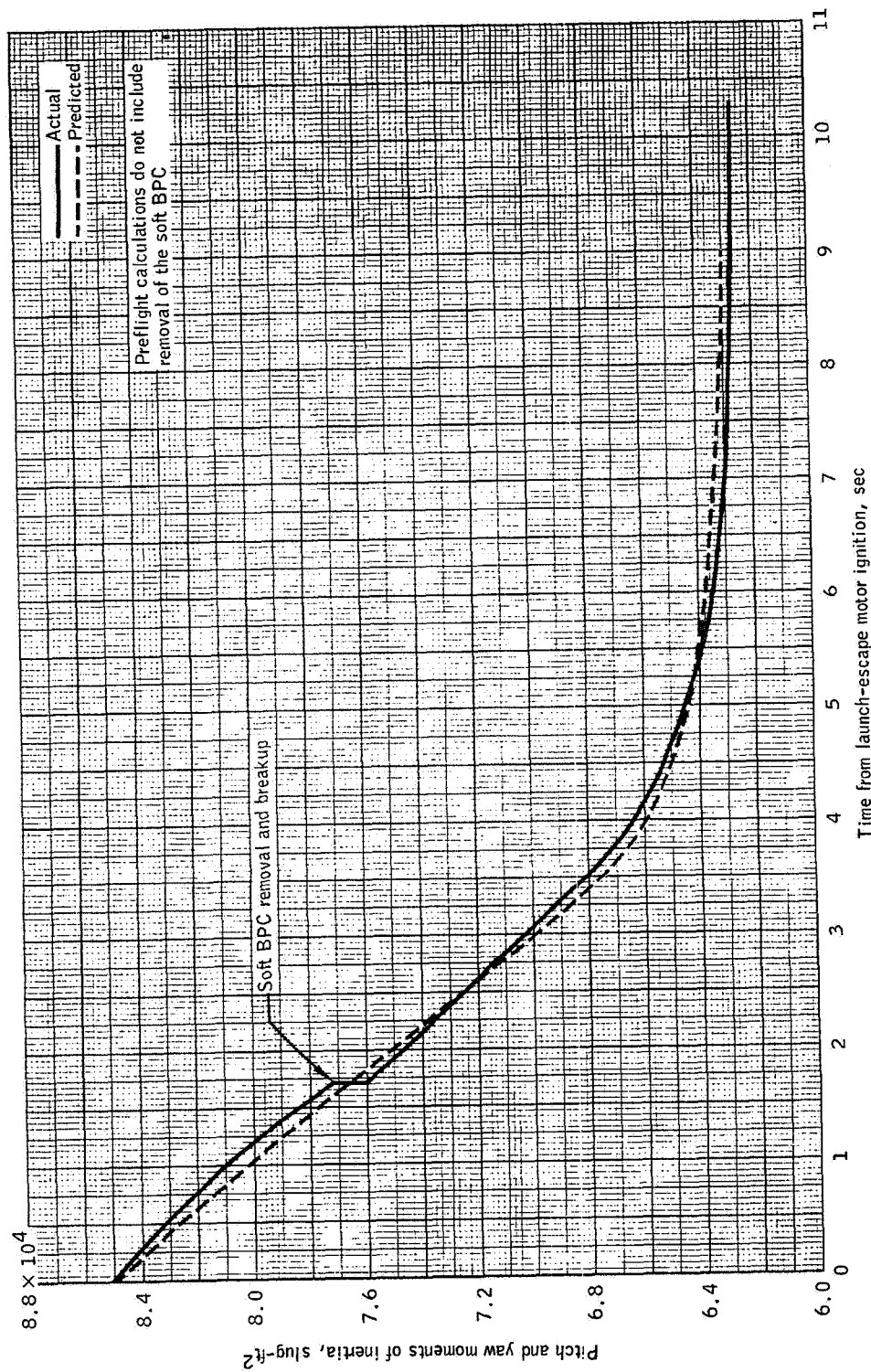


Figure 3.3-6.- Apollo Mission A-004 time history of launch-escape vehicle pitch and yaw moments of inertia.

## 4.0 MISSION TRAJECTORY ANALYSIS

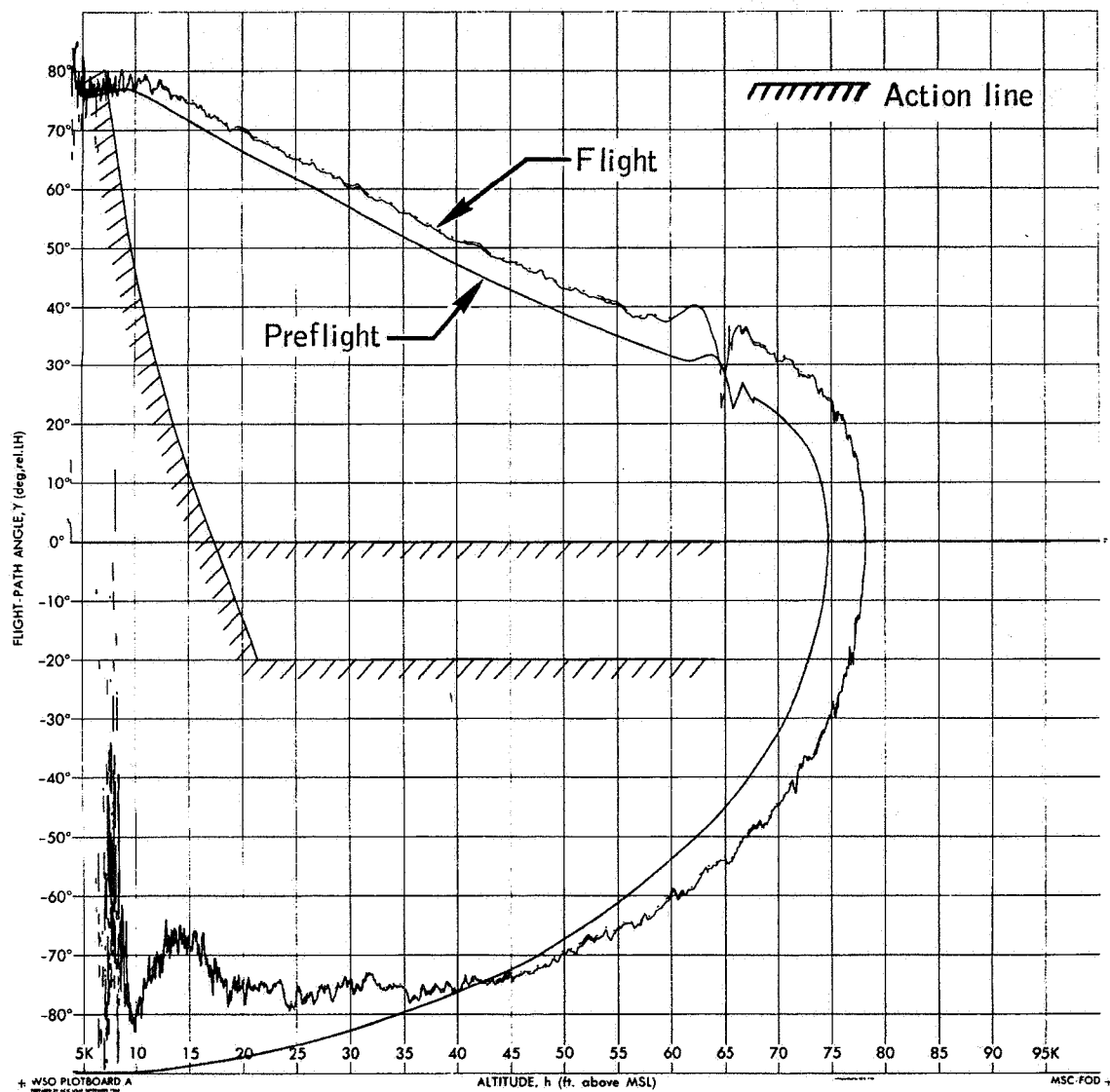
### 4.1 Real-Time Flight Dynamics Control

This mission, as in previous Apollo missions launched at WSMR with the Little Joe II launch vehicle, made use of the range real-time data system (RTDS) in connection with inflight control. The four plotboards, A, B, C, and D, which presented the real-time data during the flight, are shown in figure 4.1-1(a) to (d). (Also see section 10.3.) The pre-flight data included on the plotboards presented appropriate trajectory parameters based on nominal vehicle performance, the WSMR December atmosphere, and no wind. Plotboards A and B included the action lines for control of the mission. Plotboard B also showed the Little Joe II vehicle performance envelope.

The WSMR December atmosphere without wind was used in the RTDS for the actual mission. On the basis of the information presented by the RTDS, the Flight Dynamics Officer initiated the pitch-up maneuver by radio signal to the launch vehicle when the real-time trajectory trace of Mach number plotted against dynamic pressure crossed the action line on plotboard B (as required by ref. 7). The action line was derived so that 2.8 seconds after pitch-up (the nominal time between the pitch-up maneuver and abort initiation), the command module would experience the abort initiation conditions which were expected to result in the desired  $11.1 \pm 1.5$  psid. (See fig. 24, ref. 8.) If the launch vehicle failed, plotboard A (flight-path angle plotted against altitude) would be used for abort control in order to recover the command module intact, if possible.

The WSMR December atmosphere and the launch-time atmosphere are compared in figures 10.5-1 to 10.5-6.

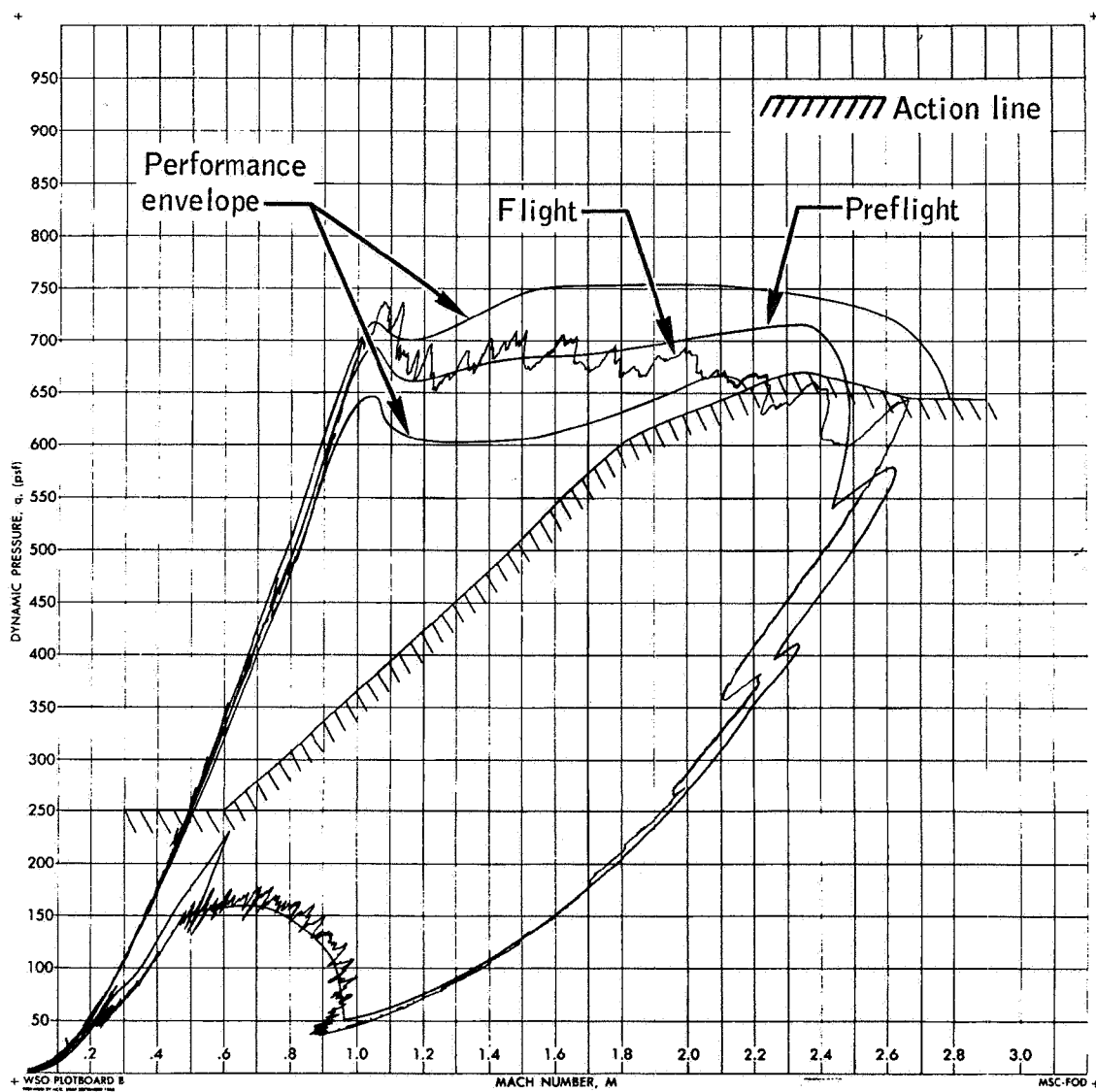
NASA-S-66-3737 APR 15



(a) Plotboard A.

Figure 4.1-1.- Apollo Mission A-004 RTDS plotboard displays.

NASA-S-66-3741 APR 15



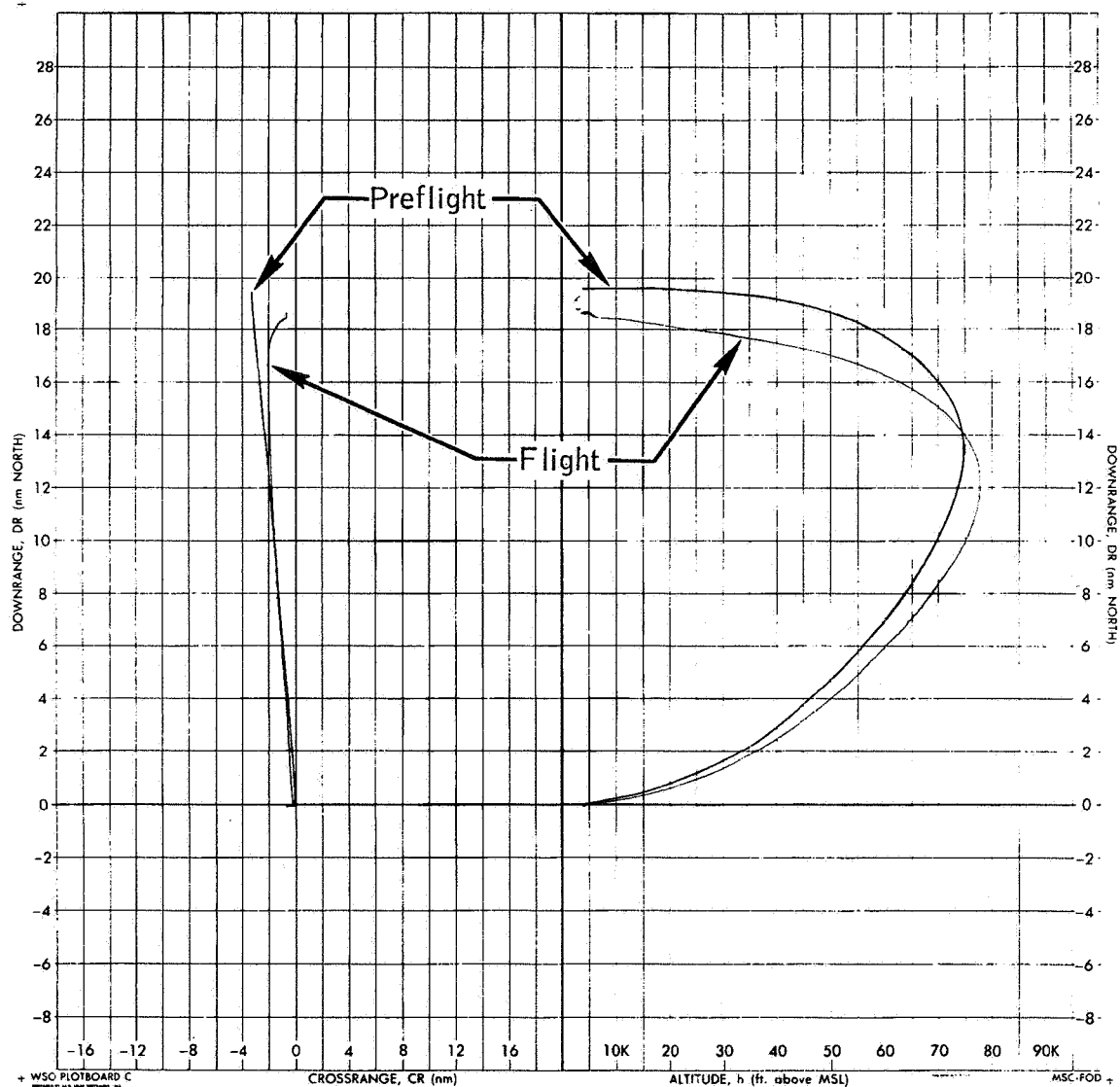
(b) Plotboard B.

Figure 4.1-1.- Continued.



4-4

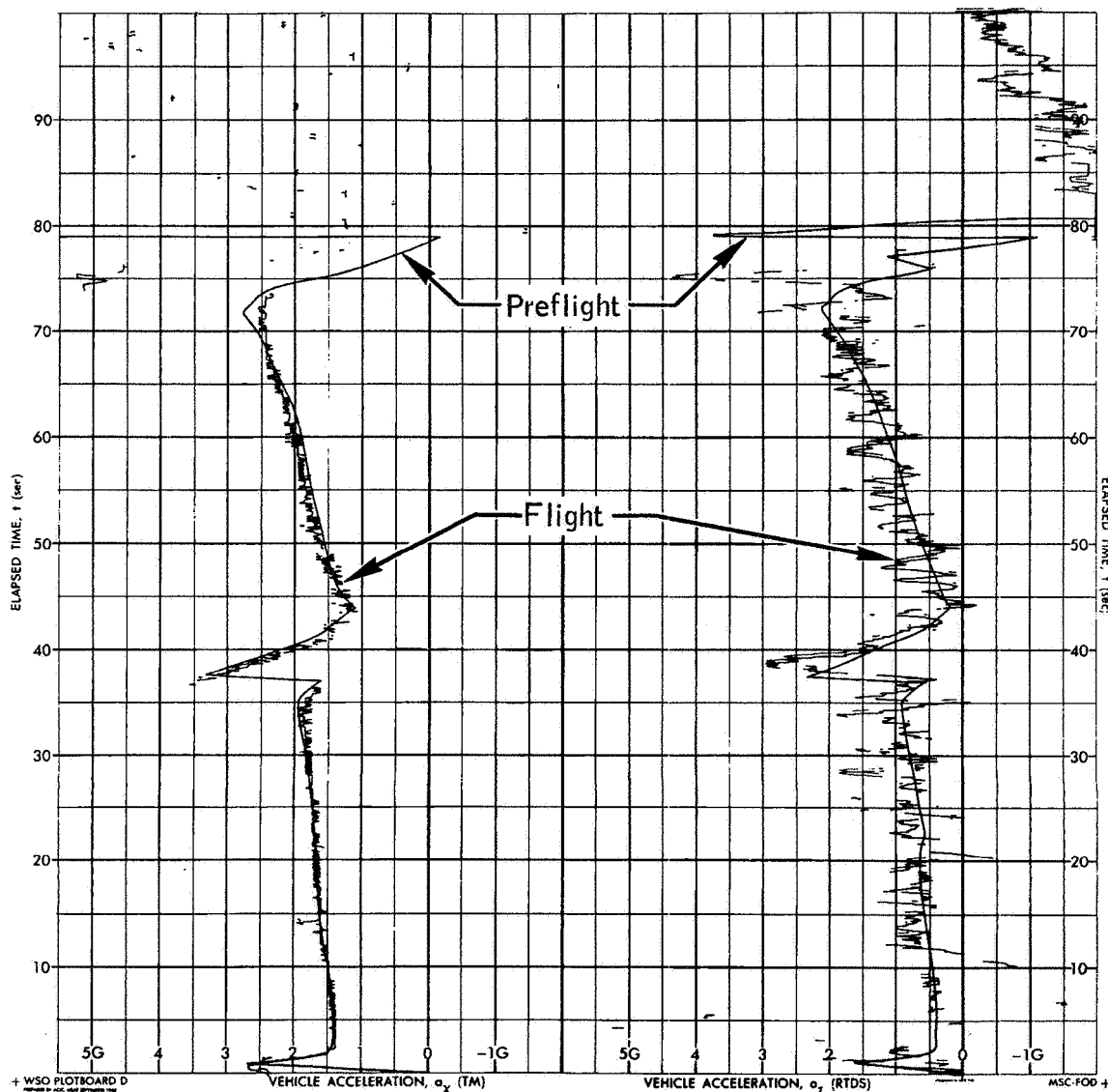
NASA-S-66-3745 APR 15



(c) Plotboard C.

Figure 4.1-1.- Continued.

NASA-S-66-3749 APR 15



(d) Plotboard D.

Figure 4.1-1.- Concluded.

## 4.2 Comparison of Flight with Preflight and Postflight Simulations

The values of several trajectory parameters at significant events in Mission A-004 are shown in table 4.2-I. Values for the actual mission were derived from radar and optical tracking. In addition, two prelaunch predictions and one postlaunch prediction are included. A brief discussion of each trajectory follows.

(a) Prelaunch prediction based on WSMR December atmosphere - This prelaunch trajectory simulation was based on nominal vehicle performance and the standard WSMR December atmosphere without wind. Trajectory parameters on the plotboards used by the RTDS during Mission A-004 were from this simulation.

(b) Prelaunch prediction with January atmosphere - This preflight prediction was based on the final weight and balance data from WSTF and the standard January WSMR atmosphere without winds. Because the changes were so slight from the values based on the WSMR December atmosphere which were already drawn on the plotboards, the decision was made to use the standard WSMR December atmosphere for conducting the mission.

(c) Actual flight results - Flight results were primarily obtained from the replay of the RTDS flight tapes with the launch-time atmosphere and winds as shown in figures 10.5-1 to 10.5-6. In addition, optical tracking was used where it was available. Flight event times are based on telemetry for the launch vehicle and on the recording of onboard timer functions for the spacecraft.

(d) Postflight trajectory simulations were made using the following flight-derived inputs: (1) launch-time atmosphere and winds, (2) the actual times of pitch-rate initiation, staging, pitch-up, and abort initiation, (3) flight thrust as shown in figures 6.1-1 to 6.1-4, and (4) flight weight and balance as discussed in section 3.3.

Figure 4.2-1 shows plotboard B in which the T-2 hour atmosphere and winds were used to recalculate Mach number and dynamic pressure. This plotboard was used for early assessment of the flight.

Flight results, including time histories of altitude, Mach number, dynamic pressure, total velocity, and flight-path angle, are presented in figures 4.2-2 to 4.2-8. Altitude with respect to range and a ground track of the command module are also shown. Figure 4.1-1(a) shows that as soon as discernible, the flight-path angle was higher than predicted, even though the nominal  $84^\circ$  launch elevation was used. This higher flight-path angle combined with an approximate 1-second delay in the start of the pitch programmer caused the trajectory to be higher than nominal for a given range, as seen on figure 4.1-1(c). This higher

altitude and the denser atmosphere, as seen on figure 10.5-4, combined to place the real-time Mach number/dynamic pressure trace at the action line approximately 5 seconds earlier than nominal.

The pitch-up RF command was sent, and abort initiation occurred 2.9 seconds later. Flight results, in terms of Mach number and dynamic pressure, indicated that the Little Joe II launch vehicle placed the command module well within the planned altitude-velocity test region. (See figs. 5.0-1 and 5.0-2.)

Launcher azimuth was set at  $348^{\circ}29'$  to compensate for the predominately westerly wind shown in figure 10.5-5. Figure 4.2-8 illustrates the amount of parachute drift caused by this wind.

TABLE 4.2-I.- MISSION A-004 TRAJECTORY PARAMETERS

Event or parameter	Preflight predictions		Flight results	Postflight simulation
	December atmosphere	January atmosphere		
Launch azimuth, deg E. of N. . . .	351	351	348°29'	348°29'
Launch elevation, deg . . . . .	84	84	84	84
Staging				
Time, sec . . . . .	37.0	37.0	36.4	36.4
Altitude, ft m.s.l. . . . .	17 854	17 936	18 243	18 023
Mach number . . . . .	0.793	0.798	0.81	0.807
Dynamic pressure, lb/sq ft . . .	480	482	475	485
Downrange, ft N. . . . .	3 806	3 882	3 520	3 767
Crossrange, ft W. . . . .	638	651	785	571
Flight-path angle, deg . . . . .	68.4	68.4	71.5	71.2
Pitch-up maneuver				
Time, sec . . . . .	76.1	75.85	70.81	70.8
Altitude, ft m.s.l. . . . .	60 040	60 037	56 985	56 319
Mach number . . . . .	2.484	2.489	2.24	2.27
Dynamic pressure, lb/sq ft . . .	659.7	659.5	610	648
Downrange, ft N. . . . .	42 652	42 422	32 940	34 216
Crossrange, ft W. . . . .	6 886	6 851	4 465	3 775
Total velocity, ft/sec . . . . .	2 351	2 365	2 140	2 179
Flight-path angle, deg . . . . .	31.57	31.84	38.4	37.53
Angle of attack, deg . . . . .	1.70	1.73	2.3	1.67
Abort initiation				
Time, sec . . . . .	78.9	78.65	73.73	73.73
Altitude, ft m.s.l. . . . .	63 449	63 489	61 083	60 359

TABLE 4.2-I.- MISSION A-004 TRAJECTORY PARAMETERS - Continued

Event or parameter	Preflight predictions		Flight results	Postflight simulation
	December atmosphere	January atmosphere		
Mach number . . . . .	2.444	2.460	2.43	2.448
Dynamic pressure, lb/sq ft . . .	539.5	543.9	577	619
Downrange, ft N. . . . .	48 253	48 026	38 090	39 454
Crossrange, ft W. . . . .	7 779	7 745	5 235	4 506
Total velocity, ft/sec . . . . .	2 328	2 348	2 315	2 343
Flight-path angle, deg . . . . .	31.55	31.89	39.2	38.87
Angle of attack, deg . . . . .	-16.32	-16.35	-13.5	-16.0
Canard deployment				
Time, sec . . . . .	89.9	89.65	84.8	84.8
Altitude, ft m.s.l. . . . .	72 151	72 410	72 845	70 989
Mach number . . . . .	1.571	1.583	1.56	1.48
Dynamic pressure, lb/sq ft . . .	145.4	145.6	134	134
Downrange, ft N. . . . .	67 923	67 796	56 370	57 360
Crossrange, ft W. . . . .	11 082	11 065	7 718	7 282
Total velocity, ft/sec . . . . .	1 512	1 526	1 500	1 418
Flight-path angle, deg . . . . .	17.25	17.75	27.8	23.51
Apogee				
Time, sec . . . . .	101.7	102.0	102.2	99.4
Altitude, ft m.s.l. . . . .	74 663	75 096	78 180	74 824
Mach number . . . . .	1.104	1.098	0.94	0.96
Dynamic pressure, lb/sq ft . . .	63.7	61.6	38	48
Downrange, ft N. . . . .	82 206	82 841	75 060	72 865

TABLE 4.2-I.- MISSION A-004 TRAJECTORY PARAMETERS - Concluded

Event or parameter	Preflight predictions		Flight results	Postflight simulation
	December atmosphere	January atmosphere		
Crossrange, ft W. . . . .	13 557	13 673	9 655	9 643
Total velocity, ft/sec . . . . .	1 066	1 061	905	921
Tower jettison				
Time, sec . . . . .	188.8	189.0	193.8	185.9
Altitude, ft m.s.l. . . . .	24 003	23 886	23 050	23 250
Mach number . . . . .	0.533	0.526	0.48	0.53
Dynamic pressure, lb/sq ft . . .	168.8	164.0	135	168
Downrange, ft N. . . . .	119 498	119 797	110 405	108 040
Crossrange, ft W. . . . .	20 123	19 728	8 036	9 958
Total velocity, ft/sec . . . . .	552	543	500	557
Main parachute deployment (pilot parachute mortar fire)				
Time, sec . . . . .	237.4	237.7	237.6	234.0
Altitude, ft m.s.l. . . . .	10 554	10 486	10 450	10 189
Mach number . . . . .	0.200	0.200	0.21	0.20
Dynamic pressure, lb/sq ft . . .	40.6	40.6	43	41
Downrange, ft N. . . . .	119 460	120 028	112 400	110 150
Crossrange, ft W. . . . .	19 955	19 810	4 842	6 460
Total velocity, ft/sec . . . . .	218	218	226	220
Command module landing				
Time, sec . . . . .	426.2	424.5	410	413.1
Altitude, ft m.s.l. . . . .	4 000	4 000	4 062	4 000
Downrange, ft N. . . . .	119 422	119 989	113 624	110 958
Crossrange, ft W. . . . .	19 947	19 802	3 328	4 949
Total velocity, ft/sec . . . . .	28.18	28.21	27.5	27.78

NASA-S-66-3753 APR 15

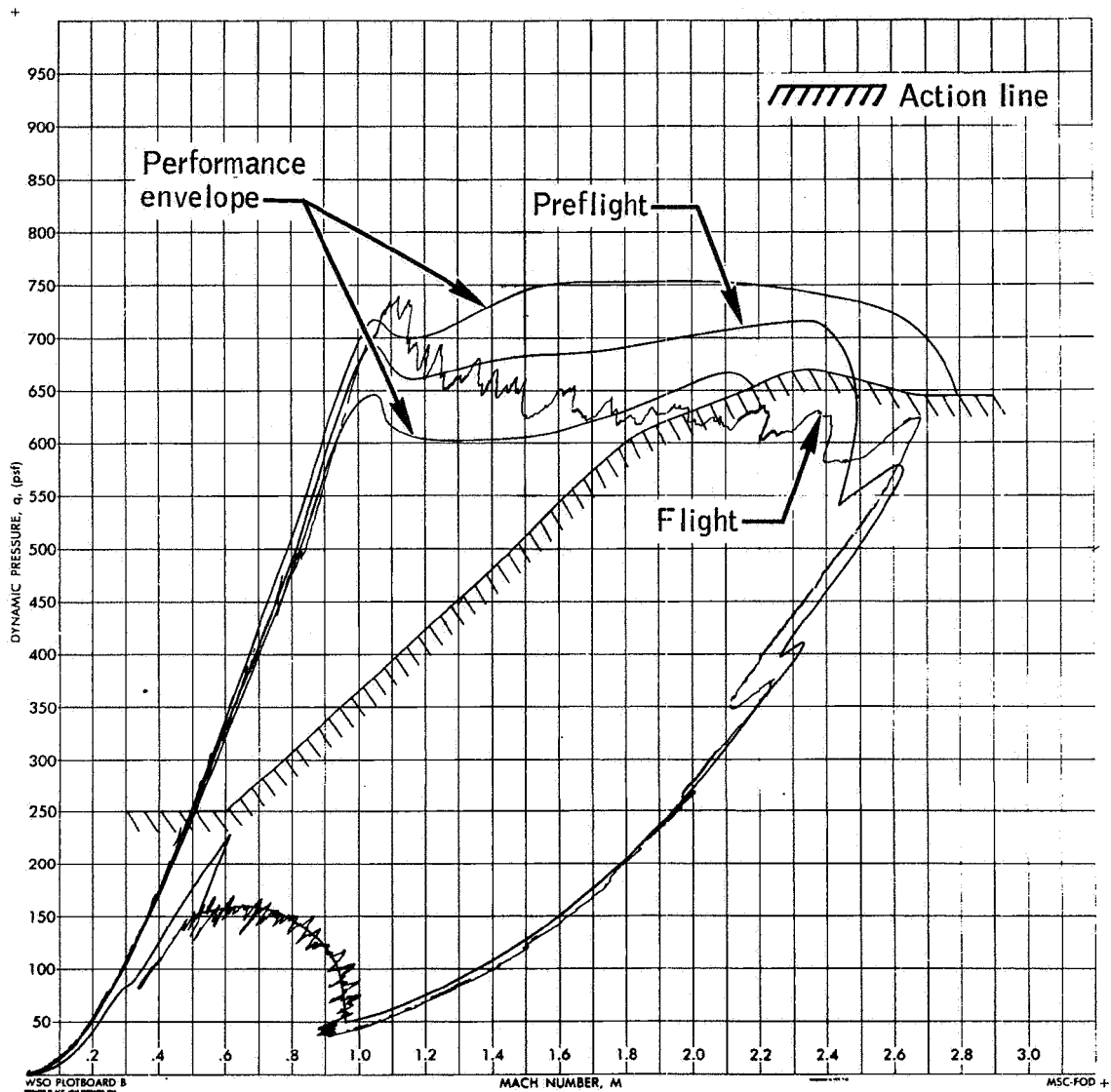


Figure 4.2-1.- Apollo Mission A-004 RTDS plotboard B with T-2 hour weather.



NASA-S-66-3757 APR 15

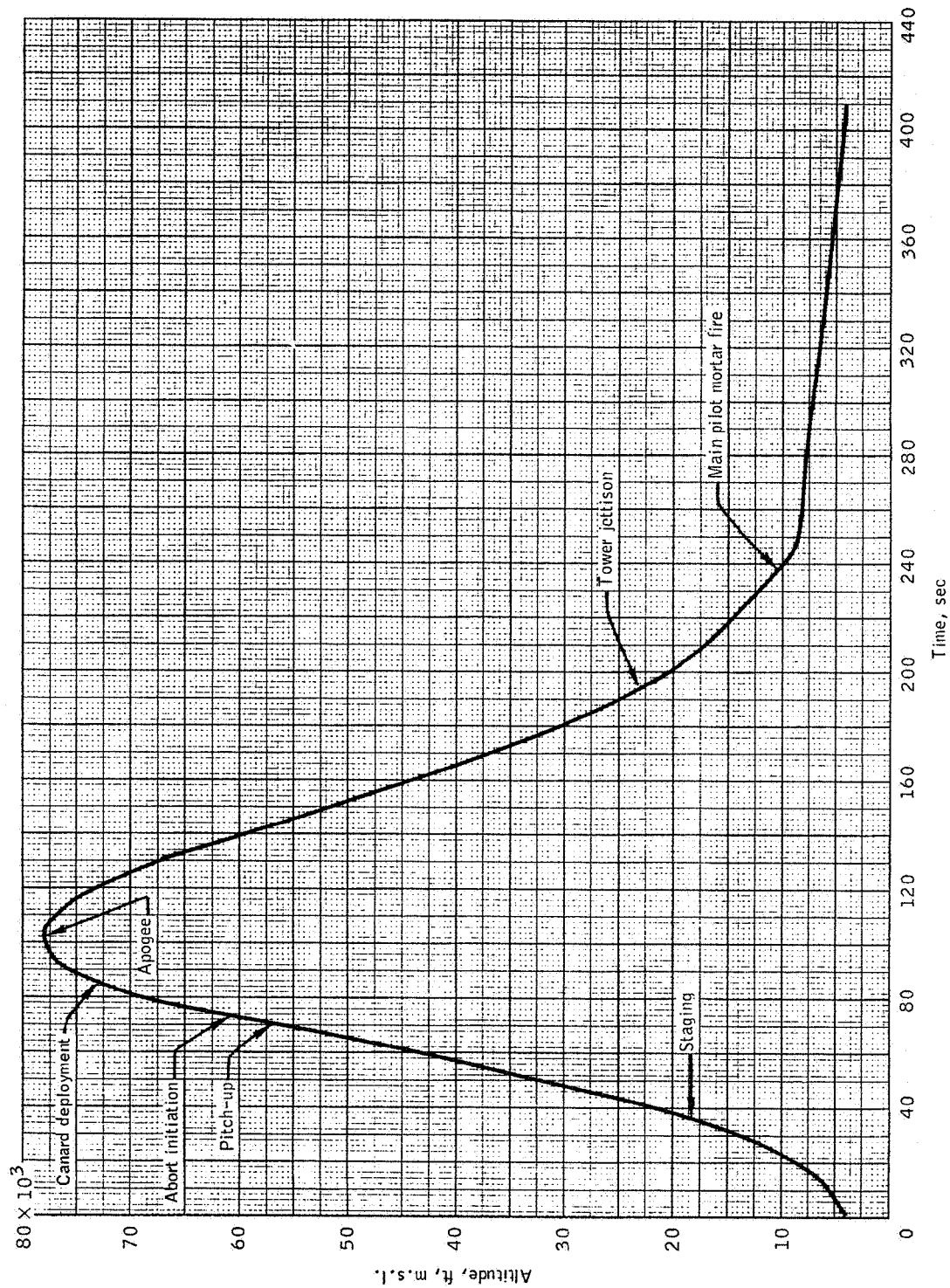


Figure 4.2-2.- Altitude plotted against time, Apollo Mission A-004.

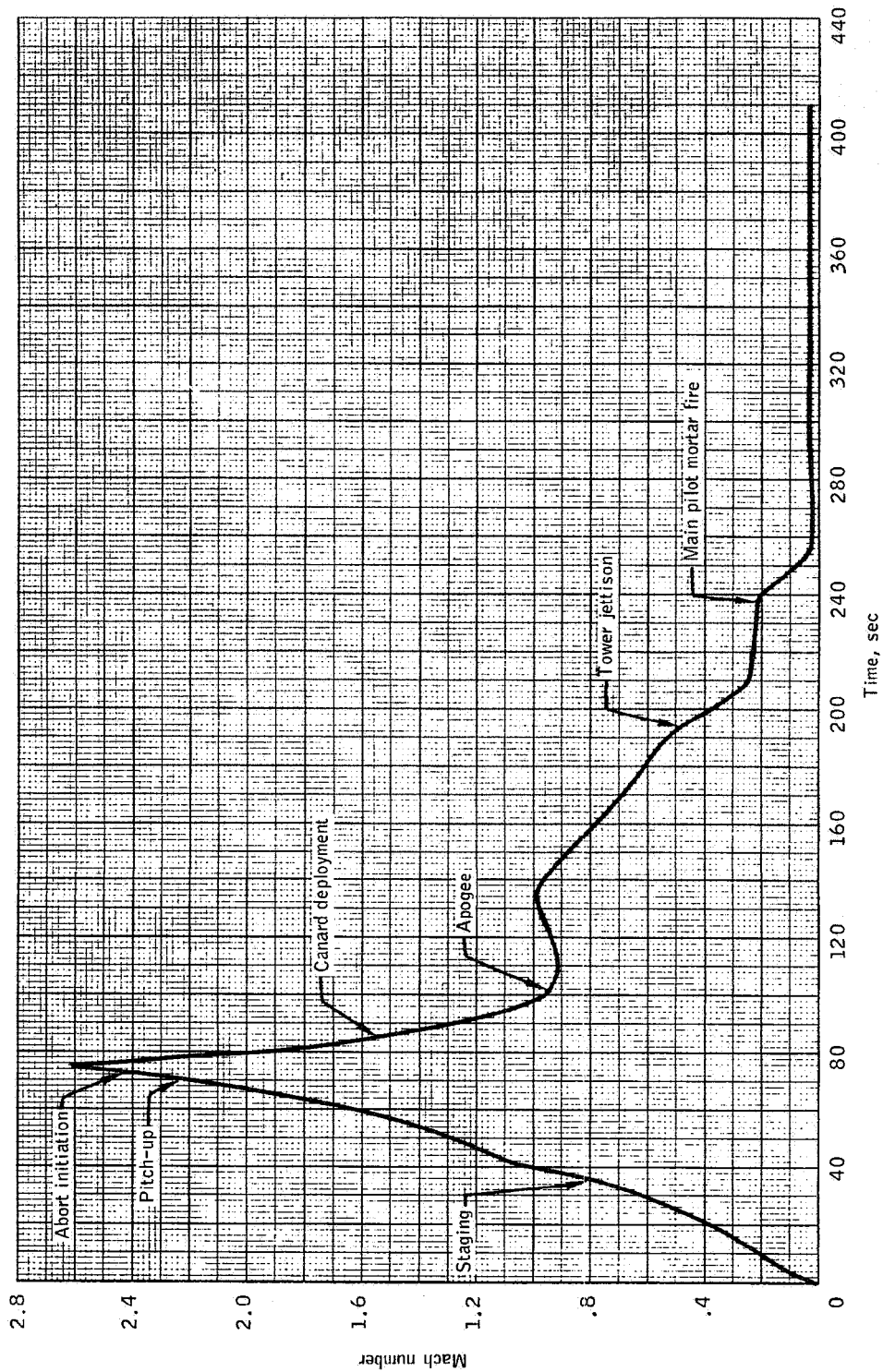


Figure 4.2-3.- Mach number plotted against time, Apollo Mission A-004.

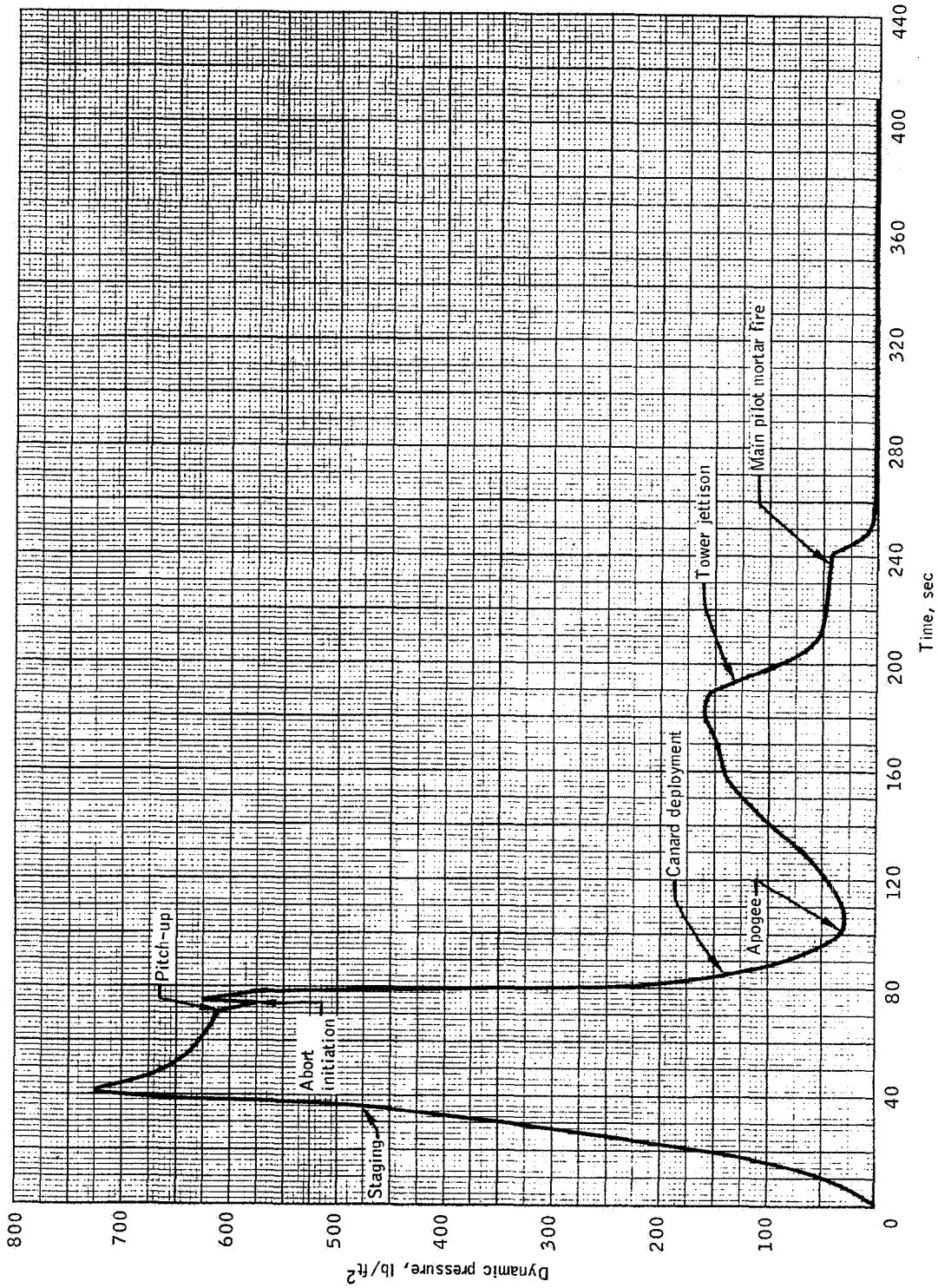


Figure 4.2-4.- Dynamic pressure plotted against time, Apollo Mission A-004.

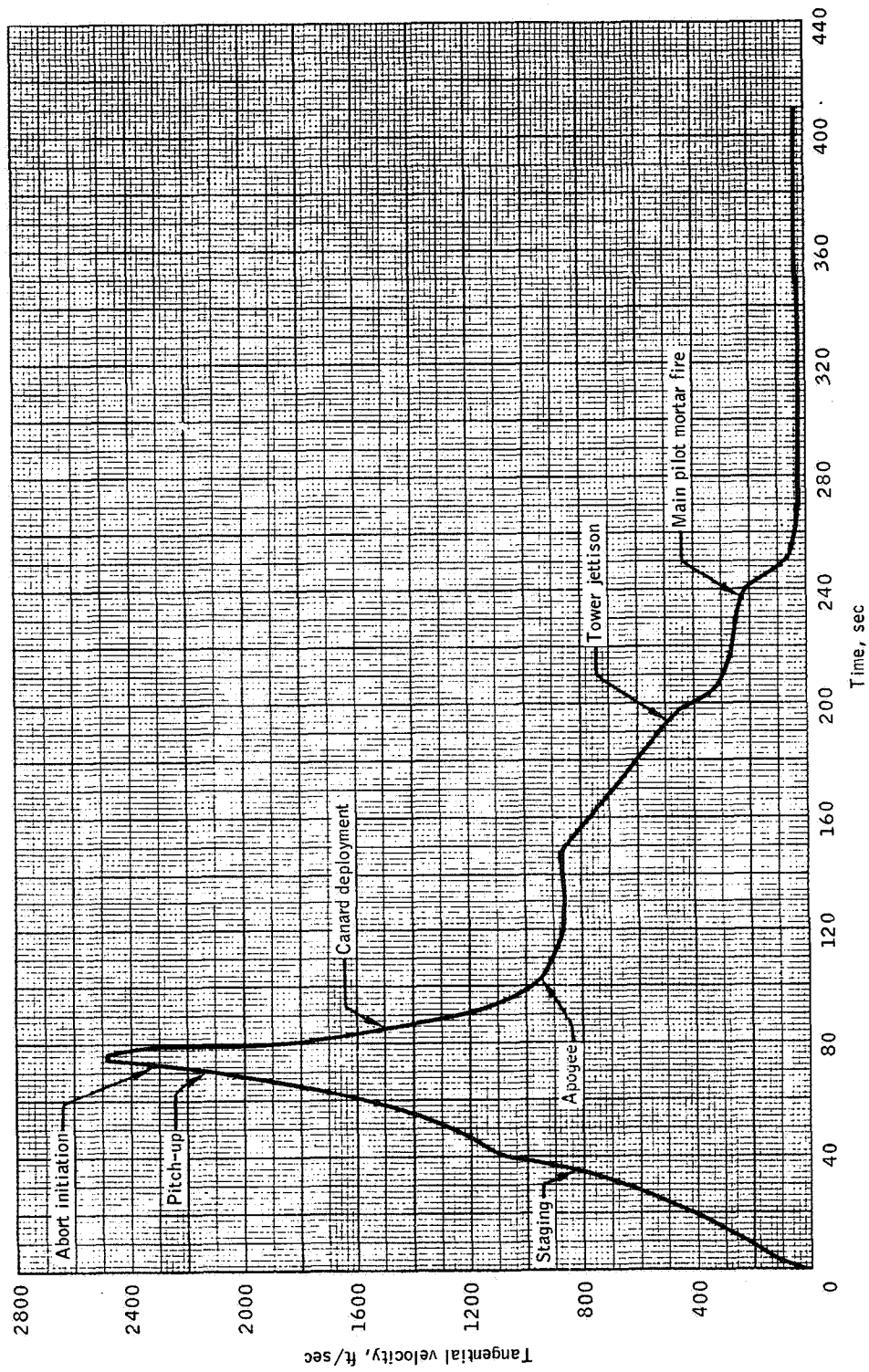


Figure 4.2-5.- Tangential velocity plotted against time, Apollo Mission A-004.

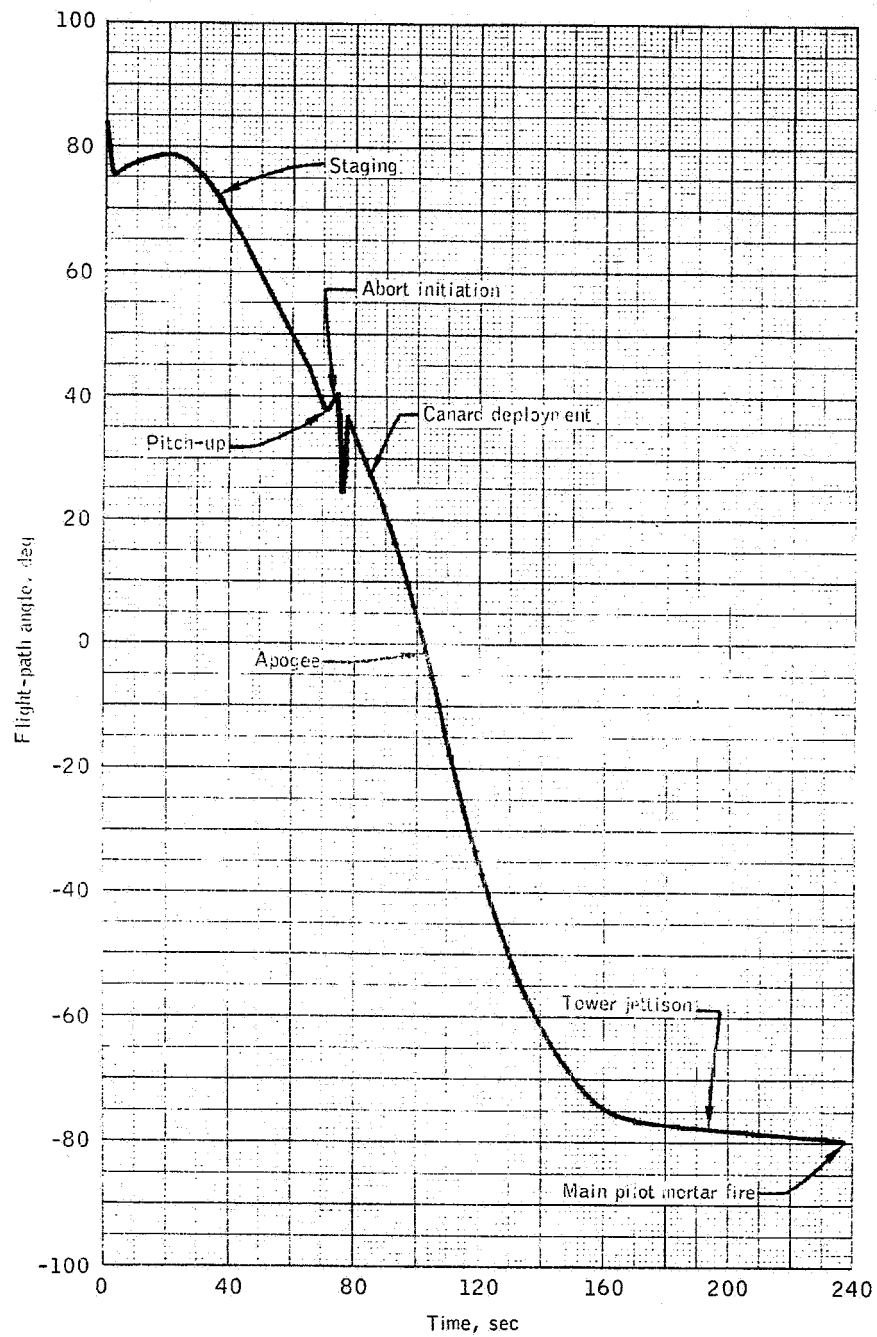


Figure 4.2-6.- Flight-path angle plotted against time, Apollo Mission A-004.

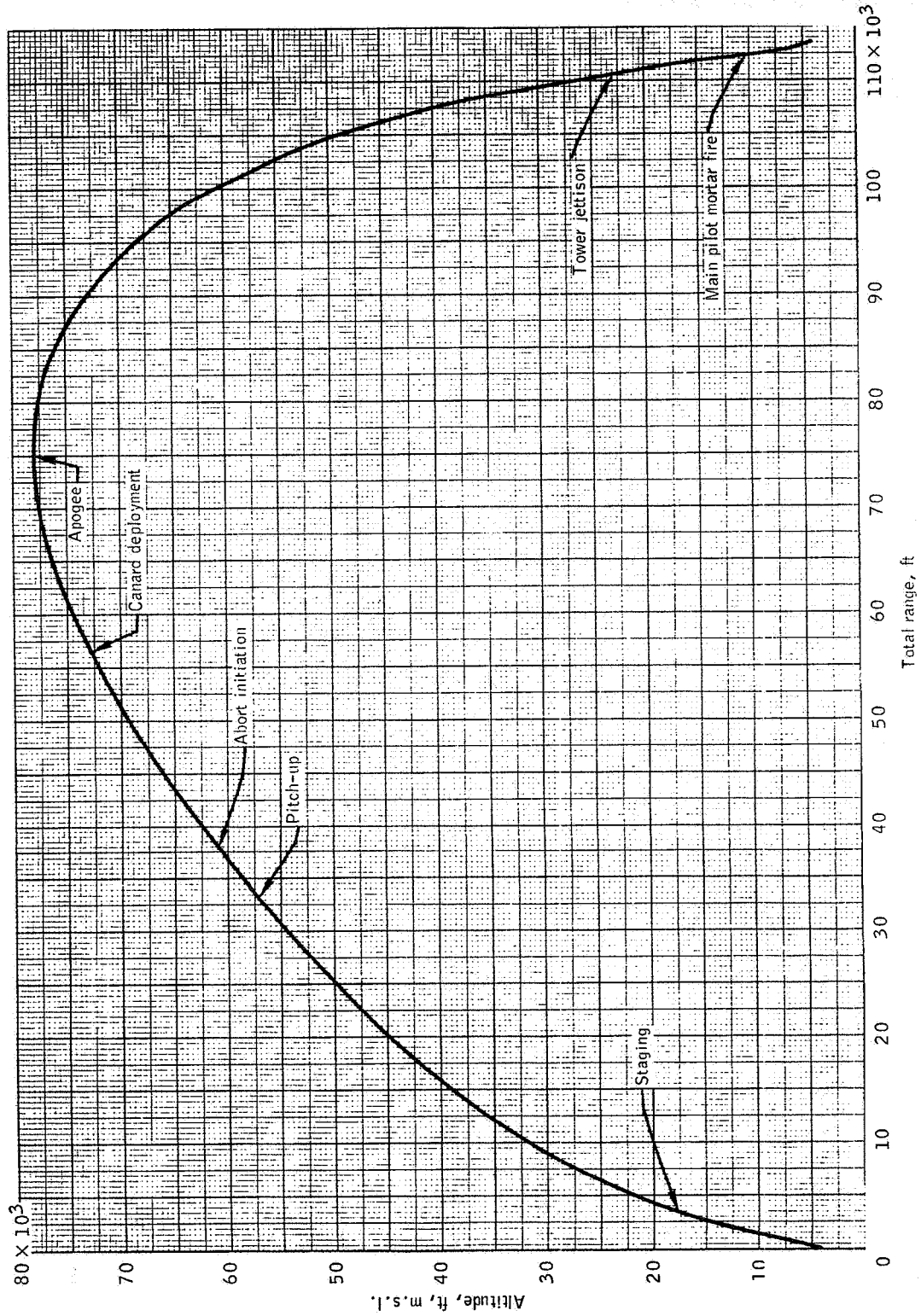


Figure 4.2-7.- Altitude plotted against total range, Apollo Mission A-004.

NASA-S-66-3781 APR 15

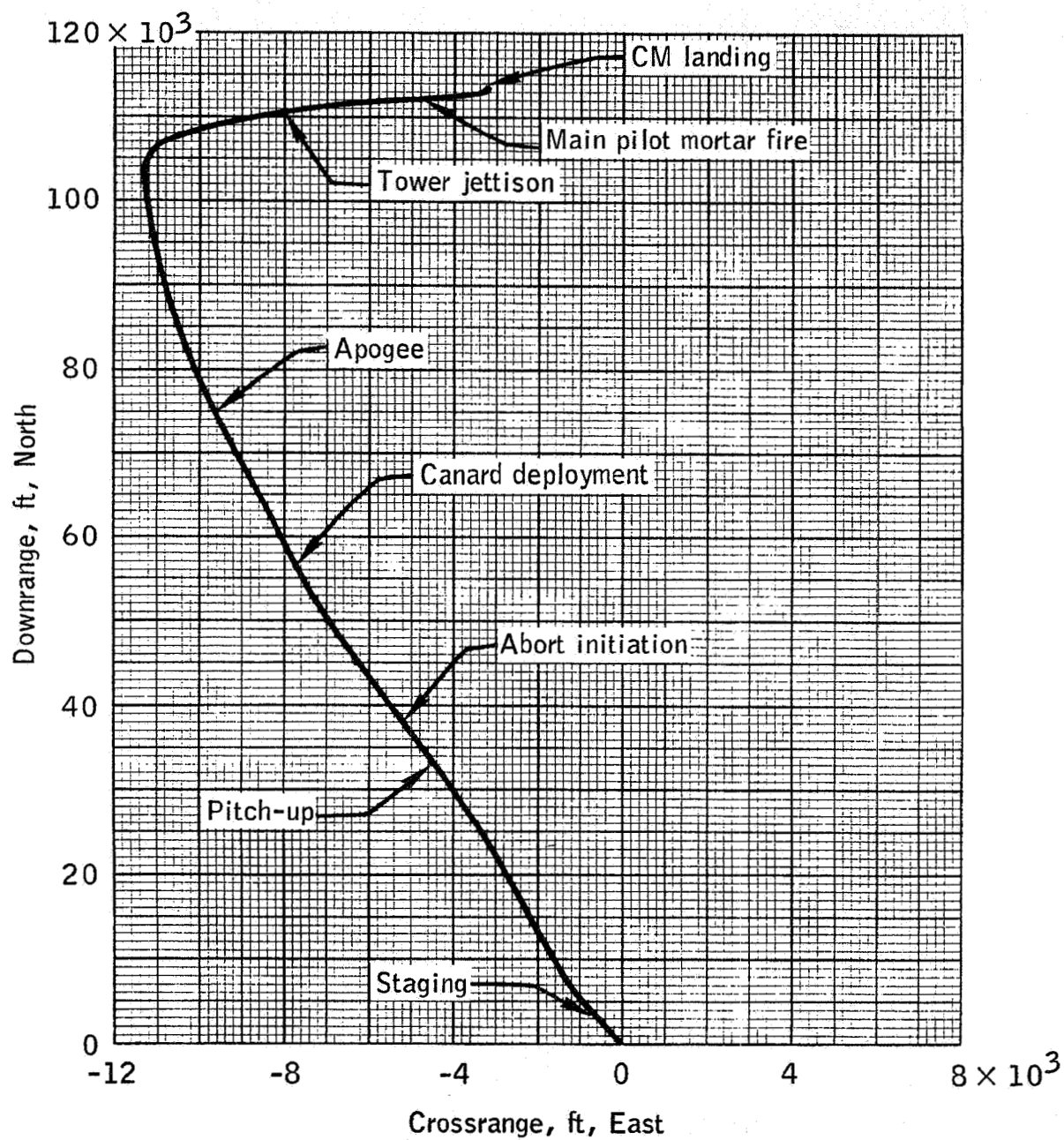


Figure 4.2-8.- Ground track, Apollo Mission A-004.



## 5.0 SPACECRAFT PERFORMANCE

The Mission A-004 test point relationship to the Saturn launch vehicle performance envelope and other WSMR missions is shown in figure 5.0-1. In conformance with the first-order test objectives, this test point was located within the region of the power-on tumbling boundary. The boundary was based on the structural load capability of the spacecraft and the altitude and velocity at which the launch-escape vehicle (LEV) could be allowed to tumble, during the power-on phase of the abort, without experiencing greater than design limit loads. The structural loading of primary interest in the above definition was the local pressure differential across the command module (CM) exterior wall caused by the difference between the internal cavity pressure and the combined external effects of the aerodynamic and launch-escape motor plume impingement pressures. The spacecraft design limit load for this condition is 11.1 psid.

Figure 5.0-2 shows an expanded view of the test region. The planned and actual abort points are indicated on the figure. The test region is bounded by the predicted Little Joe II (LJ II) maximum and minimum performance trajectories and an allowable differential pressure dispersion of  $\pm 1.5$  psi. As shown in the figure, a differential pressure of approximately 11.8 psid should have been developed during the actual abort of Mission A-004 with nominal LEV performance. The plume impingement pressure data used in the mission design were approximated from data taken in wind-tunnel tests (ref. 9). The approximation assumed the impingement pressures to be a direct function of free-stream dynamic pressure and the relationship between plume and free-stream momentum.



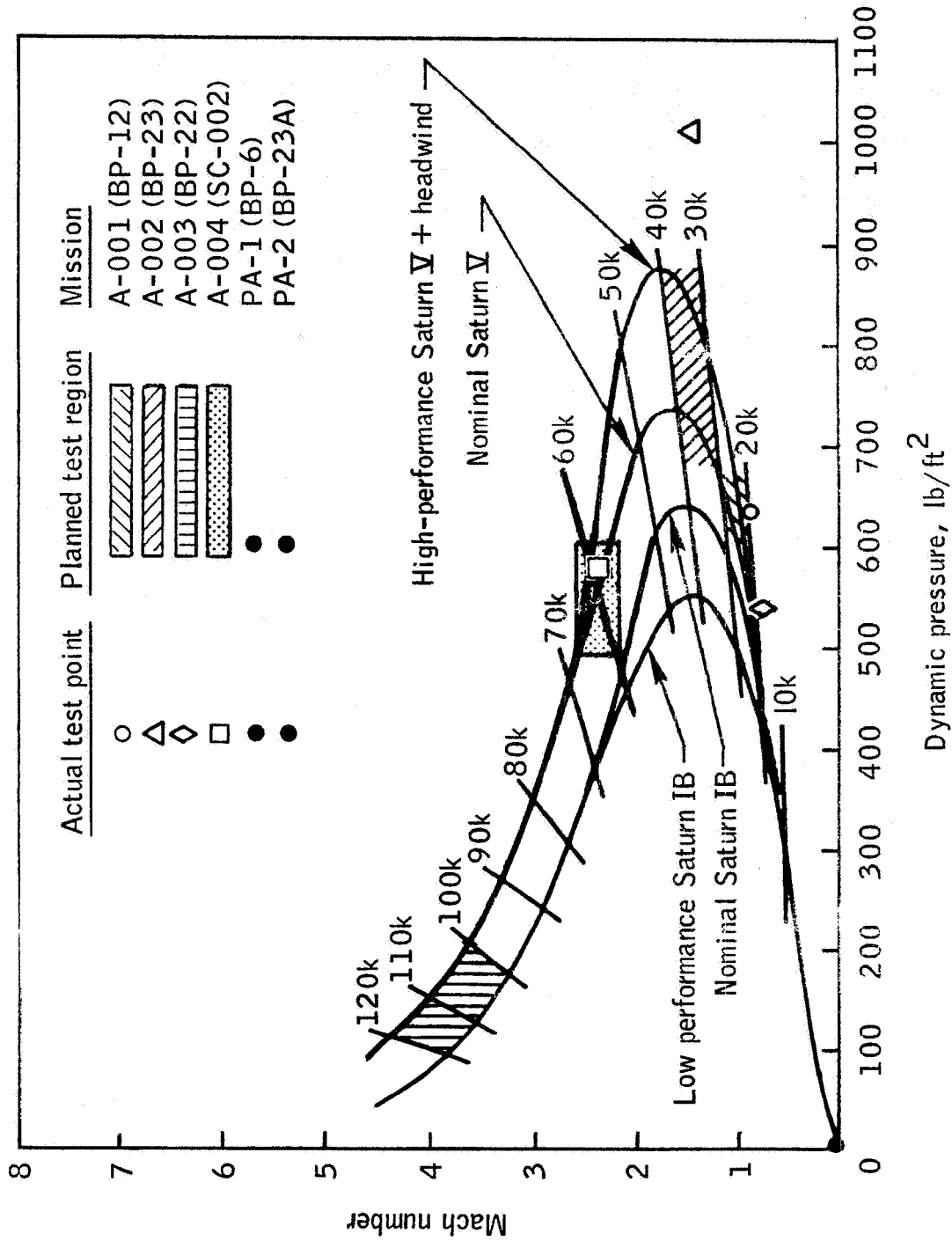


Figure 5.0-1.- WSMR abort points in relation to Saturn boost flight envelope.

NASA-S-66-3656 APR 15

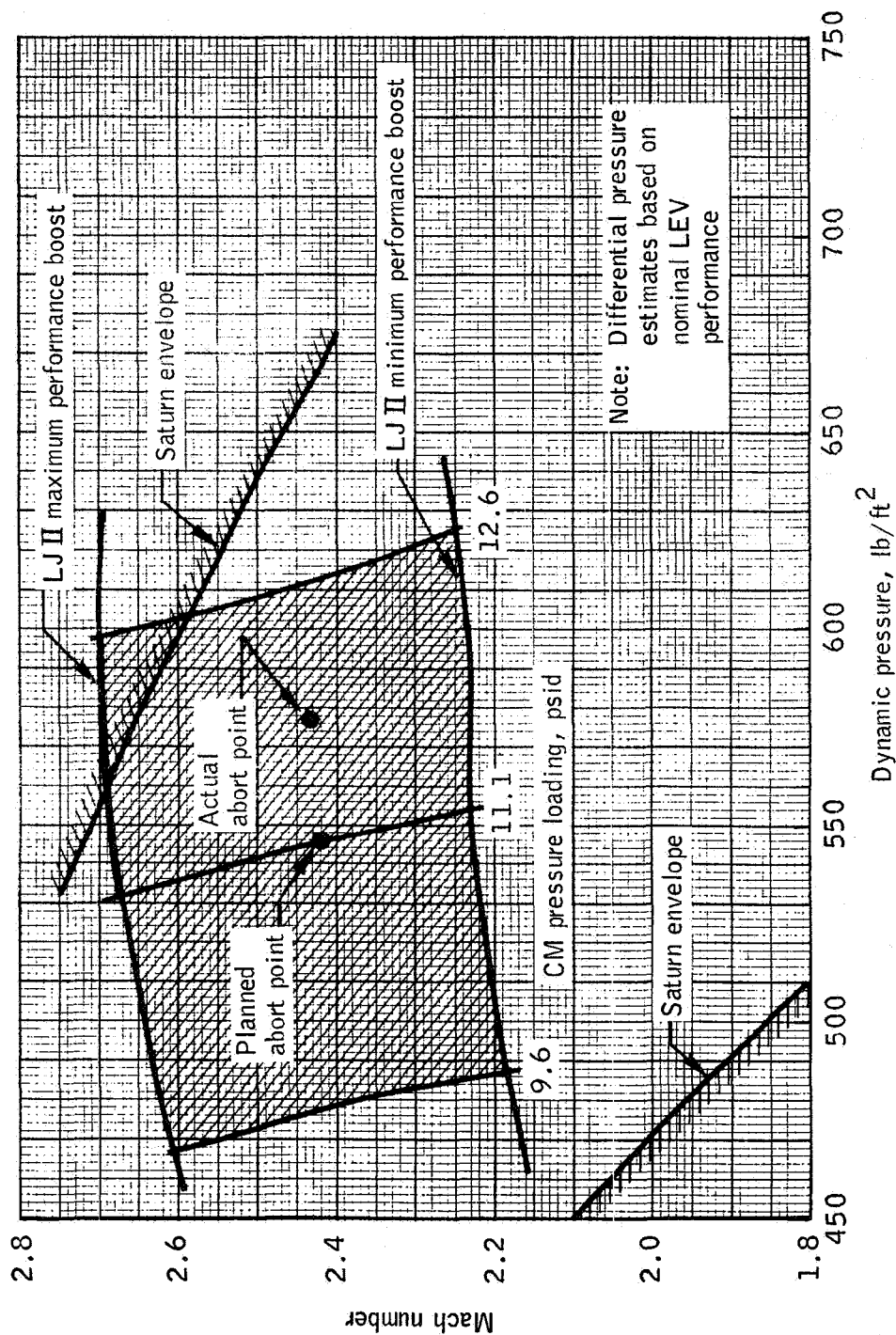


Figure 5.0-2.- Test region and abort points, Apollo Mission A-004.

## 5.1 Aerodynamics

A manned spacecraft would have a low probability of experiencing tumble during an abort at the altitude-velocity conditions of this test. However, because design limit pressure loads during a tumbling abort were desired, and because of the test vehicle structural limitations imposed on the pitch-up maneuver, the launch-escape vehicle (LEV) was configured to insure power-on tumble. This was accomplished by using the pitch-control motor at the abort altitude, moving the LEV center-of-gravity by using ballast, and setting the launch-escape subsystem (LES) thrust vector to its extreme destabilizing position. (See section 3.3 and figure 3.1-3.)

As a result of this configuration, the vehicle did tumble and the loads and the rotational rates were higher than would be expected during a normal spacecraft abort in this altitude-velocity region. The pitch and yaw rates displayed peak values of 160 deg/sec, while the roll rate reached a peak of -70 deg/sec during the power-on portion of the abort. The longitudinal load factor peaked at about +15g during peak thrust with the vehicle oriented main heat shield forward. The Y-axis load was oscillatory between  $\pm 2.5g$ , and the Z-axis load reached peaks of +2.5g and -5g.

A postflight six-degree-of-freedom simulation was conducted to determine if the LEV motions can be predicted satisfactorily by using wind-tunnel-derived aerodynamic data in the abort Mach number range. The simulation utilized actual abort initial conditions, atmosphere properties and winds measured at time of lift-off, actual thrust values, and actual mass characteristics.

The aerodynamic data used for the simulation were obtained from numerous wind-tunnel test runs conducted for limited values of Mach number, angle of attack, and thrust. The power-on tests were limited to an angle of attack,  $\alpha$ , of approximately  $50^\circ$  (for static force data). To provide additional data necessary to cover the complete range of the flight parameters expected for this mission, the power-on data were extended using power-off wind-tunnel data. Neither dynamic damping nor roll data were available for the LEV with power on.

The simulated rotational rates are compared with the flight-measured rates for the first few seconds following abort as shown in figure 5.1-1. There is good agreement between simulated and actual rates for the first 1.5 seconds subsequent to abort, whereas beyond this time the comparison becomes divergent. The flight parameters during the first 1.5 seconds are within the range of measured wind-tunnel power-on data ( $\alpha = 50^\circ$ ). After about 1.5 seconds the spacecraft had rotated to aerodynamic angles which necessitated the use of extrapolated data, which probably accounts

for most of the divergence of this portion of the simulation. The dynamic damping becomes more significant during the portion of the flight when high angular rates are encountered.

As expected for the configuration characteristics and the abort conditions, the LEV exceeded the attitude of static stability ( $\alpha \approx 35^\circ$  for this LEV) at about 1 second after abort initiation.

Based on the reasonable agreement of the flight and simulated rates during the first 1.5 seconds of LEV flight, it is indicated that the existing aerodynamic data are adequate to predict the vehicle static stability and can be used to determine operational tumbling boundaries. The results of a detailed analysis of the aerodynamic flight data in order to improve the simulation are not within the scope of this report.

The aerodynamic effectiveness of the LEV with canards extended in arresting the tumbling motions and providing damping during the descent was slightly greater than the design requirements of the operational vehicle and can be, in part, attributed to the more rearward center-of-gravity location of spacecraft 002. Flight data indicated that quasi-steady-state oscillations about 0 deg/sec were established about all axes at T+115 seconds with the maximum rate at tower jettison being 60 deg/sec and occurring in the pitch plane.

A postflight simulation of the LEV with canards was conducted using the spacecraft flight position and velocity data at the time of canard deployment (T+84.8 sec). Figure 5.1-2 shows a comparison of the envelope of the actual and simulated angular rates for approximately 50 seconds prior to tower jettison. The upper and lower boundaries of each rate envelope were obtained by connecting the peaks of the positive and negative rates for the time history period shown. There is reasonably good agreement between the simulation and flight rates during this time interval although the magnitude of the peak values from the flight were less than the simulation. It can be concluded that the canard aerodynamic data are adequate for trajectory simulation to be used for predicting vehicle rates at tower jettison.

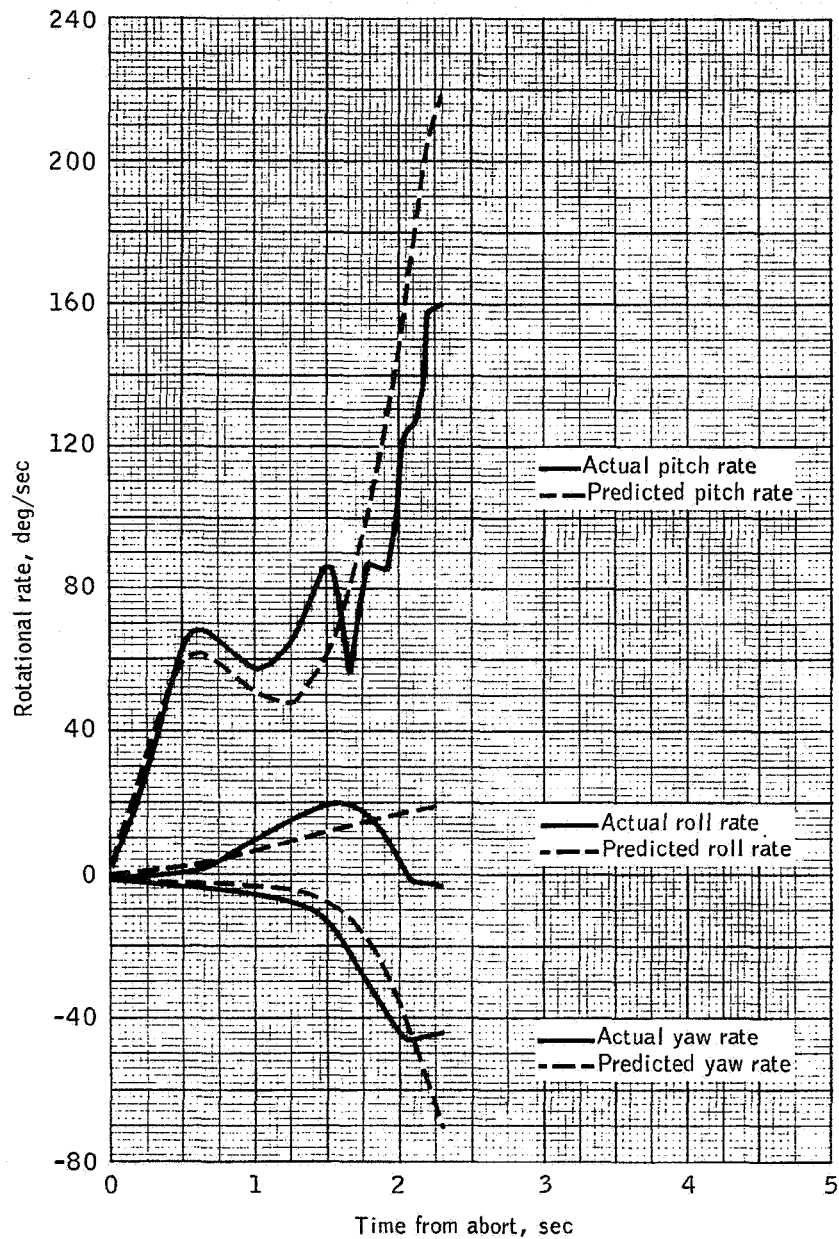


Figure 5.1-1.- Comparison of actual and predicted launch-escape vehicle spacecraft rotational rates for Apollo Mission A-004.

NASA-S-66-3668 APR 15

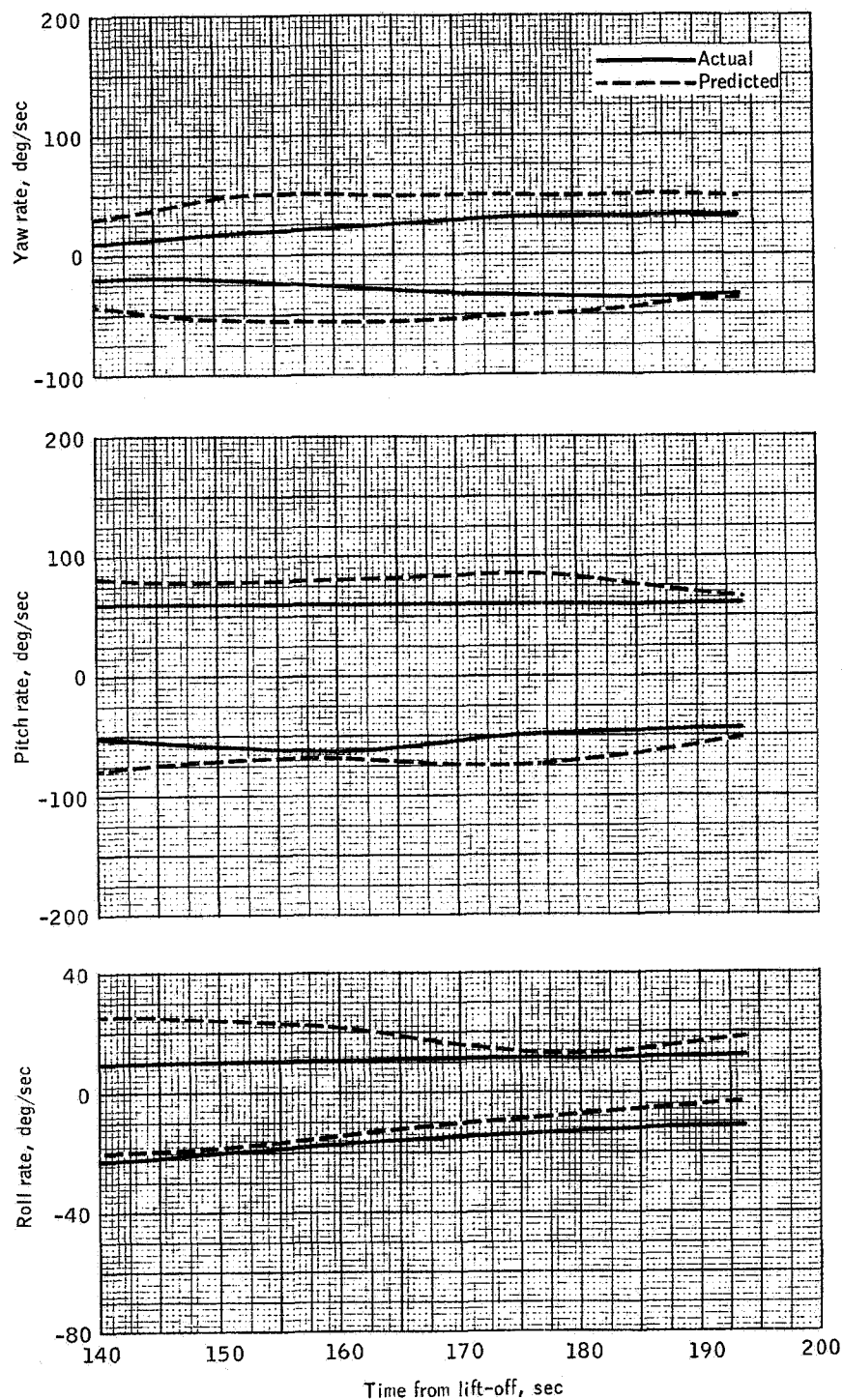


Figure 5.1-2.- Comparison of actual and predicted angular rate envelope, Apollo Mission A-004.

## 5.2 Structural Loads

5.2.1 Summary.- Analysis of the flight data indicates that spacecraft 002 performed with no structural problems throughout the flight. Interface loads calculated for the maximum load flight conditions throughout the flight show that the limit load capability of the structure was not exceeded. The maximum differential pressure measured on the command module (CM) conical heat shield during plume impingement was 7.1 psid based on flight data, although the desired differential pressure was  $11.1 \pm 1.5$  psid. Strain-gage data on the CM structure indicated low stress levels during the entire flight. Strain gages installed on the launch-escape subsystem (LES) tower legs gave maximum tension loads during the tumbling abort that reached 85.8 percent of design limit. Strain-gage instrumentation on the service module (SM) radial beam trusses and tension ties showed very low stress levels until pitch-up. At pitch-up, the stress levels were still less than 50 percent of the allowable in any member.

5.2.2 Structural description.- Mission A-004 was the first flight test of the Block I command module and service module structures; however, the Block I launch-escape subsystem structure had been previously tested on Mission A-002 (BP-23), Mission A-003 (BP-22), and Mission PA-2 (BP-23A), references 10, 4, and 11, respectively. A basic detailed description of the LES is included in reference 10 and additional information may be found in references 4 and 11.

Launch-escape subsystem: The LES used on spacecraft 002 was a Block I configuration consisting of a Q-ball assembly, a ballast compartment, the canard subsystem, launch-escape, pitch-control, and tower-jettison motors, a tower structure, and the boost protective cover. (See fig. 5.2-1.) The tower structure was a four-legged, welded, tubular, titanium alloy truss, covered with Buna-N-rubber for thermal protection. The tower structure was attached to the LES motor structural skirt by alignment bolts and attached to the command module by four explosive bolts of interim design (refs. 10 and 4). The hard portion of the boost protective cover was also attached to the tower at the CM-LES interface. Ballast plates, normally located at the interface between the Q-ball assembly and the pitch-control motor, were omitted on spacecraft 002 as a part of the LEV center-of-gravity shift to assure the tumbling required (see sections 3.3 and 5.1).

Command module: The command module structure consisted of a crew compartment inner structure, a crew compartment outer structure conical heat shield, a main heat shield, and a forward compartment heat shield (apex cover) as shown in figure 5.2-2.

The crew compartment inner structure, which was the primary load-carrying structure of the CM, was a semi-monocoque, aluminum honeycomb,

pressure vessel. The structure resembled base-opposed truncated cones, each capped by bulkheads. The flat forward bulkhead incorporated a cylindrical access tunnel capped by a flat pressure hatch cover. The aft bulkhead was spherically contoured. Longerons were incorporated in the side walls of the structure. Included in the conical structure were four windows, the astro-sextant navigational hatch, and the main crew access hatch.

The conical heat shield protecting the outer structure of the crew compartment formed the center conical portion of the command module between the forward and aft heat shields. The conical heat shield was attached to the inner structure by load-transfer stringers and frames, and included equipment access panels, four windows, two hatches, the CM-SM umbilical, and two scimitar antennas.

The main heat shield, which was not a Block I design, but was of interim configuration and material for this flight, enclosed the blunt end of the command module. Three compression and three shear - compression pads were incorporated in the main heat shield to transmit loads from the CM to the SM. At the three shear - compression pads, tension tie bolts were attached to the crew compartment inner structure.

The forward compartment heat shield (apex cover) was of interim configuration for this mission and was secured to the crew compartment inner structure by four tension tie rods which were located within the apex cover jettison thruster assemblies.

The substructures for the heat shields were constructed of brazed steel honeycomb panels with the outer surfaces covered with ablative cork to simulate the Block I heat shield.

Service module: The service module was a Block I structural shell without the Block I subsystems installed. It consisted of an outer shell, radial beams, forward and aft bulkheads, and CM-SM fairing. (See fig. 5.2-3.)

The outer shell was divided into six basic panels of aluminum honeycomb material attached to the aluminum radial beams and to the forward and the aft bulkheads. Subpanels incorporated radiators for the environmental control subsystem (ECS) and the electrical power subsystem (EPS). The radiators were inactive for this mission. Reaction control subsystem (RCS) panels included one panel complete with Block I engine nozzles, and three panels with simulated engines installed.

The quad D RCS engines were prototype Block I with the exception of the solenoid valves which were mass simulated. A prototype quad housing, two propellant tank mass simulators, and one helium tank mass



simulator completed the quad D RCS assembly. Details of the prototype engine are shown in figure 5.2-4. Each dummy assembly of quads A, B, and C consisted of a prototype housing and four dummy engines which simulated the weight and center of gravity of the prototype engines. The radial beams transferred loads from the CM to the SM outer shell. The aft bulkhead was utilized to carry ballast. The service propulsion subsystem (SPS) components were not installed.

The CM-SM interface consisted of six compression mounting pads, one at the apex of each radial beam truss. Tension ties with shear pads were installed at the interfaces on radial beams 2, 4, and 6. (See fig. 11.2-13.) A production fairing extended between the service module and the command module.

Launch vehicle adapter: A launch vehicle adapter, or mating ring, 15 inches long, was used to attach the service module to the launch vehicle. Included in the adapter was a blast barrier of laminated fiberglass construction. Venting of the service module and adapter was accomplished through holes in the adapter.

5.2.3 LES tower leg loads. - The LES tower legs were instrumented with strain gages oriented to measure axial strain and calibrated in pounds of force (refer to table 11.2-I for exact location and range of the strain gages). A comparison of the maximum tensile and compressive measured flight loads with limit design loads is given in table 5.2-I. It should be noted that the limit design loads shown are based on Saturn V flight conditions.

During launch and pitch-up the loads experienced were low compared to the limit design loads based on a Saturn V launch. After abort initiation and separation from the launch vehicle, the spacecraft 002 LEV configuration was similar to the design condition configuration except for the center-of-gravity mass characteristics. The flight loads measured for the LEV during the tumbling abort were higher and more nearly comparable to the design loads, with the maximum being 85.8 percent of the design limit.

Figures 5.2-5 and 5.2-6 show time histories of the total bending moment and the total axial force at the LES-CM interface. These loads were calculated using the strain-gage data from the tower legs. As can be seen in these figures, the maximum bending moment experienced at this interface occurred during pitch-up, the maximum compressive axial force occurred during staging, and the maximum tensile axial force occurred during power-on abort.

If, as shown in table 5.2-I, the tower legs are considered individually, the combined bending moment and axial force during pitch-up

produced the maximum compressive load per leg, although the maximum total compressive axial force at the interface occurred during staging. The maximum tensile load per leg occurred during the tumbling abort as did the maximum total tensile interface load.

5.2.4 Command module loads.- Command module internal loads: Strain gages were installed in the CM as indicated in figures 11.2-6 to 11.2-9. Stresses calculated from the flight data for each of the instrumented members are shown in table 5.2-II for the launch, staging, pitch-up, tumbling abort, tower jettison, main parachute deployment, and earth-landing impact phases of the flight. The stresses shown in table 5.2-II for the heat shield hatch were the only ones indicating the maximum and minimum principal stresses for the conical heat-shield substructure. With the exception of levels measured during earth landing, the stress levels shown in table 5.2-II were very low, and indicate that the substructure was lightly loaded during the mission. The stresses measured in the crew compartment heat shield at impact were high in comparison with stresses measured during the flight, but were well below the capability of the brazed stainless steel honeycomb structure.

CM plume impingement loads: During the abort, the LEV tumbled as planned. The IES motor plumes impinging on the CM conical surface created high static pressures on the surface within the plume. The planned mission was to obtain a differential pressure across the conical heat shield of  $11.1 \pm 1.5$  psid in order to demonstrate the capability of the CM structure to withstand the limit design load. (Also see sections 5.0 and 5.1.) Figure 5.2-7 shows the maximum absolute pressures measured during the plume impingement and the internal cavity pressures measured at the same flight time. It can be seen in figure 5.2-7 that the maximum differential pressure indicated was 6.8 psid, based on the aft equipment compartment pressure measurement near the +Y axis, or 7.1 psid, based on the aft equipment compartment pressure measurement near the -Z axis. The measured differential pressure was lower than the planned pressure because: (a) the plume impingement pressures were approximately 80 percent of those predicted for a nominal mission, and (b) the internal pressure in the aft compartment was higher than planned by approximately 1.5 psi. (Refer to section 5.13.) Figure 11.2-5 shows the locations of the pressure measurements.

The CM aft equipment compartment vent system was designed in such a manner that compartment pressure would remain within  $\pm 1.0$  psi of ambient during flight. Preflight calculations for Mission A-004 showed that aft compartment pressure for the nominal mission was approximately 0.5 psi above ambient during abort. Postflight inspection and post-flight tests at the contractor's Downey facility (see section 5.13 and 8.2) indicated that there was inflight venting of the crew compartment, past the seals of the crew access inner hatch, into the area under the

conical heat shield structure (including the aft compartment). Additional air from the crew compartment could place an additional load on the aft equipment compartment venting arrangement.

Figure 5.2-8(a) to (c) shows the comparison of conical surface static pressures on the upwind pitch-plane surface, on the yaw-plane surface, and on the downwind pitch-plane surface. The cross-hatched area represents the pressure range from wind-tunnel data if the angle of attack were varied by  $\pm 5^\circ$ . The angles of attack represented by the plotted wind-tunnel data are calculated values for the spacecraft 002 flight, assuming no roll or yaw. Good agreement between the flight and wind-tunnel data is indicated on the upwind surface until about T+74.8 seconds.

The flight data show that at T+75 seconds the LEV rolled approximately  $5^\circ$  and yawed approximately  $8^\circ$ . To obtain a better comparison between the flight and wind-tunnel data, a more accurate measurement of angle of attack would be necessary. The uncertainty in accuracy of angle-of-attack measurement could possibly explain part of the disagreement between the flight and wind-tunnel data at the highest angle of comparison ( $\alpha = 48^\circ$ ). The pressures on the yaw plane and downwind surfaces do not vary as much with angle of attack as those on the upwind surface; therefore an error in angle-of-attack measurement is not as apparent.

The method used to obtain the wind-tunnel data shown in figure 5.2-8 consisted of using the pressures measured in the wind tunnel with no scaling applied to free-stream dynamic pressure. This was possible because the plumes envelope the command module, and the free-stream flow does not directly affect the surface pressures. This, in effect, means that the pressures within the plume are not a direct function of free-stream dynamic pressure but are primarily affected by altitude conditions.

**5.2.5 Service module internal loads.**— Strain gages were installed on both the inboard and outboard legs of the six radial beam trusses and on the three CM-SM tension ties (refer to table 11.2-I for location and range). All strain measurements on the truss members were calibrated in microinches per inch while those on the three tension ties were calibrated in pounds of force.

The axial strain on each truss member and the tension tie loads were converted to axial stress and are shown in table 5.2-III for the lift-off, staging, and pitch-up events. Also shown are the maximum stresses experienced during the mission and the times at which they occurred.

The largest stress experienced by the inboard truss members was 43 percent of its allowable (based on critical buckling stress of 47 000 psi) while the largest stress experienced by the outboard truss members was 39 percent of its allowable (based on a compressive yield of 71 000 psi for the material). The maximum stress experienced by a tension tie during flight was 30 percent of its allowable limit of 90 000 psi.

Generally, most of the strain experienced by the truss members was low during the greater part of the flight, and was less than 5 percent of the full-scale range of the instrumentation. The maximum measured values for the truss members were only 5 to 10 percent of full scale, and the maximum measurements for the tension ties were approximately 20 percent of full scale.

5.2.6 Interface body loads.- During Mission A-004 the maximum quasi-steady loads experienced by the spacecraft structural interfaces occurred during lift-off, staging, pitch-up, and the first abort tumble.

The net body loads at the LES-CM and CM-SM interfaces were calculated using the flight trajectory parameters together with wind-tunnel aerodynamic data. In figure 5.2-9 loads calculated at the CM-SM and SM-adaptor interfaces are compared with the interface limit load capability. A summary of the flight trajectory parameters used to determine these loads is shown in table 5.2-IV. None of the load conditions shown in figure 5.2-9 exceeded the limit load capability of the interfaces. Load condition 6 in figure 5.2-9 was on the limit load design envelope itself because the axial force at the time of abort was approximately twice the planned value. The axial force was high because of the early abort, at which time the launch vehicle thrust was approximately 5 to 6 times as high as for the planned time for the abort. (See table 4.1-I and figs. 6.1-3 and 6.1-4.)

Strain-gage instrumentation on the LES tower legs, on the SM radial beam trusses, and on CM-SM tension ties were also utilized to calculate interface loads for these two interfaces. The data from the instrumentation on the tower legs were used to calculate both axial force and bending moment. The structural geometry of the CM-SM interface restricted the use of the flight data to the determination of axial forces only.

Table 5.2-V shows a comparison of the LES-CM interface axial loads calculated using flight trajectory parameters, those calculated from strain-gage data, and the limit design loads. The flight loads shown did not exceed the limit design, and the calculated loads were in good agreement.

The CM-SM interface loads calculated from flight trajectory parameters and from strain-gage data are presented in table 5.2-VI. Axial force agreement is only fair. Calculations of bending moment and shear using strain-gage data were not considered valid.

TABLE 5.2-1.- LAUNCH-ESCAPE SUBSYSTEM TOWER LEG LOADS, MISSION A-004

Strain gage location	Maximum LES tower leg loads, lb				Limit design load (a)		Flight loads versus limit design loads, percent (b)
	Lift-off	Staging	Pitch-up	Tumbling abort	Flight condition	Load, lb	
Tower leg load +Y, +Z	-6 550	-10 110	4 120	34 470	Lift-off Tumble abort (max q)	-27 200 45 800	37.2 75.40
Tower leg load +Y, -Z	-7 260	-11 550	-15 200	30 690	Lift-off Tumble abort (max q)	-27 200 35 800	55.9 85.80
Tower leg load -Y, +Z	-6 090	-8 390	-2 900	36 590	Lift-off Tumble abort (max q)	-27 200 45 800	30.8 79.90
Tower leg load -Y, -Z	-7 310	-8 350	-14 800	29 430	Lift-off Tumble abort (max q)	-27 200 35 800	54.4 82.40

<sup>a</sup>Based on Saturn V flight conditions<sup>b</sup>Based on maximum flight loads shown

TABLE 5.2-II.- COMMAND MODULE SUBSTRUCTURE STRESSES, MISSION A-004

Strain gage location	Stress, psi						
	Lift-off (T=0.5 sec)	Staging (T=36.5 sec)	Pitch-up (T=72.7 sec)	Tumble abort (T=73.7 to 79.0 sec)	Tower jettison (T=193.8 sec)	Main parachute deployment (T=237.6 sec)	Landing impact (T=409.7 sec)
Tower longeron no. 2 gusset, side	-1 570.00	-651.00	164.40	-2 420.00	-1 271.00	(a)	(a)
Tower longeron no. 2 gusset, edge	454.00	1 050.00	1 621.00	-2 440.00	-124.50	(a)	(a)
Tower longeron no. 4 gusset, side	-369.00	143.20	-369.00	-1 027.00	-510.00	(a)	(a)
Tower longeron no. 4 gusset, edge	-1 513.00	-1 010.00	-644.00	-5 740.00	-925.00	(a)	(a)
Tower longeron no. 8 gusset, side	923.00	1 262.00	1 448.00	-2 675.00	327.00	-109.90	469.00
Tower longeron no. 8 gusset, edge	505.00	894.00	1 623.00	-3 650.00	-532.00	-313.00	-408.00
Top forward longeron no. 2, outer	-735.00	-1 367.00	-2 640.00	5 610.00	290.00	-211.00	-3 740.00
Top forward longeron no. 2, inner	(b)	(b)	(b)	(b)	-1 450.00	-1 227.00	-8 570.00
Bottom forward longeron no. 2, outer	-437.00	-525.00	-665.00	-4 920.00	-129.90	-219.00	-1 075.00
Bottom forward longeron no. 2, inner	(b)	(b)	(b)	(b)	-612.00	-985.00	-4 000.00
Top forward longeron no. 4, outer	-495.00	-2 760.00	1 260.00	10 880.00	103.20	112.90	2 522.00
Top forward longeron no. 4, inner	383.50	-1 612.00	1 360.00	9 240.00	3 160.00	3 150.00	-844.00

<sup>a</sup>Tape recorder "F" stopped at T=210 sec (refer to section 5.12).

<sup>b</sup>Flight data invalid during flight (refer to section 5.12).

Note: Stresses included in this table are the maximums occurring during each of the noted events.

TABLE 5.2-III.- COMMAND MODULE SUBSTRUCTURE STRESSES, MISSION A-004 - Continued

Strain gage location	Stress, psi						
	Lift-off (T=0.5 sec)	Staging (T=36.5 sec)	Pitch-up (T=72.7 sec)	Tumble abort (T=73.7 to 79.0 sec)	Tower jettison (T=193.8 sec)	Main parachute deployment (T=237.6 sec)	Landing impact (T=409.7 sec)
Bottom forward longeron no. 4, outer	-2 077.00	-2 310.00	-840.00	-5 040.00	-1 162.00	-844.00	-5 190.00
Bottom forward longeron no. 4, inner	-2 890.00	-6 190.00	17.44	9 390.00	-1 382.00	-1 260.00	-3 110.00
Top forward longeron no. 8, outer	-1 289.00	-2 680.00	-4 090.00	4 840.00	-975.00	-848.00	-2 100.00
Top forward longeron no. 8, inner	565.00	1 012.00	1 059.00	2 620.00	266.00	210.00	-5 040.00
Bottom forward longeron no. 8, outer	-1 148.00	-1 080.00	-1 440.00	-3 190.00	-121.80	(a)	(a)
Bottom forward longeron no. 8, inner	-2 190.00	-2 270.00	-3 640.00	5 920.00	-148.40	(a)	(a)
Vertical gage, outer, hatch beam	-671.00	-744.00	-597.00	-644.00	-514.00	-588.00	-4 080.00
Vertical gage, inner, hatch beam	-286.50	-1 710.00	-2 170.00	-2 140.00	-428.00	-355.50	-3 980.00
Hatch heat shield, horizontal, outer	2 510.00	646.00	672.00	2 715.00	670.00	335.00	14 530.00
Hatch heat shield, horizontal, inner	-1 190.00	-709.00	-351.00	-5 790.00	-172.80	-3 540.00	11 900.00
Hatch heat shield, vertical, outer	2 100.00	890.00	-357.00	101.40	284.00	-796.00	12 700.00
Hatch heat shield, vertical, inner	-856.00	-1 330.00	-335.00	-6 990.00	-473.00	-3 210.00	14 500.00

<sup>a</sup>Tape recorder "F" stopped at T=210 sec (refer to section 5.12).

Note: Stresses included in this table are the maximums occurring during each of the noted events.



TABLE 5.2-II.- COMMAND MODULE SUBSTRUCTURE STRESSES, MISSION A-004 - Concluded

Strain gage location	Stress, psi						
	Lift-off (T=0.5 sec)	Staging (T=36.5 sec)	Pitch-up (T=72.7 sec)	Tumble abort (T=73.7 to 79.0 sec)	Tower jettison (T=193.8 sec)	Main parachute deployment (T=237.6 sec)	Landing impact (T=409.7 sec)
Side heat shield, horizontal, outer	(b)	(b)	(b)	(b)	(b)	(b)	(b)
Side heat shield, horizontal, inner	-975.00	-1 190.00	-2 495.00	4 290.00	-526.00	-314.00	6 700.00
Side heat shield, vertical, outer	-290.00	1 185.00	1 185.00	8 360.00	3 050.00	2 335.00	6 940.00

<sup>b</sup>Flight data invalid during flight (refer to section 5.12).

Note: Stresses included in this table are the maximums occurring during.

TABLE 5.2-III.- SERVICE MODULE RADIAL BEAM TRUSS AND TENSION TIE STRESSES DURING MISSION A-004

Gage location	Stress, psi			Maximum stress	
	Lift-off (T=0.5 sec)	Staging (T=36.5 sec)	Pitch-up (T=72.7 sec)	Stress, psi	Time, sec
Tension tie, beam 2	15 650	5 210	16 000	21 100	13.260
Tension tie, beam 4	15 950	9 550	6 990	21 370	2.914
Tension tie, beam 6	19 200	14 500	483	27 050	2.518
Inboard leg, beam 1	-4 630	-8 920	-9 080	-9 539.35	73.601
Outboard leg, beam 1	-10 500	-18 930	-21 000	-28 165.51	73.702
Inboard leg, beam 2	-8 400	-15 920	-7 980	-15 477.52	38.044
Outboard leg, beam 2	-15 220	-19 850	-17 980	-19 904.85	40.020
Inboard leg, beam 3	-3 460	-8 100	-3 560	-8 758.15	70.020
Outboard leg, beam 3	-13 940	-21 700	-15 650	-22 929.06	68.533
Inboard leg, beam 4	-8 940	-11 600	-11 000	-14 629.86	70.020
Outboard leg, beam 4	-13 600	-19 080	-17 100	-19 244.08	70.020
Inboard leg, beam 5	-4 460	-8 340	-13 300	-13 797.42	73.663
Outboard leg, beam 5	-17 950	-21 200	-19 950	-21 221.65	36.567
Inboard leg, beam 6	-8 820	-12 550	-18 380	-20 076.00	73.663
Outboard leg, beam 6	-9 970	-7 120	-6 500	-10 974.70	36.467

Tension tie allowable limit, psi . . . . . 90 000  
 Inboard leg critical buckling stress, psi . . . . . 47 000  
 Outboard leg compressive yield stress, psi . . . . . 71 000

TABLE 5.2-IV.- MISSION A-004 FLIGHT TRAJECTORY PARAMETERS FOR  
INTERFACE LOAD CONDITIONS

[Refer to fig. 5.2-9]

Time from lift-off, sec	Mach number	Dynamic pressure, lb/ft <sup>2</sup>	$\alpha$ , deg	$\beta$ , deg	$\ddot{X}/g$	$\ddot{Y}/g$	$\ddot{Z}/g$	$\ddot{\theta}$ , rad/sec <sup>2</sup> (a)
T+0.5	-	-	-	-	2.72	0.025	-0.15	$\approx 0$
T+36.56	0.82	480	2.2	-4.4	3.6	-.12	-.20	$\approx 0$
T+39.44	1.02	690	2.3	-2.0	2.3	-.12	-.22	$\approx 0$
T+70.0	2.2	613	2.1	0.5	2.55	.1	-.32	-0.01
T+72.7	2.39	588	-11.7	.6	2.55	.14	1.50	.30
T+73.6	2.42	580	-11.1	.4	2.35	.16	1.40	.03

<sup>a</sup>The  $\ddot{\theta}$  values used were calculated using rate gyro and linear accelerometer data and therefore must be considered approximate.

Note.- Related mission events: Lift-off, staging (36.4 sec), max q (40.1 sec) pitch-up (70.8 sec), and abort (73.7 sec).

TABLE 5.2-V.- COMPARISON OF LES-CM INTERFACE LOADS

Time from lift-off, sec (a)	Loads calculated using flight trajectory parameters	Loads calculated using strain-gage data	Limit design loads
	Axial force, lb	Axial force, lb (b)	Axial force, lb
T+0.5	-21 100	-21 365	-98 800
T+36.56	-30 400	-36 738	-98 800
T+39.44	-21 000	-24 422	-98 800
T+70.0	-24 100	-25 281	-98 800
T+72.7	-24 800	-23 337	-98 800
T+73.6	-23 000	-18 800	-98 800
T+75.39	--	112 130	163 200
T+75.69	--	113 974	163 200

<sup>a</sup>See table 5.2-IV for condition flight parameters.

<sup>b</sup>Includes effects of structural dynamics.

Note.— Related mission events: Lift-off, staging (36.4 sec),  
Max q (40.1 sec), pitch-up (70.8 sec), and abort (73.7 sec).

TABLE 5.2-VI.- COMPARISON OF CM-SM INTERFACE LOADS FROM  
STRAIN DATA AND FLIGHT PARAMETERS

Flight time, sec (a)	Loads calculated using flight trajectory parameters			Loads calculated using strain-gage data
	Shear, lb	Axial force, lb	Bending moment, in. -lb	Axial force, lb
T+0.5	2 870	-51 400	$0.458 \times 10^6$	-64 703
T+36.56	6 600	-85 600	.065	-97 244
T+39.44	6 800	-94 200	.187	-106 030
T+70.0	1 010	-88 100	.569	-102 838
T+72.7	1 600	-91 600	1.105	-92 005
T+73.6	1 800	-86 400	1.903	-90 913

<sup>a</sup>See table 5.2-IV for condition flight parameters.

Note.- Related mission events: Lift-off, staging (36.4 sec),  
Max q (40.1 sec), pitch-up (70.8 sec), and abort (73.7 sec).

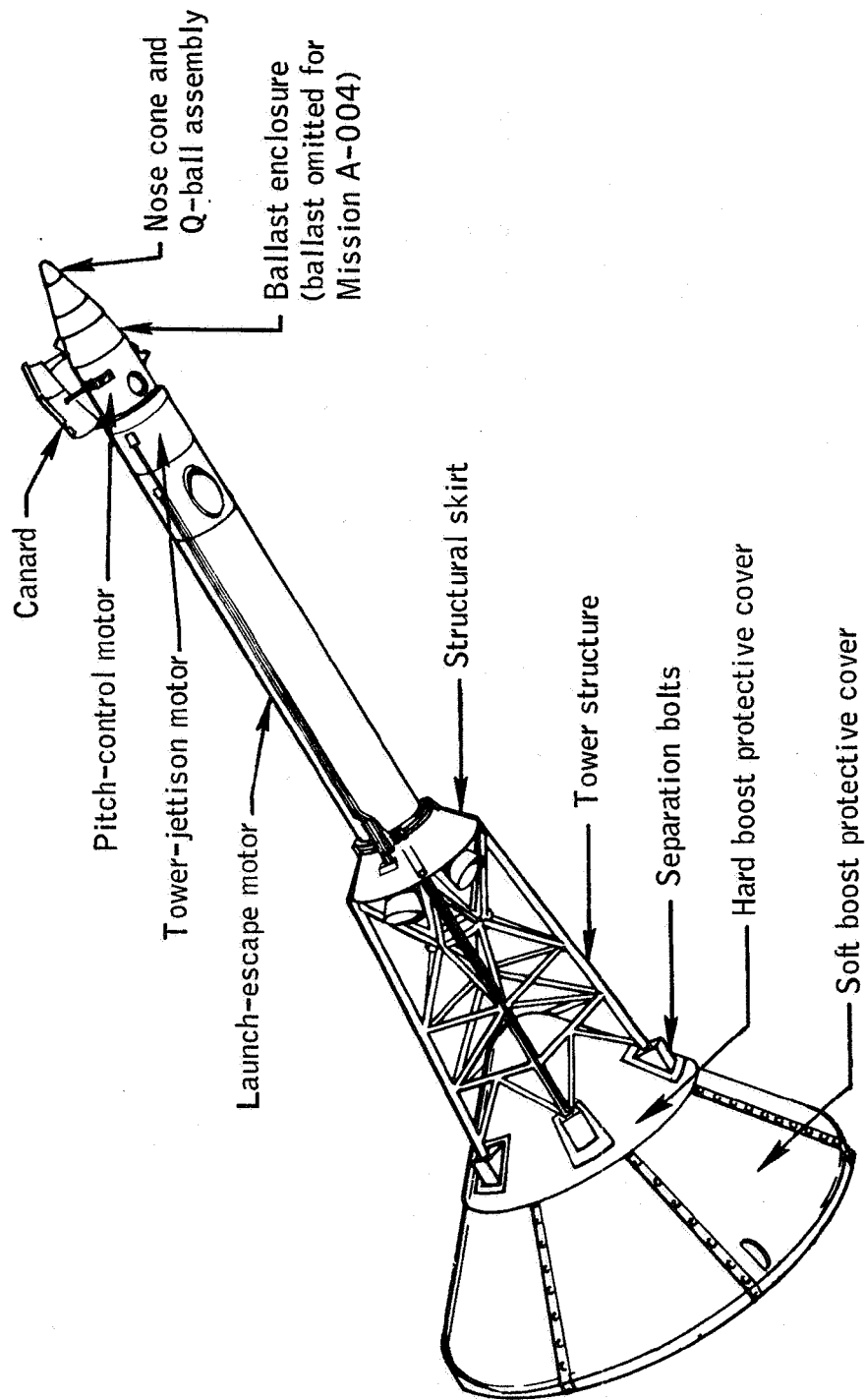


Figure 5.2-1.- Launch-escape subsystem structure, Apollo Mission A-004.

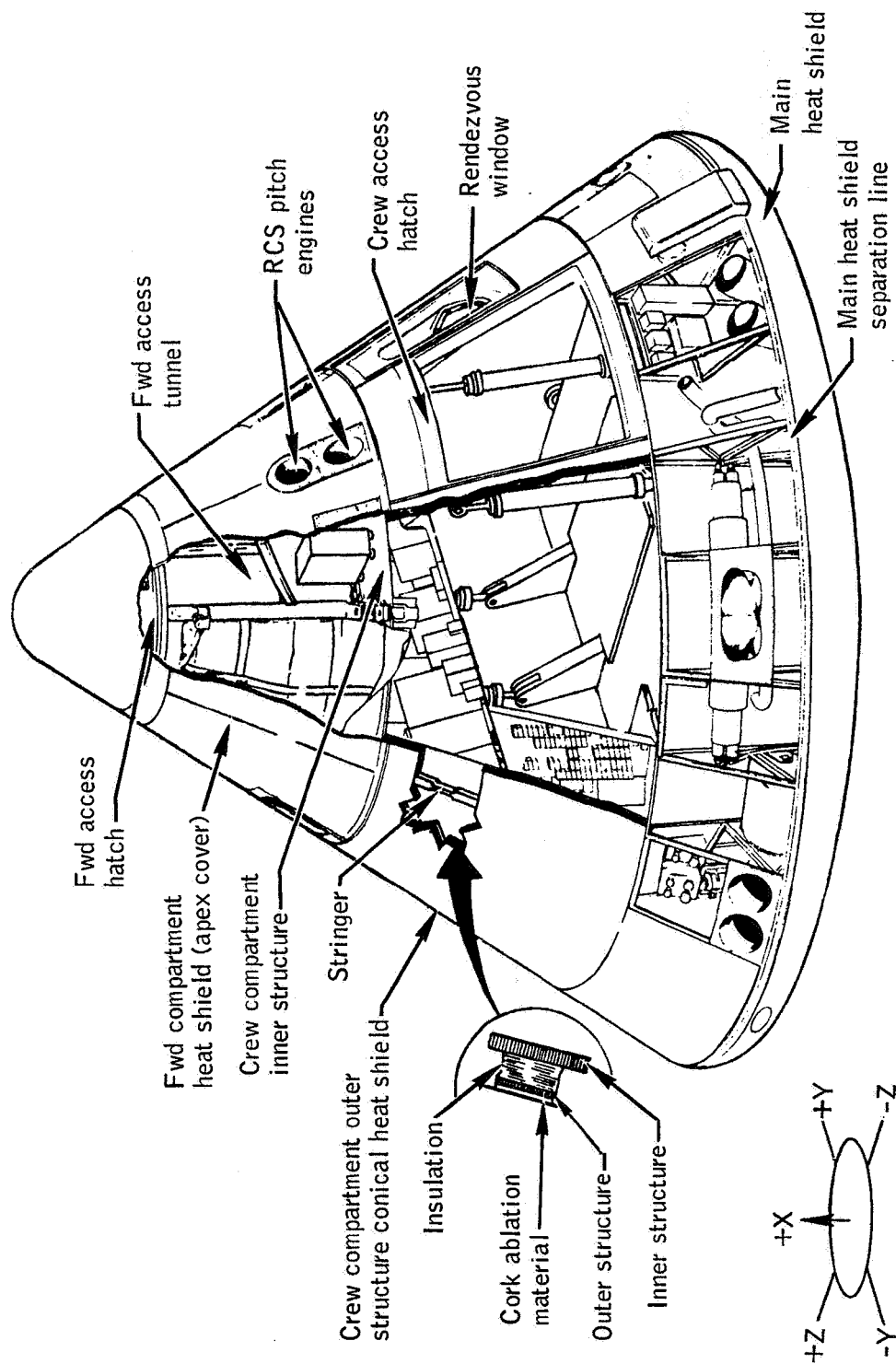


Figure 5.2-2.- Command module structure, Apollo Mission A-004.

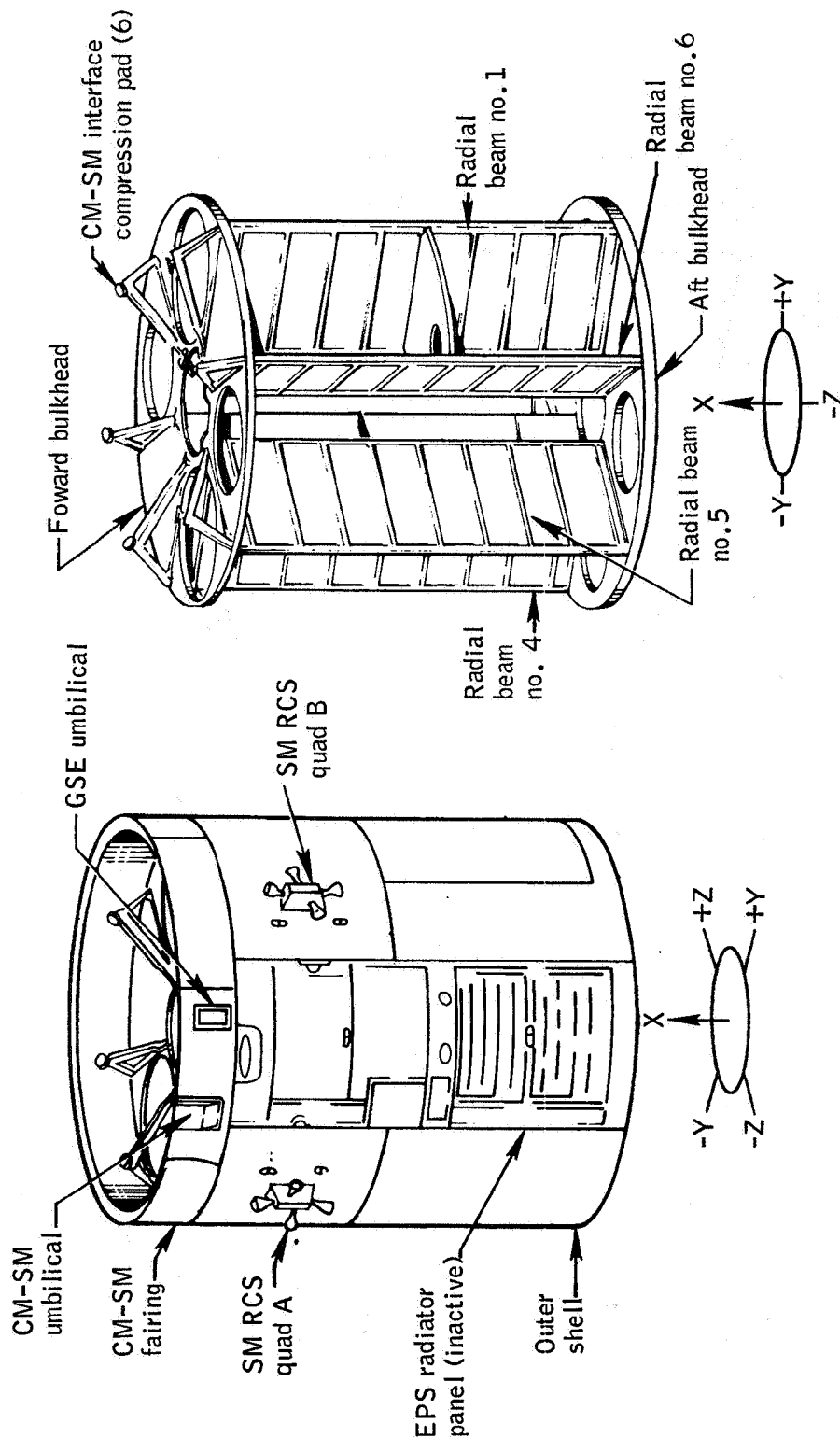
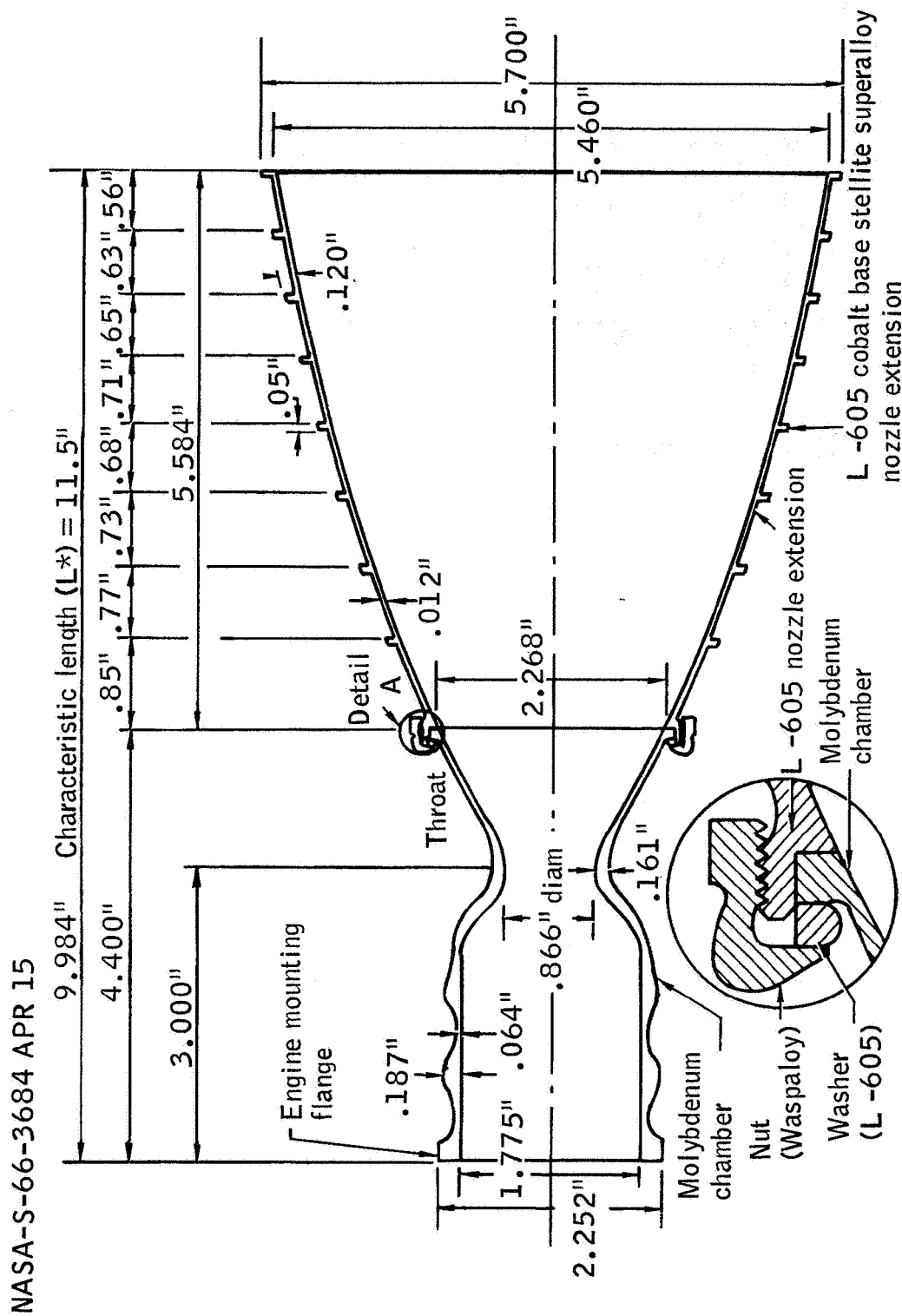


Figure 5.2-3.- Service module construction, Apollo Mission A-004.





Chamber-nozzle extension joint at an expansion area ratio ( $A_c/A_t$ ) of 7.0.

Figure 5.2-4.- Quad D prototype SM RCS engine chamber and nozzle extension, Apollo Mission A-004

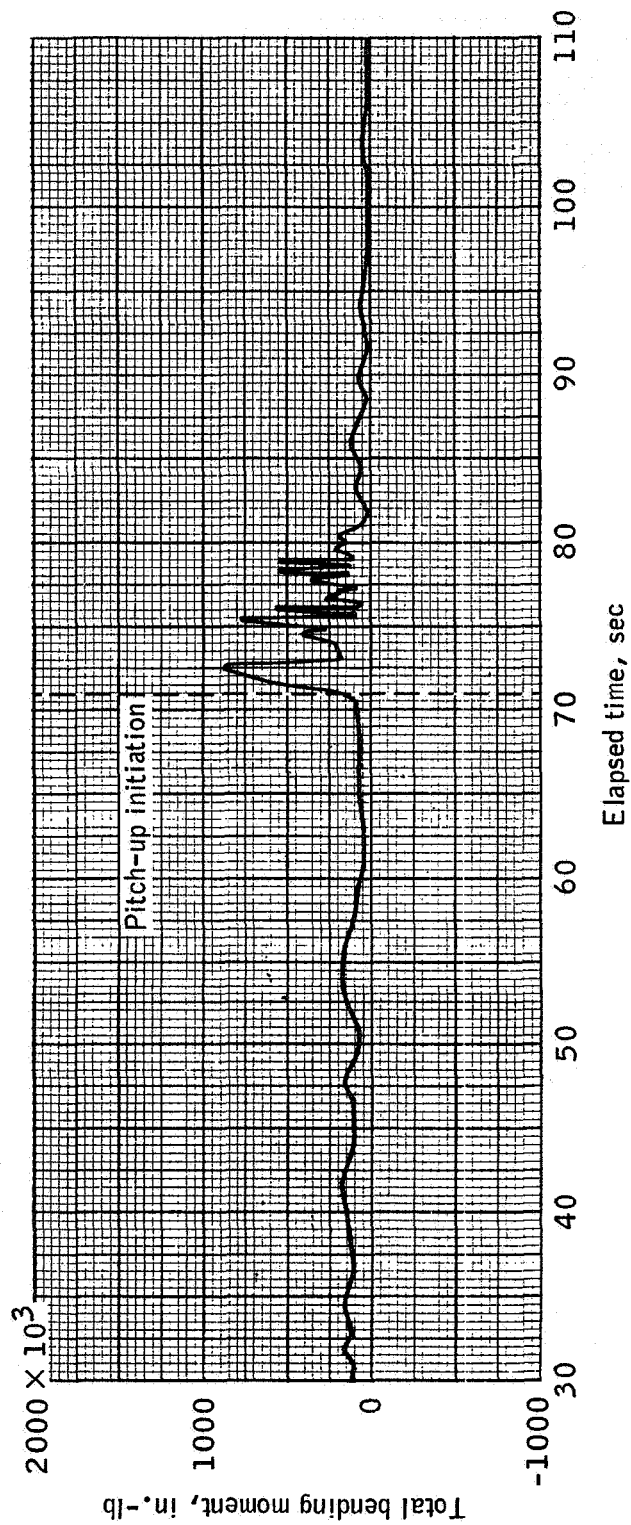


Figure 5.2-5.- LES-CM interface total bending moment calculated from tower leg strain gage data, Apollo Mission A-004.

NASA-S-66-3692 APR 15

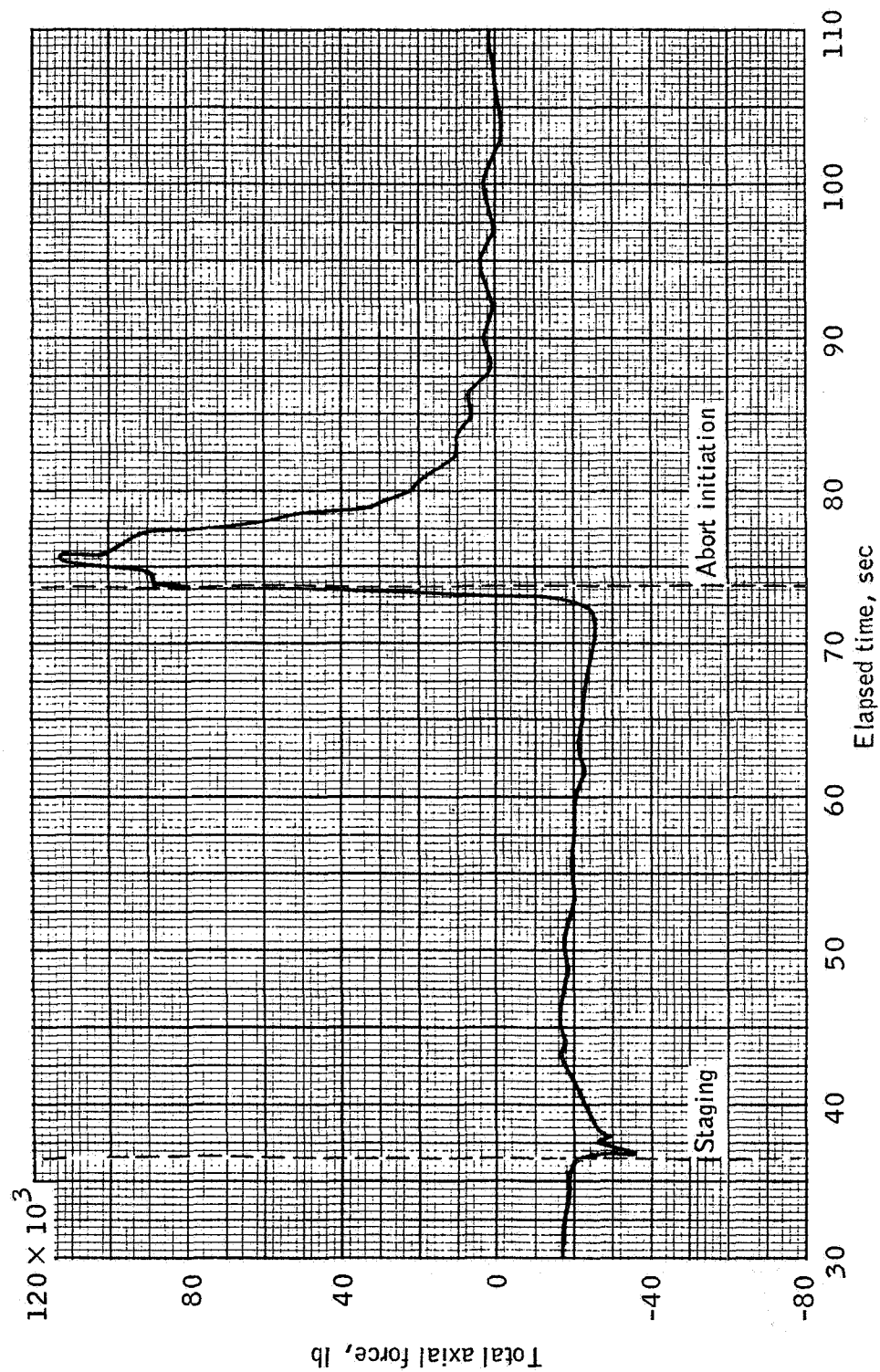


Figure 5.2-6.- LES-CM interface total axial force calculated from tower leg strain gage data, Apollo Mission A-004.

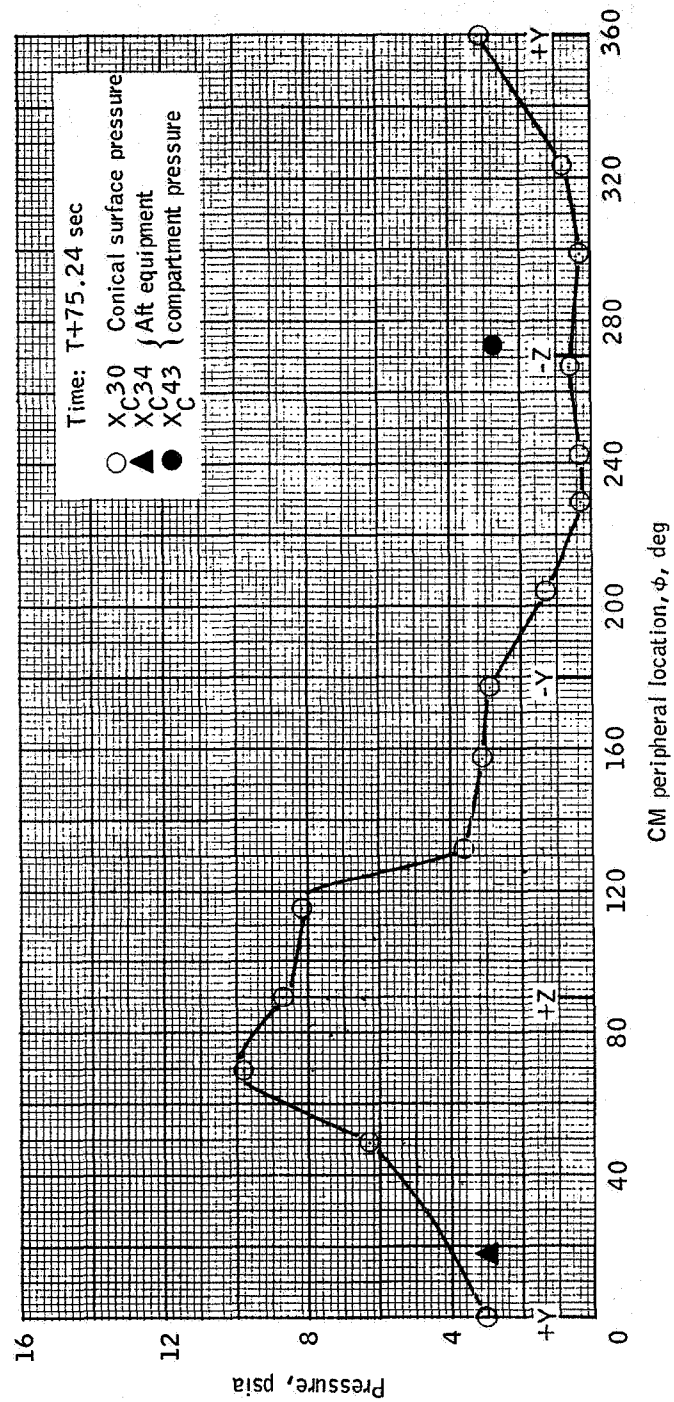


Figure 5.2-7.- Maximum conical surface plume impingement pressure and aft equipment compartment pressure measured on CM, Apollo Mission A-004.

5-30

NASA-S-66-3700 APR 15

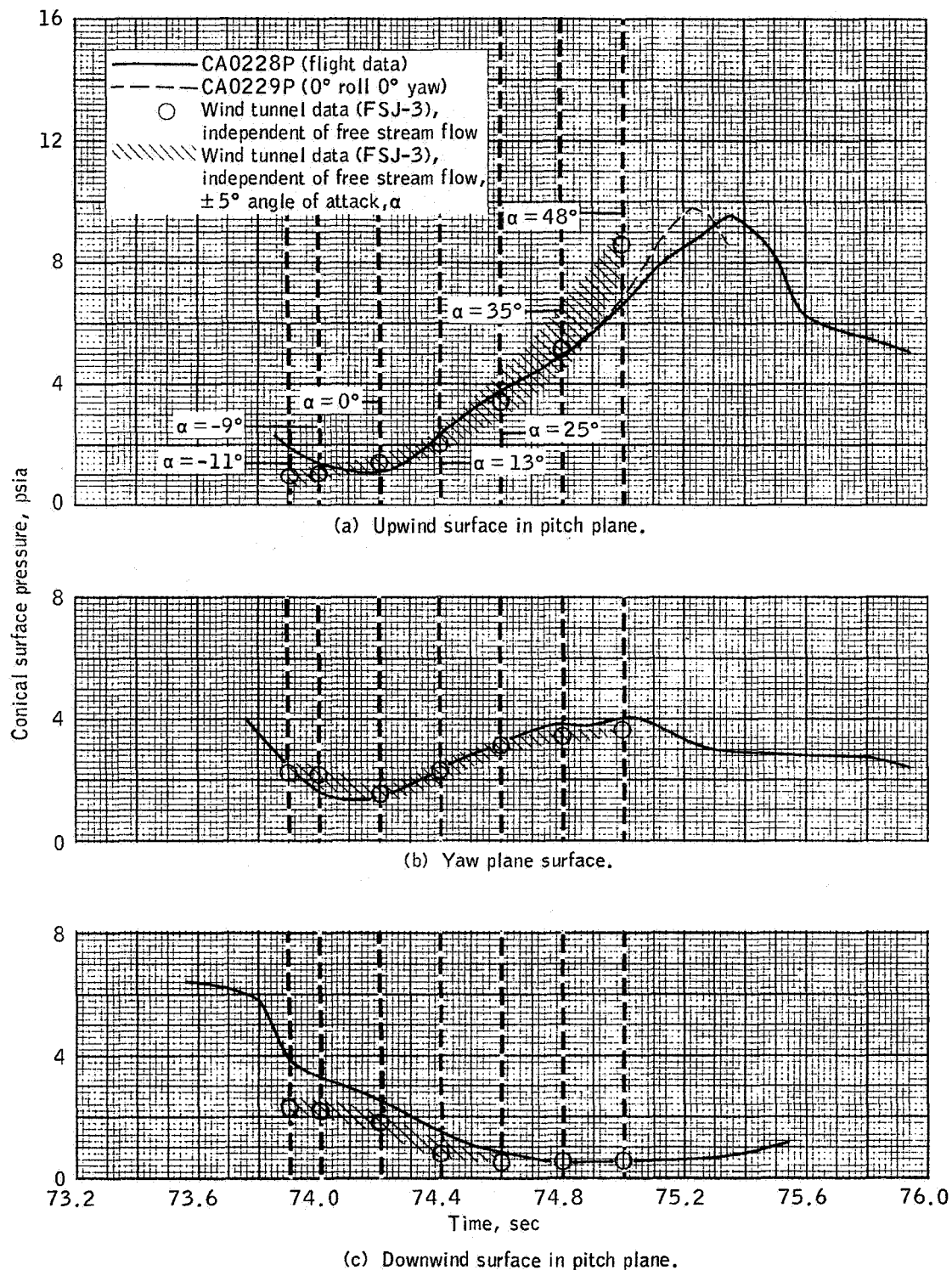


Figure 5.2-8.- Conical surface plume impingement pressures on Mission A-004.

Load condition ident a	Time, sec	Related Mission events
1	0.5	Lift-off
2	36.56	Staging (36.4)
3	39.44	Max q (40.1)
4	70.0	Pitch-up (70.8)
5	72.7	
6	73.6	Abort (73.7)

$4 \times 10^6$  a See Table 5.2-IV

Limit design load notes:

- (a) Loads at 312°F
- (b) Pretension 12 000 lb
- (c) Envelope indicates capability of tension tie only
- (d) SM truss or CM pad capability could be less than tension tie
- (e) Failure mode:  
Tension: Rupture of tension tie  
Compression: Unspecified
- (f) Method of determining failure:  
Tension: Analysis (original Block I loads)  
Compression: Design loads use as capability
- (g) Capability is affected by shear

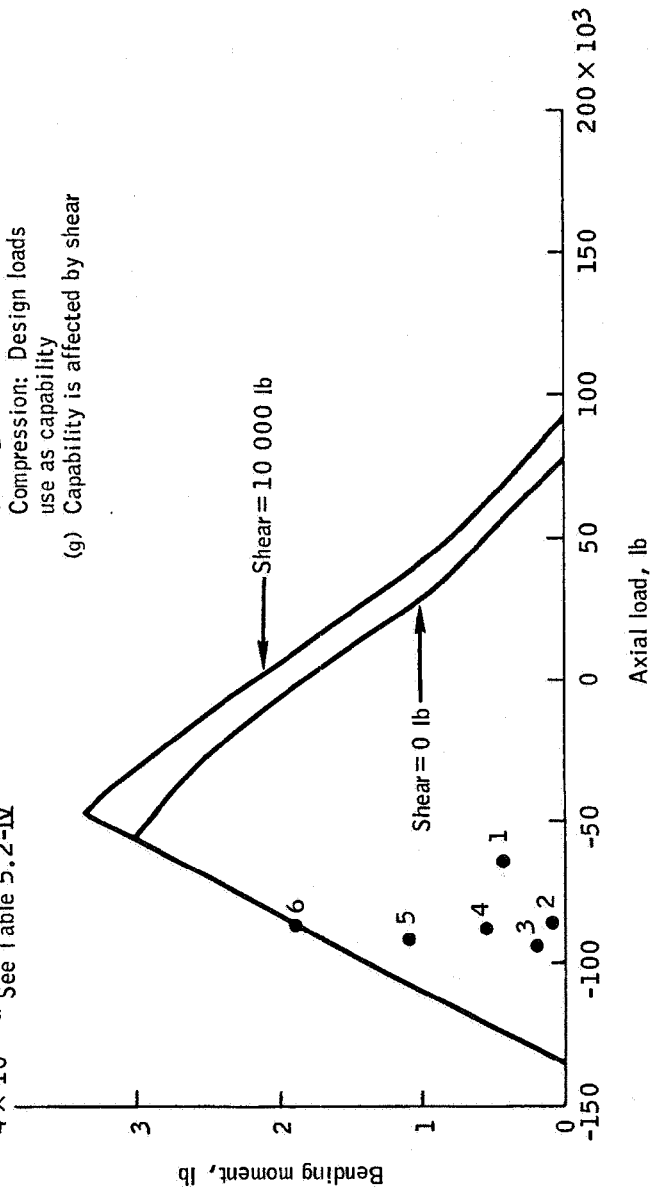


Figure 5.2-9.- CM-SM interface (station X<sub>A</sub>1010) Block I limit design load capabilities envelope and maximum load conditions, Apollo Mission A-004.

### 5.3 Structural Dynamics

5.3.1 Summary.- Examination of all spacecraft strain, pressure, and acceleration data indicated that the spacecraft performed adequately in the launch environment.

Command module X-axis oscillatory accelerations of 2.4g peak-to-peak were measured at engine staging. The predominant frequency was 14 cps. These oscillations damped out within 1 second and are of no consequence structurally.

Power spectral analyses of Y- and Z-axis accelerations showed a predominant frequency of 36 cps throughout the powered phase of flight. Small excitations of the first and second free-free bending modes of the launch vehicle were noted in oscillograph records. The first free-free bending mode of the launch escape vehicle (LEV) was excited at abort. Maximum bending moments caused by these oscillations were low and of no structural consequence.

Service module fluctuating pressure data show levels approximately the same as those of boilerplate flights; however, the effects of the larger angle of attack on the complete pressure environment could not be assessed since no measurements were made on the windward side of the spacecraft.

Service module outer shell and interior vibration data show levels much lower than those obtained in acoustic tests simulating the flight environment. One exception to this is the vibration level of the inner flange of radial beam 5 which was approximately the same as that obtained in the acoustic tests, although the spectral distribution was different. This high level indicates a much greater transmissibility from the outer shell to the radial beam inner flange than was obtained in the acoustic tests. At present this phenomenon is not understood.

Service module RCS engine nozzles experienced vibration levels approximately twice those obtained on the simulated nozzles of BP-15 (ref. 12). At present the mode associated with the predominant frequency of vibration, 490 cps, is unknown.

Service module strain data showed extremely low levels which were generally within the noise of the instrumentation system.

Acoustic data taken inside the CM indicated levels lower than those of simulated flight environment in ground tests.

Command module vibration data show levels lower than those obtained in acoustic tests. The majority of data throughout flight were close to the noise of the instrumentation system.

### 5.3.2 Vehicle low frequency vibrations.-

CM X-axis vibrations: Two accelerometers, located in the CM as shown in figure 11.2-5, were used to measure X-axis low-frequency vibrations.

The maximum boost low-frequency vibration occurred at T+36.5 seconds, the time of second-stage ignition, as shown in the rms time history of figure 5.3-1. Oscillograph records indicate that the magnitude of the vibration was 2.4g peak-to-peak at a frequency of 14 cps at this time. Figure 5.3-2 is an acceleration spectral density plot which shows all vibratory energy in the period from T+36.5 seconds to T+39.5 seconds to be concentrated at this frequency. The oscillation was damped out completely within 1 second after staging, and is therefore considered to be of no consequence.

Y-axis and Z-axis vibrations: The test vehicle was instrumented with eight accelerometers which measured low-frequency vibrations along the Y-axis and Z-axis of the vehicle. Two measurements, LA0011A and LA0012A, were provided in the forward extremity of the LES, and two measurements, CA0005A and CA0007A, in the CM. Four measurements were located in the LJ II launch vehicle. Two measurements, BB0122A and BB0123A, were on the forward bulkhead, and two measurements, BB0048A and BB0049A, on the aft bulkhead. The LES and CM accelerometers were ranged  $\pm 5g$ , and the launch vehicle accelerometers were ranged  $\pm 2g$ .

The Z-axis LES accelerometer showed maximum low-frequency vibrations during launch and abort to be 2g and 9.7g peak-to-peak, respectively. The maximum level for the launch phase occurred at a frequency of 36 cps and lasted from T+30 seconds to T+55 seconds. This frequency is shown to possess maximum energy in the acceleration spectral density plot of figure 5.3-3. The maximum LEV abort vibration level also occurred at 36 cps. These frequencies are well above those of the lowest predicted test vehicle and LEV free-free bending mode shapes. The associated mode of vibration is unknown; however, vibration at this frequency is of little concern since the maximum displacements produced are 0.015 inch and 0.072 inch, respectively.

The rms time history of the Z-axis tower accelerometer is shown in figure 5.3-4. In general, the Y-axis tower accelerometer showed the same vibration characteristics with slightly lower levels.



Analysis of the LES data showed small excitation of the lower free-free bending modes for both the LEV and the SC-002/LJ II test vehicles during flight. The acceleration of the test vehicle at lift-off was 1.3g peak-to-peak at 3 cps. The predicted value for this first free-free bending mode frequency was 3.4 cps. The acceleration spectral density plot of figure 5.3-5 shows the maximum energy concentrated at approximately 3 cps. At T+15 seconds, a maximum response of 0.7g peak-to-peak was noted at the predicted second bending mode frequency of 11 cps. After abort, a maximum response of 7.5g peak-to-peak was obtained at 9 cps. The predicted frequency for this LEV first free-free bending mode was 9.7 cps.

Oscillations at the first mode frequencies of the two configurations produce maximum interface bending moments as shown in the following table. These bending moments, when combined with the static moments, lie well within the limit-load capability.

Configuration	First free-free bending mode frequency, cps	Interface bending moment			
		LES skirt-tower $X_A = 1221$ , in-lb	Tower-CM $X_A = 1083$ , in-lb	CM-SM $X_A = 1010$ , in-lb	SM-fairing $X_A = 838$ , in-lb
SC-002/LJ II	3	$2.09 \times 10^5$	$4.19 \times 10^5$	$4.99 \times 10^5$	$5.31 \times 10^5$
LEV	9	$6.75 \times 10^5$	$2.76 \times 10^5$	--	--

The CM Y-axis and Z-axis acceleration data exhibited similar waveforms at corresponding times. As was expected, the magnitudes for the CM measurements were much lower than those given by the LES measurements (see ref. 1).

### 5.3.3 Service module dynamics.

Fluctuating pressures: Spacecraft 002 was instrumented with two pressure transducers to measure SM fluctuating pressures during atmospheric flight. Transducer SA0957P was located on the SM exterior surface near the -Y axis and 26.8 inches forward of the RCS quad D centerline (see fig. 11.2-19) which was within an area in which pressure levels change rapidly with axial distance from the RCS engine.

Figure 5.3-6, which presents rms pressure plotted against vehicle station obtained from PSTL-1 wind-tunnel data, illustrates the effect of the RCS protuberance in this region during transonic flight. No previous flights had transducers at this exact position. However, data from measurement SA0186P (Mission A-101, ref. 13) and SA0957P (Mission A-004), indicated approximately the same overall sound pressure level and are shown for comparison of figure 5.3-7. Additional comparison of SM fluctuating pressure can be made using measurements SA0958P (Mission A-004), SA0166P and SA0164P (Mission A-102, ref. 12), located at comparable SM position. This comparison is made in figure 5.3-8. All figures indicate data which are corrected to dynamic pressures of SC-002 flight trajectory. The maximum overall sound pressure levels obtained from the rms time histories of figures 5.3-9 and 5.3-10 are 161.5 dB (0.345 psi) and 157.6 dB (0.22 psi) for SA0957P and SA0958P, respectively.

In general, maximum overall sound pressure levels of the SC-002 transducers agree with levels obtained in previous flights at comparable SM locations. These values are compared with data from previous flights in figure 5.3-11.

It is worth noting that the SC-002 maximum overall SPL's occurred at a Mach number of approximately 0.85 while previous flights showed maximum levels occurring at  $M = 0.80$ . This Mach number shift, as illustrated in rms Mach histories of figure 5.3-8, is believed to have been caused by the larger angles of attack obtained in the SC-002 flight. This phenomenon has been noticed in wind-tunnel tests as angle of attack,  $\alpha$ , is increased from 0 degrees (refs. 14 and 15). This effect is caused by a delay of the subsonic flow separation from the windward CSM shoulder. Figure 5.3-12 presents a comparison of angle of attack plotted against Mach number for Missions A-004, A-101, and A-102. The angle-of-attack effect is also known to cause pressure fluctuations which are larger on the leeward half of the SM than on the windward half for angles of attack greater than 0 degrees (ref. 16). As much as 5 dB differences have been noted between windward and leeward sides of the SM at  $\alpha = 4^\circ$  (ref. 15).

The two SC-002 measurements are known to lie on the leeward side of the SM and, therefore, would be expected to indicate the maximum values for their respective axial and circumferential locations as opposed to similar locations on the windward side of the SM. Since the SC-002 angle of attack was generally greater than  $3.5^\circ$  during the transonic region of Mission A-004, it is possible that the SC-002 data represent maximum pressures rather than pressures which are more or less symmetrically distributed around the SM, as were the pressures on previous flights. If this case exists, the fluctuating pressure environment of the complete SM, as well as the corresponding SM vibration response, could be down as much as 50 percent from that of previous

flights. Further analysis will be required to determine if such a case did exist.

The pressure spectral density, when compared with applicable data from Mission A-102 (BP-15) in figure 5.3-13, seems to possess approximately the same frequency distribution of energy. The lower energy levels can be attributed to the large time slice used in the data reduction which encompassed the large drop in pressure that occurred between T+37 seconds and T+39 seconds (fig. 5.3-10). The pressure spectral densities for the two SC-002 measurements are given in figures 5.3-14 and 5.3-15.

Outer shell vibrations: Nine radial vibration measurements were made on the SM. One of these measurements was located on the fairing at station  $X_S$  373.1 at 187.5°. These measurements were ranged to measure amplitudes of 1000g peak-to-peak with a frequency response from 10 to 400 cps. All measurement locations are shown in figure 11.2-19.

Plots of rms time histories are presented in figures 5.3-16 and 5.3-17. These plots indicate that the maximum vibration levels occur during the lift-off, transonic, and supersonic periods. Vibration values range from 17.1g (rms) to 36.0g (rms) during the transonic period of flight. Maximum values during both transonic and supersonic periods are presented in the following table:

Accelerometer number	Transonic region		Supersonic region	
	Mach number	Maximum level, g(rms)	Mach number	Maximum level, g(rms)
SA0940D	0.78	22.0	1.83	22.5
SA0944D	.84	31.0	1.72	30.0
SA0945D	.84	36.0	1.68	28.0
SA0946D	.84	27.5	1.55	20.8
SA0947D	.84	22.0	1.62	20.0
SA0948D	.87	17.1	1.55	14.9
SA0949D	.84	20.5	1.90	18.0
SA0950D	.84	19.0	1.62	18.0
SA0952D	.84	29.0	Data invalid beyond T+55 sec	

These values show rms levels approximately 30 to 50 percent of those experienced in the spacecraft 007 acoustic tests. (See ref. 17.)

The frequency composition of energy during transonic flight is presented in spectral density plots (figs. 5.3-18 and 5.3-19). A comparison of the frequency distribution of SM measurements indicated no consistent trend as was indicated in boilerplate flights. Energy levels were approximately 10 percent of the levels experienced in the SC-007 acoustic tests.

Figure 5.3-20 is representative of shell vibration energy distribution for the lift-off period and illustrates the significant difference in frequency distribution of energy when compared with the transonic condition of figure 5.3-19(b).

Interior vibrations: Four vibration measurements were made on the interior structure of the SM at locations shown in figures 11.2-17 and 11.2-18.

Measurement SA0994D located on the inner flange of beam 5 at station X<sub>S</sub> 275, R22, indicated a low response of the flange for the first 40 seconds after lift-off. The time history plot (fig. 5.3-21) shows that the maximum rms vibration of 117g occurred at T+42.2 seconds. This value decreased to 40g (rms) at the time of CM-SM separation. A lag of approximately 5 seconds was indicated between the time of maximum fluctuating pressure and vibration levels on the exterior of the SM and maximum response of beam 5 inner flange. Examination of the data and instrumentation system indicates these values to be based on valid data. The frequency composition of the vibratory energy during transonic flight is shown in figure 5.3-22 and for a condition of high response in figure 5.3-23. During this period, an oscillograph recording of the composite waveform shows maximum peak-to-peak values of 300g. The major period of the data, from T+40 seconds to separation, gives peak-to-peak values of approximately 150g. These values, when considering the low outer shell vibration levels, are extremely high. Acoustic ground tests of SC-007 created vibration levels of the magnitude experienced in SC-002 flight and at the same location, but only when the vibration levels on the SM shell were much higher than those of the SC-002 SM shell (ref. 17). No explanation for this apparent increase in transmissibility has been found. If additional accelerometers had been included on the radial beam inner flange, providing data for intermediate or associated conditions, the abnormal behavior associated with this measurement could possibly have been resolved.

Measurement SA0995D, located on the aft bulkhead at station X<sub>S</sub> 203, R62, was excited beyond its calibration range ( $\pm 50g$ ) at lift-off and during the transonic period ( $M = 0.8$  to  $1.0$ ). Figure 5.3-24 is a time history of  $g(rms)$  for this measurement. These data were considered invalid after T+33 seconds for reasons explained in section 5.12. This made it impossible to determine the level of maximum excitation. Hence, the frequency spectrum could only be defined by selecting a time sample during a period of valid data. Figure 5.3-25 gives the acceleration spectral density for SA0995D on the aft bulkhead at T+29 seconds to T+31 seconds.

Time histories and lift-off and transonic spectral density plots for measurements SA0996D and SA0997D, located on the forward bulkhead and center of the hydrogen tank shelf, are shown in figures 5.3-26 to 5.3-29. Comparison of SA0996D and SA0997D data to vibration acceleration spectral density levels established during acoustic tests on SC-007 indicated that the flight levels are approximately 10 percent of the acoustic test levels.

Reaction control subsystem vibrations: The SM RCS for SC-002 consisted of one prototype quad assembly (D) and three simulated quad assemblies (fig. 5.3-30). Mass simulation of all RCS helium and propellant tanks was included. For a detailed description of the prototype RCS engine assembly, see reference 12 and the structural description in section 5.2.2. The prototype RCS was instrumented with accelerometers to measure vibration levels encountered by the engine nozzles, the oxidizer tank support, and the RCS panel as shown in figures 11.2-19 and 5.3-31. All accelerometers were ranged  $\pm 500g$ , except the tank support accelerometer which was ranged  $\pm 75g$ . All measurements had a frequency response of 10 to 400 cps.

An examination of the oscillograph record and the rms time history of SA0953D shows the vibration level of the RCS panel to be within the noise of the instrumentation system throughout the majority of the launch phase. This indicates a small vibration input, generally less than  $7g$  rms, transmitted to the RCS engine housing and propellant tanks from the panel.

An rms time history of RCS oxidizer tank support vibration is shown in figure 5.3-32. The maximum vibration occurs just prior to transonic conditions. Figure 5.3-33 shows the maximum energy during this time to exist at approximately 45 cps. This tank support bracket had been modified structurally prior to flight because of the failure which occurred during the SC-007 acoustic test.

Vibration levels of the four accelerometers mounted in the engine nozzles were considerably higher than the levels obtained on the

simulated nozzles of BP-15 (ref. 12). A typical rms time history, which shows vibration of the counterclockwise nozzle in the radial direction, is illustrated by figure 5.3-34. An acceleration spectral density plot for this measurement (SA0955D), figure 5.3-35, shows maximum nozzle vibratory energy existing at approximately 490 cps. At present, the mode of vibration associated with this frequency is unknown. Vibration records indicate that the structural integrity of the nozzles was maintained throughout the flight.

Outer shell strains: The outer shell of the SM was instrumented with strain gages SA0936S through SA0939S to measure bending and extensional strains in the axial and circumferential directions at  $X_S$  273, 252.75°. The gages were ranged for amplitudes of  $\pm 7000 \mu\text{in./in.}$  with a frequency response of 0 to 400 cps (ref. 18).

All data were of very low magnitude and within the noise of the instrumentation system; therefore, no usable strain data were obtained from the SM outer shell.

Radial beam web strains: Fourteen channels of instrumentation were used to record the web strains on radial beams 2, 4, and 5 continuously. (See fig. 5.3-36 for location of the instrumented radial beams.) The exact location of all the strain gages, and the frequency response and range of the measurements, are shown in table 5.3-I. The purpose of the strain measurements was to evaluate the dynamic response of the webs to the launch acoustic environment, and also to compare the fluctuating stresses from flight data with those from the ground tests of SC-007 (ref. 17). This was done to determine a measure of the resistance of the radial beam webs to fatigue failure.

Adhesive-backed "damping" tape was installed on one side of the web panels of radial beam 2. It was planned that the four strain gages on the web panels of beam 2 would indicate the effectiveness of the damping tape in reducing the web dynamic response.

The magnitude of the fluctuating strains on the radial beam webs indicated by Mission A-004 flight data was unexpectedly low. The magnitude of the overall rms strain of a typical strain gage on a web panel of radial beam 5, from lift-off until abort initiation, is shown in figure 5.3-37. The maximum rms strain response of this particular gage (SA0728S) was only  $120 \mu\text{in./in.}$  This maximum response was indicated at the time of lift-off and during transonic flight. Figure 5.3-37 also presents the rms of web panel strain response to the acoustic environment of SC-007 ground tests which simulated the environment of earlier boilerplate flights. There is no technical explanation at this time for the large discrepancy between the two sets of strain results.

Because of the low response levels that were recorded at all 14 strain-gage locations, it could not be determined whether the strain levels on beam 2 were reduced or increased as a result of the application of the damping tape.

#### 5.3.4 Command module dynamics.-





Acoustics: The SC-002 command module was instrumented with two microphones to measure internal noise levels, measurements CK0034Y and CK0035Y. (For a discussion of the crew compartment internal noise levels, see section 5.9.)

The one-third octave band sound level obtained from measurement CK0035Y at T+38 seconds was used to obtain an estimated CM external acoustic environment based on the CM attenuation of SC-007. The one-third octave band noise attenuation values, determined during SC-007 ground acoustic tests, were approximately 35 dB (ref 18). These attenuation values were added to spacecraft 2 reduced flight data to obtain the estimate of the exterior acoustic environment as indicated in figure 5.3-38. The estimated external level for Mission A-004 compared with the measured value for Mission A-101 (BP-13) indicates that the external acoustic level for Mission A-004 was considerably lower. This could account for the unexpectedly low vibration response in the CM and SM structures on Mission A-004. Additional study of the CM acoustic attenuation characteristics would be necessary to establish confidence in this comparison.

Vibrations: The spacecraft 002 CM was instrumented with a total of 12 accelerometers located as shown in figure 11.2-5. Each measurement was ranged  $\pm 100g$  with a frequency response of 10 to 2500 cps and 0 to 600 cps, as given in table 11.2-I.

Magnitudes of all vibration levels measured were considerably lower than had been anticipated. Throughout the flight, acceleration was less than 5g rms for all measurements with the exception of measurement CA0123D, located on the crew compartment heat shield at station X<sub>C</sub> 33, which showed levels of 10g to 40g rms (fig. 5.3-39). Peak-to-peak values measured at this location, were 80g during the transonic period and 200g at T+70 seconds. These values were at the upper range of the instrumentation system and are considered valid. All other measurements were within the noise of the instrumentation system and are being reduced further for additional evaluation. Figure 5.3-39 gives the rms time history of measurement CA0123D. This plot shows an increase in vibration level from the transonic period to T+70 seconds. This trend is characteristic of all vibration measurements on the CM. For spectral density information on measurement CA0123D, see reference 1.

TABLE 5.3-1.- LOCATIONS OF STRAIN GAGES ON WEBS OF SERVICE MODULE RADIAL BEAMS

Beam no.	Strain gage designation	Location	Gage direction	Range, $\mu$ in./in.	Frequency, cps	Gage type
2	SA0721S	X <sub>S</sub> 268, R74.12	Radial membrane	$\pm 5000$	0 to 400	 BLH FA-25-35-S13 NTN 2.1.1.5.1
2	SA0722S	X <sub>S</sub> 340.5, R74.12	Radial membrane	$\pm 5000$	0 to 400	
2	SA0723S	X <sub>S</sub> 305, R74.12	Radial membrane	$\pm 5000$	0 to 400	
2	SA0724S	X <sub>S</sub> 218, R74.12	Radial membrane	$\pm 5000$	0 to 400	
5	SA0725S	X <sub>S</sub> 340.5, R74.12	Radial membrane	$\pm 5000$	0 to 600	
5	SA0726S	X <sub>S</sub> 268, R74.12	Radial membrane	$\pm 5000$	0 to 600	
5	SA0728S	X <sub>S</sub> 305, R74.12	Radial membrane	$\pm 5000$	0 to 400	
4	SA0727S	X <sub>S</sub> 305, R74.34	Radial membrane	$\pm 5000$	0 to 600	 BLH FABR-50-35-S13 NTN 2.1.1.13.1
5	SA0865S	X <sub>S</sub> 217, R74.12	Axial membrane	$\pm 4000$	0 to 600	
5	SA0866S	X <sub>S</sub> 217, R74.12	Radial membrane	$\pm 4000$	0 to 600	
5	SA0867S	X <sub>S</sub> 217, R74.12	45° membrane	$\pm 4000$	0 to 600	
5	SA0868S	X <sub>S</sub> 219, R74.12	Axial bending	$\pm 4000$	0 to 600	
5	SA0869S	X <sub>S</sub> 219, R74.12	Radial bending	$\pm 4000$	0 to 600	
5	SA0870S	X <sub>S</sub> 219, R74.12	45° bending	$\pm 4000$	0 to 600	



5-42

NASA-S-66-3834 APR 15

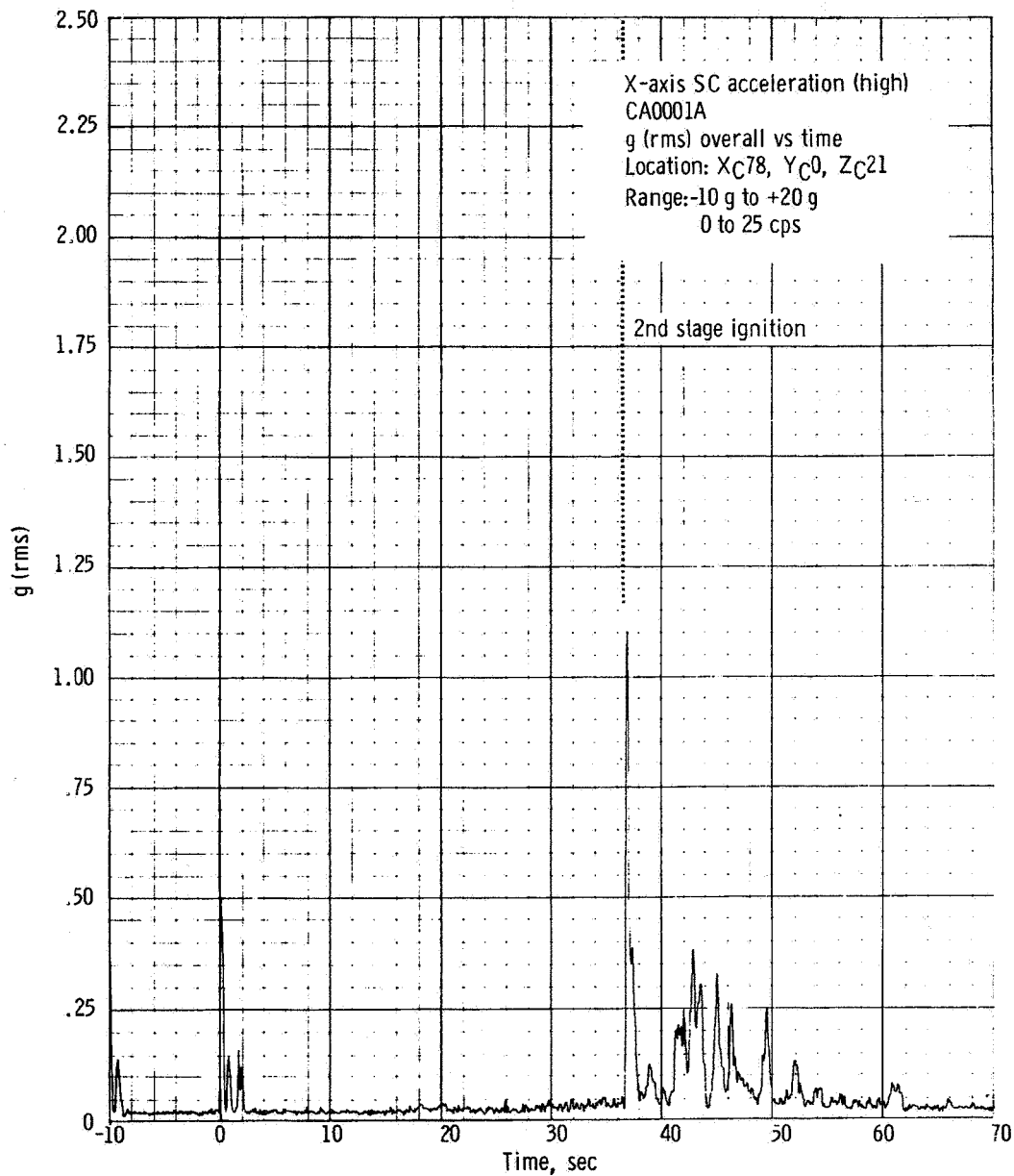


Figure 5.3-1. - rms time history of CM X-axis acceleration, Apollo Mission A-004.

NASA-S-66-3838 APR 15

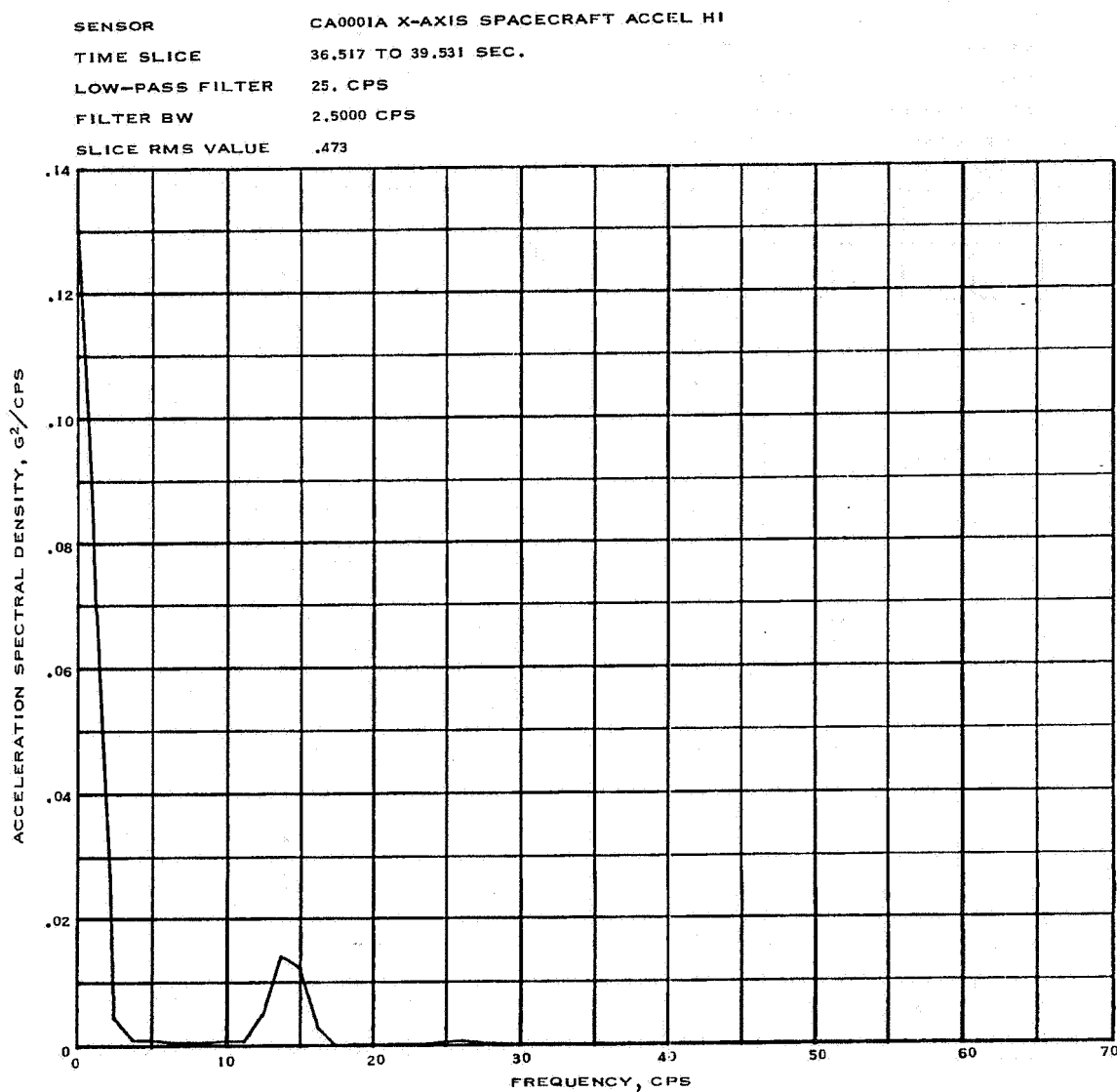


Figure 5.3-2.- X-axis acceleration spectral density during staging,  
Apollo Mission A-004.

5-44

NASA-S-66-3842 APR 15

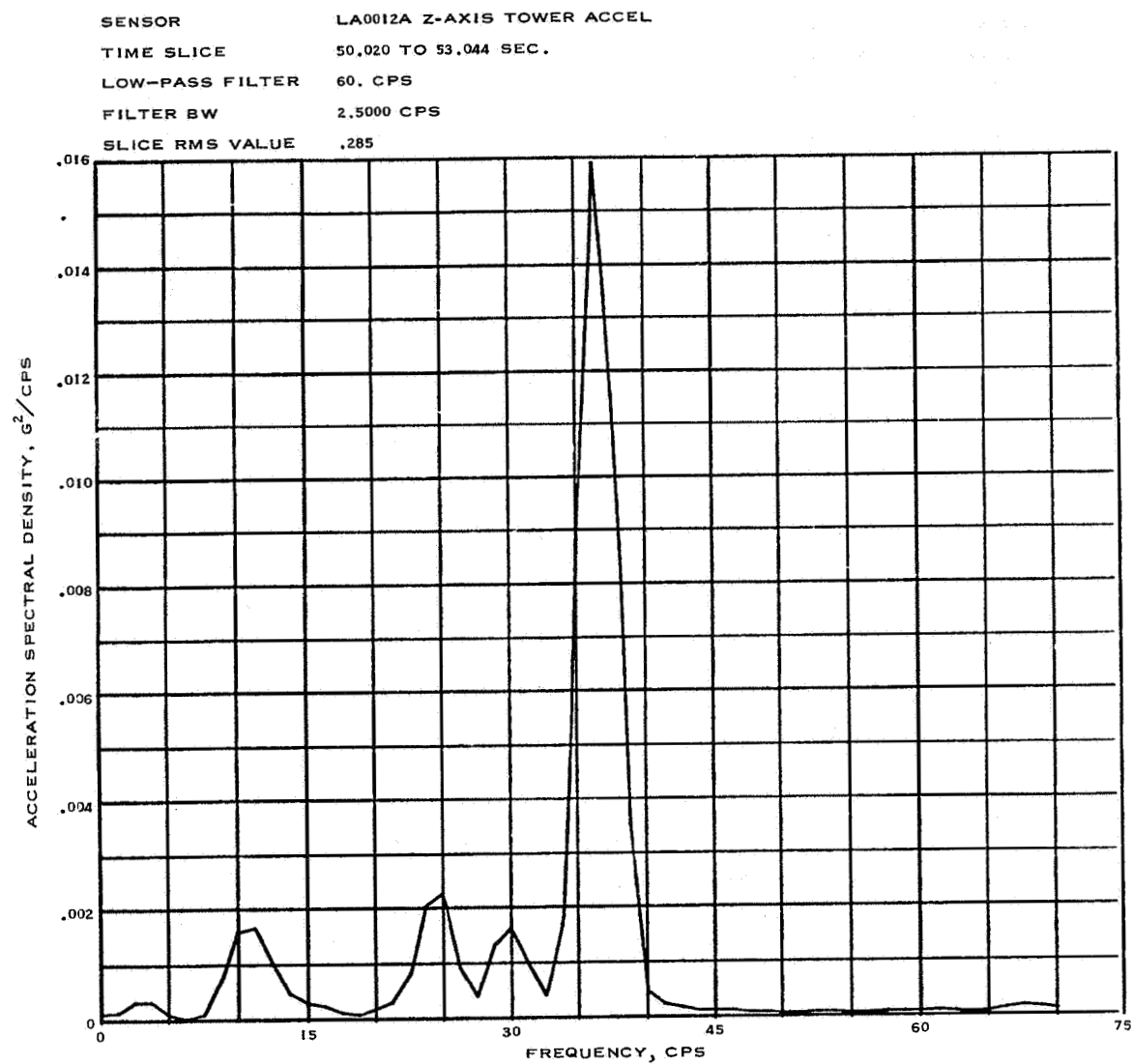
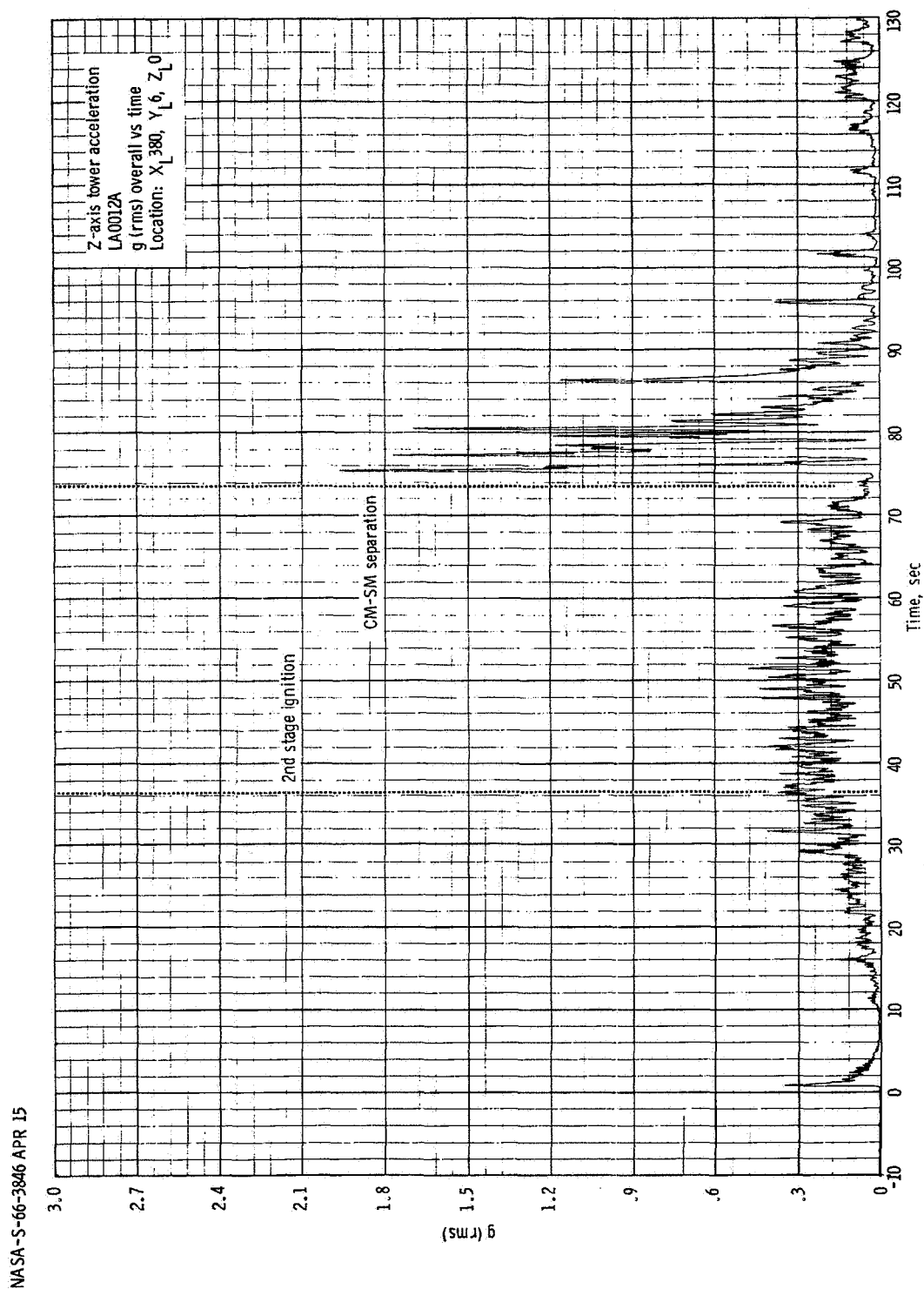


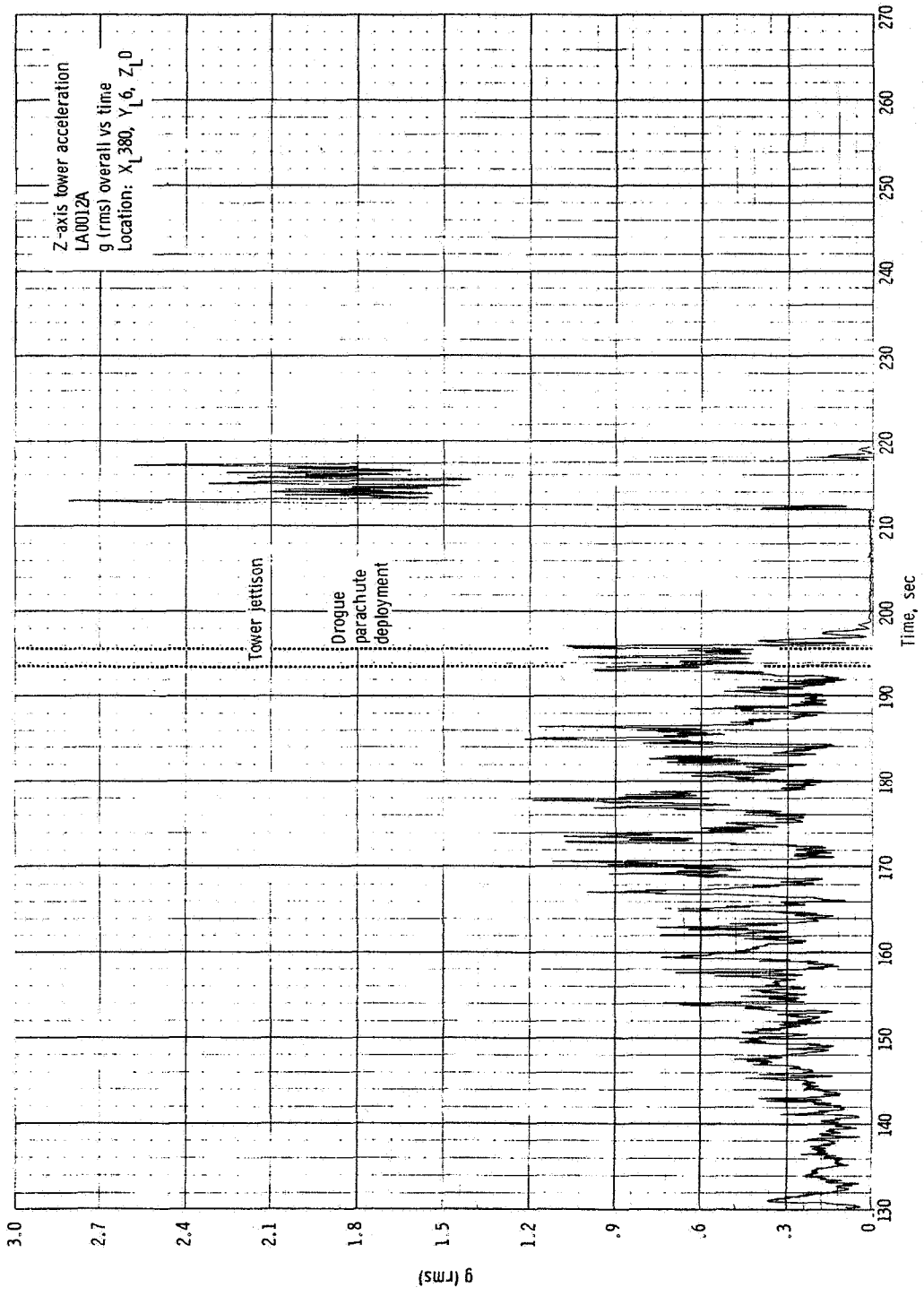
Figure 5.3-3.- Z-axis acceleration spectral density at T+51.5 second, Apollo Mission A-004.



(a) -10 to 130 seconds.

Figure 5.3-4. - rms time history of Z-axis tower acceleration, Apollo Mission A-004.

NASA-S-66-3850 APR 15



(b) 130 to 270 seconds.  
Figure 5.3-4. - Concluded.

NASA-S-66-3655 APR 15

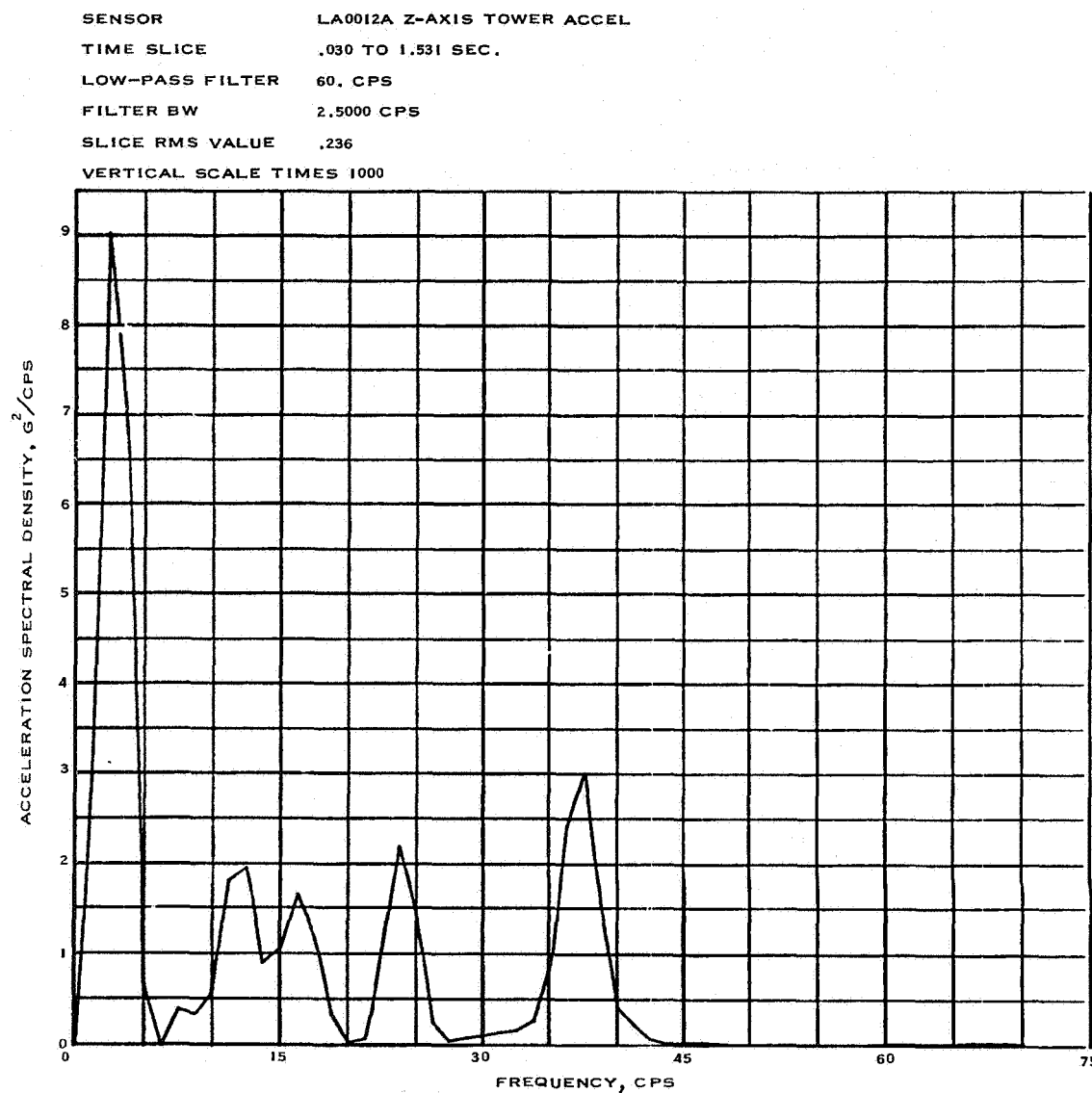


Figure 5.3-5.- Z-axis acceleration spectral density at lift-off,  
Apollo Mission A-004.

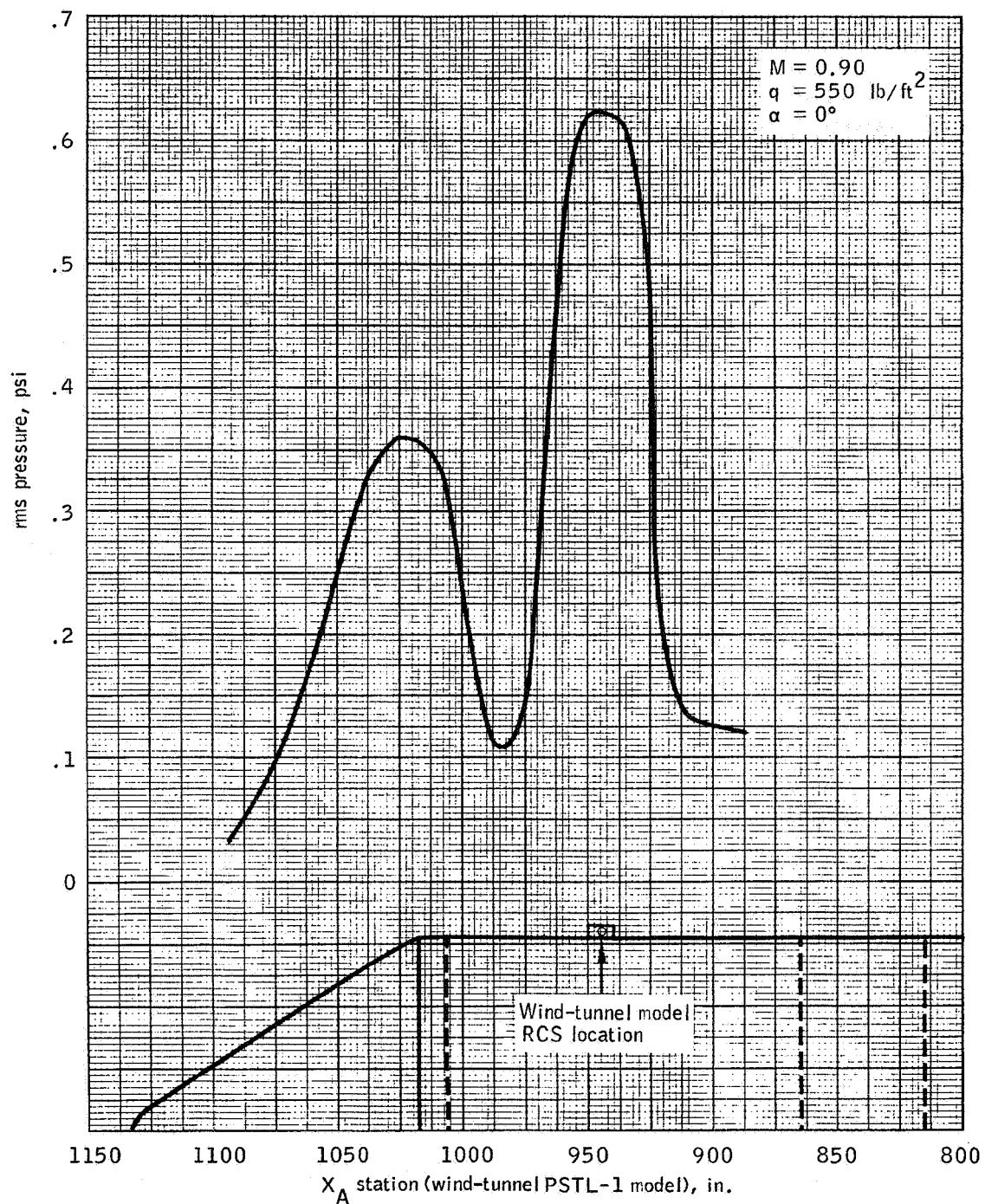


Figure 5.3-6.- Effect of RCS protuberance of SM fluctuating pressure levels as shown by wind tunnel data.

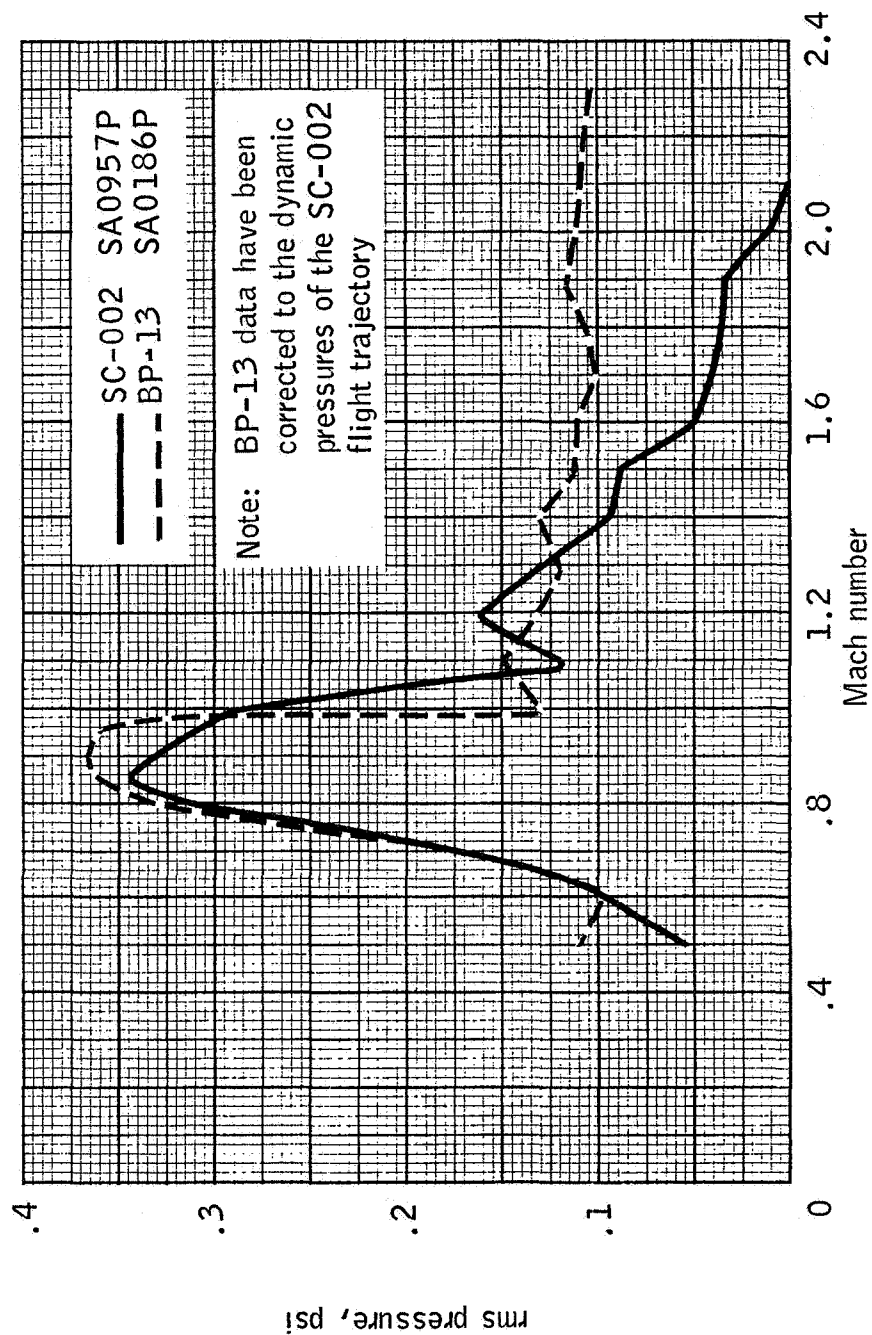


Figure 5.3-7.- Comparison of SC-002 and BP-13 fluctuating pressure in vicinity of RCS engines on Apollo Missions A-004 and A-101.



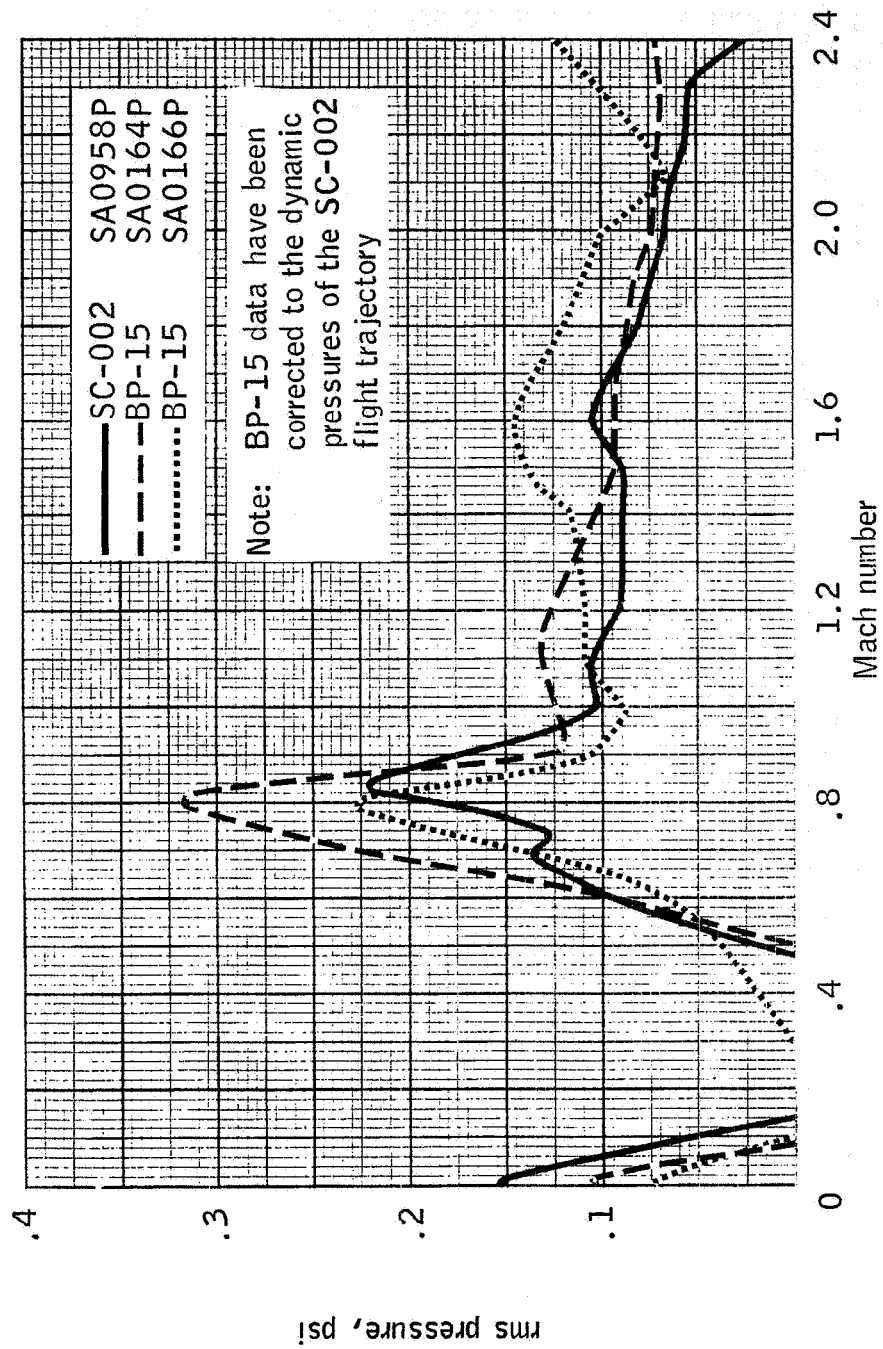


Figure 5.3-8.- Comparison of SC-002 and BP-15 fluctuating pressure environments on Apollo Missions A-004 and A-102.

NASA-S-66-3675 APR 15

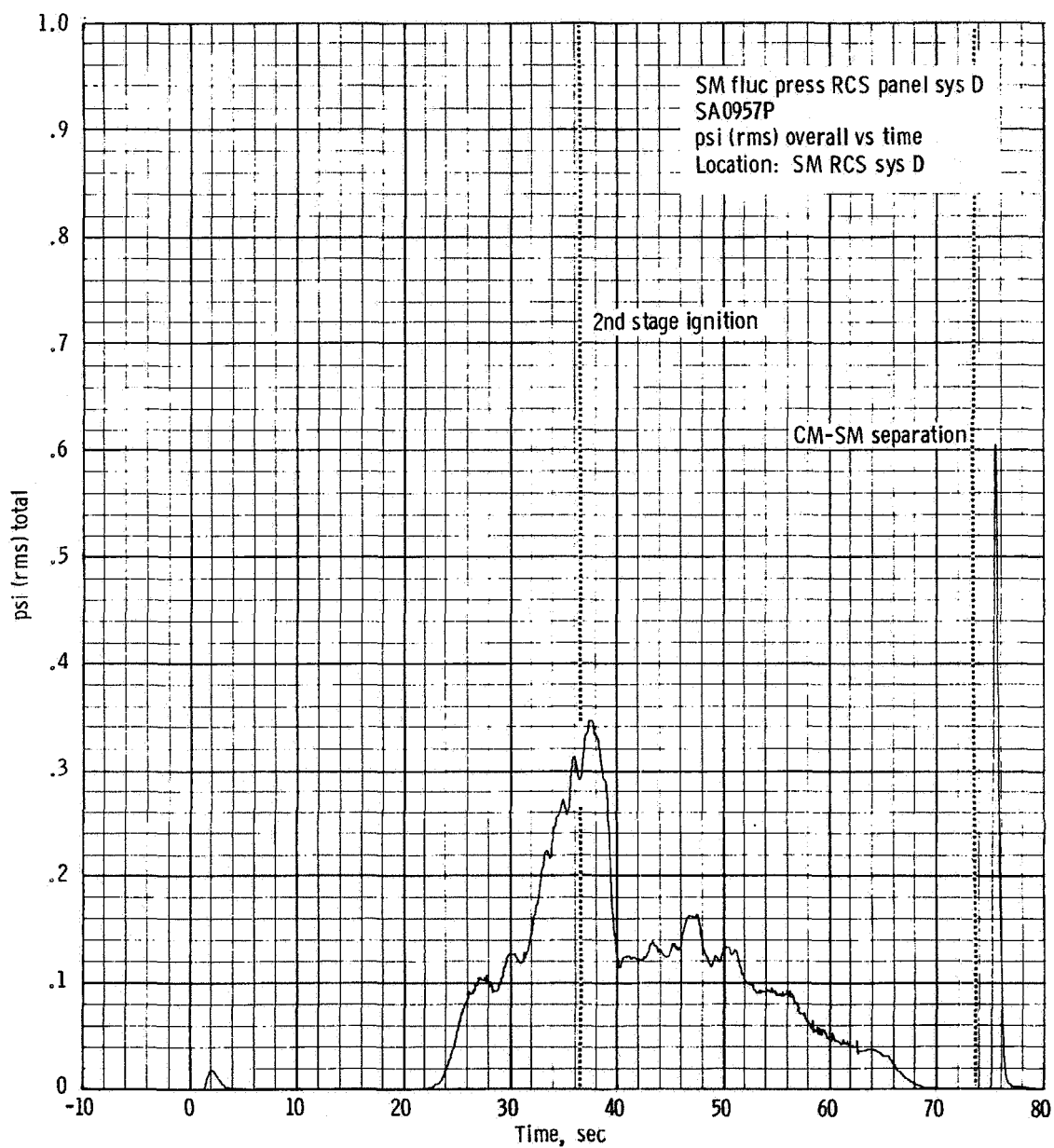


Figure 5.3-9. - Service module fluctuating pressure time history for RCS panel, Apollo Mission A-004.

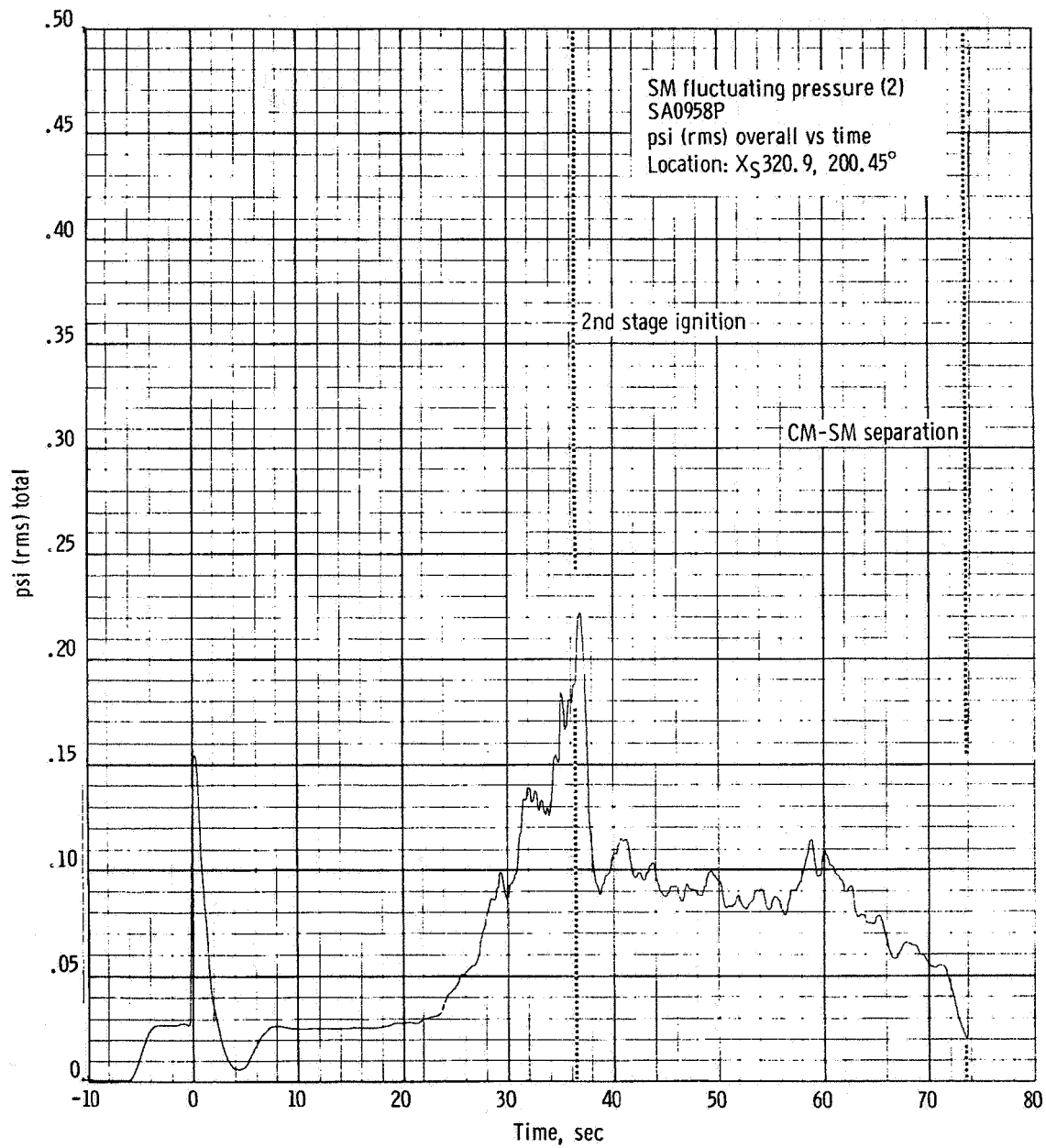


Figure 5.3-10. - Service module shell fluctuating pressure time history, Apollo Mission A-004.

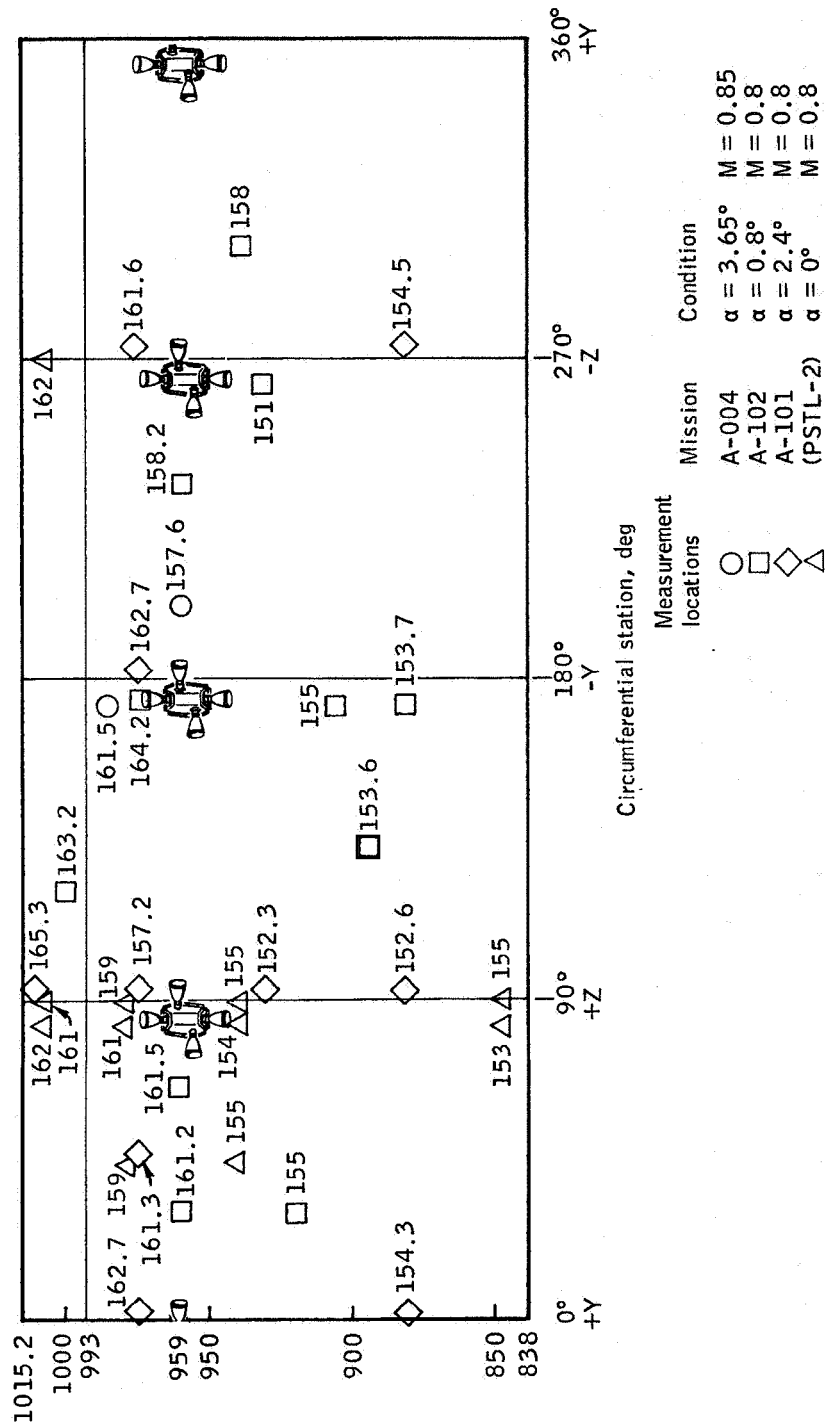


Figure 5.3-11.- Comparison of overall sound pressure levels (dB) on the service module, Apollo Mission A-004.

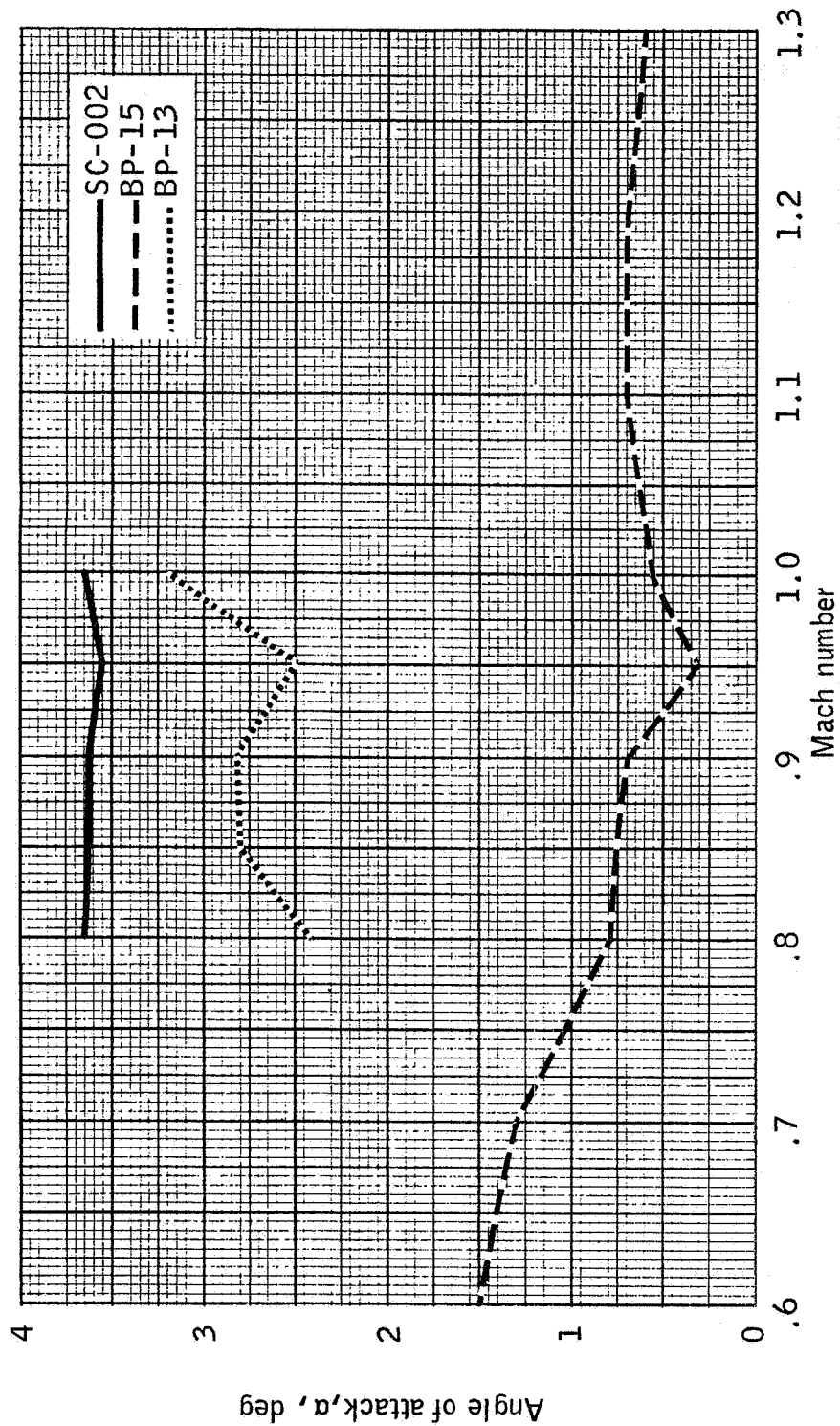


Figure 5.3-12.- Comparison of angle of attack for Apollo Missions A-004 (SC-002), A-101 (BP-13), and A-102 (BP-15).

NASA-S-66-3691 APR 15

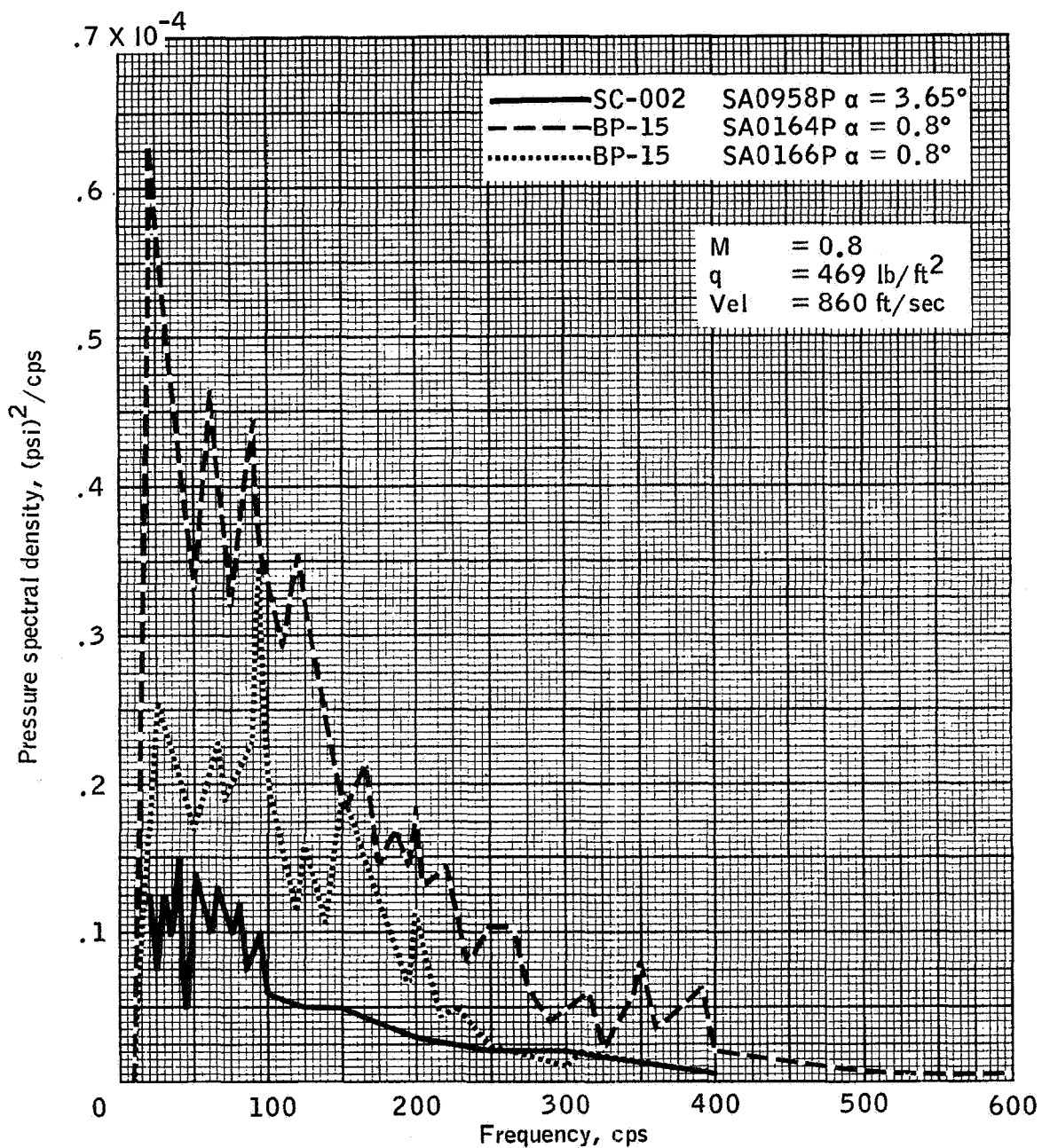


Figure 5.3-13.- Comparison of pressure spectral density for similar locations on the SM for Apollo Missions A-004 (SC-002) and A-102 (BP-15).

5-56

NASA-S-66-3695 APR 15

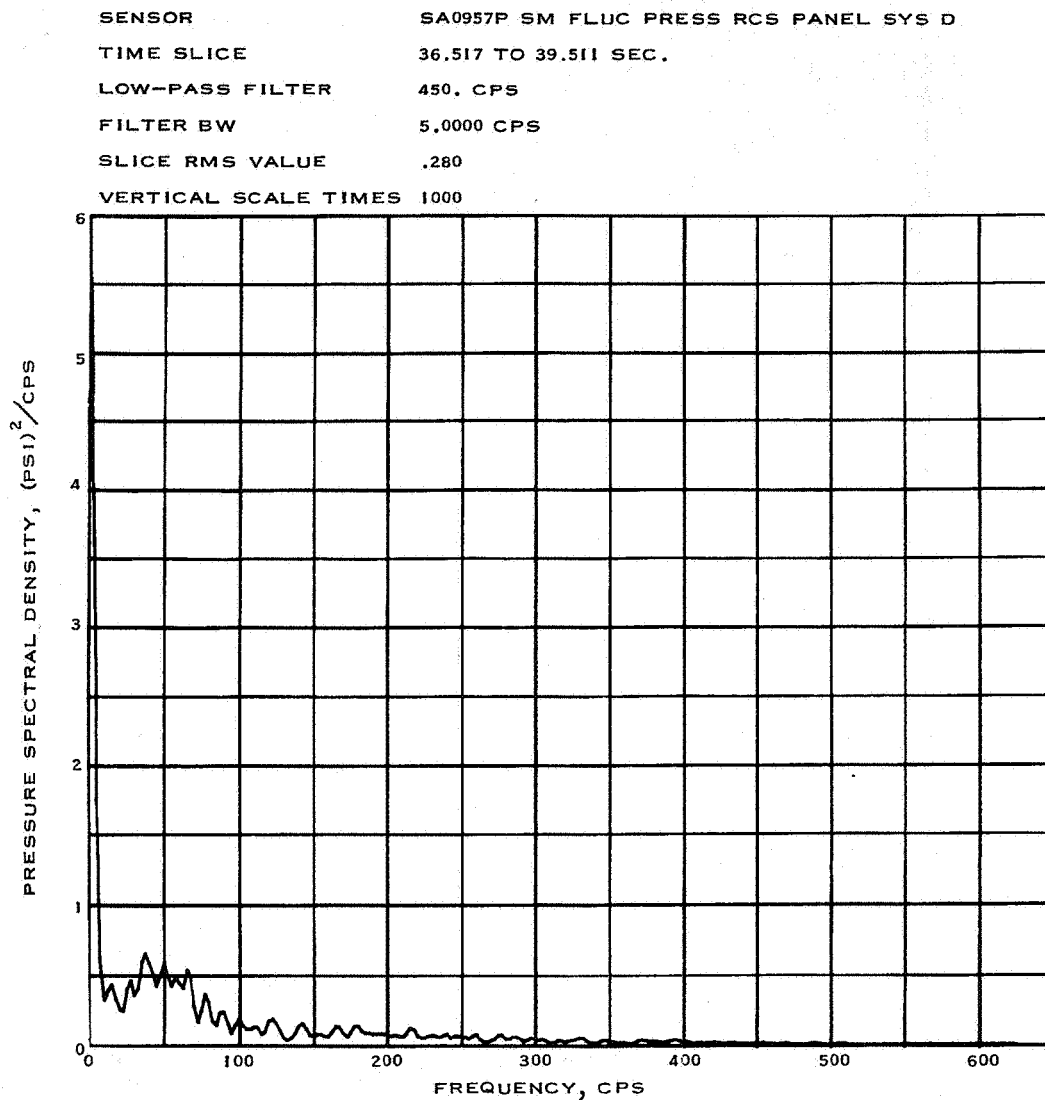


Figure 5.3-14.- SM RCS panel fluctuating pressure spectral density during transonic flight, Apollo Mission A-004.

NASA-S-66-3699 APR 15

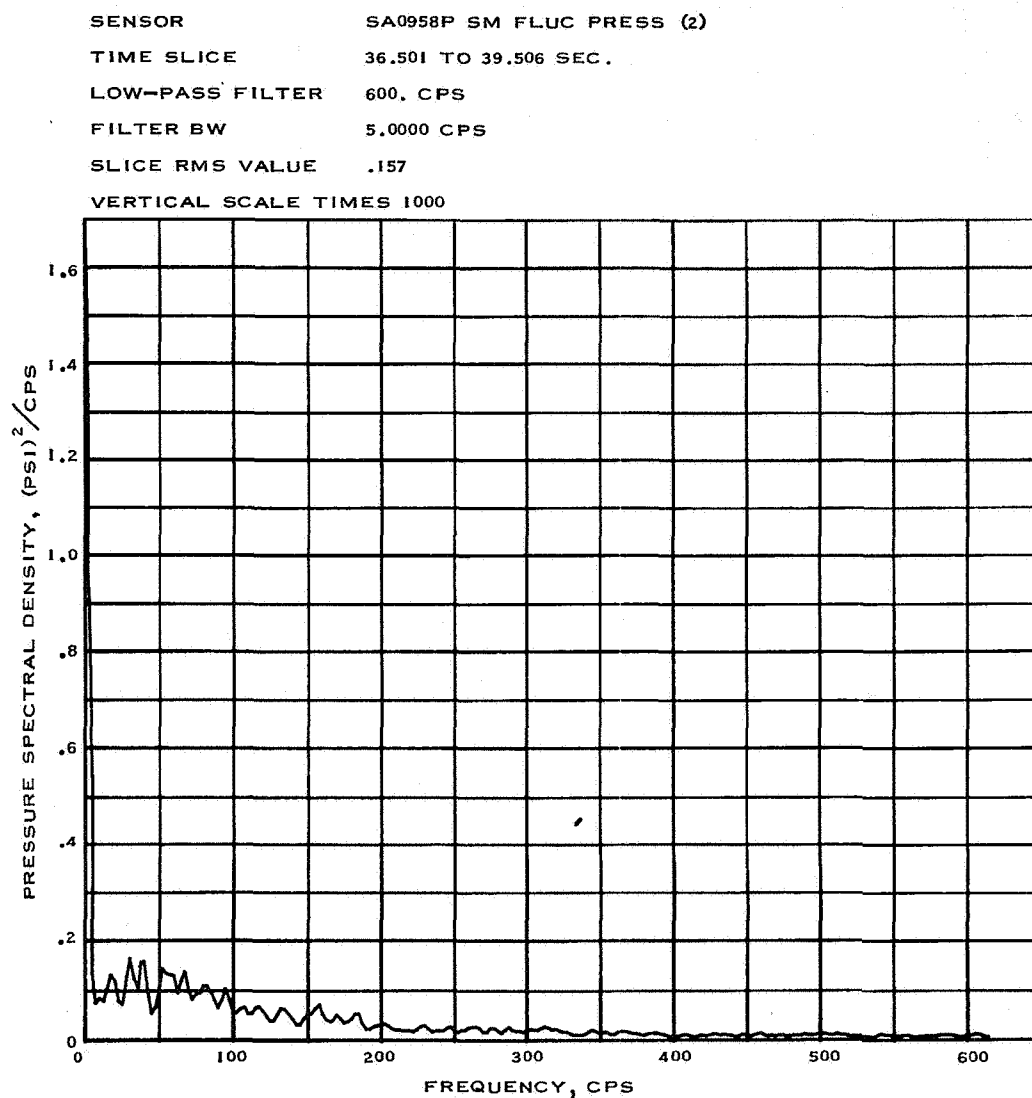


Figure 5.3-15.- SM fluctuating pressure spectral density during transonic flight, Apollo Mission A-004.



5-58

NASA-S-66-3703 APR 15

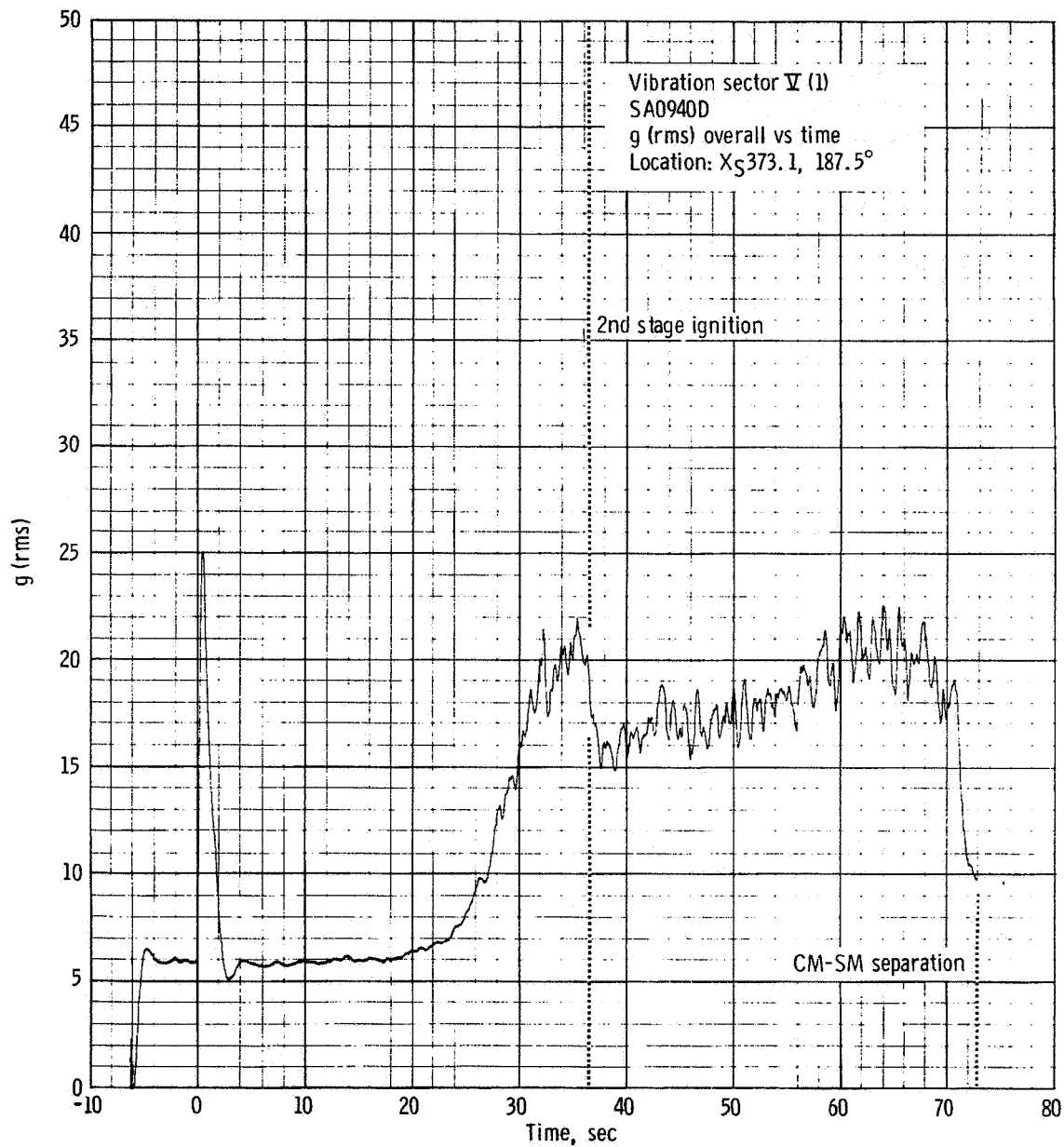
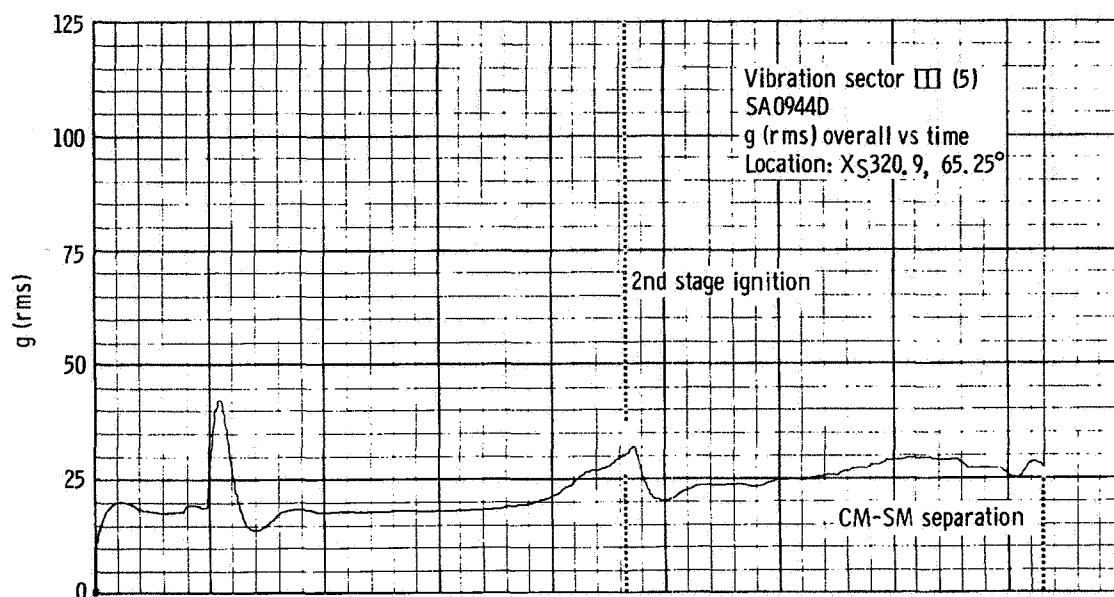
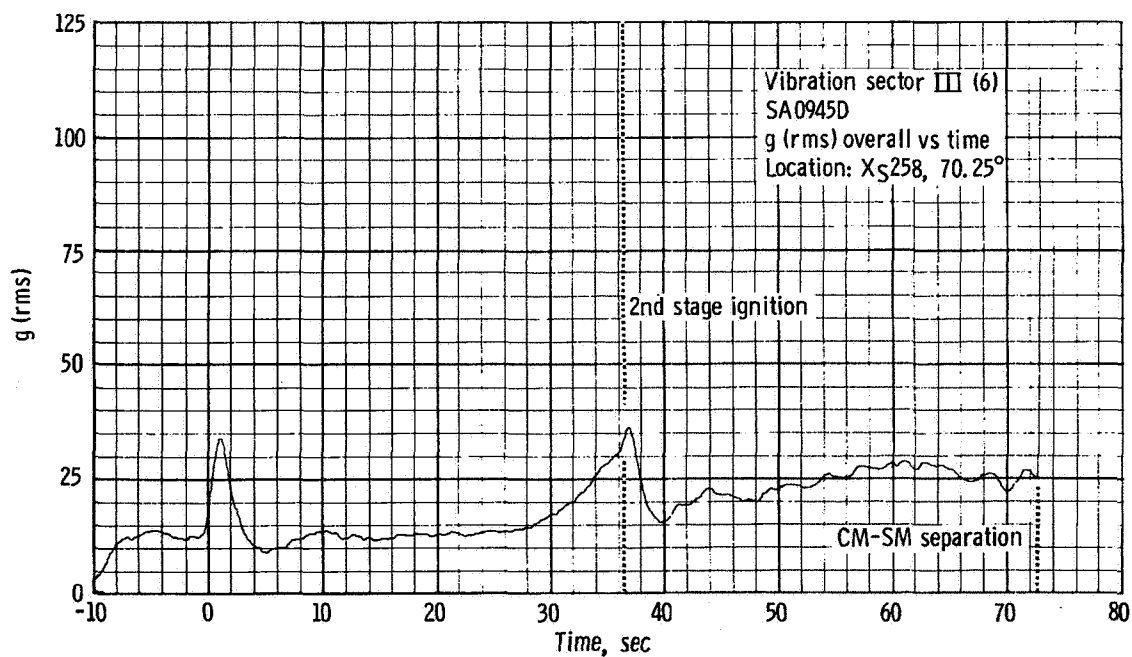


Figure 5.3-16. - rms time history of CSM fairing vibration, Apollo Mission A-004.

NASA-S-66-3707 APR 15



(a) Measurement SA0944D.

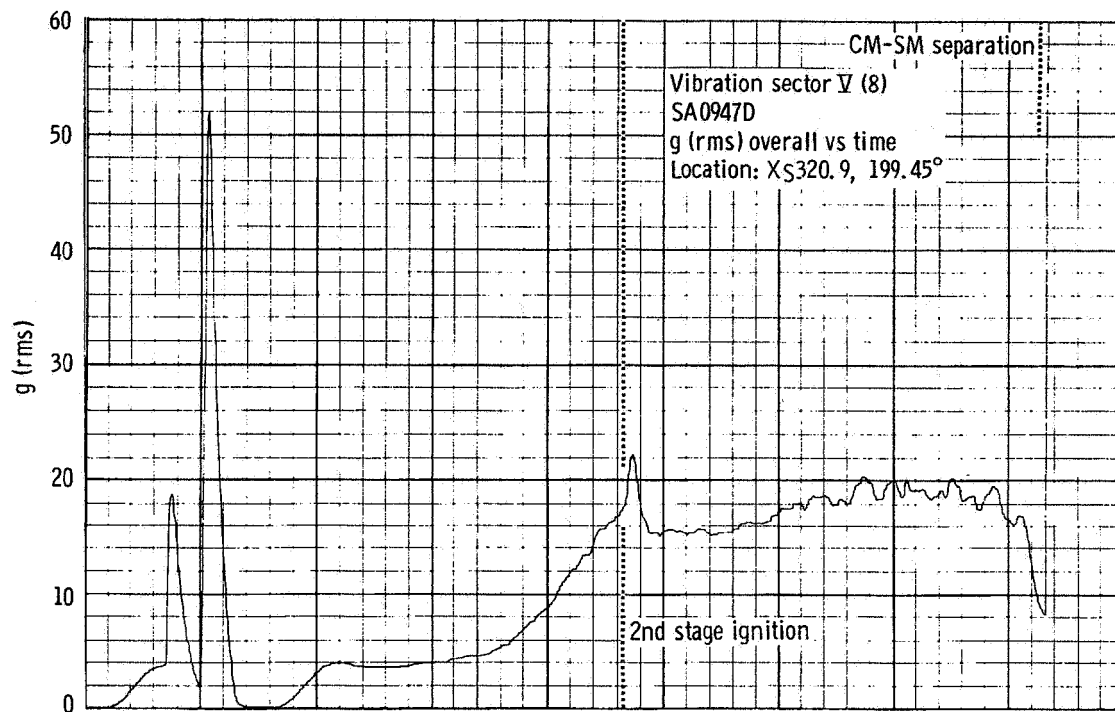


(b) Measurement SA0945D.

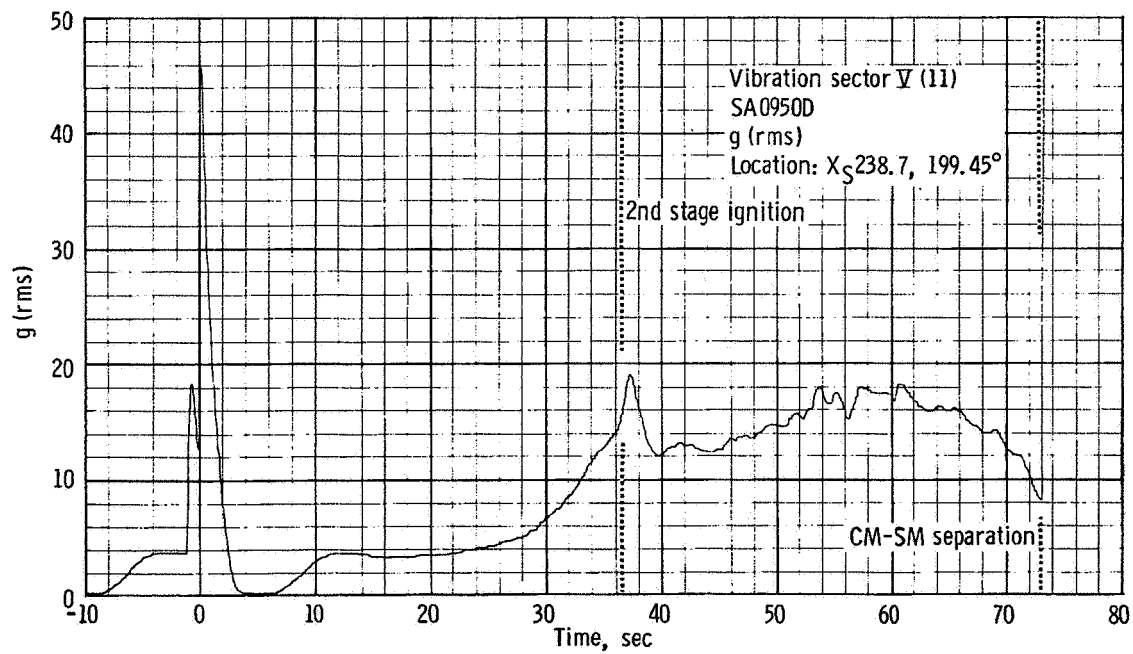
Figure 5.3-17. - rms time history of SM vibration, Apollo Mission A-004.

5-6C

NASA-S-66-3711 APR 15



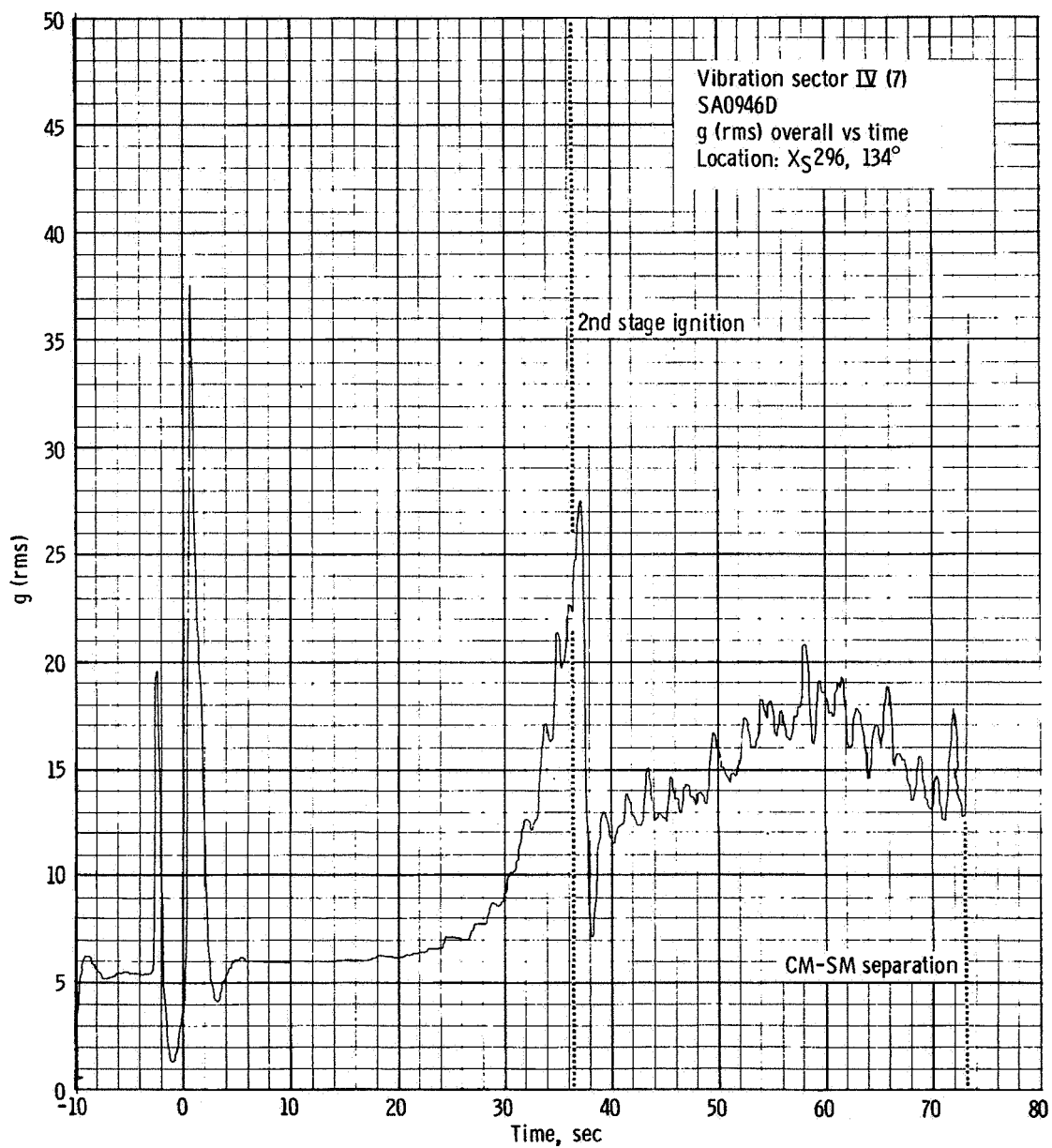
(c) Measurement SA0947D.



(d) Measurement SA0950D.

Figure 5.3-17. - Continued.

NASA-S-66-3715 APR 15

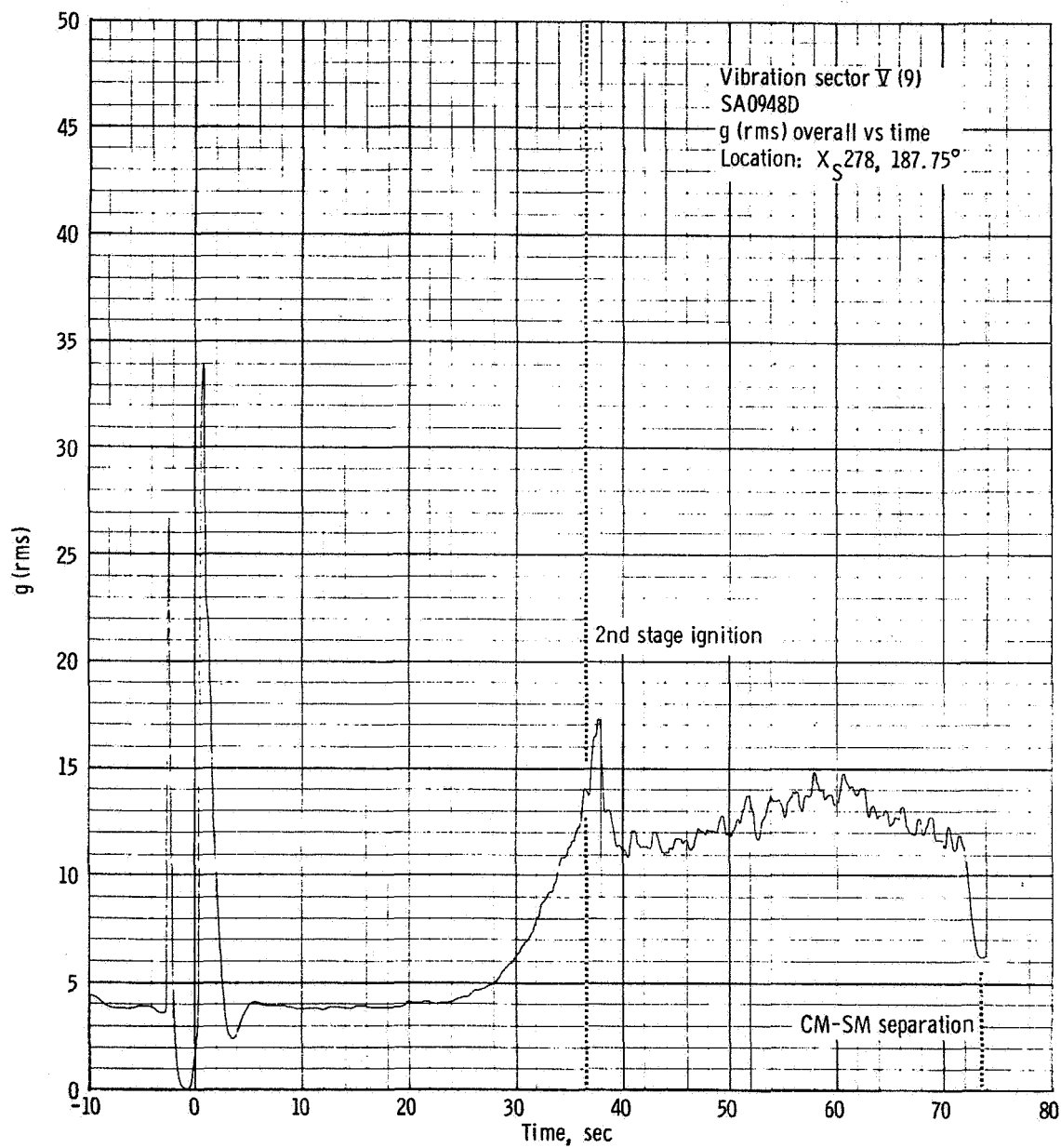


(e) Measurement SA0946D.

Figure 5.3-17. - Continued.

5-62

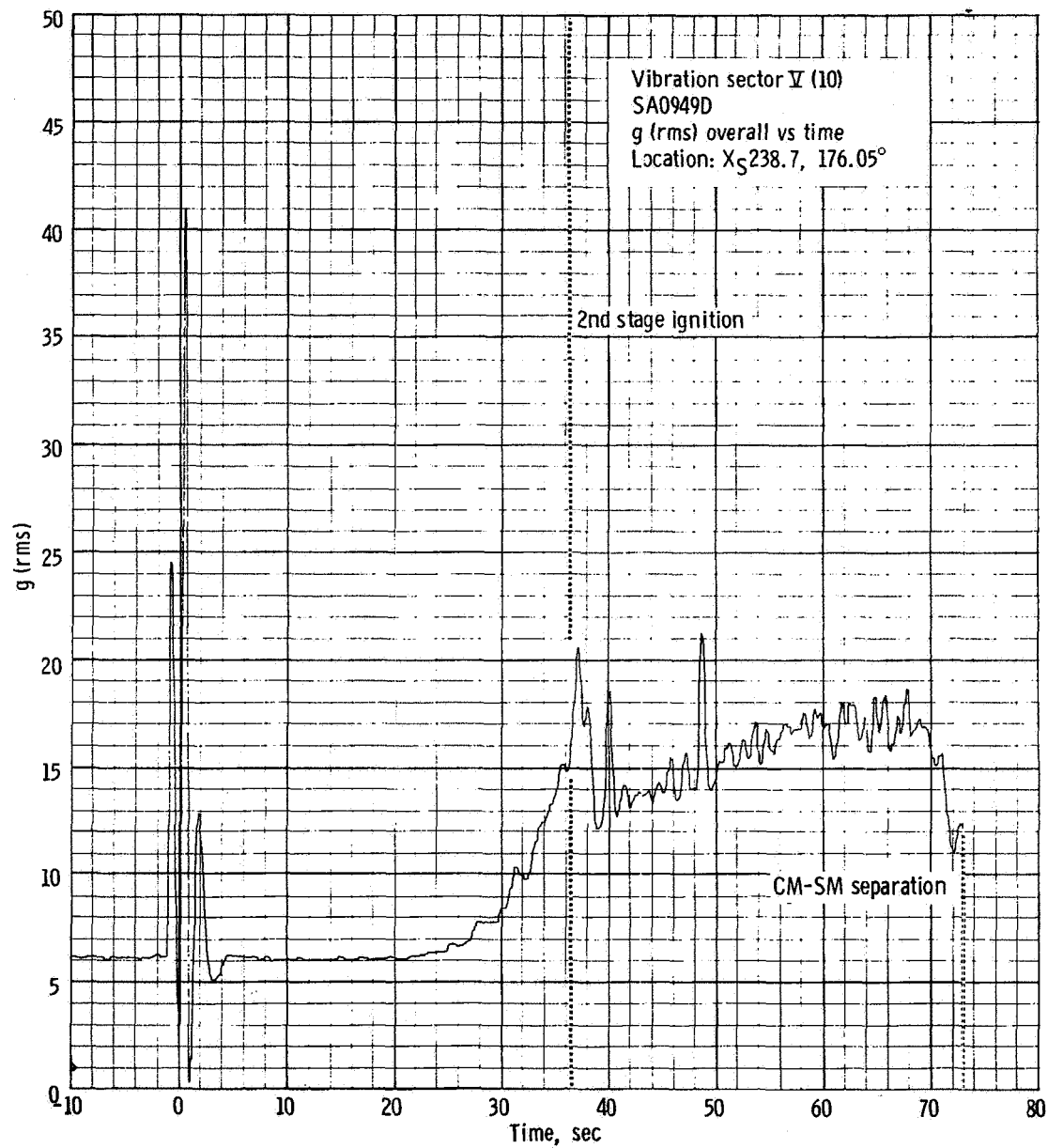
NASA-S-66-3719 APR 15



(f) Measurement SA0948D.

Figure 5.3-17. - Continued.

NASA-S-66-3723 APR 15

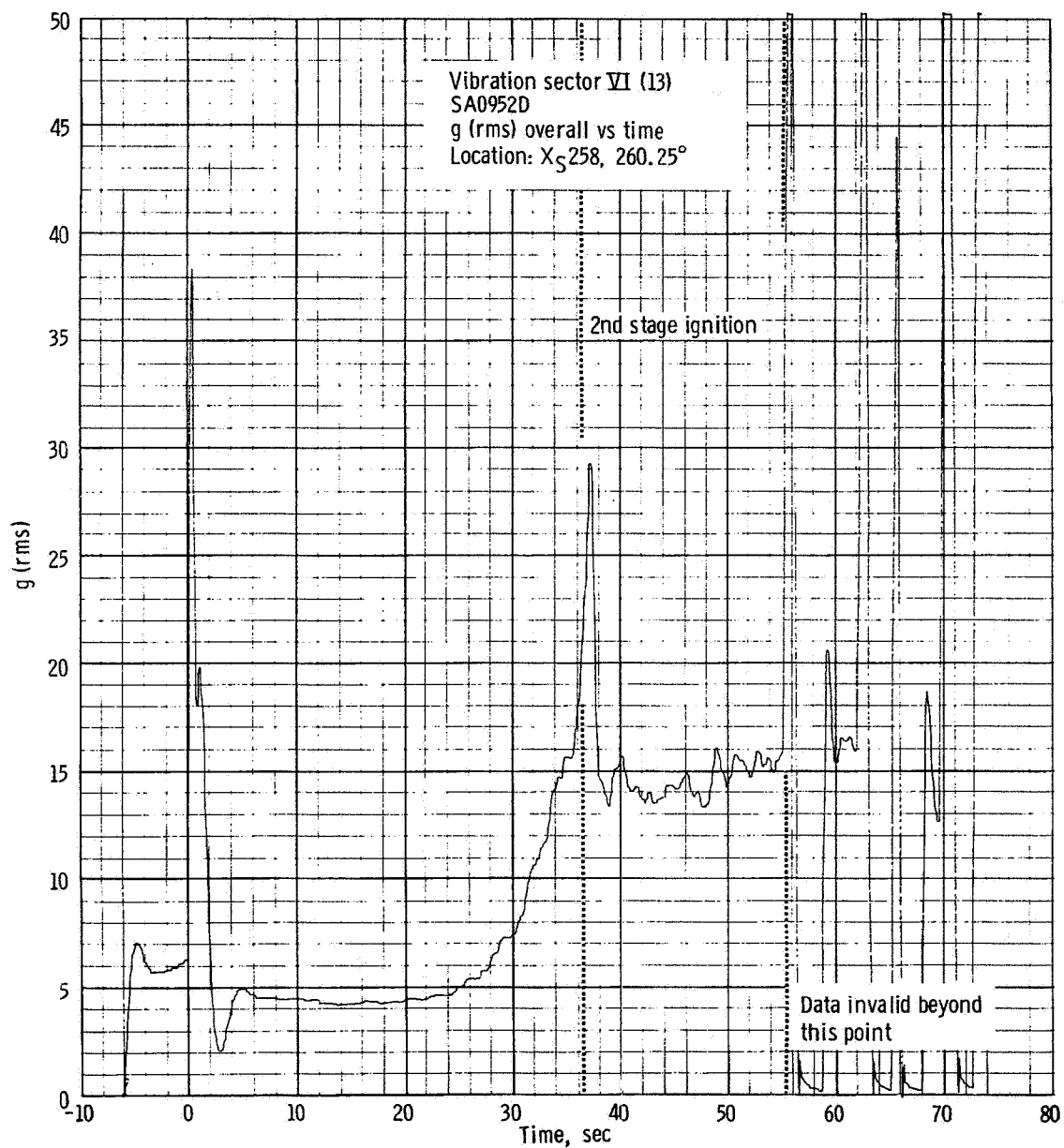


(g) Measurement SA0949D.

Figure 5.3-17. - Continued.

5-64

NASA-S-66-3727 APR 15



(h) Measurement SA0952D.

Figure 5.3-17. - Concluded.

NASA-S-66-3731 APR 15

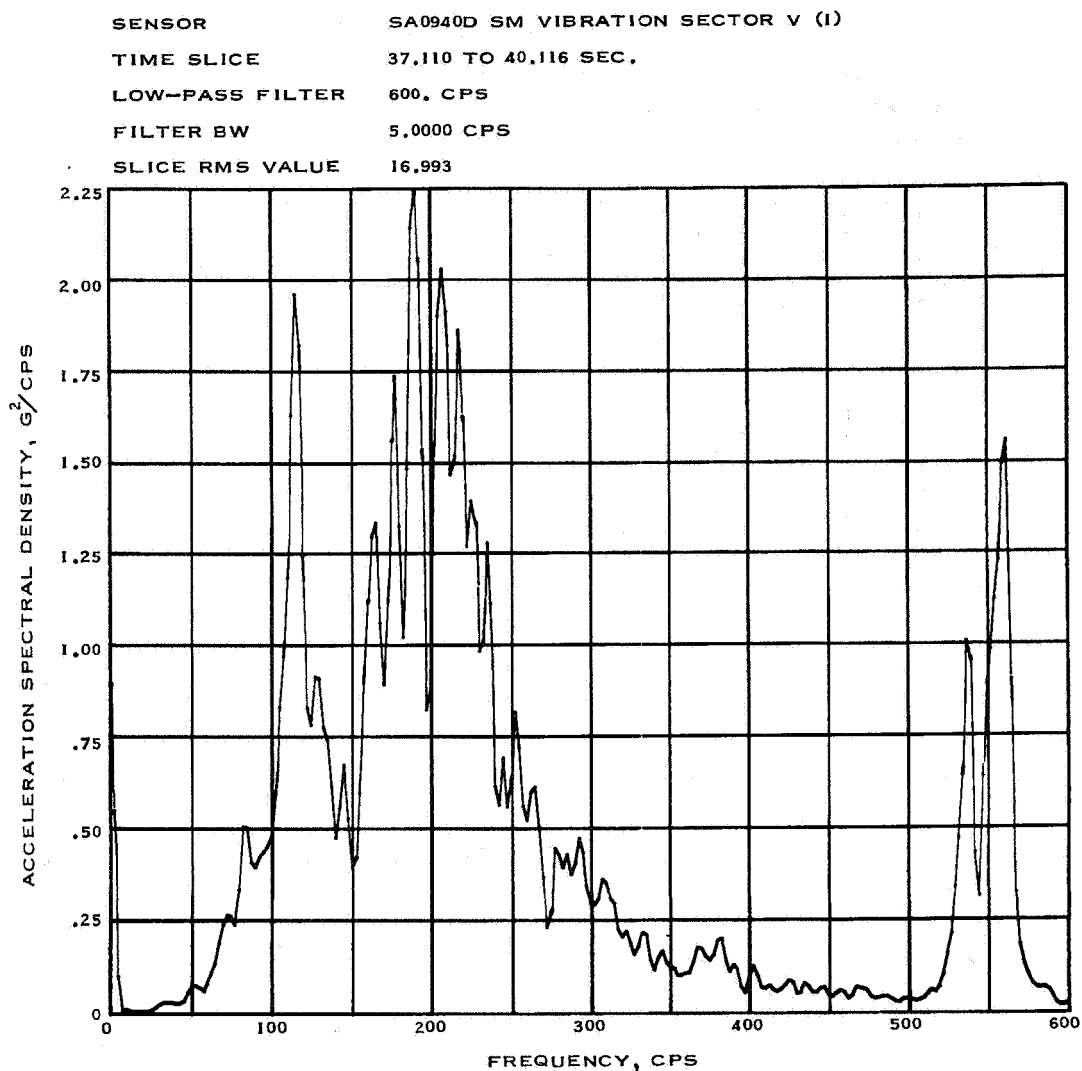
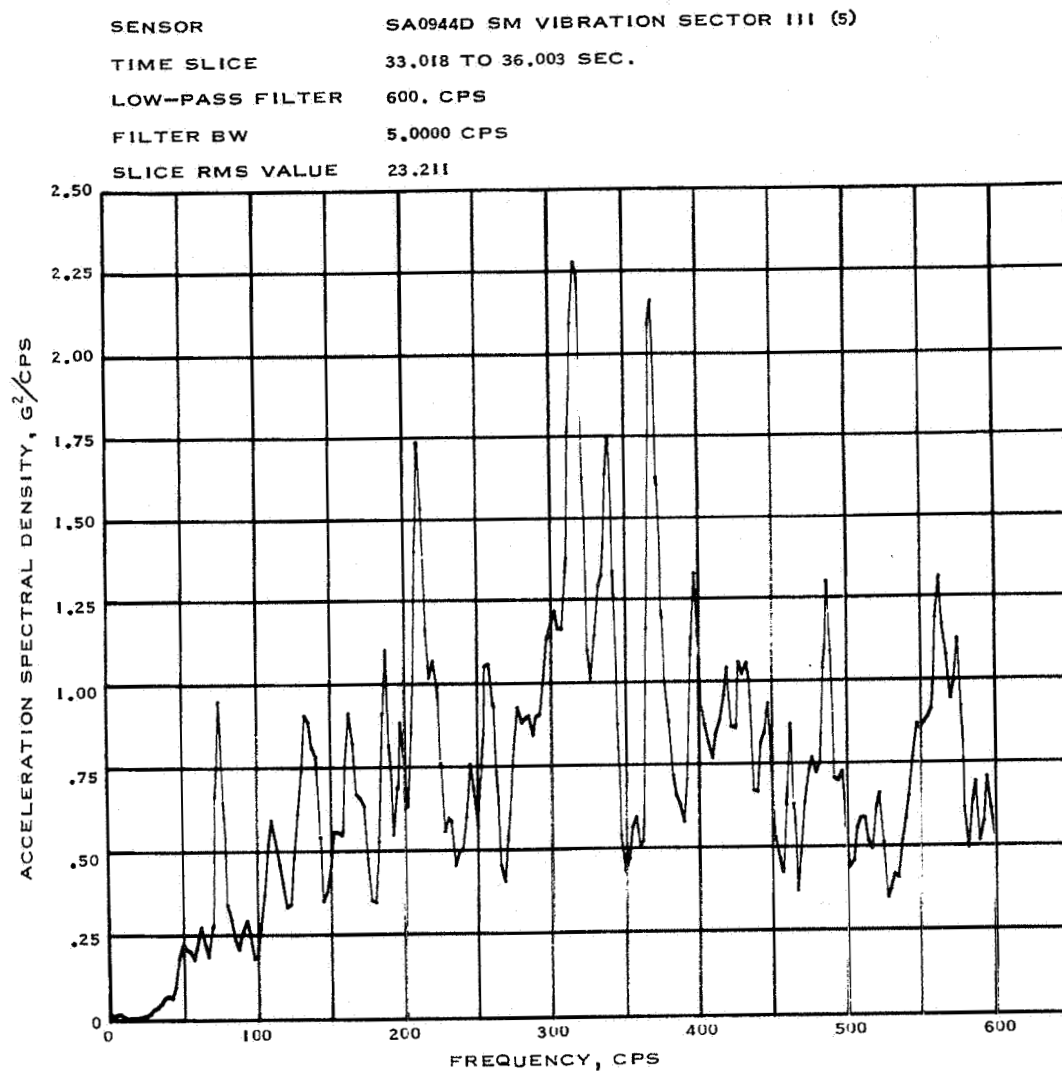


Figure 5.3-18.- CSM fairing acceleration spectral density during transonic flight, Apollo Mission A-004.



5-66

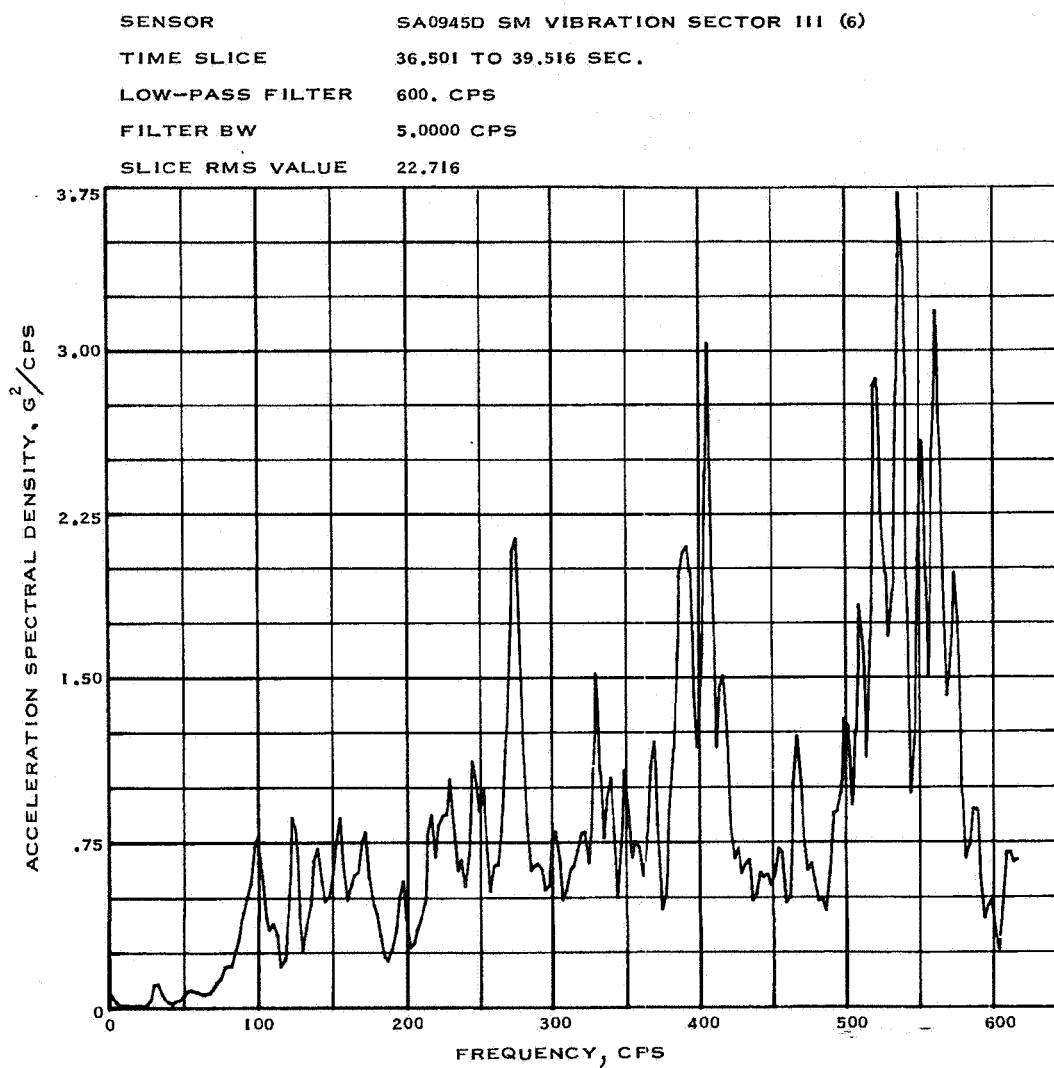
NASA-S-66-3735 APR 15



(a) Measurement SA0944D.

Figure 5.3-19.- SM shell acceleration spectral density during transonic flight, Apollo Mission A-004.

NASA-S-66-3739 APR 15

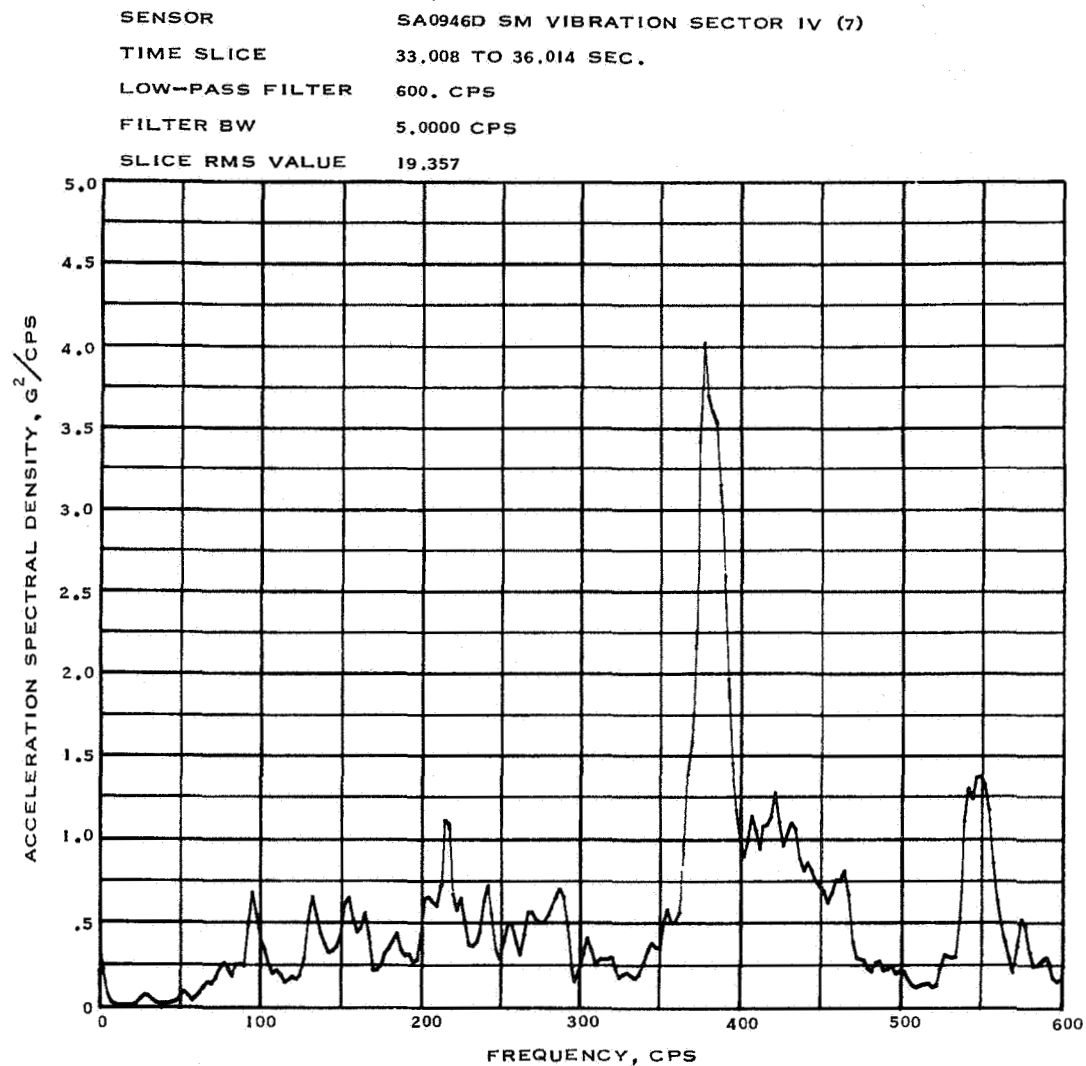


(b) Measurement SA0945D.

Figure 5.3-19.- Continued.

5-68

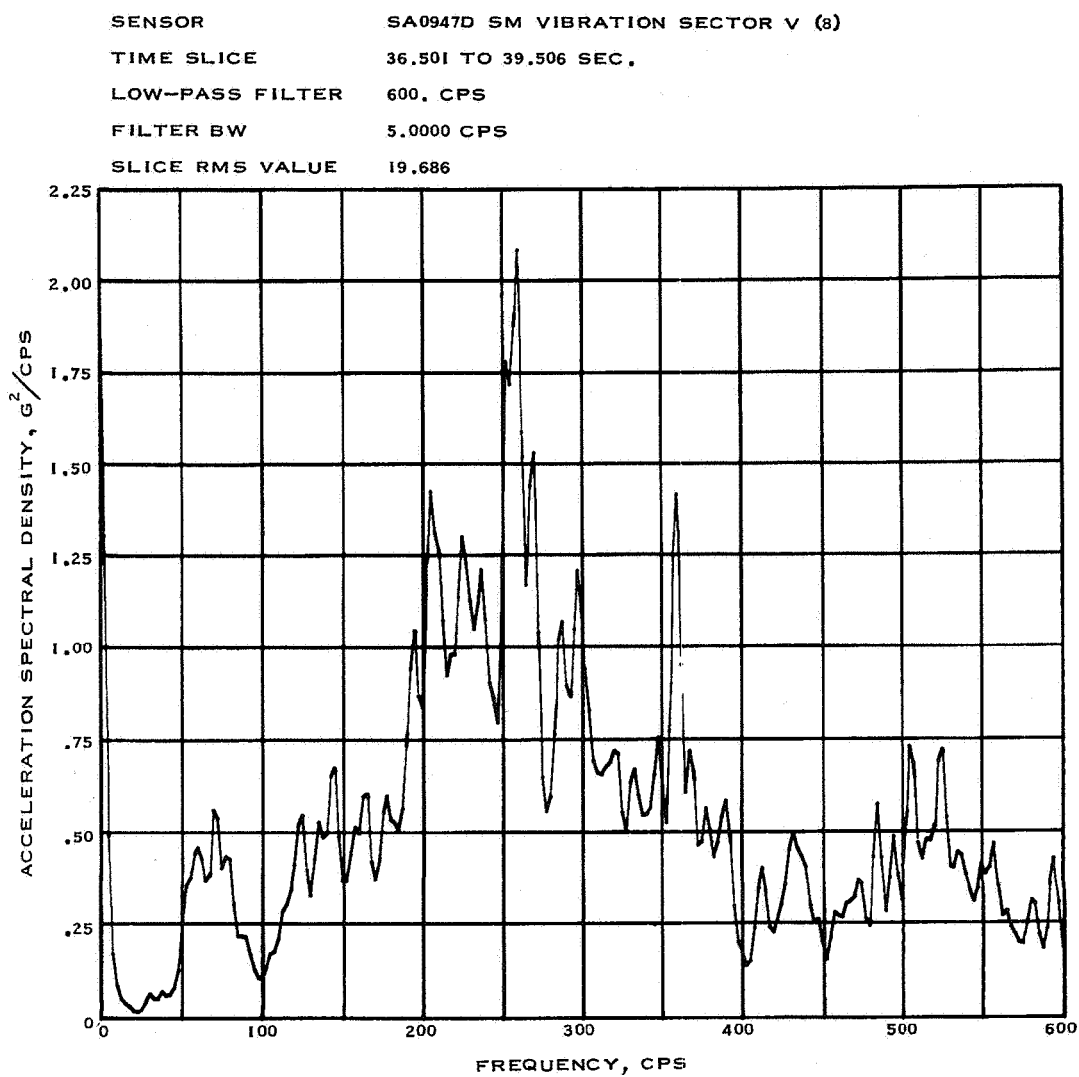
NASA-S-66-3743 APR 15



(c) Measurement SA0946D.

Figure 5.3-19.- Continued.

NASA-S-66-3747 APR 15

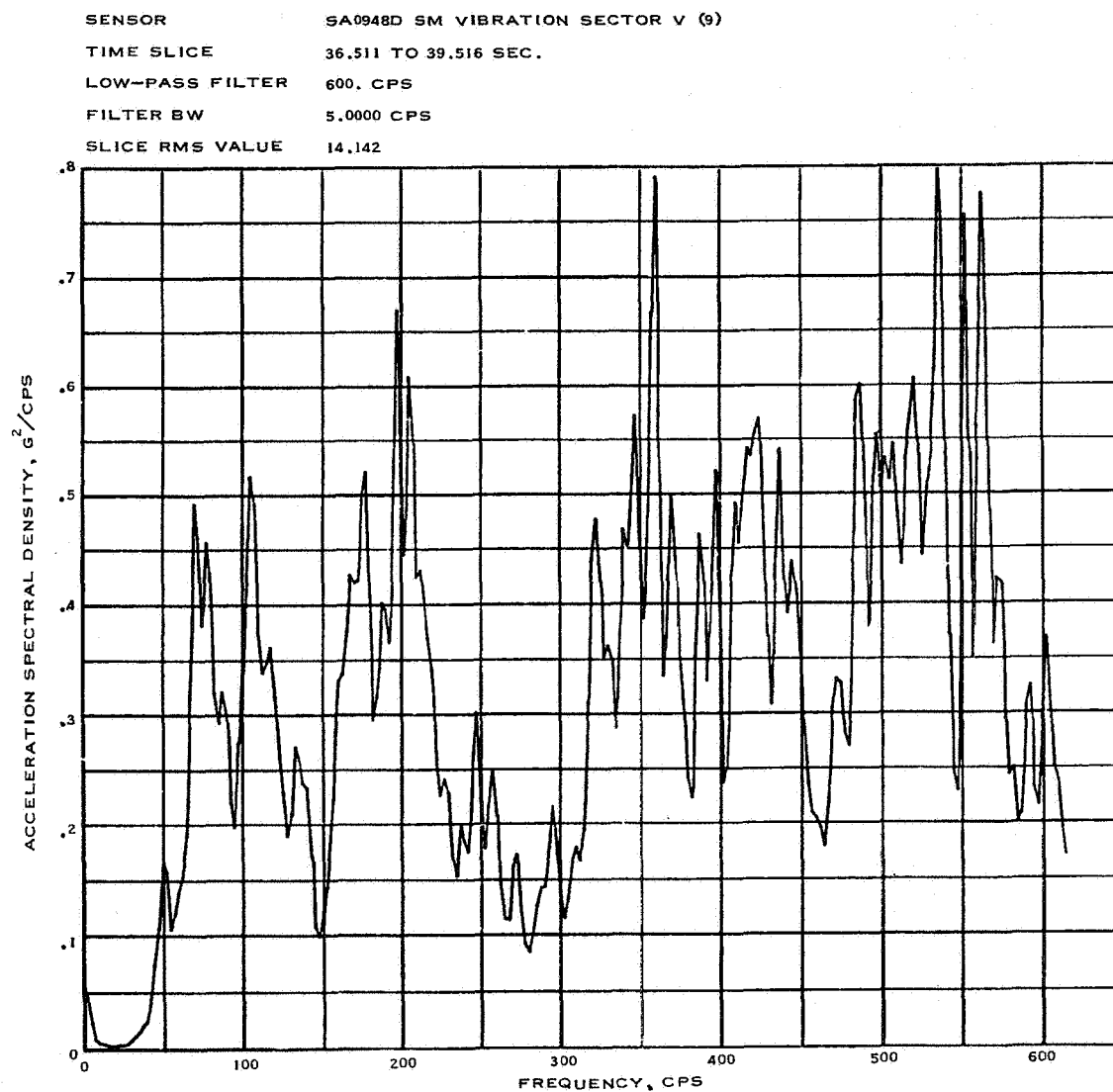


(d) Measurement SA0947D.

Figure 5.3-19.- Continued.

5-70

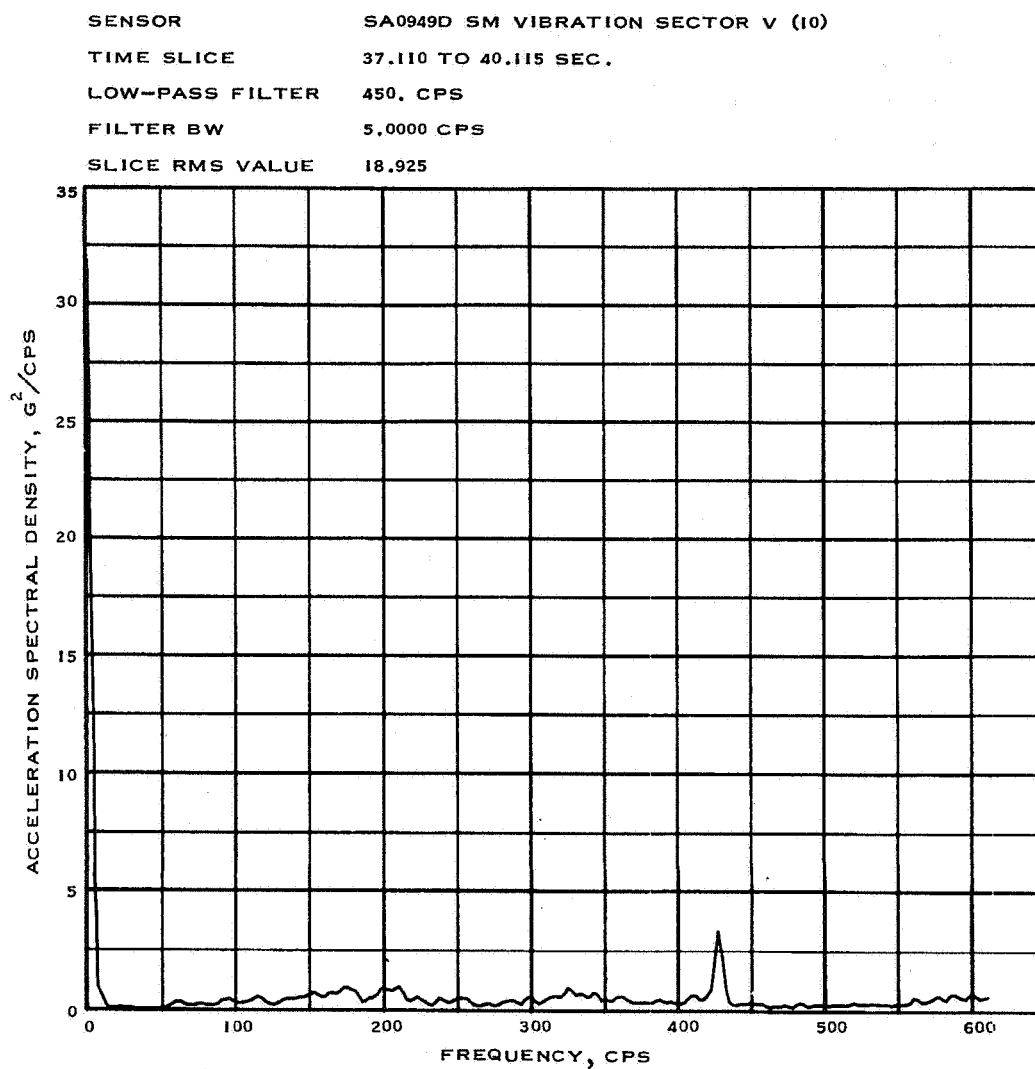
NASA-S-66-3751 APR 15



(e) Measurement SA0948D.

Figure 5.3-19.- Continued.

NASA-S-66-3755 APR 15

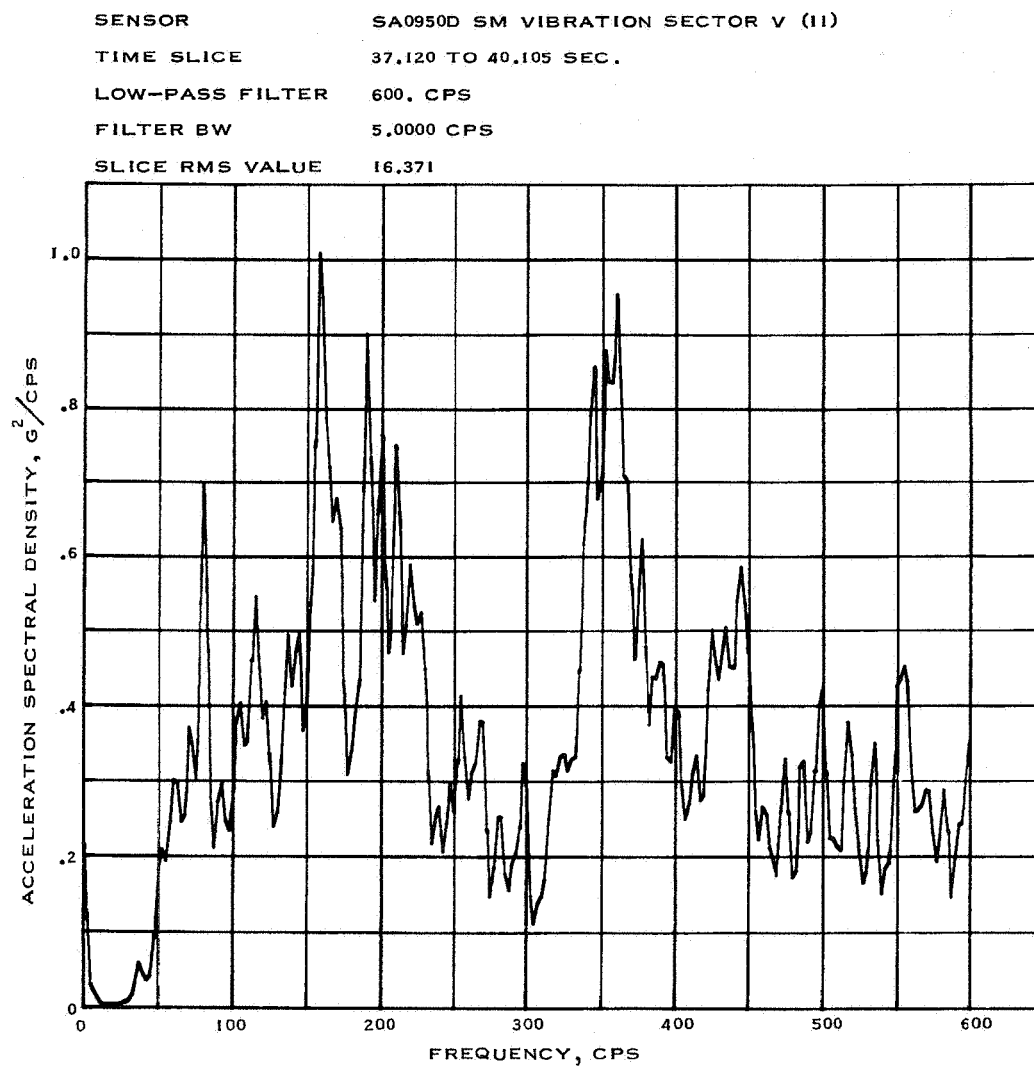


(f) Measurement SA0949D.

Figure 5.3-19.- Continued.

5-72

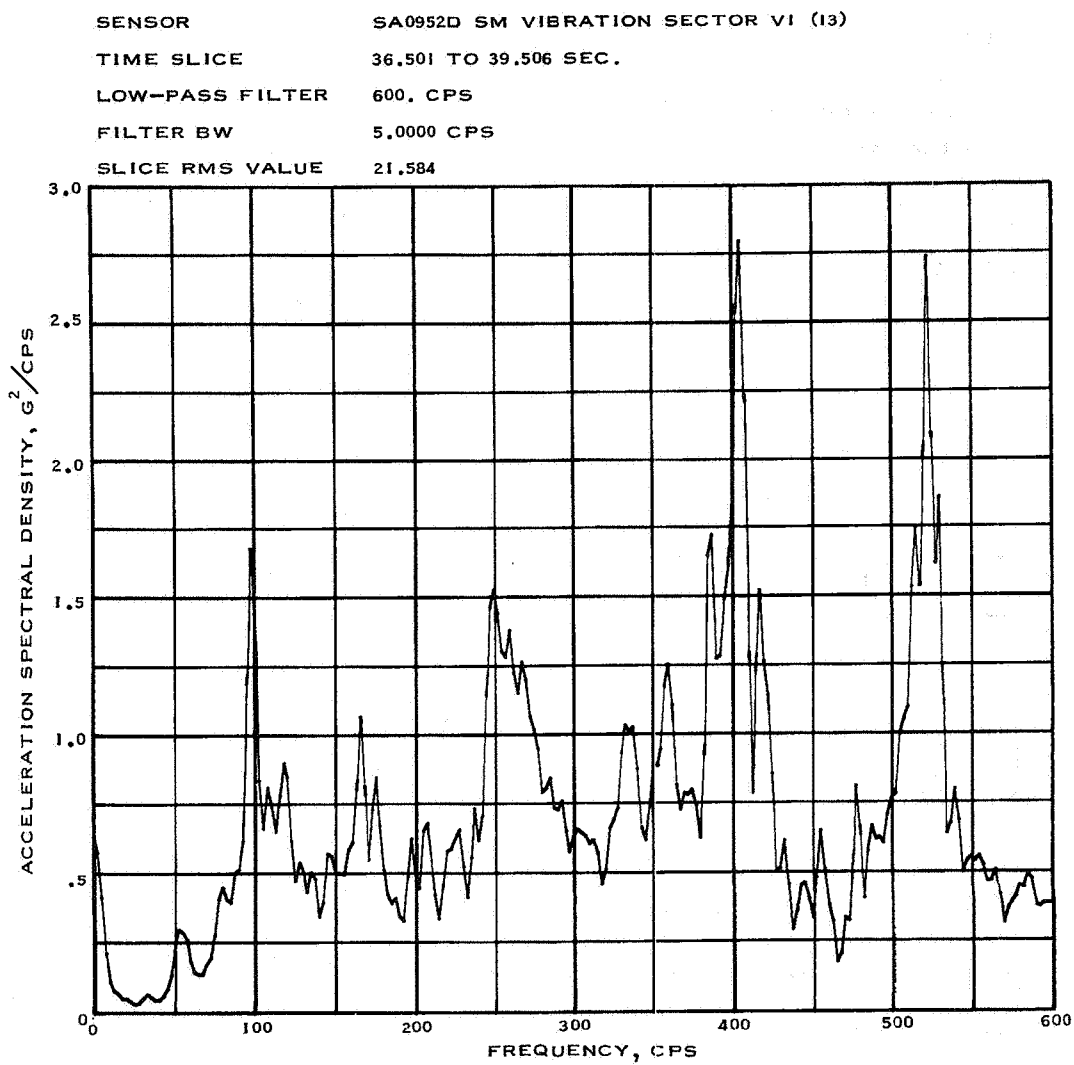
NASA-S-66-3759 APR 15



(g) Measurement SA0950D.

Figure 5.3-19.- Continued.

NASA-S-66-3763 APR 15



(h) Measurement SA0952D.

Figure 5.3-19.- Concluded.



5-74

NASA-S-66-3767 APR 15

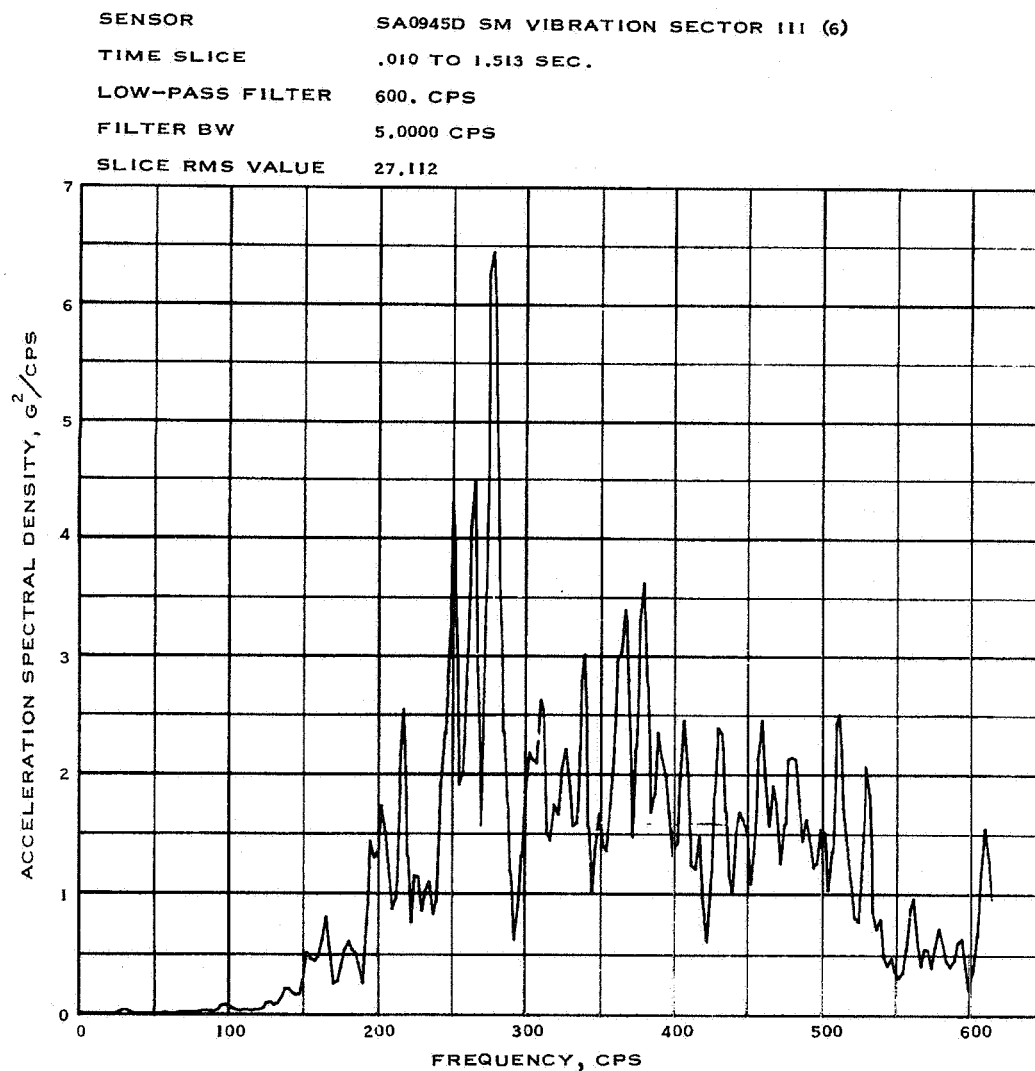


Figure 5.3-20.- SM shell acceleration spectral density at lift-off, Apollo Mission A-004.

NASA-S-66-3771 APR 15

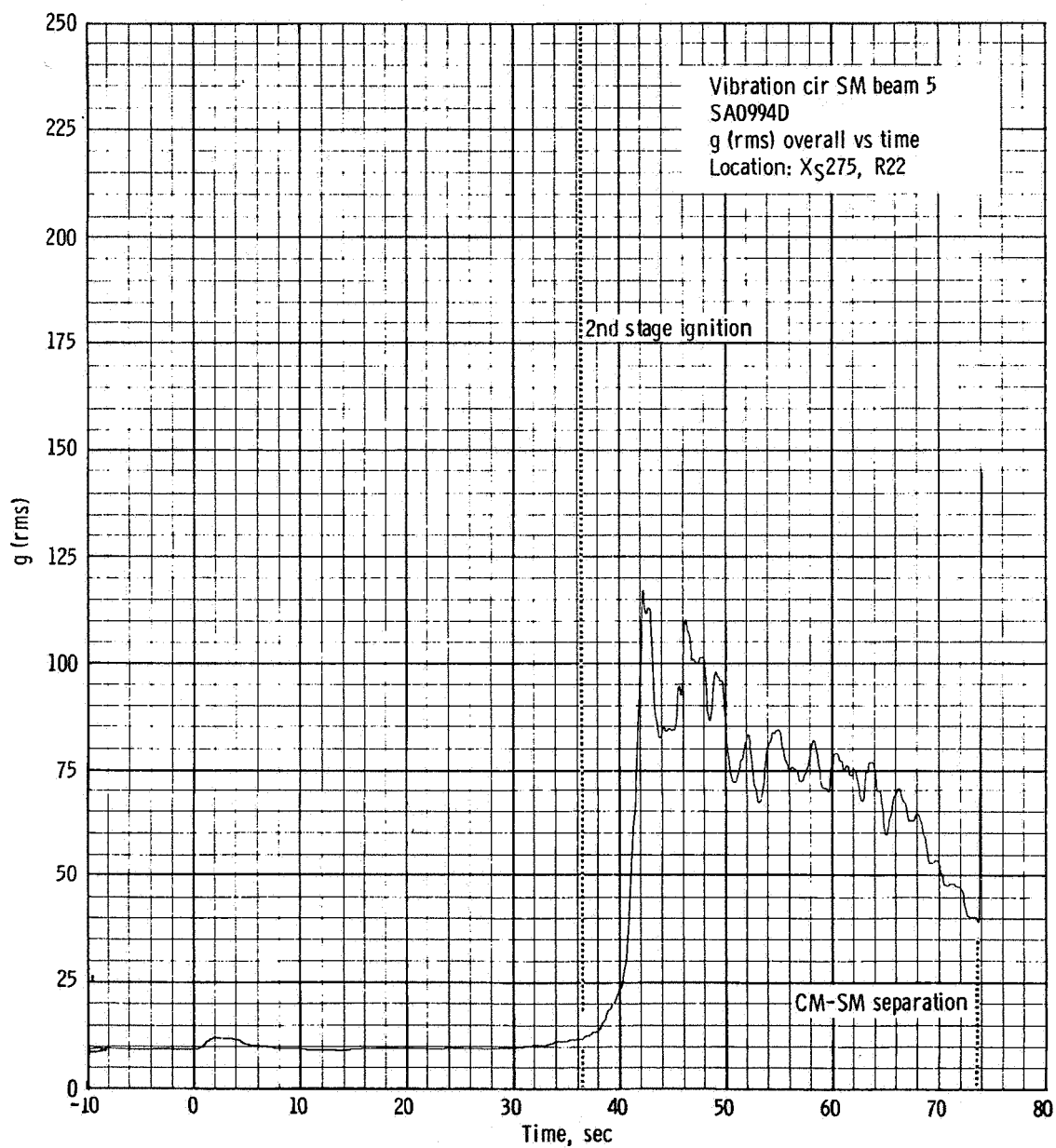


Figure 5.3-21. - rms time history of radial beam circumferential vibration, Apollo Mission A-004.

5-76

NASA-S-66-3775 APR 15

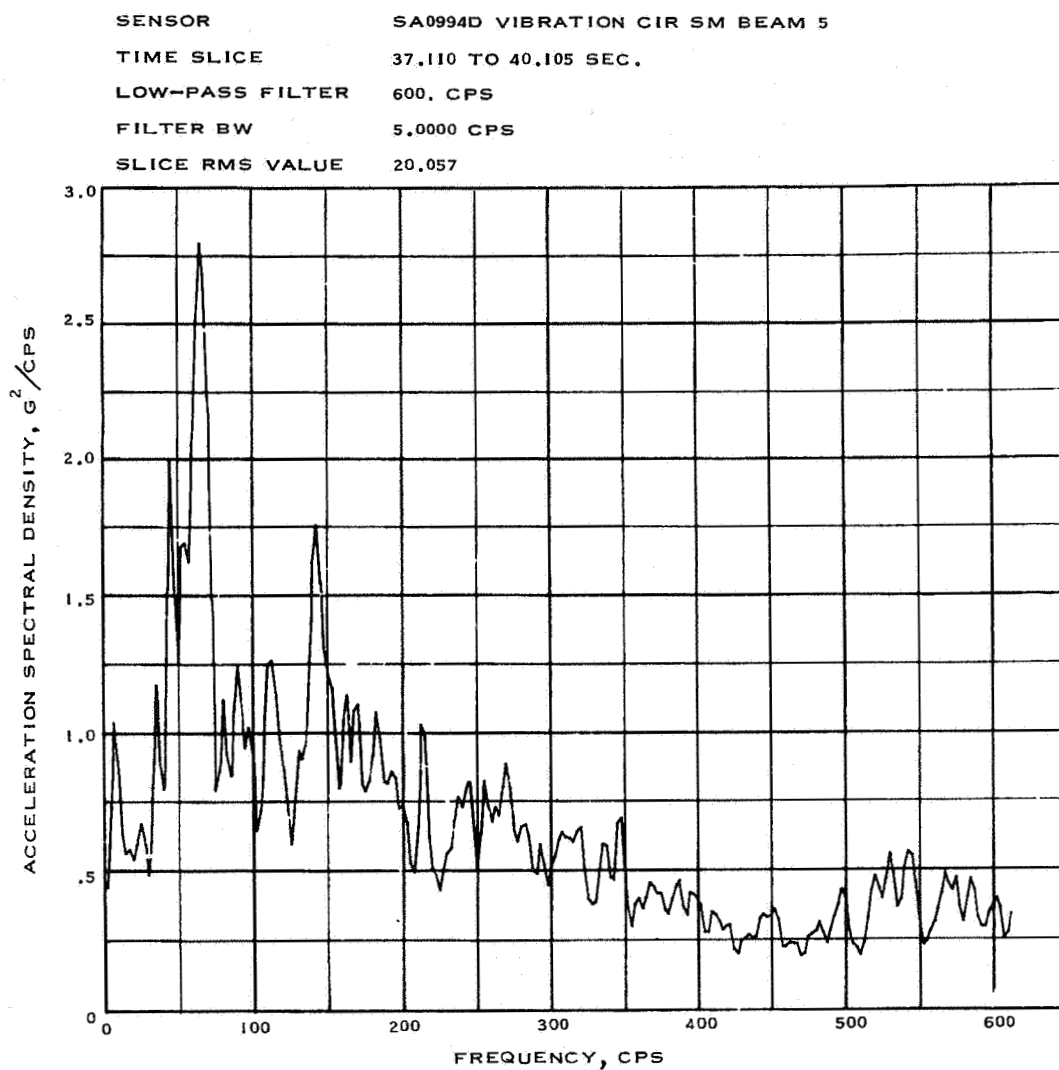


Figure 5.3-22.- Radial beam acceleration spectral density during transonic flight, Apollo Mission A-004.

NASA-S-66-3779 APR 15

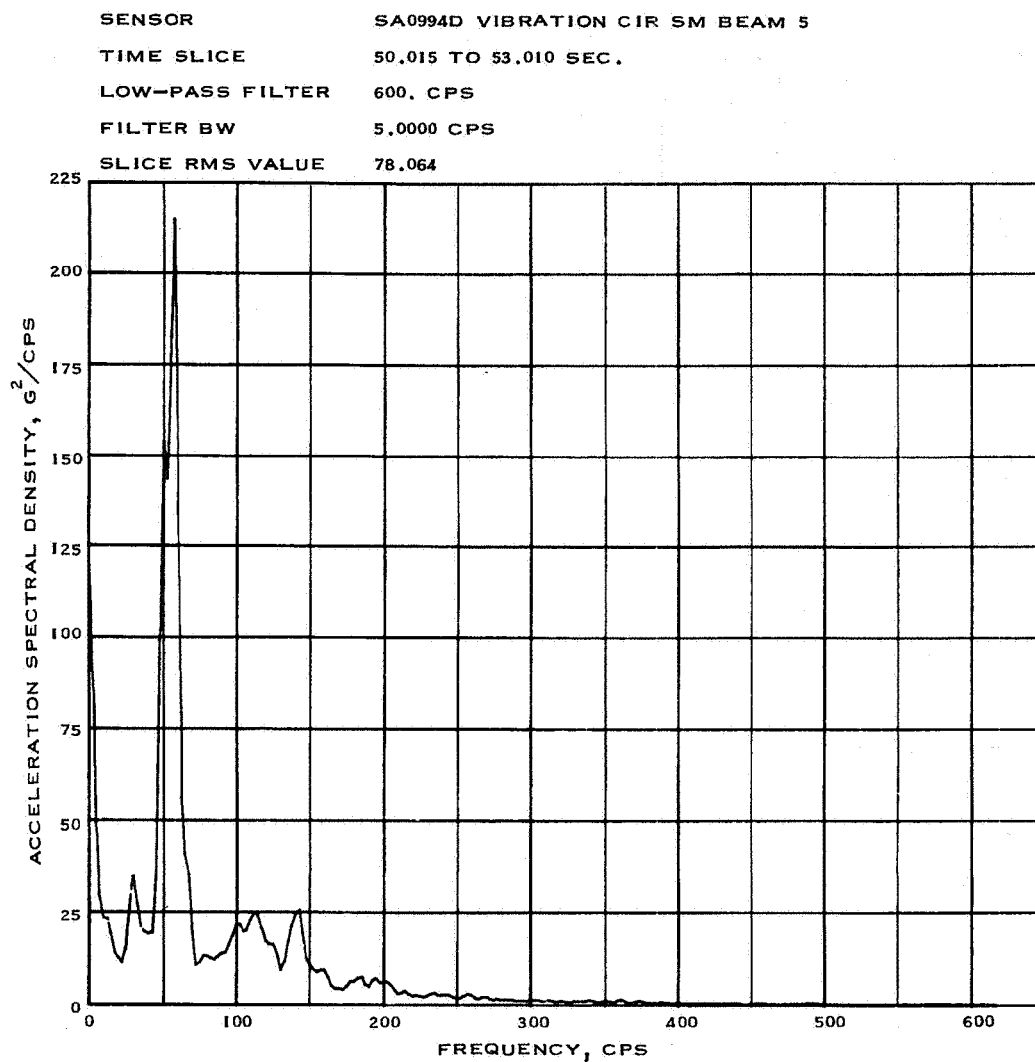


Figure 5.3-23.- Radial beam acceleration spectral density during supersonic flight, Apollo Mission A-004.

NASA-S-66-3783 APR 15

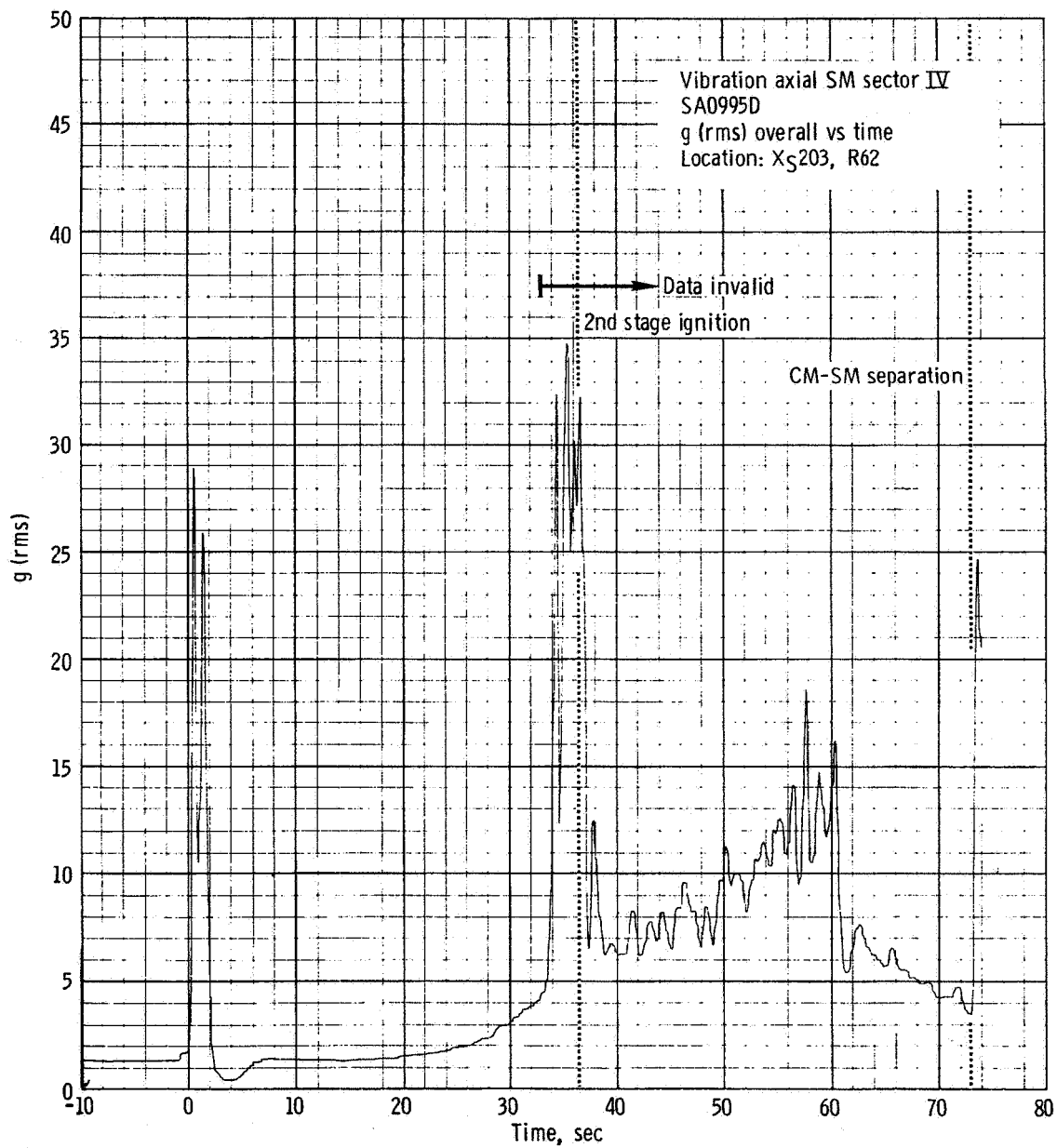


Figure 5.3-24. - rms time history of aft bulkhead vibration, Apollo Mission A-004.

NASA-S-66-3787 APR 15

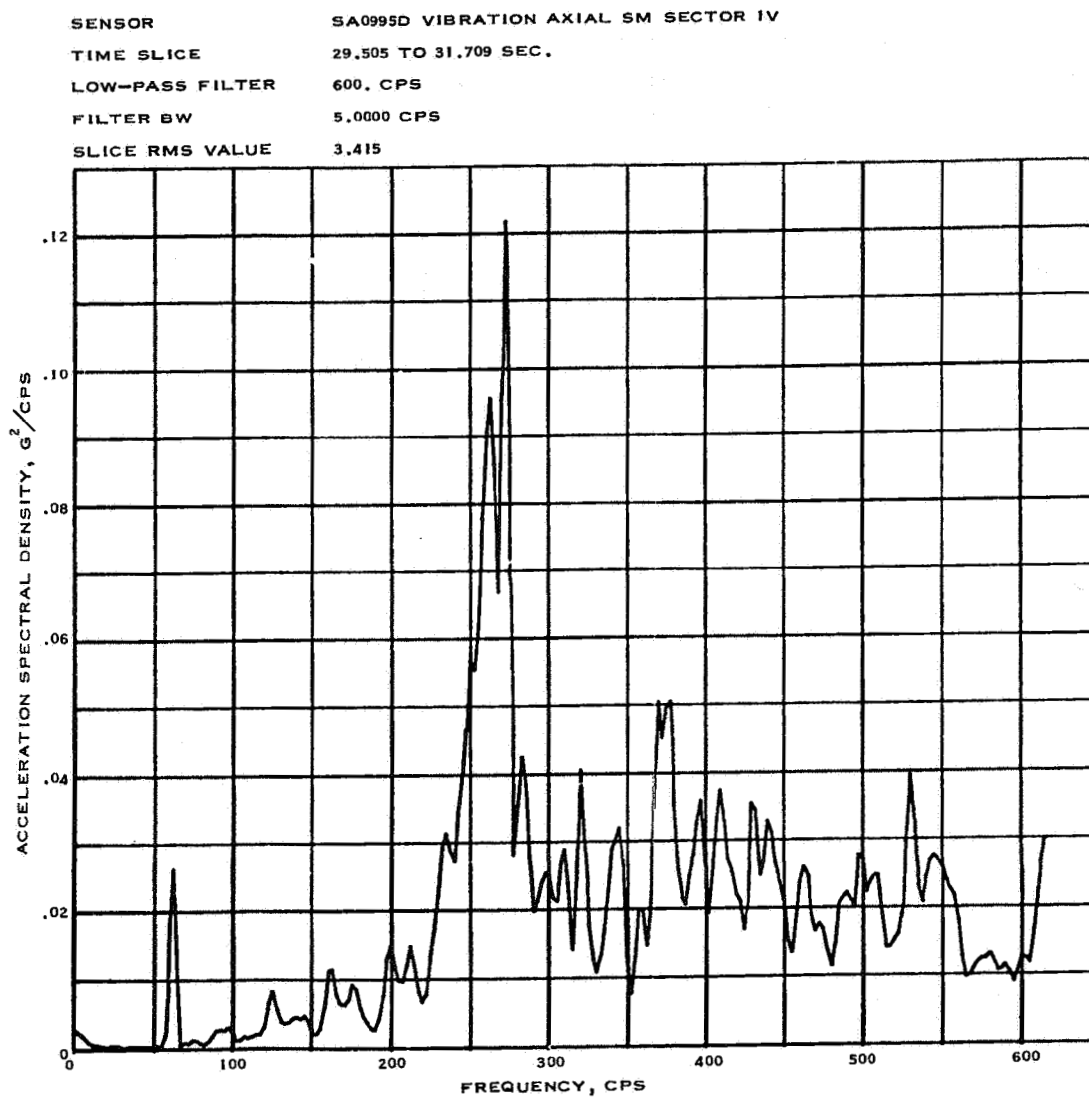


Figure 5.3-25.- Aft bulkhead acceleration spectral density,  
Apollo Mission A-004.

NASA-S-66-3791 APR 15

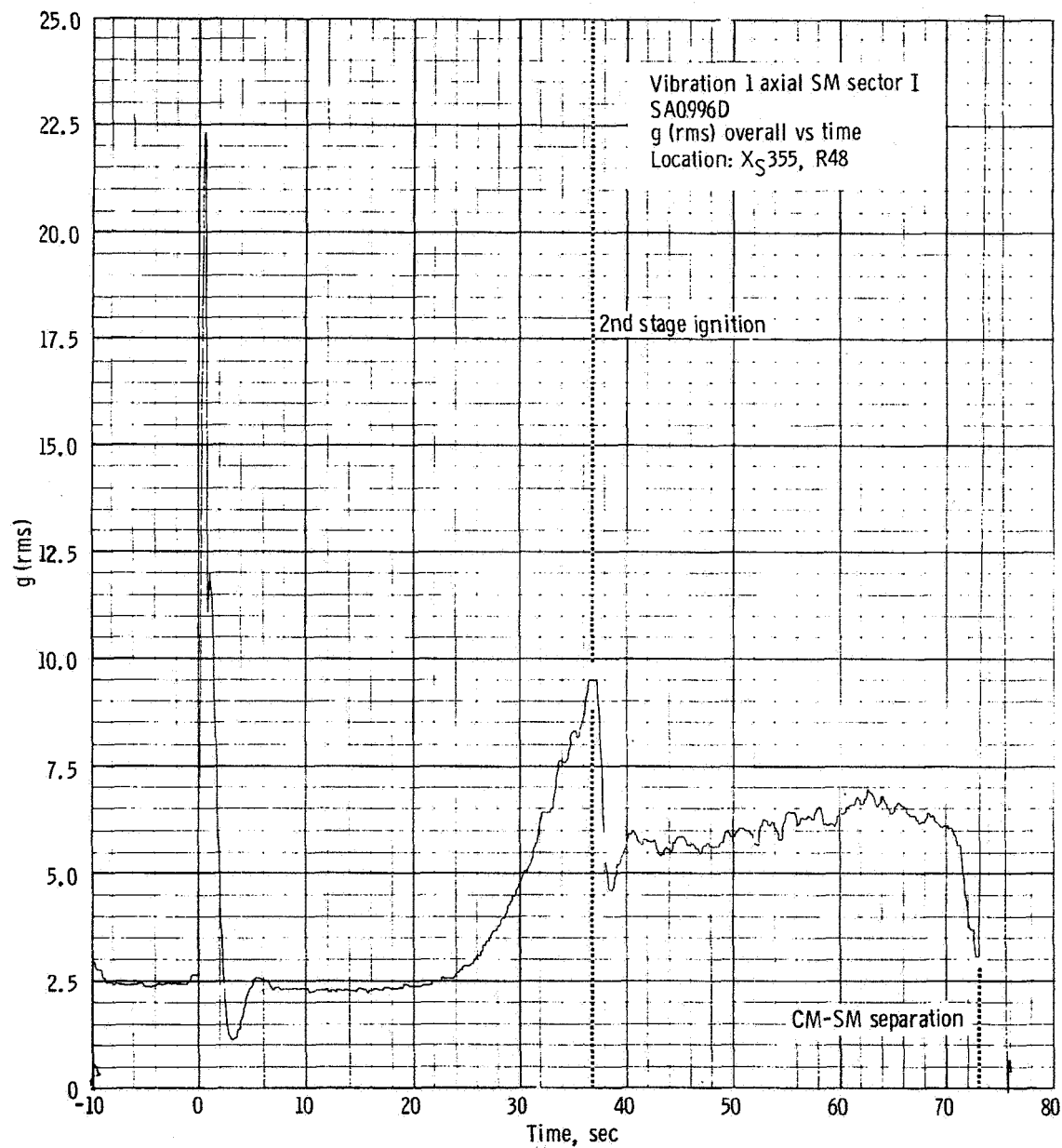
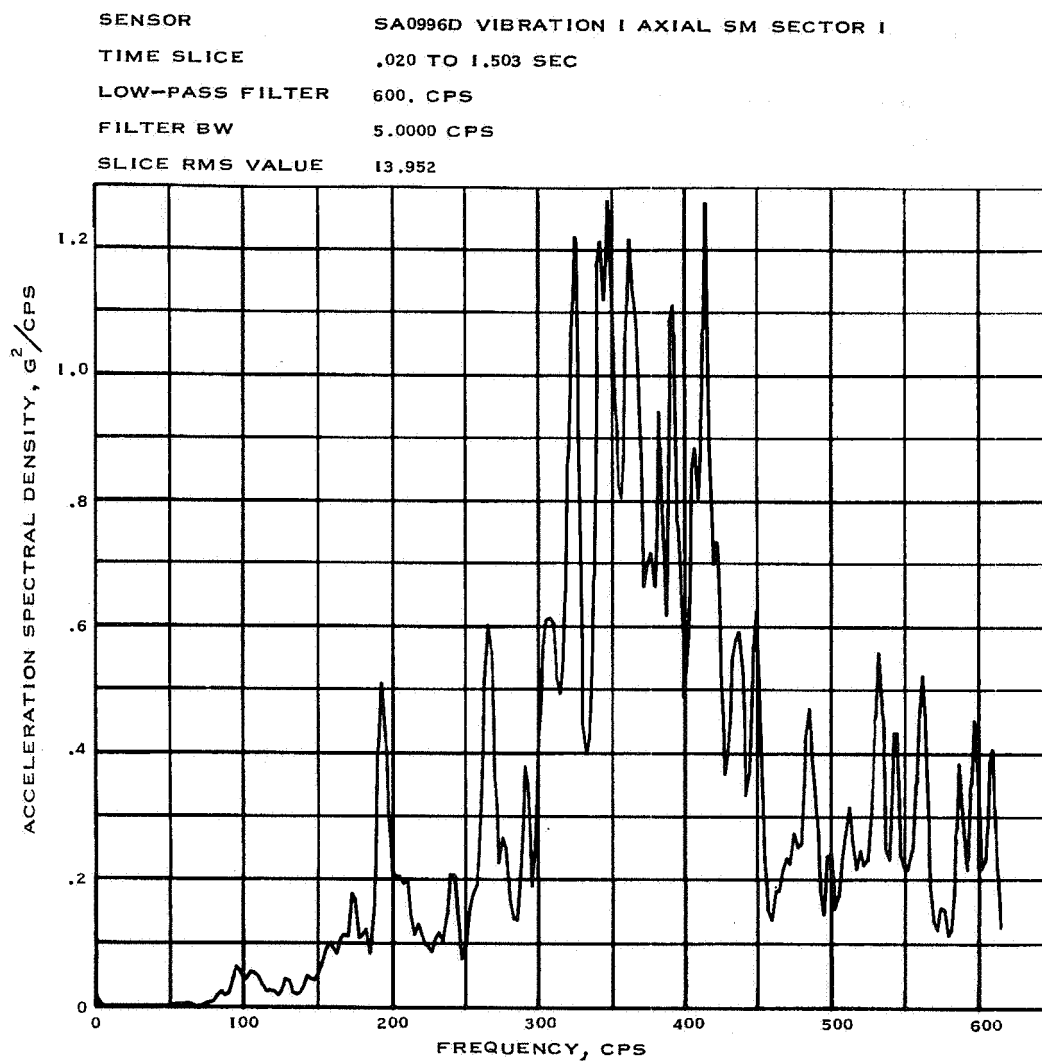


Figure 5.3-26. - rms time history of forward bulkhead vibration, Apollo Mission A-004.

NASA-S-66-3795 APR 15



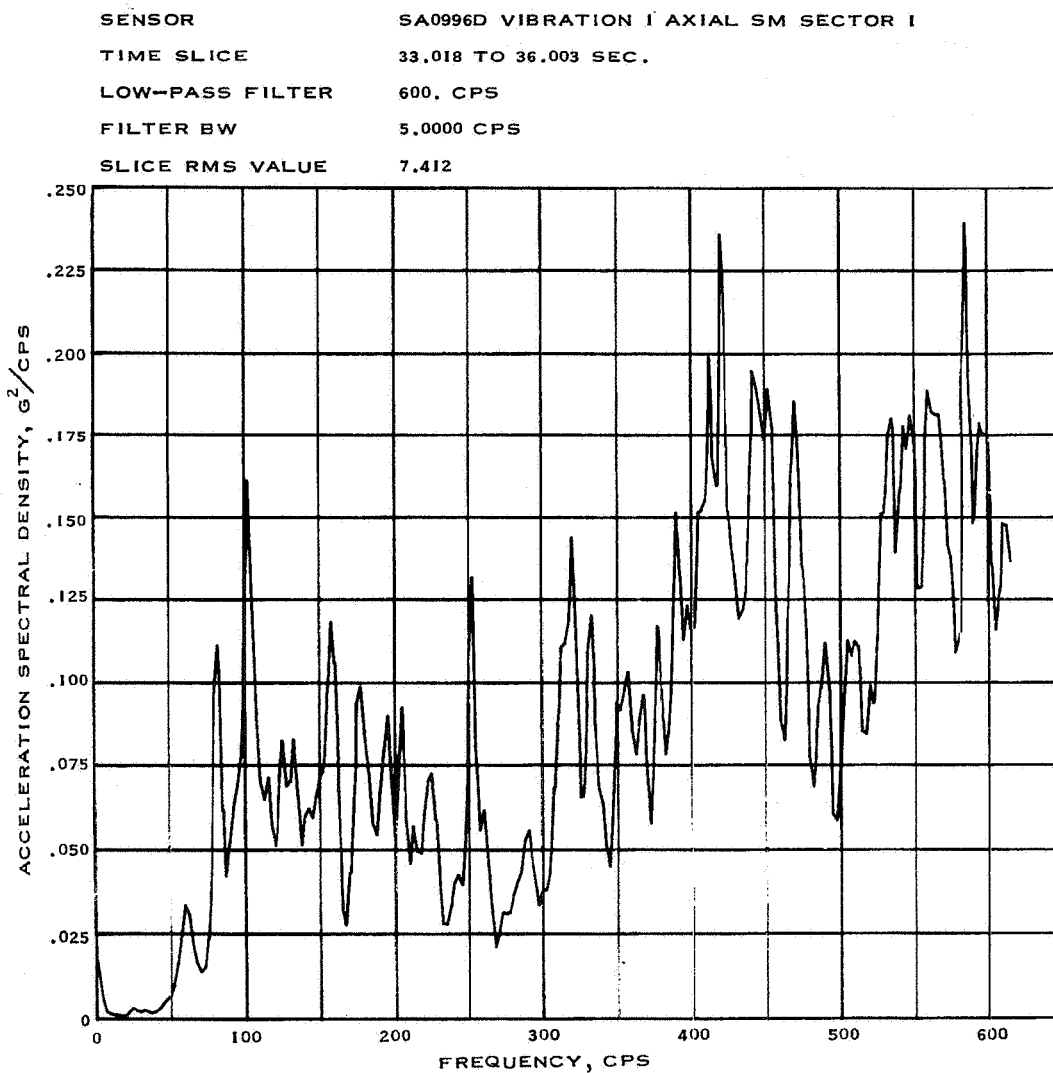
(a) Lift-off.

Figure 5.3-27.- Forward bulkhead acceleration spectral density,  
Apollo Mission A-004.



5-82

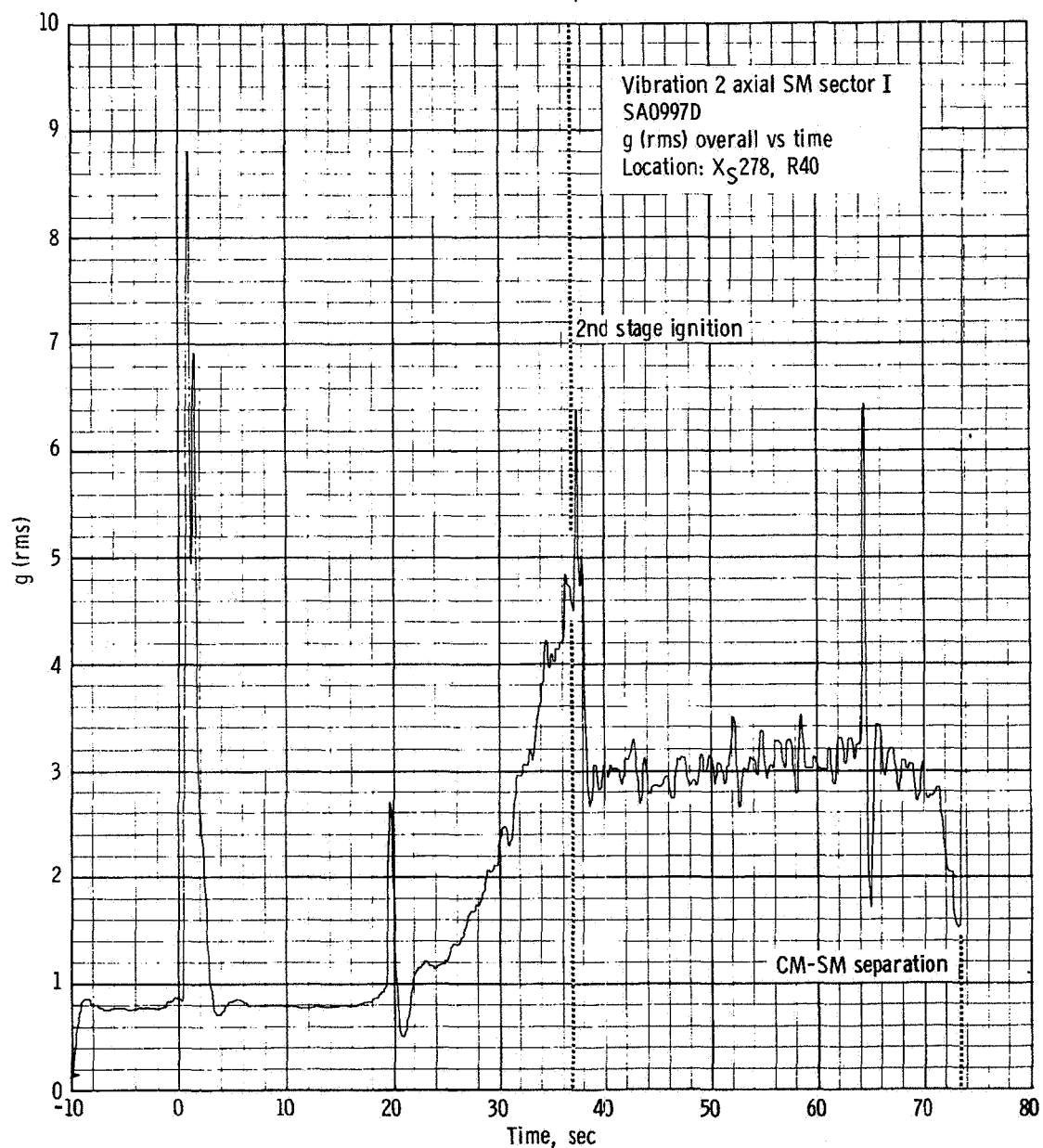
NASA-S-66-3799 APR 15



(b) During transonic flight.

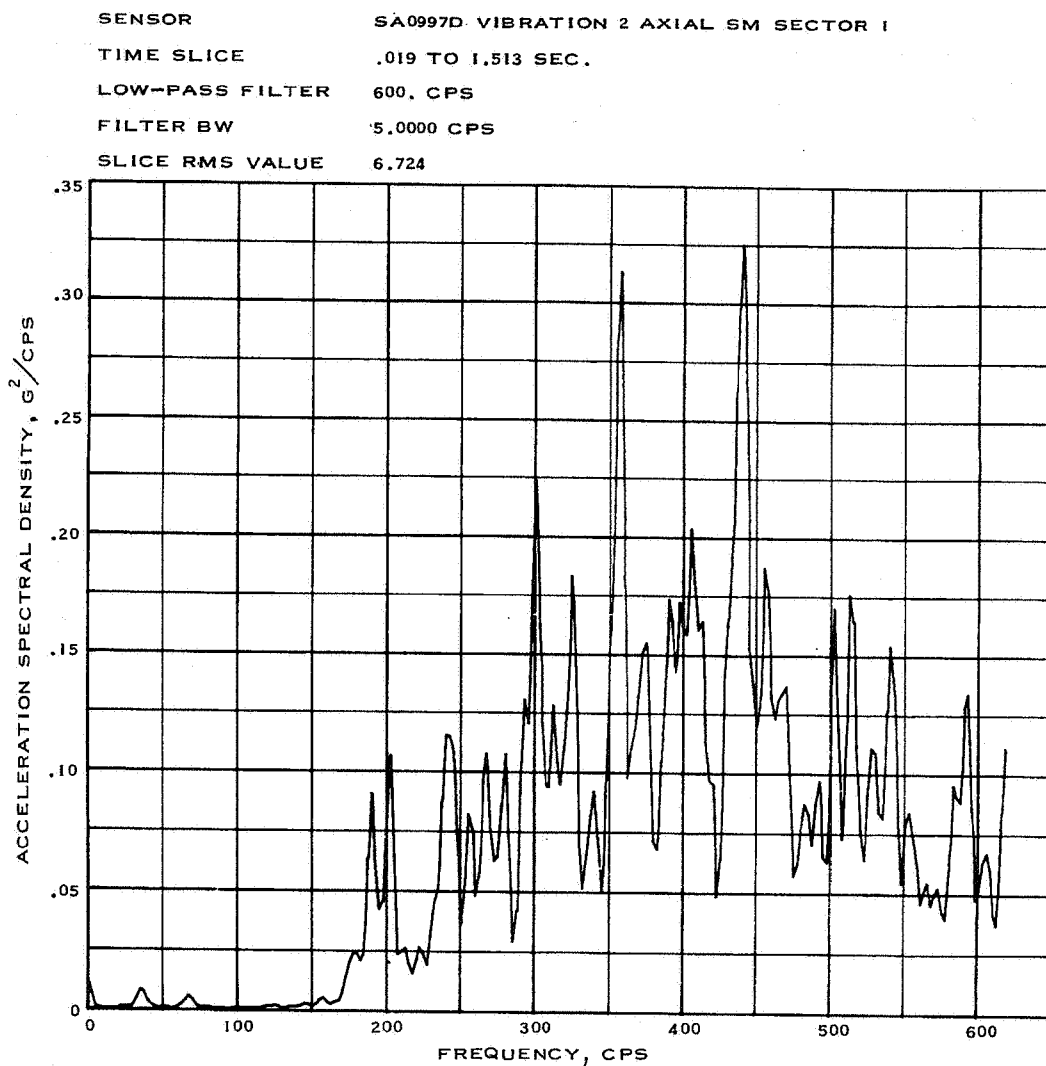
Figure 5.3-27.- Concluded.

NASA-S-66-3803 APR 15

Figure 5.3-28. - rms time history of H<sub>2</sub> tank shelf vibration, Apollo Mission A-004.

5-84

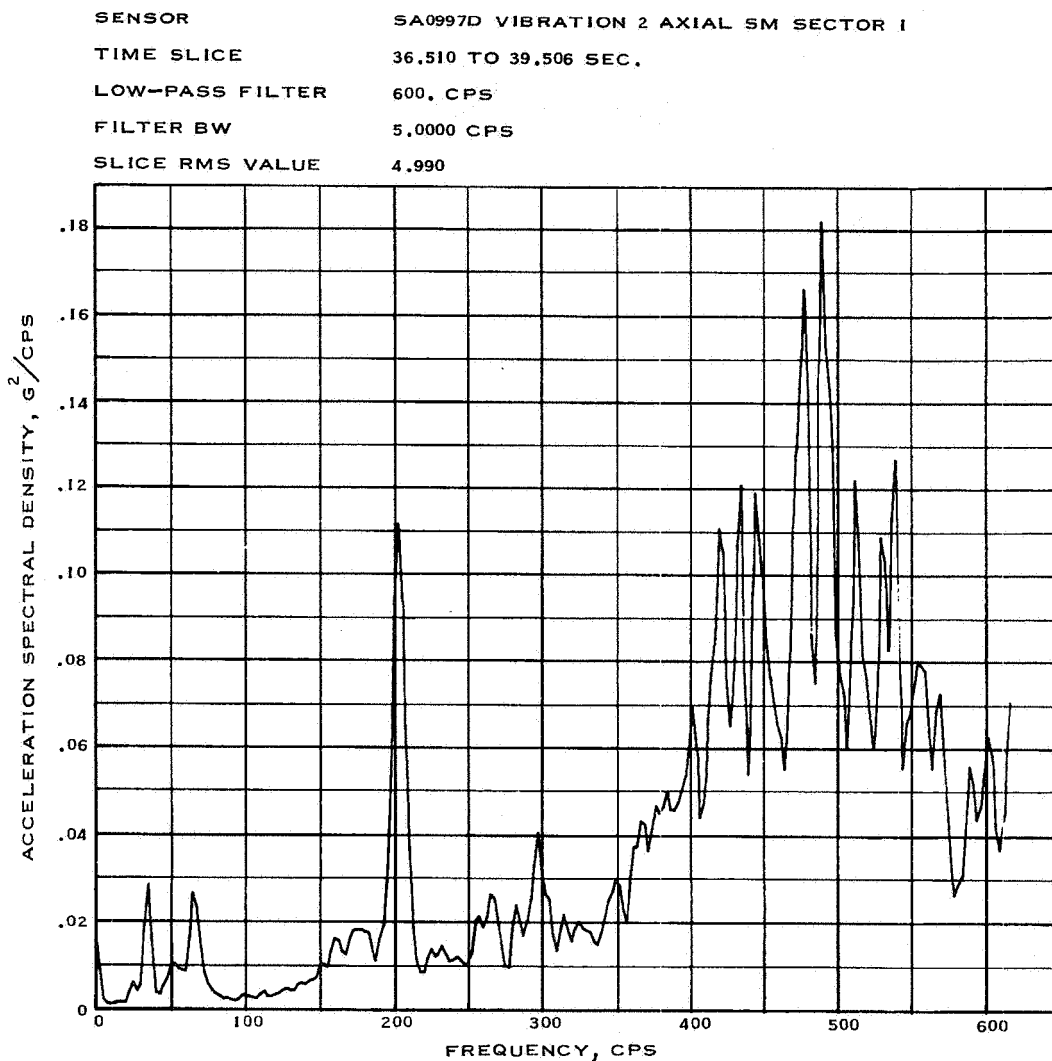
NASA-S-66-3807 APR 15



(a) Lift-off.

Figure 5.3-29.-  $H_2$  tank shelf acceleration spectral density,  
Apollo Mission A-004.

NASA-S-66-3811 APR 15



(b) During transonic flight.

Figure 5.3-29.- Concluded.

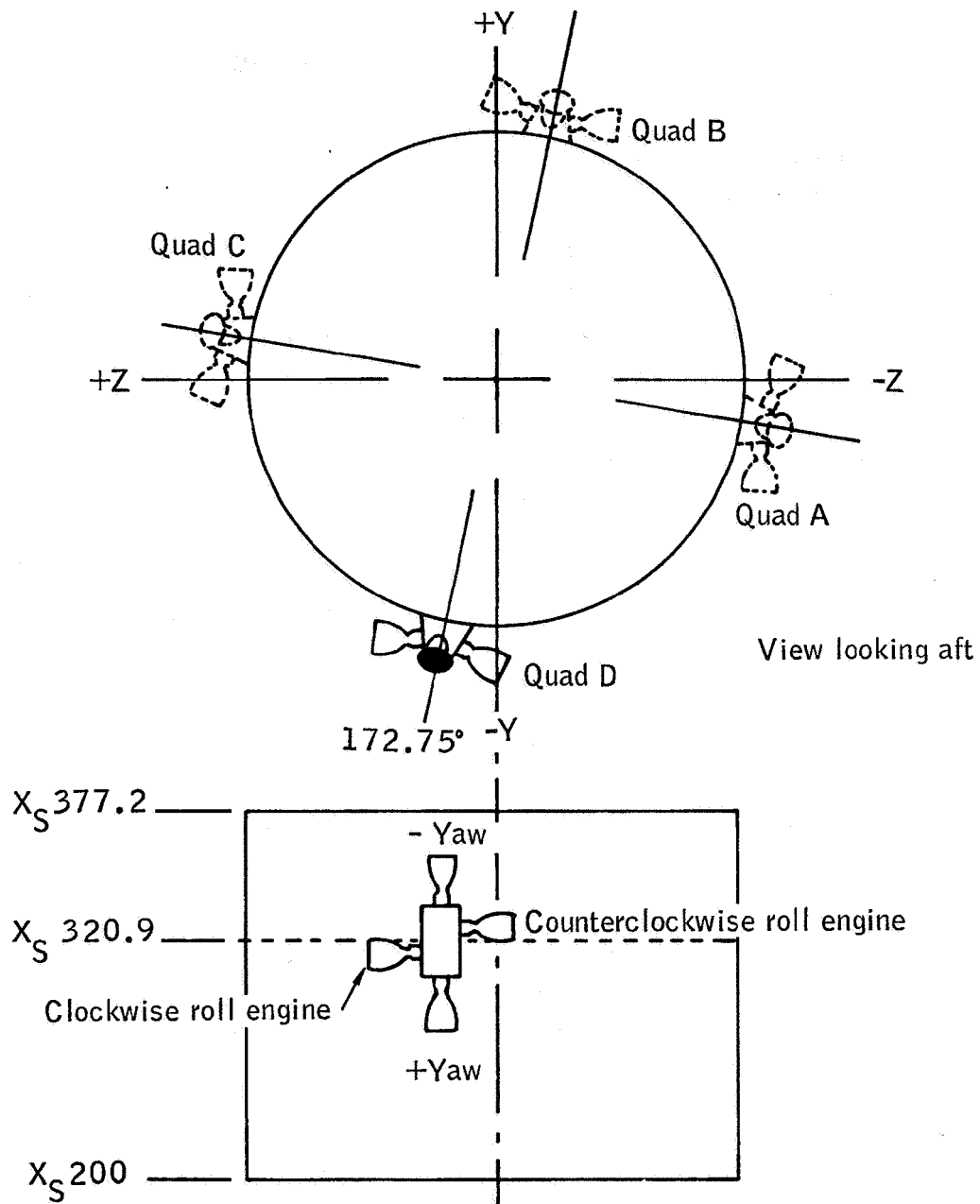
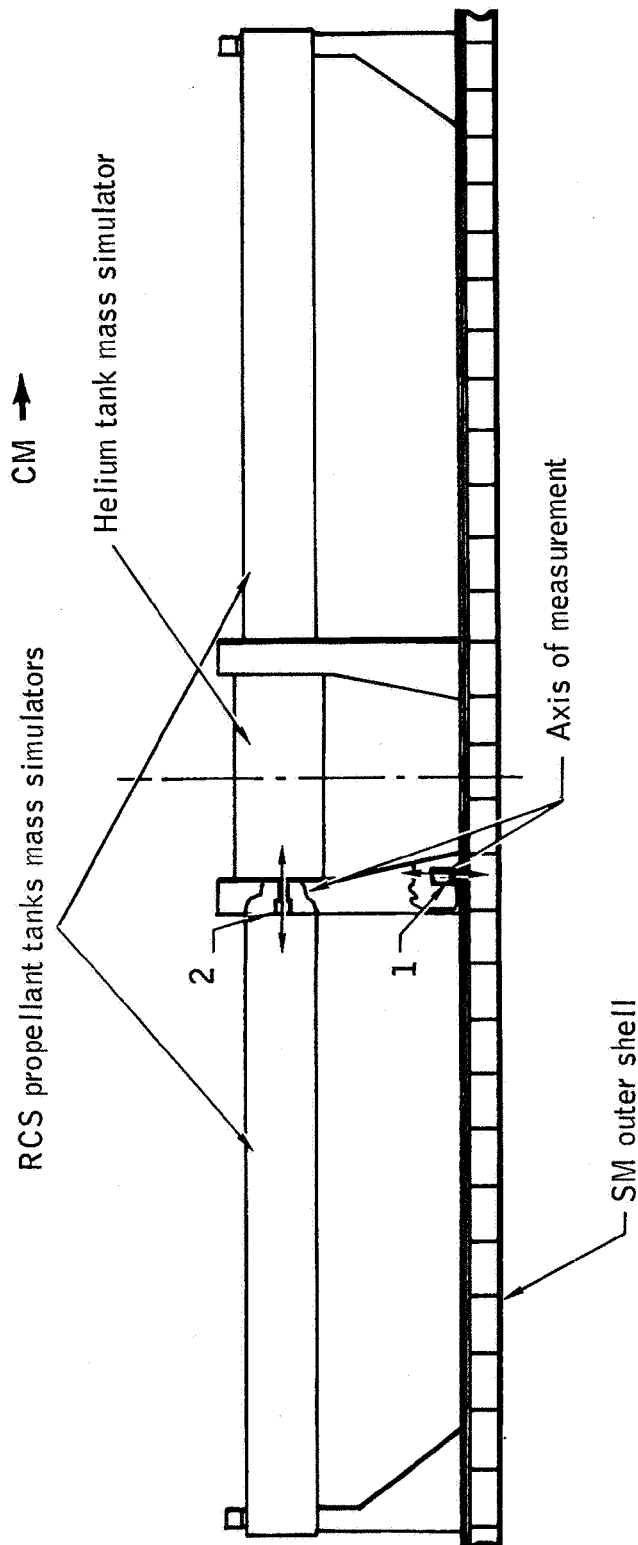


Figure 5.3-30.- Location of SM RCS quad D, Apollo Mission A-004.



<u>Measurement</u>	<u>Location</u>
SA0953D	1
SA0954D	2

Figure 5.3-31.- Location of accelerometers on SM RCS panel and propellant tank bracket, Apollo Mission A-004.

5-88

NASA-S-66-3823 APR 15

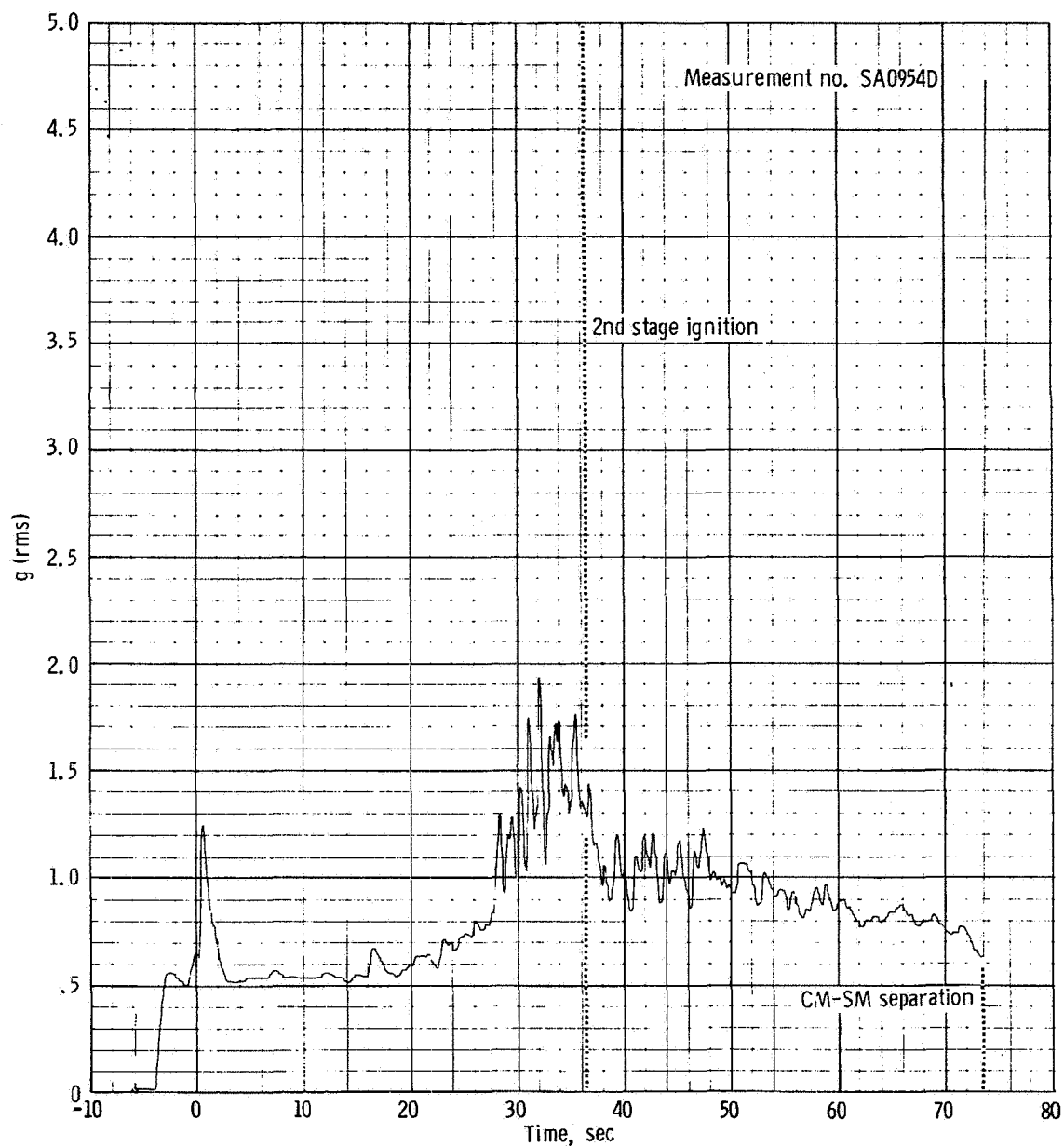


Figure 5.3-32. - X-axis vibration measured on the oxidizer tank support bracket of quad D, SM RCS, Apollo Mission A-004.

NASA-S-66-3827 APR 15

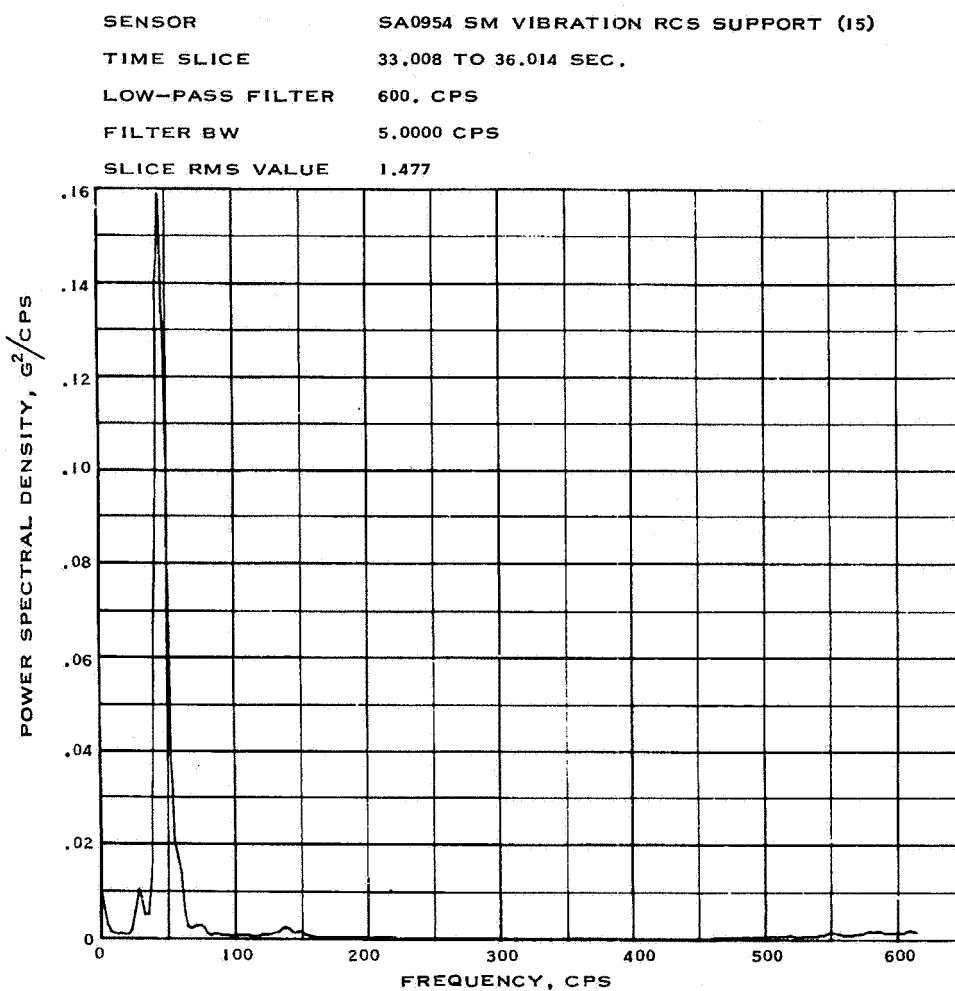


Figure 5.3-33.- Digital power spectral density of X-axis vibration measured from T+33.008 to T+36.014 seconds on the oxidizer tank support bracket of quad D, SM RCS, Apollo Mission A-004.



5-90

NASA-S-66-3831 APR 15

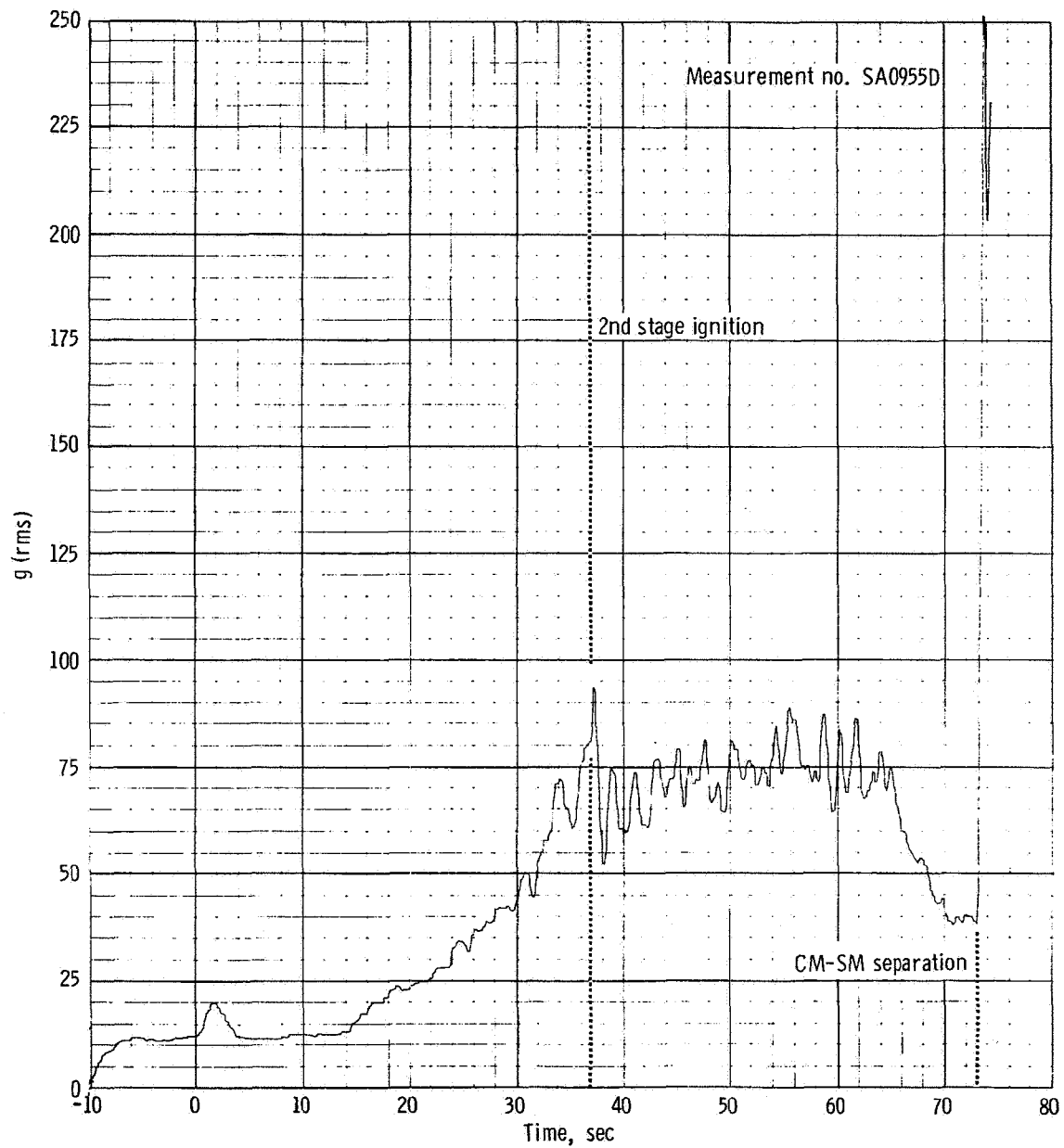


Figure 5.3-34. - Radial vibration measured in the counterclockwise roll engine nozzle of quad D, SM RCS, Apollo Mission A-004.

NASA-S-66-3835 APR 15

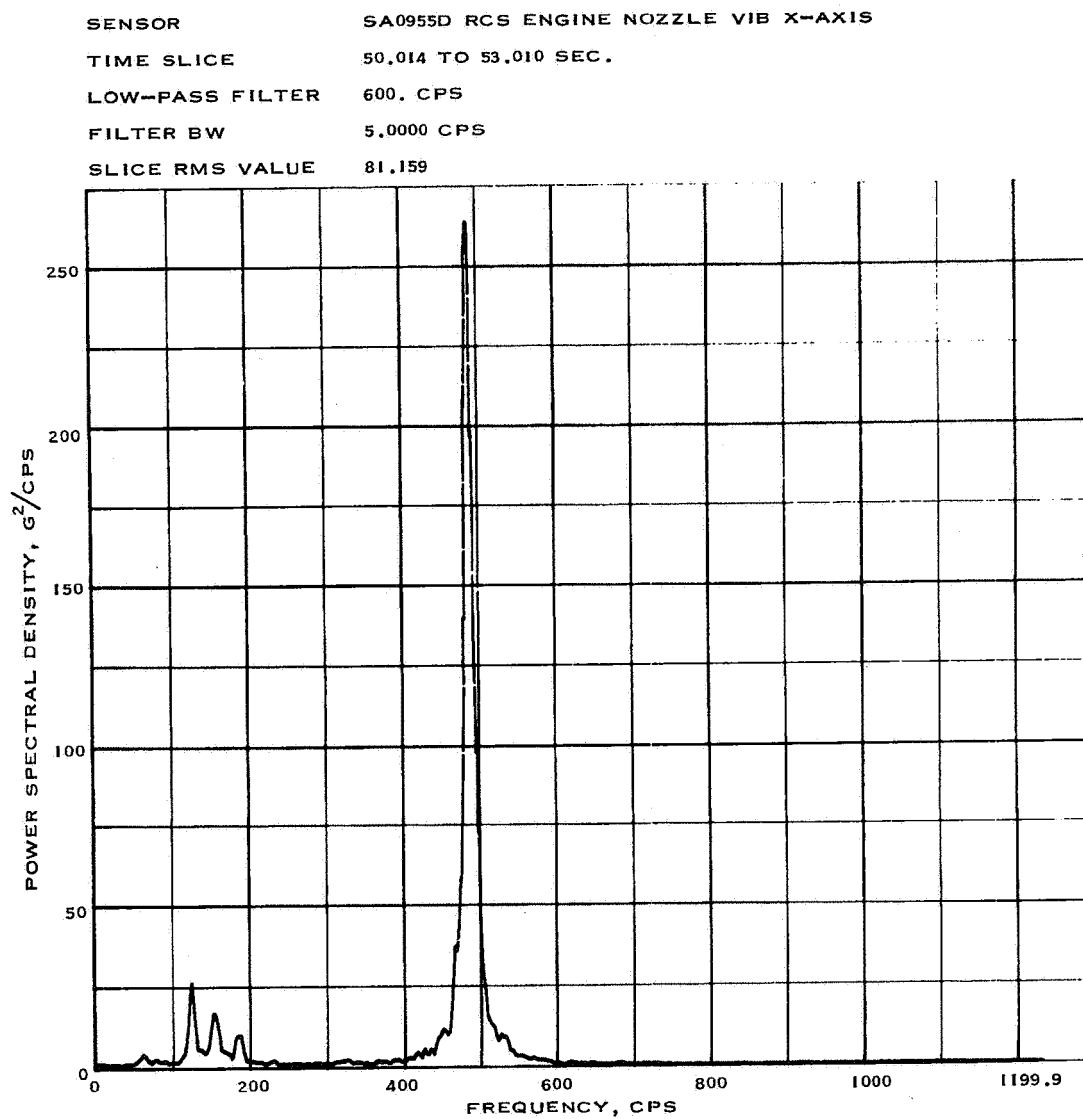


Figure 5.3-35.- Digital power spectral density of radial vibration measured from T+50.014 to T+53.010 seconds in the counter-clockwise roll engine nozzle of quad D, SM RCS, Apollo Mission A-004.

5-92

NASA-S-66-3839 APR 15

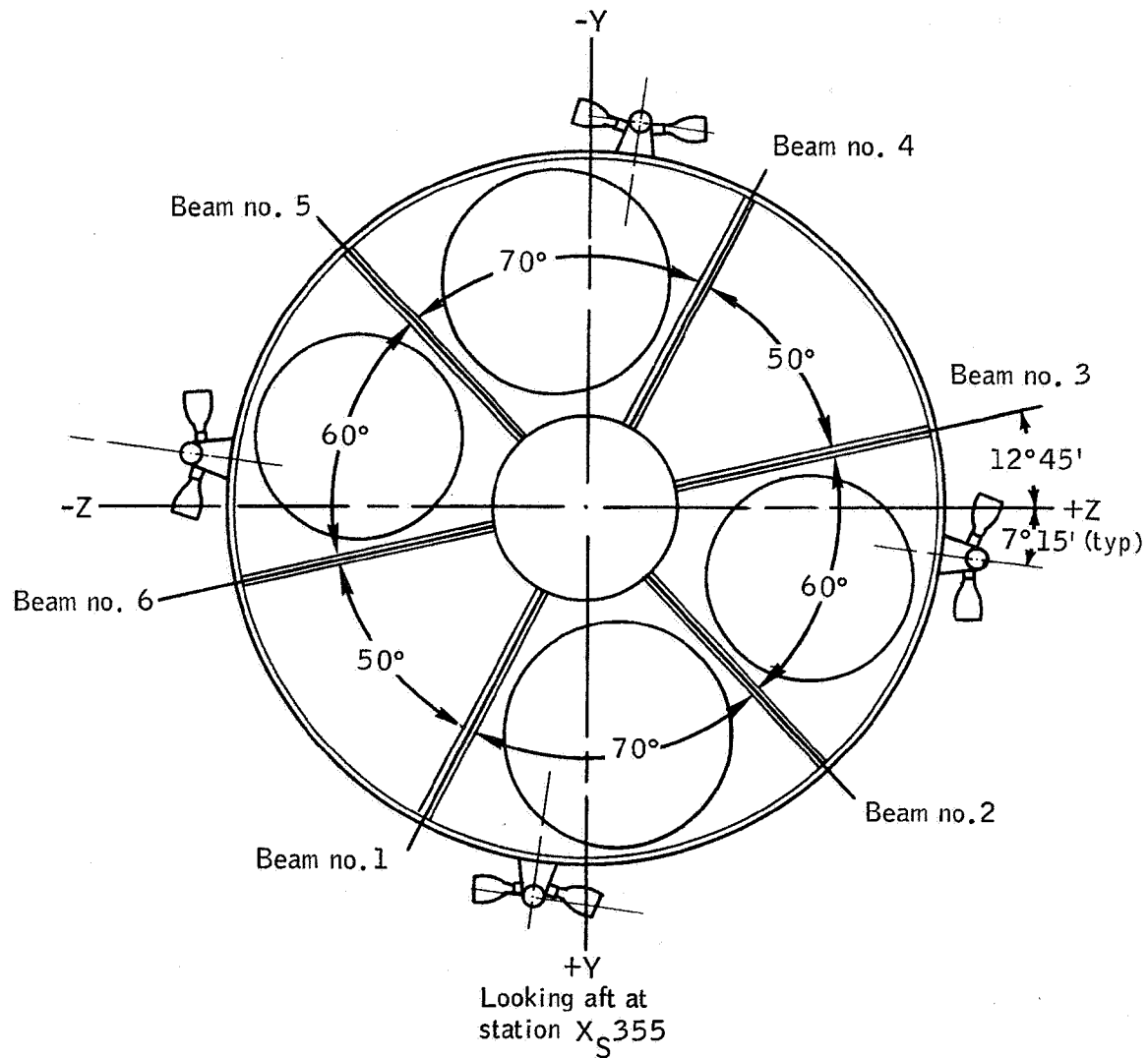


Figure 5.3-36.- Location of radial beams in service module for Apollo Mission A-004.

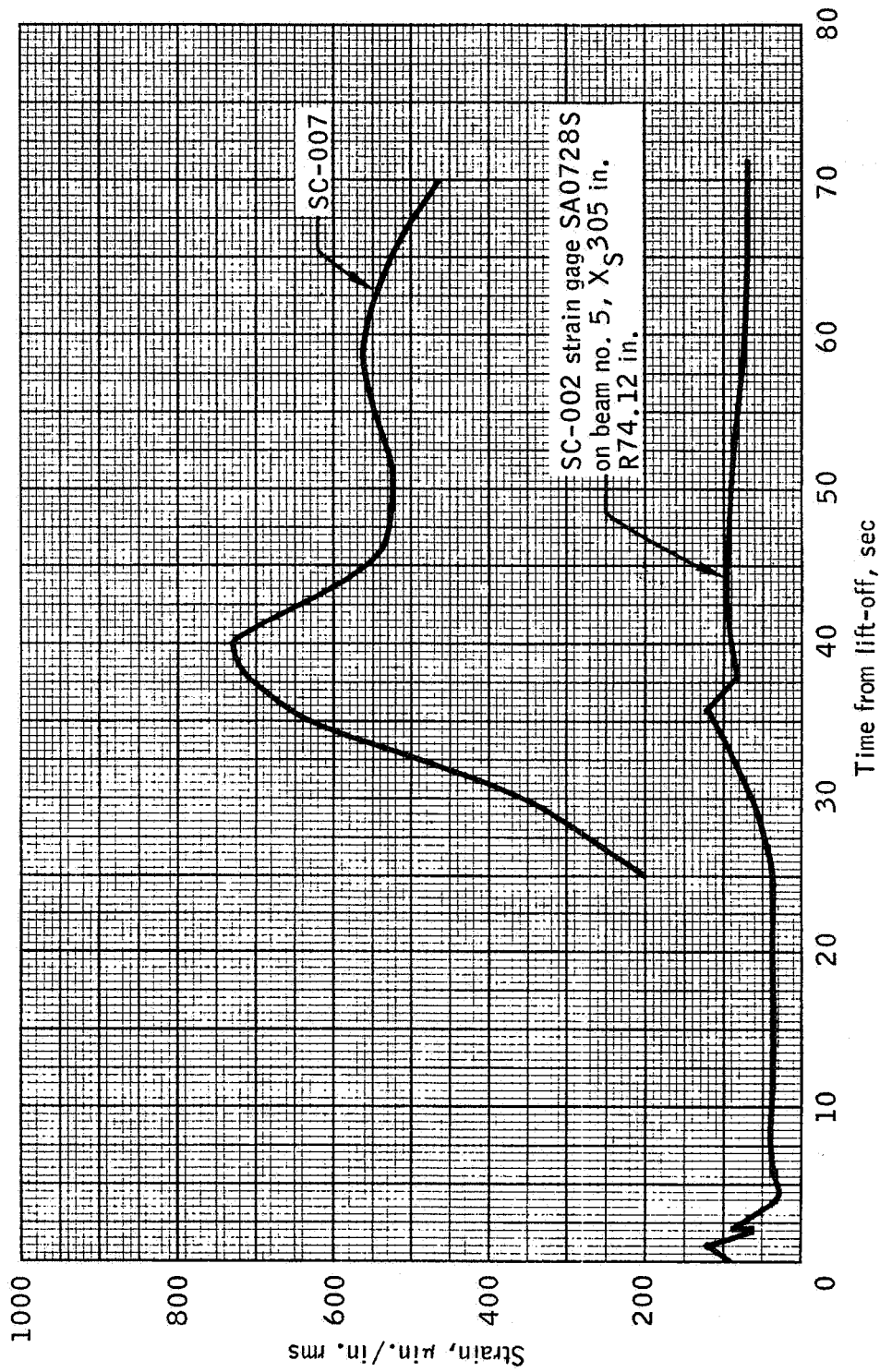


Figure 5.3-37.- Comparison of rms strain history from typical radial beam web panel on SC-002 (Apollo Mission A-004) with strain from ground acoustic test of SC-007.

NASA-S-66-3847 APR 15

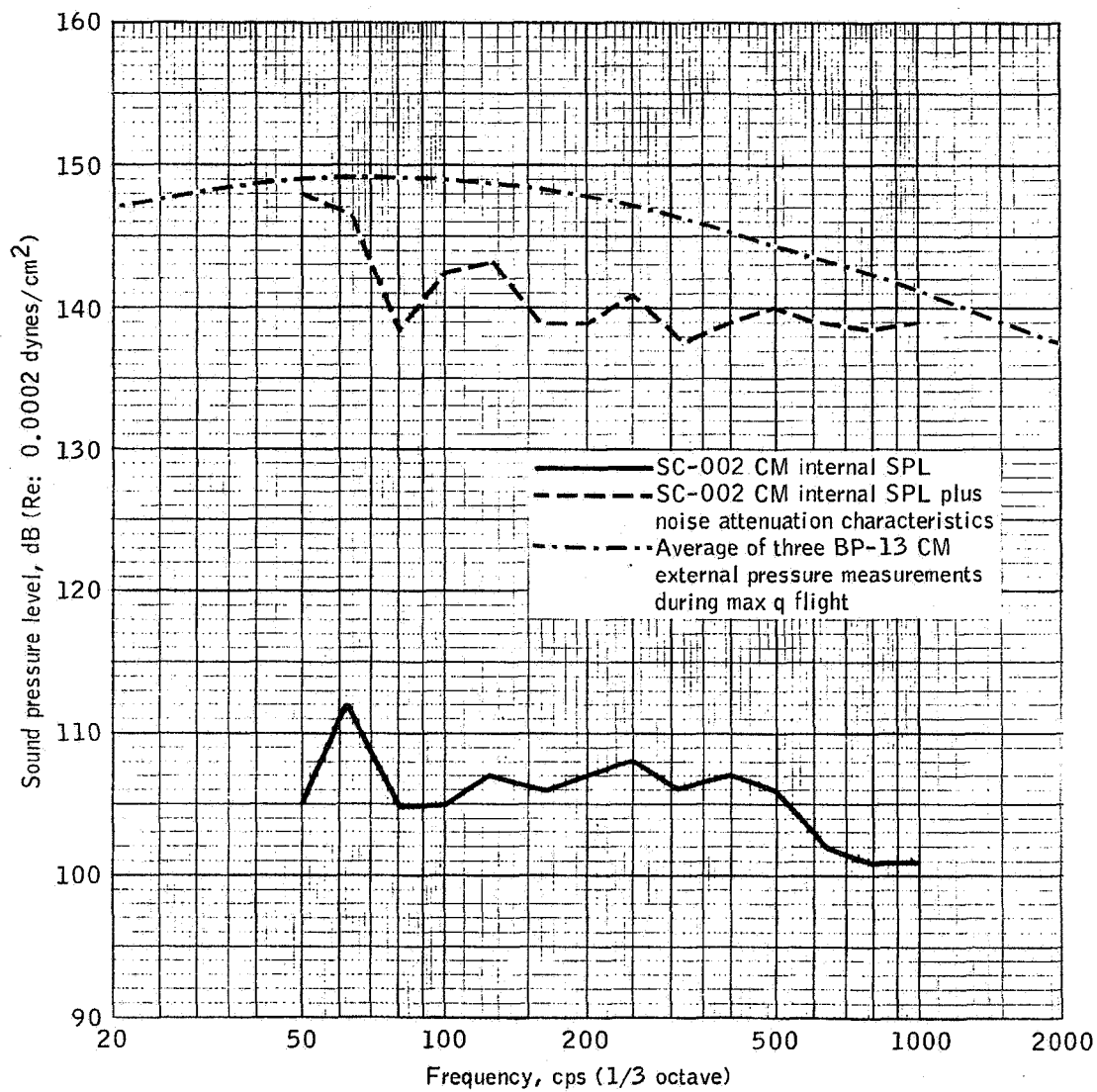


Figure 5.3-38.- Comparison between BP-13 measured and SC-002 calculated CM external acoustic environment on Apollo Missions A-101 and A-004.

NASA-S-66-3851 APR 15

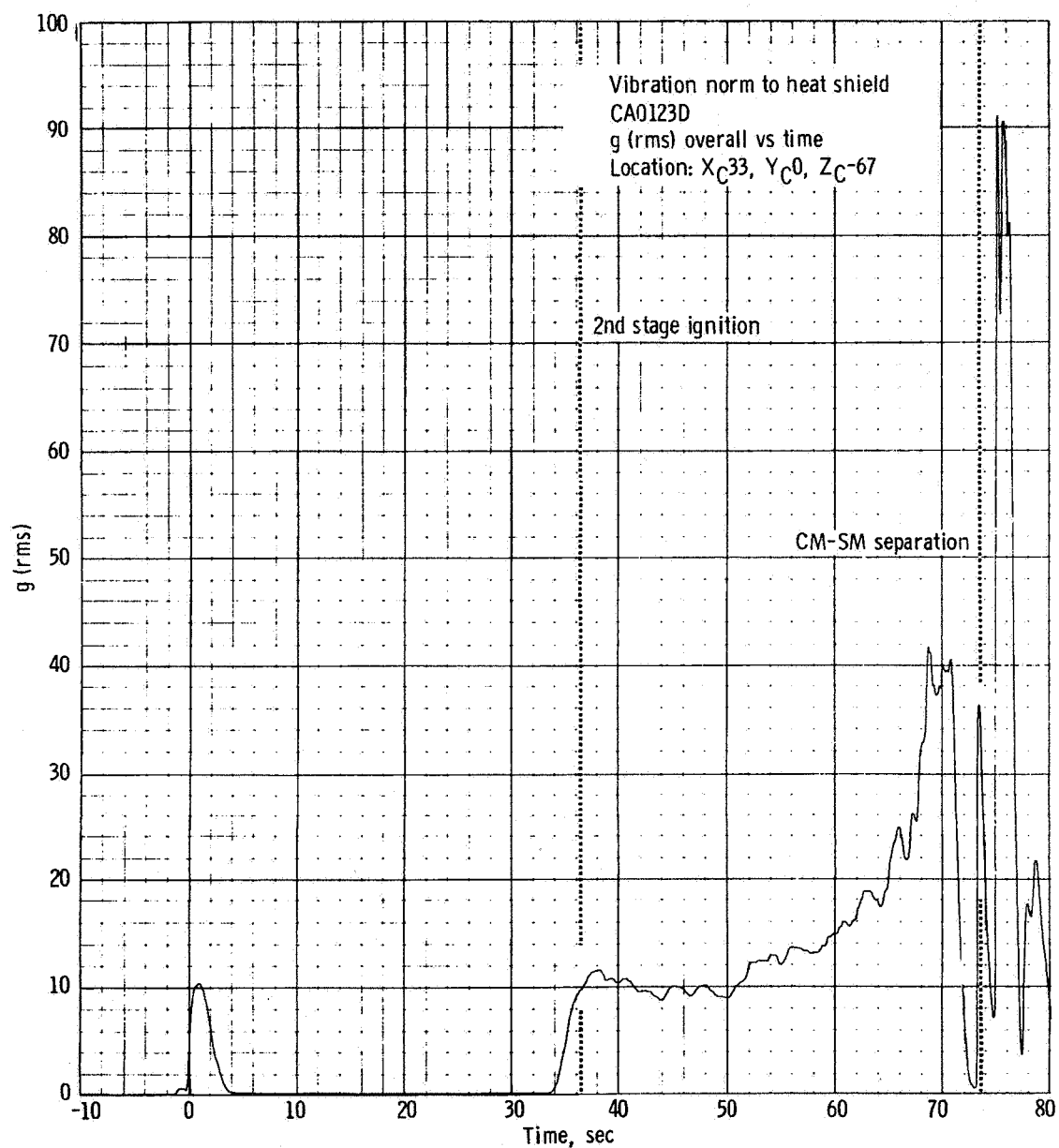


Figure 5.3-39. - rms time history of CM heat shield vibration, Apollo Mission A-004.

#### 5.4 Boost Protective Cover

Description.- The boost protective cover (BPC) consisted of a hard cover over the apex portion of the command module (CM), and a soft cover made up of seven panels over the remainder of the conical portion of the CM (see fig. 5.4-1). The boost protective cover was of Block I configuration and construction except for the interface of the hard cover to soft cover on six of the seven soft cover panels. The interface on the panel containing the side access hatch did have the Block I interface structure. The cover was also modified to accommodate the installation of 36 pressure measurements, and 6 calorimeter measurements. This instrumentation was mounted on the CM heat shield through individual bosses, and mated to matching holes in the BPC so that the transducer surfaces were flush with the BPC outer surface. The basic installation was the same as that on BP-22 (ref. 4).

The hard cover over the CM apex was constructed of ablative cork bonded to a fiberglass honeycomb substructure. The soft panels were laminated with a layer of teflon impregnated glass cloth, a second covering of nylon fabric, and an outer layer of cork. An additional panel over the hatch area was removable with all other panels installed. Incorporated in this panel was a circular window coinciding with the CM hatch window. Protuberances covering the CM-SM umbilical, scimitar antennas, and CM venting systems were incorporated in the soft panels. The BPC was fastened together with mechanical fasteners at all joints.

Instrumentation.- Four static pressure transducers were installed to measure the pressure between the boost protective cover and CM heat shield. One of the measurements was under the hard cover and three under the soft cover. (See section 11.2 for exact locations and range.) These pressures in conjunction with the external conical surface pressures were used to obtain the differential pressure across the cover. In addition, six calorimeters were installed on the external surface to measure heating rates throughout the mission.

Performance.- The essential function of the boost protective cover is to protect the CM crew compartment heat shield and thermal control coating from ablating, charring, or discoloring during launch. It also serves to reduce the sooting on the CM windows and CM thermal control coating following the firing of the tower-jettison motor. The test objective for the boost protective cover on this flight was to demonstrate its structural capability to withstand the launch environment. There is no requirement for the cover to remain intact following an abort.

Based on tracking and onboard films, in addition to the pressure data, the boost protective cover performed as planned. There was no

evidence from these data of any breathing or flutter of the soft cover, or any other structural problems occurring during launch and pitch-up. The cover remained intact until after abort initiation when the soft cover failed, as expected. Based on the pressure data and film coverage, the soft cover failure started during the first launch-escape vehicle (LEV) tumble, approximately 1.5 to 2 seconds after abort initiation. Recovery evidence indicated that the hard cover was removed with the launch-escape subsystem (LES) as planned.

Figure 5.4-2 shows typical pressure conditions for the SC-002 flight. As can be seen, the differential pressure across the cover in the areas of instrumentation was in a direction to press the cover to the CM surface.

Six calorimeters were located on the command module, flush with the boost protective cover, to measure the heat flux resulting from LES motor plume impingement during the mission abort. All six calorimeters had ranges from 0 to 100 Btu/ft<sup>2</sup>/sec (see fig. 11.2-10 and table 11.2-I). An examination of the flight data indicated that the boost protective cover received considerable heat flux from the LES motor plume, which expanded much more than on previous flights because of the high-altitude abort conditions. Reference 1 (figs. CAR-145, CAR-146, CAR-147) contains the measured heat flux on the boost protective cover. The following table shows the heat-flux maximums measured.

Calorimeter location		Maximum heat flux	
Y and Z	X <sub>C</sub>	Time, sec (a)	Btu/ft <sup>2</sup> /sec
+Z	28	2	94
+Z	59	2	78
+Z	48	2	63
-Z	34	3	70
-Z	48	3	65
-Y	34	< 1	35

<sup>a</sup>Time after LES motor ignition



The flight times showing high static pressures due to plume impingement during the tumbling of the LEV after abort initiation (see section 5.2) correlated with the measured heat flux impingement. The period of heat flux impingement was less than 6 seconds over the entire command module, which compares to the major thrusting period of LES motor burn (see section 5.6).

Visual inspection of the CM after recovery showed it to be scorched and covered with soot. However, the condition did not indicate any problem for the heat protection subsystem for a power on tumbling boundary abort.

The temperature measurements on the CM heat shield underneath the boost protective cover did not indicate any change during the entire flight, thus indicating that the simulated cork heat shield provided adequate insulation (ref. 1, figs. CAT-189, CAT-190, CAT-191, and CAT-192).

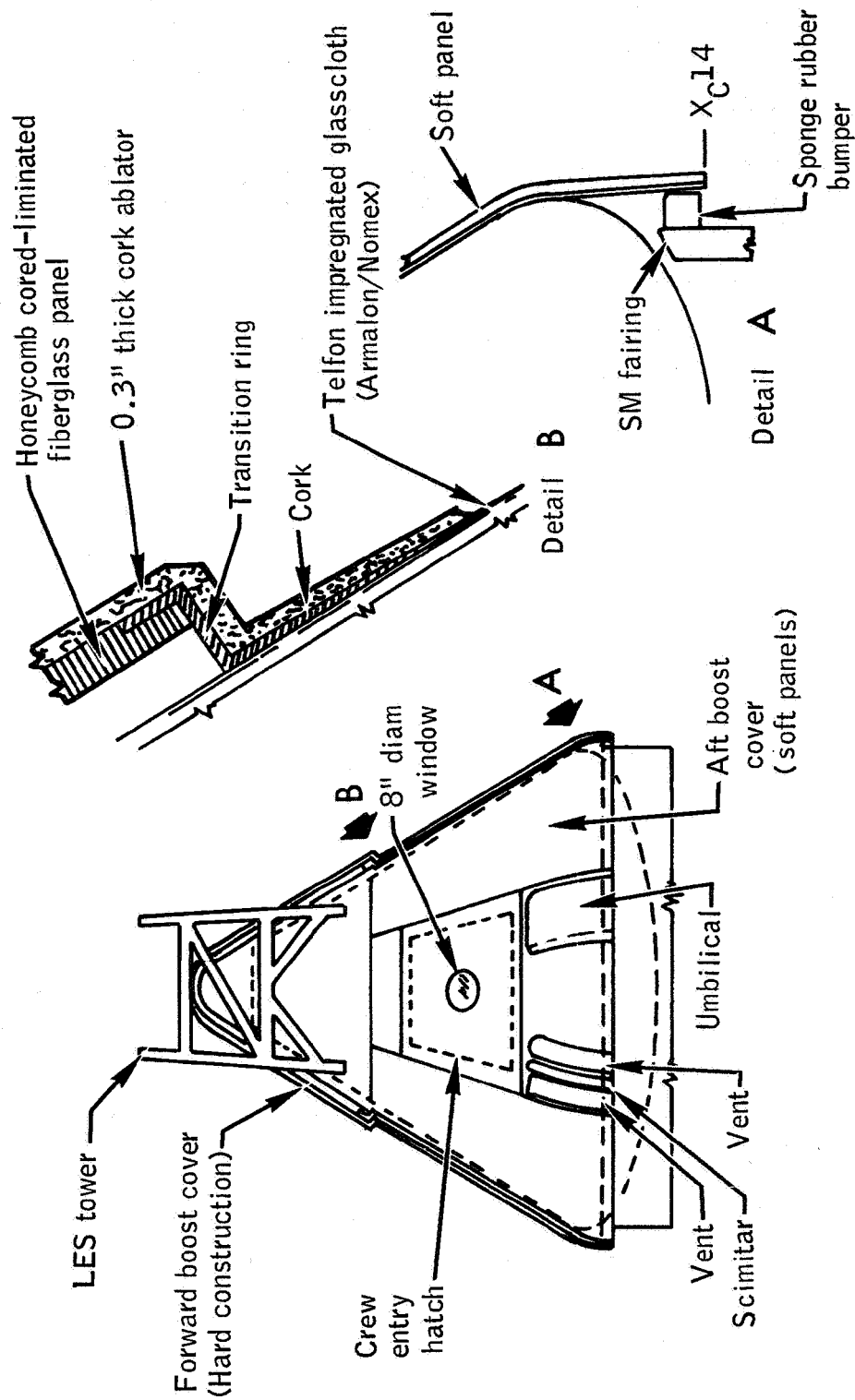
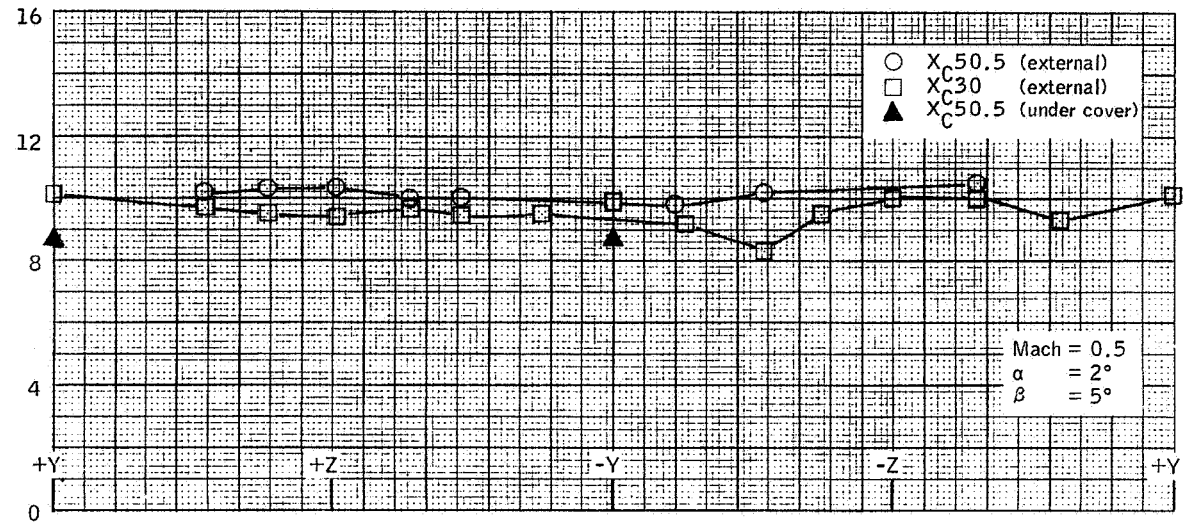


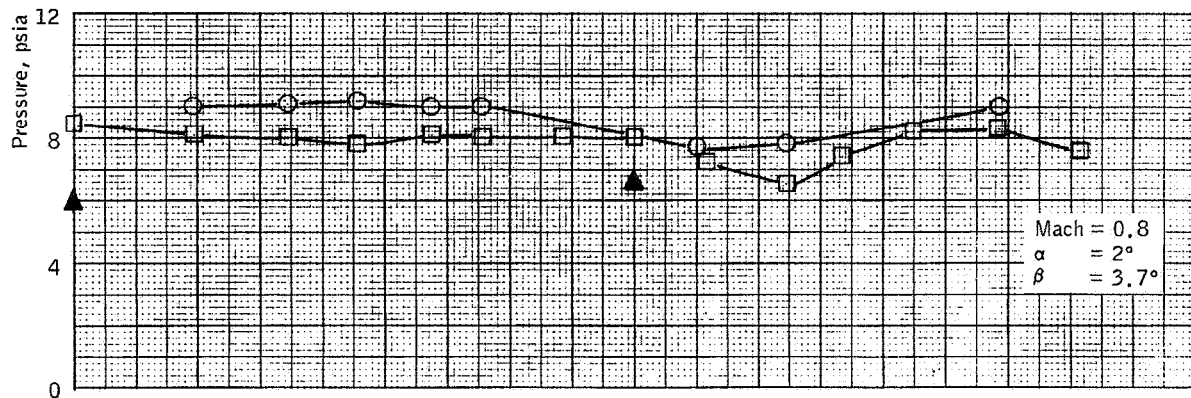
Figure 5.4-1.- Boost protective cover assembly and details, Apollo Mission A-004.

5-100

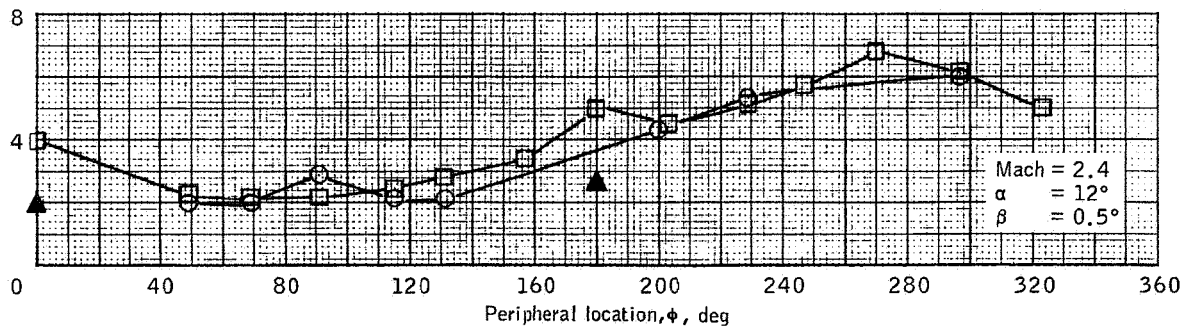
NASA-S66-3862 APR 15



(a) T + 25 seconds.



(b) T + 36 seconds.



(c) T + 73 seconds.

Figure 5.4-2.- Mission A-004 soft boost protective cover static pressures.

## 5.5 Mechanical Subsystems

Summary. - Components of the mechanical subsystems flown on Mission A-004 included the canard subsystem, the uprighting subsystem canisters (with packed bags), the deployment mechanisms for the recovery aids, the latching mechanisms for the side pressure and side ablative hatches, and a modified latching mechanism for the astro-sextant door. All components performed satisfactorily. The following paragraphs describe each component and its performance.

Canard subsystem. - Mission A-004 was the fourth mission to use the canard subsystem. The subsystem consisted of two deployable aerodynamic surfaces located between the forward end of the tower-jettison motor and the Q-ball assembly. A detailed description of the subsystem is presented in references 4 and 10.

The sequence of events of the canard subsystem was as planned and compared favorably with the sequences of the previous flights. The canards functioned properly. The canard-deployment relays in the mission sequencer closed approximately 11 seconds (T+84.76 sec) after abort initiation, activating the cartridges in the pyrotechnic thruster. Post-flight examination of the thruster revealed that both cartridges had fired. Canard deployment started at T+84.78 seconds, and the canards reached the full-open position by T+84.99 seconds. (See fig. 5.5-1.) The 0.21 second required for deployment was well within the design limit. Photographic coverage of the launch-escape subsystem showed that the canards were open until earth impact (T+266 sec).

The strain-gage outputs from both actuator links were approximately the same during canard deployment and are presented in figures 5.5-2 and 5.5-3. The time-history plots of these strain-gage outputs during canard deployment were as planned and as previously experienced (refs. 4 and 10. At the time of full canard deployment, dynamic pressure was  $134 \text{ lb/ft}^2$  as compared with a maximum of  $185 \text{ lb/ft}^2$  for Mission A-003, and  $175 \text{ lb/ft}^2$  for Mission A-002. After full deployment, the load oscillated for 0.20 second at approximately 31 cps, which is essentially the natural frequency of the canards in the open position. A similar inertial oscillation was also observed on the previous flights. During the time that the launch-escape vehicle was tumbling, the link loads varied very slowly between +1500 pounds and -1500 pounds until tower jettison (figs. 5.5-4 and 5.5-5).

Uprighting subsystem canisters. - Two canisters were flown on SC-002 to verify compatibility with the earth landing subsystem (ELS). They were not scheduled to operate for this mission.

The canisters contained the inflatable bags of the uprighting subsystem. The double-bag canister was attached to the +Z side of gusset 1 on the CM upper deck, and the single-bag canister was attached to the -Y side of gusset 2 (figs. 5.5-6 and 5.5-7).

Both canisters were inspected in place after the flight. There was no evidence of contact with the ELS during parachute deployment. However, the deployable part of the double-bag canister shifted down (in the X-axis direction) approximately three-eighths of an inch (fig. 5.5-7). The canister was still latched satisfactorily and appeared to have slipped at earth impact.

Recovery aids deployment mechanisms.- The deployment mechanisms for the postlanding recovery aids included those used with the two VHF antennas, the flashing light, and the sea dye marker/swimmer umbilical. Although the antennas and light were required to deploy, they were not scheduled to function on Mission A-004.

The deployment spring-operated mechanisms for the antennas and flashing light were identical. When the main parachutes were deployed, the pull on the lanyard attached to the parachute caused the activation of the 8-second time-delay cutter device, which released the spring-operated deployment mechanisms. The deployment springs used on SC-002 were not representative of the springs to be used on future flights. Stronger springs are scheduled for all future spacecraft beginning with SC-009. The antenna elements were not actual flight hardware, but were of nonrepresentative materials and were shorter in length. One VHF antenna was located in the forward compartment on the inboard +Z side of gusset 1, while the other antenna was located on the inboard -Y side of gusset 2 (figs. 5.5-6 and 5.5-7). The flashing light was located on the inboard +Y side of gusset 4 (fig. 5.5-8).

Postflight inspection of the VHF antennas and flashing light confirmed that all three systems erected as planned. The weak deployment springs allowed some "play" in the mechanisms when erect and the antenna elements (of nonrepresentative materials) were badly bent, as expected. (See figs. 5.5-6 and 5.5-7.) Examination of the mechanisms revealed no apparent damage during the flight or at impact.

The sea dye marker/swimmer umbilical deployment mechanism consisted of a rectangular canister which was spring-loaded on a deployment platform located in the -Z bay of the CM upper deck (fig. 5.5-8). The canister contained the swimmer inter-phone connection plug and a simulated sea dye cake. The canister was not scheduled nor fitted for deployment on Mission A-004. There was no evidence of contact with ELS components during the mission.

Side ablative hatch latching mechanism. - The side ablative hatch was located on the -Z side of the CM conical surface outer structure. The latching mechanism, mounted on the inner face of the hatch, could be manually operated from either inside or outside the CM as indicated in figure 5.5-9. An ablative plug is normally inserted in the clearance hole (for a 7/16-inch hex head male operating tool) which permits access to the mechanism from the outside. For this mission the plug was omitted. Manual rotation of the actuating shaft and handle caused rotation of the roller latches which engage the ramp-type striker plates on the heat-shield structure frame. An override spring retained the latches in either the latched or unlatched condition. An auxiliary plunger with a strike face located in the forward compartment, operating between the heat-shield structure and inner structure, supplied an alternate means of externally releasing the hatches after landing.

The side ablative hatch latching mechanism performed satisfactorily on this flight. The mechanism retained the hatch in place during flight and was operable after landing. Preflight torque required to latch the mechanism was 240 in.-lb; postlanding torque required to unlatch the mechanism was 150 in.-lb. (Latch torque limit is specified as 260 in.-lb.) Visual examination of the mechanism indicated no damage.

Side pressure hatch latching mechanism. - The side pressure hatch was located on the -Z side of the CM and relied on the inside cabin pressure for the "hard" seal against the CM inner structure (fig. 5.5-10). The latching mechanism, mounted on the outer face of the hatch, was used to hold the hatch in place and to obtain the initial "soft" seal for the cabin. The mechanism could be manually operated from either inside or outside the CM by rotating a drive shaft which penetrated the hatch through a hermetically sealed gear unit. A pinion gear on the output side of the unit operated a drive bar by means of a rack. Parallel-operating hook-type latches on the aft edge of the hatch were driven by links attached to the drive bar (figs. 5.5-10 and 5.5-11). The hooks were engaged by cam action with roller-type striker bars mounted on the CM inner structure. After the hooks were engaged, the additional travel of the hooks caused a limited "pull down" wedging action to produce initial sealing contact on the hatch O-ring sealing surfaces. Full sealing of the hatch is dependent upon the pressure differential between cabin pressure and ambient. The present sealed drive unit/pinion gear design was proven unsatisfactory during ground handling. A new design will be incorporated on SC-011 and subsequent vehicles. The present pinion is torque limited to 100 in.-lb before failure.

The side pressure hatch latching mechanism performed satisfactorily for this mission although cabin pressure was not maintained. The hatch remained latched satisfactorily during flight; however, internal pressure of the command module apparently leaked past the two hatch O-ring

seals. Figure 5.5-12 shows the evidence of seal leakage discovered when the hatch was inspected during recovery operations. Impressions from the two O-rings could clearly be seen in the surface of the tape located on the hatch -X and +Y edges. This tape had been applied to all the hatch edges to eliminate preflight gaps between the hatch seal surface and frame seal surface. Only intermittent impressions were visible across the +X edge, and no seal impressions were visible along most of the -Y edge. In addition, sooting was visible along most of the -Y hatch edge and portions of the +X edge. These soot deposits were inside the first O-ring and portions of the deposits were inside the second O-ring.

The latching mechanism was torqued to 295 in.-lb at preflight hatch installation and required 120 in.-lb torque to unlatch at recovery. (Latch torque limit is specified as 100 in.-lb.) Visual examination of the mechanism after recovery indicated no damage was incurred during flight.

On final preflight installation, one tooth on the pinion was broken off, but this did not prevent positive latching of the hatch. Two more teeth were broken in recovery area operation.

Astro-sextant door mechanism. - The astro-sextant door mechanism of the command module is used to latch and to deploy the doors during manned missions. For this mission, only the latches were used and they were not required to be operable at any time during the flight. The two latches held the doors in place during the flight.

NASA-S-66-3712 APR 15

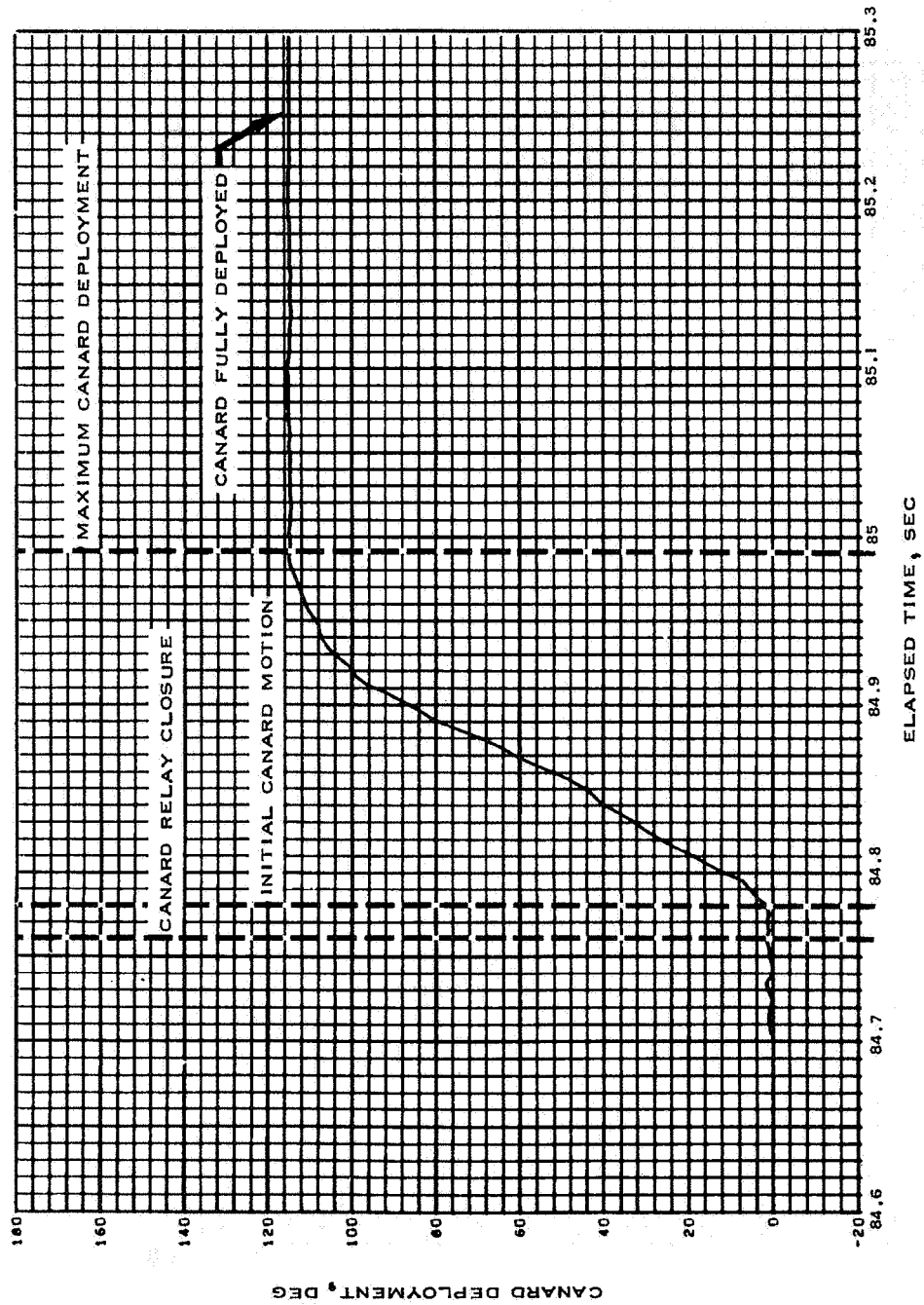


Figure 5.5-1.- Canard deployment time history, Apollo Mission A-004.



NASA-S-66-3716 APR 15

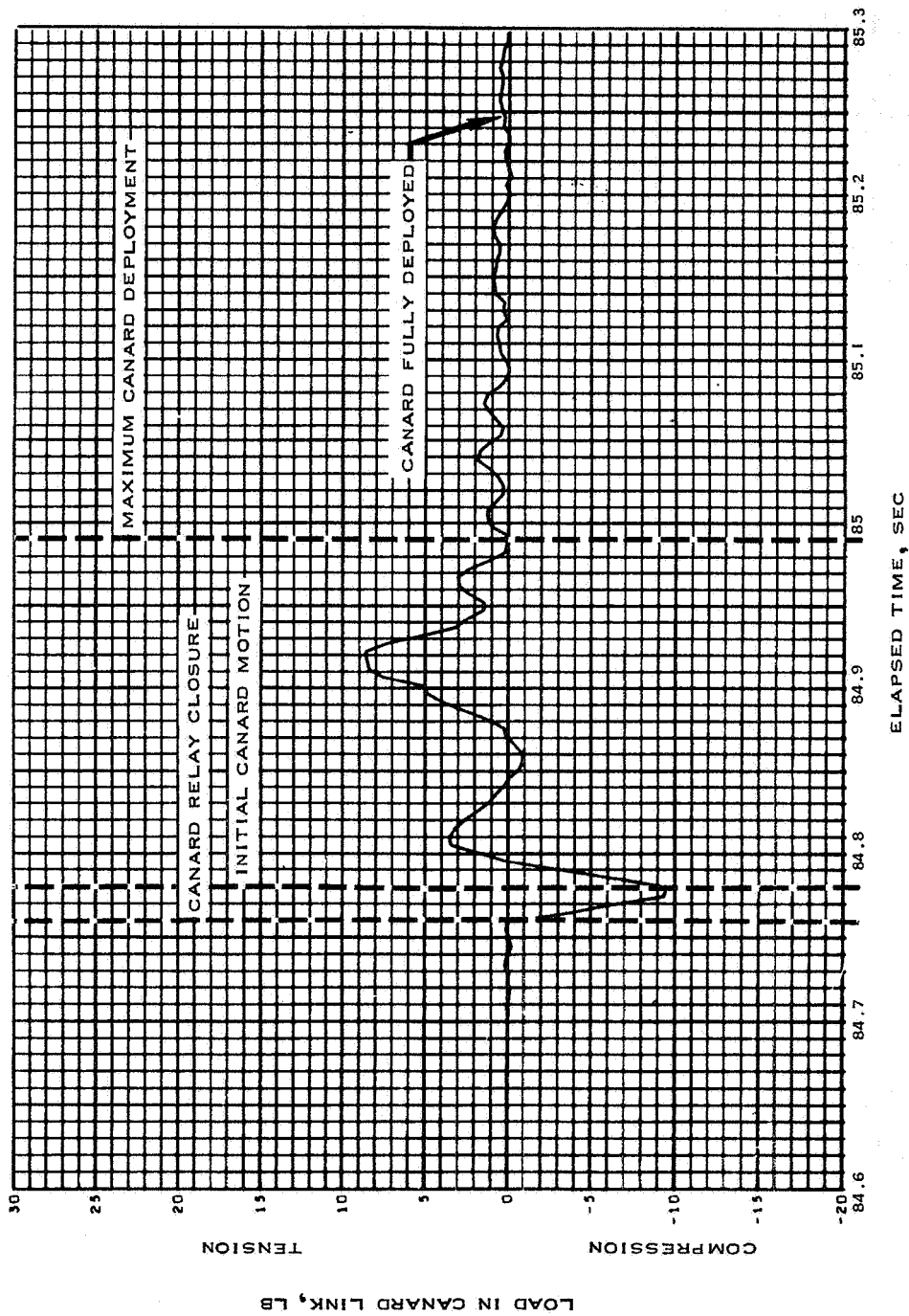


Figure 5.5-2.- Canard +Y link load time history during deployment, Apollo Mission A-004.

NASA-S-66-3720 APR 15

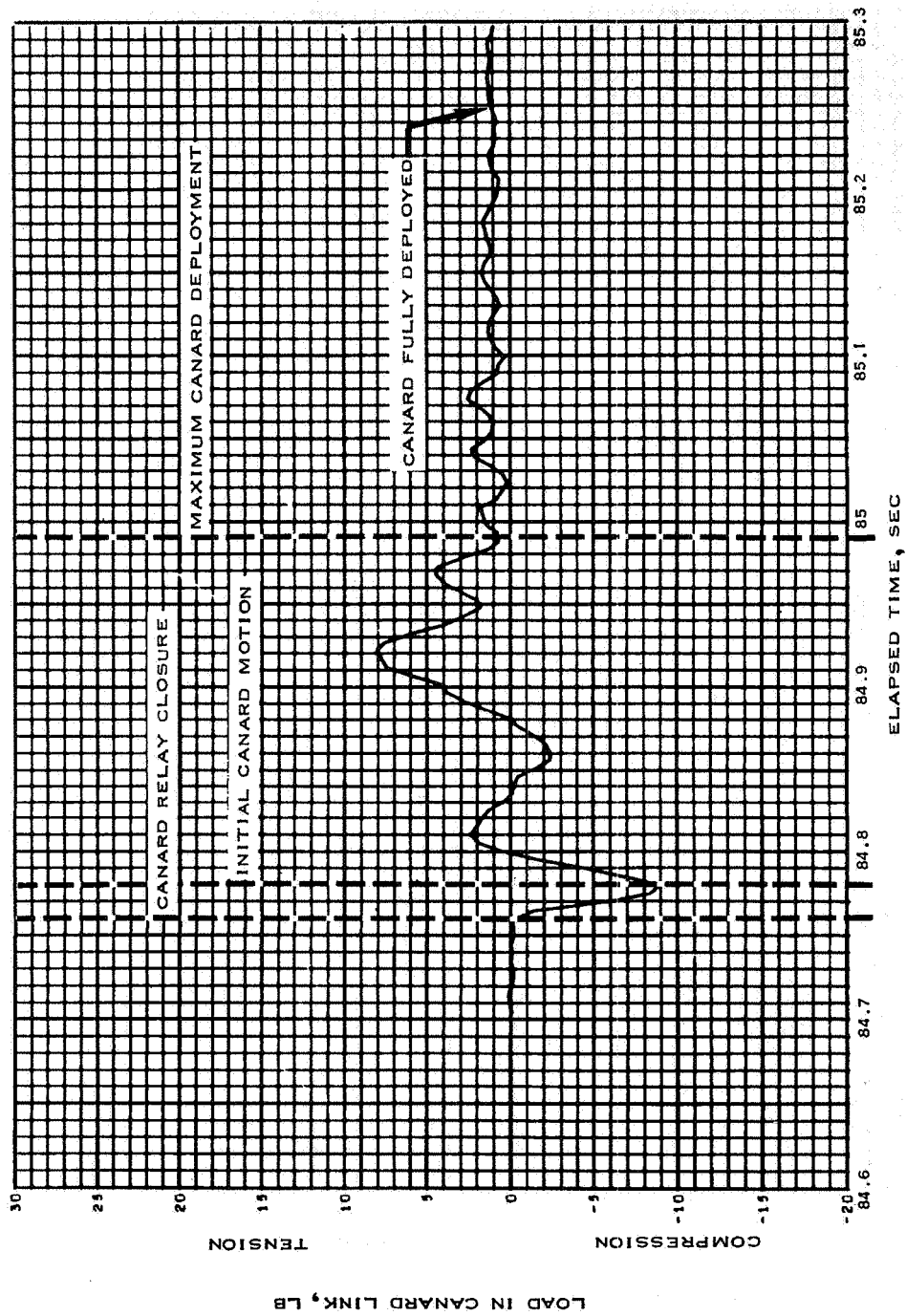


Figure 5.5-3.- Canard -Y link load time history during deployment, Apollo Mission A-004.

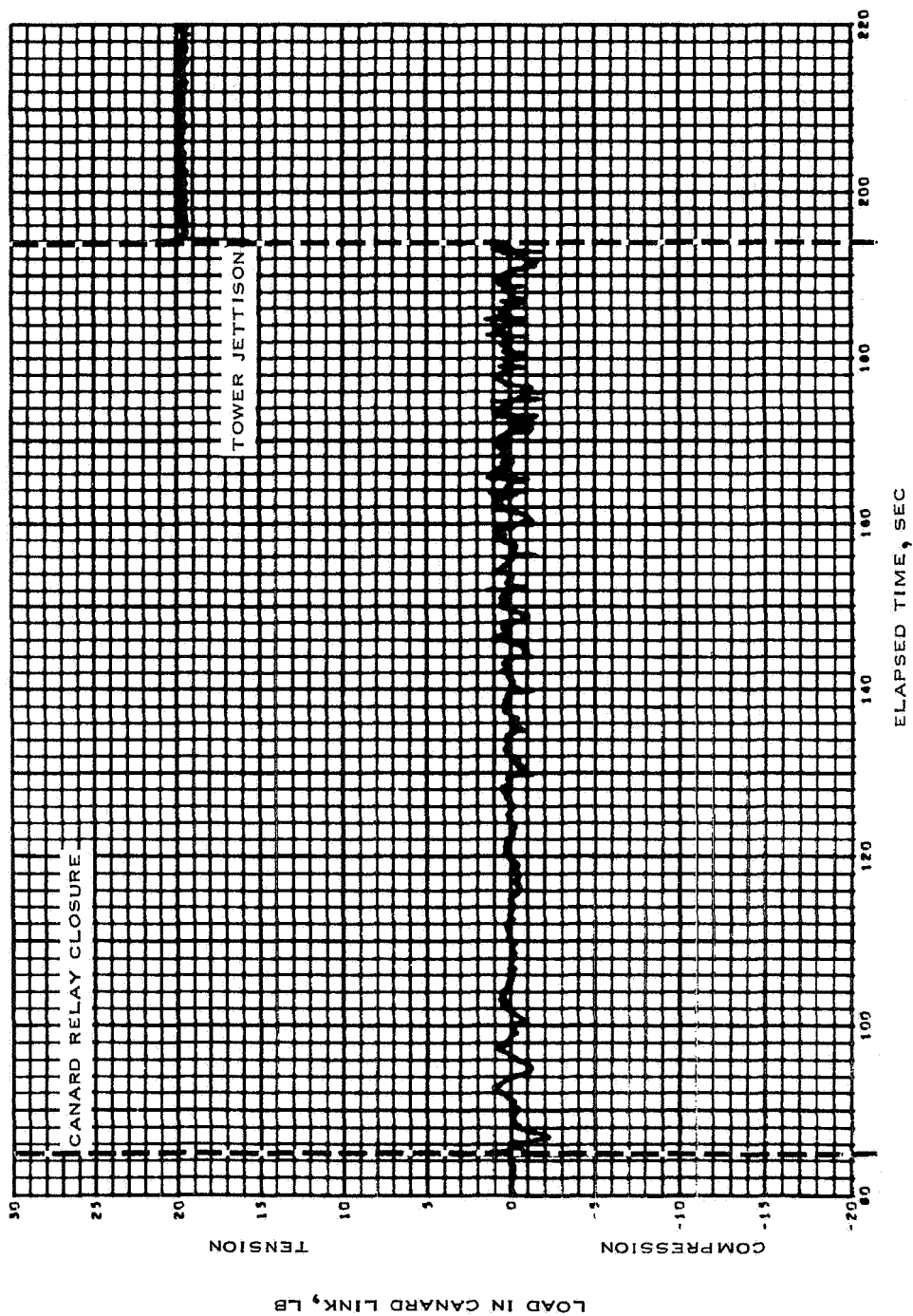


Figure 5.5-4.- Canard +Y link load time history, Apollo Mission A-004.

NASA-S-66-3724 APR 15

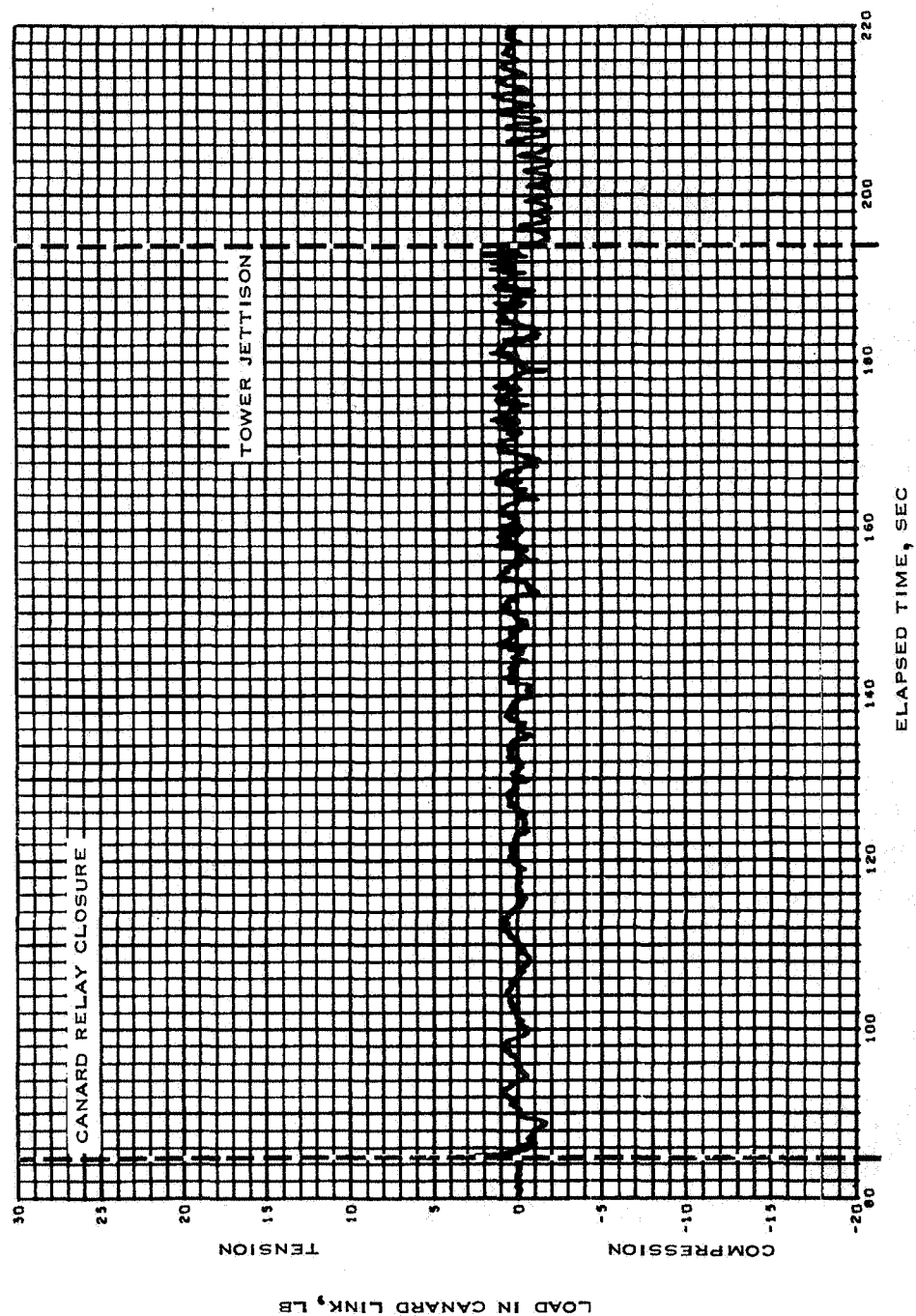


Figure 5.5-5.- Canard -Y link load time history, Apollo Mission A-004.

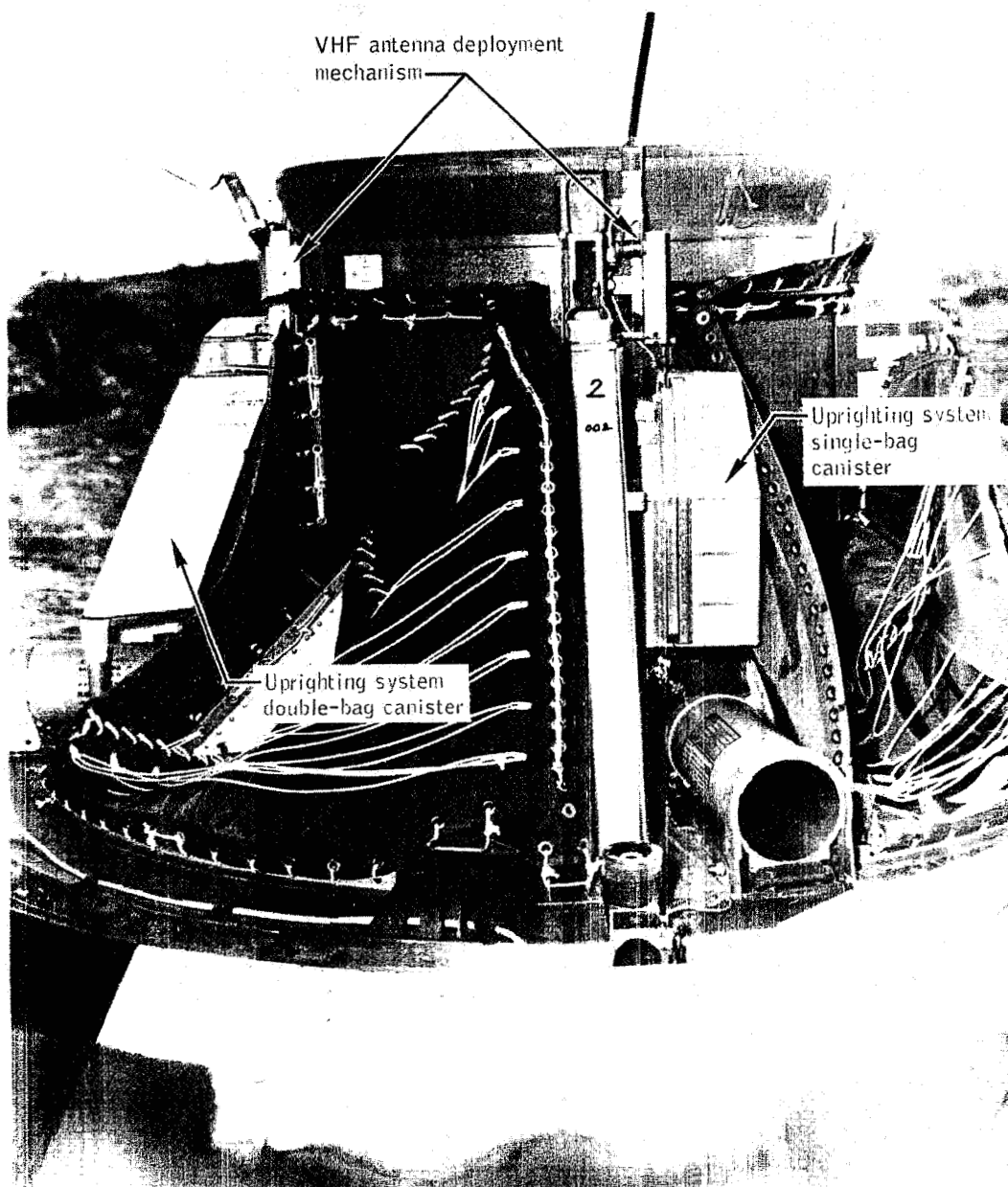


Figure 5.5-6.- Uprighting system canisters and VHF recovery aids, Apollo Mission A-004.

NASA-S-66-3732 APR 15

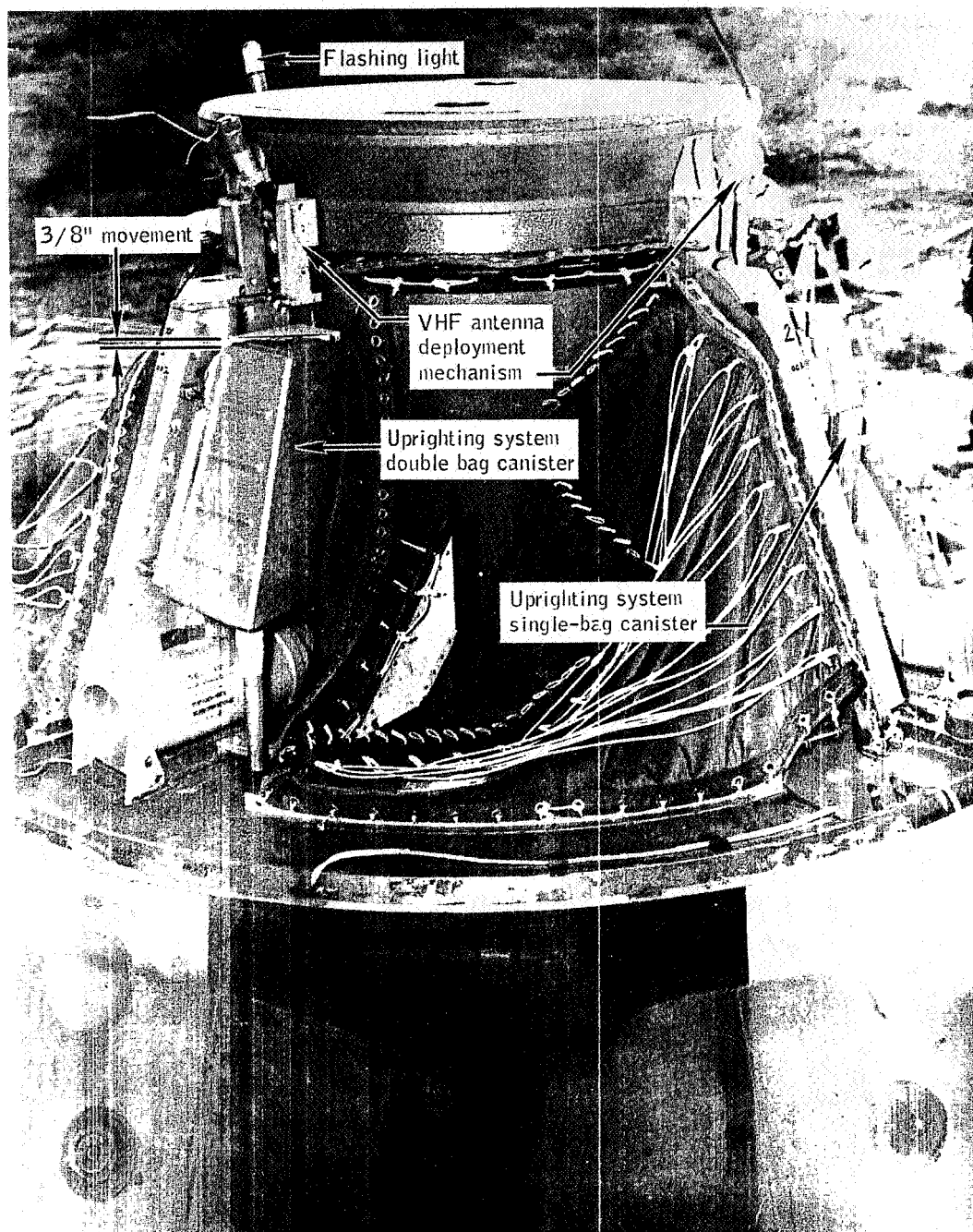


Figure 5.5-7.- Uprighting system canisters and recovery aids, Apollo Mission A-004.

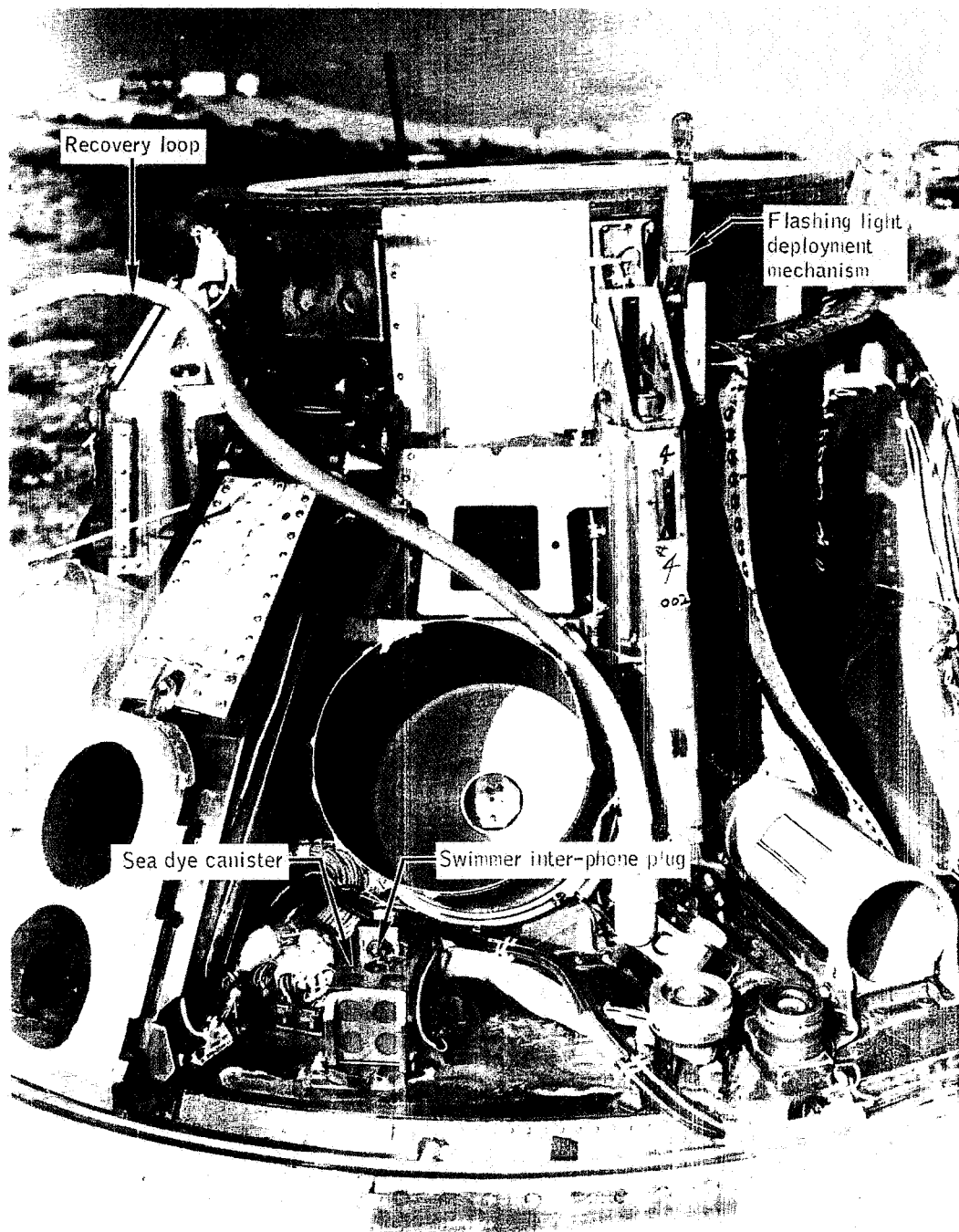


Figure 5.5-8.- Sea dye canister and flashing light recovery aids, Apollo Mission A-004.

NASA-S-66-3740 APR 15

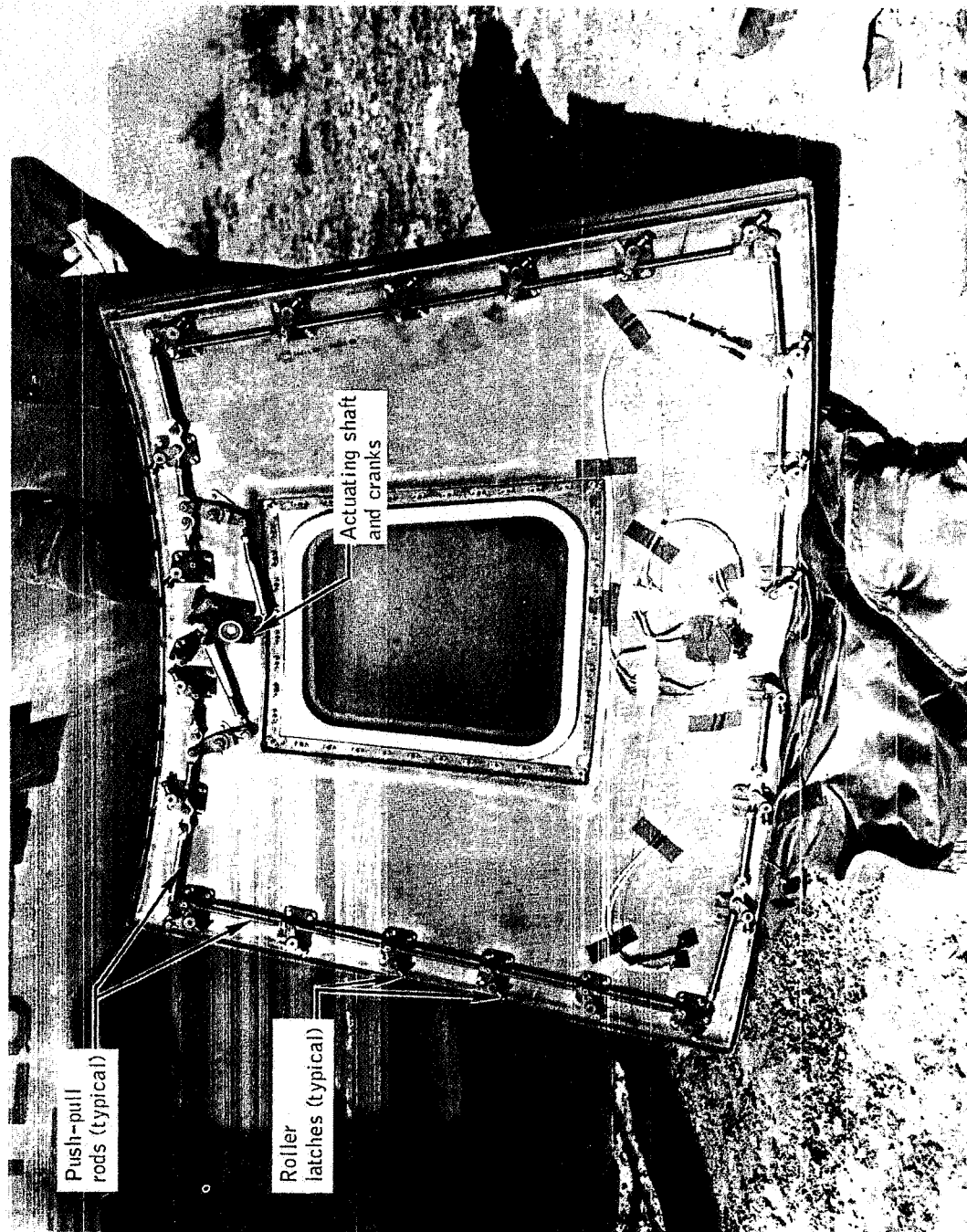


Figure 5.5-9.- Inner surface of side ablative hatch and latching mechanism, Apollo Mission A-004.



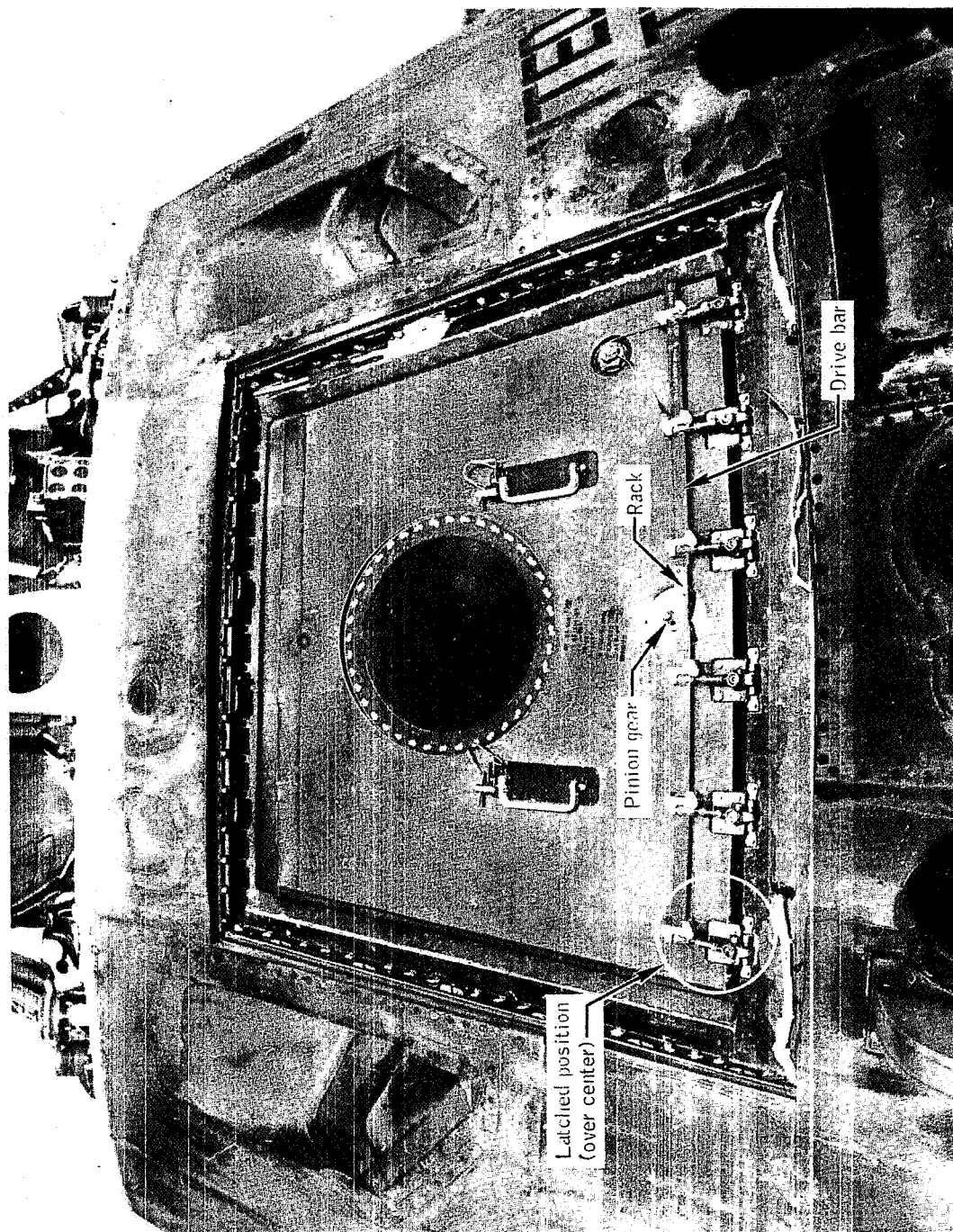


Figure 5.5-10.- Latched side pressure hatch at recovery, Apollo Mission A-004.

NASA-S-66-3748 APR 15

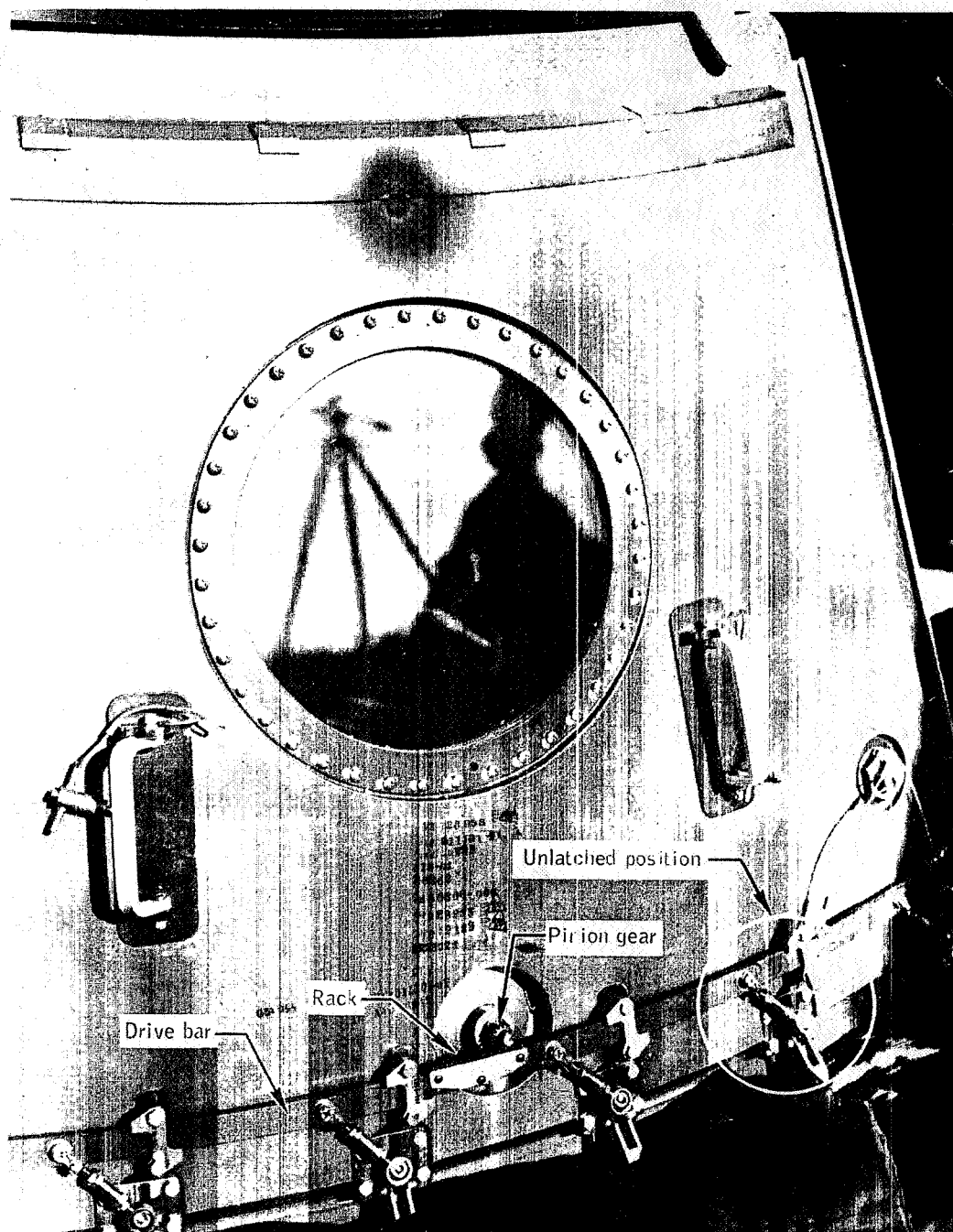


Figure 5.5-11.- Unlatched side pressure hatch after recovery, Apollo Mission A-004.

5-116

NASA-S-66-3752 APR 15

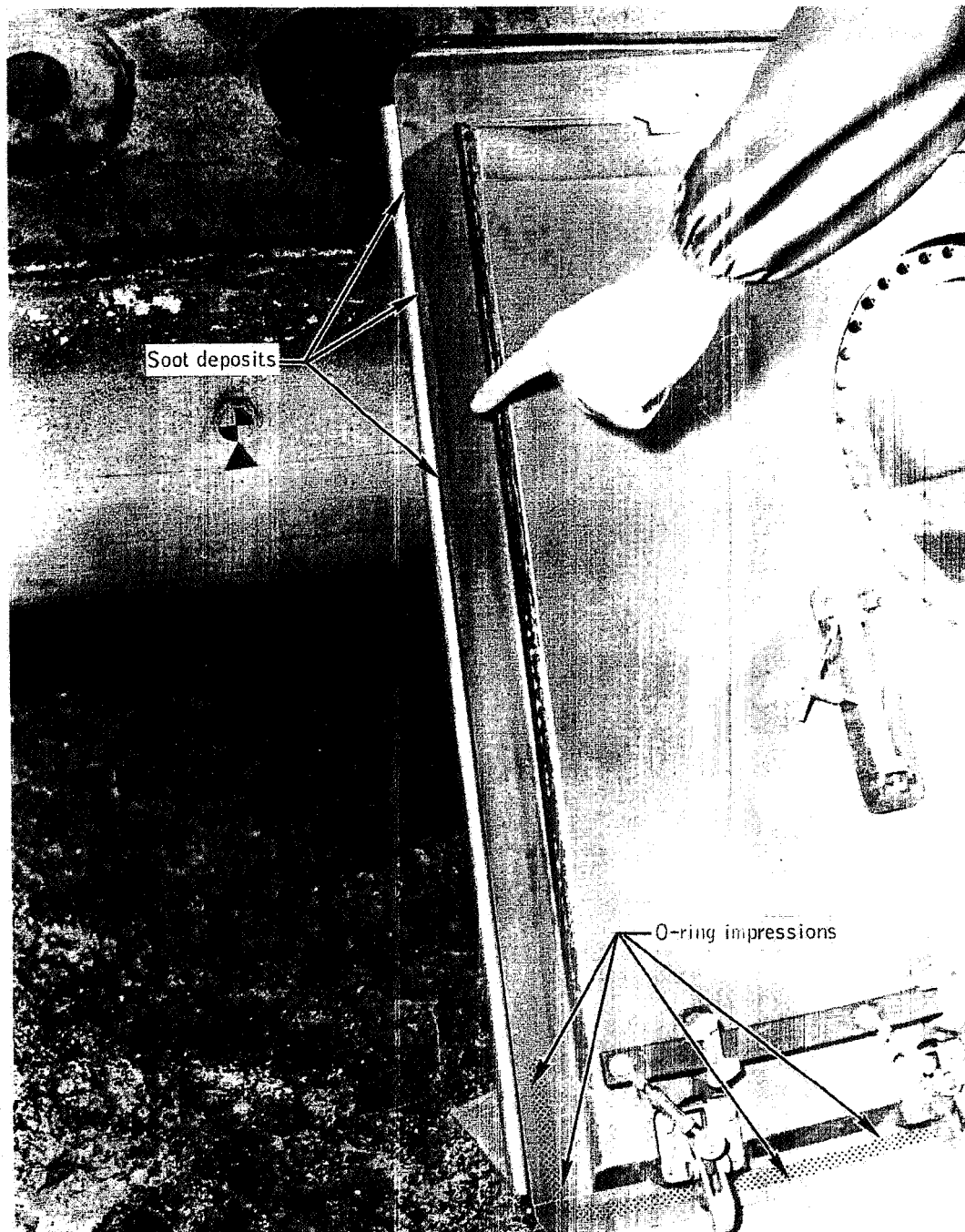


Figure 5.5-12.- Side pressure hatch postflight inspection, Apollo Mission A-004.

### 5.6 Launch-Escape Propulsion Subsystem

The launch-escape propulsion subsystem for Apollo Mission A-004 consisted of qualified launch-escape and pitch-control motors and a conditionally qualified tower-jettison motor. The configuration and instrumentation of the subsystem were the same as those used for Mission A-003 (ref. 4).

The launch-escape propulsion subsystem satisfactorily performed its intended purpose for Mission A-004. All instrumentation functioned satisfactorily, and the performance of the launch-escape and pitch-control motors when corrected for motor grain temperature was approximately as predicted. Thermocouple landline data indicated that the temperature of both the launch-escape motor and the pitch-control motor was  $35 \pm 5^\circ$  F at the time of launch.

A summary of the individual motor performance is presented in table 5.6-I. Figures 5.6-1 and 5.6-2 present the vacuum thrust time histories for the launch-escape and pitch-control motors, respectively.

TABLE 5.6-I.- MOTOR PERFORMANCE SUMMARY

[VACUUM CORRECTED]

Parameter	Launch-escape motor (a)	Pitch-control motor (a)	Tower-jettison motor (b)
Web burn-time average thrust, lb . . .	139 900	2356	30 150
Maximum thrust, lb . . . . .	154 000	2633	32 000
Total impulse, lb-sec . . . . .	614 500	1773	36 570
Action time, sec . . . . .	6.39	1.05	1.36
Web burn-time, sec . . . . .	3.42	0.63	1.15
Total time, sec . . . . .	10.30	1.50	1.5
Propellant weight, lb . . . . .	3160	8.84	206.8

<sup>a</sup>Delivered<sup>b</sup>Predicted at sea level

NASA-S-66-3756 APR 15

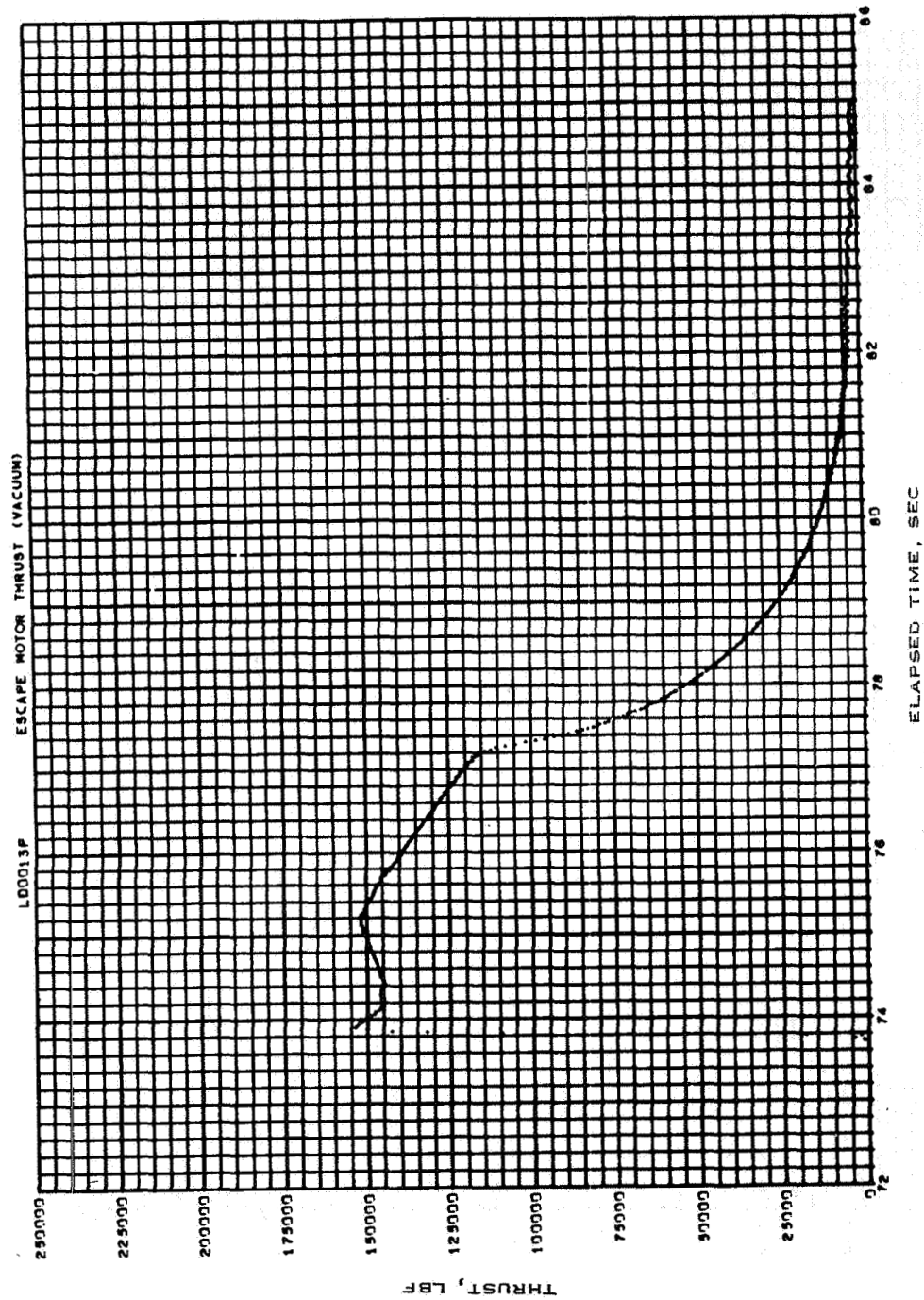


Figure 5.6-1.- Launch-escape motor vacuum thrust time history, Apollo Mission A-004.

NASA-S-66-3760 APR 15

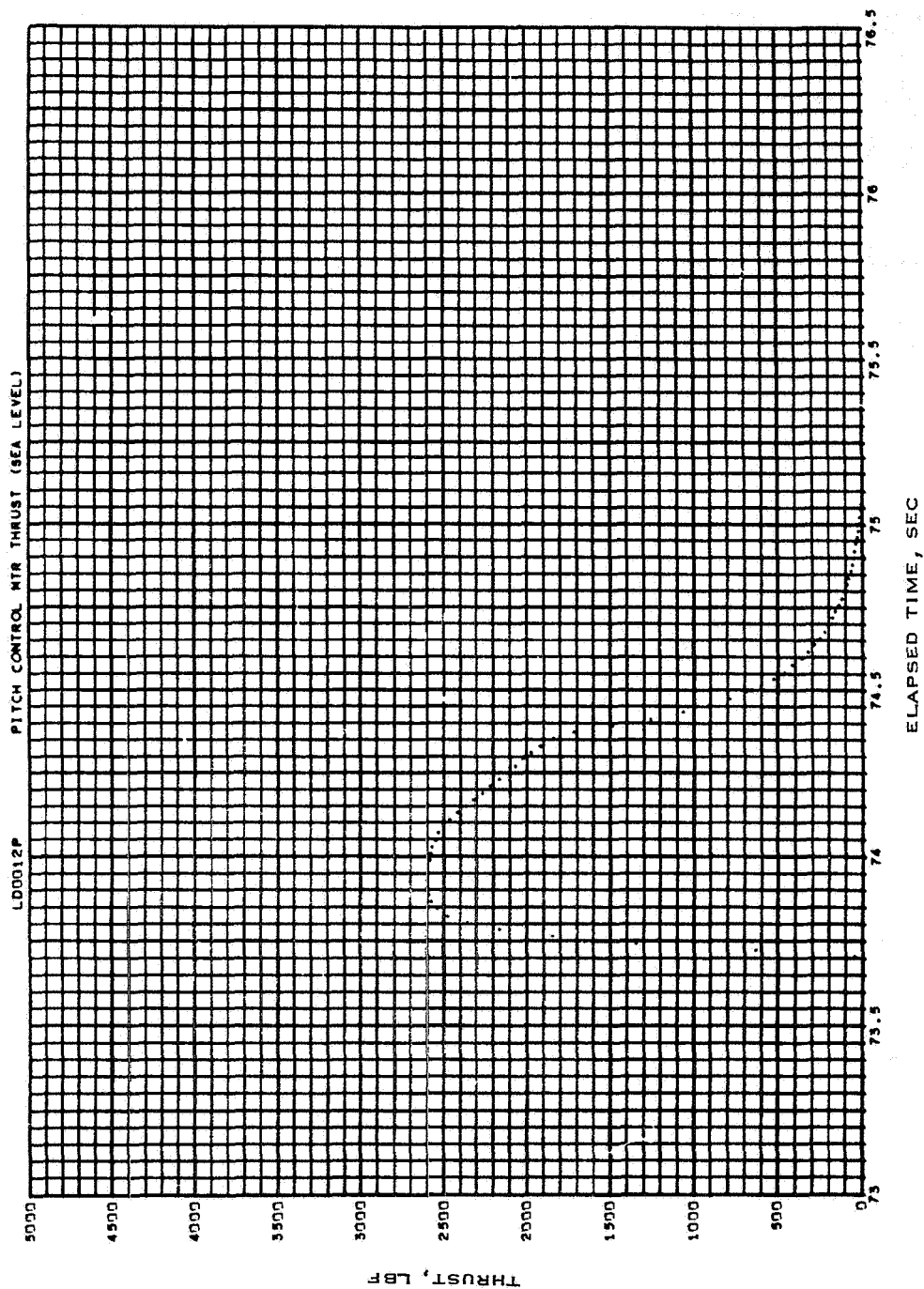


Figure 5.6-2.- Pitch-control motor vacuum thrust time history, Apollo Mission A-004.

## 5.7 Pyrotechnic Devices

There were five pyrotechnic devices on SC-002 being flight-tested for the first time: the recovery aids line cutter, the apex-cover thruster pressure cartridge, the CM-SM umbilical guillotine, the standard Apollo circuit interrupter, and the main parachute disconnect guillotine. Four of these were Block I configuration. The type VI pressure cartridge (apex-cover thruster) was an interim design.

The recovery aids line cutter was actually an additional application of the Block I reefing-line cutter configuration which performed successfully on Mission PA-2 (ref. 11).

The main parachute disconnect guillotine was previously flown on Mission A-003 as an inert device.

The apex-cover thruster cartridges were similar to those used on Mission A-003 with the following modifications:

(a) The total pressure buildup was decreased by the addition of an end closure welded in the base of the cartridge below the main charge pellets.

(b) The curing cycle time for the pyrotechnic mix was increased by an additional hour at 300° F for better control of the pressure rise time.

The CM-SM umbilical guillotine used on Mission A-004 was the standard Block I configuration. The guillotine design provided redundant opposing blades on each side of the umbilical. Initiation of the explosive train was provided by two Apollo standard detonators which fired a mild detonator fuse (MDF) crossover manifold to all four blades. The crossover manifold insured that at least one blade on each side of the umbilical would fire. Figures 5.7-1 and 5.7-2 illustrate the general configuration of the guillotine.

Four electrical circuit interrupters were used on Mission A-004 to deadface electrical connections between the CM and SM just prior to severance of the umbilical. Two 18-pin and two 104-pin connectors were installed with dual Apollo standard initiators to provide positive electrical isolation of hot electrical circuits for LES abort and normal CM-SM separation. The electrical circuit interrupters used on Mission A-004 were of the Block I configuration. Figure 5.7-3 shows a cutaway drawing of a typical circuit interrupter.



The main parachute disconnect consisted of two pressure-cartridge-propelled guillotines. (See fig. 5.8-3.) One guillotine was provided for each of the two parachute harness legs. The cartridge utilized was the type 200 pressure cartridge (ME 453-0005-0232).

Of the other pyrotechnic devices which had been flight-tested previously, all were Block I configuration except the type VI pressure cartridge (apex-cover jettison). The Block I pressure cartridge, type VI, will be flown on SC-009.

The pyrotechnic devices and the functions performed on Mission A-004 are listed in table 5.7-I.

All pyrotechnic devices used on Mission A-004 functioned satisfactorily and in proper sequence. Visual inspection of the recovered pyrotechnic devices (all were recovered except the CM-SM umbilical guillotine) verified that each device had been totally expended. Inspection of the cleanly severed umbilical on the command module indicated that the guillotine functioned properly. All separation systems severed cleanly and in proper sequence.

TABLE 5.7-I.- PYROTECHNIC DEVICES FOR MISSION A-004 (SC-002)

Function	Explosive component and part number	Number required	Device		Initiator	
			Lot	Serial number	Lot	Serial number
Launch-escape motor ignition	Igniter cartridge, type I (ME 453-0014-0091)	2	AJJ	0017	AFH	0029
			AJJ	0005	AFH	0007
Pitch-control motor ignition	Igniter cartridge, type I (ME 453-0014-0091)	2	AJJ	0013	AFH	0021
			AJJ	0012	AFH	0018
Tower-jettison motor ignition	Igniter cartridge, type II (ME 453-0014-0092)	2	ARW	0035	ANX	0040
			ARW	0034	ANX	0024
Tower separation	Explosive bolt assembly (ME 111-001-0026)	4	APB	0009	AKN	0405
					AKN	0441
			APB	0005	ALH	0047
					ALH	0034
			APB	0011	AKN	0296
			APB	0012	AKN	0423
Drogue parachute deployment	Pressure cartridge, type I (ME 453-0005-0081)	4			AKN	0415
					AKN	0409
			AJN	0025	ACU	0315
			AJN	0026	ACU	0311
Pilot parachute deployment	Pressure cartridge, type II (ME 453-0005-0082)	6	AJN	0068	ACU	0053
			AJN	0002	ACU	0054
			AJP	0015	ACU	0156
			AJP	0079	ACU	0135
			AJP	0059	ACU	0132
			AJP	0018	ACU	0001
Apex cover jettison	Pressure cartridge, type VI (ME 453-0005-0056)	2	AJP	0059	ACU	0117
			AJP	0052	ACU	0121
Drogue parachute disconnect	Linear shaped charge cartridge (V16-576260-61) (V16-576260-71)	2	ACU	0109	AFJ	0408
			ACU	0094	AFJ	0412
Canard deployment	Pressure cartridge (V15-590220-41)	2	LOT 1	0050	-	-
			LOT 1	0011	-	-
Main parachute disconnect	Pressure cartridge, type 200 (ME 453-0005-0232)	2	ACV	0266	ACE	0261
			ACV	0126	ACE	0294
		2	AAB	0005	AFJ	0503
			AAB	0007	AFJ	0029
		2	ALL	0084	AGG	0097
			ALL	0088	AFV	0161

TABLE 5.7-I. - PYROTECHNIC DEVICES FOR MISSION A-004 (SC-002) - Continued

Function	Explosive component and part number	Number required	Device		Initiator	
			Lot	Serial number	Lot	Serial number
CM-SM separation system tension tie cutters	Linear shaped charges (V17-590049)	6	LOT 1	1234	-	-
			LOT 1	1235	-	-
			LOT 1	1240	-	-
			LOT 1	1241	-	-
			LOT 1	1236	-	-
			LOT 1	1237	-	-
	Detonator cartridge (ME 453-0021-0005)	6	ACX	0153	ADV	0463
			ACX	0056	ADV	0322
			ACX	0057	ADV	0321
			ACX	0039	ADV	0172
			ACX	0204	ADV	0397
			ACX	0159	ADV	0268
CM-SM separation system						
Umbilical guillotine	Detonator cartridge (ME 453-0021-0005)	2	ACX	0203	ADV	0335
			ACV	0143	ACS	0321
Electrical circuit interrupter	Type I - 104 pins (ME 453-0010-0001)	2	-	-	AKP	0168
			-	-	AKP	0082
			-	-	AKP	0123
			-	-	AKP	0205
	Type II - 18 pins (ME 453-0010-0003)	2	-	-	AKP	0214
			-	-	AKP	0157
			-	-	AKP	0104
			-	-	AKP	0131
Recovery aids						
Flashing light	Line cutter (ME 901-0001-0024)	2	AAF	0715	-	-
			AAF	0667	-	-
Longeron no. 1 antenna release	Line cutter (ME 901-0001-0024)	2	AAF	0666	-	-
			AAF	0631	-	-
Longeron no. 2 antenna release	Line cutter (ME 901-0001-0024)	2	AAF	0608	-	-
			AAF	0618	-	-
Disreef drogue parachutes	Reefing line cutter (NV-5844-8)	8	AAF	0583 #2	-	-
			AAE	0538	-	-
			AAF	0639	-	-
			AAF	0640	-	-
			AAF	0662 #1	-	-
			AAF	0675	-	-
			AAF	0680	-	-
			AAF	0764	-	-

TABLE 5.7-1.- PYROTECHNIC DEVICES FOR MISSION A-004 (SC-002) - Concluded

Function	Explosive component and part number	Number required	Device		Initiator	
			Lot	Serial number	Lot	Serial number
Disreef main parachutes	Reefing line cutter (NV-5844-8)	18	AAC	0330 +Y	-	-
			AAC	0323	-	-
			AAC	0326	-	-
			AAC	0324	-	-
			AAC	0264	-	-
			AAC	0265	-	-
			AAC	0328 +Z	-	-
			AAC	0308	-	-
			AAC	0309	-	-
			AAC	0279	-	-
			AAC	0288	-	-
			AAC	0271	-	-
			AAC	0318 -Y	-	-
			AAC	0284	-	-
			AAC	0285	-	-
			AAC	0322	-	-
			AAC	0334	-	-
			AAC	0335	-	-

NASA-S-66-3780 APR 15

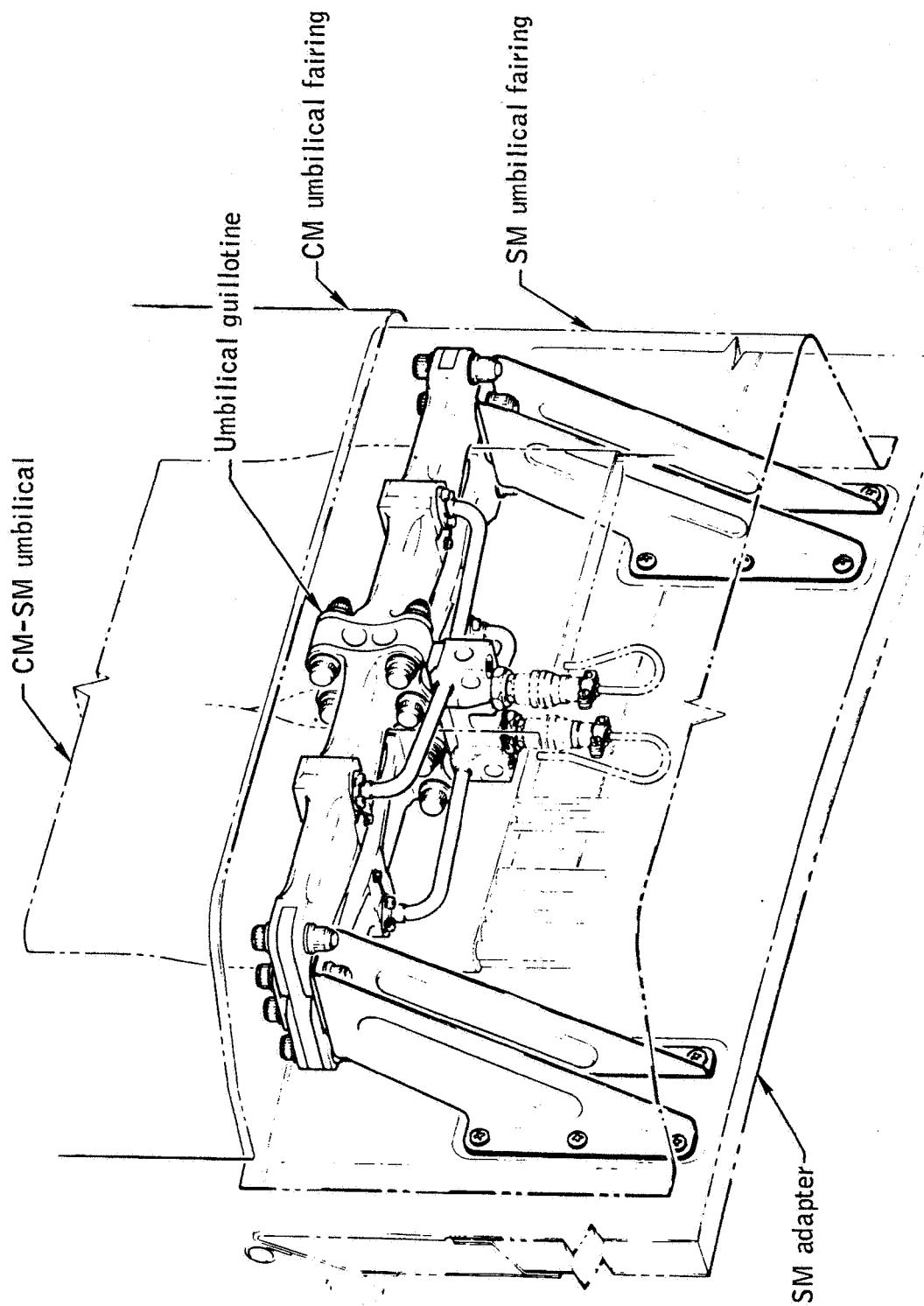


Figure 5.7-1.- CM-SM umbilical disconnect, Apollo Mission A-004.

NASA-S-66-3768 APR 15

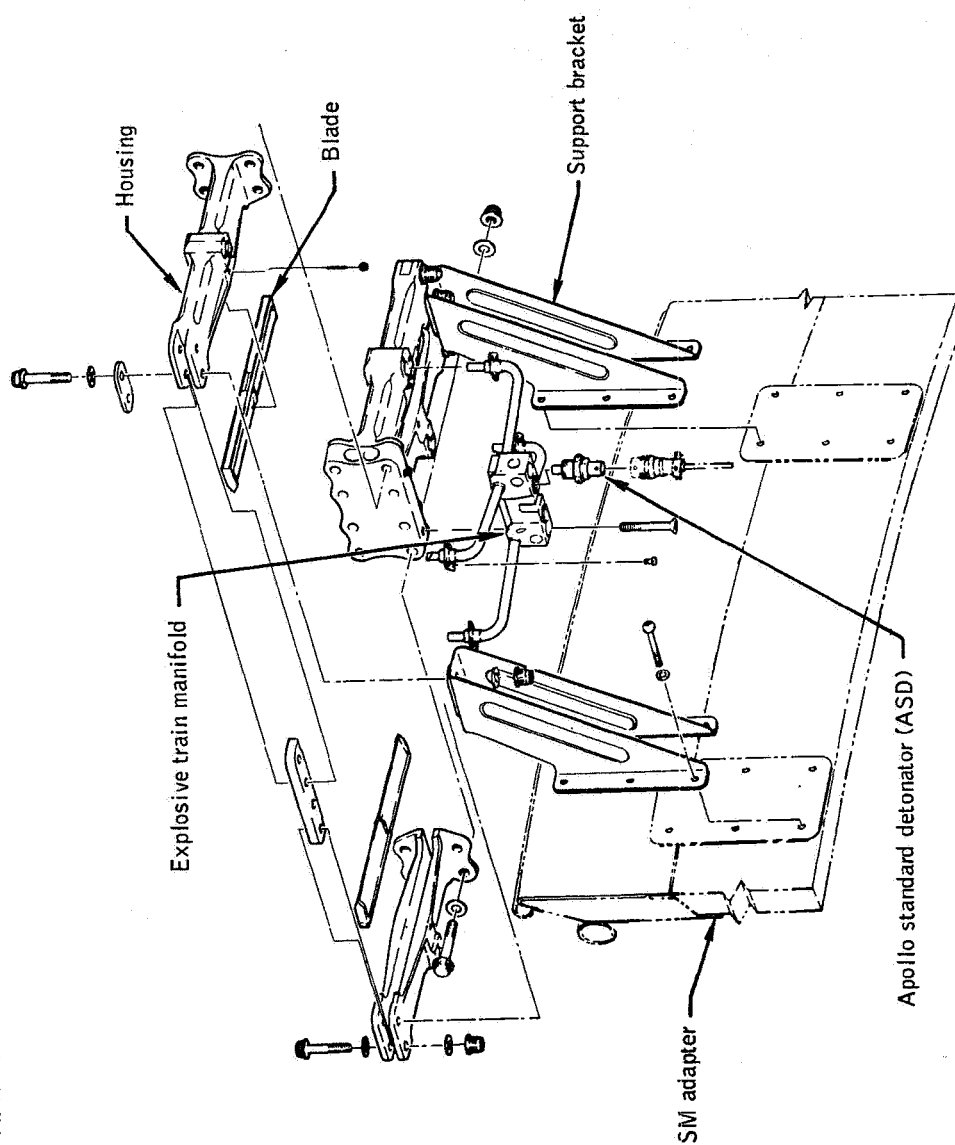


Figure 5.7-2.- CM-SM umbilical separation system components on Apollo Mission A-004.

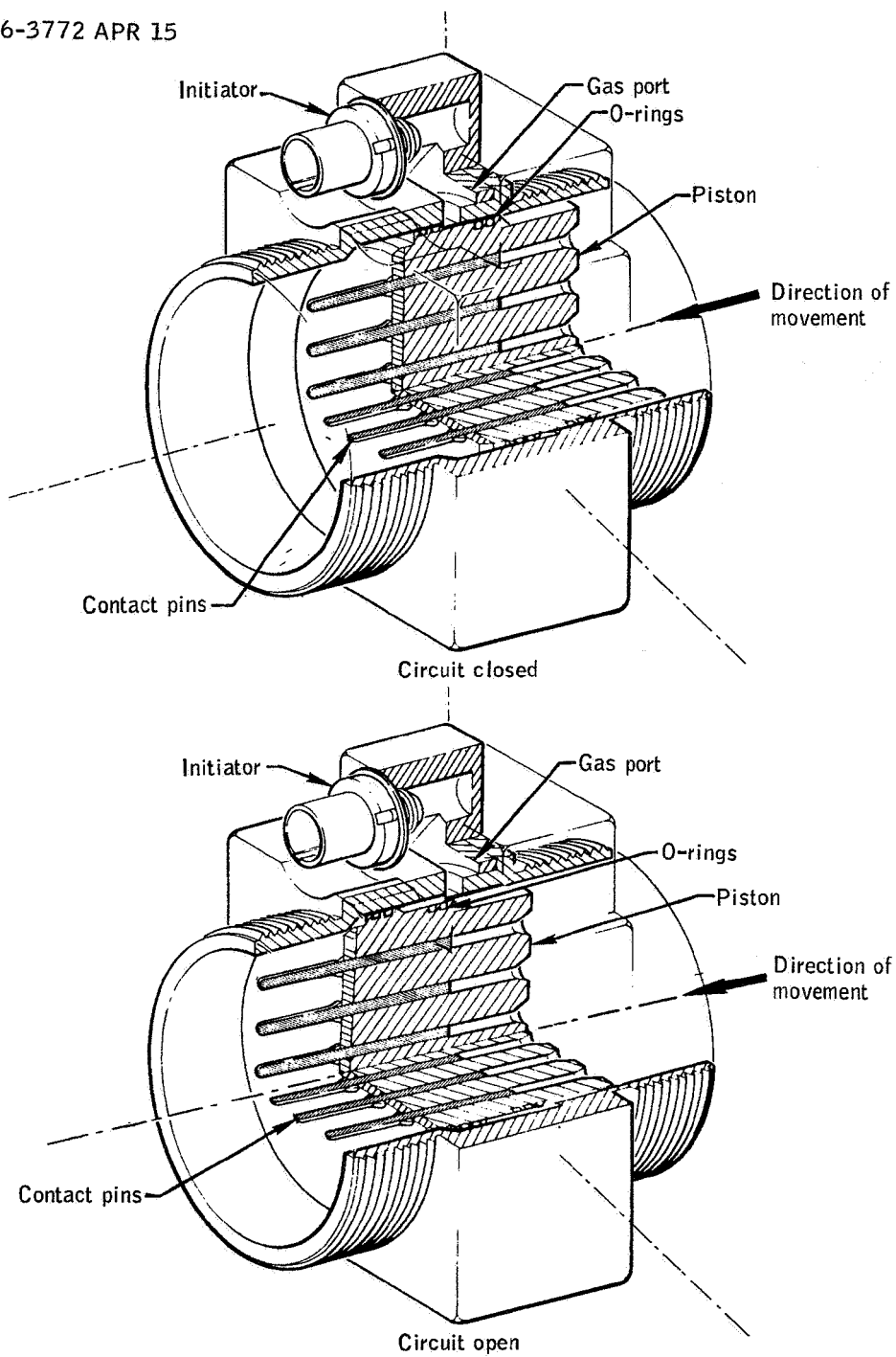


Figure 5.7-3.- Apollo electrical circuit interrupter.

## 5.8 Earth Landing and Impact Attenuation

5.8.1 Earth landing subsystem. - Of the major components and assemblies of the earth landing subsystem (ELS), the main parachute harness with attach fittings, the sequencer controller, and the drogue parachute subsystem disconnect were Block I configuration and had been successfully flight-tested previously on Mission A-003 (ref. 4). The main parachute disconnect was Block I and had been flown previously (Mission A-003) as an inactive component. The main parachute disconnect inertial switch was Block I configuration and was being flight-tested for the first time. The drogue parachute subsystem, pilot parachute subsystem, and the main parachute subsystem were very near the Block I configuration.

Drogue parachute subsystem: The Mission A-004 drogue parachute subsystem (fig. 5.8-1) differed from Block I (ref. 2) and from that previously flown on Mission PA-2 (ref. 11) as follows:

	Reefing line cutter	Cutter lanyard	Lanyard knot
A-004	C-6200-8	650 lb	Two half hitches
PA-2	B-6110-8	250 lb	Two half hitches
Block I	C-6200-8	650 lb	Chinese finger

Pilot parachute subsystem: The Mission A-004 pilot parachute subsystem was the same as that previously flown on Mission PA-2 (ref. 11) and differed from Block I (ref. 2) in that the metal lid/foam retainer was not Block I. (See fig. 5.8-2.)

Main parachute subsystem: The Mission A-004 main parachute subsystem differed from Block I (ref. 2) and from that previously flown on Mission PA-2 (ref. 11) as follows:

	Retention flaps	Deployment bag
A-004	Nylon	Hard pack
PA-2	Nylon	Loose pack
Block I	Nomex	Hard pack



Main parachute harness disconnect: The Mission A-004 disconnect (fig. 5.8-3), a Block I configuration flown active for the first time, is discussed in section 5.7 of this report.

Main parachute disconnect inertial switch: The Mission A-004 inertial switch (see section 5.7) was a 3g to 5g water-landing Block I configuration.

ELS performance: Flight data and postflight inspection indicate that all components of the ELS functioned properly and effected the safe recovery of the command module.

As planned for the Mission A-004 abort mode, an electrical arming signal from the mission sequencer applied logic power (at T+87.7 sec) to the earth landing subsystem sequence controller (ELSSC) 3.0 seconds after canard deployment. Closure of the ELSSC high-altitude baroswitches initiated tower jettison at an altitude of 23 055 feet m.s.l. (T+193.8 sec). Simultaneous with closure of the high-altitude baroswitches the 0.4-second apex-cover jettison delay timer of the mission sequencer and the ELSSC 2.0-second drogue mortar fire delay timer were started. Apex-cover jettison was initiated at T+194.2 seconds (0.4-sec time delay) at an altitude of 22 860 feet m.s.l.

Drogue mortar fire was initiated at T+195.8 seconds (2.0-sec time delay) at an altitude of 22 065 feet m.s.l. Drogue disconnect and pilot mortar fire were initiated by closure of the ELSSC low-altitude baroswitches at an altitude of 10 480 feet m.s.l. (T+237.6 sec). A nominal descent to landing followed (rate of descent was 27.1 ft/sec at a pressure altitude of 5000 ft), with the CM coming to rest in an upright position after the initial rocking action which followed touchdown. Main parachute disconnect was initiated at touchdown by the ELS impact inertial switch.

Both the high-altitude and low-altitude baroswitches operated within the barometric pressure altitude ranges specified. Reefing-line cutters fired and cutter lanyards were undamaged. Both main parachute harness legs were cleanly cut (fig. 5.8-4) although the postflight inspection showed that the cutter blade on leg no. 2 was broken (fig. 5.8-5).

The ELS event times (table 5.8-I) were obtained from onboard tape recorder H. The m.s.l. altitudes corresponding to the event times were obtained from the WSMR radar tracking plots. Cloud cover in the recovery area obscured optical and visual reference to ELS performance until after main parachute full inflation.

Postflight examination of the ELS and CM upper deck structure showed that there was no contact of the drogue parachute steel cable risers with the airlock lip, indicating that the CM was stabilized in a favorable heat-shield-forward attitude at the time of drogue parachute deployment. Minimal contact of the main parachute harness legs with the drogue mortar cans and no evidence of undue abrasion between the main parachute deployment bags, uprighting system canisters, longerons, or airlock, indicated a favorable main heat-shield-forward attitude at the time of main parachute deployment. The absence of apparent contact between the ELS components and the CM upper deck structure was an indication of satisfactory sequential deployment of the ELS. (See figs. 5.8-6 to 5.8-10.)

Although postflight examination indicated no contact between the apex cover and ELS components, the indication of reddish scuff marks (fig. 5.8-6) on the -Z pitch motor panel of the simulated CM RCS correlates with the red RTV sealant used on the apex cover around the RCS cutout.

A 2-inch split was found in the +Z main parachute fiberglass retention strip (fig. 5.8-11). No evidence of scrapes, impact, or abrasion on the strip or surrounding structure was observed. Prelaunch photographs do not show this split.

5.8.2 Impact attenuation subsystem. - The purpose of the impact attenuation subsystem on SC-002 was to provide support and impact attenuation for the equipment platform installed in place of the crew couches on this unmanned earth-impact mission. This was the first flight test for the impact attenuation components, and they were not instrumented. However, stroke measurements were made before and after flight. Additional measurements and analysis by the contractor at Downey, California, were not complete at the time of publication of this report.

The impact attenuation system consisted of four crushable honeycomb ribs mounted in a 120° sector of the +Z section of the CM, and eight impact struts. (See fig. 5.8-12.) The X-X and Z-Z strut stroking loads were developed by the combination of a frictional device and the crushing of aluminum honeycomb. These struts could stroke in either tension or compression. The Y-Y strut loads were developed by the crushing of aluminum honeycomb alone and operated only in compression.

The struts and ribs used in SC-002 were similar to the Block I type but were modified for higher load values for earth impact since the equipment on the platform was capable of withstanding greater accelerations than those acceptable for man. In addition, the X-X struts

were left in the high-load locked condition throughout the flight. The lockout provision on manned missions prevents undesirable stroking during selected periods.

Figure 5.8-13(a) to (d) illustrates the predicted load stroke curves for Mission A-004. After an initial stroke of either the X-X or Z-Z struts, in either tension or compression, the return load is supplied only by the friction device until honeycomb core is again encountered. This process can continue until the available honeycomb core is entirely crushed and, therefore, the frictional load alone is predictable. The initial high load indicated is due to the lockout feature. As shown in the figure, the Y-Y struts use only honeycomb crushing and operate only in compression.

Although the impact attenuation subsystem was not instrumented, strut action can be evaluated on the basis of field measurements of stroking (see table 5.8-II). Strokes were measured in the field to an accuracy of approximately  $\pm 1/16$ th inch.

Impact loads information was not available from flight data. However, loads on the X-X struts did not reach the level required to break out the lockout device, and only limited stroking of the Z-Z and Y-Y struts was indicated. Field inspection indicated that no stroking of the crushable ribs occurred.

TABLE 5.8-I.- EARTH LANDING SUBSYSTEM EVENTS FOR MISSION A-004

Event	Time from lift-off, sec			Dynamic pressure, lb/sq ft
	Planned	A	B	
Abort initiation (reference)	78.65	73.7	73.7	
Canard deployment (reference)	89.65	84.9	84.8	
ELS sequencer A start, relays A and B	92.65	87.9	87.9	
ELS sequencer B start, relays A and B	92.65	87.8	87.8	
Tower jettison (reference)	189.0	193.8	193.8	
Baroswitch lock-in, relay close A and B	189.0	193.8	193.8	
CM apex cover jettison (reference)	189.4	194.2		136.0
Drogue parachute deployment, relay close A and B		195.9	195.8	146.0
Drogue parachute deployment shear wire	195.8	No data	No data	
Drogue parachutes 1 and 2 line stretch		No data	No data	
Drogue parachutes 1 and 2 disreef		No data	No data	
Drogue parachute release - pilot mortar fire, relay A and B	237.6	237.6	237.6	43.0
Main parachutes off deck		No data		
Main parachutes disreef		No data		
Main parachutes full open		No data		

TABLE 5.8-II.- APOLLO MISSION A-004  
FIELD MEASUREMENTS OF IMPACT STRUT STROKES

Strut and location	Length before, in.	Length after, in.	Stroke, in.
X-X head			
+Y side	$36\frac{3}{4}$	$36\frac{3}{4}$	0
-Y side	$36\frac{3}{4}$	$36\frac{3}{4}$	0
X-X foot			
+Y side	$31\frac{3}{16}$	$31\frac{1}{16}$	$\frac{1}{8}$ compression
-Y side	$31\frac{3}{8}$	$31\frac{1}{2}$	$\frac{1}{8}$ tension
Z-Z struts			
+Y side	$38\frac{3}{4}$	$38\frac{5}{8}$	$\frac{1}{8}$ compression
-Y side	$38\frac{1}{4}$	$39\frac{3}{4}$	$1\frac{1}{2}$ tension
Y-Y struts			
+Y side	No data	Measured gap	$\frac{3}{4}$ compression
-Y side	No data	Measured gap	$\frac{1}{2}$ compression

Note: Measurement tolerance approximately  $\pm\frac{1}{16}$  in.

NASA-S-66-3776 APR 15

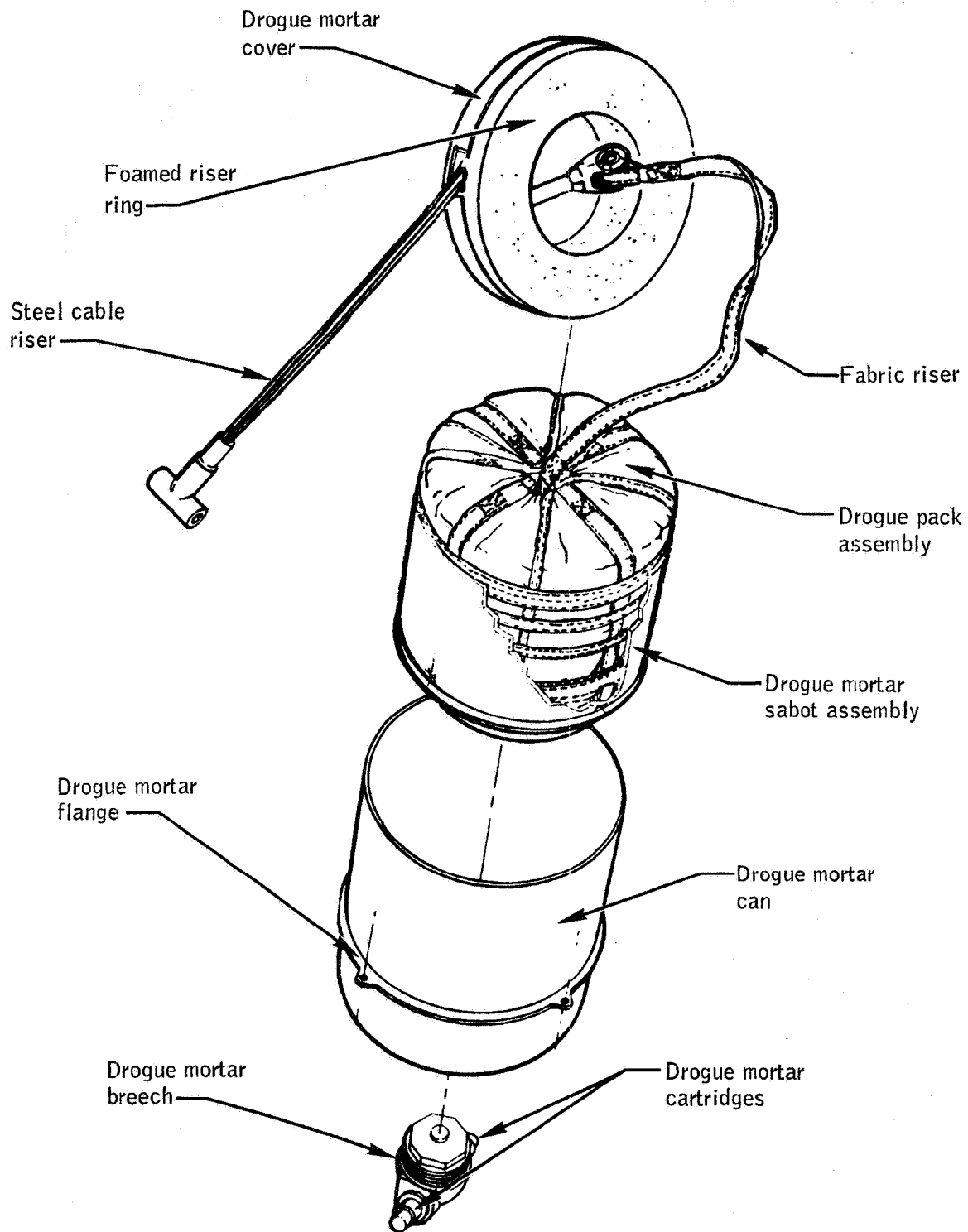


Figure 5.8-1.- Drogue parachute subsystem (Block I), Apollo Mission A-004.

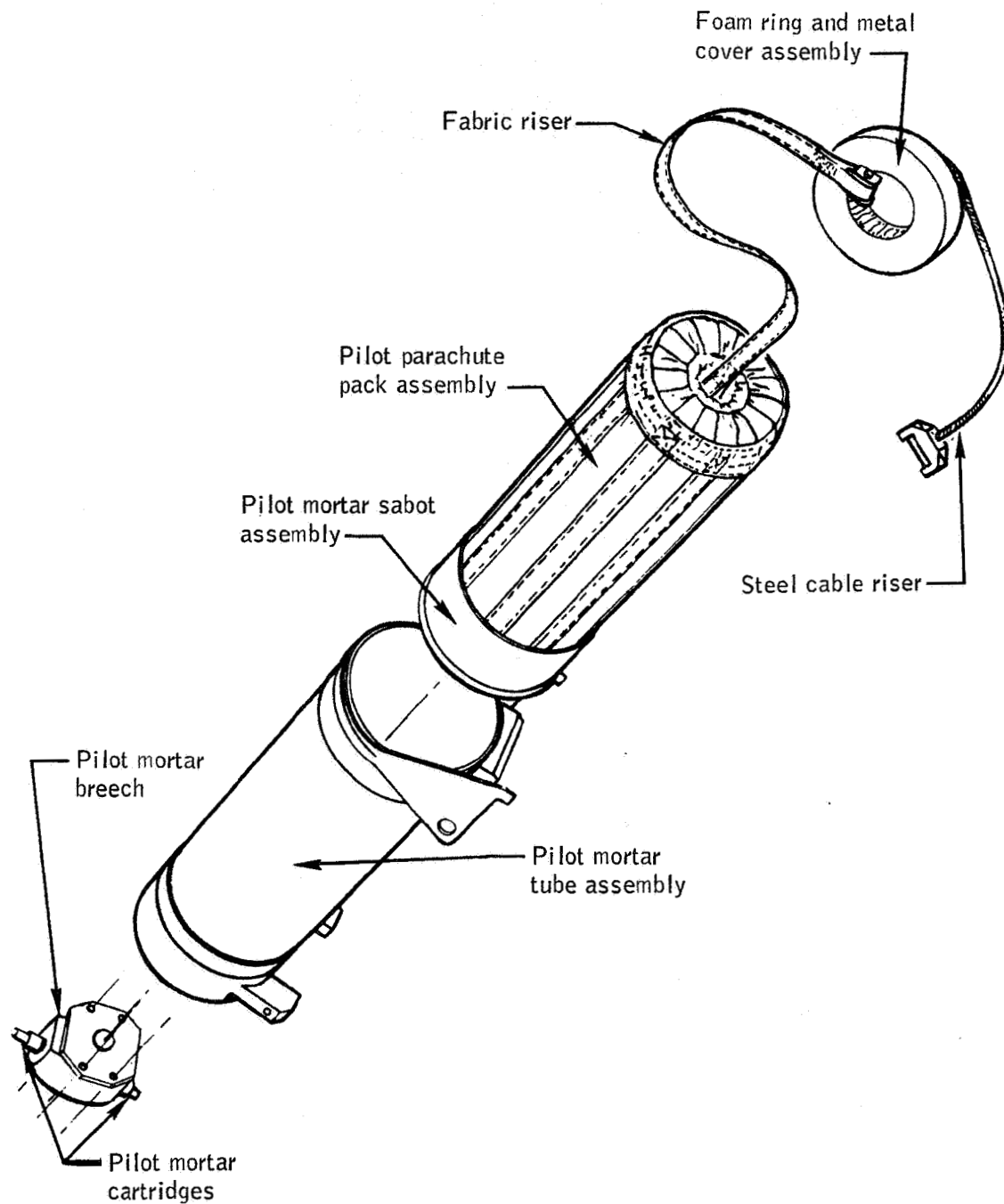


Figure 5.8-2.- Pilot parachute subsystem (Block I) except for metal cover, Apollo Mission A-004.

NASA-S-66-3764 APR 15

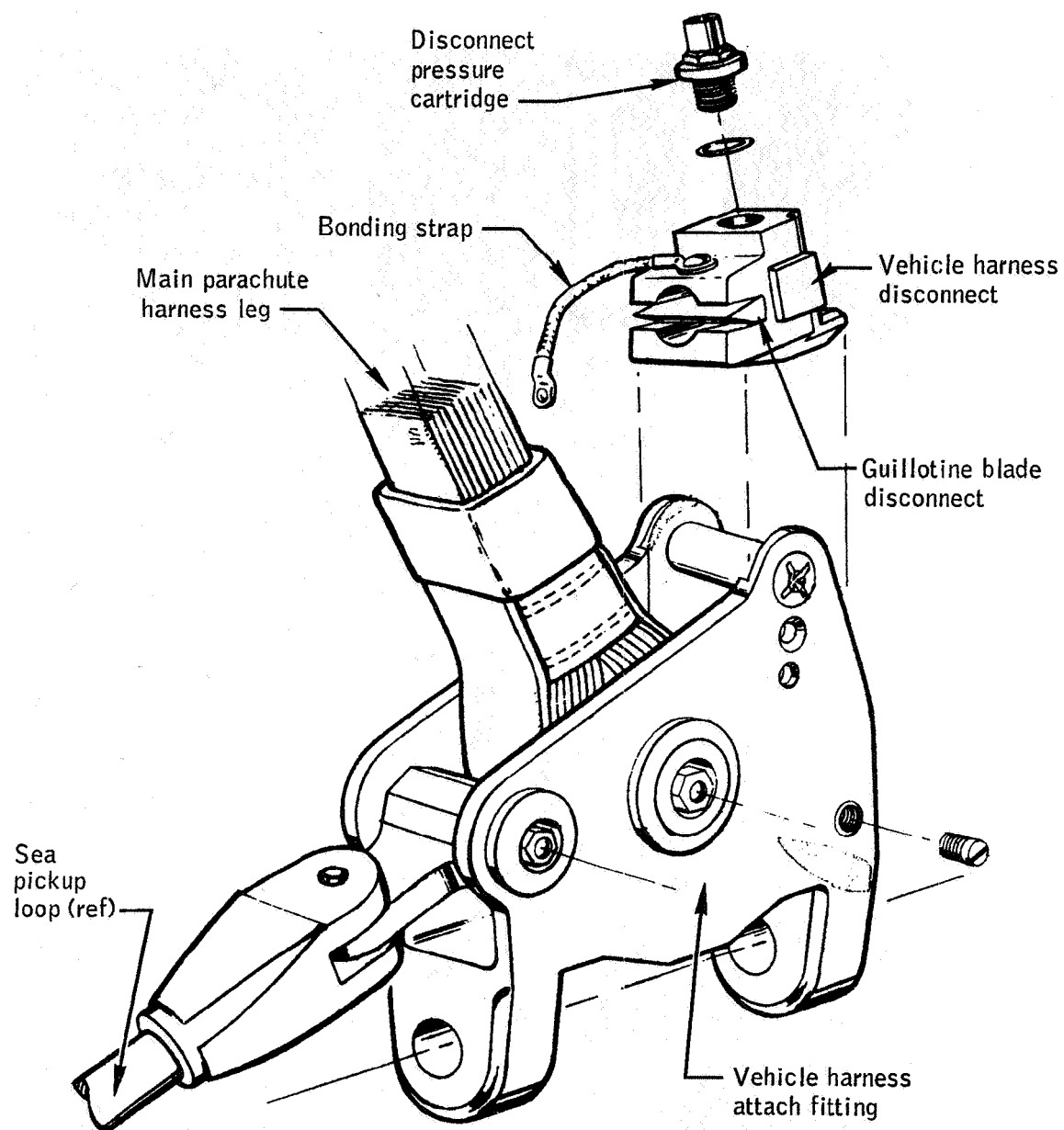


Figure 5.8-3.- Vehicle harness attach fitting and vehicle harness disconnect, Apollo Mission A-004.



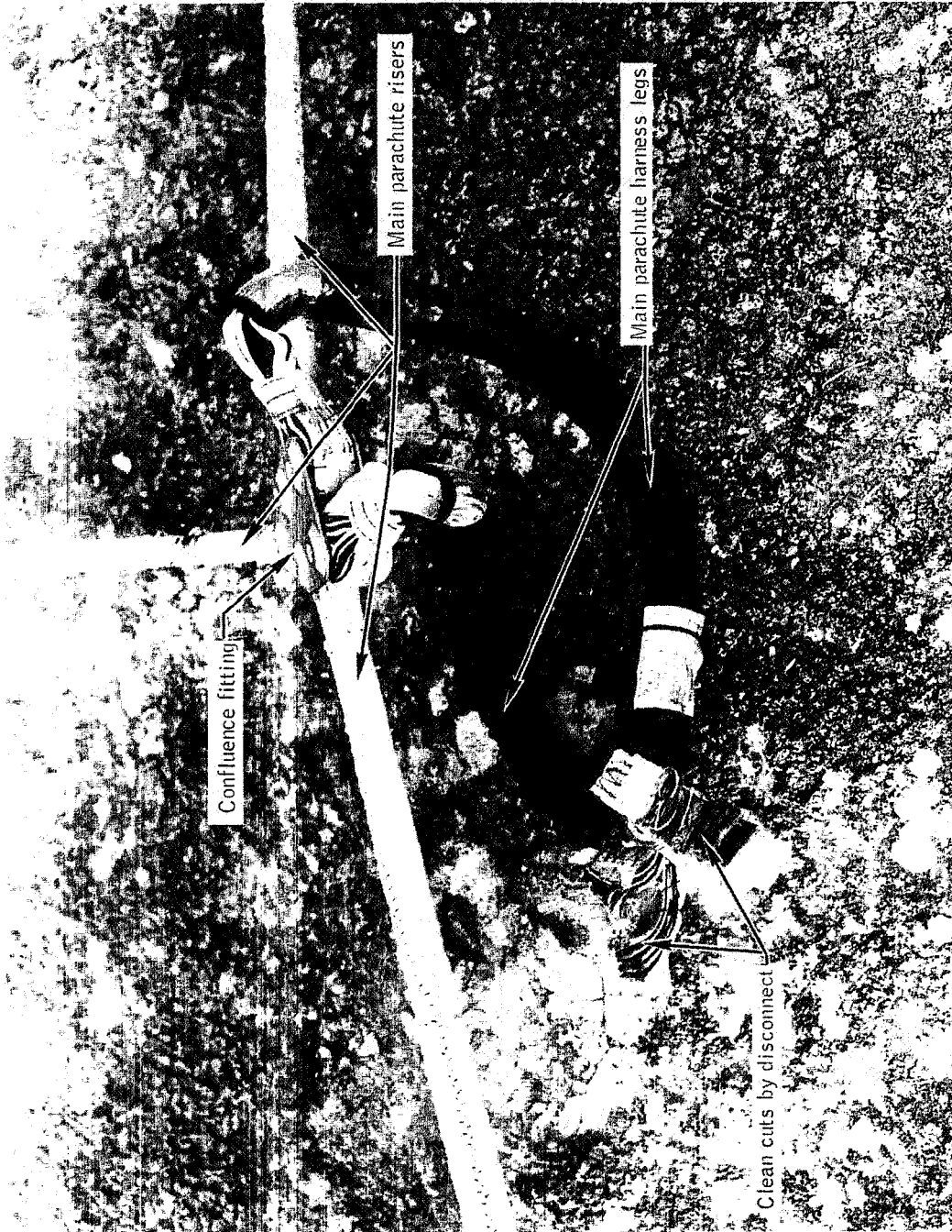


Figure 5.8-4.- Main parachute harness showing disconnect cut on Apollo Mission A-004.

NASA-S-66-3800 APR 15



Figure 5.8-5.- No. 2 main parachute attach fitting and disconnect, Apollo Mission A-004.

5-140

NASA-S-66-3788 APR 15

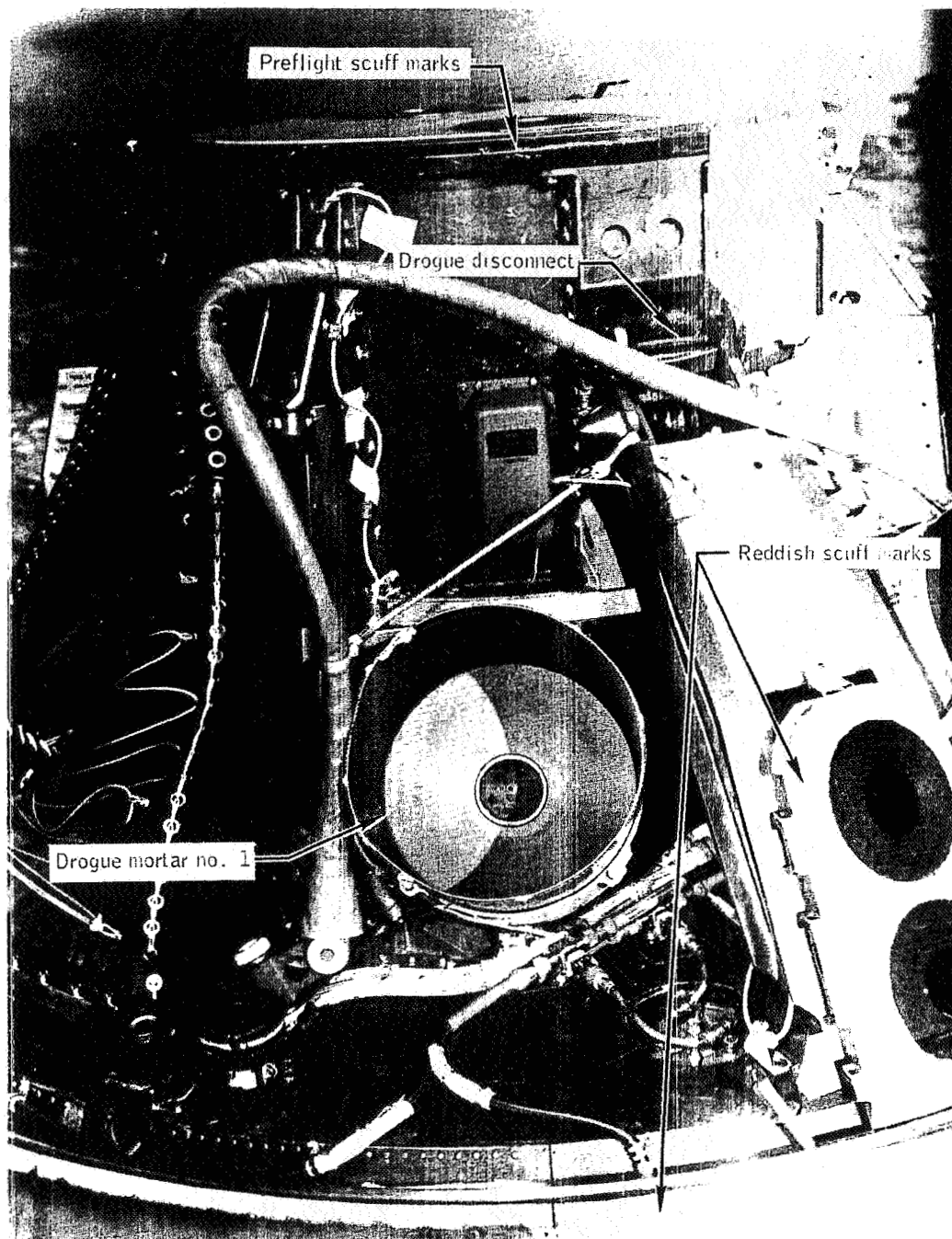


Figure 5.8-6.- Parachute (-Z) quadrant showing drogue mortar no. 1, Apollo Mission A-004.

NASA-S-66-3796 APR 15

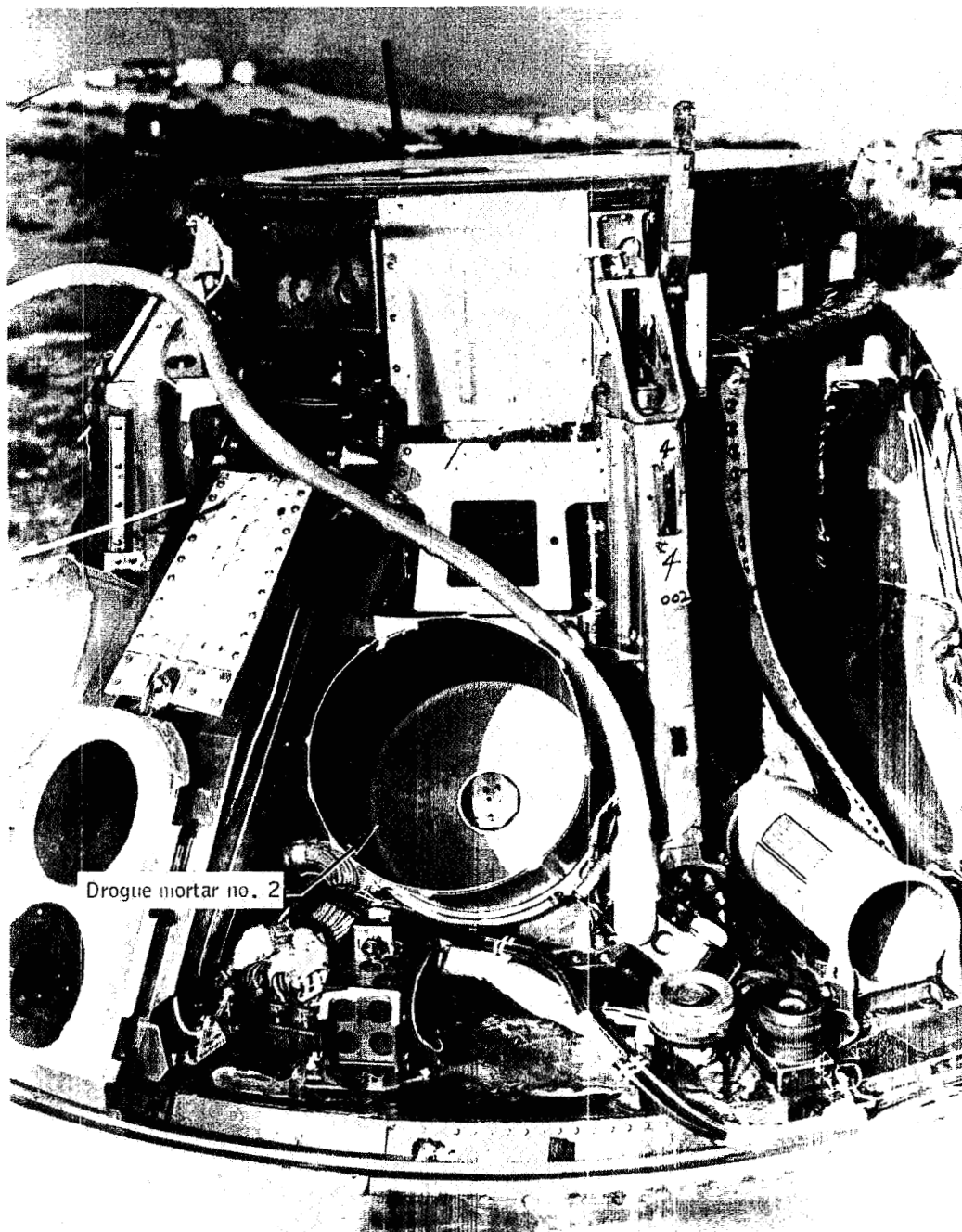


Figure 5.8-7.- Parachute (-Z) quadrant showing drogue mortar no. 2, Apollo Mission A-004.

NASA-S-66-3812 APR 15

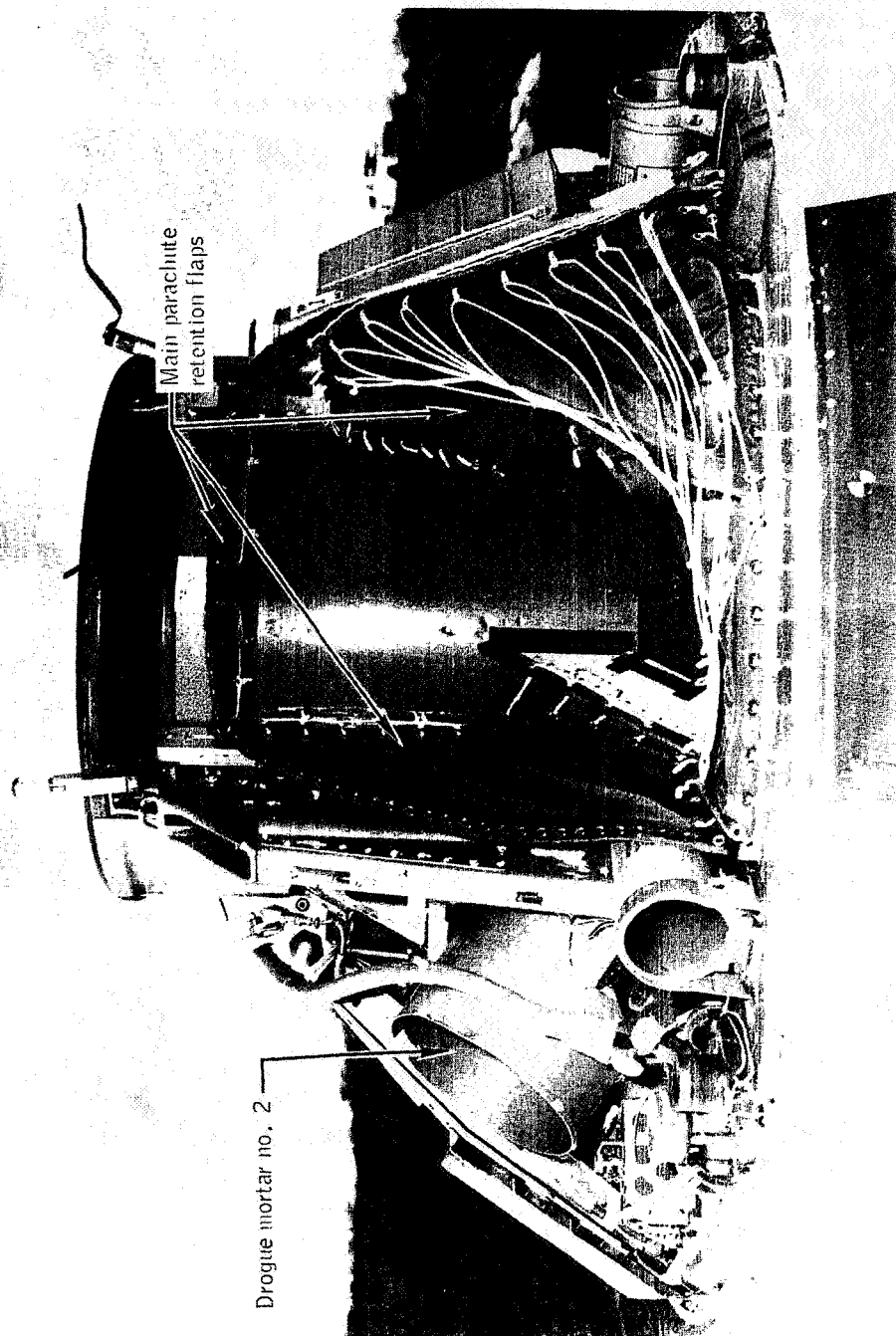


Figure 5.8-8.- Main parachute (+Y) quadrant, Apollo Mission A-004.

NASA-S-66-3832 APR 15

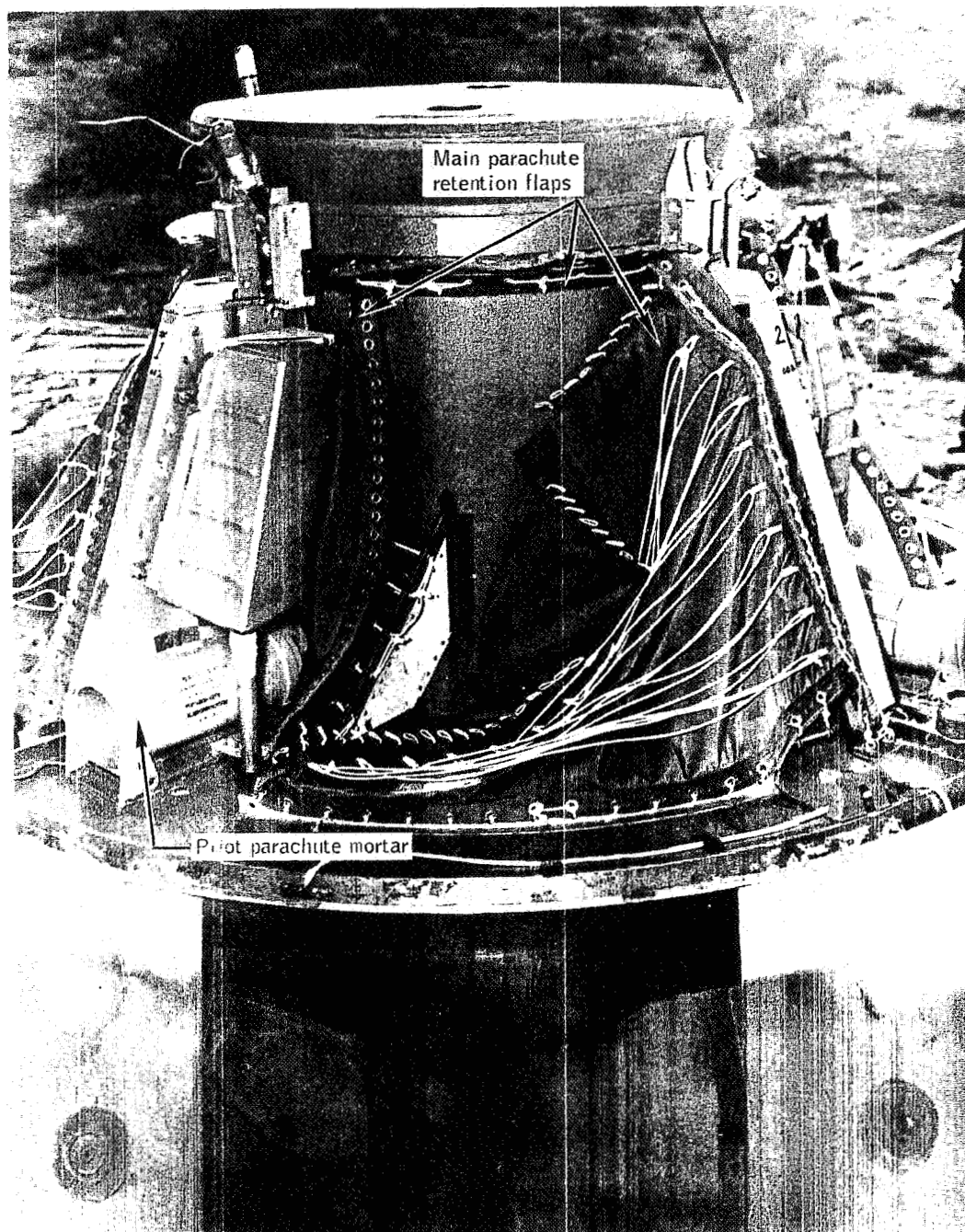


Figure 5.8-9.- Main parachute (+Z) quadrant, Apollo Mission A-004.

5-144

NASA-S-66-3792 APR 15

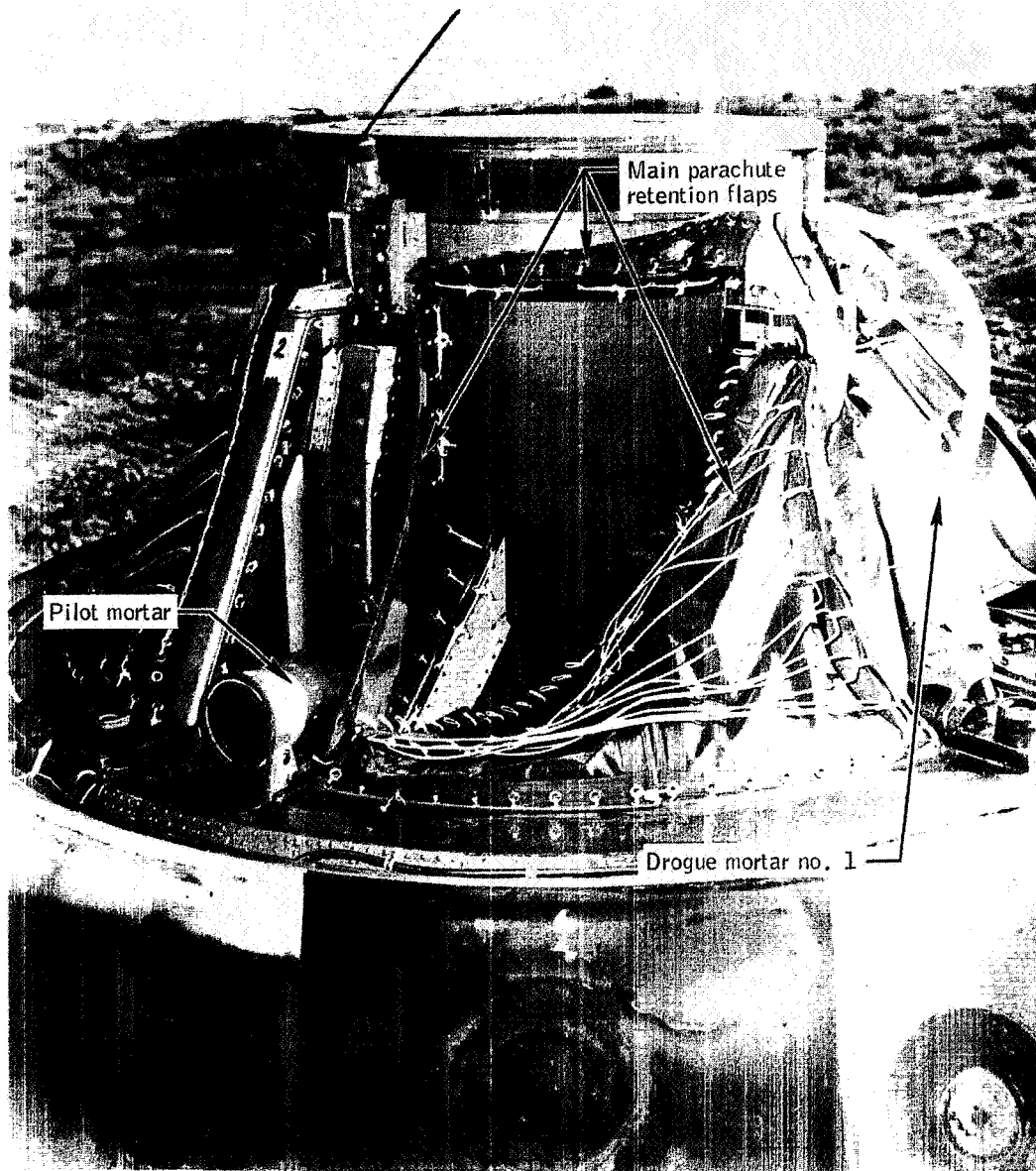


Figure 5.8-10.- Main parachute (-Y) quadrant, Apollo Mission A-004.



NASA-S-66-3804 APR 15

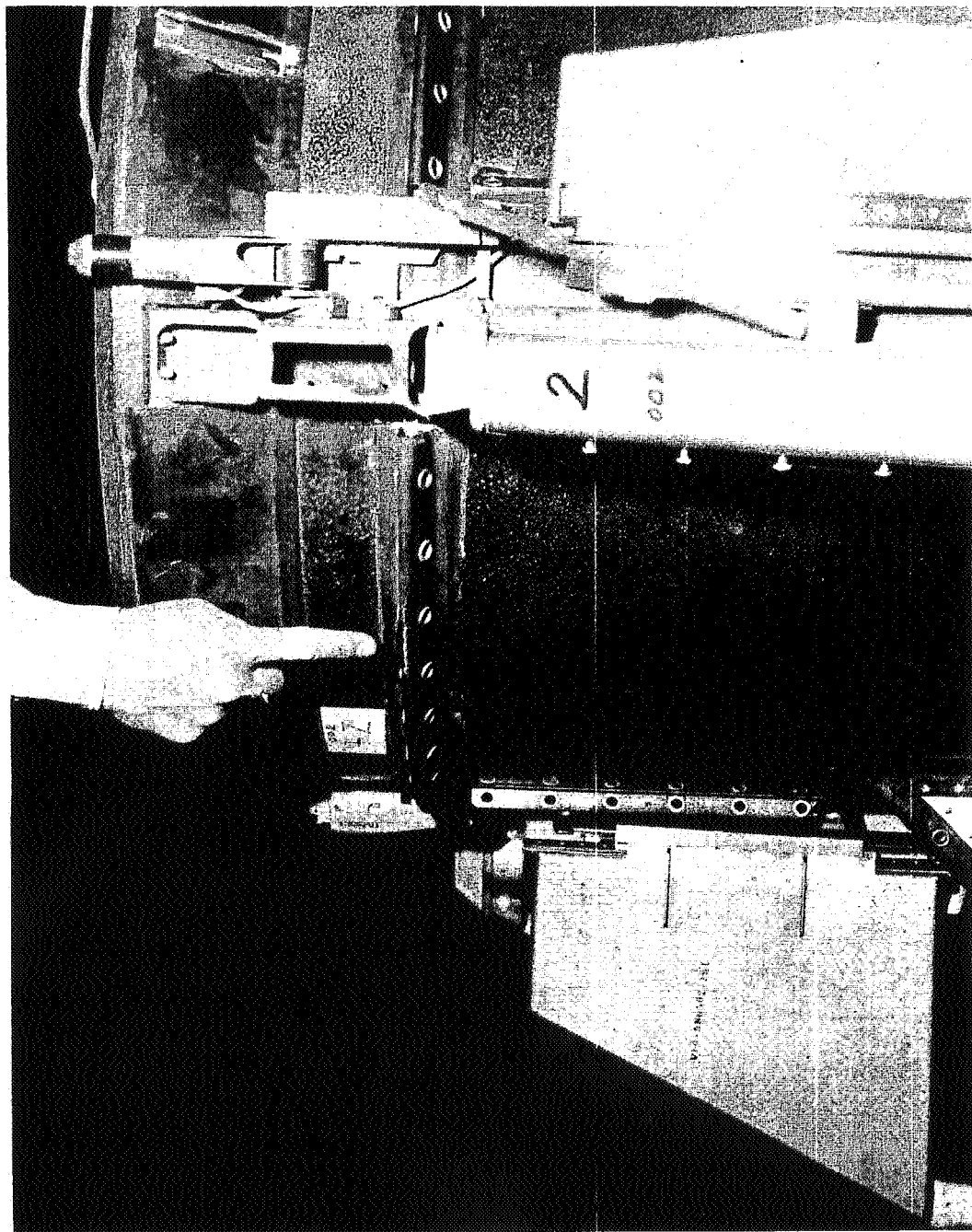
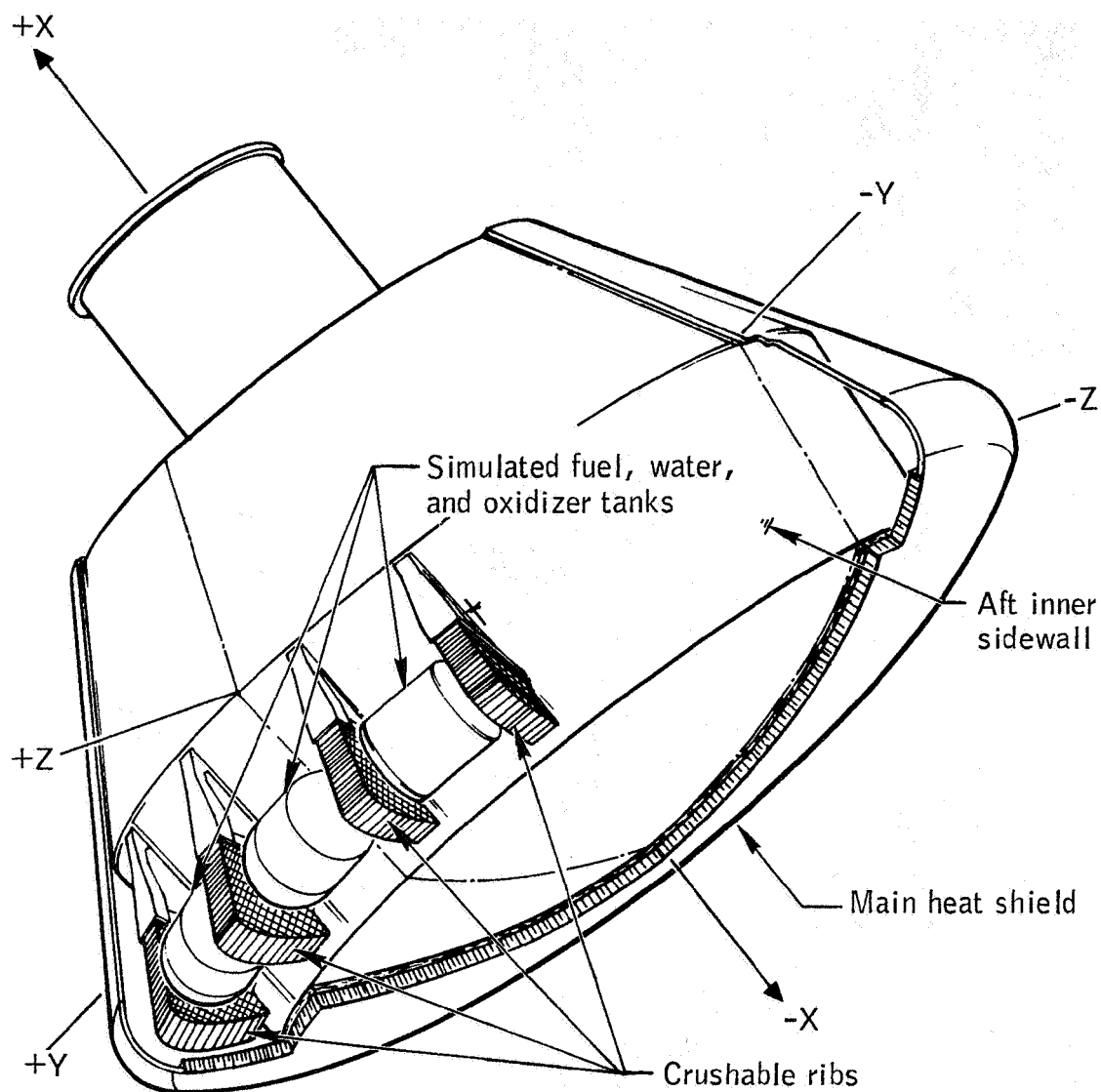


Figure 5.8-11.- Split retention strip (+Z) quadrant, Apollo Mission A-004.

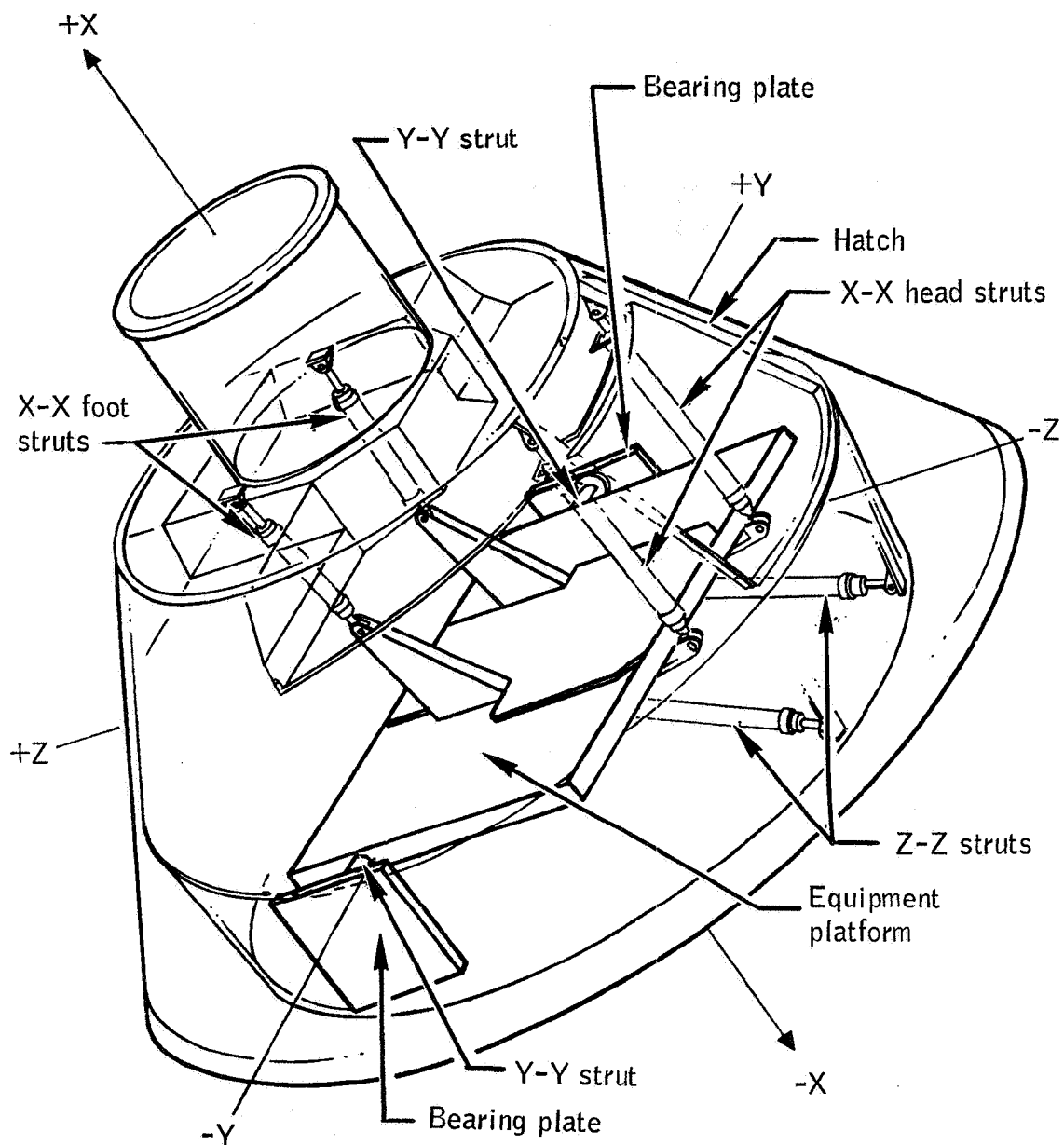




(a) External configuration.

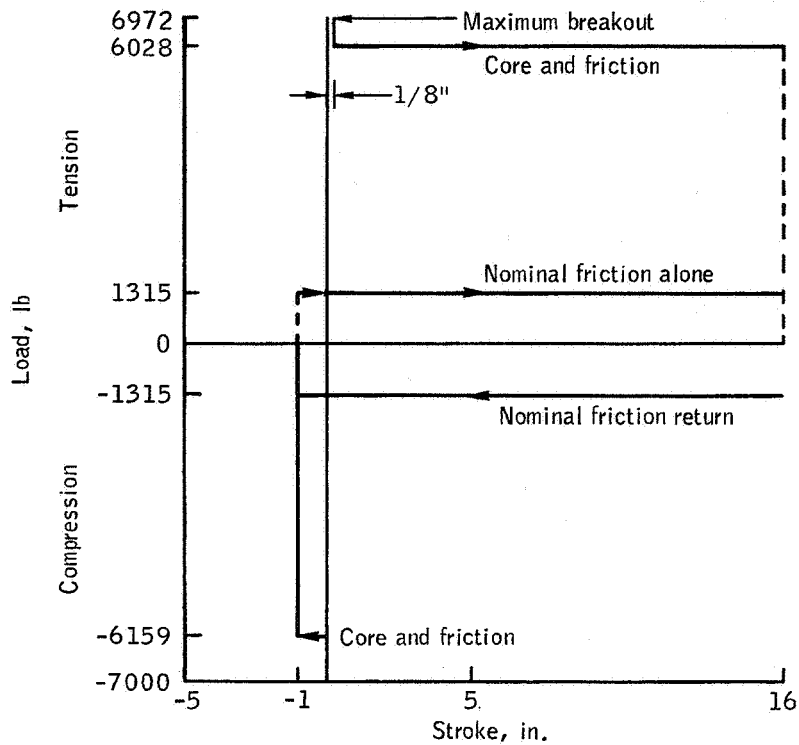
Figure 5.8-12.- Command module attenuation subsystem,  
Apollo Mission A-004.

NASA-S-66-3820 APR 15

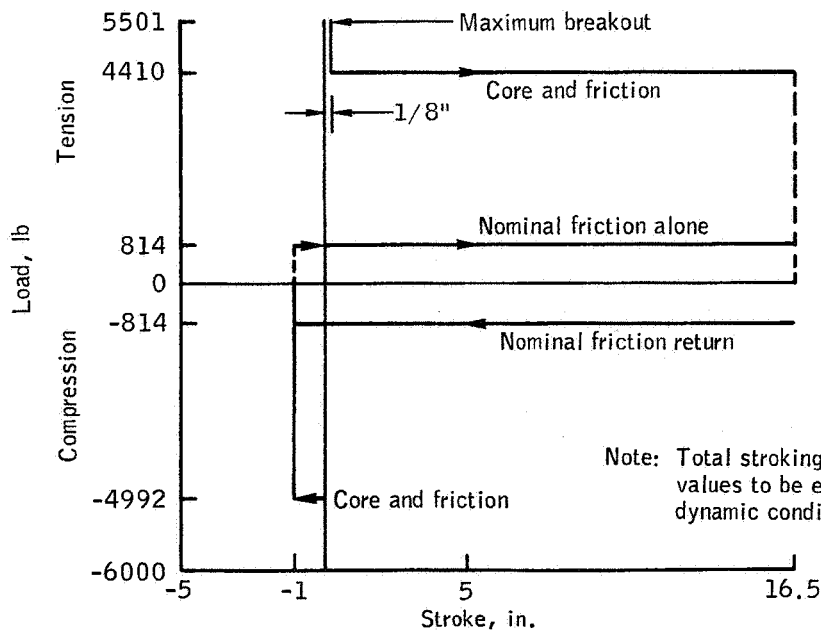


(b) Internal configuration.

Figure 5.8-12.- Concluded.



(a) X-X foot strut.



Note: Total stroking loads are maximum values to be expected under dynamic conditions

(b) X-X head strut.

Figure 5.8-13.- Impact attenuation struts, Apollo Mission A-004 predicted load-stroke curves.

NASA-S-66-3828 APR 15

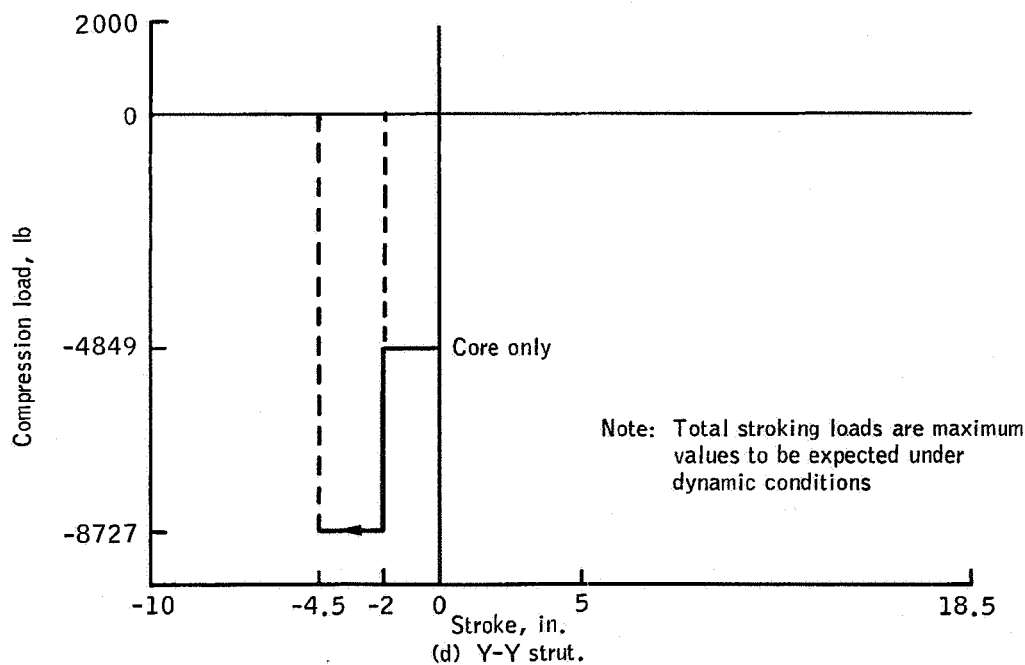
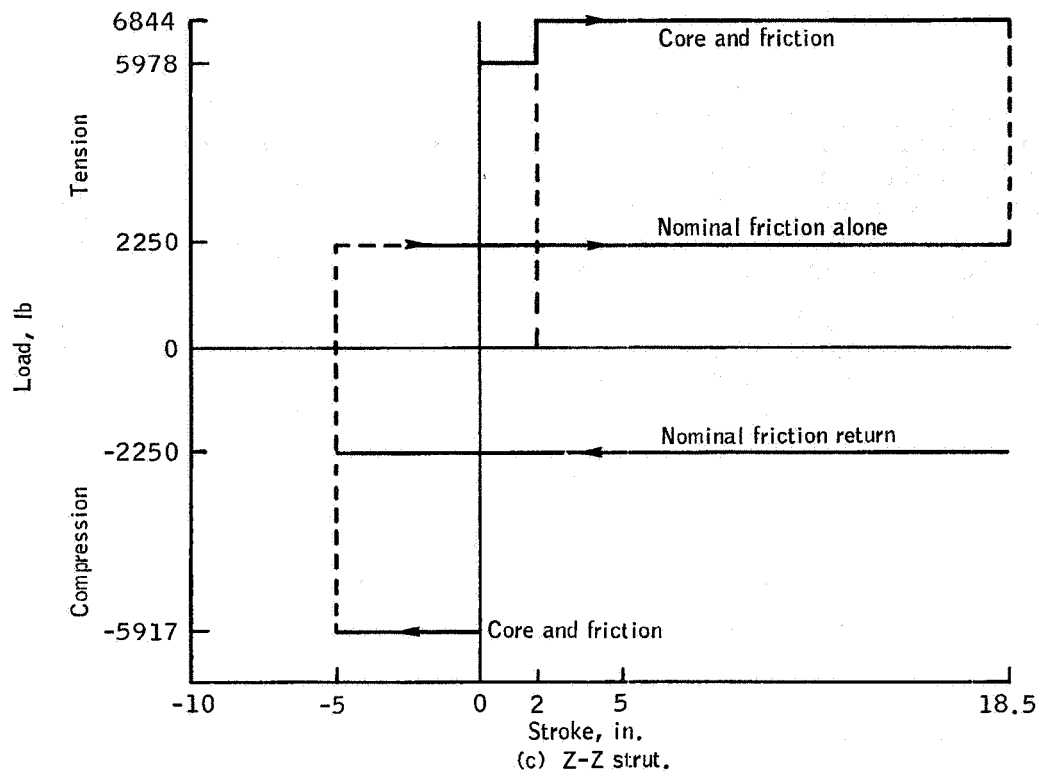


Figure 5.8-13.- Concluded.

### 5.9 Crew Station Acoustics

Description. - A third-order objective for Mission A-004 was to obtain acoustic data at a crewman's station. The environment of interest was the noise generated aerodynamically during the region of maximum dynamic pressure and the noise during abort. From the available wind-tunnel data (ref. 19) collected on the Apollo spacecraft configuration, a maximum overall sound pressure level (SPL) of 168 decibels (dB, re:  $0.0002 \text{ dyne/cm}^2$ ) had been predicted on the CM-SM interface for a nominal Saturn trajectory. Sound pressure levels of 167 dB and 169 dB were measured at the CM-SM interface of the instrumented boilerplate spacecraft on Missions A-001 and A-002 (refs. 20 and 10).

Two microphones were mounted in the crew compartment on the equipment platform in SC-002. (See fig. 5.9-1.) The measurement CK0034Y microphone, located at  $X_C 50.0$ ,  $Y -0.5$ ,  $Z -18.0$ , had an SPL range of 110 to 150 dB, and the measurement CK0035Y microphone, located at  $X_C 50.0$ ,  $Y 0.5$ ,  $Z -18.0$ , had a range of 100 to 140 dB. The microphones sensed the crew station noise and vibration, but a compensating accelerometer, operating in opposition to the microphone, removed the vibration component; therefore, only the noise was recorded. Preflight calibrations showed that the microphones and their terminal equipment were linear with SPL and had a flat frequency response ( $\pm 1$  dB) from 20 to 5 kc/sec. Both measurements were recorded on the wide-band FM tape recorder. A more complete description of the acoustic instrumentation system can be found in reference 21.

Performance. - Acoustic data at the crew station were obtained and the results are presented in figures 5.9-2 to 5.9-4. The recorded data were reduced in an analog format using a rms meter, octave band analyzer, and X-Y plotter. The data, consisting of overall SPL and one-third octave band SPL time histories, were reduced from data from microphone CK0035Y only because microphone CK0034Y failed at T+48 seconds. Up to that time, the instruments were giving the same readings.

Figure 5.9-2 shows the overall SPL time history of crew station acoustics for the period from T-10 to T+90 seconds. After launch vehicle engine ignition, the noise reaching the crew compartment increased to a maximum level of 117 dB at T+0.6 seconds. As the vehicle accelerated, the SPL in the crew compartment decreased and became insignificant at approximately T+4 seconds. At T+23.2 seconds, the aerodynamic noise became predominant in the crew compartment and continued to increase until T+38.8 seconds (Mach number of 1). The noise remained intense throughout the high dynamic pressure region until abort. At T+73.5 seconds, the acoustic measurement saturated for 0.5 second; the data are difficult to interpret from T+74 seconds to T+78 seconds because the

intensity and frequency are changing rapidly. The maximum SPL during this 4-second period was 132 dB, which was recorded at T+76.5 seconds. Levels as low as 96 dB were also recorded during this 4 seconds. At T+88 seconds, the noise levels at the crew station fell below the instrumentation range and were not significant during the remainder of the flight.

One-third octave band time histories were used to calculate spectrum levels (SPL per cycle) for discrete flight times. Figure 5.9-3 shows the noise spectrum at a Mach number of 1 (T+38.8 sec), maximum dynamic pressure (T+41.5 sec), and just prior to abort (T+73.3 sec). These data, collected at the crew station, indicate that a flat spectrum was recorded and that the acoustic energy was concentrated at frequencies below 500 cps. Figure 5.9-4 shows the noise spectrum during abort at T+74.3, T+75.6, T+76.6, and T+78.8 seconds. Criteria values based on the high q abort design (ref. 22) have been included in figure 5.9-4 for comparison.

NASA-S-66-3840 APR 15

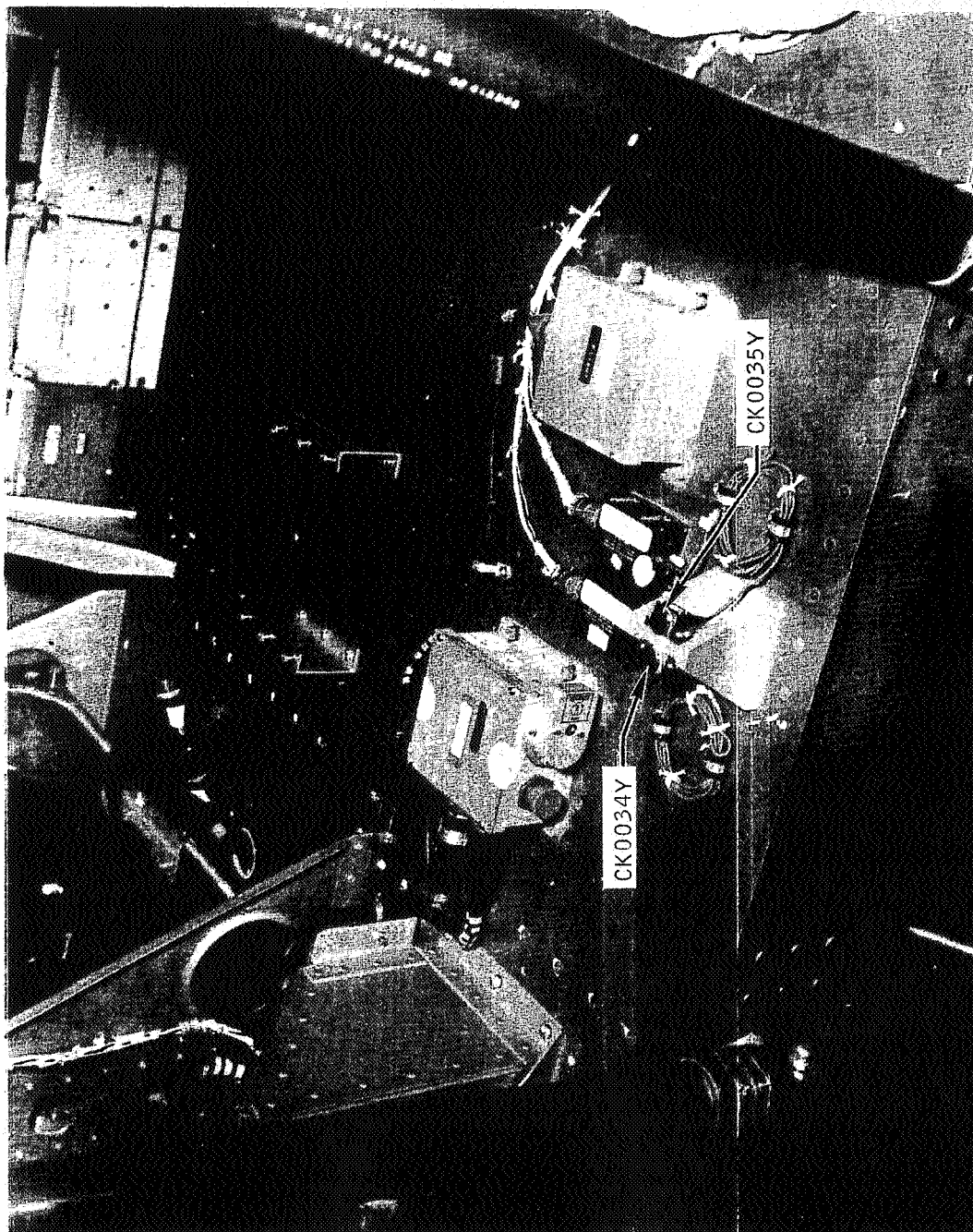


Figure 5.9-1.- Microphone mountings on equipment platform at the crew station, Apollo Mission A-004.

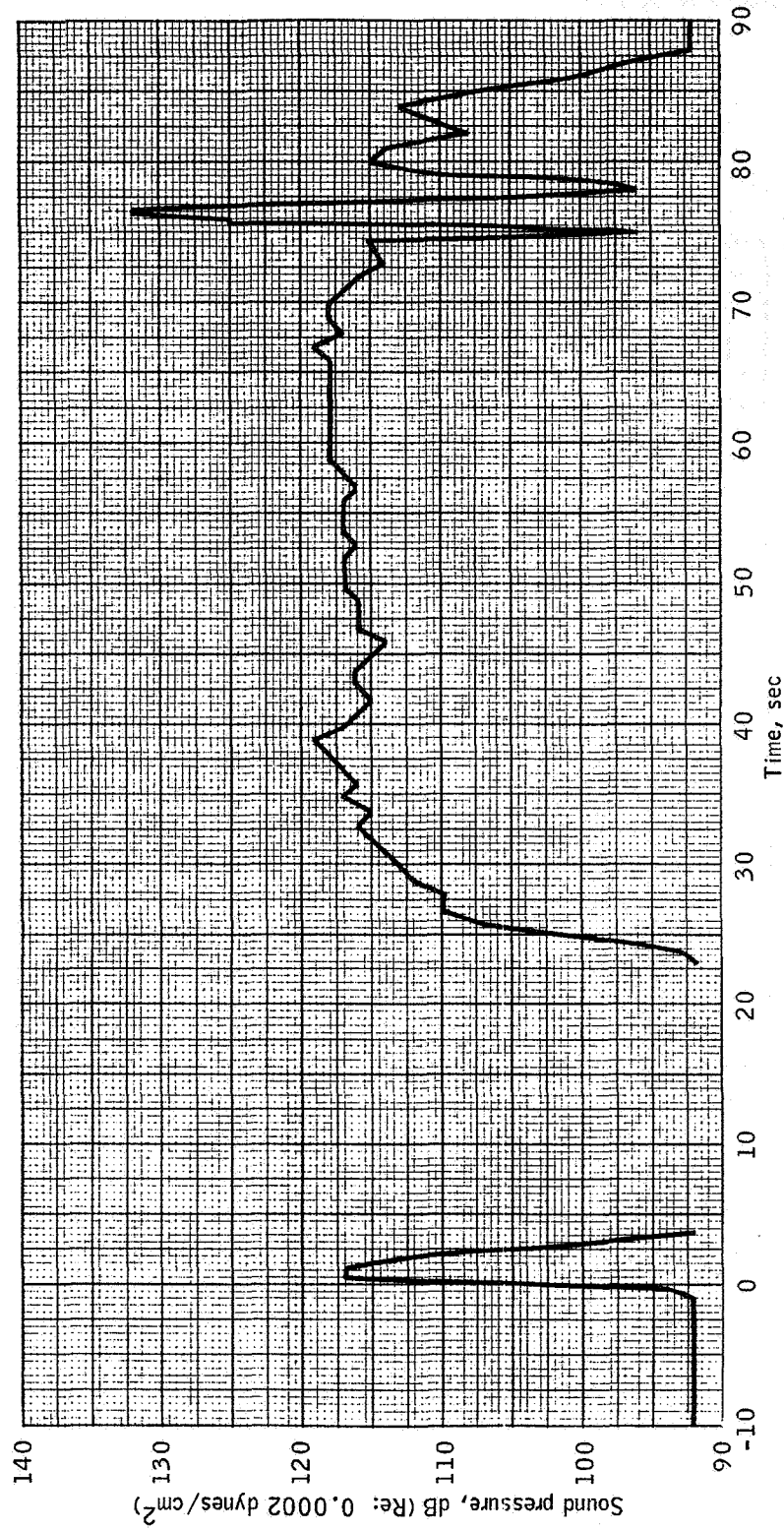


Figure 5.9-2.- Overall sound pressure level time history of crew station acoustics CK0035Y, Apollo Mission A-004.



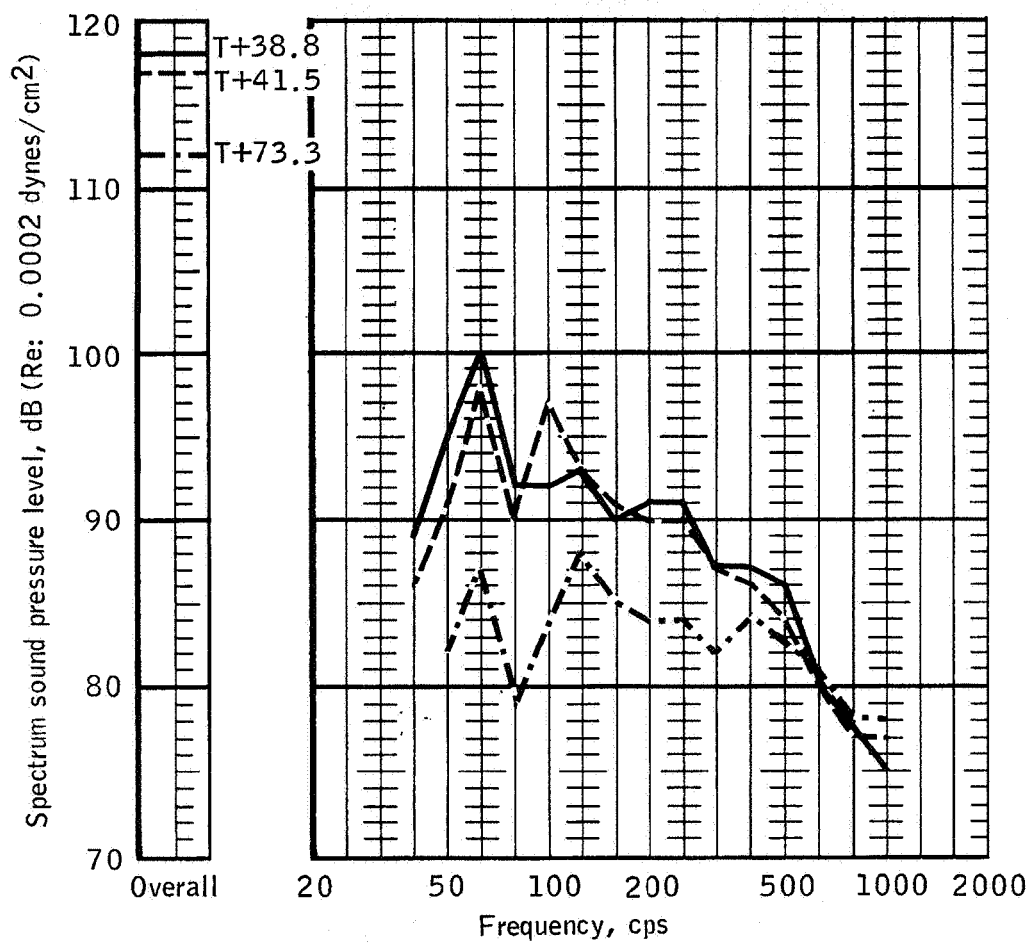


Figure 5.9-3.- Spectrum sound pressure levels (SPL per cycle) for CK0035Y at T+38.8 (Mach 1), T+41.5 (max q), and T+73.3 (prior to abort) for Apollo Mission A-004.

NASA-S-66-3808 APR 15

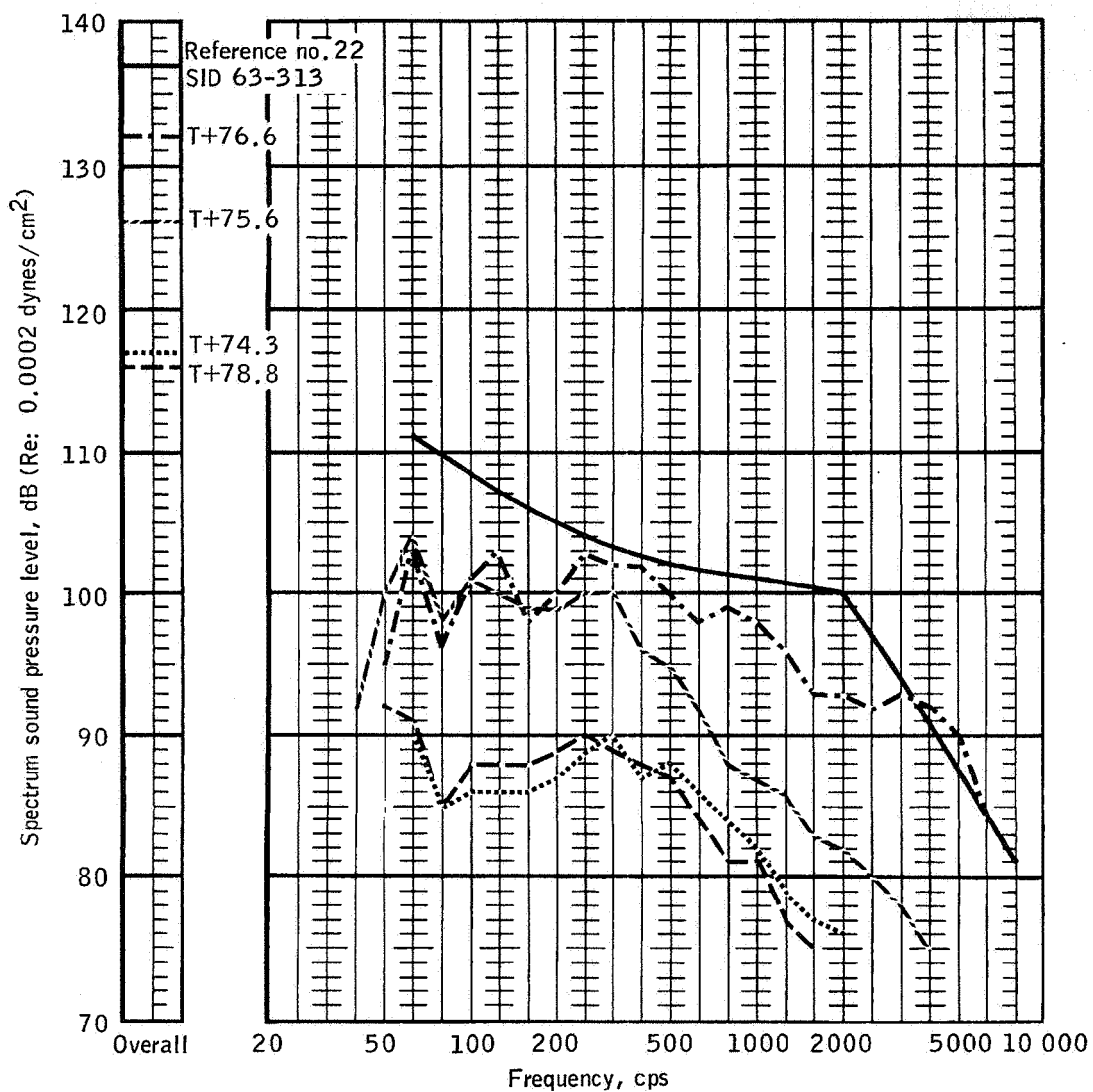


Figure 5.9-4.- Spectrum sound pressure levels (SPL per cycle) for CK0035Y at T+74.3, 75.6, 76.6, and 78.8 sec during abort for Apollo Mission A-004.

### 5.10 Sequential Subsystem

Description.- The sequential subsystem installed on SC-002 included a mission sequencer, a separation sequencer, a tower sequencer, an impact switch box, an abort backup timer, and an ELS sequence controller. (See fig. 5.10-1.) Functions performed by the first three sequencers mentioned are those that will be performed by the master events sequence controller on future Block I spacecraft.

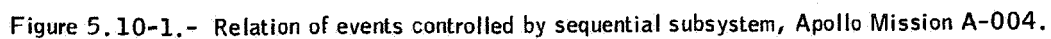
The mission sequencer, tower sequencer, abort backup timer, and impact switch box were R and D units identical to those used on Mission A-003 (BP-22, ref. 4) with the following exceptions:

(a) Both the BP-22 and SC-002 mission sequencers included circuits to initiate CM-SM umbilical deadfacing and separation, but because SC-002 used a Block I CM-SM umbilical for the first time the separation sequencer was added to SC-002 to delay umbilical separation until 0.4 second after deadfacing. Since BP-22 did not use a Block I CM-SM umbilical, the output wiring harness for the umbilical deadfacing and separation circuits was not installed in BP-22.

(b) The BP-22 impact switch box included fuses that simulated the pyrotechnics used to disconnect the main parachutes. Live pyrotechnics were used on SC-002.

The Block I earth landing subsystem sequence controller (ELSSC) consisted of two independent redundant units and was identical to the Block I controller successfully tested on BP-22. A pyrotechnic verification box was installed in the CM of SC-002 to permit verification of the pyrotechnic circuits prior to launch. Spacecraft 002 was the first spacecraft to have this box installed.

Performance.- The sequential subsystem operated properly during the flight and all time-delay relays operated within acceptable time limits. Event times are listed in figure 2.0-2. Figure 5.10-2 shows the fuses which were blown during the pyrotechnic bus voltage excursions discussed in section 5.11.



NASA-S-66-3717 APR 15

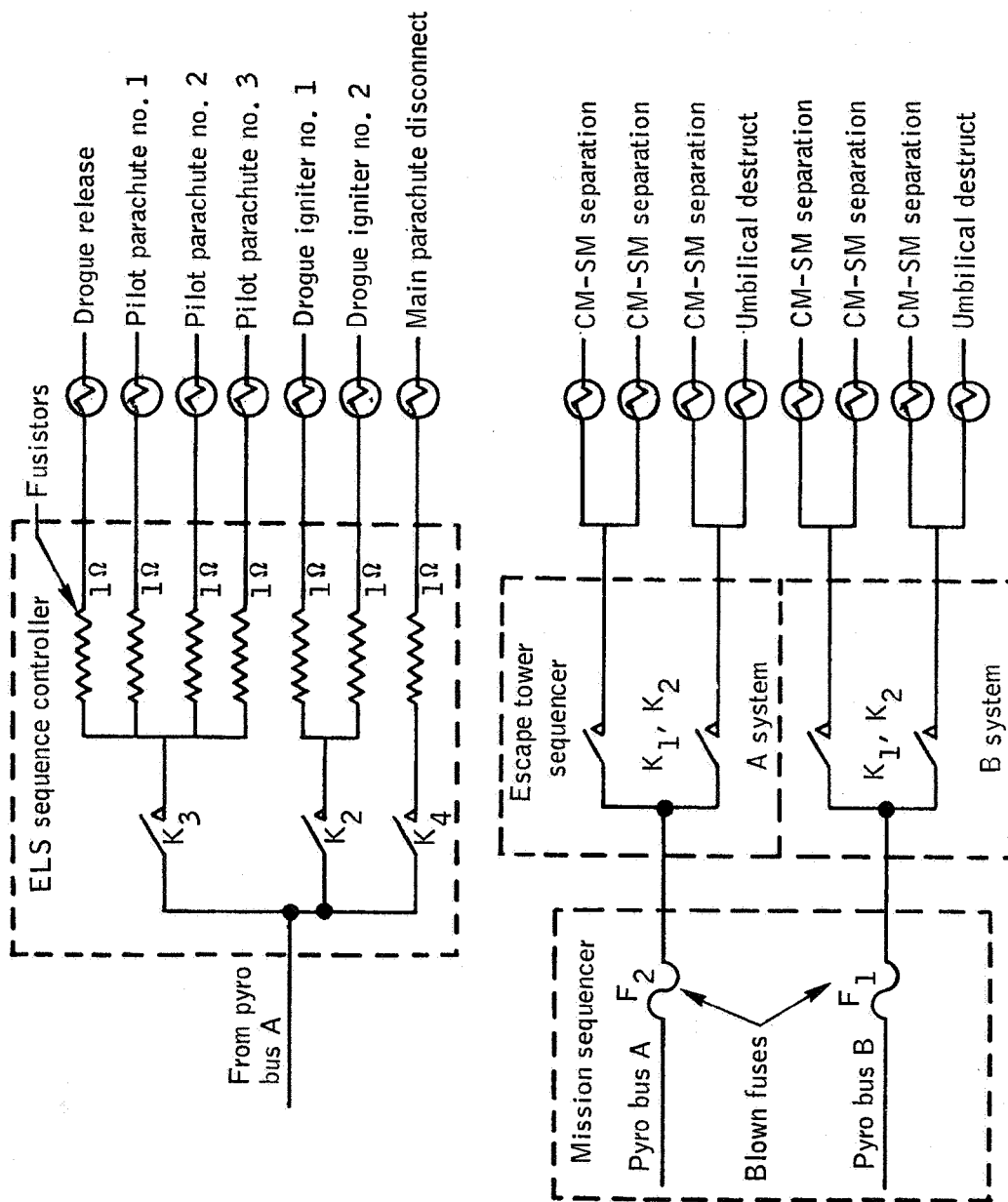


Figure 5.10-2.- Blown fuses and fusistor locations in mission sequencer and ELS sequence controller for Apollo Mission A-004.

### 5.11 Electrical Power Subsystem

Description.- The electrical power subsystem (EPC) provided power for the instrumentation and communications subsystem, the sequential subsystem, and pyrotechnic loads as shown in figure 5.11-1. The EPS included six silver-zinc batteries: two main batteries, two logic batteries, and two pyro batteries. All batteries were successfully flight-tested on Apollo Mission A-003 and are described in reference 4. The two pyro batteries were Block I configuration.

Electrical power for the two camera systems was provided by two camera batteries MAR 4090-11A; each battery included an additional 13-volt tap for camera operation.

Performance.- The electrical power subsystem operated properly during the flight. There were no abnormal variations in either current or voltage of instrumentation buses A and B; those slight variations noted reflected the varying instrumentation loads. The lowest instrumentation bus voltage recorded was 27.9 volts on bus B, which was recorded at T+200 seconds and was accompanied by a 3-ampere transient increase in total instrumentation current. This time coincides approximately with the malfunction of the onboard tape recorder discussed in section 5.12. Records of total instrumentation direct current and voltages from main buses A and B for the flight are shown in figure 5.11-2.

The variations during flight of logic buses A and B voltages are shown in figure 5.11-3. The normal decrease in voltage from abort initiation until impact was caused by the increasing sequencer logic load during this period. Bus voltage remained within the range expected.

Variations in pyro buses A and B voltages during flight are shown in figure 5.11-4. With the exception of the two excursions discussed in the following paragraphs, variations were within the normal range. Other than these excursions the lowest voltage recorded was 30.1 volts, which occurred at T+193.8 seconds (tower jettison).

A major decrease in bus voltage occurred simultaneously on both pyro buses at T+73.7 seconds (abort initiation). Bus A dropped to 5.0 volts and bus B dropped to 7.5 volts. However, both recovered within 1 second. This decrease in voltage indicated an extremely low resistance short in the pyro ignition circuit which was immediately removed as fuses F<sub>1</sub> and F<sub>2</sub> in the mission sequencer blew. A plot of bus A voltage during this incident is shown in figure 5.11-5, and fuse locations are shown in figure 5.10-2. Postflight bench testing of the command module associated circuitry and simulations with groups of initiators of the same type have indicated no apparent fault in the CM

circuitry and associated components. It is possible that the magnitude of either the firing current or pin-to-case leakage current during firing could be sufficient to cause this effect when fuses are used in the circuit in lieu of fusistors with their current-limiting ability. Further examination has shown that conditions exist on the spacecraft which could account for the shorting conditions. An example of this is initiator wires which were frayed back 2 to 3 inches from the end by explosion and wind whipping in several initiator locations. It should be noted that the shorting conditions do not constitute a failure of either the power or sequencer systems since the fuses were installed in anticipation of shorts of this nature occurring in the pyro subsystem. These fuses functioned properly.

The second major drop in pyro bus B voltage occurred at T+237.6 seconds (pilot parachute deployment) when pyro bus B dropped to 30.1 volts. Recovery occurred in approximately 5 seconds with data indications that a fusistor in the earth landing subsystem sequence controller (ELSSC) removed the heavy load. An expanded plot of bus voltage during this incident is shown in figure 5.11-6. Fusistor locations are shown in figure 5.10-2. Postflight testing by the contractor revealed that all fusistors are still functional which leaves the anomaly unexplained.

Camera battery performance is indicated in section 5.12.

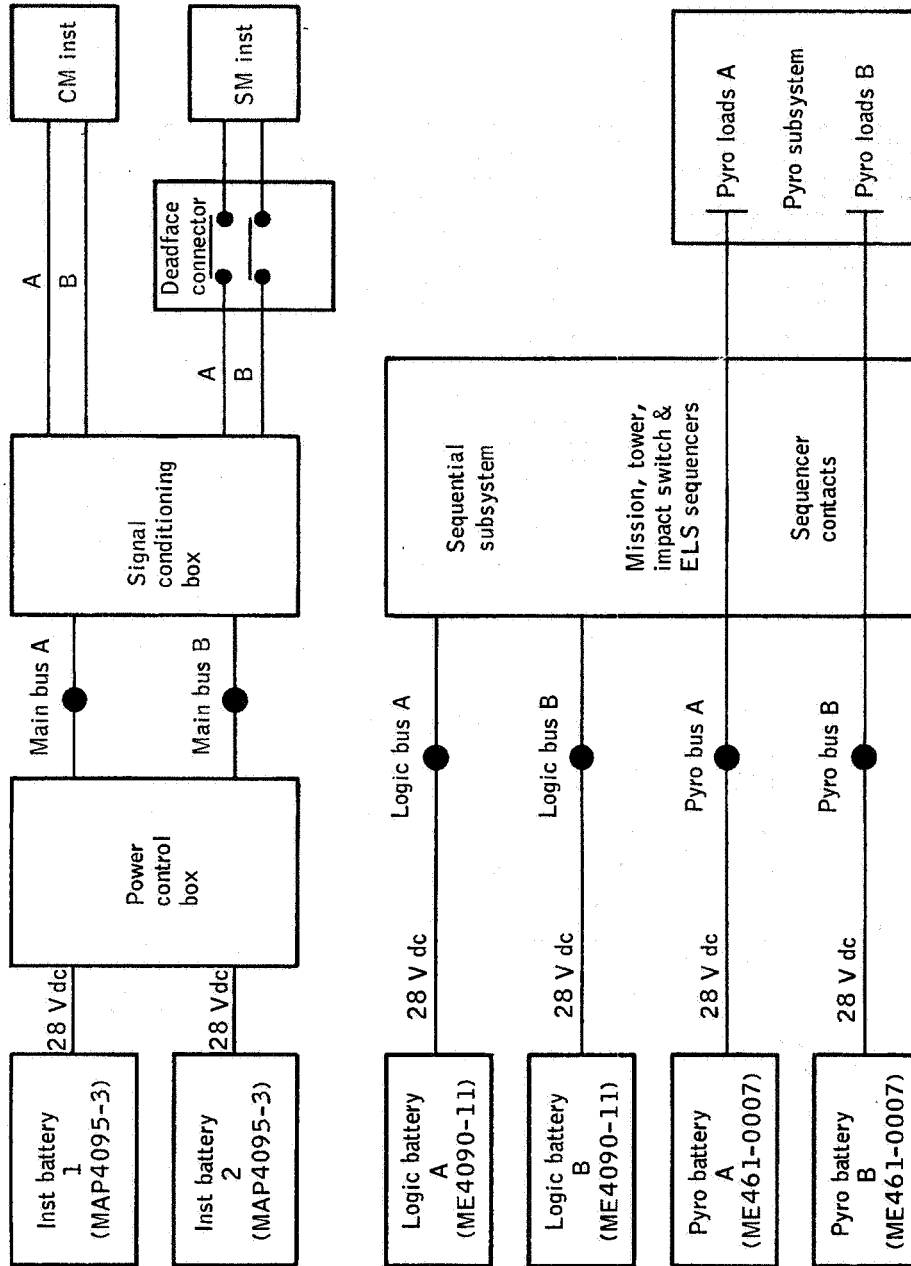


Figure 5.11-1.- Electrical power subsystem block diagram, Apollo Mission A-004.



NASA-S-66-3863 APR 15

0.00 SEC LIFT OFF  
 73.70 SEC ABORT INITIATION  
 73.70 SEC LES MOTOR FIRE  
 193.80 SEC TOWER JETTISON  
 237.60 SEC MAIN CHUTE

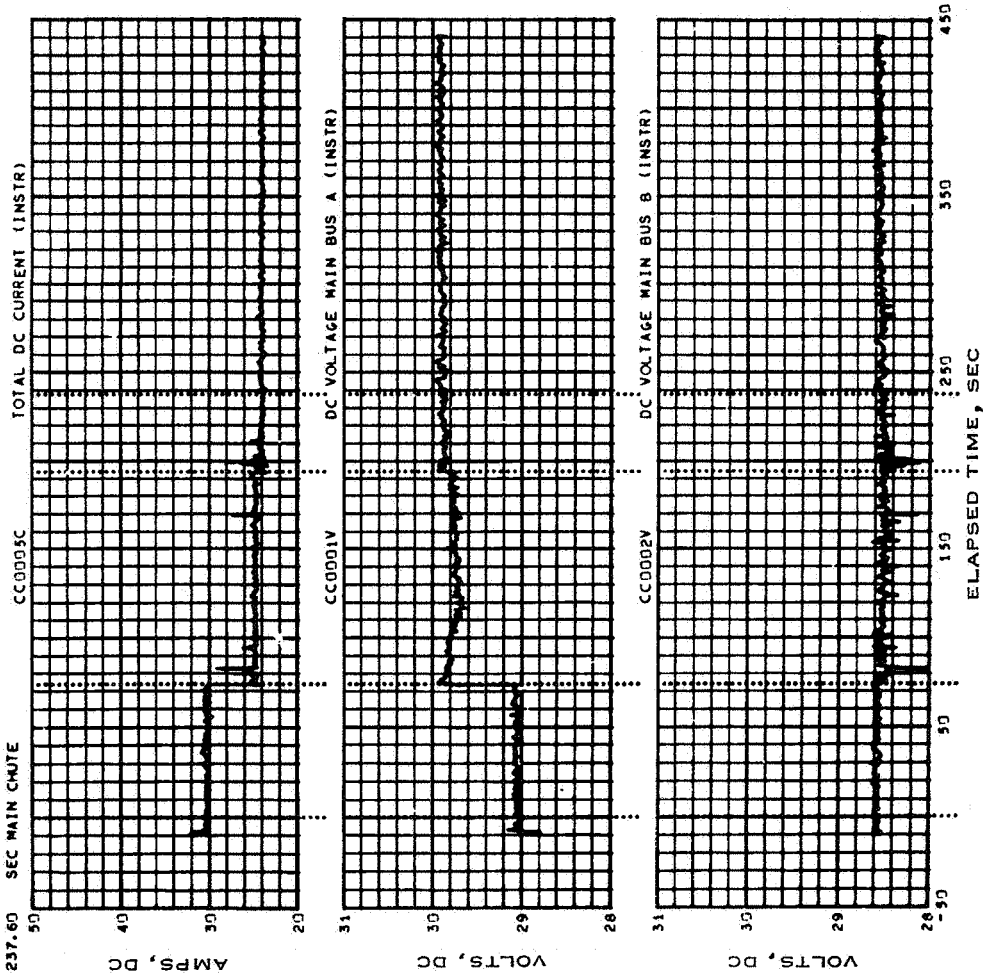


Figure 5.11-2.- Time histories of dc current and main bus voltage, Apollo Mission A-004.

NASA-S-66-3889 APR 15

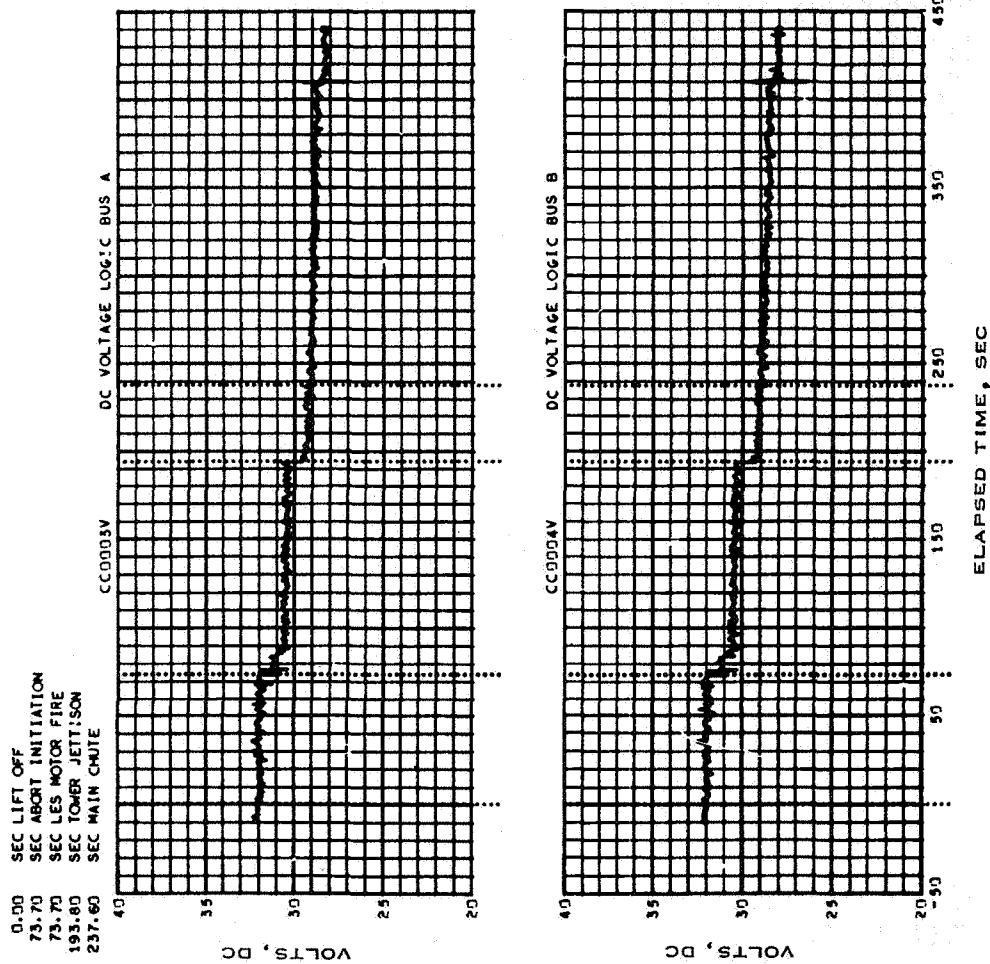
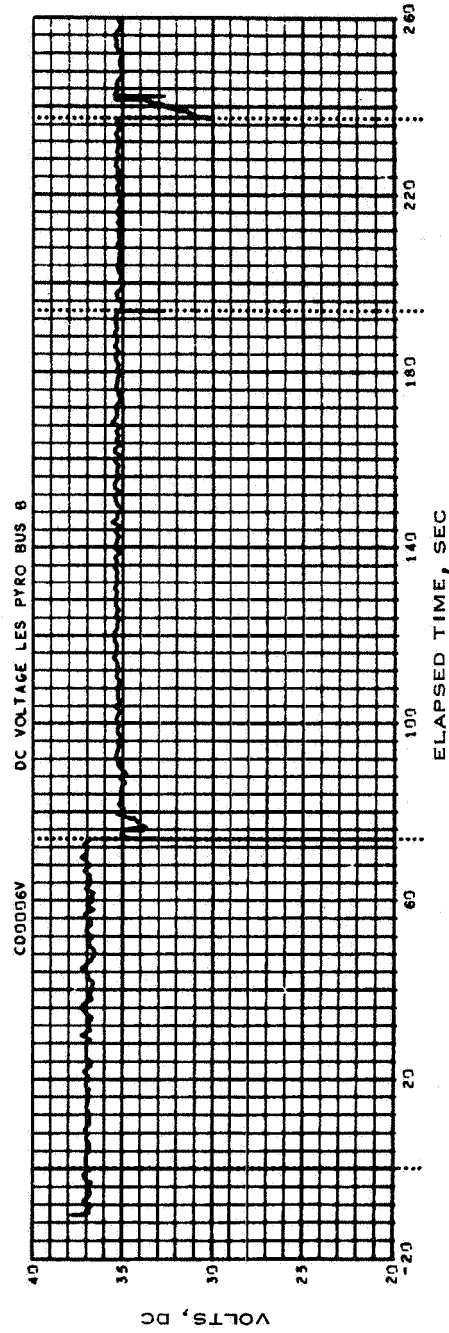
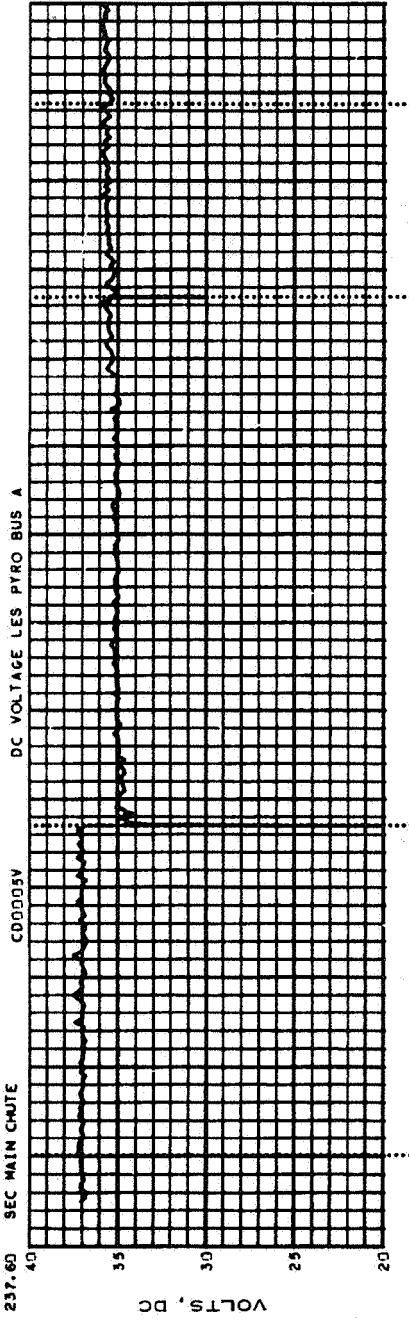


Figure 5.11-3.- Time histories of logic bus A and B voltage, Apollo Mission A-004.

NASA-S-66-3886 APR 15

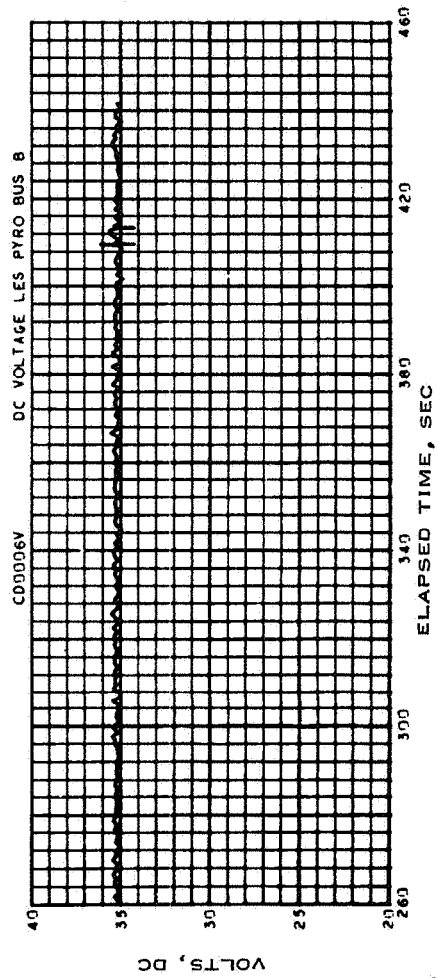
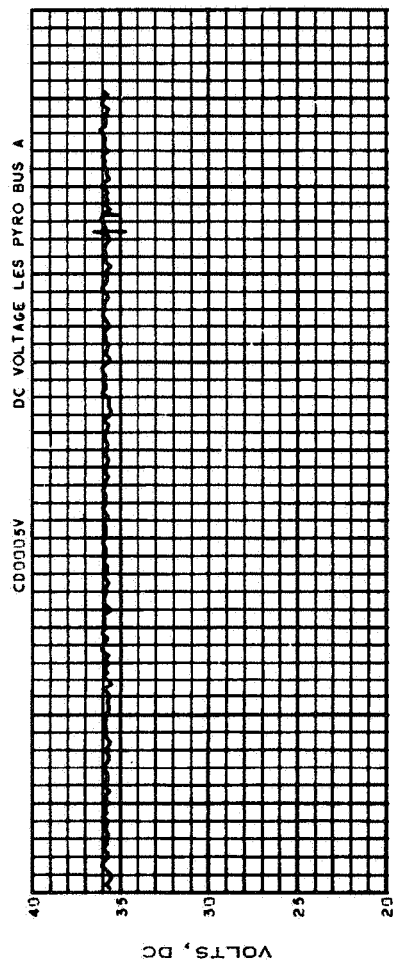
0.00 SEC LIFT OFF  
73.70 SEC ABORT INITIATION  
73.70 SEC LES MOTOR FIRE  
193.80 SEC TOWER JETTISON  
237.60 SEC MAIN CHUTE



(a) -20 to 260 seconds.

Figure 5.11-4.- Time histories of pyro bus A and B voltages, Apollo Mission A-004.

NASA-S-66-3883 APR 15



(b) 260 to 460 seconds.

Figure 5.11-4.- Concluded.

5-166

NASA-S-66-3868 APR 15

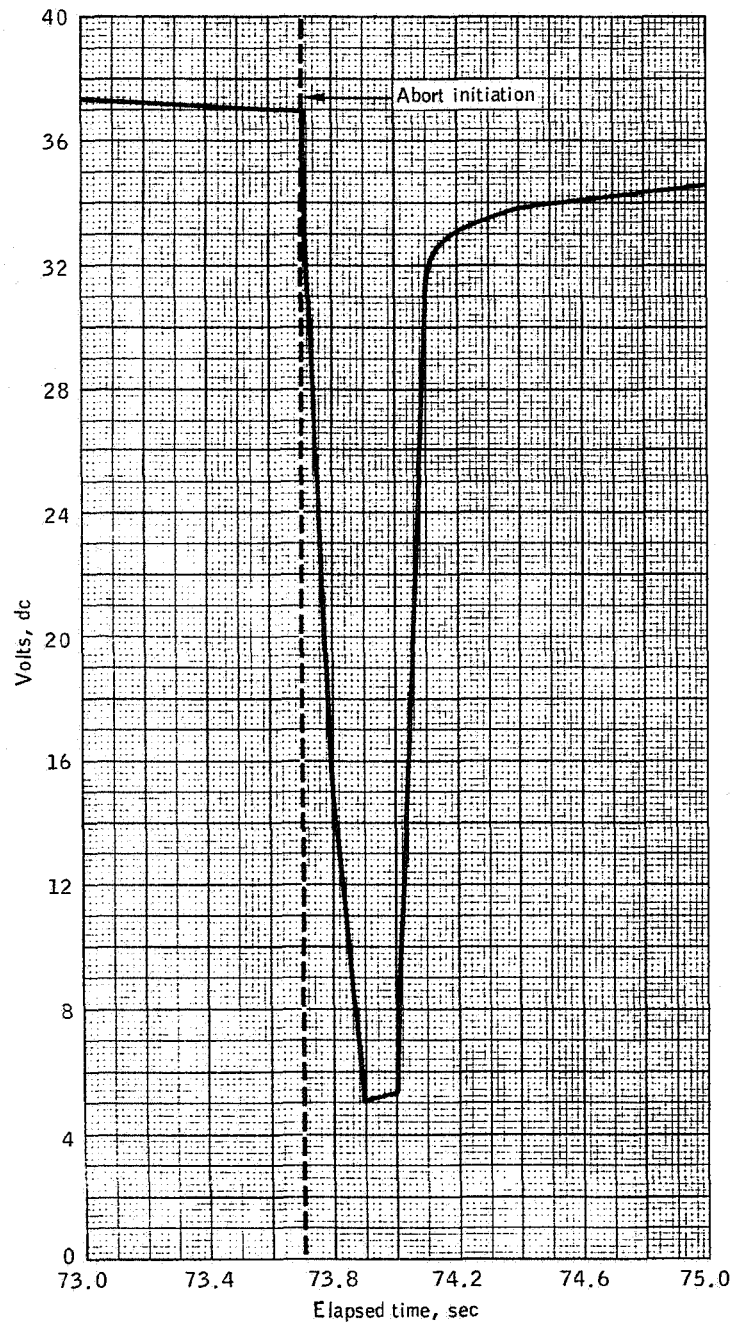


Figure 5.11-5.- Pyro bus A voltage, Apollo Mission A-004.

NASA-S-66-3871 APR 15

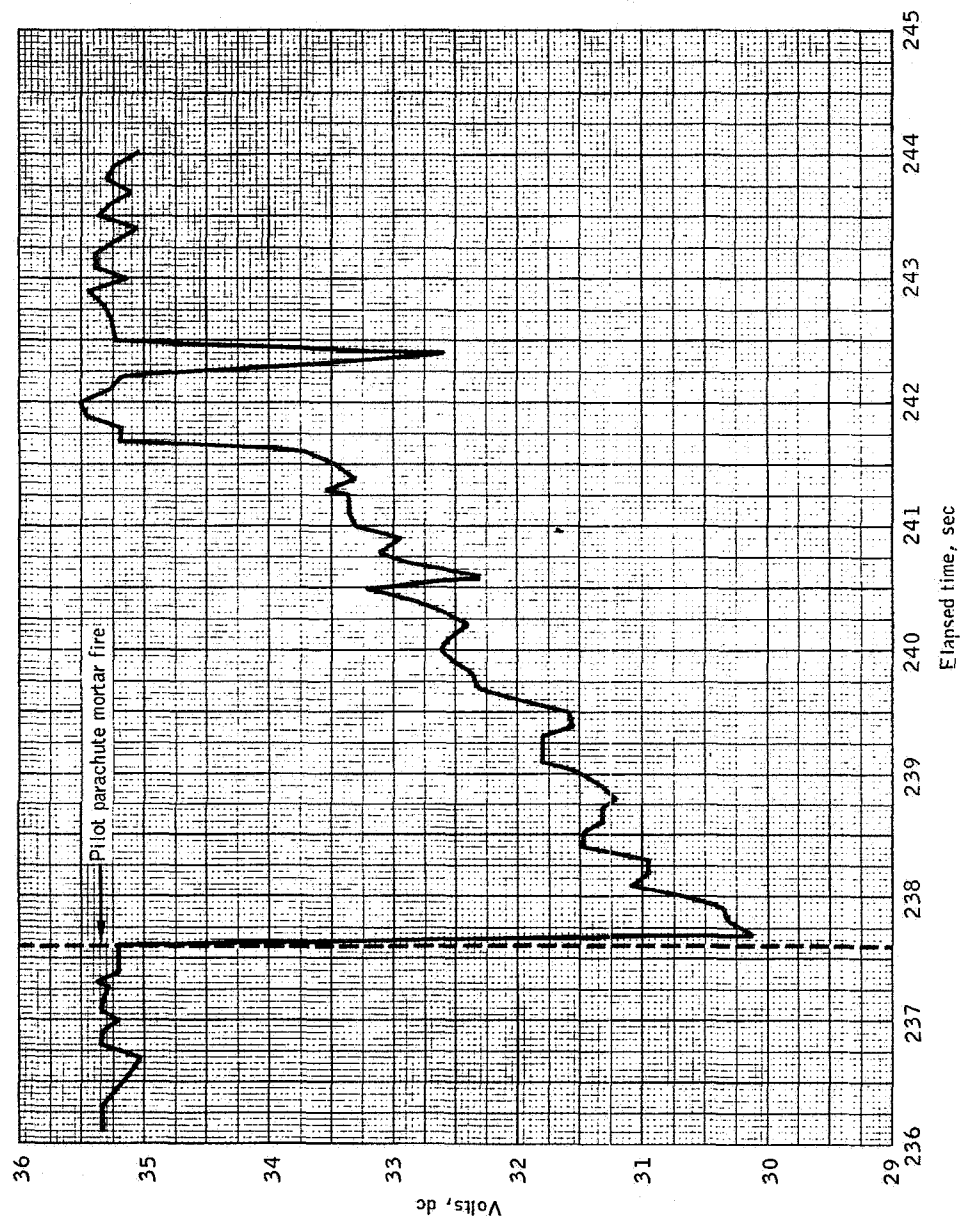


Figure 5.1.1-6.- Pyro bus B voltage, Apollo Mission A-004.

## 5.12 Spacecraft Instrumentation and Communication Subsystem

Summary.- Pertinent data were obtained from 237 of the total 242 onboard measurements. Failure of the single operational-type scimitar antenna following abort caused a loss of both radio-frequency telemetry links at T+74.7 seconds. However, data transmitted by these links were recorded on the onboard tape recorders, as planned, such that significant information was recovered for the mission evaluation.

Description.- The SC-002 instrumentation and communication subsystem was a standard PAM/FM/FM system similar to that flown on the previous boilerplate flights, but it employed upgraded components qualified to higher environmental levels. The subsystem consisted of two 15-channel PAM/FM/FM telemetry links, signal conditioners, and transducers to measure and monitor vehicle performance. Two 14-track onboard tape recorders provided additional facilities for recording high-frequency data, as well as providing back-up recording of the telemetered data. Figures 5.12-1 to 5.12-3 are block diagrams illustrating the telemetry systems, F tape recording system, and H tape recording system, respectively. A complete description of the instrumentation and communication subsystem is contained in reference 21.

Performance.- Loss of telemetry signals occurred at T+74.7 seconds because of the failure of the single scimitar antenna (the second antenna was non-functional) at the time of the abort maneuver. Visual inspection of the antenna after command module recovery revealed a crack around the fairing of the antenna base, indicating that the antenna had been struck with a significant force. (See fig. 5.12-4.) Soot in the crack established that the impact occurred during the period of launch-escape motor burning. This was the first flight test for the operational scimitar antenna.

Postflight field inspection of the antenna cabling revealed that the coaxial conductor, which was permanently attached to the antenna, was loose and could be moved in and out of the antenna approximately 1/16 inch. In-line watt meter checks gave a normal reading of 1/2 watt reflected power and 10 watts forward power with the cable pushed in. With the cable moved out, the reflected power increased to 6 watts, indicating a failure of the internal connection. Subsequent examination of the antenna and lead wire at the contractor's facility at Downey, California, indicated that the antenna lead wire had parted at the base plate/exterior epoxy interface because of motion at the interface after bond failure.

The F tape recorder jammed at T+209.5 seconds, between the time of drogue parachute deployment and main parachute deployment. This difficulty had also been encountered during preflight checkout of the

spacecraft. Approximately 12 feet of tape was unwound on the take-up side of the recorder, indicating that movement of the take-up reel had been restricted. A postflight functional check confirmed normal recorder operation and that no component failure had occurred. Playback of the 50 kc tape recorder compensation data, which is a measure of tape speed variation, indicated that both recorders were severely stressed from T+76 to T+77 seconds. In addition, there was evidence that the take-up reel momentarily stopped at T+190 seconds and then recovered, causing a distinct variation in tape speed.

Service module RCS engine nozzle vibration measurement (SA0956D) and sector VI vibration measurement (SA0952D) malfunctioned at T+38 seconds and T+56 seconds, respectively. Oscillograph playbacks indicate that the data are valid up to time of malfunction. The instrumentation for these measurements were not recovered for failure analysis; however, the abrupt change in the data at these times and the character of the succeeding data indicated failures of the coaxial cable between the accelerometer and amplifier.

Command module strain measurements CA1601S and CA1603S, located on longeron 2, exhibited an intermittent condition for varying periods prior to and during abort. After T+80 seconds the measurements responded normally. Postflight investigations revealed no malfunction or intermittent condition in either the amplifier or cabling.

Service module aft bulkhead vibration measurement SA0995D had indications of noise at lift-off and for 4 seconds at T+34 seconds. Data between these times were valid. Since the instrumentation was not recovered, no failure analysis on the specific units could be performed. Laboratory tests simulating failures which would produce similar results indicated that a broken accelerometer connector could be the cause.

Command module acoustic measurement CK0034Y, located on the crew couch platform at X<sub>C</sub> 50.0, Y 0.5, Z -18.0, responded normally until T+48 seconds. It was erratic from T+48 seconds until abort where it again responded normally. Postflight analysis of this acoustic measurement system revealed no component or equipment malfunction. Also, the flight recorder was evaluated in conjunction with the acoustic measurement system. No malfunction or intermittent condition of the flight recorder was observed. The most probable cause is a loose connection.

The two C-band transponders used on the command module to aid in tracking were interrogated satisfactorily by three FPS-16 radars during flight. Satisfactory return signals were received from both transponders.



Two 16-mm motion picture cameras were installed on SC-002 with photographic coverage as illustrated in figure 5.12-5. The tower camera operated at 64 frames per second and ran from lift-off through launch-escape tower jettison. The command module camera, which viewed the left-hand rendezvous window for sooting, operated at 16 frames per second, covering the period from T+70 seconds to approximately T+240 seconds. Both cameras operated as programmed. The tower camera provided good coverage throughout the powered phase. As in previous flights, coverage was limited after launch-escape-motor burning because of lens sooting from motor exhaust. Soft boost protective cover separation in the first tumbling revolution allowed sooting of the rendezvous window from the burning LES motors but useful data were obtained from the command module film.

NASA-S-66-3721 APR 15

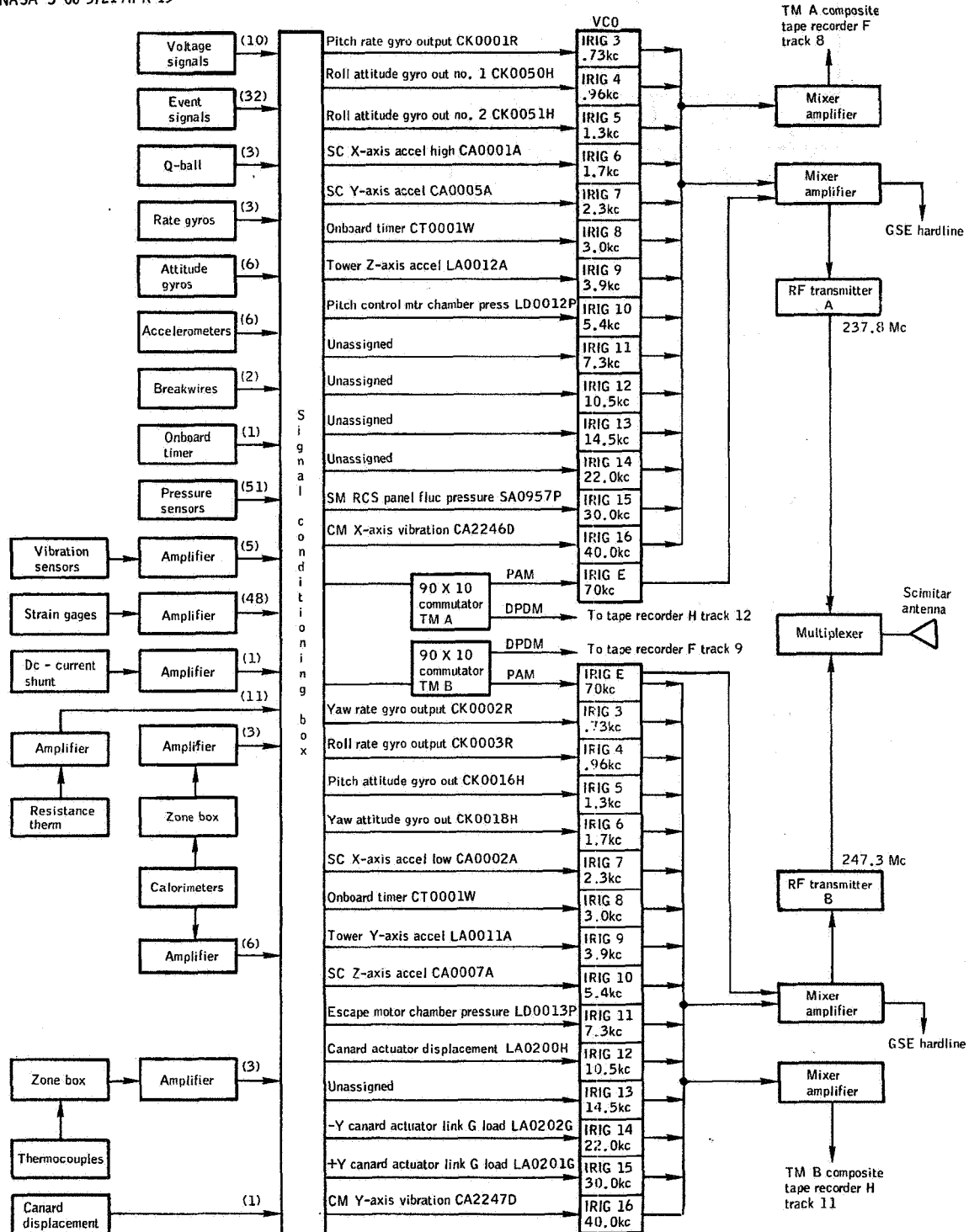


Figure 5.12-1. - Telemetry subsystem block diagram, Apollo Mission A-004.

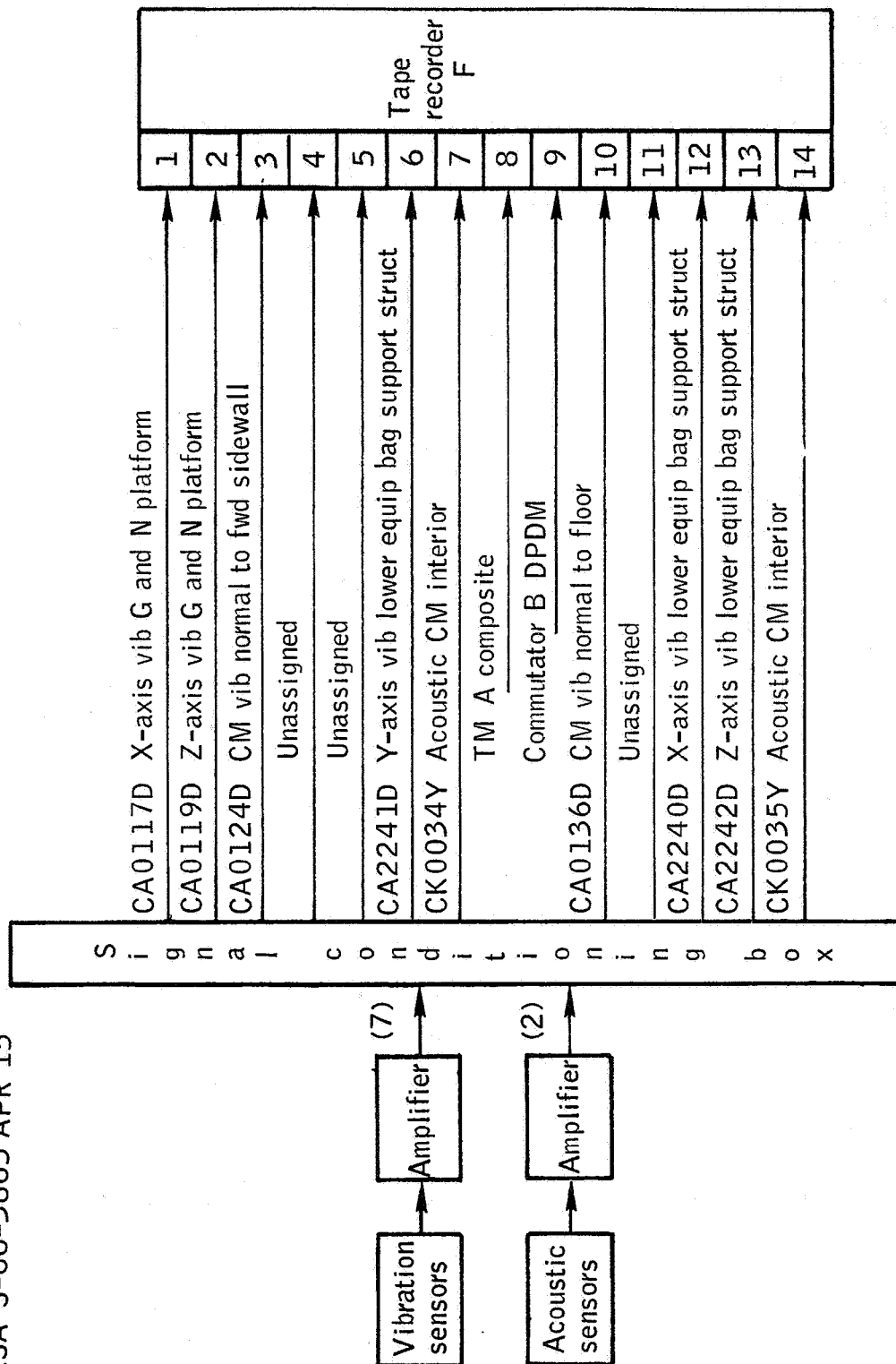


Figure 5.12-2.- Onboard tape recorder F block diagram, Apollo Mission A-004.

NASA-S-66-3869 APR 15

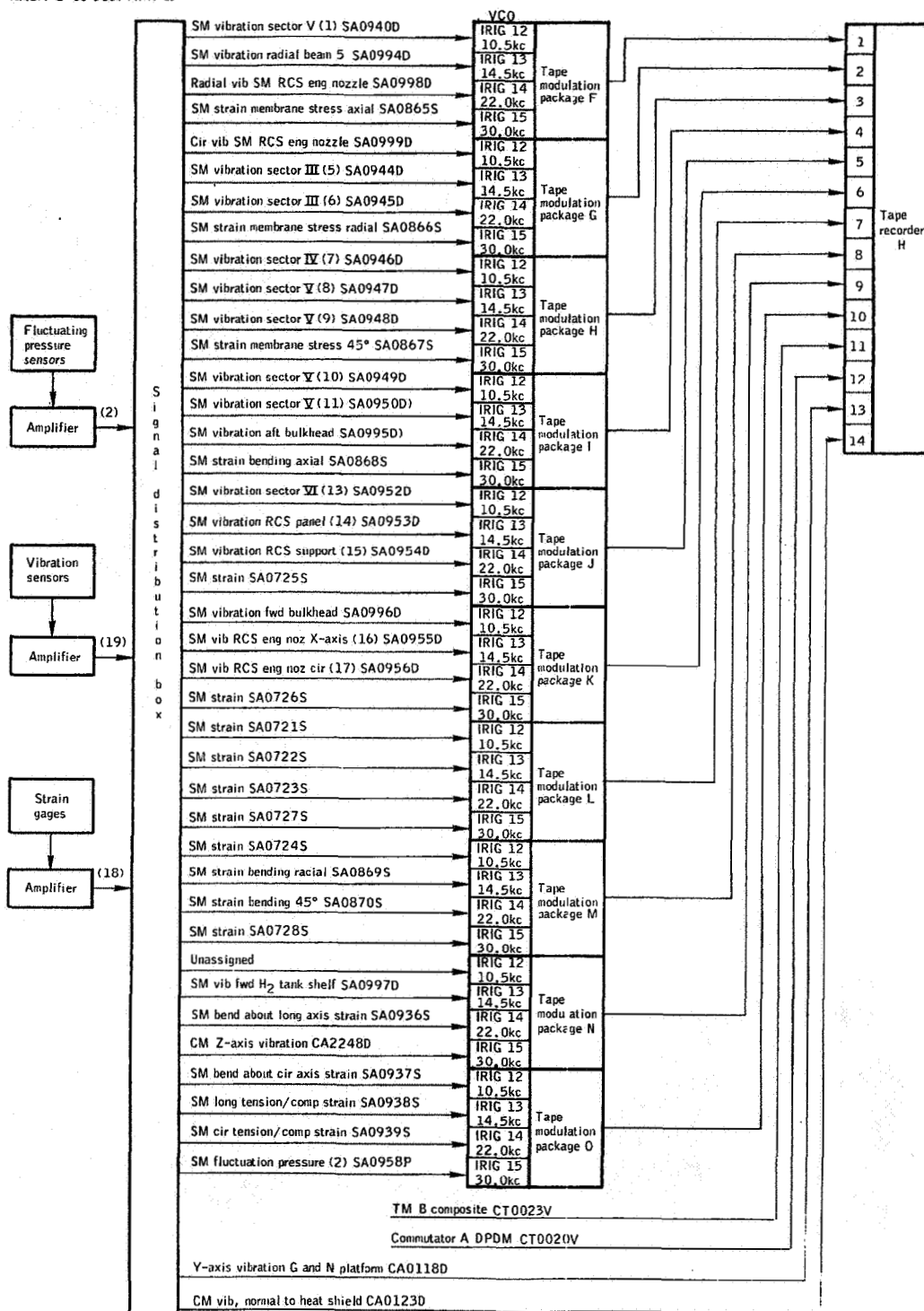


Figure 5.12-3. - Onboard tape recorder H block diagram, Apollo Mission A-004.

5-174

NASA-S-66-3866 APR 15

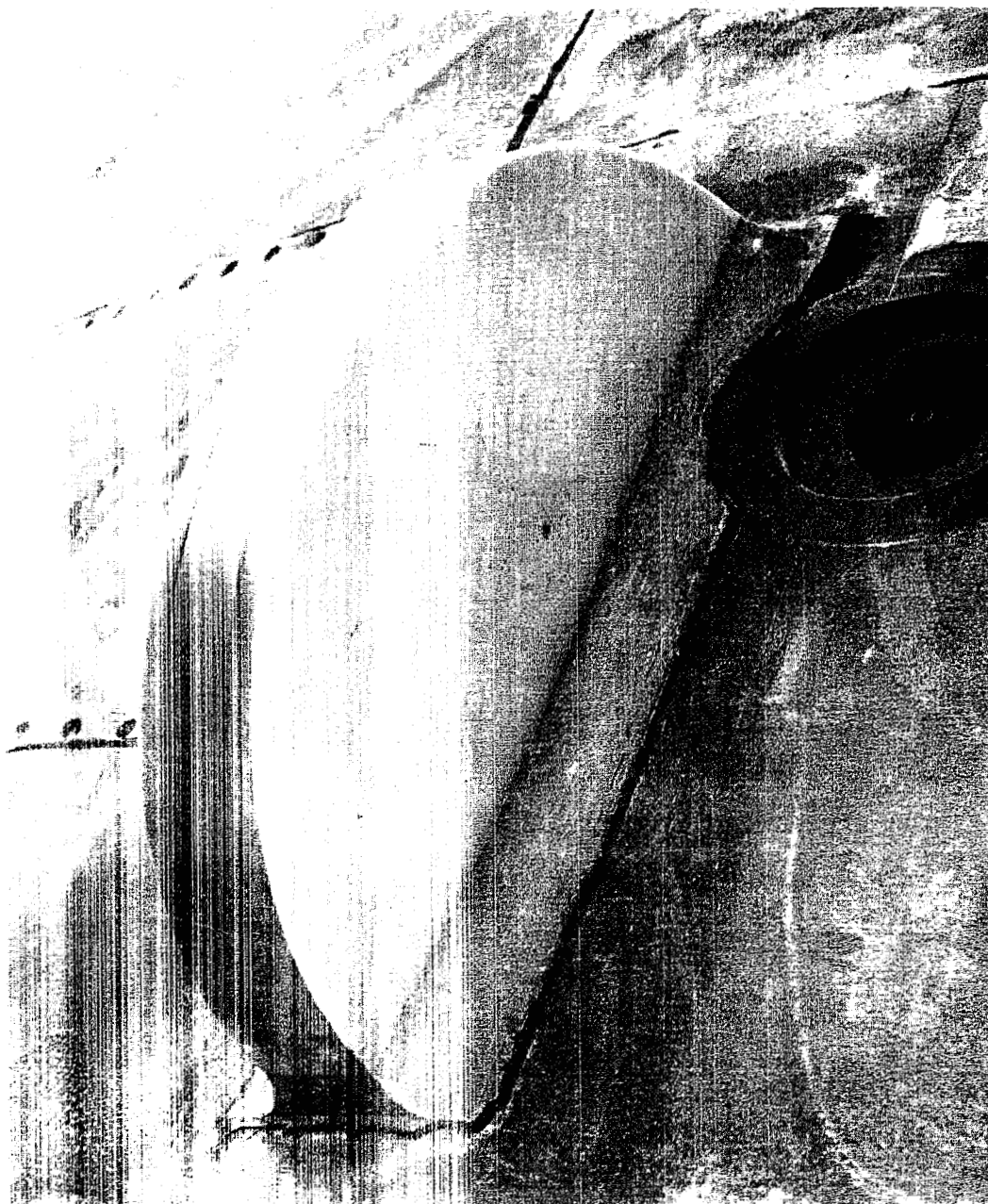


Figure 5.12-4.- Scimitar antenna damage, Apollo Mission A-004.

NASA-S-66-3864 APR 15

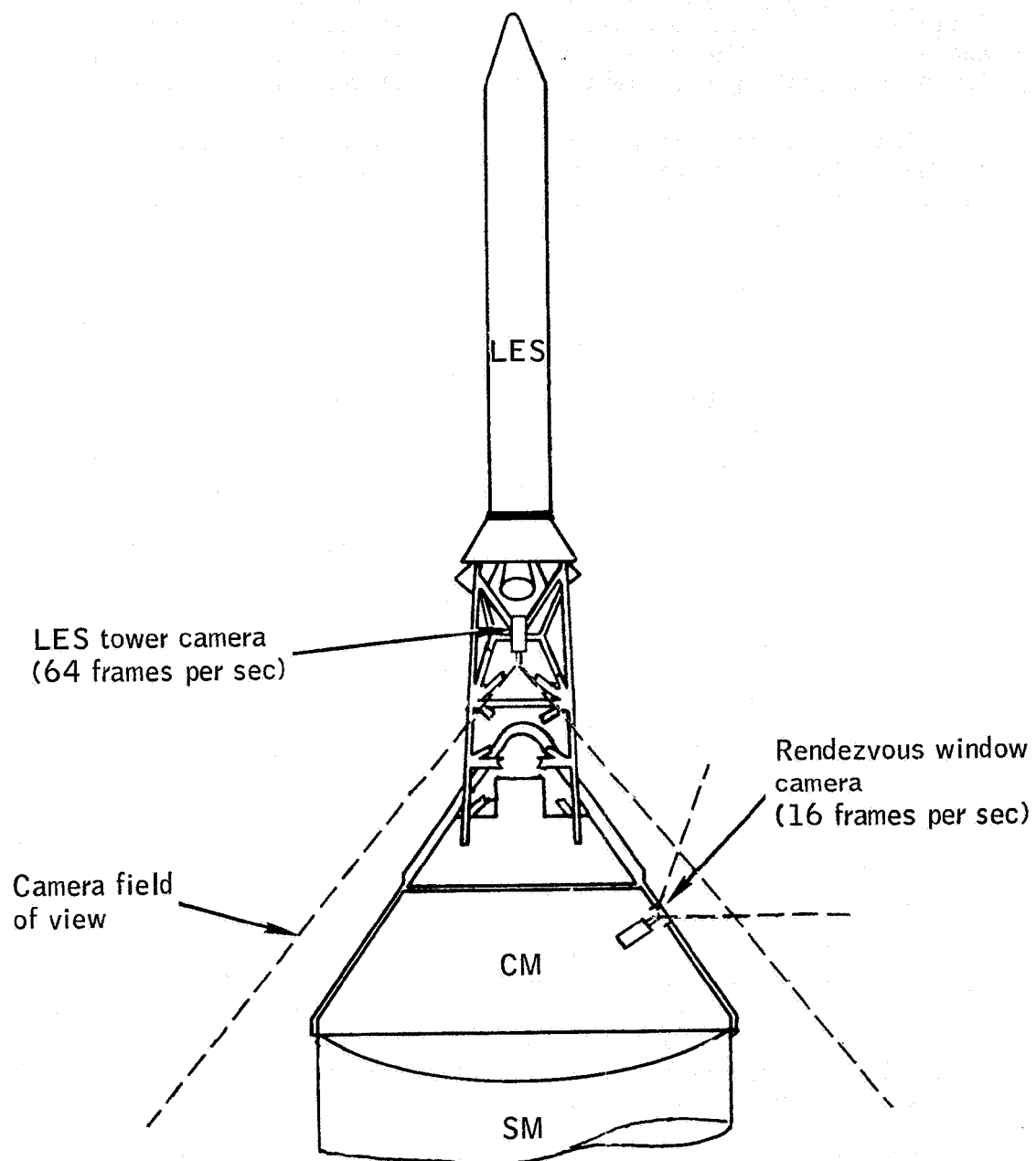


Figure 5.12-5.- Tower and CM camera installation, Apollo Mission A-004.

### 5.13 Environmental Control Subsystem Cabin Pressure Relief Valve

Description.- The partial environmental control subsystem (ECS) installed on SC-002 consisted of a modified cabin pressure relief valve and steam duct. The remainder of the ECS, including CM pressure regulation and cooling equipment, was not included in SC-002.

The cabin pressure relief valve provides positive pressure relief of the cabin during spacecraft ascent and negative pressure relief during descent. Specification requirements for positive pressure relief are  $6(+0.2, -0.4)$  psid and 0.36 to 0.90 psid for negative pressure relief.

The SC-002 valve was similar to the qualification test unit except for the manual controls and locking position, which were not installed on the valve in SC-002. A section of teleflex cable was utilized to lock the valve in the normal, or automatic, position in lieu of the manual controls. The relief valve was mounted on the steam duct in the left-hand equipment bay. The steam duct penetrated both the inner pressure wall and outer moldline of the heat shield. Two pressure sensing lines, attached to the ambient sensing ports on the valve, penetrated the pressure wall and sensed ambient pressure in the unpressurized area, providing an ambient reference pressure for the valve diaphragms.

Flight performance.- Postflight analysis of the SC-002 flight data and subsequent postflight tests conducted at the contractor's facilities at Downey, California, indicate that CM interior pressure control was not achieved during Mission A-004 due to an excessive CM leakage rate. Figure 5.13-1 indicates that the CM interior pressure began to decrease immediately after lift-off and continued to decrease until a minimum pressure of 0.86 psia was attained at  $T+147.5$  seconds into the flight. The predicted minimum CM interior pressure of 6.53 psia and predicted CM interior pressure profile (fig. 5.13-2), based upon negligible CM leakage and a normally operating cabin pressure relief valve, were not attained due to the excessive CM leak rate.

The cabin pressure relief valve did not actuate during ascent since the valve requires a differential pressure of 5.6 to 6.2 psid, sensed between the aft compartment and cabin, to provide pressure relief of the cabin. The maximum differential pressure obtained between the aft compartment and cabin was 2.45 psid, which was insufficient to cause valve operation.

Figure 5.13-2 indicates that the cabin pressure relief valve operated during spacecraft descent, since the differential pressure between the cabin and ambient pressures remained within the valve specification range of 0.36 to 0.90 psid. However, a quantitative estimate for the degree of valve operation relative to the CM leakage is undetermined.

Postflight testing.- Postflight testing was conducted on the ECS cabin pressure relief valve at the contractor and subcontractor facilities, respectively, to check the positive and negative relief pressures, and to learn whether the valve was sticking in the open position. Prior to checking the relief pressure, contractor personnel verified that the valve was closed by applying a vacuum of 29.2 in. Hg to the ECS steam duct. A vacuum level of this magnitude could not be obtained if the valve were in the open position.

Positive pressure was applied to the steam duct to test for negative pressure relief. Negative pressure relief occurred at 0.60 psig differential pressure. Insufficient checkout equipment at the contractor facility prevented completion of the positive pressure relief tests, so the valve was removed from SC-002 and delivered to the subcontractor for completion of the tests.

The valve was installed in an altitude chamber for launch profile testing. Results of the three launch profile tests indicated that positive pressure relief occurred at differential pressures of 6.1, 6.1, and 6.2 psig, respectively, denoting satisfactory performance of the valve.

Before removal of the cabin pressure relief valve from SC-002, a cabin leak test was performed by the contractor. Test results indicated that the major portion of cabin leakage occurred at the inner hatch - inner structure interface seal. During the testing, it was demonstrated that the inner hatch could be improperly installed, preventing the effective sealing of the hatch. The lack of an effective inner hatch seal would result in premature loss of cabin pressure.

Results of the postflight testing of the cabin pressure relief valve and cabin leakage indicated that the valve would have operated satisfactorily during Mission A-004 if the cabin leakage rate past the inner hatch had been reduced to an acceptable level prior to flight.



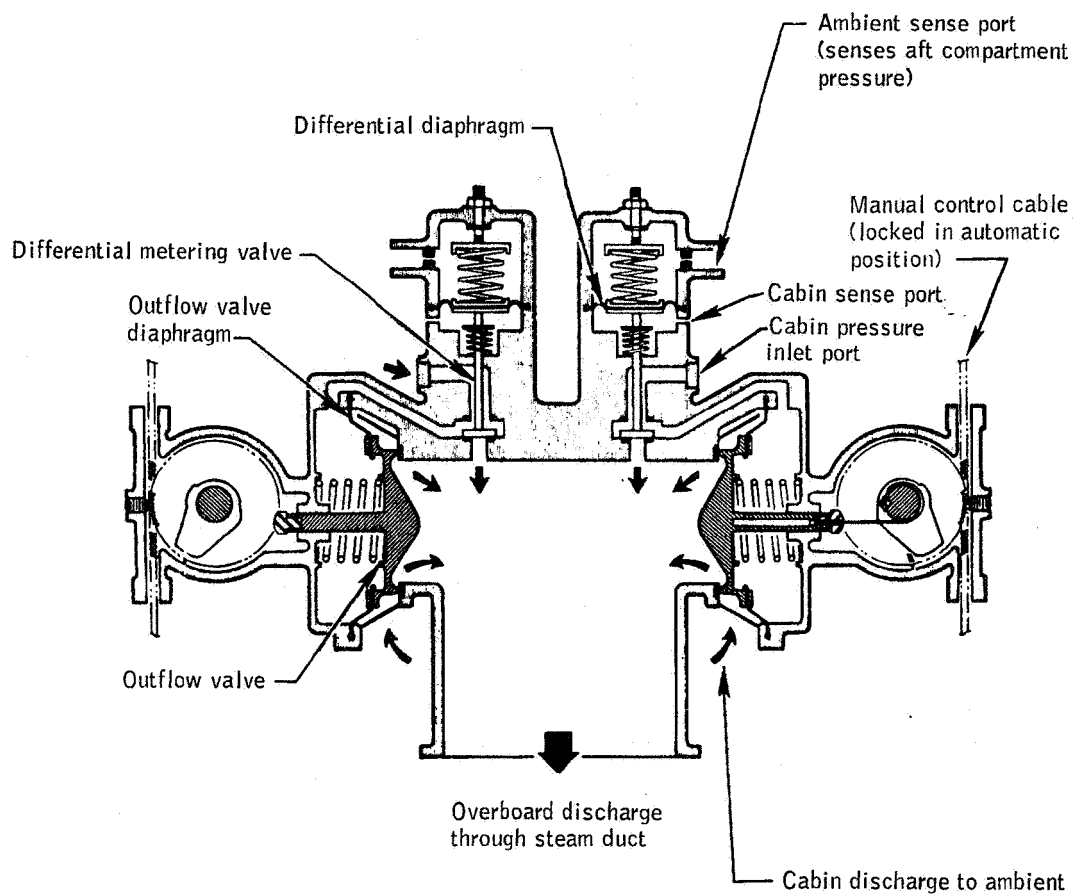


Figure 5.13-1.- ECS cabin pressure relief valve, Apollo Mission A-004.

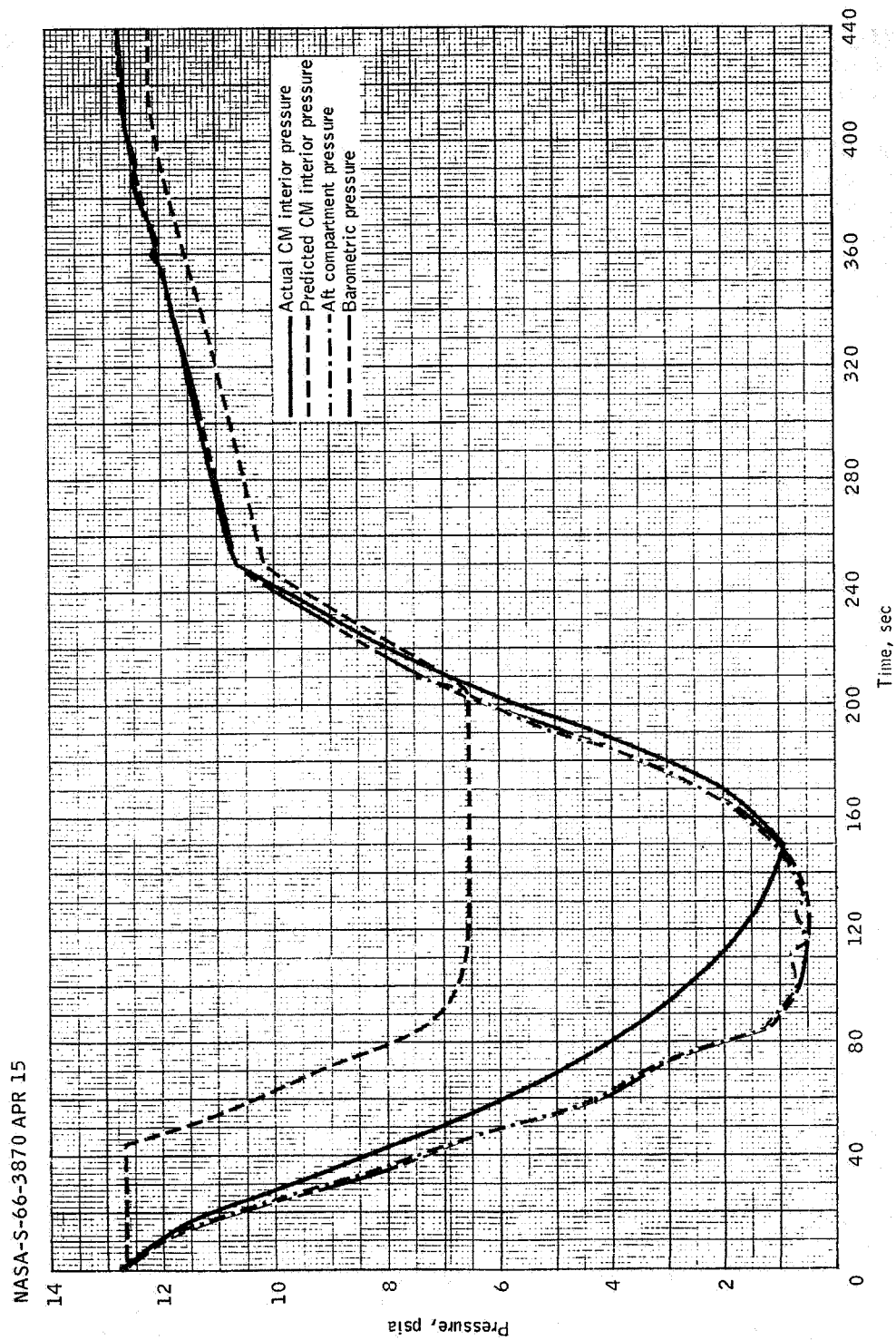


Figure 5.13-2.- SC-002 command module interior pressure profiles, Apollo Mission A-004.

## 5.14 Crew Windows

Description. - The command module (CM) window subsystem installed on the command module was Block I configuration except the antiglare and reflective coatings were omitted from the glass surfaces.

The CM window subsystem consisted of one hatch window, two side windows, and two rendezvous windows (see fig. 5.14-1). The hatch window was approximately 12 inches square and was located in the -Z axis. The side windows were approximately 7 by 10 inches and were located symmetrically  $59^\circ$  from the -Z axis. The rendezvous windows were located symmetrically  $32^\circ$  from the -Z axis and were approximately 6 by 12 inches and set approximately  $32^\circ$  from the Y-Z plane.

The three panels in each side and rendezvous window used in this flight were installed as follows: two panels, each 0.20 inch thick, were installed with a 0.175-inch air space between them in the pressure cabin structure; the third panel, 0.70 inch thick, was installed in the heat shield structure, approximately 1 inch from the inner panels. The glass for the inner panels was aluminosilicate (Corning code 1723); the glass for the outer panel was amorphous fused silica (Corning code 7940 (optical grade quartz)). None of the panels were coated.

A 16-mm camera was installed at the eye level point of the planned position for the command pilot behind the left-side rendezvous window and was directed approximately normal to the window surface. The camera subsystem was independent of the spacecraft subsystem, and was powered by a camera battery.

Performance. - A timer was started by an inertial switch at lift-off which in turn started the camera at T+70 seconds. The film speed was 16 frames per second and operated for approximately 170 seconds (from T+70 to T+240 sec). In frame 44 (T+72.8 sec) the panel of the soft boost protective cover is seen to disappear for a clear view through the window.

In frame 53 (T+73.3 sec) two soot spots are seen in the center of the window, and in frame 60 (T+73.8 sec) light deposits are seen to form in the corners of the panel. The deposits continued to build up throughout the abort sequence. This deposit resulted in a translucent condition around the window and covered approximately 20 percent of the window area. (See figs. 5.14-2 and 5.14-3.)

The visibility through the remaining 80 percent of the window changed only slightly during the time period from frame 60 to frame 259 (T+86 sec), at which time two large and six smaller black soot spots appeared scattered throughout the center portion of the window. Cloud formations and the horizon were still readily discernible, indicating acceptable window visibility.

A vapor trail was easily detected through the window approximately 42 seconds after abort (T+116 sec). Stabilization as a result of canard deployment was noticeable by the decrease in oscillation rate of the shadow from the edge of the window across the viewing field.

Tower-jettison-motor ignition was observed as an orange flare, and the visibility through the window deteriorated rapidly with definition of exterior image activity ceasing after a momentary glimpse of drogue parachute movement at approximately T+196 seconds. Camera coverage ended before the command module emerged below the cloud cover.

Postflight inspection showed that all windows were covered with a layer of gray material which was considerably darker around the edges of the window than in the center area. The preliminary examination of the window indicated that the high loss of visibility through the windows would make it extremely difficult, if not impossible, for the crew to detect horizon or ground landmarks. The white light transmission loss through the window was greater than 85 percent.

After the windows were removed, they were subjected to a spectral transmission test, and emission and infrared analysis of the gray deposit at Atomic's International, Canoga Park, California. The results of the emission analysis of the gray deposits are listed in table 5.14-I. The results of the infrared analysis are not available at the time of publication of this report.

In summary, it appears that the removal of the boost protective cover did not affect the visibility through the command pilot rendezvous window during launch-escape-motor burn although some soot appeared, mainly during tail off. The greatest visibility loss did not appear until time of tower jettison. From the time of tower jettison until command module landing the window visibility loss increased to the extent that postflight subjective visual tests indicated that no difference could be seen between the horizon line and ground landmarks.

The spectral transmission was performed at two locations on the left-hand rendezvous window. Point 1 was the lighter center area of the window. Point 2 was the very dark area at the left-hand corner edge where sooting from the LES started after soft boost protective cover break-up. The readings were taken normal to the glass surface.

The spectral transmission through point 1 of the left rendezvous window was 10 to 60 percent in the infrared (9000 to 16 000 angstroms) and 2 to 20 percent in the visual (4000 to 7000 angstroms). The transmissions through point 2 was 1 to 10 percent for infrared and less than 1 percent for the visual. The results of the emission spectrographs are shown in table 5.14-I.

TABLE 5.14-I.- ELEMENTS FOUND IN LES ENGINE DEPOSITS ON THE  
SC-002 LEFT-HAND RENDEZVOUS WINDOW

a. Impurities in deposit<sup>a</sup>

Sample area	Al	Ca	Cu	Fe	Mg	Na	Pb	Si	Sm	Ti	Zn
1. Center area of window	10	<10	10	75	3	200	1000	10	<10	20	300
2. Edge of window	20	<10	5	30	10	<200	500	50	<10	75	400
3. Soot smudge	10	<10	5	20	3	<200	300	40	<10	20	50
4. Edge of ablator	200	20	5	150	150	<200	500	400	10	100	100

b. Gravimetric analysis of carbon

Sample area	Percent by weight
1. Center area of window	4 to 6
2. Edge of window	3 to 5
3. Soot smudge	4 to 6
4. Edge of ablator	4 to 6

<sup>a</sup>Numbers represent relative units of mass for the particular sample.

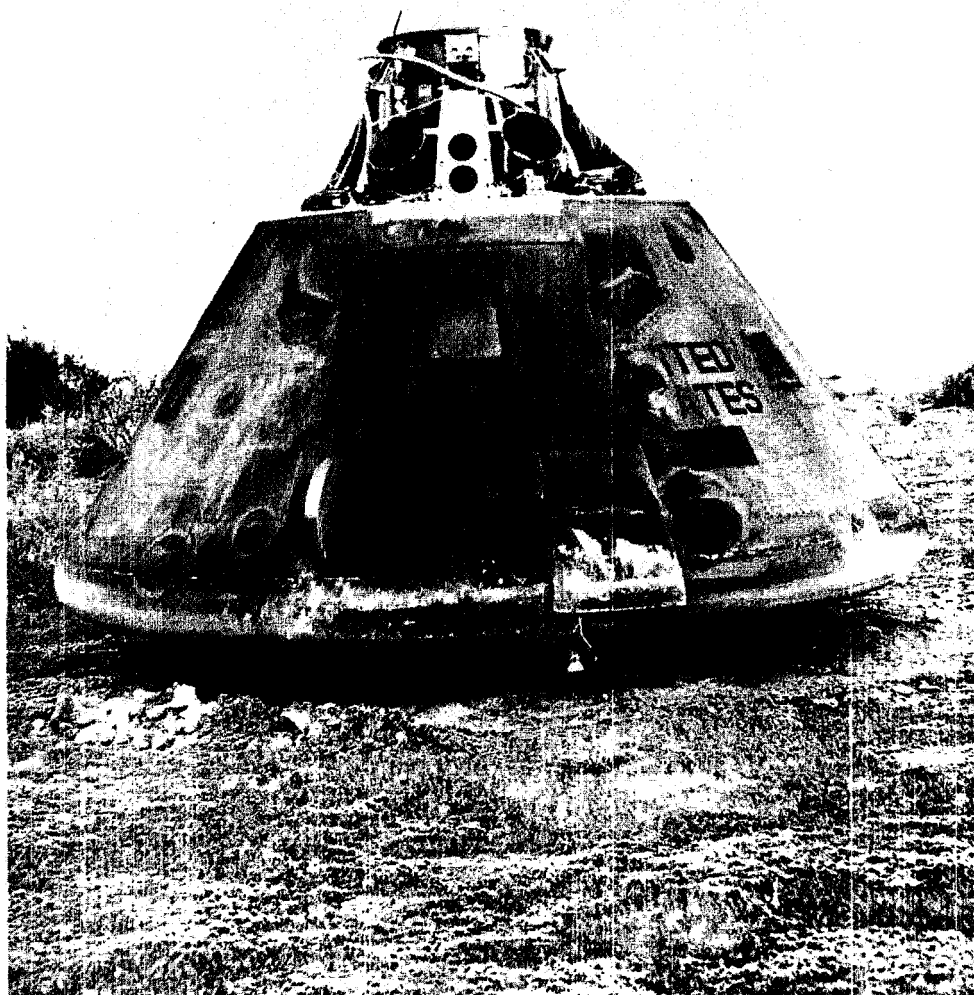
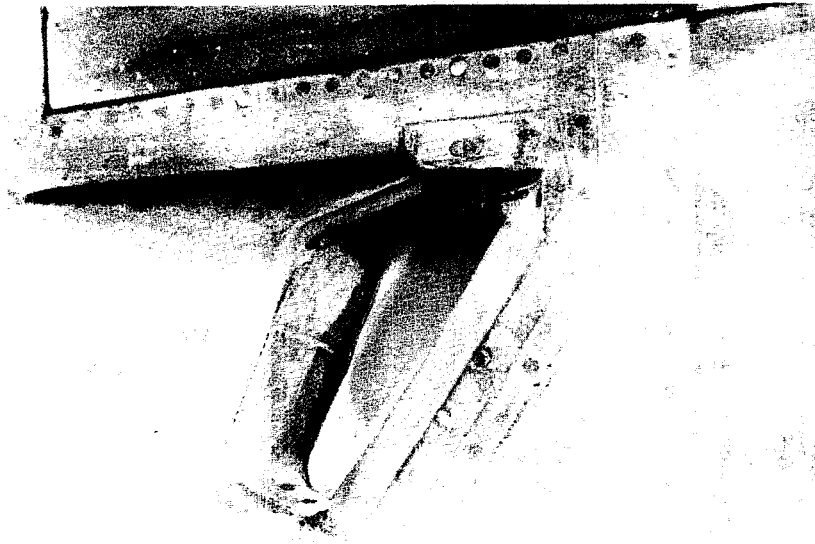
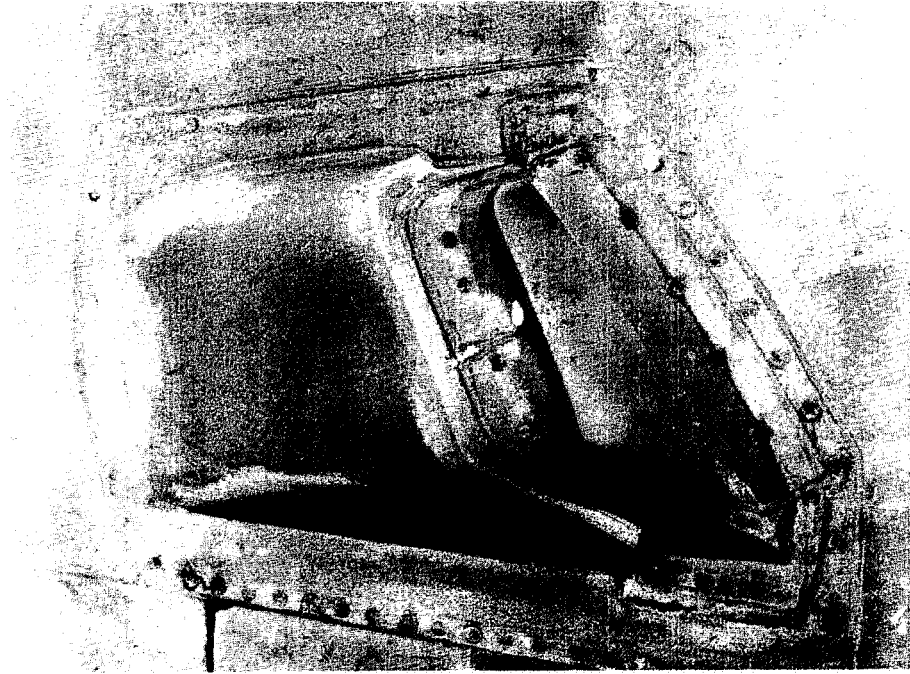


Figure 5.14-1.- Command module after landing showing general condition of windows, Apollo Mission A-004.

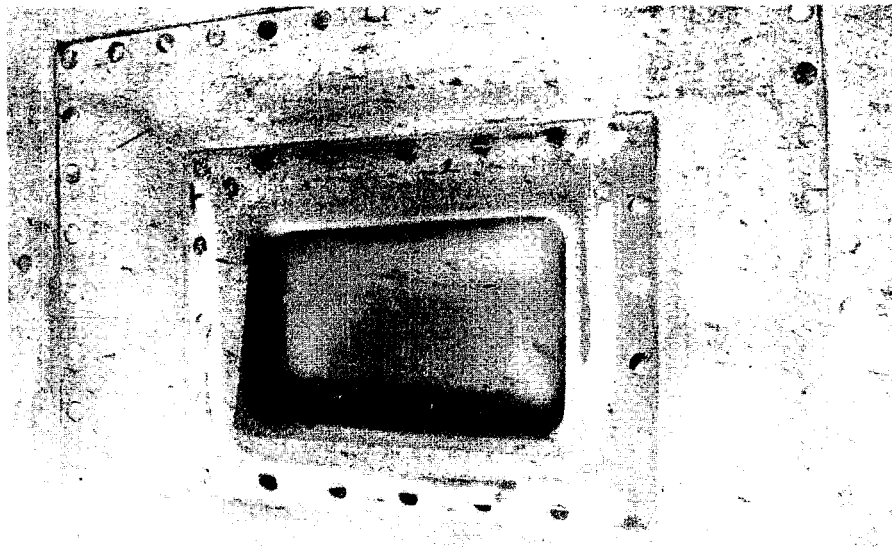


Left rendezvous and docking window

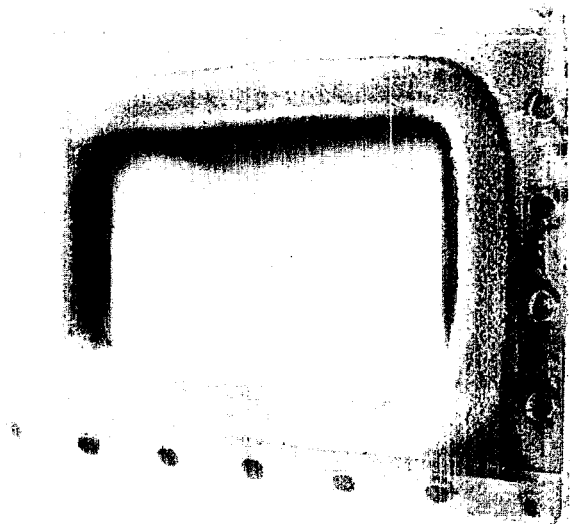


Right rendezvous and docking window

Figure 5.14-2. - Left and right rendezvous and docking windows after landing, Apollo Mission A-004.



Right crew window



Left crew window

Figure 5.14-3. - Left and right crew windows after landing, Apollo Mission A-004.



## 6.0 LAUNCH VEHICLE PERFORMANCE

### 6.1 Propulsion

Description.- The propulsion subsystem for the Little Joe II launch vehicle consisted of four Algol 1D Mod I and five Recruit TE-29 rocket motors. The five Recruit motors and two of the Algols (positions 2 and 5) were used as first-stage propulsion, and the remaining two Algols (positions 1 and 4) acted as second-stage propulsion. The motors were bolted to the six peripheral rings and one center retaining ring in the thrust bulkhead of the vehicle afterbody, and the Algol motors were laterally supported by the bulkhead at vehicle station 34.75. Figure 3.2-1 shows the location of the motors. A detailed description of the Algol and Recruit motors is presented in reference 10.

The propulsion flight instrumentation consisted of one chamber pressure measurement for each Algol motor. Data from the pressure transducers were sampled 20 times per second. All instrumentation functioned satisfactorily until abort. Recruit motors were not instrumented.

Landline instrumentation indicated that the Algol motor temperatures were approximately 70° F at time of launch.

Performance.- Examination of the chamber pressure data indicated that the general performance of all Algol motors was satisfactory. Deviation of the specific performance of the individual motors from the predicted performance based on average thrust for a respective period of time is as follows:

Motor position	Operation time, sec	Thrust deviation, percent
1	38	-1.0
2	41	0
4	38	-0.3
5	41	+0.5

The flight thrust time histories are presented in figures 6.1-1 to 6.1-4.

Postflight examination.- The motors remained attached to the vehicle until ground impact. They were not returned to the assembly area and no detailed inspection was made.

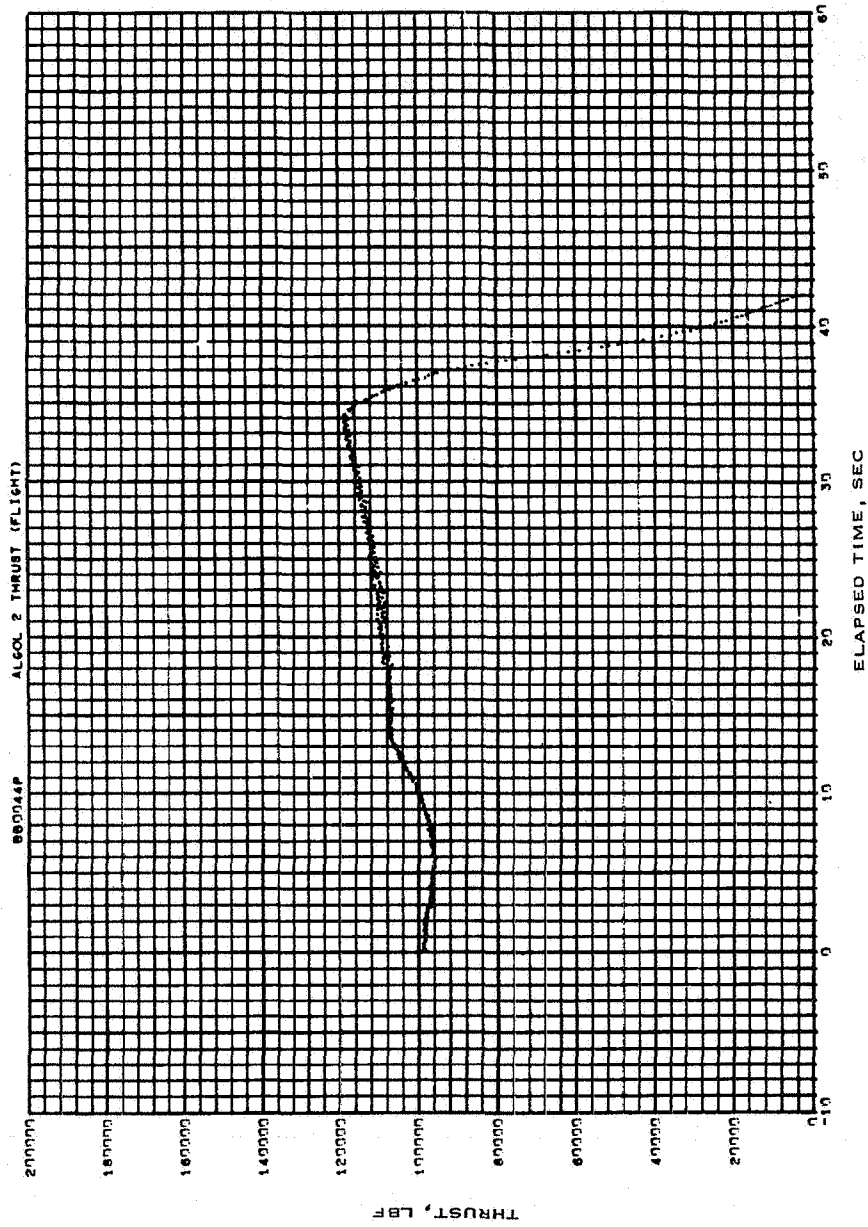


Figure 6.1-1.1.- First-stage Alcol motor no. 2 flight thrust time history, Apollo Mission A-004.

NASA-S-66-3789 APR 15

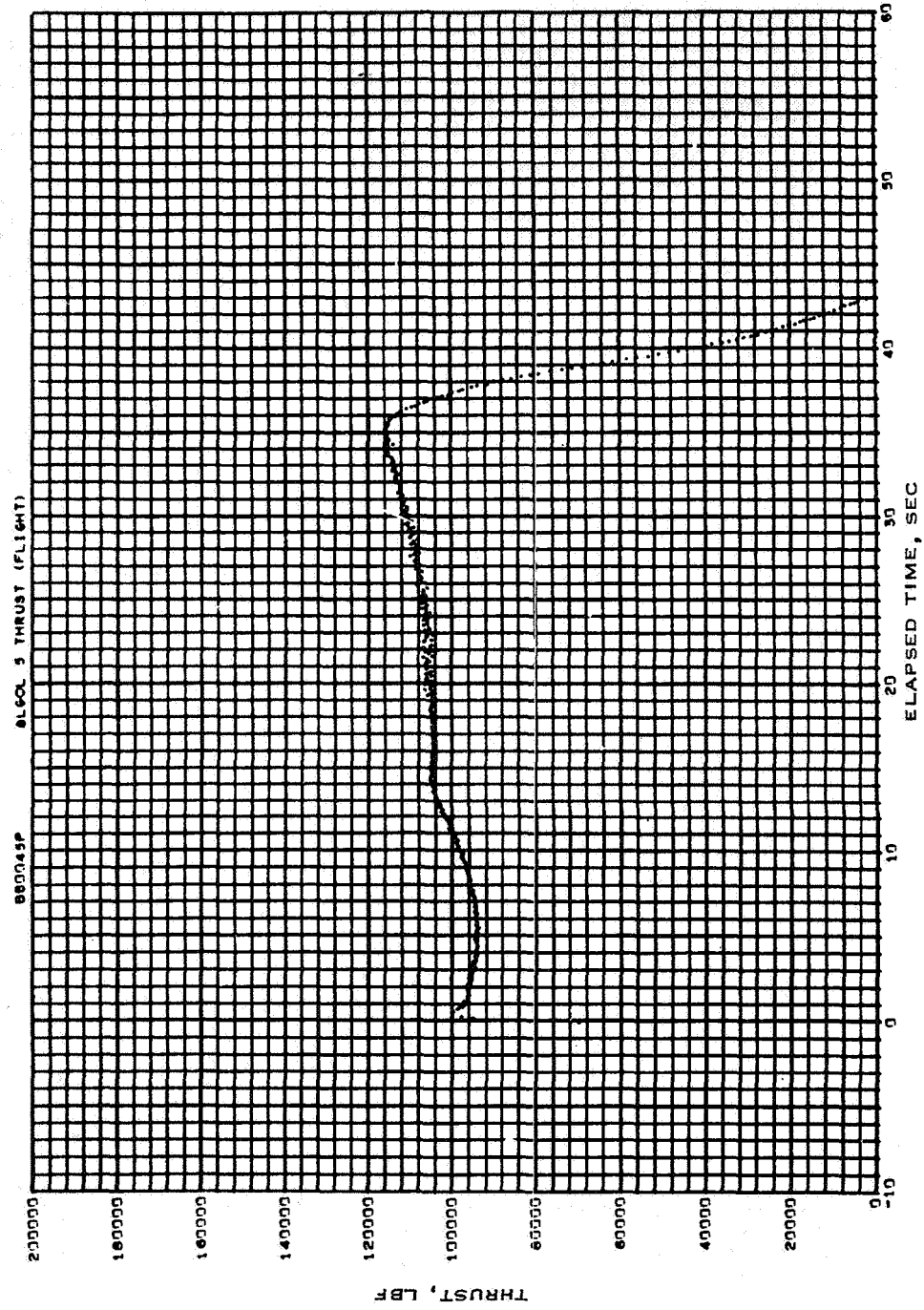


Figure 6.1-2.- First-stage Algol motor no. 5 flight thrust time history, Apollo Mission A-004.

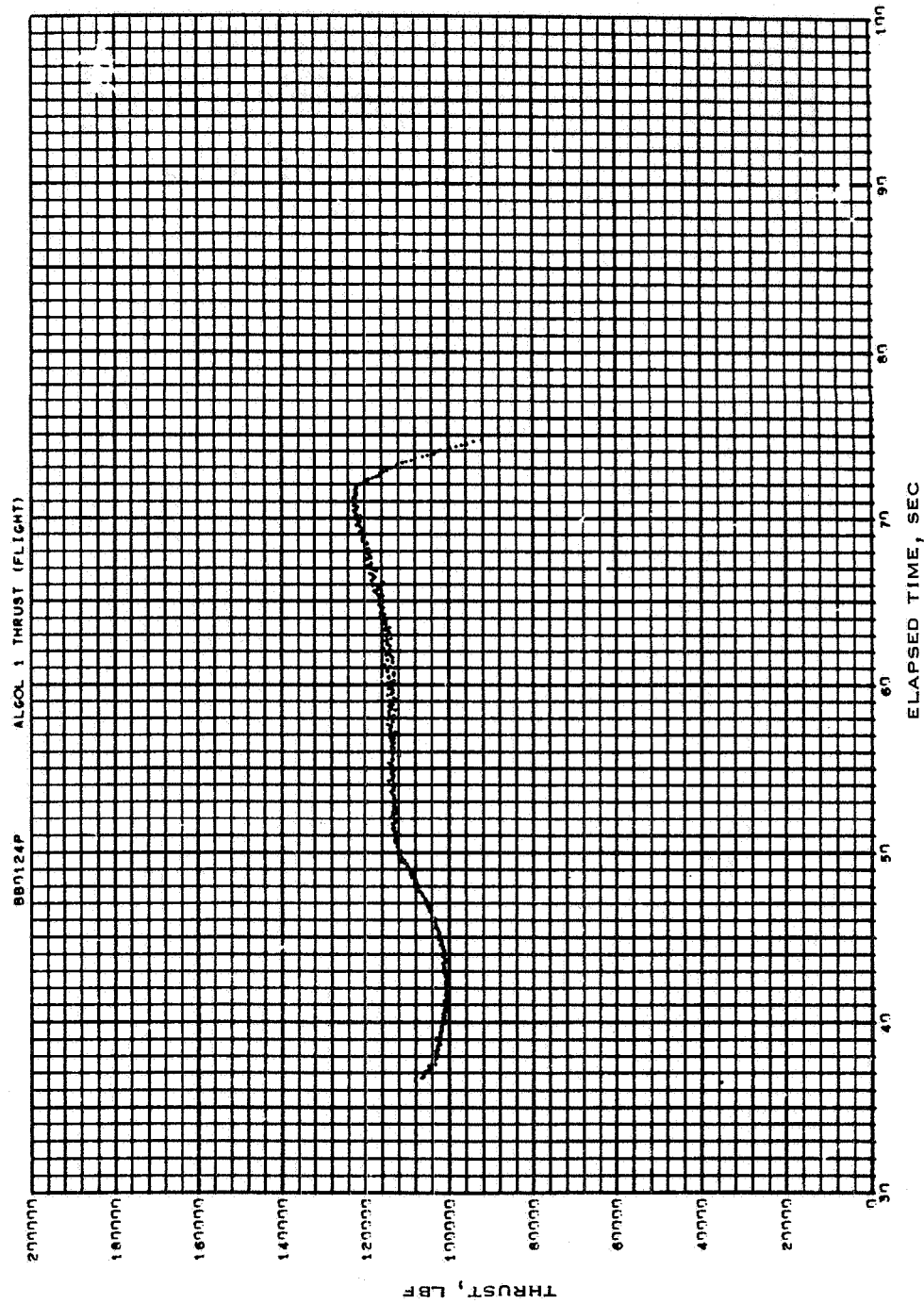


Figure 6.1-3.- Second-stage Algol motor no. 1 thrust time history, Apollo Mission A-004.

NASA-S-66-3797 APR 15

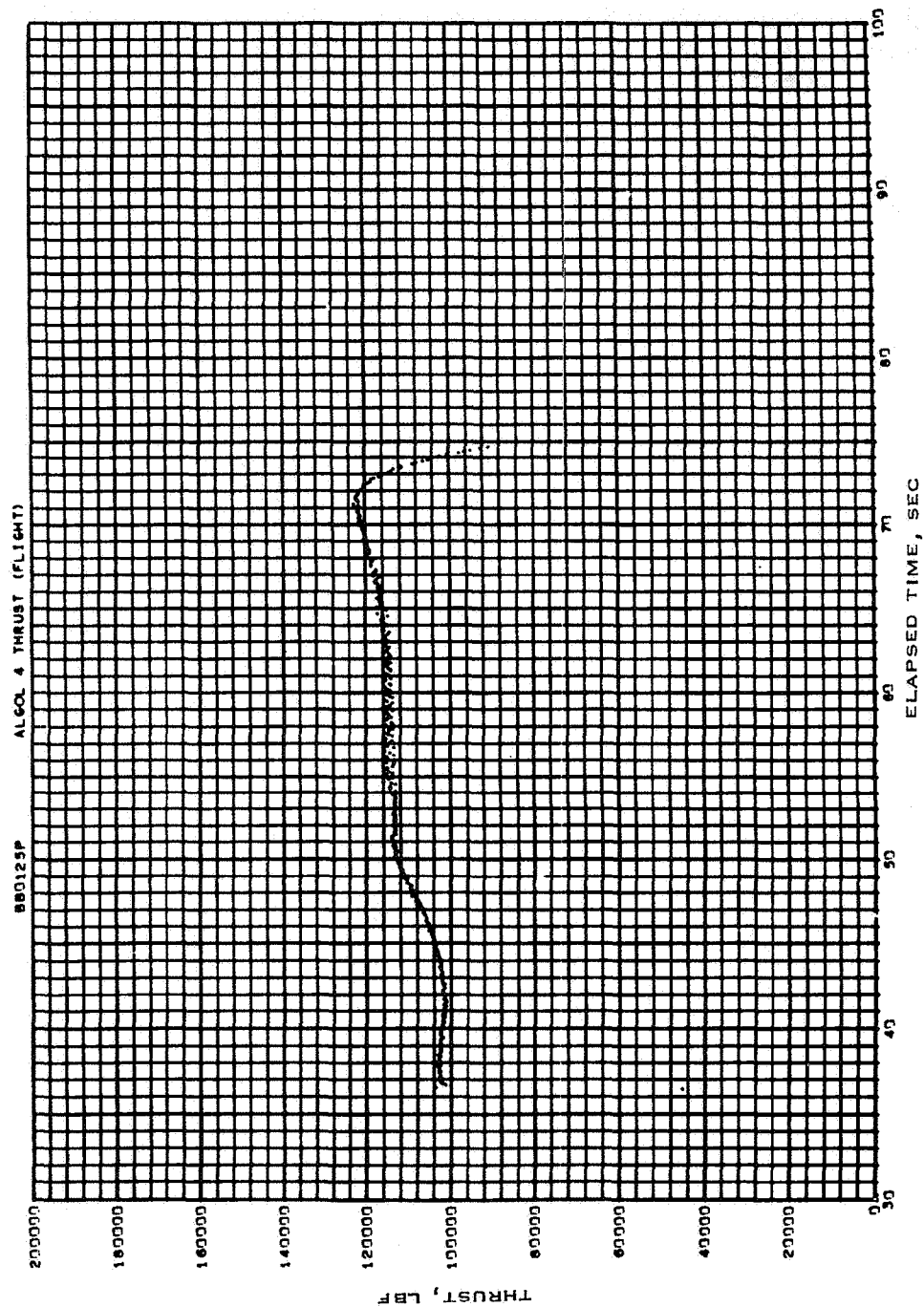


Figure 6.1-4.- Second-stage Alcol motor no. 4 thrust time history, Apollo Mission A-004.

## 6.2 Launch Vehicle Pyrotechnic Devices

Description. - The launch vehicle pyrotechnic devices consisted of initiators and motor igniters for ignition of the Algol and Recruit motors, and the range safety subsystem pyrotechnics. All devices were the same type as used on earlier Apollo - Little Joe II flights. For a detailed description of the launch vehicle pyrotechnic devices, see reference 10.

The Algol motor initiators were Holec AGC, part no. 360871, lot no. 332602, and the Recruit motor initiators were Space Ordnance Systems, S01-266-6, lot no. 25. Lot no. 25 initiators have been used for the Recruit motors throughout this program. The initiator serial numbers were as follows:

Algol motor 1 . . . . .	Serial nos. 513 and 529
Algol motor 2 . . . . .	Serial nos. 514 and 501
Algol motor 4 . . . . .	Serial nos. 512 and 549
Algol motor 5 . . . . .	Serial nos. 509 and 530
Recruit motor 3 . . . . .	Serial nos. 12053 and 12141
Recruit motor 6 . . . . .	Serial nos. 12066 and 12092
Recruit motor 7 . . . . .	Serial nos. 12074 and 12080
Recruit motor 8 . . . . .	Serial nos. 12332 and 12052
Recruit motor 9 . . . . .	Serial nos. 12302 and 12064

Performance. - All initiators and igniters functioned properly. One bridge of each initiator of the first-stage motors was expended by system no. 1 before the redundant second system was activated. Initiator bridges in the Algol motors were expended within 3 milliseconds, and those in the Recruit motors within 1 millisecond. The initiators were not removed for postflight inspection.

The range safety subsystem was armed at lift-off, but was not required to function because of the nominal flight of the launch vehicle.

### 6.3 Attitude Control Subsystem

Description. - The attitude control subsystem (fig. 6.3-1) for the Mission A-004 launch vehicle was identical to the one used on Mission A-003 (ref. 4) with the following exceptions:

(a) The radio-frequency command pitch-up capability was included since there was a requirement for a pitch-up maneuver on this flight. The pitch command signal was equivalent to a vehicle attitude error of  $29.5^\circ$  with a time constant of 0.52 second.

(b) The pitch-down signal commanded by the pitch programmer was set at 1 deg/sec to be initiated at T+20 second.

(c) The reaction control subsystem was deleted because there was no requirement for this system on this flight.

(d) The autopilot gains for aerodynamic control set at time of launch were as follows:

	Attitude, control surface deflection/ vehicle angular displacement, deg/deg	Rate, control surface deflection/ vehicle angular rate, deg/deg/sec
Pitch	1.5	1.5
Yaw	1.5	1.5
Roll	0.4	0.2

Performance. - The attitude control subsystem performed satisfactorily throughout the flight, including the critical phases of lift-off, staging (initiation of the second pair of Algol engines), and pitch-up. The vehicle was launched at an initial pitch attitude of  $84^\circ$ , and at T+21 seconds the pitch programmer was initiated, which caused the vehicle to pitch over at the planned rate of approximately 1 deg/sec throughout the remainder of the flight (figs. 6.3-2 and 6.3-3). At lift-off, normal ignition transients caused outputs from the pitch and roll rate gyros of 11.8 deg/sec (peak-to-peak) and 4.8 deg/sec (peak-to-peak), respectively, at 20 cps; however, the duration was less than 0.5 second. The disturbance in the yaw axis was negligible.

Staging occurred at T+36.4 seconds and had no noticeable effect on the control system as shown by the rate gyro outputs (figs. 6.3-3

and 6.3-4). Pitch-up was initiated at T+70.8 seconds and the body elevation angle was increased from  $36^\circ$  to approximately  $54^\circ$  as planned. (fig. 6.3-2.)

As expected, the largest attitude errors occurred shortly after lift-off (from T+4 to T+10 sec); however, these errors were rapidly reduced to a small value and remained small throughout the remainder of the flight. Figure 6.3-5 shows that the vehicle started to roll in a positive direction at lift-off (counterclockwise looking aft), and reached a maximum excursion of approximately  $3^\circ$  at T+4 seconds; however, the vehicle had fully recovered at T+10 seconds. At T+3 seconds the vehicle began to pitch up (fig. 6.3-6) and reached a maximum excursion of approximately  $3^\circ$  at T+9 seconds; however, this error had been eliminated by T+13 seconds. At T+4 seconds the vehicle began to yaw in a positive direction (to the left, looking aft) and reached a maximum value of approximately  $2.5^\circ$  at T+9 seconds. By T+15 seconds this attitude error had been eliminated (fig. 6.3-5).

The steady-state error (approximately  $1^\circ$ ) in the yaw and roll axes during much of the flight was not abnormal and was probably caused by thrust misalignments or winds, or both. In the pitch axis, a steady-state error of approximately  $2^\circ$  is normal as the vehicle lags behind the commanded attitude. This effect has been verified by simulation studies.

During pitch-up, the vehicle rolled approximately  $5^\circ$  (fig. 6.3-5) because the control system gains were not perfectly balanced, which is a normal situation for the system. Figure 6.3-7 shows that elevons 1 and 4 are displaced approximately  $20^\circ$  counterclockwise, and figure 6.3-8 shows that elevons 2 and 3 are displaced approximately  $19^\circ$  clockwise. The net difference is in a direction to cause positive roll of the vehicle. The roll attitude was corrected before abort.

Performance of the hydraulic system was correct in all aspects throughout the flight. Figure 6.3-9 shows hydraulic pressure plotted against time until abort of the payload. Approximately 175 cu in. of hydraulic fluid were used by each fin out of approximately 710 cu in. available for each fin.

Figure 6.3-10 shows that launch vehicle system power (28 V dc) was normal throughout the flight.



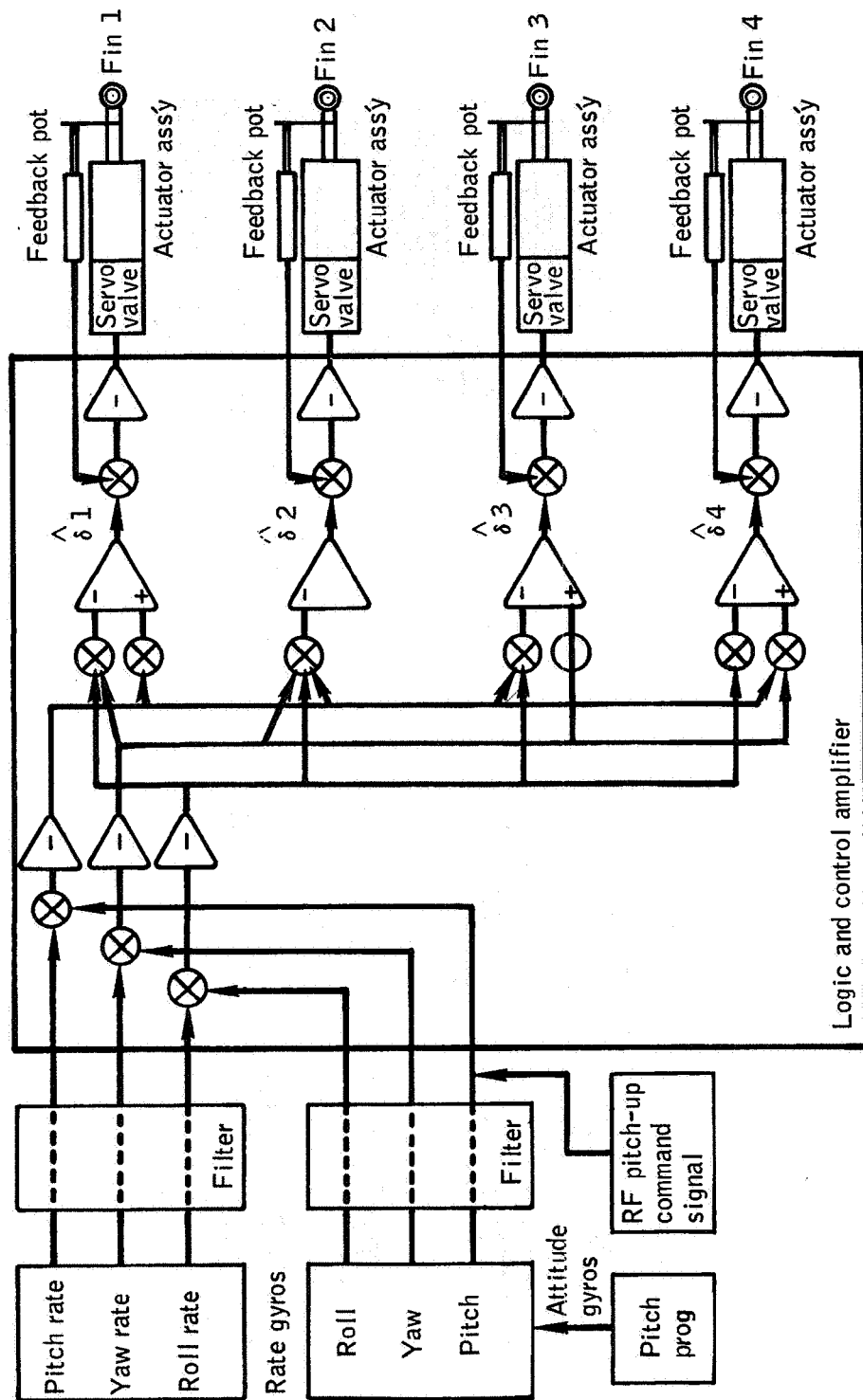


Figure 6.3-1.- Launch-vehicle attitude control subsystem block diagram, Apollo Mission A-004.

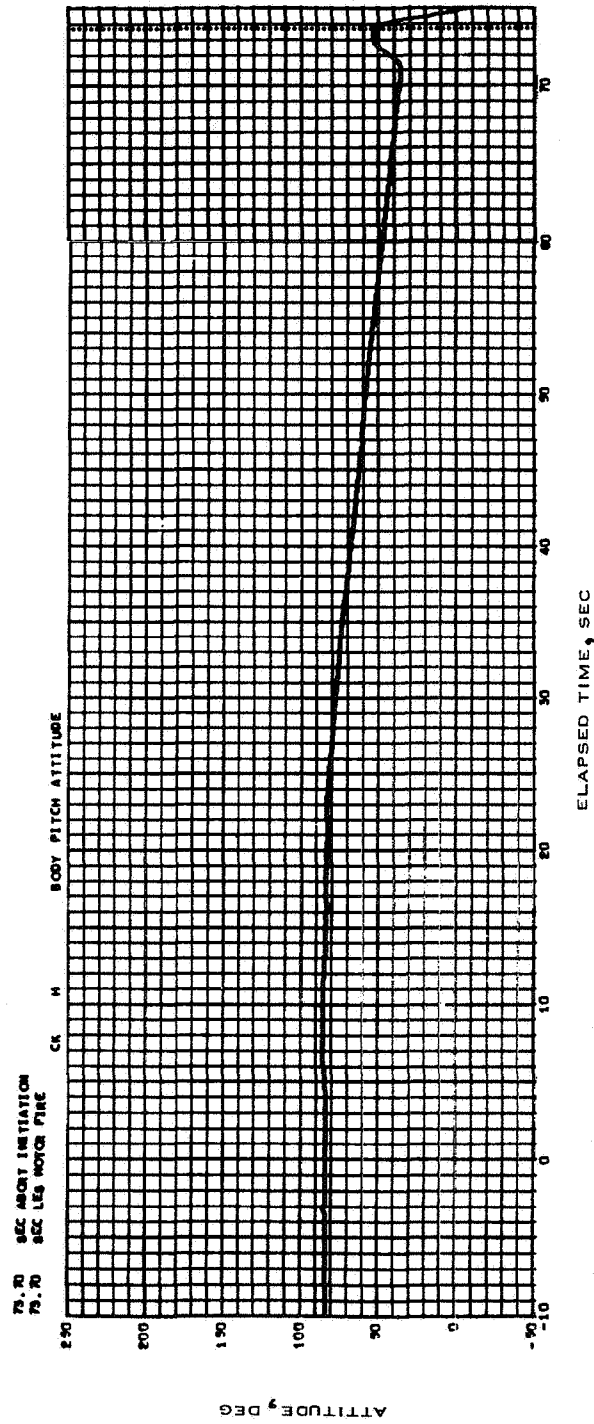


Figure 6.3-2.- Launch-vehicle pitch attitude plotted against time, Apollo Mission A-004.

NASA-S-66-3809 APR 15

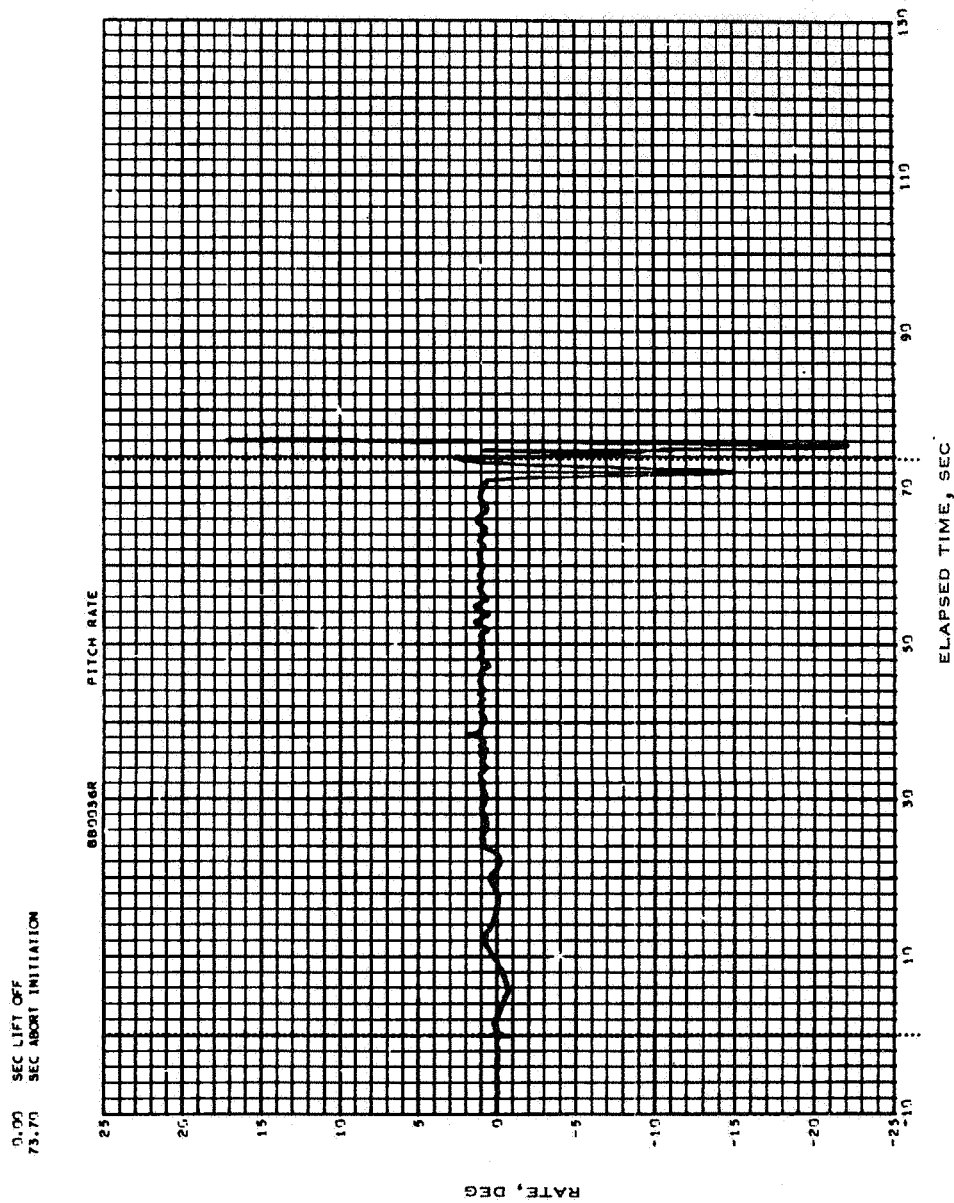


Figure 6.3-3.- Time history of launch-vehicle pitch rate, Apollo Mission A-004.

NASA-S-66-3813 APR 15

0.00 SEC LIFT OFF  
73.70 SEC ABORT INITIATION

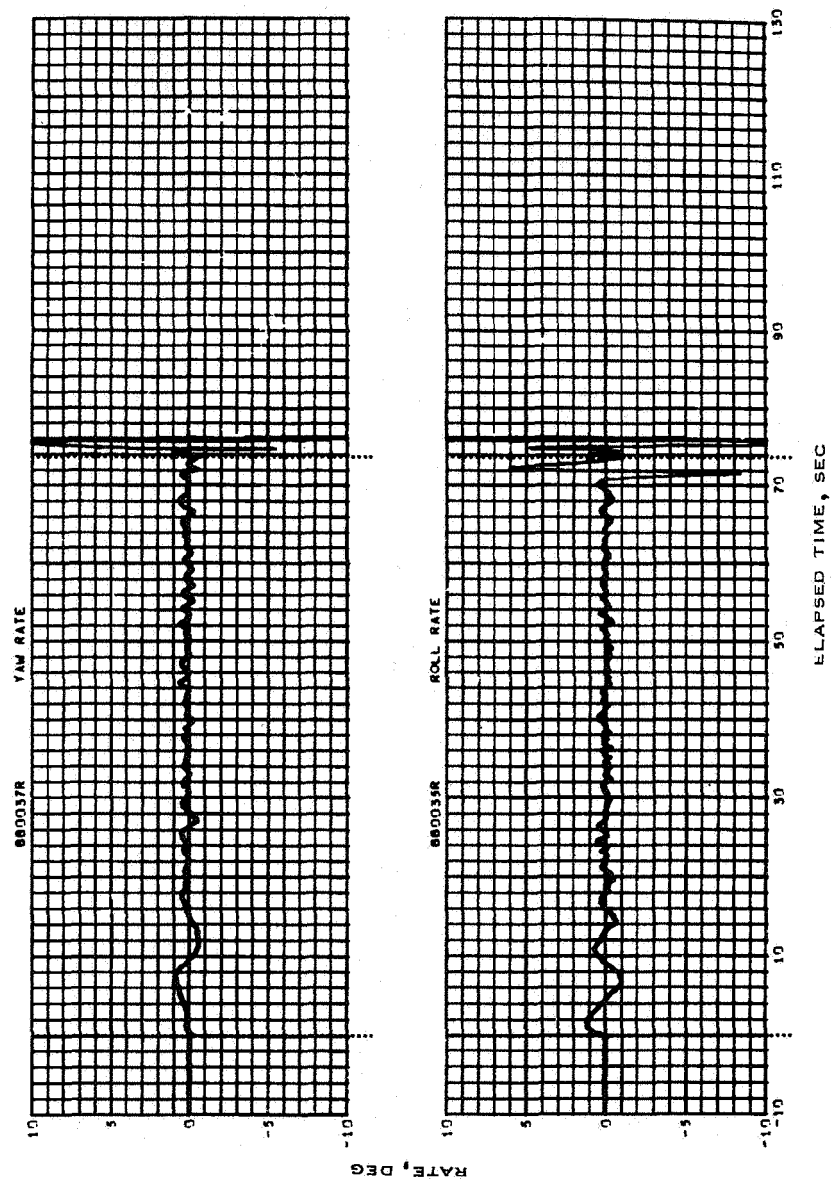


Figure 6.3-4.- Time history of launch-vehicle yaw and roll rates, Apollo Mission A-004.

NASA-S-66-3817 APR 15

0.00 SEC LIFT OFF  
73.70 SEC ABORT INITIATION

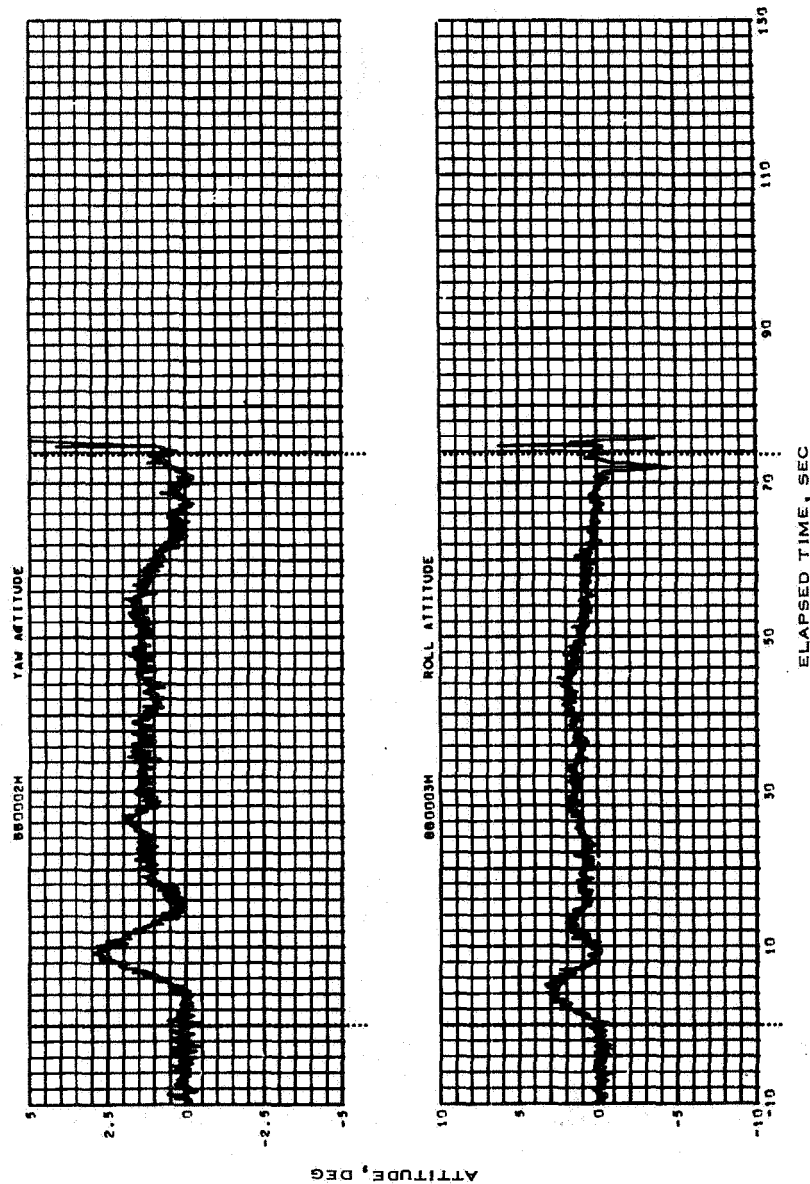


Figure 6.3-5.- Time history of launch-vehicle roll and yaw attitudes, Apollo Mission A-004.

NASA-S-66-3821 APR 15

0.00 SEC LIFT OFF  
73.70 SEC ABORT INITIATION

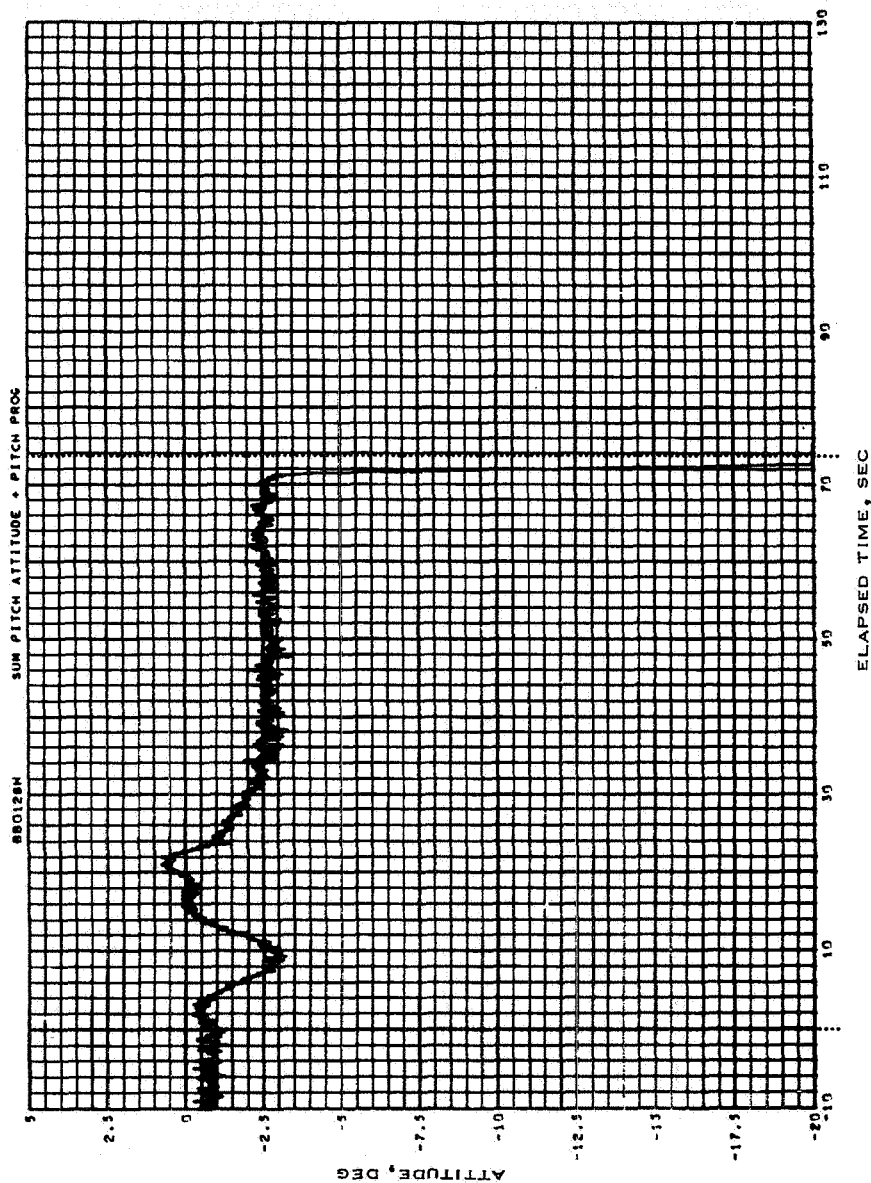


Figure 6.3-6.- Time history of launch-vehicle sum of pitch attitude gyro plus pitch programmer, Apollo Mission A-004.

NASA-S-66-3825 APR 15

0.00 SEC LIFT OFF  
73.70 SEC ABORT INITIATION

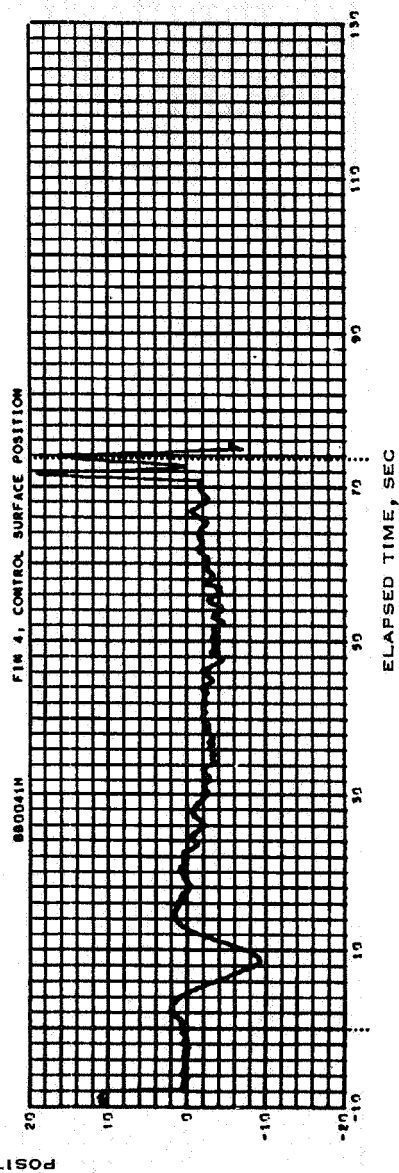
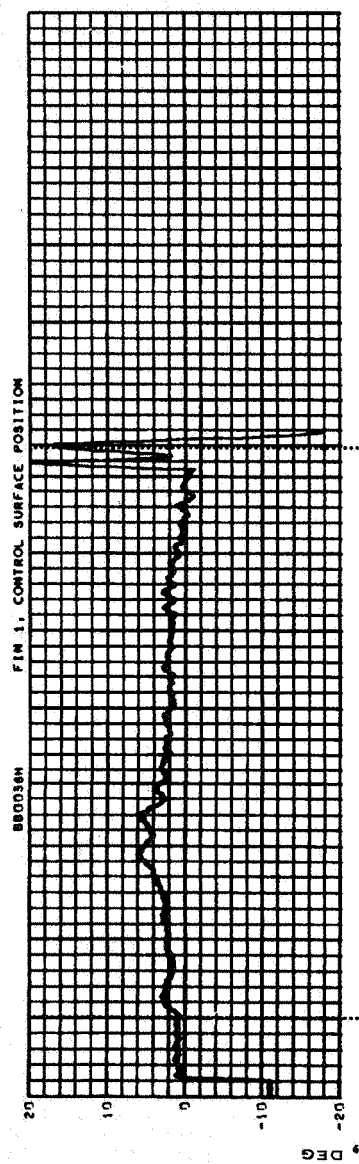


Figure 6.3-7.- Time history of position of launch-vehicle elevons no. 1 and 4, Apollo Mission A-004.

NASA-S-66-3829 APR 15

0.00 SEC LIFT OFF  
73.70 SEC ABORT INITIATION

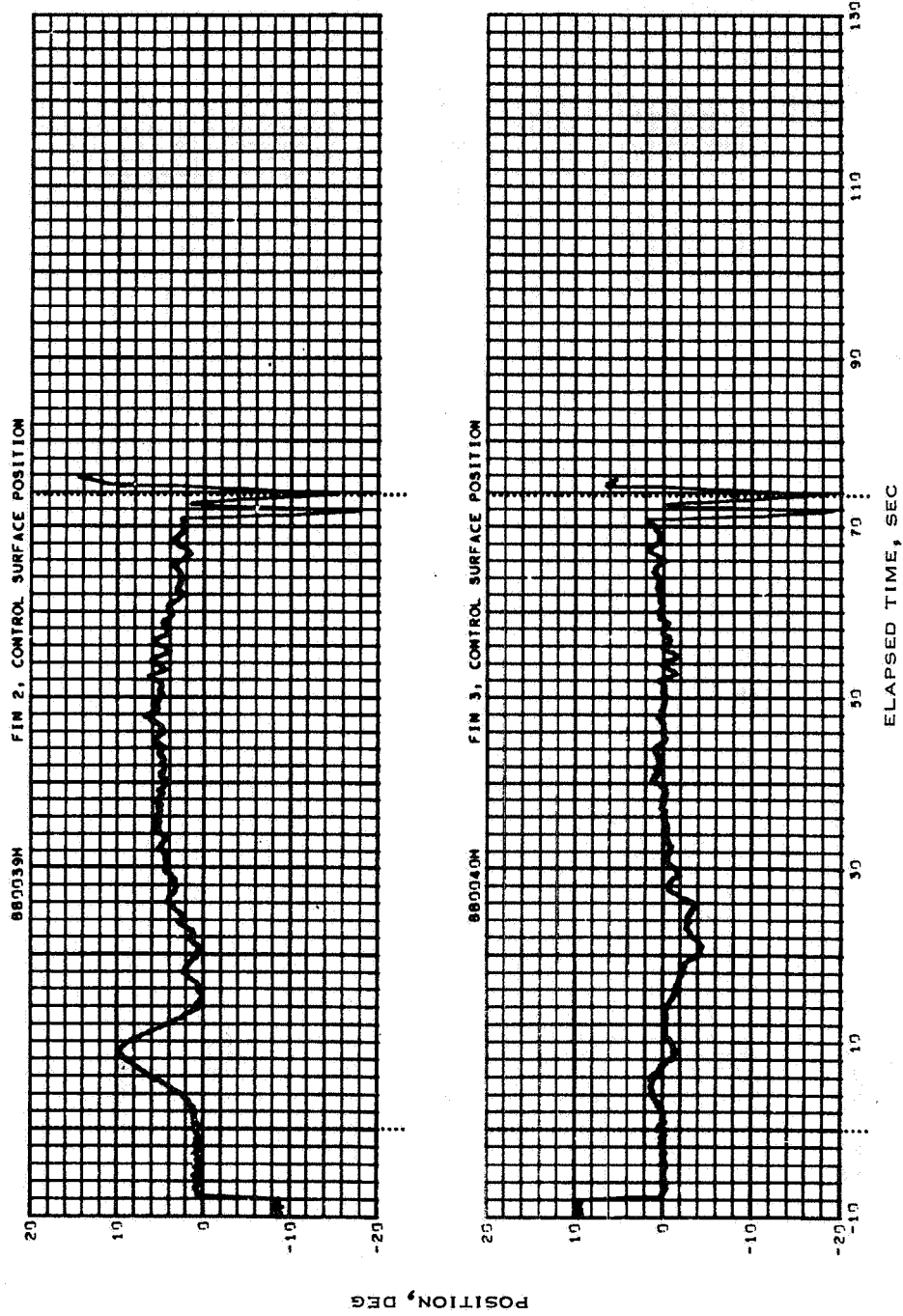
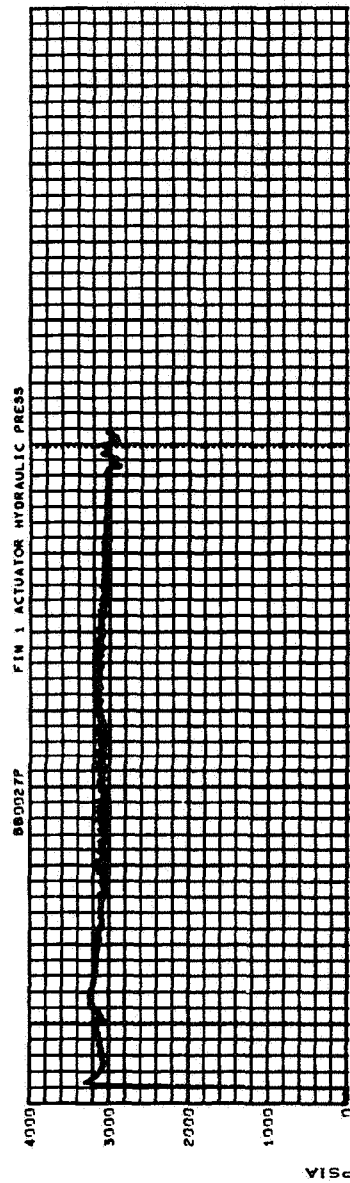


Figure 6.3-8.- Time history of position of launch-vehicle elevons no. 2 and 3, Apollo Mission A-004.

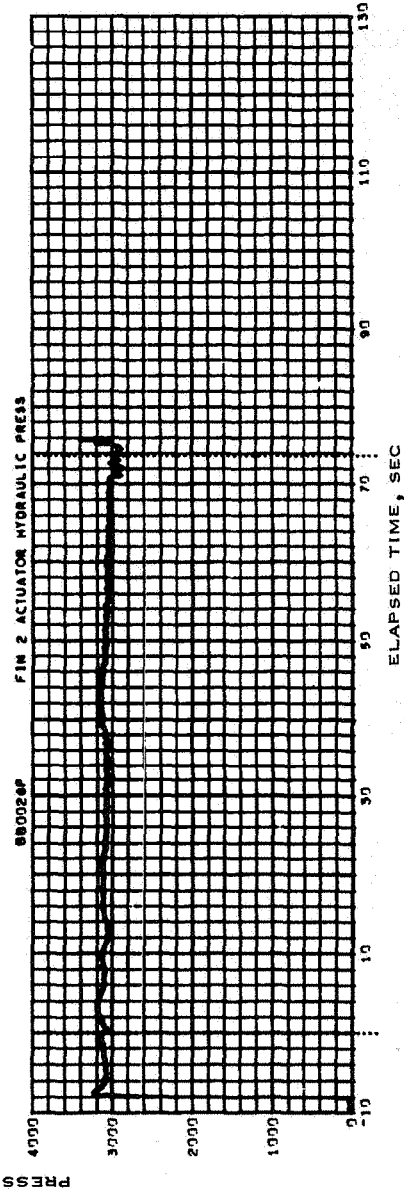


NASA-S-66-3833 APR 15

0.00 SEC LIFT OFF  
73.70 SEC ABORT INITIATION



(a) Elevon no. 1.

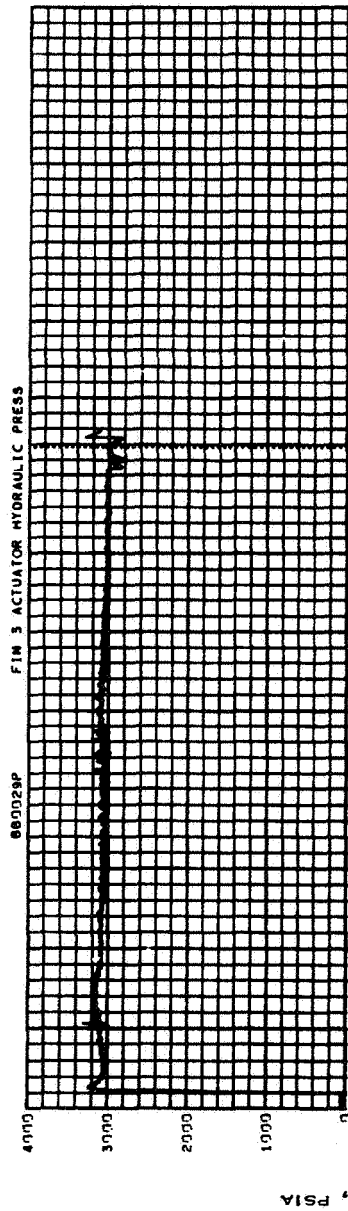


(b) Elevon no. 2.

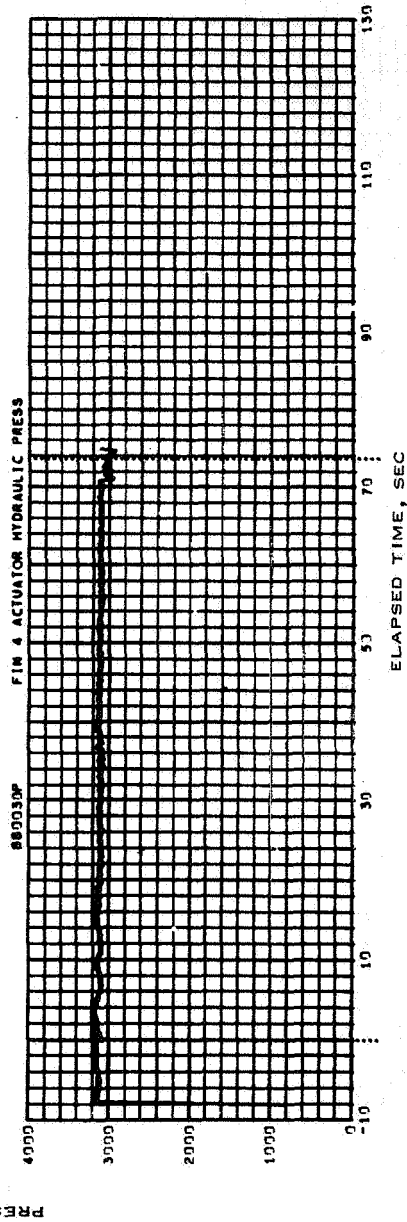
Figure 6.3-9.- Time history of launch-vehicle hydraulic pressures, Apollo Mission A-004.

NASA-S-66-3837 APR 15

0.00 SEC LIFT OFF  
73.70 SEC ABORT INITIATION



(c) Elevon no. 3.



(d) Elevon no. 4.

Figure 6.3-9.- Concluded.

NASA-S-66-3841 APR 15

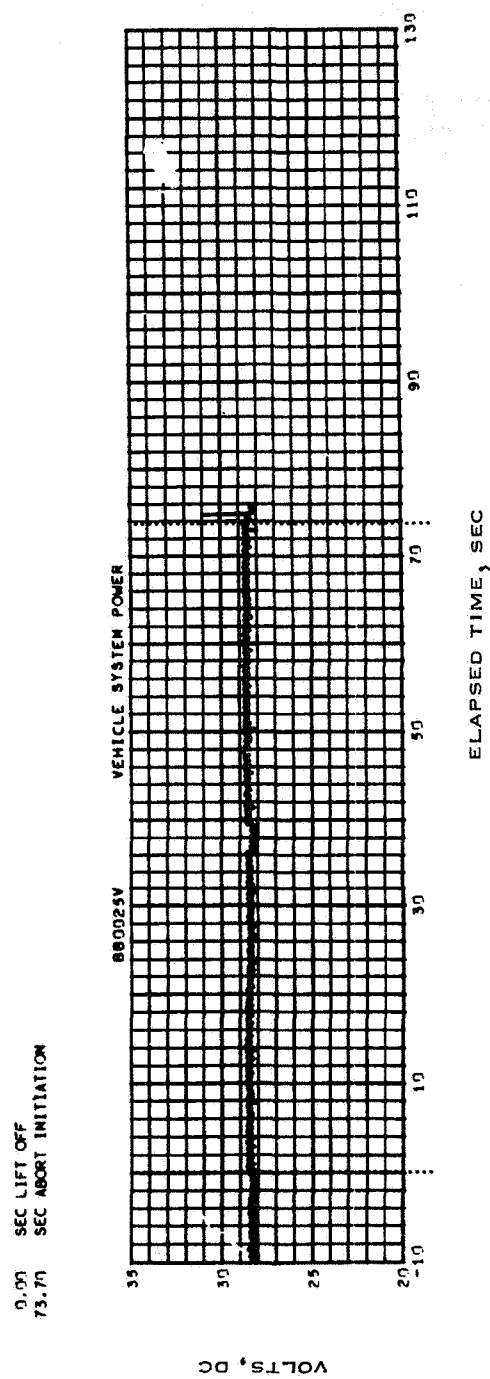


Figure 6.3-10.- Time history of launch-vehicle electrical power, Apollo Mission A-004.

#### 6.4 Launch Vehicle Aerodynamics

The variation of power-on drag with Mach number of the Little Joe II launch vehicle is a function of altitude, thrust level, number of each type of motor, and the base arrangement. Since no power-on wind-tunnel drag data were available, the preflight drag estimate for the Little Joe II launch vehicle model 12-51-3 was based on drag data from previous flights of Little Joe II and other launch vehicles which had various combinations of the above-mentioned factors that affect the drag. The estimated maximum and minimum power-on drag coefficients shown in figure 6.4-1 were used in preflight performance predictions. Figure 6.4-1 also includes the actual drag coefficients computed from the longitudinal high-range accelerometer data (ref. 1, fig. CAA), the flight weight (fig. 3.3-7), flight thrust (figs. 6.1-1 to 6.1-4), and the flight dynamic pressure. As indicated in figure 6.4-1, flight drag values were within the estimated drag envelope during the launch except for the period of overlap of stage 1 and stage 2 motor burning (Mach numbers from 0.8 to 1.1).

The launch vehicle was controlled and was statically stable from lift-off to abort. The vehicle had a positive static margin of 0.055 body diameter (diam. = 154 in.) at lift-off and 0.2 diameter at abort. Performance of the control system is discussed in section 6.3.

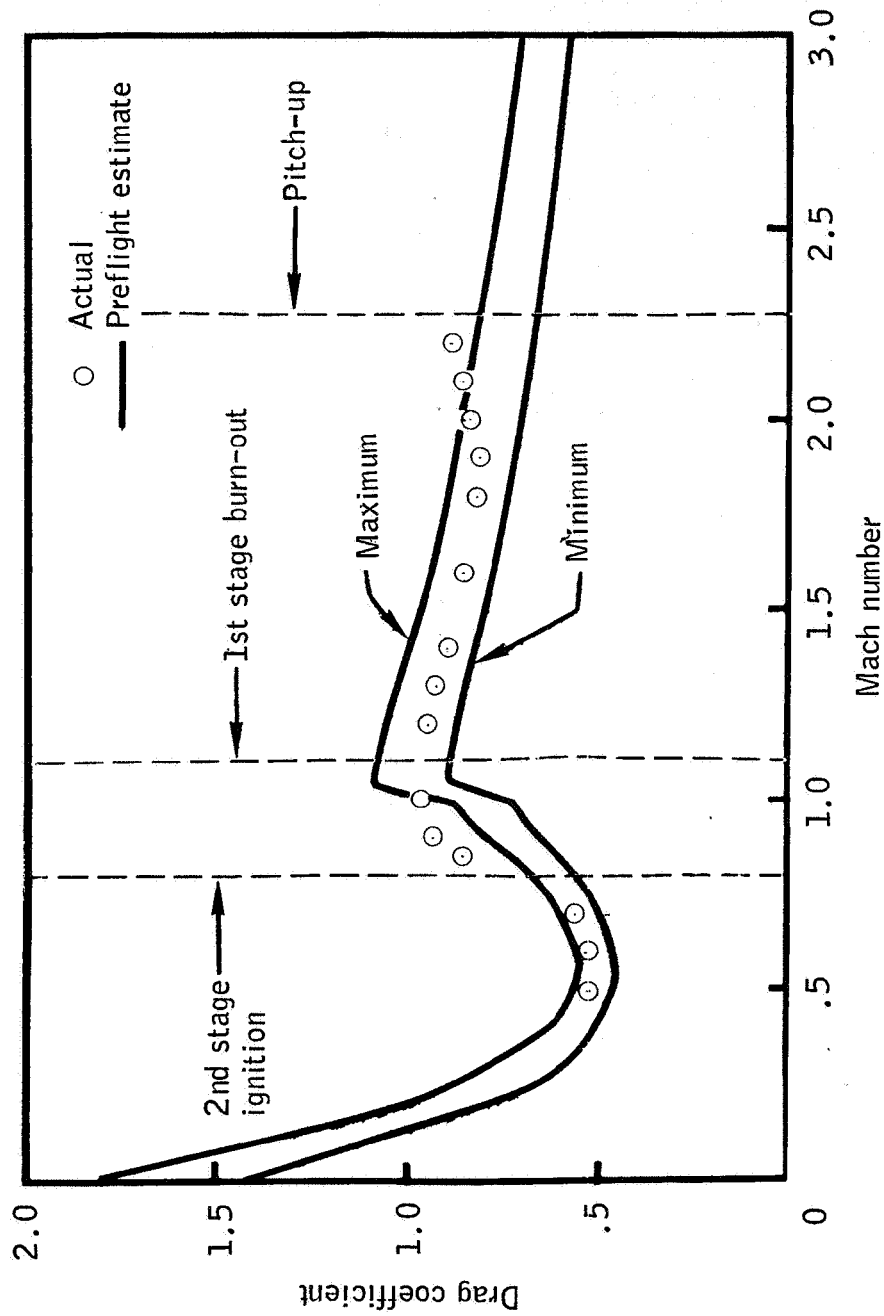


Figure 6.4-1.- Comparison of estimated power-on drag with two Algol motors with actual drag coefficients for various Mach numbers, Apollo Mission A-004.

## 6.5 Launch Vehicle Structures

The Little Joe II launch vehicle was a fin-stabilized airframe, and was structurally the same as the launch vehicle described in reference 4. The airframe consisted of the vehicle body and four fins. Hydraulically operated aerodynamic control elevons were attached to the trailing edges of the fixed portion of the fins. The body consisted of a forebody and an afterbody section of semimonocoque construction fabricated from truncated-form corrugated aluminum sheets stabilized by ring frames. Each fin was of a monospar structure with the skin stabilized by ribs and chordwise stiffeners. The elevons of essentially the same construction were attached to the trailing edge of each fin by four hinges. For a detailed description, see reference 6.

The only structurally oriented instrumentation were accelerometers mounted on the forward and aft bulkheads and oriented to measure the Y and Z components of acceleration. These accelerometers were ranged primarily to detect possible excitation of body bending modes. Data from these accelerometers, together with the linear accelerometer data from the spacecraft and LES, show amplitudes of the first body bending mode at lift-off that were small enough that the resulting body bending moments were small.

Based on these data and engineering films of the flight, the Little Joe II launch vehicle proved structurally adequate and performed the required mission with no problems. The films also show that the launch vehicle remained essentially intact until earth impact.

## 6.6 Launch Vehicle Electrical Power Subsystem

Description. - The launch vehicle electrical power subsystem consisted of two independent power sources: (1) instrumentation power, and (2) vehicle power for autopilot functions. Except for the incorporation of a separate control for each of the two sources when operating from external power, the subsystem was identical to that on LJ II described in reference 4.

Performance. - Telemetry data indicate that the electrical subsystem performance was satisfactory throughout the mission.

## 6.7 Launch Vehicle Instrumentation Subsystem

Description.- The launch vehicle instrumentation subsystem was similar to that used on Mission A-002 (ref. 10) and consisted of a single PAM/FM/FM telemetry link, signal conditioners, and transducers. The performance of the launch vehicle subsystems was monitored during flight by 39 telemetered measurements. During preflight checkout through lift-off, the launch vehicle performance was monitored by 33 landline measurements.

A block diagram of the instrumentation subsystem is shown in figure 6.7-1, and the landline measurements are shown in figure 6.7-2. The measurement list and the transducer locations are included in section 11.2 of this report. For a detailed description of the launch vehicle instrumentation subsystem, refer to section 3.0 of reference 20.

Performance.- Telemetry reception and recording were of good quality. All 39 measurements functioned properly and acceptable telemetry signals were obtained from lift-off until termination of launch vehicle telemetry transmission at T+73.7 seconds, following abort initiation.

At approximately T+30 seconds and continuing throughout the duration of the launch-vehicle flight, a baseline drift was observed in the PAM output of the 90 by 10 commutator. Reference and data pulses did not drift; thus all commutated data were recovered with no loss in accuracy.

The performance of the landline instrumentation was satisfactory.



NASA-S-66-3849 APR 15

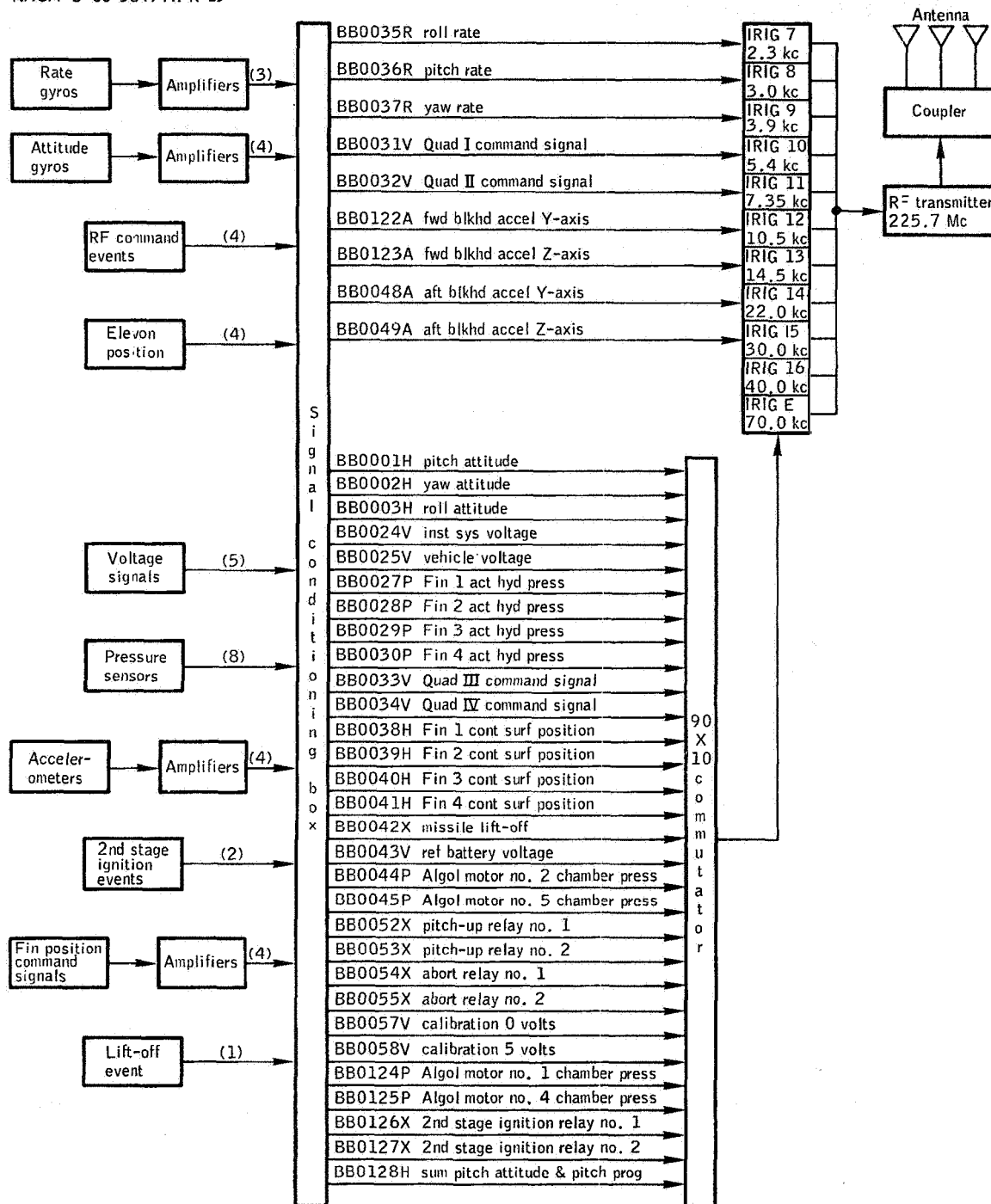


Figure 6.7-1. - Launch-vehicle instrumentation subsystem, Apollo Mission A-004.

NASA-S-66-3853 APR 15

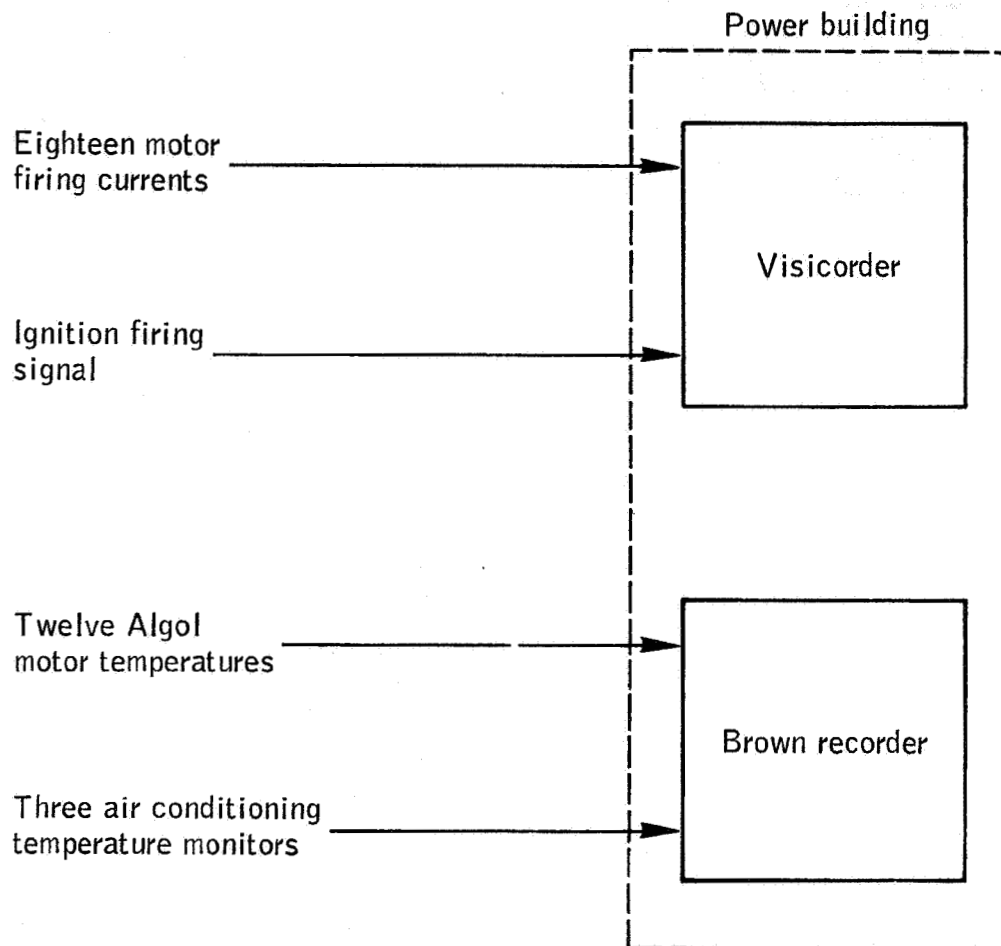


Figure 6.7-2.- Launch-vehicle landline instrumentation block diagram, Apollo Mission A-004.

## 6.8 Radio-Frequency Command Subsystem

The radio-frequency (RF) command subsystem, shown in figure 6.8-1, consisted of two independent, identical, redundant circuits to initiate the pitch-up and abort sequence from a coded ground transmission. The subsystem was essentially the same as that employed on vehicle 12-51-1 (Mission A-002); however, it did not include integral back-up timers and the abort hot-line was not wrapped around the range safety subsystem primacord. An additional "abort only" command function was included for use in the event the pitch-up maneuver was not desired because of flight conditions.

The RF command subsystem performed the pitch-up and abort functions as intended. At T+70.81 seconds, the pitch-up command was received, initiating the pitch-up maneuver. This signal also started the operation of a 2.8-second time-delay relay which actuated at T+73.7 seconds, initiating the abort sequence. Telemetry data verified that both circuits operated at these times.

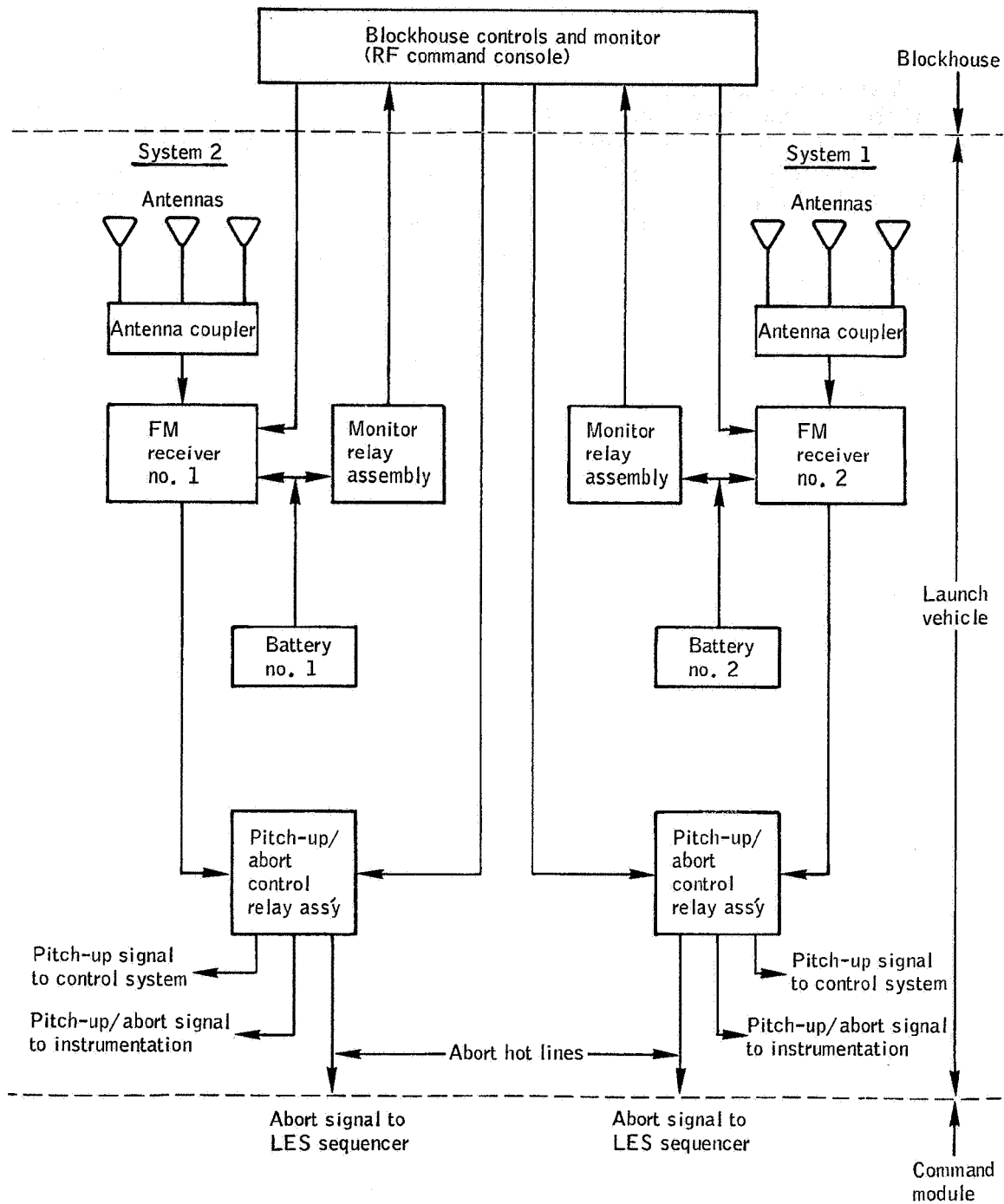


Figure 6.8-1.- Launch-vehicle RF command subsystem block diagram, Apollo Mission A-004.

## 6.9 Range Safety Subsystem

The range safety subsystem (fig. 6.9-1) provided the means for terminating launch vehicle thrust by splitting the Algol motor cases with pyrotechnics in the event of a range safety requirement. The system was controlled by the WSMR Range Safety Officer and could be actuated by ground station transmission of a coded radio-frequency command. Other than controlling the thrust termination of four, rather than six, Algol motors the subsystem was essentially the same as that employed on vehicle 12-51-2 (Mission A-003).

Range safety action during the flight was not required. Recovery of both safe and arm blocks after the flight indicated that the units were properly armed at lift-off.

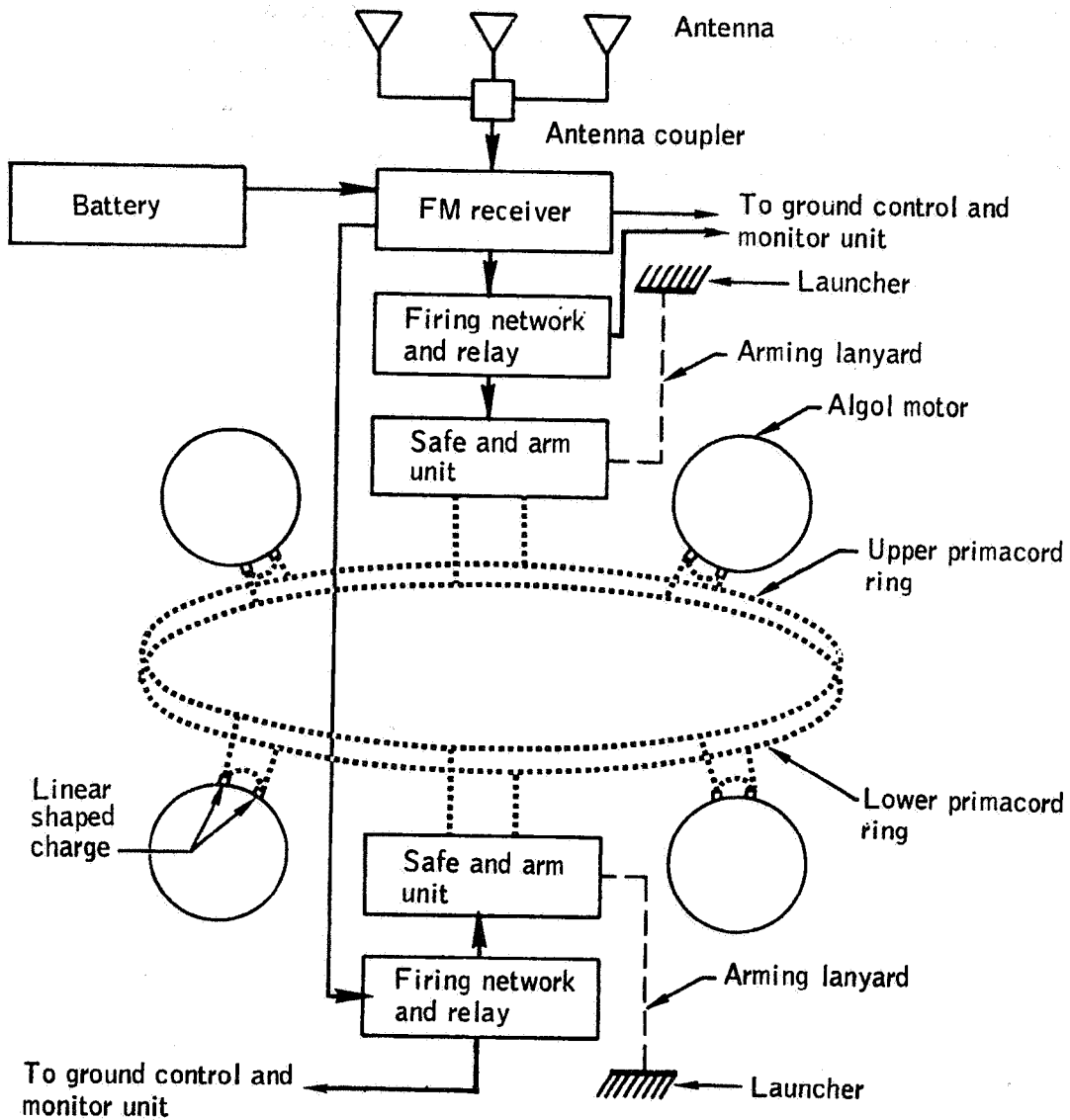


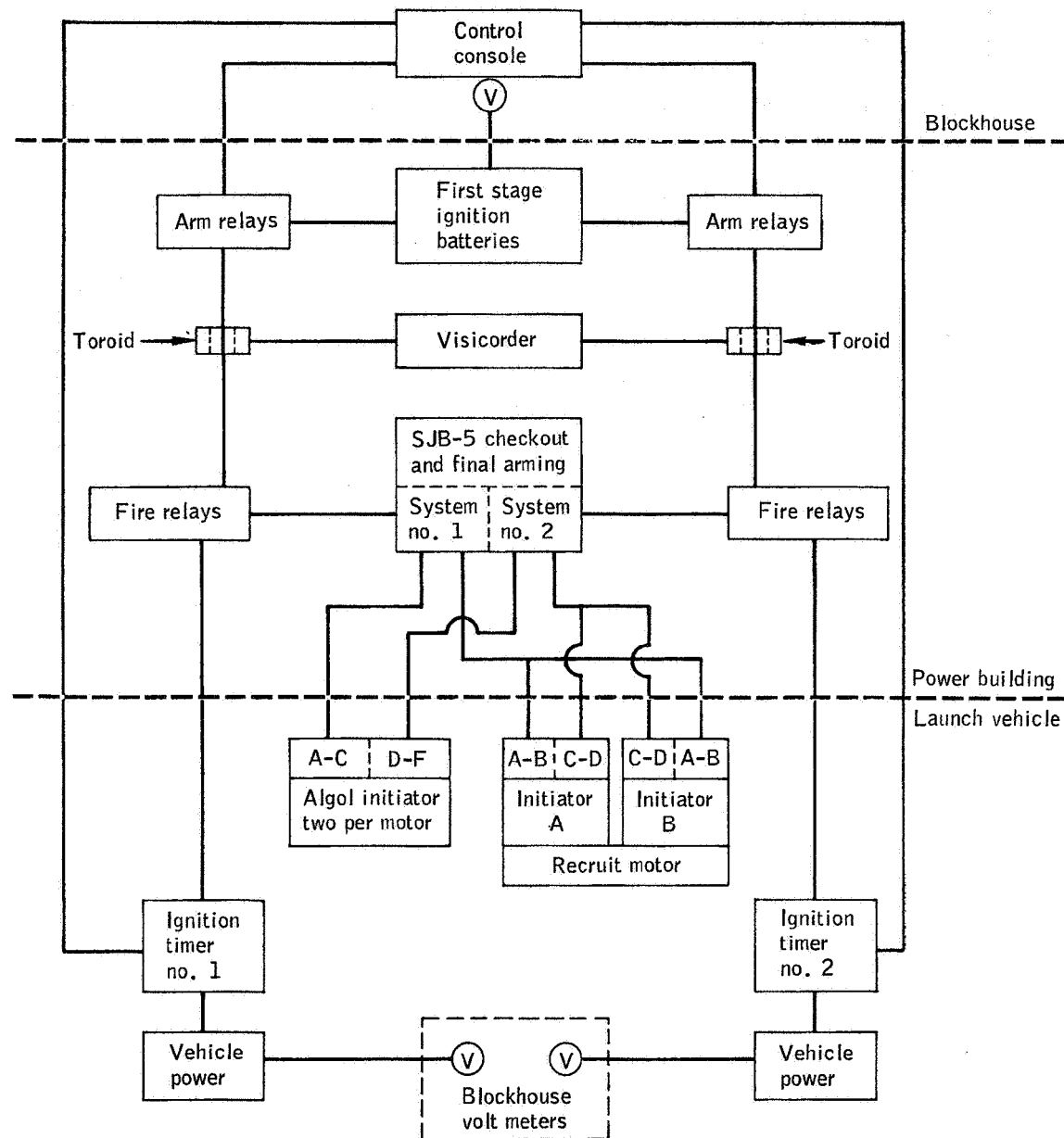
Figure 6.9-1.- Range safety subsystem, Apollo Mission A-004.

### 6.10 Launch Vehicle Ignition

The launch vehicle first-stage and second-stage ignition systems for Mission A-004 (fig. 6.10-1(a) and (b)) were similar to those used for Mission A-003 (see ref. 4, section 6.9).

Ignition of both stages was satisfactory (at T-0 and T+36.4 sec). The visicorder record in the power building indicated that first-stage ignition was initiated by timer 1 at 8:17:00.625 a.m. m.s.t. Fixed-camera coverage of first-stage ignition indicated no appreciable variation in Recruit motor burn-outs and no apparent hang-fires.

Timer 1 led timer 2 by 0.5 second, indicating that the ignition of the second-stage Algol motors was initiated by timer 1. This was the first two-stage ignition on a Little Joe II flight, and the first successful ignition of Algol motors for a second stage.

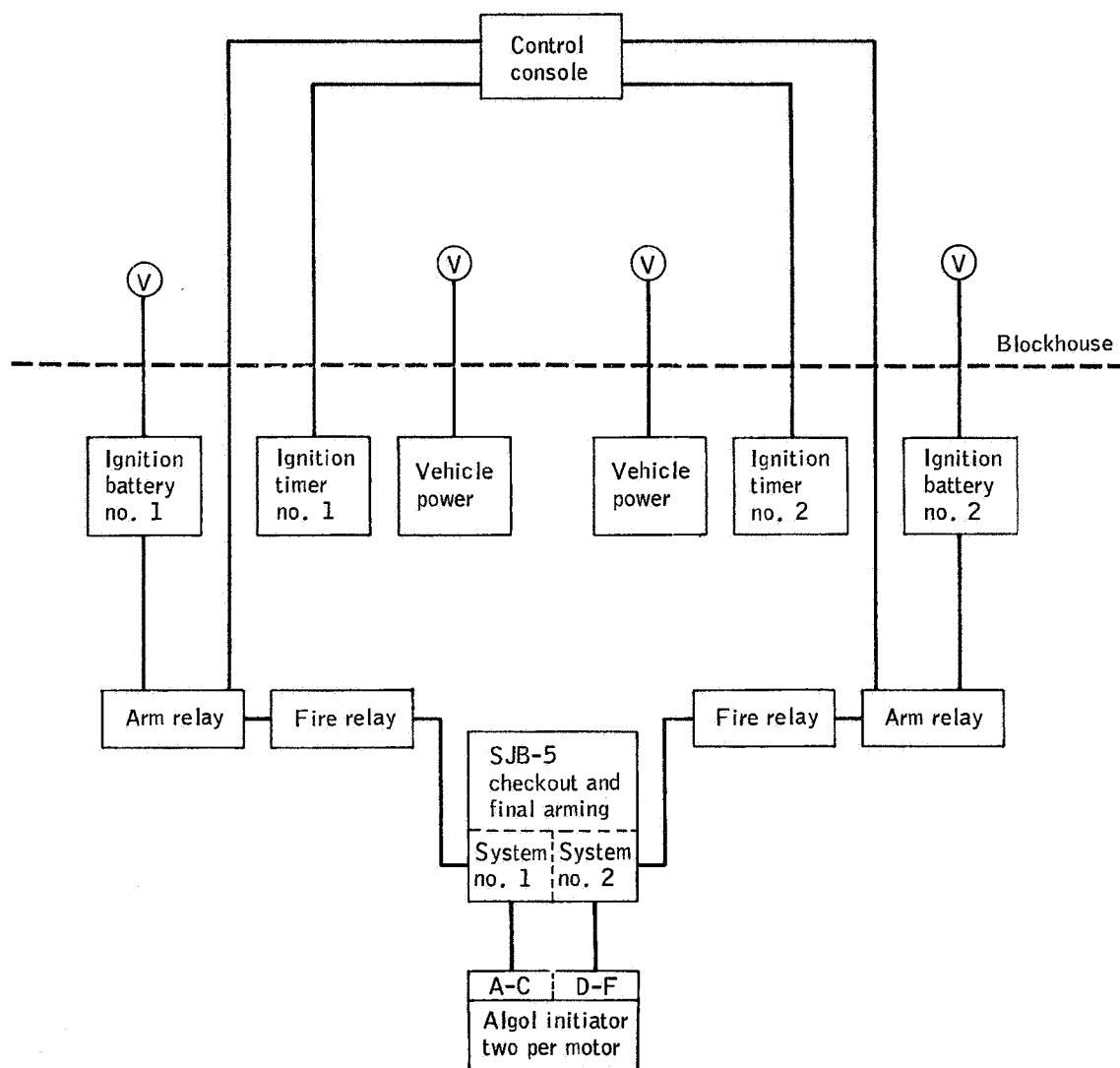


(a) First stage ignition system.

Figure 6.10-1.- Apollo Mission A-004 launch-vehicle ignition subsystem.  
Typical for each motor.



NASA-S-66-3666 APR 15



(b) Second stage ignition system.

Figure 6.10-1.- Concluded.

## 7.0 RECOVERY OPERATIONS

Recovery teams for the command module (CM) and the launch-escape subsystem (LES) were prepositioned at radar tracking site NE30, whereas the recovery team for the launch vehicle (LV) was at site SE30. (See fig. 7.0-1 for a map of the area.) The ground teams first observed the CM at approximately 9500 ft m.s.l. descending through an overcast sky on all three main parachutes. Descent was steady with very little side-ward motion and with the CM in normal descent attitude. Main parachute disconnect was observed at the instant the CM first contacted the ground. Immediately following disconnect, the CM was seen to rock back and forth to a maximum angle of approximately 60° from vertical before coming to rest in an upright position.

The drogue parachutes touched down approximately 3000 feet north-east of the CM. There was no damage to the drogue parachutes, no fraying of cables, and no evidence of riser cable kinking.

The apex cover was observed falling 2000 feet east of the CM. The cover was in excellent condition and there were neither cracks nor chips from impact.

NASA-S-66-3690 APR 15

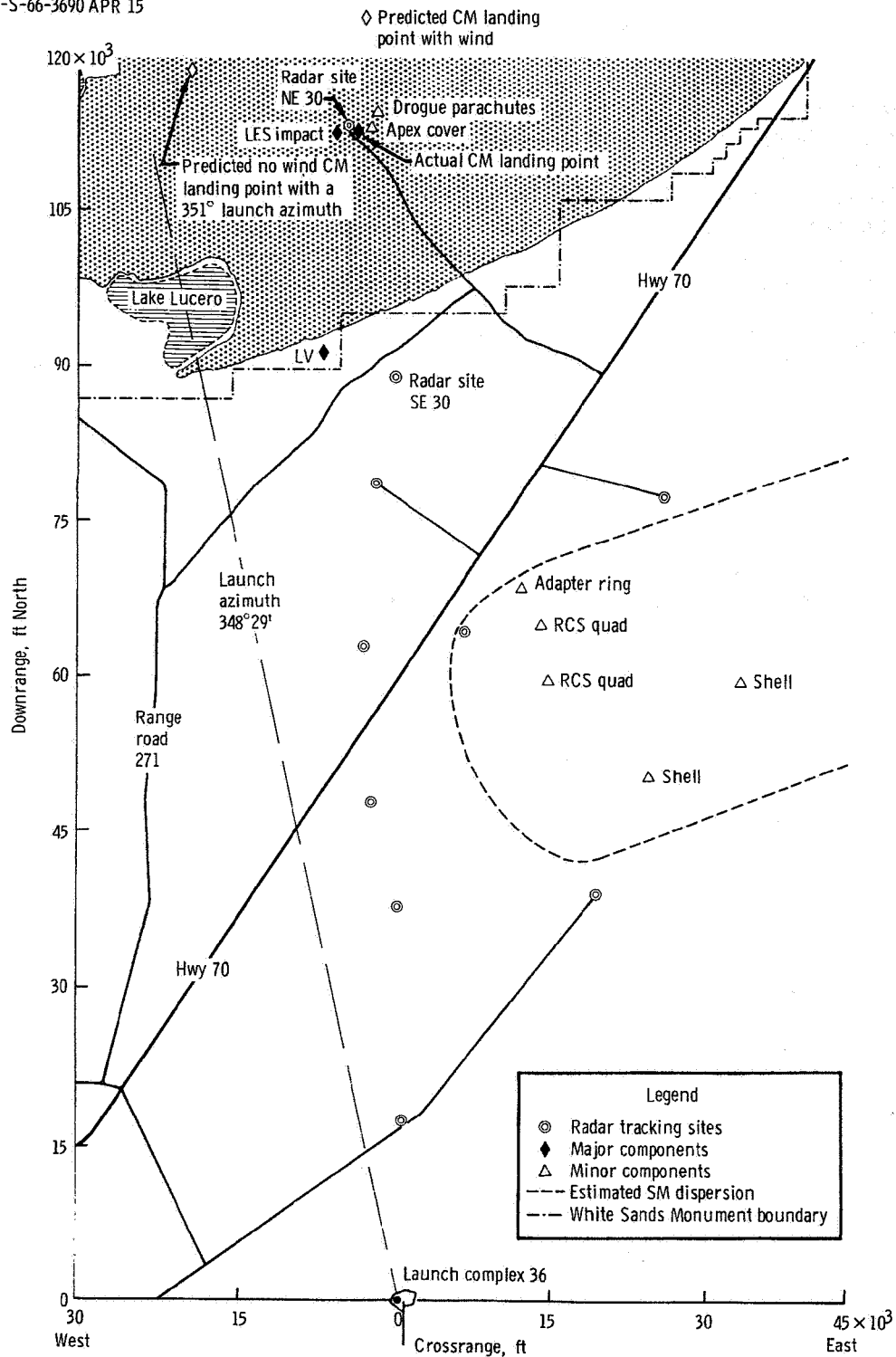


Figure 7.0-1. - Location of recovered components, Apollo Mission A-004.

## 7.1 Command Module

On-scene inspection of the CM revealed the following:

- (a) Almost the entire CM conical surface was discolored and sooted.
- (b) The three main parachutes were at full suspension-line length, one toward the north, one toward the south, and one toward the southeast.
- (c) The main heat shield was shifted approximately  $1/4$  inch toward the -Z axis. A 4-foot-long piece of the cork ablator was broken off the +Z axis (approximate location of first contact with the ground). The underlying stainless steel structure was also damaged (fig. 7.1-1). Two fine-line cracks were observed, each 1 foot long and approximately 2 feet from the outer edge. One crack was between the -Y and +Z axes, and the other between -Z and +Y axes.
- (d) All windows were covered with soot, reducing light transmission to approximately 20 to 30 percent of normal (fig. 5.14-1).
- (e) The -Z axis scimitar antenna was shifted toward the -Y axis and soot was found in the crack marks at the base (fig. 5.12-4).
- (f) The outer hatch (side ablative hatch) was not sprung and required a 150-lb torque wrench pressure to release. (See section 5.5.) Sooting had penetrated to the inner door through the hatch release socket hole. The inner door (side pressure hatch) was in good condition and required a 120-lb torque wrench pressure to release. (See section 5.5.) A tooth of the inner door sprocket was broken off during removal. Another tooth was broken off while the inner door was being replaced for transport back to the Vehicle Assembly Building (VAB).
- (g) The platform inside the CM was swinging free with approximately  $3/4$  inch of sideward (Y-Y) movement. Pins were replaced, as planned, to secure the platform for transport back to VAB. Strut stroke measurements made in the recovery area are presented in section 5.8.
- (h) Pressure ports were clean except for a small amount of potting compound on the external surface. The inside of the ports was blackened with soot.
- (i) The CM-SM umbilical was cut cleanly by the guillotine.
- (j) The flashing light was deployed, but not to the full vertical position. Preflight adjustment of the stop screw, made necessary because of the weak deployment springs, restricted the extent of full deployment. (See section 5.5.)

(k) The VHF antennas were deployed, but not to the vertical position. Preflight adjustment of the stop screw, made necessary because of weak deployment springs, had restricted the extension. The VHF antenna at the -Y axis was cracked half-way through at the base and was bent toward the center of the CM. The other VHF antenna (all copper) at the +Z axis was bent but was not cracked. Potting at the base of either antenna was not cracked. These antennas are not representative of actual flight hardware. (See section 5.5.)

(l) Red apex cover silicon sealant strains were noticed on the CM above the hatch door.

(m) Main parachute disconnects were severed cleanly. One cutter blade was broken. The cutter left heavy grooves on the pins. (See fig. 5.8-11.)

(n) All tower separation bolts were fired, leaving edges clean. The expander body bolt protectors which cover the sharp edges of the sheared bolts were removed and replaced by bolts to accommodate the 3-point cable-lifting sling.

(o) The canister holding the uprighting bag on the +Z side was jarred downward  $3/8$  inch (see section 5.5).

(p) Drogue cans were clean and indicated no damage during deployment. One drogue can was slightly bent during pick-up by the recovery loop (fig. 7.1-2). Figure 5.5-8 shows the drogue can before the CM was lifted by the recovery loop.

(q) Drogue disconnects were cut cleanly. One connector of a drogue disconnect (C-20 SQ7 P-1) was broken due to the initiator charge.

(r) All apex cover thrusters were deployed satisfactorily.

(s) None of the three pilot parachute cans were damaged. (See figs. 5.8-8 to 5.8-10.)

(t) The CM was first lifted by the recovery loop but, because of the  $30^\circ$  tilt angle (fig. 7.1-2), could not be aligned properly for loading on the MM-1 terracruiser. Therefore, the alternate 3-point sling was used (fig. 7.1-3). The CM was loaded on the terracruiser and departed for the VAB by T+4 hours.

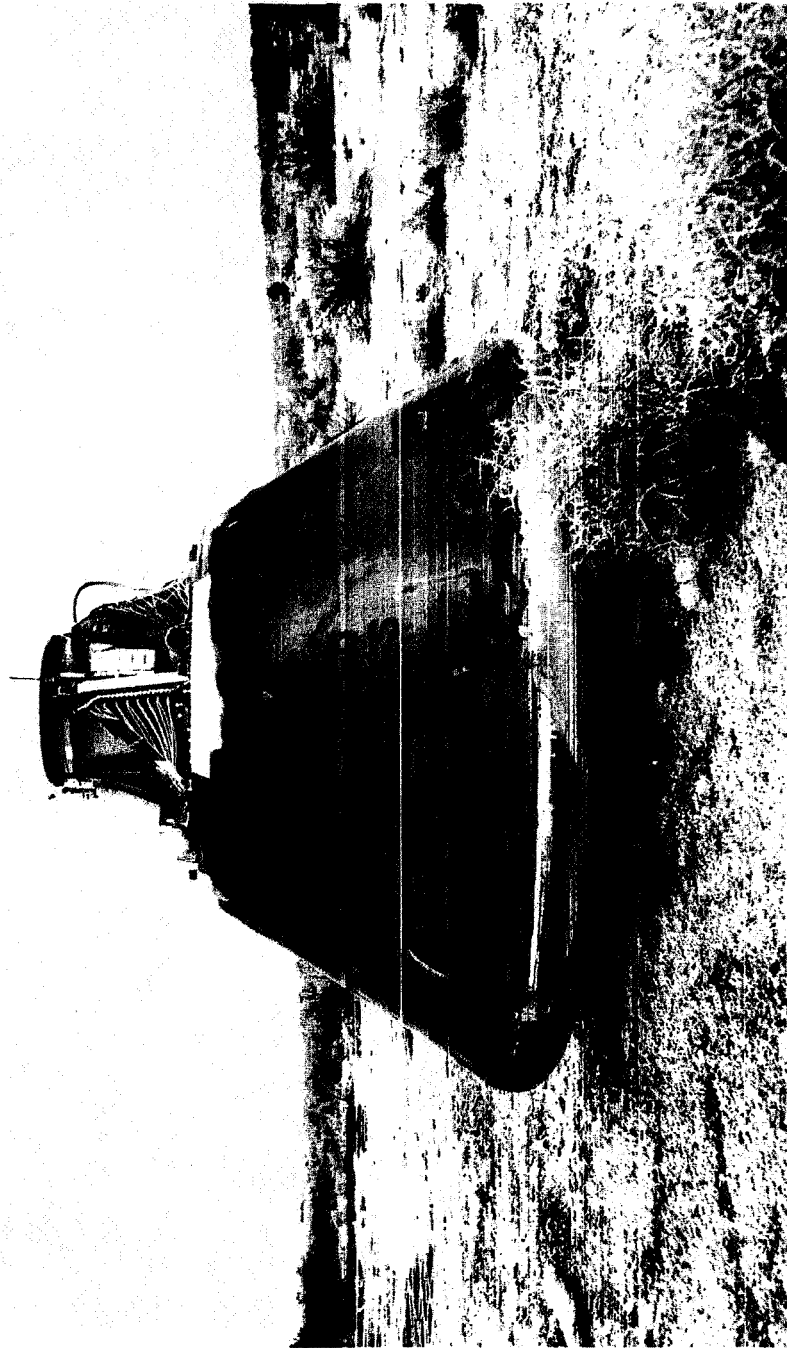


Figure 7.1-1.- Apollo Mission A-004 command module after landing, showing cork ablator broken from impact.

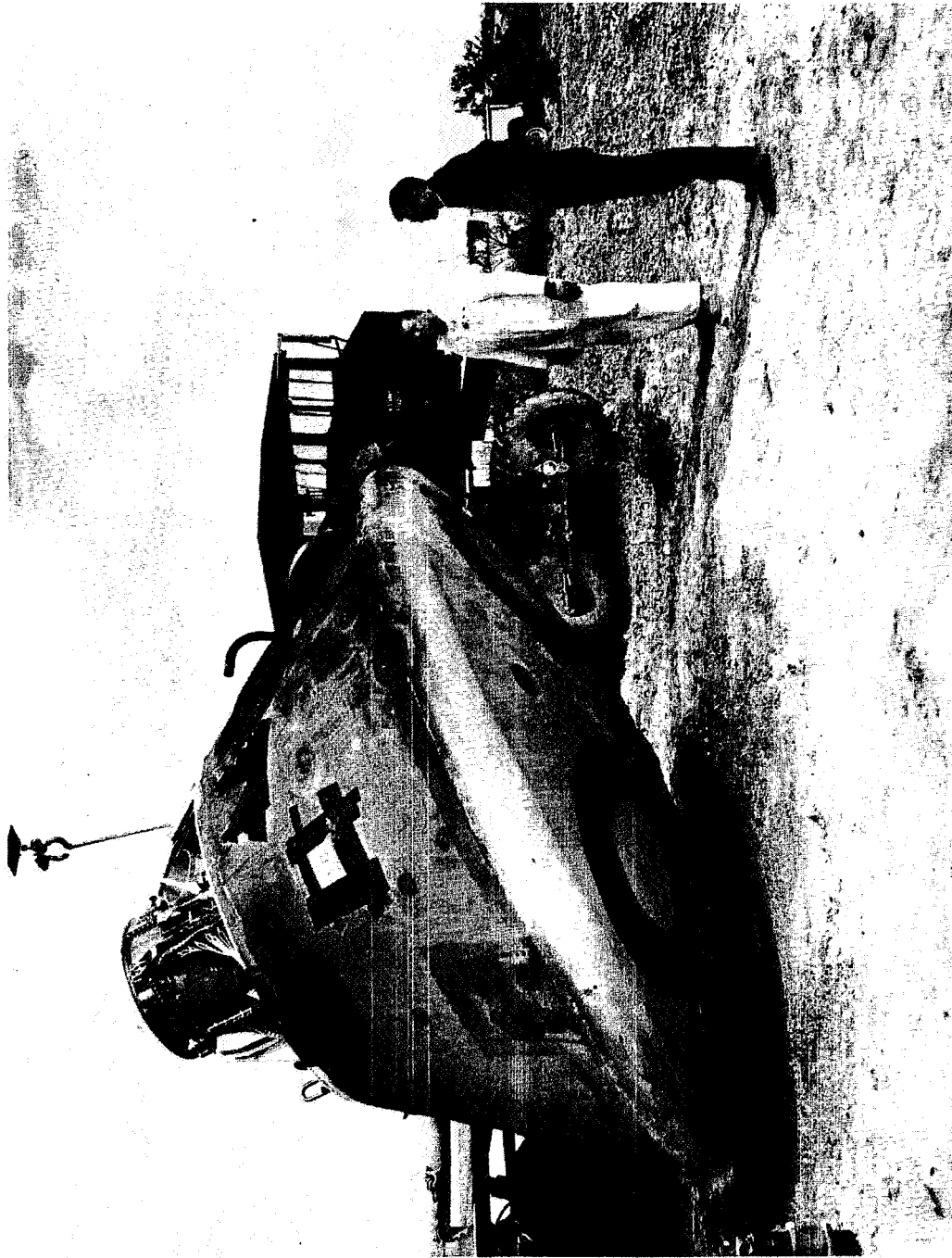


Figure 7.1-2.- Lifting Apollo Mission A-004 command module by the recovery loop.

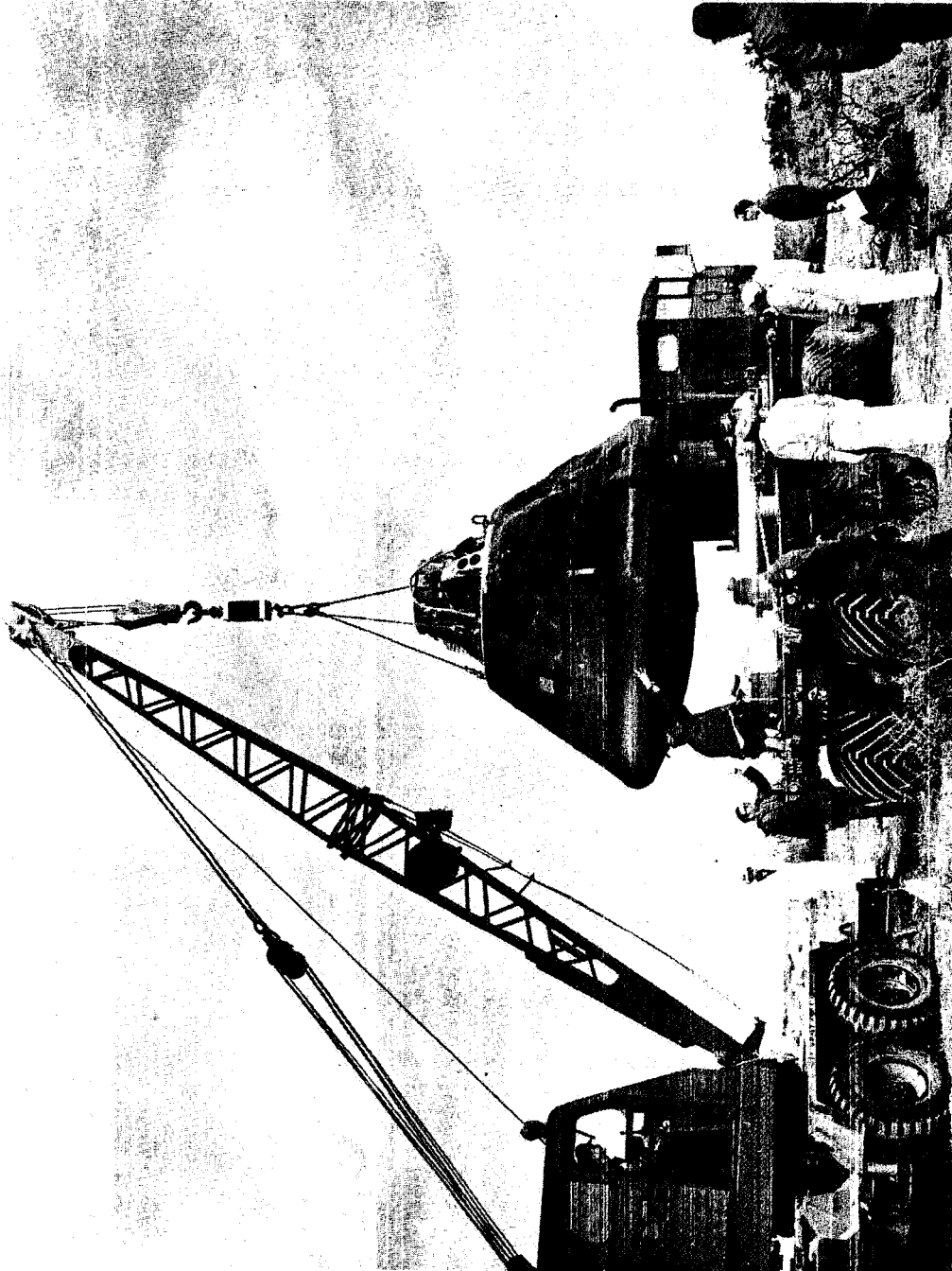


Figure 7.1-3.- Lifting Apollo Mission A-004 command module by alternate three-point sling.



## 7.2 Launch-Escape Subsystem

The launch-escape subsystem (LES) fell in a nearly horizontal position and broke upon impact which was observed by the ground recovery crew stationed at NE30. Impact was approximately 3500 feet west of the CM landing point (fig. 7.2-1).

Following are observations of the recovery team:

(a) The LES camera was found in place but the protective covering was knocked loose during impact.

(b) The launch-escape motor, tower-jettison motor, and pitch-control motor were completely expended. There was no evidence of hot spots on any of the remaining intact parts.

(c) The aft section of the launch-escape motor and the phenolic exit cones were sheared off on impact (fig. 7.2-1). All four nozzles contained their graphite throat inserts when recovered.

(d) The tower-jettison motor showed no abnormal erosion marks.

(e) The pitch-control motor remained with the canard section and was in good condition.

(f) The canard actuation system contained residual gas pressure in both cylinders. This gas pressure was released and shorting plugs were installed in the initiators as a precautionary measure.

(g) The Q-ball external structure was in one piece, whereas the internal parts were scattered.

(h) The tower was broken upon impact.

(i) Each of the four explosive bolts indicated a clean break.

(j) The tower structure, camera case, and hard boost protective cover exterior surfaces were discolored and sooted but not badly burned.



Figure 7.2-1.- Apollo Mission A-004 LES impact area.

### 7.3 Service Module

The service module (SM) broke up shortly after abort and pieces were scattered over an area covering 50 square miles (fig. 7.0-1). Because of inclement weather, high winds, and the large dispersion pattern, the first pieces of the SM were not found until T+2 days.

Parts of the service module that were found included the following:

- (a) Two RCS quads (quads B and C)
- (b) One section (2 ft by 4 ft) of an SM radial beam (sectors 2 and 5)
- (c) One CM support beam and tension tie (V 1734 001-11)
- (d) One signal distribution box (1.9.1.1.2)
- (e) One tape module (3.11.1.1.1)
- (f) Nineteen amplifiers
- (g) Other small pieces of skin and radial beams.

The SM-LJ II adapter ring was found in one piece except for impact damage. The fiberglass bulkhead was shattered with only the jagged edges left in the mating ring.

#### 7.4 Launch Vehicle

The launch vehicle was observed by the recovery crew to be falling intact, aft end first. Impact was approximately 7200 feet northwest of site SE30 just inside the White Sands National Monument (fig. 7.0-1). Maximum dispersion of the launch vehicle was approximately 100 yards (fig. 7.4-1). Immediately after impact the launch vehicle started burning, and it was T+130 minutes before the recovery team could enter the impact area because of the intense heat.

The launch vehicle separation at the top ring was indicated by the clean shear of the rivets. This was verified when the bottom ring of the service module was found 2 days later.

The following observations were made by the recovery teams:

(a) Seven of the eight nitrogen tanks were ruptured. The eighth tank was not located.

(b) Two safe and arm destruct units used to detonate the linear shaped charge for destructing the Algol motors were found in the armed position.

(c) Other items recovered were:

Launch sequence timers (only one was returned to VAB)

RF command receiver

Logic and control unit (found in three pieces)

Pitch programmer

Fin, including pallet and actuator

These were the only items requested for recovery. All remaining launch vehicle items were disposed of by Army Ordnance Disposal.

7-12

NASA-S-66-3686 APR 15

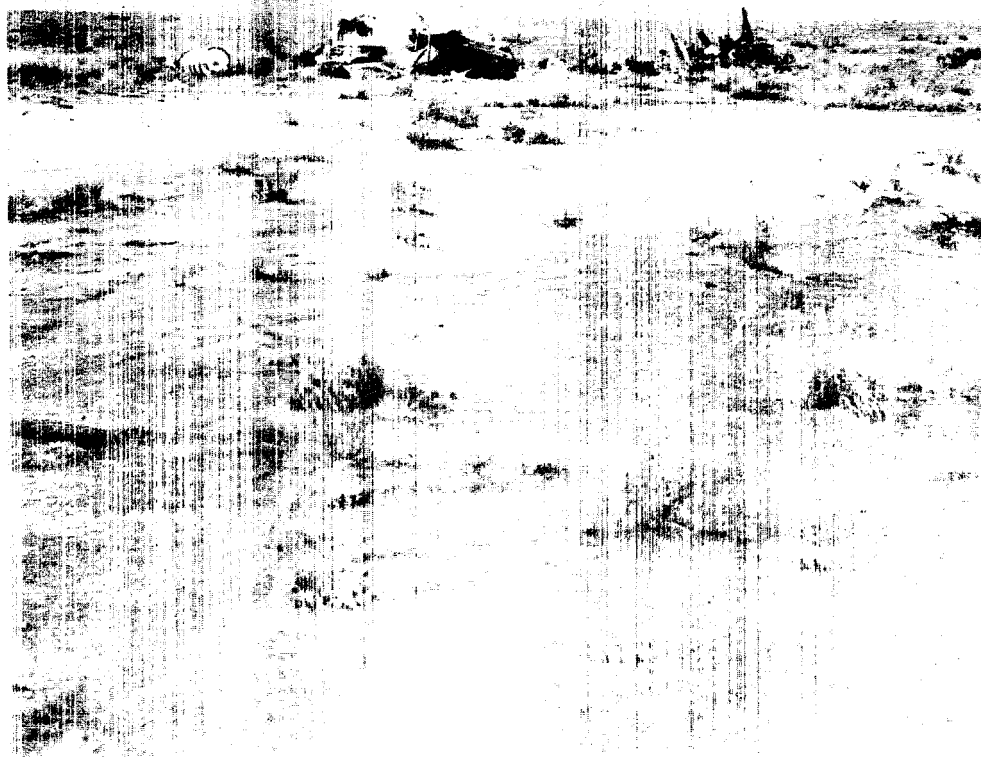


Figure 7.4-1.- Apollo Mission A-004 Little Joe II  
launch vehicle impact area.

## 8.0 POSTFLIGHT TESTING AND ANOMALY SUMMARY

### 8.1 Postflight Testing

Planned postflight testing for analysis of subsystem performance and the resolution of anomalies occurring during the flight of Mission A-004 have been completed and the results analyzed. Each item is discussed in the area where testing occurred as noted in the section referenced in parenthesis.

1. Scimitar Antenna - The scimitar antenna was field inspected, and then removed from the spacecraft. A radiation bench test was conducted on the antenna, and X-rays were taken to observe structural condition. The final test involved complete sectioning of the antenna for analysis (section 5.12).

2. Pyro buses A and B - Electrical continuity checks of pyro buses A and B were conducted in the spacecraft with the sequencers in place. Bench tests were conducted on the sequencer after it was removed from the vehicle (section 5.11).

3. Cabin Pressure Relief Valve Tests - Pressurization and vacuum tests were conducted on the cabin pressure relief valve while it was still installed in the spacecraft. The valve was removed and shipped to AiResearch Manufacturing Co. where further pressure and vacuum tests were conducted (section 5.13).

4. Command Module Leak Tests - All cracks in the aft bulkhead of the command module pressure vessel were bagged and a vacuum was applied to the bagged area prior to a complete CM pressure check. The cracks were sealed and a pressure check was conducted on the total CM through the vent port on the crew access hatch prior to the removal of the cabin pressure relief valve (section 5.13).

5. Crew Window Tests - The crew windows were removed at the contractor's Downey facilities and shipped to Atomic International for visibility, transmissibility, and chemical analysis (section 5.14).

6. Instrumentation Measurements (5) Tests - Postflight electrical continuity tests were conducted on all questionable instrumentation measurements prior to removing any equipment from the vehicle. Calibrations were completed on those measurements requiring such action (section 5.11).

7. Flotation Bag Canister Test - The flotation bag canister was removed from the spacecraft and shipped to MSC for testing. Operational tests have been completed on this item (section 5.5).

## 8.2 Summary of Malfunctions and Deviations

The flight test of Mission A-004 did not reveal any malfunctions or deviations which could be considered a serious system failure or design deficiency. However, 10 deviations did occur and are summarized here for documentary purposes.

Corrective measures were recommended for some of the items listed. These are marked with an asterisk. Each item is discussed in the area where the deviation occurred as noted in the section referenced in parenthesis.

1. RF telemetry was lost, starting approximately 2 seconds after abort due to scimitar antenna failure (section 5.12).
2. At abort, pyro bus A and B voltage dropped to approximately 5 volts for approximately 0.2 second (section 5.11).
3. Cabin pressure relief valve did not control cabin pressure during ascent because of excessive inner hatch seal leakage (section 5.12).\*
4. All windows on the command module sustained severe sooting during the flight (section 5.14).
5. There was damage (pitting) to the aft heat shield in the area of the CM-SM tension ties (section 5.2.4).\*
6. The onboard tape recorder F jammed at T+209 seconds (section 5.12).
7. Five measurements yielded questionable data (section 5.12).
8. The flotation bag canister shifted during flight (section 5.5).
9. Pyro bus B voltage dropped to approximately 30 volts at the time of pilot mortar/drogue disconnect firing (section 5.11).
10. One drogue parachute disconnect cutter blade was broken during flight (section 5.8.1).\*

## 9.0 CONCLUDING REMARKS

Mission A-004 demonstrated the satisfactory performance and structural integrity of the Apollo launch escape vehicle Block I type airframe structure during a power-on tumbling abort.

The desired differential pressure ( $11.2 \pm 1.5$  psid) loads on the command module structure were not achieved because of the combination of higher than predicted aft compartment pressure and lower than expected plume impingement pressure.

The Block I type service module airframe structure performed during the launch phase and pitch-up maneuver as required.

After canard deployment, the spacecraft 002 launch escape vehicle with specially configured mass characteristics, quickly oriented from a high tumbling rate to a stabilized, main heat shield forward attitude.

The boost protective cover performed during the launch phase and pitch-up maneuver as required.

The single scimitar antenna was broken during the first tumble and soft boost protective cover break up after abort initiation.

Improper installation of the inner hatch resulted in excessive cabin air leakage.

With the exceptions already noted, all Block I type spacecraft 002 subsystems performed satisfactorily.

Dynamic loads and structural response values determined from the flight data were within design limits and predicted values.

The desired flight measurements were obtained, although they were incomplete from drogue deployment to landing because one onboard tape recorder jammed.

The Little Joe II launch vehicle placed the Apollo launch escape vehicle within the planned altitude-velocity test region.



## 10.0 APPENDIX A

### 10.1 Test Vehicle History

The launch vehicle was assembled at the contractor's plant and after acceptance was disassembled and shipped to Launch Complex 36 at White Sands Missile Range, New Mexico. The checkout of assemblies and subsystems and the integrated subsystem tests were performed in accordance with operational checkout procedures (OCP's). Significant OCP's are listed in table 10.1-I.

Launch vehicle testing was divided into four phases: manufacturing acceptance evaluation (MAE), pre-delivery acceptance test (PAT), field test, and integrated system tests. The MAE was completed on July 1, 1965, the PAT was completed on October 7, 1965, and the post-PAT acceptance review was held on October 8, 1965. The launch vehicle was shipped from San Diego, California, on October 11, 1965, and arrived at White Sands Test Facility on October 14, 1965.

Assembly of the spacecraft command module, service module, and launch-escape subsystem structure was completed at the contractor's plant on September 16, 1965. After completion of subsystem and integrated system tests (Sept. 30, 1965), the spacecraft was formally accepted at the customer acceptance readiness review (CARR) on October 1, 1965, and shipped to the Vehicle Assembly Building (VAB) at the White Sands Test Facility (WSTF).

The service module was shipped October 6, 1965, and received at the VAB on October 7, 1965. After pre-mating preparations, the service module was moved to the launch pad and mated to the launch vehicle on October 23, 1965.

The command module was shipped on October 8, 1965, and received at the VAB on October 9, 1965. It was moved to the launch pad on October 29, 1965, and mated to the launch vehicle/service module stack.

The launch-escape tower was shipped on October 7, 1965, and received at the VAB on October 10, 1965. Launch-escape subsystem (LES) build-up was completed on October 20, 1965. The hard boost protective cover and LES were mated to the command module on October 30, 1965. On November 22, 1965, the soft boost protective cover was installed to complete the assembly of the spacecraft.

The simulated countdown was completed on November 30, 1965. At the Flight Readiness Review, December 3, 1965, the spacecraft and launch vehicle were declared ready for a December 8, 1965, launch, pending

investigation of a reported failure of a LJ II attitude control subsystem logic and control unit.

The subsequent investigation revealed faulty solder connections. As a result of this, on December 4 the launch was cancelled and rescheduled for December 18 in order to correct and requalify LJ II.

During a telephone Flight Readiness Review on December 17, the Flight Readiness Review Board was advised that the LJ II launch vehicle was unacceptable for flight, and the scheduled December 18 launch was cancelled. After a series of planning meetings between the launch vehicle contractor and NASA, the launch was rescheduled for January 18, 1966. A chronological history of activities related to the launch vehicle logic and control units is presented in table 10.1-II.

At the Flight Readiness Review conducted January 14, 1966, the spacecraft and launch vehicle were declared ready for launch. On January 18 launch was rescheduled for January 20, 1966, because of bad weather. Launch was satisfactorily completed January 20, 1966, at 8:17:00.776 a.m. m.s.t.

TABLE 10.1-I.- OPERATIONAL CHECKOUT PROCEDURES FOR MISSION A-004

OCP number	Title	Date completed
Spacecraft		
A-9030	GSE installation and checkout	Oct. 13, 1965
A-2013	LES build-up	Oct. 20, 1965
A-3038	LES weight and balance	Oct. 16, 1965
	SM receiving inspection	Oct. 19, 1965
	SM build-up	Oct. 22, 1965
A-3023	SM-IV mate	Oct. 23, 1965
	CM receiving inspection	Oct. 9, 1965
A-3027	Top deck build-up	Oct. 21, 1965
A-3035	Horizontal weight and balance	Oct. 22, 1965
A-3036	Vertical weight and balance	Oct. 25, 1965
A-3039	Thrust vector alignment	Oct. 27, 1965
	Quality control shakedown	Oct. 28, 1965
A-3015	SM-CM-LES mate	Oct. 30, 1965
	Antenna checkout	Nov. 5, 1965
A-10002	Cable up for SC checkout	Nov. 4, 1965
	Open item review	Nov. 4, 1965
A-0100	Spacecraft systems checkout	Nov. 8, 1965
	Install BPC	Nov. 22, 1965
	Pyro checkout and no-voltage check	Jan. 5, 1966
	Tape recorder checkout	Jan. 6, 1966

TABLE 10.1-I. - OPERATIONAL CHECKOUT PROCEDURES

FOR MISSION A-004 - Continued

OCP number	Title	Date completed
Spacecraft - concluded		
A-10002	Preparation of systems checkout	Jan. 6, 1966
	Systems checkout	Jan. 7, 1966
	Data review	Jan. 10, 1966
	Quality control shakedown	Jan. 11, 1966
	Battery preparation	Jan. 14, 1966
Launch vehicle		
A-85173	Facility installation and checkout	July 30, 1965
	Receiving inspection	Oct. 15, 1965
	Flight component testing	Jan. 18, 1966
	Vehicle build-up	Nov. 2, 1965
	Fin checkout and installation	Nov. 1, 1965
	Open item review	Oct. 22 and Nov. 18, 1965
	Launch vehicle systems checkout	Oct. 28, Nov. 4, 12, and 17, 1965
	Receive and functional test instruction L & C and 799 monitor box	Jan. 7, 1966
12-83132 12-83133	Checkout sensors and L & C unit	Jan. 9, 1966
12-83131	Integrated checkout attitude control system	Jan. 10, 1966

TABLE 10.1-I.- OPERATIONAL CHECKOUT PROCEDURES

FOR MISSION A-004 - Concluded

OCP number	Title	Date completed
Launch vehicle - concluded		
12-83116	Data review	Jan. 12, 1966
	Quality control shakedown and open item review	Jan. 12, 1966
	Service fins	Jan. 12, 1966
	Battery preparation	Jan. 11, 1966
Spacecraft-launch vehicle		
A-10002	Interface/integrated preparations	Nov. 19, 1965
A-1099	Interface/integrated test	Nov. 22, 1965
A-1099	Data review	Nov. 23, 1965
A-1099	Quality control shakedown	Nov. 24, 1965
A-1099	Open item review	Nov. 29, 1965
A-0010 (simulated)	Simulated countdown	Nov. 30, 1965
	FRR	Dec. 3, 1965
	Simulated countdown	Jan. 13, 1966
	Data review and FRR	Jan. 14, 1966
	Final systems checks	Jan. 16, 1966
	Closeout	Jan. 17, 1966
	Countdown (rescheduled)	Jan. 18, 1966
	Countdown	Jan. 20, 1966

TABLE 10.1-II. - PROBLEM HISTORY OF LAUNCH VEHICLE

Date	Unit status
Nov. 30, 1965	Logic and control (L&C) unit SN-6 failed function test inspection (FTI) at WSTF.
Dec. 2, 1965	L&C unit SN-6 failure verified at San Diego.
Dec. 3, 1965	FRR conducted at WSTF.
Dec. 3, 1965	Failure analysis of SN-6 completed at San Diego.
Dec. 3, 1965	NASA informed of failure analysis results.
Dec. 5, 1965	Method of failure resting resolved and reverification required on SN-4.
Dec. 6, 1965	L&C unit SN-4 removed from the launch vehicle and exhibited the same problem as SN-6.
Dec. 7 to 9, 1965	Failure cause and corrective action accomplished. L&C unit SN-4 repaired and reverification tests started.
Dec. 10, 1965	L&C unit SN-4 reverification completed and the unit returned to WSTF for FTI.
Dec. 11, 1965	L&C unit SN-4 installed in the vehicle, OCP 12-83133 started, and an intermittent fluctuation noted.
Dec. 12, 1965	Troubleshooting started with no significant conclusions.
Dec. 13, 1965	Troubleshooting appeared to isolate the problem to the yaw attitude amplifier. After replacement, another intermittent fluctuation was noted with different characteristics.
Dec. 14, 1965	Troubleshooting appeared to isolate the problem to the L&C unit $\pm 15$ V dc power supply and L&C unit SN-7 was shipped from San Diego.

TABLE 10.1-II. - PROBLEM HISTORY OF LAUNCH VEHICLE - Continued

Date	Unit Status
Dec. 15, 1965	Parts of SN-4 and SN-7 installed in SN-7 which was reverified and reinstalled in the vehicle.
Dec. 16, 1965	OCP 12-83133 started and successfully completed.
Dec. 17, 1965	Pre-count successfully completed.
Dec. 17, 1965	FRR held by telephone; mission postponed.
Dec. 18, 1965	NASA-Contractor meeting at MSC; rescheduled mission for mid-January with minimum rework to logic and control unit and instrumentation system.
Dec. 22, 1965	NASA-Contractor meeting at MSC; scheduled mission for January 19; defined detail tasks to be accomplished.
Dec. 23, 1965	New launch data of January 18, 1966 established.
Dec. 28 and 29, 1965	Instrumentation wiring checkout completed.
Dec. 29, 1965 to Jan. 7, 1966	TZ-5 box modification, amplifier failure, and TZ-5 box function acceptance.
Jan. 6, 1966	L&C unit SN-7D received at WSTF, and FTI complete.
Jan. 7, 1966	OCP 12-83132 completed.
Jan. 8, 1966	OCP 12-83133 started and 799 box power supply problem found.
Jan. 9, 1966	OCP 12-83133 completed.
Jan. 9, 1966	OCP 12-83131 completed, but review of data disclosed improperly adjusted roll gains.
Jan. 10, 1966	OCP 12-83133 rerun and successfully completed. OCP 12-83131 successfully completed.

TABLE 10.1-II.- PROBLEM HISTORY OF LAUNCH VEHICLE - Concluded

Date	Unit status
Jan. 11, 1966	Complete data review confirmed successful completion of testing.
Jan. 13, 1966	Simulated countdown successfully completed.
Jan. 14, 1966	Final FRR conducted at WSTF.



## 10.2 Launch Procedure

Final preparation for launch, including countdown, was divided into three operations as indicated in figures 10.2-1 to 10.2-4. The overall operation is shown in figure 10.2-1. The first operation included final system checks, stray voltage checks, and installation of all vehicle pyrotechnic initiators. The second operation included close-out of the command module, service module, and launch-escape subsystem, and the hydraulic and gaseous nitrogen servicing for the Little Joe II attitude control subsystem. The third operation included arming of the total vehicle, gantry removal, launcher positioning, and the terminal portion of the countdown. The terminal portion of the countdown was stopped approximately 1 hour before launch on January 18, 1966, because of bad weather. The launch was rescheduled to January 20, 1966.

Operation 1. - The final system checkout included detailed telemetry checks, C-band radar beacon checks, launch-vehicle autopilot checks, range-safety and RF command system checks, and finally, a simulated mission with all onboard systems active (see fig. 10.2-2 and OCP-0010). All support radars and transmitters used for flight were turned on and directed toward the launch pad. The results of this testing were satisfactory. The power-on stray voltage checks of all vehicle firing lines with all systems, radars, and transmitters on were satisfactory.

When the absence of stray voltage had been verified, the ordnance installation began. Algol and Recruit motor initiators were installed, and shorting plugs were connected to all units. All spacecraft initiators were installed and firing lines were connected to them, except for the initiators for the tower-jettison and launch-escape motors.

Operation 2. - Spacecraft closeout began immediately after completion of operation 1, and was completed satisfactorily. (See fig. 10.2-3.) Major tasks are listed in table 10.2-I. The servicing of launch-vehicle systems following spacecraft closeout progressed without incident. The gaseous nitrogen top-off concluded operation 2.

Operation 3. - Upon verification that controlled radiation was of a safe level, tower-jettison and launch-escape motors were armed (see fig. 10.2-4 and OCP-0010). The flight safety crew (WSMR personnel) then closed out the range safety system. No problems were encountered and the launch pad was cleared. The launch vehicle crew then armed the second-stage motors, finished the operation on schedule, and all personnel cleared the pad area for a complete vehicle power-up.

After system checks, all power was turned off and the gantry was removed. Power was applied to the launcher and the launcher was rotated to the firing position of  $348.29^\circ$  azimuth and a launch angle

of 84°. The launch pad was then cleared for launch vehicle power-up and first-stage arming.

Final checks of the spacecraft and launch-vehicle systems continued through T-15 minutes, at which time a hold was called because of bad weather. At 8:30 a.m. m.s.t. on January 18, 1966, the mission was rescheduled for 3:00 p.m. m.s.t. the same day. Later the mission was rescheduled for 8:00 a.m. m.s.t. January 20, 1966. Launch vehicle ordnance personnel then installed shorting plugs to all initiators, and flight safety personnel disarmed the range safety system. The spacecraft remained in ready condition.

Launch procedure was resumed on January 20, 1966 (fig. 10.2-4). The count proceeded satisfactorily until T-3 minutes. At this time the range called a hold because two of the seven telemetry ground stations were unable to support launch. With five telemetry stations supporting the launch, the count was resumed. Launch was completed at 8:17 a.m. m.s.t.

TABLE 10.2-I.- MAJOR TASKS OF SC-002 SPACECRAFT CLOSE-OUT

Service module close-out
<ul style="list-style-type: none"> <li>(a) Remove instrumentation orifice covers</li> <li>(b) Quality control final review</li> <li>(c) Install SM hatch</li> </ul>
Command module close-out
<ul style="list-style-type: none"> <li>(a) Install batteries and safety wire switch</li> <li>(b) Remove instrumentation orifice covers</li> <li>(c) Install CM camera system</li> <li>(d) Quality control final review</li> <li>(e) Install CM hatch</li> <li>(f) Install boost protective cover hatch</li> <li>(g) Pot screw holes in boost protective cover</li> </ul>
Launch-escape subsystem close-out
<ul style="list-style-type: none"> <li>(a) Install camera system</li> <li>(b) Remove nozzle covers</li> <li>(c) Install and pot remaining tower leg covers</li> </ul>
GSE securing and pad clean-up
<ul style="list-style-type: none"> <li>(a) Remove pyrotechnic simulators</li> <li>(b) Stow or remove all loose items from gantry</li> <li>(c) Sand bag junction boxes</li> <li>(d) Clean up pad and gantry</li> </ul>

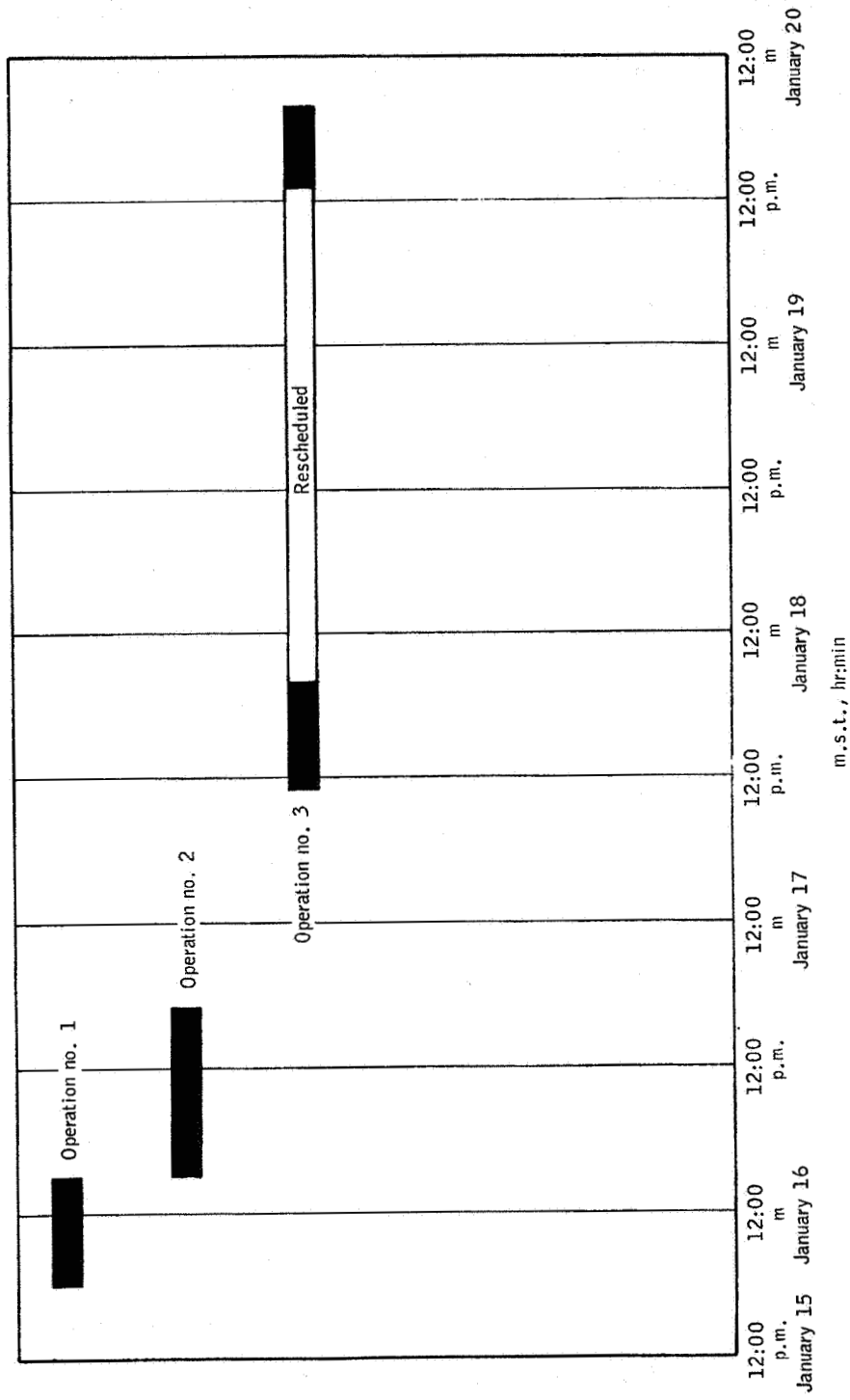


Figure 10.2-1.- Final preparation and countdown schedule, Apollo Mission A-004.

NASA-S-66-3702 APR 15

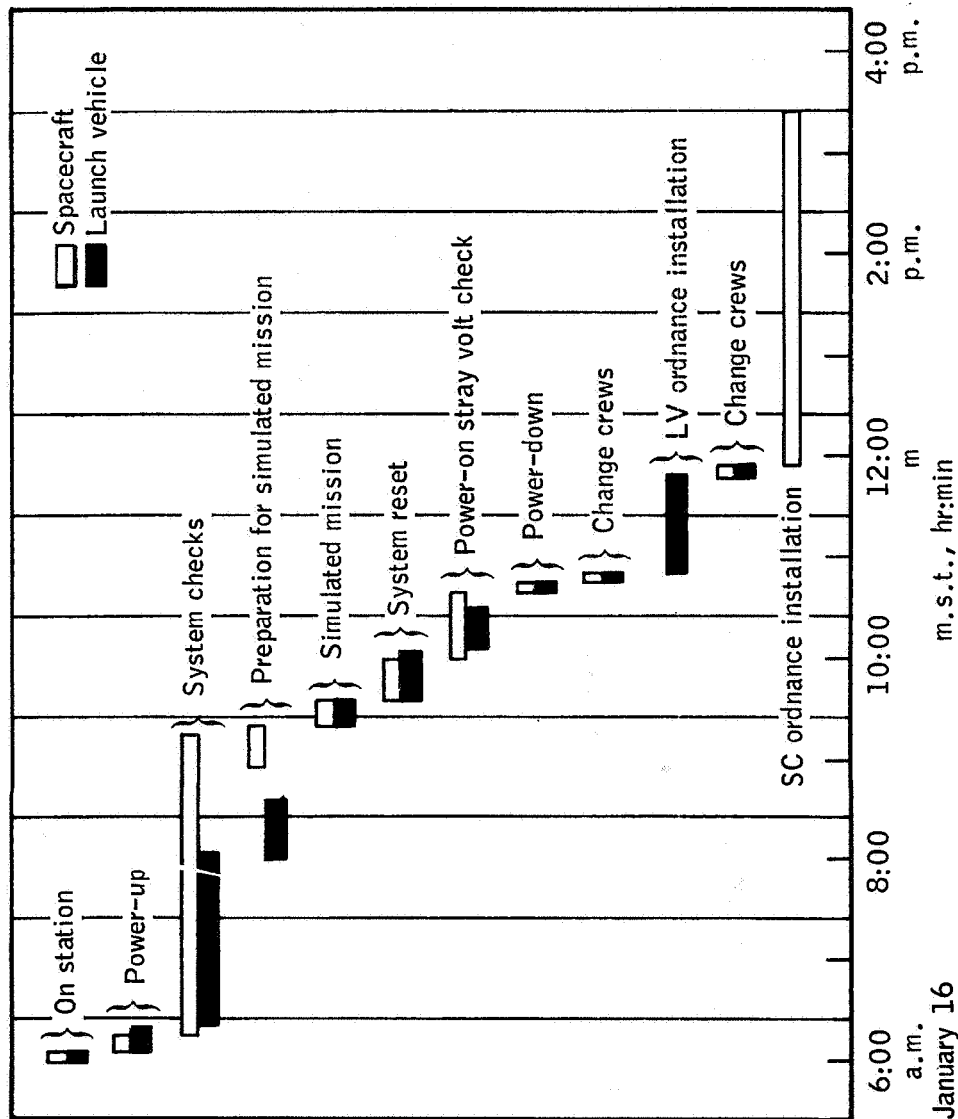


Figure 10.2-2.- Final preparation and countdown schedule of operation no. 1, Apollo Mission A-004.

NASA-S-66-3706 APR 15

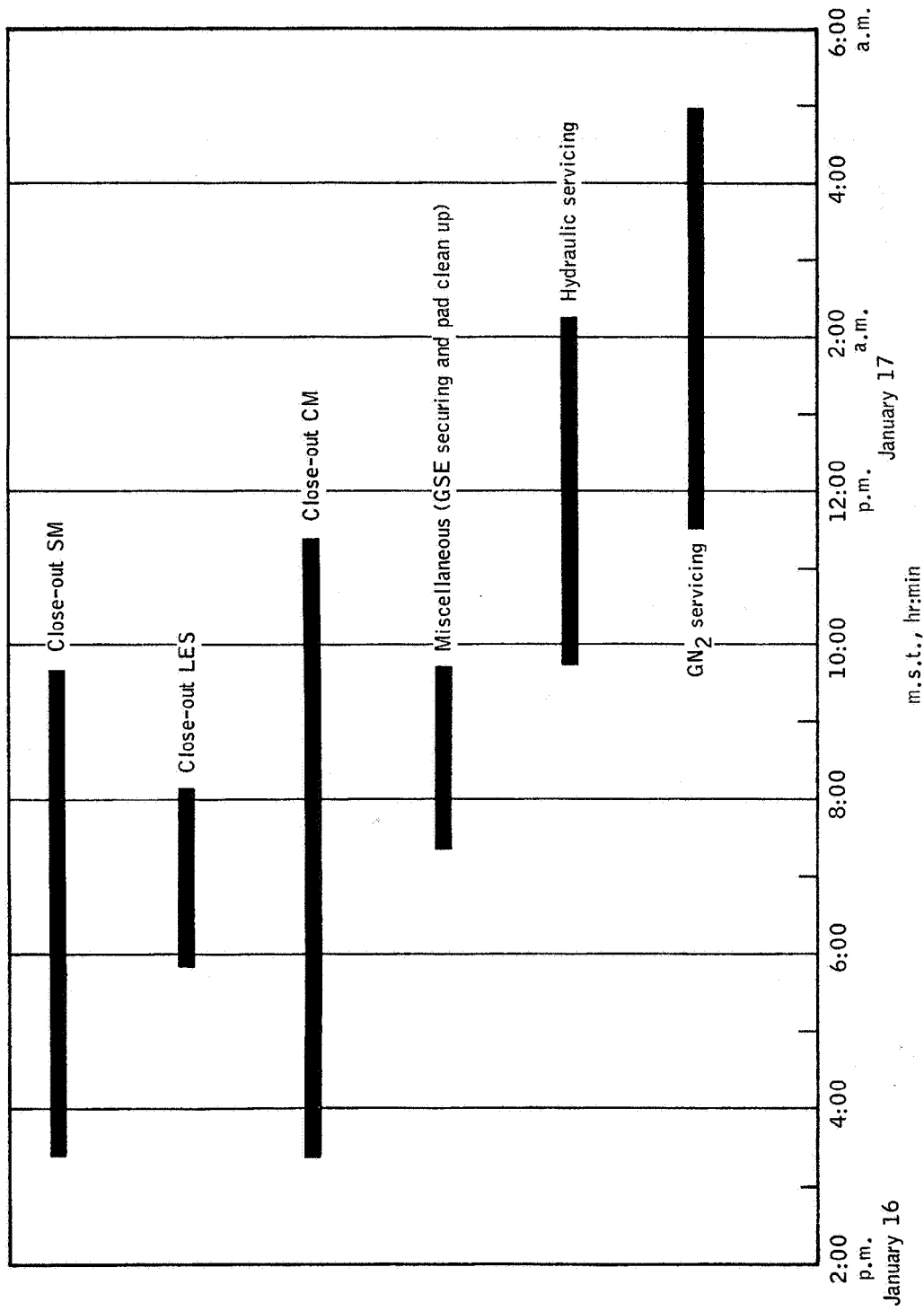


Figure 10.2-3.- Final preparation and countdown schedule of operation no. 2, Apollo Mission A-004.

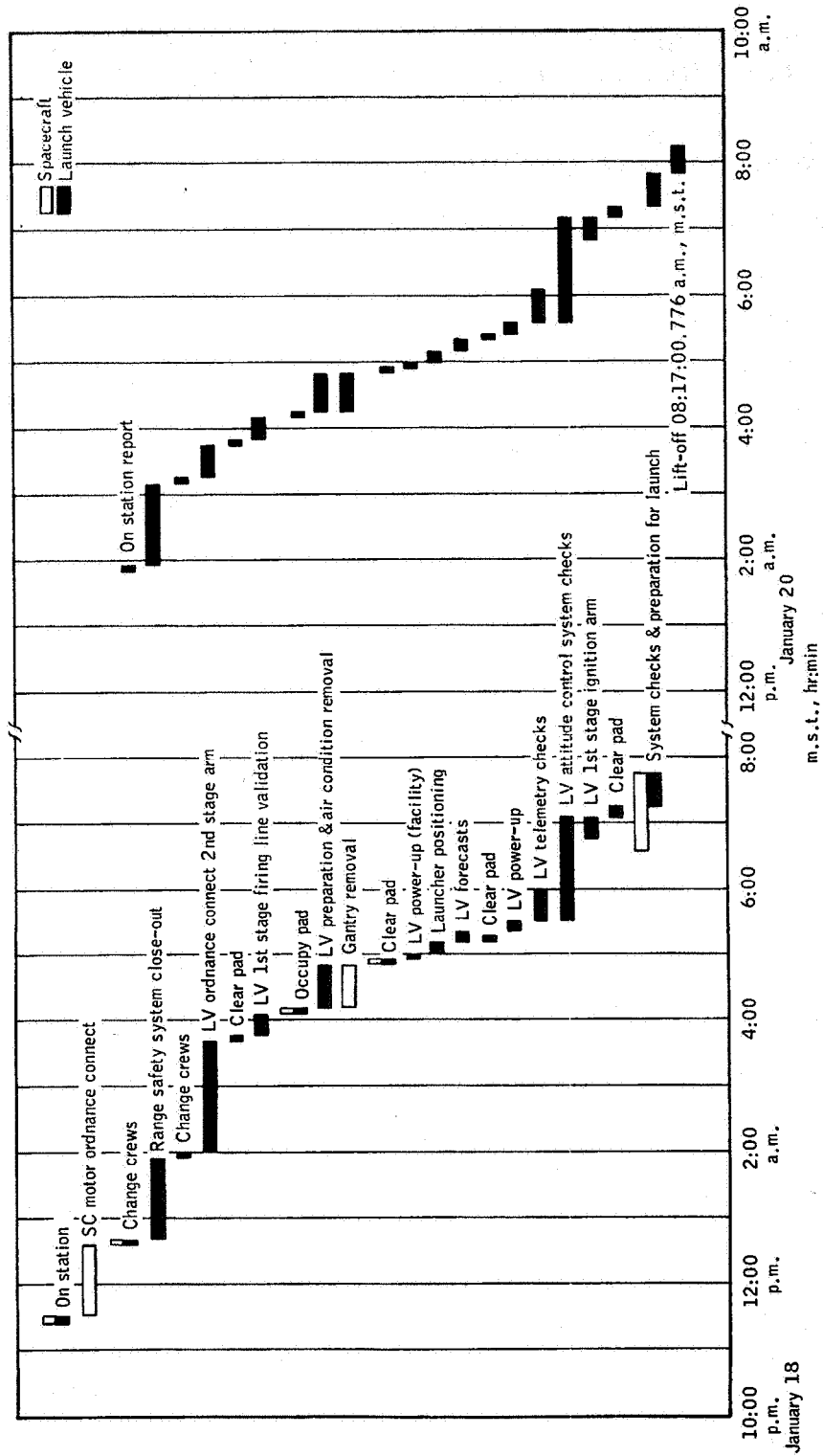


Figure 10.2-4. - Final preparation and countdown schedule of operation no. 3, Apollo Mission A-004.

### 10.3 Real-Time Data System

The configuration of the White Sands Missile Range (WSMR) real-time data system (RTDS) to support Mission A-004 consisted of the following:

- (a) Two FPS-16 radars at C station
- (b) Two FPS-16 radars at site King I
- (c) An IBM 7094 II computer and its output display devices in building 1512
- (d) Digital data links from the radars to the computer
- (e) Lift-off signal from the launcher to the computer
- (f) Timing signals to the computer and the radars
- (g) WSMR Telemetry Ground Station, Jig-3

Displays provided to the Flight Dynamics Officer for control of the mission included four plotboards, one digital panel, and one sweep-second-hand "plus time" clock. The plotboards displayed the following information:

- (a) Flight-path angle plotted against altitude (plotboard A)
- (b) Dynamic pressure plotted against Mach number (plotboard B)
- (c) Crossrange plotted against downrange (plotboard C)
- (d) Altitude plotted against downrange (plotboard C)
- (e) Acceleration (RTDS) plotted against time (plotboard D)
- (f) Acceleration (telemetry) plotted against time (plotboard D)

The digital display panel indicated time, altitude, Mach number, dynamic pressure, and flight-path angle. The sweep-second-hand "plus time" clock, which was started by a lift-off signal from the launcher, provided elapsed time.

Checkout and qualification testing of the real-time data system for support of Mission A-004 was conducted from the first part of October, 1965 to the end of November, 1965. The system was requalified during the first week of January, 1966. The Computer Augmented Trajectory Simulator (CATS) program provided a method of testing the



real-time data system under conditions closely approximating the expected trajectory of Mission A-004. Final testing of the RTDS was conducted during the launch countdown at T-45 minutes, utilizing fly-by aircraft equipped with C-band beacon. The aircraft made three passes and completed the prelaunch testing 3 minutes prior to the allotted time.

The RTDS was the prime reference for initiating the pitch-up maneuver during Mission A-004. All phases of the real-time data system performed satisfactorily. The data were also used in connection with the quick-look and final analysis of the flight (see section 4.0).

#### 10.4 Range Operations

The White Sands Missile Range (WSMR) provided communications, range timing, radio-frequency radiation controls, optical tracking, radar tracking, telemetry, documentary photography, meteorological data, and geodetic survey in support of Apollo Mission A-004. Support similar to that given previous Apollo abort CSM developmental missions included the following:

The range command ready-hold network provided the formal communication channel between range users and range operating personnel for transmitting range readiness and countdown information.

The telemetry network linked all range telemetry stations with the telemetry systems controller and a NASA representative located in the blockhouse at Launch Complex 36 (LC 36). Prelaunch calibrations and telemetry requirements were also coordinated over this network.

The flight-control network consisted of five stations linked together to relay launcher positioning coordinates, real-time data system performance, meteorological conditions, and inflight events observed by the visual observers.

The missile flight surveillance network included intercommunications between personnel in the LC 36 blockhouse, FRW-2 transmitter, radar display room in C station, data display room in technical center building 1512. The network was used for checkout of the abort commands and the range-safety subsystem.

Extension radio and telephone facilities were provided for recovery and general support of the mission.

A tape recording of the Time Announcer, Test Director, Flight Dynamics Officer, and the spacecraft, launch vehicle, telemetry, and range isolation networks was made on a 9-channel tape recorder located in the blockhouse. The recording was retained at WSTF.

Range-timing distribution stations for IRIG timing was provided to LC 36 on a 24-hour basis. The test vehicle lift-off signal triggered the start of the "plus" time from lift-off clocks and reset the frame counters on cinetheodolite cameras in order to correlate the data film easily. The timing system performed satisfactorily. The times recorded by the timing generator at lift-off were as follows:

20 days 15 hours 17 minutes 0.776 second, G.m.t.

20 days 8 hours 17 minutes 0.776 second, m.s.t.

Radio frequency (RF) electromagnetic radiation control was maintained during the interface-integrated test, simulated countdown, final systems checks, and countdown to prevent interference with the RF systems of the mission, and to prevent a concentration of RF energy on the launch pad during installation of pyrotechnic devices.

Radar support was provided for the real-time data system, interface-integrated test, simulated countdown, final systems checks, and countdown. FPS-16 (C-band) radars located throughout the range were used to support the mission flight requirements. Four radars were used to track the beacons and one each to skin-track the launch vehicle and the LES. Figure 10.4-1 shows the location of the radar stations used to support the flight.

Telemetry support was provided by WSMR for the integrated-interface test, simulated countdown, final systems checks, and for the flight. Real-time and playback telemetry information was provided during the flight by range telemetry stations. Seven range stations were used. Data were provided by all seven stations from T-2 to T+75 seconds, at which time the spacecraft telemetry antenna failed.

At T-3 minutes during the final countdown to launch, a hold was called by WSMR because of an amplifier failure at telemetry station Jig 56. Both Jig 56 and Jig 3 were unable to support the mission. (Jig 56 was a relay station for Jig 3). WSMR reported that the duration of the hold would be approximately 5 minutes. Both stations were ready to support the mission prior to the actual launch.

In addition to the range telemetry stations, the NASA telemetry station located at LC 36 also recorded flight telemetry.

The original telemetry tapes, and a copy of each, were forwarded to MSC-Houston for data reduction.

Two television cameras, one located approximately 2000 feet southeast of the launcher and the other located on Mule Peak approximately 40 miles northeast of the launcher, provided real-time tracking information to three monitors in the LC 36 blockhouse and at MSC-Houston. The television monitors and cameras performed satisfactorily. Clouds hampered tracking; therefore coverage was intermittent throughout the flight. Television camera locations are shown in figure 10.4-2. Pre-flight and postflight documentary photography for engineering analysis was supplied by the range. Various 16-mm film copies and still prints were furnished.

Optical coverage was limited during portions of the flight due to cloud cover which prevented some stations from complete mission tracking. Generally, stations downrange were unable to obtain coverage.

At the time of actual launch, an optical limitation of 70 to 80 percent deterioration was reported by WSMR for the launch area. The optical instrumentation systems which were used and the evaluation of the films provided are presented in tables 10.4-I to 10.4-III. Optical station locations are shown in figure 10.4-2.

General weather forecasts were reported at 12-hour intervals and 1-week specific forecasts were provided as described in section 10.5.

The U.S. Coast and Geodetic Survey made location surveys of impact locations of the recovered components of the vehicle on December 20 and 21, 1965.

TABLE 10.4-I.- RANGE EVALUATION OF FILM COPIED FOR MSC

Station	Type	Focal length, mm	Frame rate, frames/sec	Film	Object tracked	Time coverage, sec	Quality		Remarks
							Images	Film	
Fixed camera									
0199 at 1195F	35mm	5	500	Color	Lift-off	0 to 2.2	Good	Good	Good fin position at lift-off and launch vehicle paint patterns
1099 at 1198F	35mm	5	1000	Color	Lift-off	Film jammed	--	--	Good lift-off
Cinetheodolites									
G-30	Contraves	60	20	Black & white	CM	1.6 to 186.7	Blurred	Dark	Fair LJ II descent
G-101	Contraves	60	30	Color	LJ II	2.0 to 187.0	Good	Fair	Good ignition, lift-off, boost phase, and abort
G-102	Contraves	60	20	Black & white	CM	1.6 to 92.0	Fair	Dark	Good boost phase and abort
G-109	Contraves	60	20	Color	LES	0 to 143	Fair	Fair	Good boost phase, boost protective cover break-up, LEV tumble, fair canard deployment
F-110	Contraves	60	20	Color	LES	1.0 to 156	Small, blurry	Fair	Good boost phase and LEV tumbling, fair pitch-up and abort
F-154	Contraves	60	20	Black & white	LES	2 to 83	Out of focus	Dark	Fair lift-off, boost phase, and abort

TABLE 10.4-I. - RANGE EVALUATION OF FILM COPIED FOR MSC - Continued

Station	Type	Focal length, mm	Frame rate, frames/sec	Film	Object tracked	Time coverage, sec	Quality		Remarks
							Images	Film	
Telescopes									
T-2 at T-2		90	60	Color	CM	36.0 to 409.0	Good	Fair	Good LJ II impact
T-9 at T-9		96	60	Color	CM	3 to 409	Good	Good	Good abort, launch-escape motor ignition, tower descent, CM descent on main parachute
T-154 at T-154		20	250	Black & white	Test vehicle	58 to 95	Good to poor	Fair	Good abort, Fair boost phase
T-154 at T-154		91	60	Color	Test vehicle	No timing	--	--	Fair boost phase, good LEV tumbling and canard deployment
T-155 at T-155		48	60	Color	LJ II	0 to 92	Good	Fair	Fair lift-off, good boost phase and paint patterns, pitch-up, abort, and SM break-up
T-198 at T-198		96	60	Color	CM	0 to 126	Very good	Very good	Good Recruit and Algol ignition, lift-off, paint patterns, fin positions, boost phase, pitch-up and abort, LEV tumbling, canard deployment, tower descent, fair CM on drogue parachutes
MT 1-1 at T-2		72	60	Color	LJ II	261 to 410	Fair	Very dark	Good LJ II descent and impact
MT 1-2 at T-2		40	250	Color	CM	280 to 416	Good	Good	Fair LJ II impact

TABLE 10.4-I.- RANGE EVALUATION OF FILM COPIED FOR MSC - Concluded

Station	Type	Focal length, mm	Frame rate, frames/sec	Film	Object tracked	Time coverage, sec	Quality		Remarks
							Images	Film	
Telescopes - concluded									
MT 1-2 at T-12		40	250	Color	LES	No report	--	--	Good CM on main parachutes, CM paint patterns, CM impact, fair CM upper deck
MT 1-2 at T-12		92	60	Color	CM/LES	280 to 416	Good	Good	Good CM on main parachutes
MT-45 at T-12		40	250	Color	CM/LES	No timing	--	--	Fair LES tower descent and impact, CM descent on main parachutes, CM color patterns, CM impact
MT-153 at T-12		48	250	Color	CM	290 to 366	Good	Fair	Poor CM on main parachutes and LES tower descent
MT-190 at T-318		90	60	Color	LJ II	4 to 209	Fair to good	Fair	Fair boost phase, good abort, LES motor ignition, and LEV tumbling

10-24

TABLE 10.4-II. - RANGE EVALUATION OF FILM NOT COPIED FOR MSC

Station	Type	Focal length, mm	Frame rate, frames/sec	Film	Object tracked	Time coverage, sec	Quality	
							Image	Film
Fixed camera								
F-1195	70mm	80	60	Color	Lift-off	Film jam and break		
F-1196	70mm	80	60	Color	Lift-off	Film jam	Poor	
F-1197	70mm	80	60	Color	Lift-off		Timing poor	
F-1198	70mm	80	60	Color	Lift-off	0 to 2.2	Good	Good
0499 at 1196F	35mm	5	500	Color	Lift-off	Timing jumbled	Good	Good
0799 at 1197F	35mm	5	500	Color	Lift-off	0 to 2.0	Good	Good
1099-1F at F1198	35mm	14	500	Color	Umbilical retraction	Good	Too hazy on launcher	
1099-2F at F-1198	35mm	14	500	Color	Elevon 4 action			
0499 at F-1196	35mm	6	60	Infrared	Flame	0 to 1.7	Good	Good
0799 at F-1197	35mm	6	60	Infrared	Flame	Jumbled	Fair	Fair
Cinetheodolites								
G-5	Askania	47	5, 1 <sup>a</sup>	Black & white	LJ II	No timing		
G-34	Askania	47	5, 1 <sup>a</sup>	Black & white	CM	37 to 231	Small	Dark
G-37	Askania	47	5, 1 <sup>a</sup>	Black & white	LES	16 to 229	Hazy	Fair
G-38	Askania	47	5, 1 <sup>a</sup>	Black & white	LES	13 to 229	Fair	Dark
G-39	Askania	47	5, 1 <sup>a</sup>	Black & white	CM	131 to 229	Fair	Fair
G-40	Askania	47	5, 1 <sup>a</sup>	Black & white	CM	12 to 228	Out of focus	Fair
G-41	Askania	47	5, 1 <sup>a</sup>	Black & white	LES	Not usable		

<sup>a</sup> 5 frames/sec to 225 seconds. After 225 seconds, track CM at 1 frame/sec.



TABLE 10.4-II. - RANGE EVALUATION OF FILM NOT COPIED FOR MSC - Continued

Station	Type	Focal length, mm	Frame rate, frames/sec	Film	Object tracked	Time coverage, sec	Quality	
							Image	Film
Cinetheodolites - concluded								
G-43	Askania	47	5, 1 <sup>a</sup>	Black & white	LJ II	Too much cloud cover		
G-46	Askania	47	5, 1 <sup>a</sup>	Black & white	LJ II	110 to 128	Poor	Fair
G-50	Askania	47	5, 1 <sup>a</sup>	Black & white	LJ II	60 to 125	Blurry	Fair
G-137	Askania	47	5, 1 <sup>a</sup>	Black & white	LES	2 to 65	Fair	Dark
G-138	Askania	47	5, 1 <sup>a</sup>	Black & white	LES	223 to 349	Fair	Fair
G-149	Askania	47	5, 1 <sup>a</sup>	Black & white	CM	68 to 225	Hazy, blurred	Fair
G-150	Askania	47	5, 1 <sup>a</sup>	Black & white	CM			
G-32	Contraves	60	30	Black & white	CM	1.1 to 114.0	Small, faint	Light
G-81	Contraves	60	20	Black & white	CM	1.0 to 316.0	Small, faint	Dark
G-108	Contraves	60	20	Color	LJ II	Film break		
F-111	Contraves	60	20	Color	CM	Film break		
F-152	Contraves	60	20	Color	CM	0 to 108	Small, blurred	Fair
Telescopes								
T-2 at T-2		40	250	Color	CM	243 to 261	Fair	Dark
T-7 at T-7		90	250	Color	Test vehicle	Film break		
T-11 at T-11		96	250	Color	CM	260 to 407	Good	Good
T-12 at T-12		96	60	Color	CM	288 to 411	Good	Good
T-126 at T-126		24	60	Color	CM	2.3 to 80.0	Fair	Fair

<sup>a</sup> 5 frames/sec to 225 seconds. After 225 seconds, track CM at 1 frame/sec.

10-26

TABLE 10.4-II. - RANGE EVALUATION OF FILM NOT COPIED FOR MSC - Continued

Station	Type	Focal length, mm	Frame rate, frames/sec	Film	Object tracked	Time coverage, sec	Quality	
							Image	Film
Telescopes - continued								
T-126 at T-126		60	60	Black & white	CM	70 to 159	Fair	Fair
T-128 at T-128		20	500	Color	LJ II	0 to 37	Fair	Fair
T-128 at T-128		48	60	Color	LJ II	0 to 89	Poor	Fair
T-155 at T-155		24	500	Black & white	Test vehicle	2.0 to 37.0	Good	Good
T-156 at T-156		48	60	Color	CM	50 to 412	Poor	Hazy
T-156 at T-156		24	250	Black & white	CM	103 to 183	No images	
T-167 at BATE		100	30	Color	CM	3 to 80	Small, blurry	Fair
T-167 at BATE		300	30	Color	CM	3 to 80	Small, blurry	Fair
T-197 at T-197		180	30	Black & white	CM	43 to 411	Poor focus	Poor
T-199 at T-199		199	96	Black & white	CM	313 to 327	Blurry	Poor
MT 1-1 at T-2		40	250	Color	LJ II	Poor timing		
MT 1-2 at T-2		71	60	Color	CM	351 to 409	Fair	Dark
MT 1-3 at T-2		40	250	Color	LEV/SM	294 to 311	Good	Dark
MT 1-3 at T-2		96	60	Color	LEV/SM	62 to 82	Fair	Fair
MT 1-1 at T-12		40	250	Color	LJ II	Poor timing		
MT 1-1 at T-12		80	60	Color	LJ II		No images	
MT-45 at T-12		72	60	Color	CM/LES	Film jam	No images	

TABLE 10.4-II. - RANGE EVALUATION OF FILM NOT COPIED FOR MSC - Concluded

Station	Type	Focal length, mm	Frame rate, frames/sec	Film	Object tracked	Time coverage, sec	Quality	
							Images	Film
Telescopes - concluded								
MT-127 at T-180		24	180	Color	LJ II		Fair	Fair
MT-127 at T-180		24	60	Infrared	LJ II	17.0 to 108.0	Fair	Fair
MT-151 at T-6		24	60	Infrared	LJ II	Film jam		
MT-151 at T-6		60	250	Black & white	LJ II	0 to 37	Good	Good
MT-152 at T-321		96	60	Color	LJ II	Did not run - mount trouble		
MT-152 at T-321		40	250	Color	LJ II	Did not run - mount trouble		
MT-153 at T-12		90	60	Color	CM	246 to 360	Good	Good
MT-173 at T-318		40	250	Color	CM	37.0 to 79.0	Off frame	Fair
MT-173 at T-318		60	60	Color	CM	3.6 to 84.6	Fair	Fair
MT-190 at T-318		48	250	Black & white	LJ II	64.0 to 117.0	Hazy, blurry	Fair

TABLE 10.4-III.- FILM EVALUATION OF BEST

## MOTION PICTURE COVERAGE FOR EVENTS

Events	Best available films for events
Algol ignition	G-101, T-198/T-198
Recruit ignition	T-198/T-198
Algol burn	G-101, T-198/T-198, RP-080
Lift-off	1099F, G-101, T-198/T-198, MSC 4969, RP-080
LJ II fin position	0199/1195, T-198/T-198
Test vehicle paint pattern	0199/1195, T-155/T-155, RP-080
Launch phase	G-101, G-102, G-109, G-110, T-198/T-198, MT-90/T318, RP-080
Staging	MSC 4969, RP-080
Pitch-up	G-101, T-155/T-155, T-198/T-198, RP-080
Abort	G-101, G-102, G-110, T9/T9, T-154/T-154, T-155/T-155, T-198/T-198, MT-190/318, RP-080
Soft boost protective cover break-up	G-109
LES motor ignition	T-9/T-9, MT-190/T-318
SM break-up	T-155/T-155, G-101
LEV tumble	G-109, G-110, T-154/T-154, T-198/T-198, MT-190/T-318, MSC 4969, RP-080
Canard deployment	T-154/T-154, T-198/T-198, T-190/318
LEV descent	T-198/T-198, T-9/T-9

TABLE 10.4-III.- FILM EVALUATION OF BEST  
MOTION PICTURE COVERAGE FOR EVENTS - Concluded

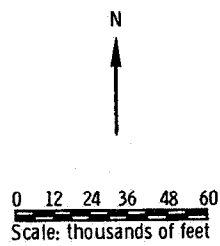
Events	Best available films for events
LJ II booster descent	MT-1-1/T-2, MT-1-2/T-2
CM on drogue parachutes	T-198
Drogue parachute disconnect	4972
CM on main parachutes	T-9/T-9, T-198/T-198, MT-1-2/T-12, MT-45/T-12, 4972, RP-080
CM paint pattern	MT-1-2/T-12, MT-45/T-12
CM landing	MT-1-2/T-12, MT-45/T-12, 4972, RP-080
Main parachute disconnect	4972, RP-080
LES tower descent	T-9/T-9, MT-45/T-12, MT-153/T-12, T-198/T-198
LES tower impact	MT-45/T-12, 4972
Apex cover descent	4972
Apex cover impact	4972
LJ II impact	T-2/T-2, MT-1-1/T-2, MT-1-2/T-2
Recovery film	4972, PAO, S66-75

Note: The following events were not photographed because of heavy cloud cover:

Tower jettison  
Drogue parachute deployment  
Pilot parachute deployment  
Main parachute deployment

10-30

NASA S-66-3714 APR 15



- Meteorological stations
- ⊙ Towers
- Telemetry stations
- ▣ NASA telemetry trailers
- ▤ Radar stations
- Launch complex 36
- ▲ CM landing
- ✱ Launcher L-224

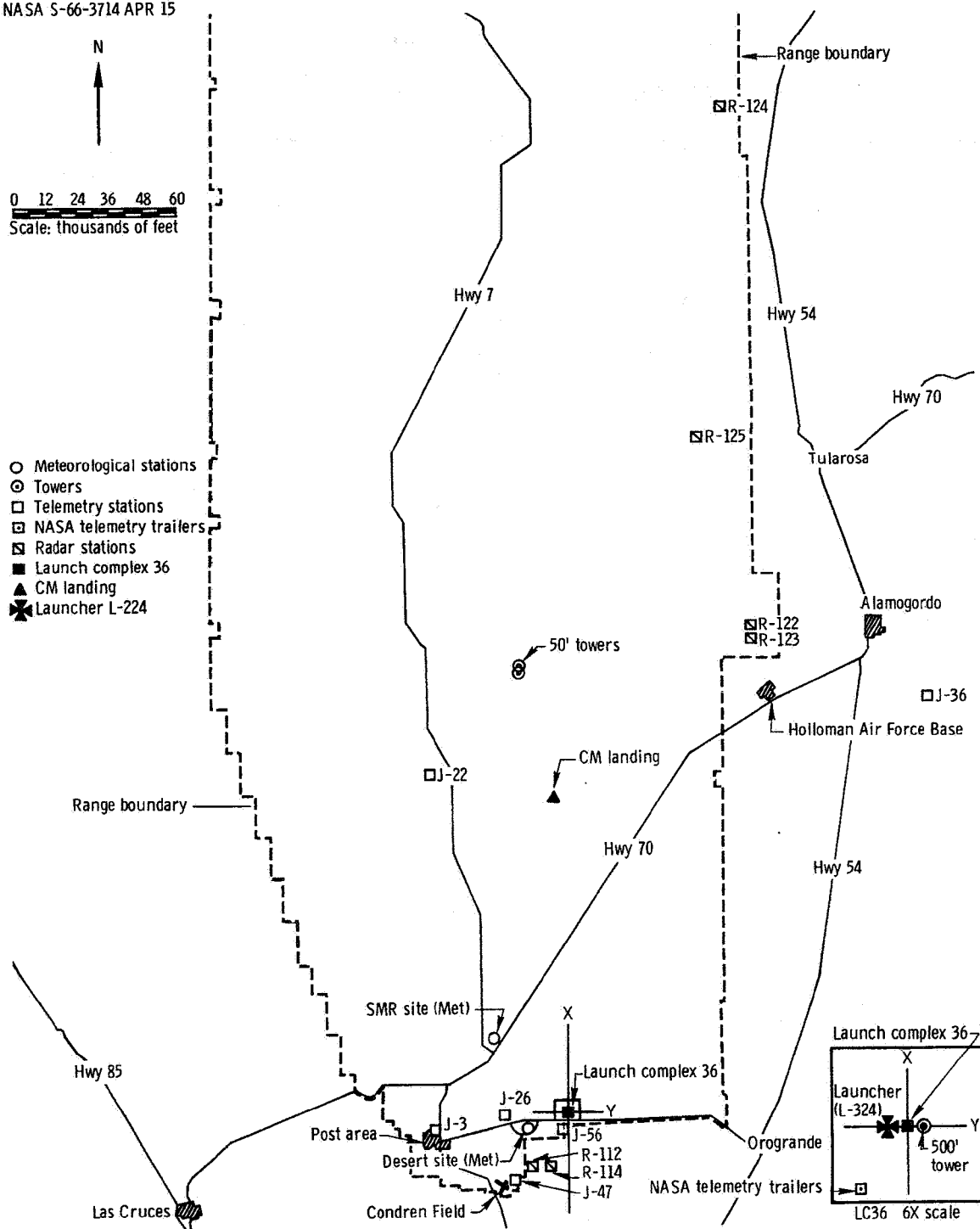


Figure 10.4-1. - Telemetry, meteorological, and radar station locations, Apollo Mission A-004.

NASA-S-66-3718 APR 15

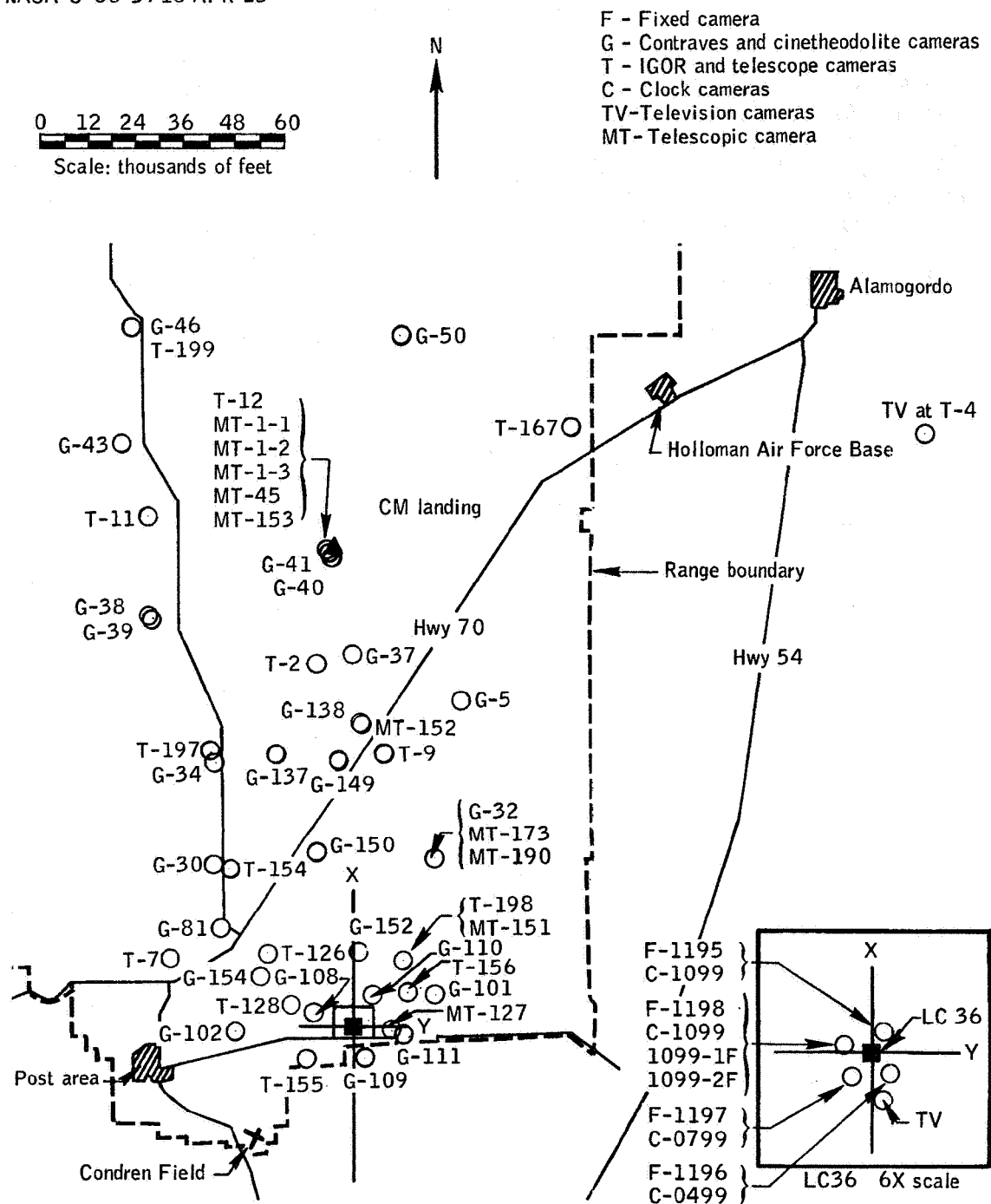


Figure 10.4-2.- Camera locations, Apollo Mission A-004.

### 10.5 Weather Conditions

Continuous weather forecasting service was provided to NASA by the WSMR Meteorological Support Office during the final 2 weeks prior to launch. The T-24 hour forecast for a January 18 launch indicated that cloud cover would be 100 percent. The countdown initiated for an 8:00 a.m. m.s.t. launch on January 18 was cancelled at 8:30 a.m. m.s.t. because of weather conditions and rescheduled for 8:00 a.m. m.s.t. on January 20. The T-24 hour forecast for a January 20 launch indicated no meteorological restrictions. The T-12 hour forecast of T = 0 conditions indicated a 0.1 to 0.2 (10 to 20 percent) cirrus condition.

Approximately 15 minutes before the planned launch time of 8:00 a.m. m.s.t., WSMR reported that a 20-percent deterioration could be expected in the quality of the optical data throughout the trajectory due to 0.1 to 0.2 (10 to 20 percent) cirrus cloud cover over the southern portion of the range. During the telemetry hold at T-3 minutes (which resulted in a 17-minute launch delay) cloud cover was moving rapidly into the southern portion of the planned trajectory. The 0.5 alto-cumulus condition continued through launch.

Prelaunch wind, pressure, and temperature measurements as a function of altitude were made from Rawinsonde releases from the Small Missile Range (SMR) at T-7 and T-4 hours and were provided to NASA Meteorological Officer for trajectory predictions. These data were also provided to NASA Flight Director Officer for use with the RTDS program. Additional wind measurements were provided to NASA Meteorological Officer from Pibal releases at T-1 hour and T-30 minutes. Wind measurements from the 500-foot tower located at LC 36 and two 50-foot towers located in predicted spacecraft landing area were provided to NASA Meteorological Officer as required for trajectory predictions and final launcher adjustments.

The T = 0 meteorological measurements for postflight analysis were reduced from data obtained by Rawinsonde released from the Small Missile Range at 8:20 a.m. m.s.t. and presented in increments from the surface (approximately 4000 feet m.s.l.) to 109 000 feet m.s.l. Wind direction and velocity, temperature, pressure, and relative humidity were measured. (See figs. 10.5-1 to 10.5-6.)



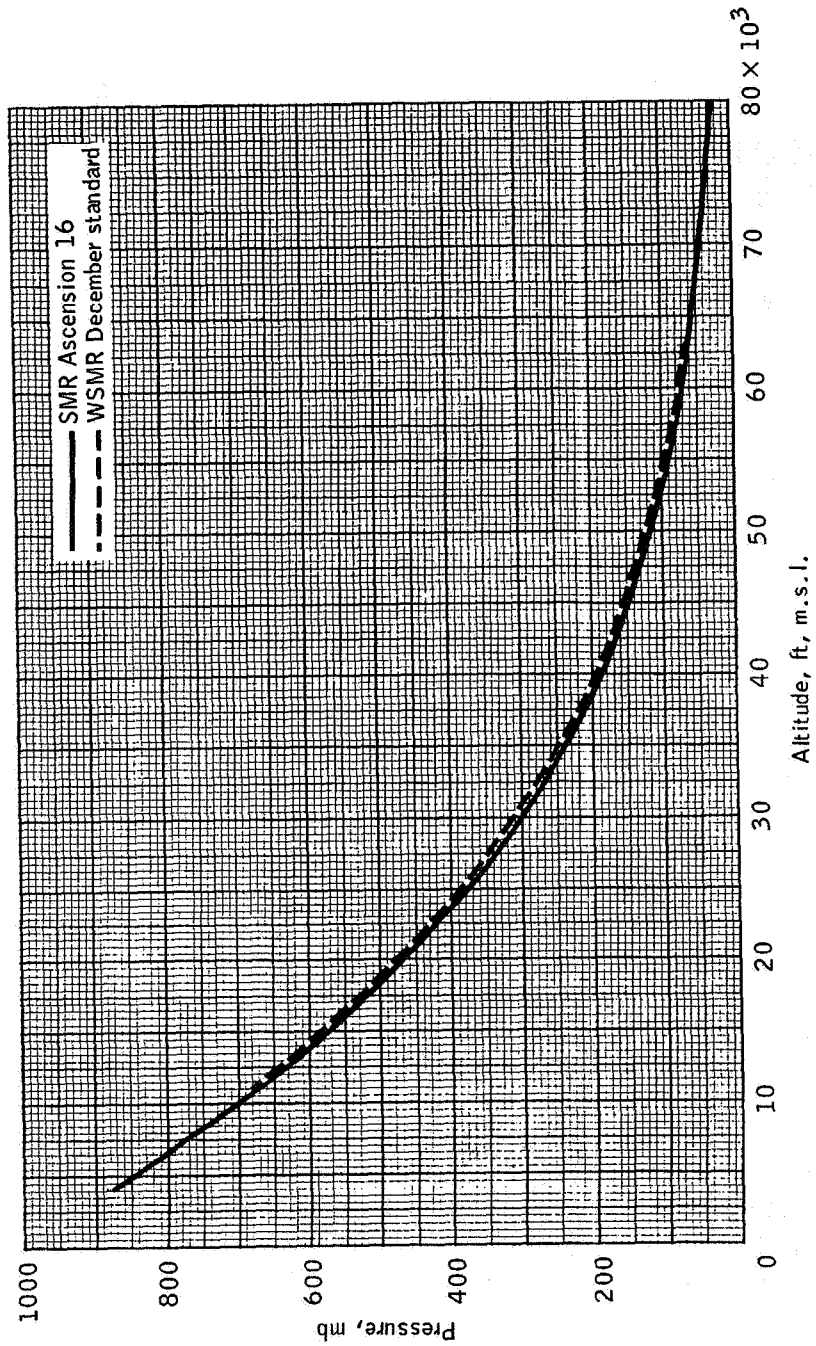


Figure 10.5-1.- Apollo Mission A-004 atmospheric pressure compared with WSMR December standard.  
(From Small Missile Range rawinsonde at 8:20 a.m. m.s.t. January 20)

NASA-S-66-3726 APR 15

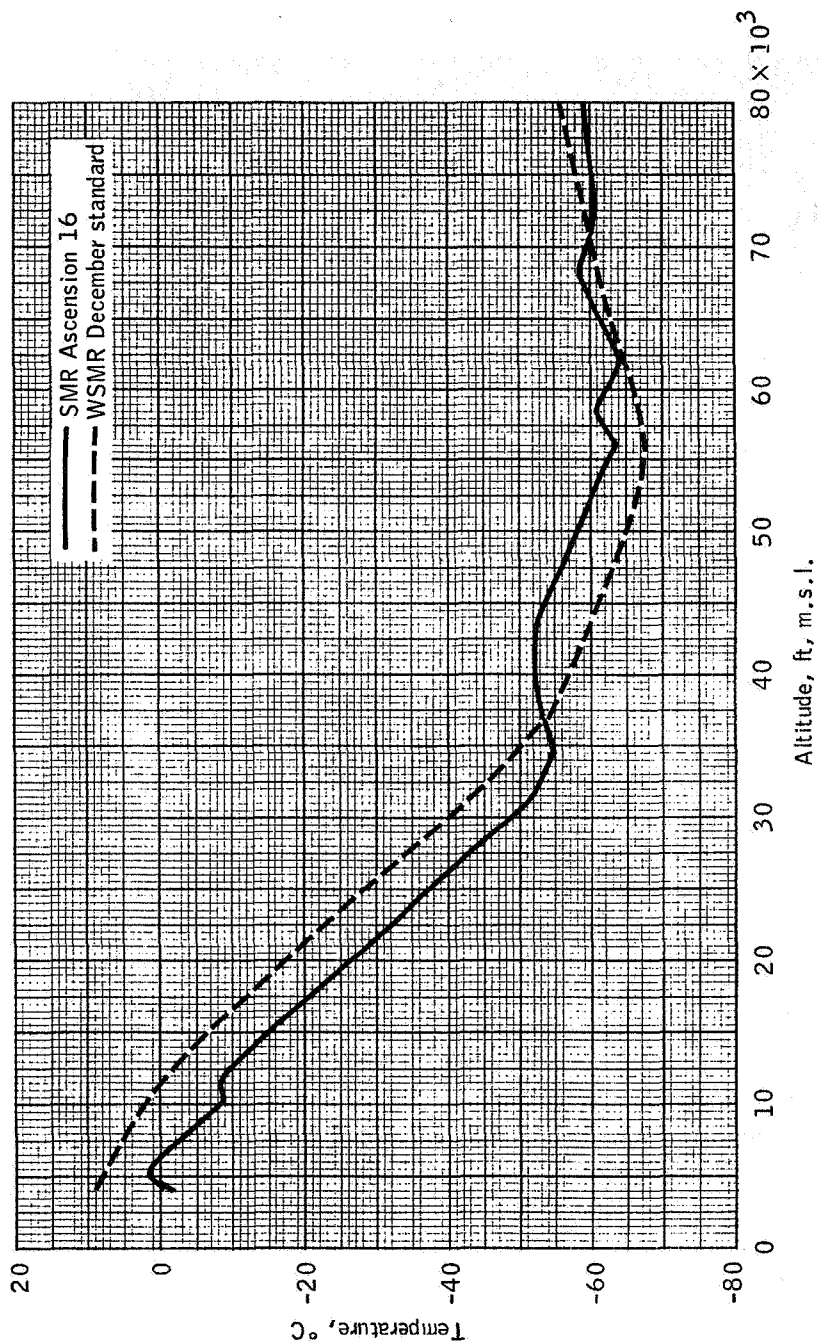


Figure 10.5-2.- Apollo Mission A-004 atmospheric temperature compared with WSMR December standard.  
(From Small Missile Range rawinsonde at 8:20 a.m. m.s.t. January 20)

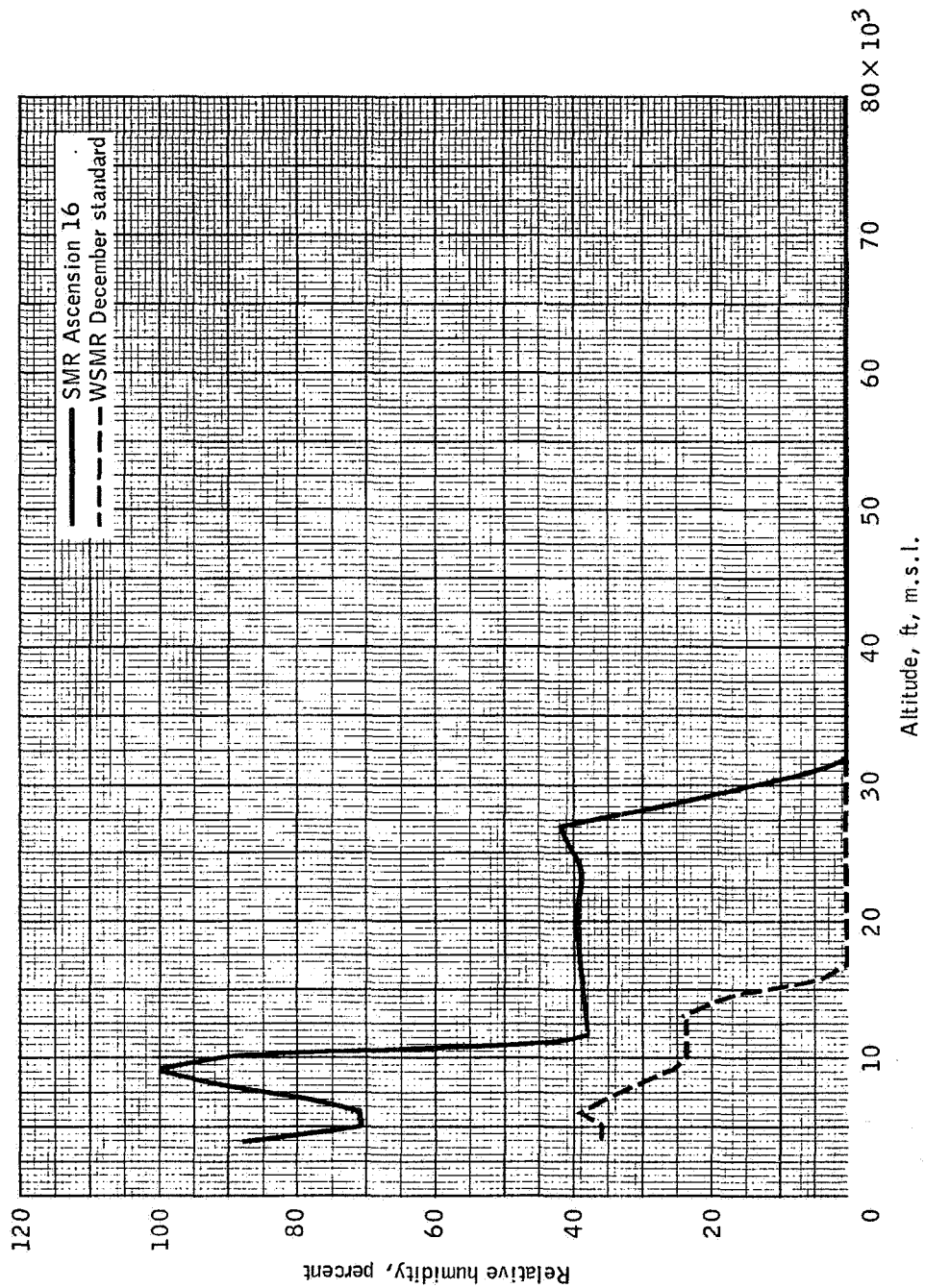


Figure 10.5-3.- Apollo Mission A-004 atmospheric humidity compared with WSMR December standard.  
(From Small Missile Range rawinsonde at 8:20 a.m. m.s.l., January 20)

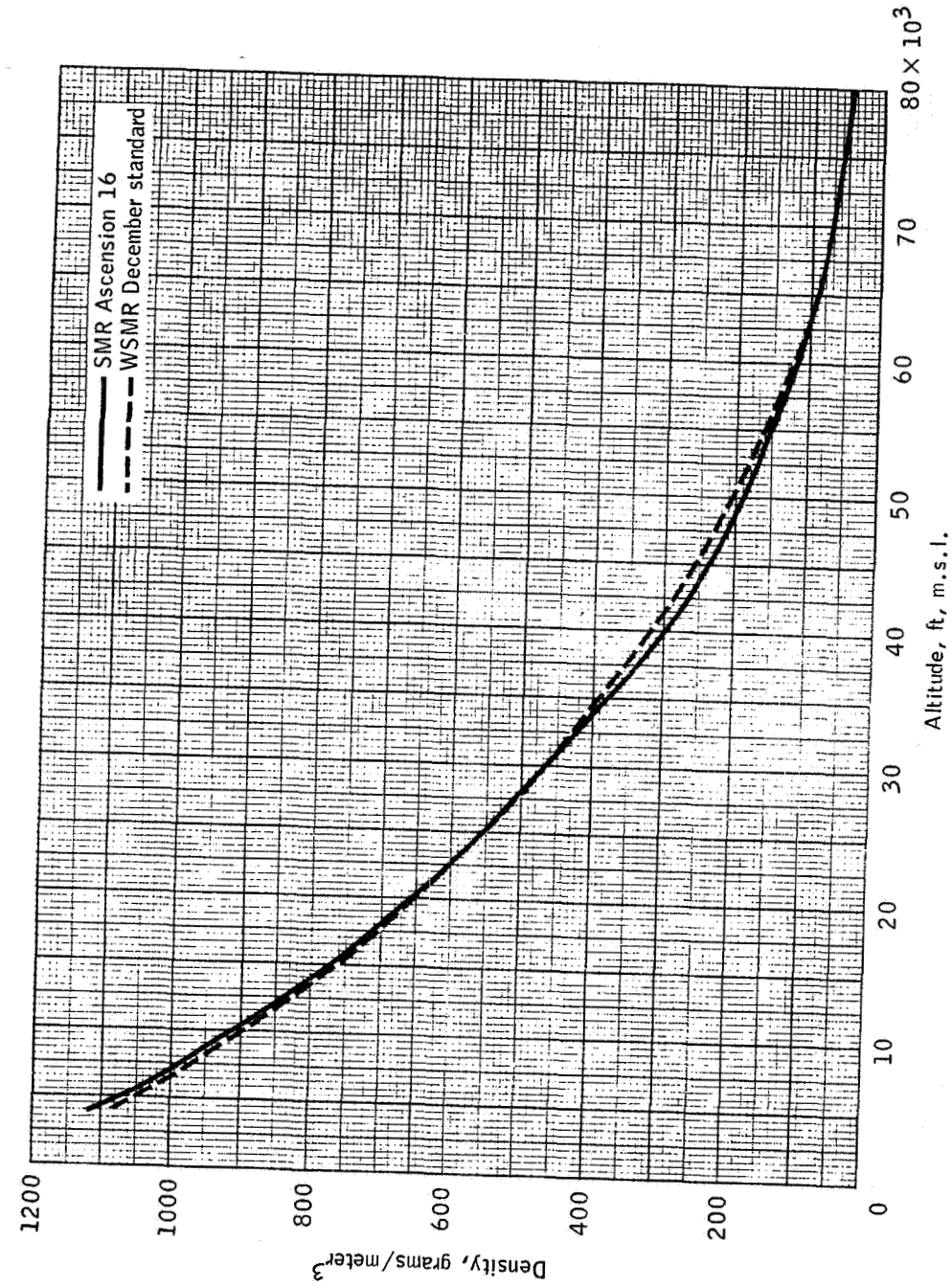


Figure 10.5-4.- Apollo Mission A-004 atmospheric density compared with WSMR December standard.  
(From Small Missile Range rawinsonde at 8:20 a.m. m.s.l. January 20)

NASA-S-66-3738 APR 15

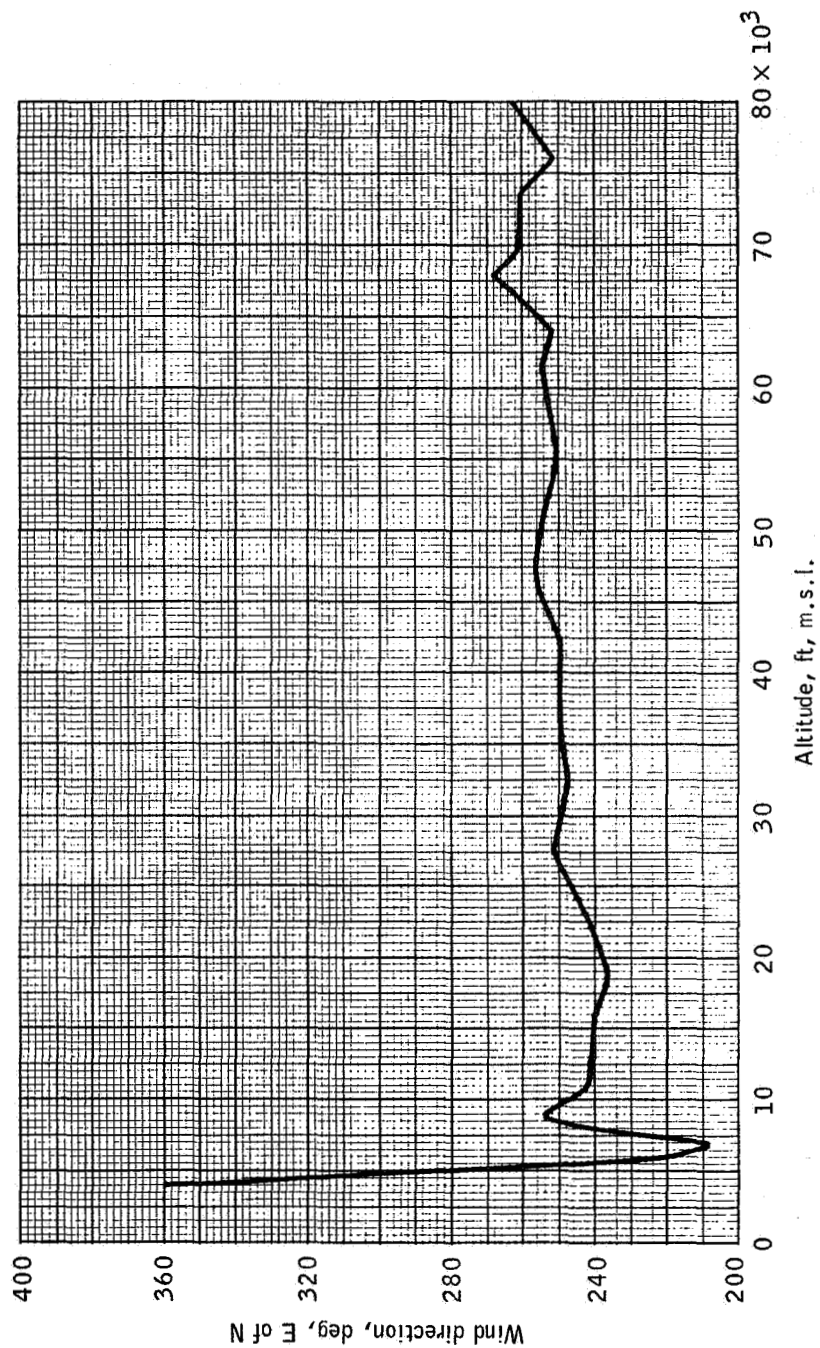


Figure 10.5-5.- Apollo Mission A-004 launch time wind direction, SMR Ascension 16.  
(From Small Missile Range rawinsonde at 8:20 a.m. m.s.l. January 20)

NASA-S-66-3746 APR 15

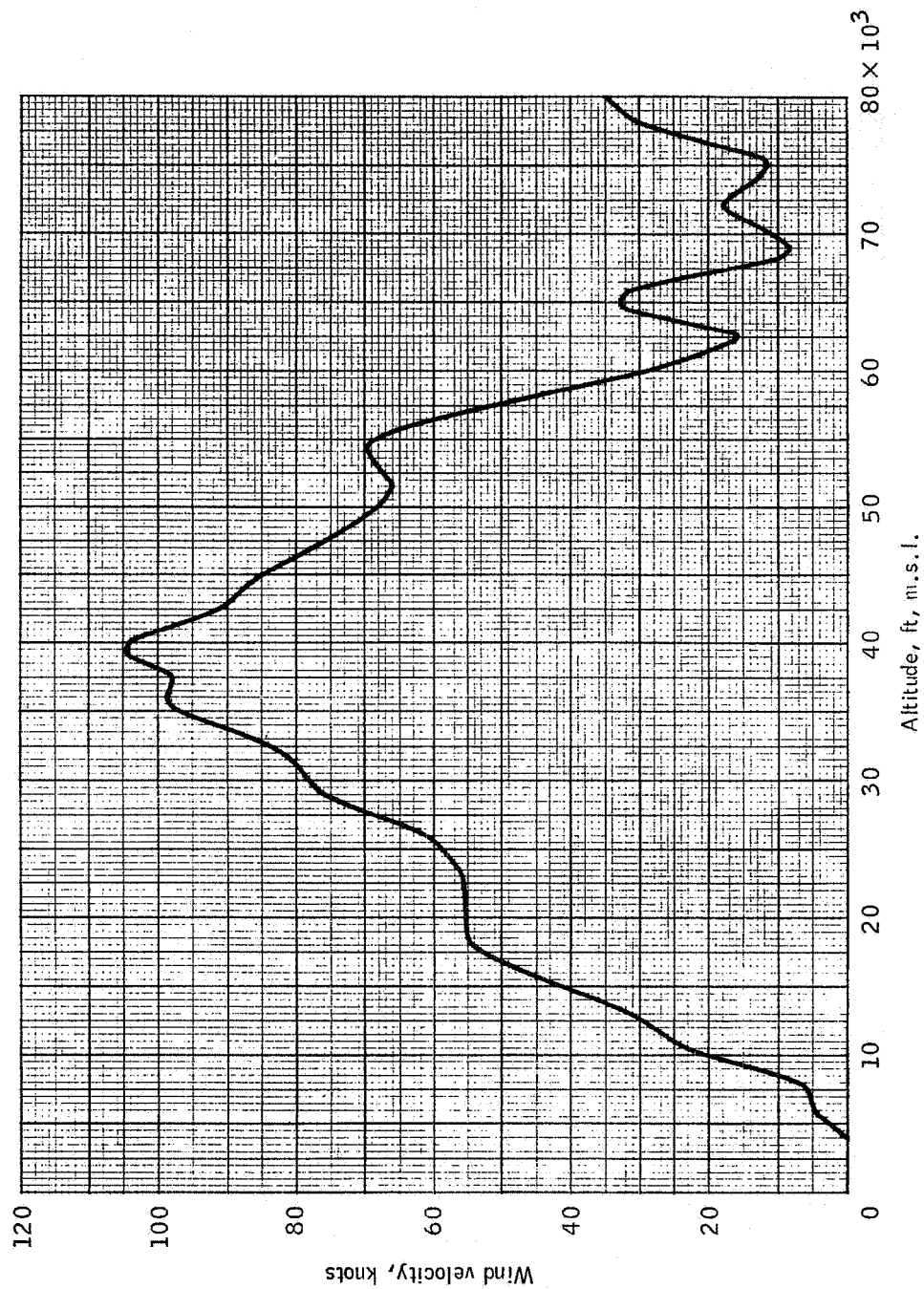


Figure 10.5-6.- Apollo Mission A-004 launch time wind magnitude, SMR Ascension 16.  
(From Small Missile Range rawinsonde at 8:20 a.m. m.s.l. January 20)

## 11.0 APPENDIX B

## 11.1 Mission A-004 Test Objectives

First-order test objectives.-

(a) Demonstrate satisfactory launch-escape vehicle (LEV) performance for an abort in the power-on tumbling boundary region.

(b) Demonstrate the structural integrity of the LEV airframe structure for an abort in the power-on tumbling boundary region.

Second-order test objectives.-

(a) Demonstrate the capability of the canard subsystem to satisfactorily reorient and stabilize the LEV with the aft heat shield forward after a power-on tumbling abort.

(b) Demonstrate the structural capability of the production boost protective cover to withstand the launch environment.

(c) Determine the static loads on the command module during the launch and the abort sequences.

(d) Determine the dynamic loading of the command module inner structure.

(e) Determine the dynamic loads and the structural response of the service module during launch.

(f) Demonstrate the capability of the command module forward heat shield thrusters to satisfactorily separate the forward heat shield after the tower has been jettisoned by the tower-jettison motor.

(g) Determine the static pressure imposed on the command module by free-stream conditions and launch-escape subsystem motor plumes during a power-on tumbling abort.

(h) Obtain data on rendezvous window visibility degradation due to launch-escape motor exhaust products for a power-on tumbling abort.

Third-order test objectives.-

(a) Demonstrate satisfactory separation of the LEV from the service module.

(b) Demonstrate the satisfactory operation and performance of the earth landing subsystem with a spacecraft vehicle.

(c) Obtain data on the structural loading of the command module during the earth landing subsystem sequence.

(d) Obtain thermal data on the boost protective cover during a power-on tumbling abort.

(e) Obtain acoustical noise data at an astronaut station inside the command module.



## 11.2 Test Vehicle Measurements

TABLE 11.2-I. - TEST VEHICLE MEASUREMENT LIST

Measurement identification	Measurement description	Telemetry link, channel, and segment	Frequency response	Measurement range	Location	Figure
Structure subsystem						
CA0001A	Spacecraft acceleration, X-axis, high	A-6	0 to 50 cps	-10 to 20g	X <sub>C</sub> 78 Y0	11.2-5 221
CA0002A	Spacecraft acceleration, X-axis, low	B-7	0 to 30 cps	-2 to 2g	X <sub>C</sub> 78 Y0	11.2-5 221
CA0005A	Spacecraft acceleration, Y-axis	A-7	0 to 30 cps	-5 to 5g	X <sub>C</sub> 78 Y0	11.2-5 221
CA0007A	Spacecraft acceleration, Z-axis	B-10	0 to 30 cps	-5 to 5g	X <sub>C</sub> 78 Y0	11.2-5 221
LA0011A	Tower acceleration, Y-axis	B-9	0 to 30 cps	-5 to 5g	X <sub>L</sub> 380 Y0	11.2-1 26
LA0012A	Tower acceleration, Z-axis	A-9	0 to 30 cps	-5 to 5g	X <sub>L</sub> 380 Y6	11.2-1 20
CA0117D	CM vibration, navigation base, axis 1	Track 1	.01 to 2.5 kcps	-100 to 100g	X <sub>C</sub> 72 Y-10	11.2-5 2-35
CA0118D	CM vibration, navigation base, axis 2	Track B-13	.01 to 2.5 kcps	-100 to 100g	X <sub>C</sub> 72 Y-10	11.2-5 2-35
CA0119D	CM vibration, navigation base, axis 3	Track 2	.01 to 2.5 kcps	-100 to 100g	X <sub>C</sub> 72 Y-10	11.2-5 2-35
CA0123D	CM vibration, normal to heat shield	Track B-14	.01 to 2.5 kcps	-100 to 100g	X <sub>C</sub> 33 Y0	11.2-5 2-67
CA0124D	CM vibration, normal to forward sidewall	Track 3	.01 to 2.5 kcps	-100 to 100g	X <sub>C</sub> 53 Y0	11.2-5 252
CA0136D	CM vibration, normal to floor	Track 10	.01 to 2.5 kcps	-100 to 100g	X <sub>C</sub> 1-3 Y0	11.2-5 20
LA0200H	Canard actuator displacement	B-12	10 to 100 cps	0 to 110°	A-frame pivot	11.2-2
LA0201G	Strain, +Y canard actuator link	B-17	0 to 31.5 cps	-15 000 to 20 000 lb	+Y actuator link	11.2-2
LA0202G	Strain, -Y canard actuator link	B-14	0 to 31.4 cps	-15 000 to 20 000 lb	-Y actuator link	11.2-2
LA0215G	Strain, tower leg	A-E-38	10 s/s	-15 000 to 50 000 lb	X <sub>L</sub> 5-5 Y23.4	11.2-3 225.3
LA0216G	Strain, tower leg	A-E-39	10 s/s	-15 000 to 50 000 lb	X <sub>L</sub> 5-5 Y23.4	11.2-3 2-25.3
LA0217G	Strain, tower leg	A-E-40	10 s/s	-15 000 to 50 000 lb	X <sub>L</sub> 5-5 Y-23.4	11.2-3 225.3
LA0218G	Strain, tower leg	A-E-41	10 s/s	-15 000 to 50 000 lb	X <sub>L</sub> 5-5 Y-23.4	11.2-3 2-25.3
CA0228P	Spacecraft conical surface pressure 1	B-E-17	10 s/s	2 to 22 psia	X <sub>C</sub> 35	11.2-4 87.5°
CA0229P	Spacecraft conical surface pressure 2	B-E-18	10 s/s	2 to 22 psia	X <sub>C</sub> 30	11.2-4 68.5°
CA0229P	Spacecraft conical surface pressure 3	B-E-19	10 s/s	2 to 22 psia	X <sub>C</sub> 30	11.2-4 10.25°
CA0229P	Spacecraft conical surface pressure 5	B-E-30	10 s/s	2 to 22 psia	X <sub>C</sub> 31	11.2-4 267°
CA0229P	Spacecraft conical surface pressure 6	B-E-31	10 s/s	2 to 22 psia	X <sub>C</sub> 30	11.2-4 242°
CA0229P	Spacecraft conical surface pressure 7	B-E-52	10 s/s	2 to 22 psia	X <sub>C</sub> 25.4	11.2-4 228.75°

TABLE 11.2-1. - TEST VEHICLE MEASUREMENT LIST - Continued

Measurement identification	Measurement description	Telemetry link, channel, and segment	Frequency response	Measurement range	Location	Figure
Structure subsystem - Continued						
CA0235P	Spacecraft conical surface pressure 8	B-E-53	10 s/s	2 to 22 psia	X <sub>C</sub> 30	11.2-4
CA0237P	Spacecraft conical surface pressure 10	B-E-54	10 s/s	2 to 22 psia	X <sub>C</sub> 30	11.2-4
CA0238P	Spacecraft conical surface pressure 11	B-E-64	10 s/s	2 to 22 psia	X <sub>C</sub> 30	11.2-4
CA0239P	Spacecraft conical surface pressure 12	B-E-56	10 s/s	2 to 22 psia	X <sub>C</sub> 30	11.2-4
CA0241P	Spacecraft conical surface pressure 14	B-E-57	10 s/s	2 to 22 psia	X <sub>C</sub> 30.5	11.2-4
CA0242P	Spacecraft conical surface pressure 15	B-E-58	10 s/s	2 to 22 psia	X <sub>C</sub> 71	11.2-4
CA0247P	Spacecraft conical surface pressure 20	B-E-59	10 s/s	2 to 22 psia	X <sub>C</sub> 71	11.2-4
CA0248P	Spacecraft conical surface pressure 21	B-E-60	10 s/s	2 to 22 psia	X <sub>C</sub> 50.5	11.2-4
CA0249P	Spacecraft conical surface pressure 22	B-E-61	10 s/s	2 to 22 psia	X <sub>C</sub> 54	11.2-4
CA0250P	Spacecraft conical surface pressure 23	B-E-62	10 s/s	2 to 22 psia	X <sub>C</sub> 50.5	11.2-4
CA0252P	Spacecraft conical surface pressure 25	B-E-63	10 s/s	2 to 22 psia	X <sub>C</sub> 50.5	11.2-4
CA0254P	Spacecraft conical surface pressure 27	B-E-55	10 s/s	2 to 22 psia	X <sub>C</sub> 50.5	11.2-4
CA0255P	Spacecraft conical surface pressure 28	B-E-65	10 s/s	2 to 22 psia	X <sub>C</sub> 71	11.2-4
CA0257P	Spacecraft conical surface pressure 30	B-E-66	10 s/s	2 to 22 psia	X <sub>C</sub> 71	11.2-4
CA0258P	Spacecraft conical surface pressure 31	B-E-67	10 s/s	2 to 22 psia	X <sub>C</sub> 71	11.2-4
CA0259P	Spacecraft conical surface pressure 32	B-E-68	10 s/s	2 to 22 psia	X <sub>C</sub> 71	11.2-4
CA0260P	Spacecraft conical surface pressure 33	B-E-69	10 s/s	2 to 22 psia	X <sub>C</sub> 65	11.2-4
CA0262P	Spacecraft conical surface pressure 35	B-E-70	10 s/s	2 to 22 psia	X <sub>C</sub> 75.7	11.2-4
CA0265P	Spacecraft conical surface pressure 38	B-E-71	10 s/s	2 to 22 psia	X <sub>C</sub> 71	11.2-4
CA0267P	Spacecraft conical surface pressure 40	B-E-73	10 s/s	2 to 22 psia	X <sub>C</sub> 50.5	11.2-4
CA0268P	Spacecraft conical surface pressure 41	B-E-74	10 s/s	2 to 22 psia	X <sub>C</sub> 25.4	11.2-4
CA0269P	Spacecraft conical surface pressure 42	B-E-75	10 s/s	2 to 22 psia	X <sub>C</sub> 30	11.2-4
CA0271P	Spacecraft conical surface pressure 44	B-E-77	10 s/s	2 to 22 psia	X <sub>C</sub> 10	11.2-4
CA0272P	Spacecraft conical surface pressure 45	B-E-78	10 s/s	2 to 22 psia	X <sub>C</sub> 34	11.2-4
CA0273P	Spacecraft conical surface pressure 46	B-E-79	10 s/s	2 to 22 psia	X <sub>C</sub> 34	11.2-4

TABLE 11.2-1.- TEST VEHICLE MEASUREMENT LIST - Continued

Measurement identification	Measurement description	Telemetry link, channel, and segment	Frequency response	Measurement range	Location	Figure
Structure subsystem - Continued						
CA027-P	Spacecraft conical surface pressure 47	B-E-80	10 s/s	2 to 22 psia	X <sub>C</sub> 102	11.2-4
CA027-P	Spacecraft conical surface pressure 49	B-E-82	10 s/s	2 to 22 psia	X <sub>C</sub> 102	11.2-4
CA0280P	Spacecraft base pressure 1	A-E-10	10 s/s	0 to 15 psia	Bottom R50	11.2-12
CA0281P	Spacecraft base pressure 2	A-E-11	10 s/s	0 to 15 psia	Bottom R50	11.2-12
CA0282P	Spacecraft base pressure 3	A-E-12	10 s/s	0 to 15 psia	Bottom R50	11.2-12
CA0283P	Spacecraft base pressure 4	A-E-13	10 s/s	0 to 15 psia	Bottom R50	11.2-12
CA0285P	Spacecraft aft equipment compartment pressure	B-E-76	10 s/s	2 to 22 psia	X <sub>C</sub> 43	11.2-5
CA0300P	Spacecraft conical surface pressure 53	B-E-86	10 s/s	2 to 22 psia	X <sub>C</sub> 74	11.2-4
CA0301P	Spacecraft conical surface pressure 54	B-E-87	10 s/s	2 to 22 psia	X <sub>C</sub> 74	11.2-4
CA0302P	Spacecraft conical surface pressure 55	B-E-88	10 s/s	2 to 22 psia	X <sub>C</sub> 102	11.2-4
CA0303P	BPC-CM interface pressure	B-E-72	10 s/s	2 to 22 psia	X <sub>C</sub> 50.5	11.2-4
CA0310P	BPC-CM interface pressure	B-E-83	10 s/s	2 to 22 psia	X <sub>C</sub> 83.5	11.2-4
CA0311P	BPC-CM interface pressure	B-E-84	10 s/s	2 to 22 psia	X <sub>C</sub> 50.5	11.2-4
CA0312P	BPC-CM interface pressure	B-E-85	10 s/s	2 to 22 psia	X <sub>C</sub> 50.5	11.2-4
CA0355P	Spacecraft aft equipment compartment pressure	B-E-81	10 s/s	2 to 22 psia	X <sub>C</sub> 34	11.2-5
CA0510S	Hatch beam axial strain, outside vertical	A-E-58	10 s/s	-5000 to 5000 $\mu$ in./in.	X <sub>C</sub> 61.7	11.2-9
CA0511S	Hatch beam axial strain, inside vertical	A-E-59	10 s/s	-5000 to 5000 $\mu$ in./in.	X <sub>C</sub> 61.7	11.2-9
CA0574R	Hatch heat flux	A-E-27	10 s/s	0 to 100 Btu/ft <sup>2</sup> /sec	X <sub>C</sub> 48	11.2-10
CA0575R	Heat flux calorimeter 23	B-E-29	10 s/s	0 to 100 Btu/ft <sup>2</sup> /sec	X <sub>C</sub> 34	11.2-10
CA0576R	Rendezvous window heat flux	B-E-31	10 s/s	0 to 100 Btu/ft <sup>2</sup> /sec	X <sub>C</sub> 34	11.2-10
CA0577R	Heat flux calorimeter 22	B-E-33	10 s/s	0 to 100 Btu/ft <sup>2</sup> /sec	X <sub>C</sub> 48	11.2-10
CA0578R	Heat flux calorimeter 21	B-E-35	10 s/s	0 to 100 Btu/ft <sup>2</sup> /sec	X <sub>C</sub> 39	11.2-10
CA0579R	Heat flux calorimeter 20	B-E-37	10 s/s	0 to 100 Btu/ft <sup>2</sup> /sec	X <sub>C</sub> 28	11.2-10
CA0610T	CM crew compartment temperature	A-E-80	10 s/s	32 to 302° F	X <sub>C</sub> 48.5	11.2-5
CA0611P	CM crew compartment pressure	A-E-82	10 s/s	0 to 15 psia	X <sub>C</sub> 45	11.2-5

TABLE 11.2-1.- TEST VEHICLE MEASUREMENT LIST - Continued

Measurement identification	Measurement description	Telemetry link, channel, and segment	Frequency response	Measurement range	Location	Figure
Structure subsystem - Continued						
SA0612T	SM interior temperature	A-E-81	10 s/s	30 to 302° F	X <sub>3</sub> 355 Y0	11.2-18
SA0613P	SM interior pressure	A-E-83	10 s/s	0 to 15 psia	X <sub>3</sub> 371.5 R21.94	11.2-18
CA0645T	Hatch window temperature	B-E-28	10 s/s	32 to 482° F	X <sub>6</sub> 48	11.2-10
CA0646T	Body temperature calorimeter 23	B-E-30	10 s/s	32 to 482° F	X <sub>6</sub> 34	11.2-10
CA0647T	Rendezvous window temperature	B-E-32	10 s/s	32 to 482° F	X <sub>6</sub> 34	11.2-10
SA0721S	Radial stress, beam 2	Track B-7-12	0 to 600 cps	-5000 to 5000 min./in.	X <sub>3</sub> 268	11.2-15
SA0722S	Radial stress, beam 2	Track B-7-13	0 to 600 cps	-5000 to 5000 min./in.	X <sub>3</sub> 340.5	11.2-15
SA0723S	Radial stress, beam 2	Track B-7-14	0 to 600 cps	-5000 to 5000 min./in.	X <sub>3</sub> 305	11.2-15
SA0724S	Radial stress, beam 2	Track B-8-12	0 to 600 cps	-5000 to 5000 min./in.	X <sub>3</sub> 218	11.2-15
SA0725S	Radial stress, beam 5	Track B-5-15	0 to 600 cps	-5000 to 5000 min./in.	X <sub>3</sub> 340.5	11.2-17
SA0726S	Radial stress, beam 5	Track B-6-15	0 to 600 cps	-5000 to 5000 min./in.	X <sub>3</sub> 268	11.2-17
SA0727S	Radial stress, beam 4	Track B-7-15	0 to 600 cps	-5000 to 5000 min./in.	X <sub>3</sub> 305	11.2-16
SA0728S	Radial stress, beam 5	Track B-8-15	0 to 600 cps	-5000 to 5000 min./in.	X <sub>3</sub> 305	11.2-17
SA0855S	Strain, membrane stress axial	Track B-1-15	0 to 600 cps	-4000 to 4000 min./in.	X <sub>3</sub> 218	11.2-17
SA0856S	Strain, membrane stress radial	Track B-2-15	0 to 600 cps	-4000 to 4000 min./in.	X <sub>3</sub> 218	11.2-17
SA0857S	Strain, membrane 45° stress	Track B-3-15	10 s/s	-4000 to 4000 min./in.	X <sub>3</sub> 218	11.2-17
SA0858S	Strain, bending stress axial	Track B-4-15	10 s/s	-4000 to 4000 min./in.	X <sub>3</sub> 218	11.2-17
SA0859S	Strain, bending stress radial	Track B-8-13	10 s/s	-4000 to 4000 min./in.	X <sub>3</sub> 218	11.2-17
SA0870S	Strain, 45° bending stress	Track B-8-14	10 s/s	-4000 to 4000 min./in.	X <sub>3</sub> 218	11.2-17
SA0876T	SM outer skin temperature	A-E-67	10 s/s	32 to 482° F	X <sub>3</sub> 273	11.2-20
SA0877T	SM inner skin temperature	A-E-68	10 s/s	32 to 482° F	X <sub>3</sub> 273	11.2-20
SA0878T	SM outer skin temperature	A-E-69	10 s/s	32 to 482° F	X <sub>3</sub> 273	11.2-20
SA0879T	SM outer skin temperature	A-E-70	10 s/s	32 to 482° F	X <sub>3</sub> 273	11.2-20
SA0936S	Strain, SM bending about longitudinal axis	Track B-9-14	0 to 400 cps	-7000 to 7000 min./in.	X <sub>3</sub> 273	11.2-20
SA0937S	Strain, SM bending about circular axis	Track B-10-12	0 to 400 cps	-7000 to 7000 min./in.	X <sub>3</sub> 273	11.2-20

TABLE 11.2-1. - TEST VEHICLE MEASUREMENT LIST - Continued

Measurement identification	Measurement description	Telemetry link, channel, and segment	Frequency response	Measurement range	Location	Figure
Structure subsystem - Continued						
SA0978S	Strain, SM longitudinal tension/compression	Track B-10-13	0 to 400 cps	-7000 to 7000 min./in.	X <sub>5</sub> 273	11.2-20
SA0979S	Strain, CM circular tension/compression	Track B-10-14	0 to 400 cps	-7000 to 7000 min./in.	X <sub>5</sub> 273	11.2-20
SA0940P	CM vibration, sector V	Track B-1-12	0 to 400 cps	-500 to 500g	X <sub>5</sub> 375.1	11.2-19
SA0944D	CM vibration, sector III	Track B-2-13	0 to 400 cps	-500 to 500g	X <sub>5</sub> 320.9	11.2-19
SA0945D	SM vibration, sector III	Track B-2-14	0 to 400 cps	-500 to 500g	X <sub>5</sub> 298	11.2-19
SA0946D	SM vibration, sector IV	Track B-3-12	0 to 400 cps	-500 to 500g	X <sub>5</sub> 296	11.2-19
SA0947D	SM vibration, sector V	Track B-3-13	0 to 400 cps	-500 to 500g	X <sub>5</sub> 320.9	11.2-19
SA0948D	SM vibration, sector V	Track B-3-14	0 to 400 cps	-500 to 500g	X <sub>5</sub> 278	11.2-19
SA0949D	CM vibration, sector V	Track B-4-12	0 to 400 cps	-500 to 500g	X <sub>5</sub> 238.7	11.2-19
SA0950D	SM vibration, sector V	Track B-4-13	0 to 400 cps	-500 to 500g	X <sub>5</sub> 238.7	11.2-19
SA0952D	SM vibration, sector VI	Track B-5-12	0 to 400 cps	-500 to 500g	X <sub>5</sub> 238.7	11.2-19
SA0953D	SM-RCS panel vibration	Track B-5-13	0 to 400 cps	-500 to 500g	X <sub>5</sub> 320.9	11.2-19
SA0954D	SM-RCS support vibration	Track B-5-14	0 to 400 cps	-75 to 75g	X <sub>5</sub> 320.9	11.2-19
SA0955P	SM-RCS engine nozzle vibration, X axis	Track B-6-13	0 to 400 cps	-500 to 500g	SM-RCS system D OCW nozzle	11.2-19
SA0956D	SM-RCS engine nozzle vibration, circular	Track B-6-14	0 to 400 cps	-500 to 500g	SM-RCS system D OCW nozzle	11.2-19
SA0957P	SM-RCS panel fluctuating pressure	A-15	0 to 400 cps	-3 to 3 psi	SM-RCS system D	11.2-19
SA0958P	CM fluctuating pressure	Track B-10-15	0 to 400 cps	-3 to 3 psi	X <sub>5</sub> 320.9	11.2-19
SA0959D	CM beam 5 circular vibration	Track B-1-13	0 to 400 cps	-500 to 500g	X <sub>5</sub> 275	11.2-17
SA0959D	CM axial vibration, sector IV	Track B-4-14	0 to 400 cps	-50 to 50g	X <sub>5</sub> 203	11.2-18
SA0959D	CM axial vibration 1, sector I	Track B-6-12	0 to 400 cps	-100 to 100g	X <sub>5</sub> 355	11.2-18
SA0977D	CM axial vibration 2, sector I	Track B-9-13	0 to 400 cps	-100 to 100g	X <sub>5</sub> 278	11.2-18
SA0998D	SM-RCS engine nozzle radial vibration	Track B-1-14	0 to 400 cps	-500 to 500g	SM-RCS system D OCW nozzle	11.2-19
SA0999D	SM-RCS engine nozzle circular vibration	Track B-2-12	10 s/s	-500 to 500g	SM-RCS system D OCW nozzle	11.2-19
CA100T	CM heat shield surface temperature	B-P-30	10 s/s	+32 to 502° F	X <sub>6</sub> 23	11.2-11
CA100T	CM heat shield surface temperature	B-P-31	10 s/s	+32 to 502° F	X <sub>6</sub> 23	11.2-11

TABLE 11.2-1.- TEST VEHICLE MEASUREMENT LIST - Continued

Measurement identification	Measurement description	Telemetry link, channel, and segment	Frequency response	Measurement range	Location	Figure
Structure subsystem - Continued						
CA1073T	CM heat shield surface temperature	B-E-43	10 s/s	+32 to 302° F	X <sub>C</sub> 23	11.2-11
CA1074T	CM heat shield surface temperature	B-E-44	10 s/s	+32 to 302° F	X <sub>C</sub> 81	11.2-11
CA1075T	Aft heat shield surface temperature	B-E-45	10 s/s	+32 to 302° F	R71	11.2-12
CA1076T	Aft heat shield surface temperature	B-E-46	10 s/s	+32 to 302° F	R39	11.2-12
CA1077T	Pressure hull temperature	A-E-84	10 s/s	+32 to 302° F	X <sub>C</sub> 44	11.2-5
CA1078T	Pressure hull temperature	A-E-85	10 s/s	+32 to 302° F	X <sub>C</sub> 80	11.2-5
CA1512S	Tower longeron 2 axial strain, gusset side	B-E-13	10 s/s	-5000 to 5000 min./in.	X <sub>C</sub> 91	11.2-8
CA1513S	Tower longeron 2 axial strain, gusset edge	B-E-14	10 s/s	-5000 to 5000 min./in.	X <sub>C</sub> 91	11.2-8
CA1514S	Tower longeron 4 axial strain, gusset side	B-E-15	10 s/s	-5000 to 5000 min./in.	X <sub>C</sub> 91	11.2-6
CA1515S	Tower longeron 4 axial strain, gusset edge	B-E-16	10 s/s	-5000 to 5000 min./in.	X <sub>C</sub> 91	11.2-6
CA1600S	Forward longeron 2 axial strain, outside	A-E-63	10 s/s	-5000 to 5000 min./in.	X <sub>C</sub> 71.5	11.2-8
CA1601S	Forward longeron 2 axial strain, inside	A-E-52	10 s/s	-5000 to 5000 min./in.	X <sub>C</sub> 69.1	11.2-8
CA1602S	Forward longeron 2 axial strain, outside	A-E-64	10 s/s	-5000 to 5000 min./in.	X <sub>C</sub> 52	11.2-8
CA1603S	Forward longeron 2 axial strain, inside	A-E-56	10 s/s	-5000 to 5000 min./in.	X <sub>C</sub> 94.4	11.2-8
CA1604S	Forward longeron 4 axial strain, outside	A-E-50	10 s/s	-5000 to 5000 min./in.	X <sub>C</sub> 71.5	11.2-6
CA1605S	Forward longeron 4 axial strain, inside	A-E-53	10 s/s	-5000 to 5000 min./in.	X <sub>C</sub> 69.1	11.2-6
CA1606S	Forward longeron 4 axial strain, outside	A-E-55	10 s/s	-5000 to 5000 min./in.	X <sub>C</sub> 52	11.2-6
CA1607S	Forward longeron 4 axial strain, inside	A-E-57	10 s/s	-5000 to 5000 min./in.	X <sub>C</sub> 94.4	11.2-6
CA1608S	Forward longeron 8 axial strain, outside	A-E-51	10 s/s	-5000 to 5000 min./in.	X <sub>C</sub> 71.5	11.2-7
CA1609S	Forward longeron 8 axial strain, inside	A-E-54	10 s/s	-5000 to 5000 min./in.	X <sub>C</sub> 69.1	11.2-7
CA1610S	Forward longeron 8 axial strain, outside	B-E-17	10 s/s	-5000 to 5000 min./in.	X <sub>C</sub> 52	11.2-7
CA1611S	Forward longeron 8 axial strain, inside	B-E-18	10 s/s	-5000 to 5000 min./in.	X <sub>C</sub> 94.4	11.2-7
CA1880S	Side heat shield axial strain, horizontal - outside	A-E-45	10 s/s	-5000 to 5000 min./in.	X <sub>C</sub> 46	11.2-11
CA1881S	Side heat shield axial strain, horizontal - inside	A-E-42	10 s/s	-5000 to 5000 min./in.	X <sub>C</sub> 48	11.2-11

TABLE 11.2-1.- TEST VEHICLE MEASUREMENT LIST - Continued

Measurement identification	Measurement description	Telemetry link, channel, and segment	Frequency response	Measurement range	Location	Figure
Structure subsystem - Continued						
CA1882S	Side heat shield axial strain, vertical - outside	A-E-45	10 s/s	-5000 to 5000 min./in.	X <sub>C</sub> 48	11.2-11 270°
CA1883S	Side heat shield axial strain, vertical - inside	A-E-44	10 s/s	-5000 to 5000 min./in.	X <sub>C</sub> 48	11.2-11 270°
CA1884S	Side heat shield axial strain, horizontal - outside	A-E-47	10 s/s	-5000 to 5000 min./in.	X <sub>C</sub> 77	11.2-11 272°
CA1885S	Side heat shield axial strain, horizontal - inside	A-E-46	10 s/s	-5000 to 5000 min./in.	X <sub>C</sub> 77	11.2-11 272°
CA1886S	Side heat shield axial strain, vertical - outside	A-E-49	10 s/s	-5000 to 5000 min./in.	X <sub>C</sub> 77	11.2-11 272°
SA2020G	Tension bolt axial strain, beam 2	A-E-60	10 s/s	0 to 40 000 lb	Beam 2	11.2-13
SA2021G	Tension bolt axial strain, beam 4	A-E-61	10 s/s	0 to 40 000 lb	Beam 4	11.2-13
SA2022G	Tension bolt axial strain, beam 6	A-E-62	10 s/s	0 to 40 000 lb	Beam 6	11.2-13
CA2240D	Lower equipment bay support structure vibration, X axis	Track 12	10 to 2500 cps	-100 to 100g	X <sub>C</sub> 28	11.2-5 233
CA2241D	Lower equipment bay support structure vibration, Y axis	Track 6	10 to 2500 cps	-100 to 100g	X <sub>C</sub> 28	11.2-5 233
CA2242D	Lower equipment bay support structure vibration, Z axis	Track 13	10 to 2500 cps	-100 to 100g	X <sub>C</sub> 28	11.2-5 233
CA2246D	CM X-axis vibration	A-16	10 to 600 cps	-100 to 100g	X <sub>C</sub> 15	11.2-5 7-55
CA2247D	CM Y-axis vibration	B-16	10 to 600 cps	-100 to 100g	X <sub>C</sub> 15	11.2-5 2-55
CA2248D	CM Z-axis vibration	Track B-9-15	10 to 600 cps	-100 to 100g	X <sub>C</sub> 15	11.2-5 2-55
CA2617S	Tower longeron 8 axial strain, gusset side	A-E-65	10 s/s	-5000 to 5000 min./in.	X <sub>C</sub> 91	11.2-7 223°
CA2618S	Tower longeron 8 axial strain, gusset edge	A-E-66	10 s/s	-5000 to 5000 min./in.	X <sub>C</sub> 91	11.2-7 223°
SA4001S	SM compression pad strain, beam 1A	A-E-87	10 s/s	-5000 to 5000 min./in.	X <sub>A</sub> 1000	11.2-14 2-15.5
SA4002S	SM compression pad strain, beam 1B	B-E-88	10 s/s	-5000 to 5000 min./in.	X <sub>A</sub> 1000	11.2-14 2-31
SA4003S	SM compression pad strain, beam 2A	B-E-3	10 s/s	-5000 to 5000 min./in.	X <sub>A</sub> 1000	11.2-14 223.8
SA4004S	SM compression pad strain, beam 2B	B-E-4	10 s/s	-5000 to 5000 min./in.	X <sub>C</sub> 3	11.2-14 243.5
SA4005S	SM compression pad strain, beam 3A	B-E-5	10 s/s	-5000 to 5000 min./in.	X <sub>A</sub> 1000	11.2-14 233.5



TABLE 11.2-1.- TEST VEHICLE MEASUREMENT LIST - Continued

Measurement identification	Measurement description	Telemetry link, channel, and segment	Frequency response	Measurement range	Location	Figure
Structure subsystem - Concluded						
SA4006S	SM compression pad strain, beam 3B	B-E-6	10 s/s	-5000 to 5000 min./in.	X <sub>A</sub> 1000 Y-25 Z66.5	11.2-14
SA4007S	SM compression pad strain, beam 4A	B-E-7	10 s/s	-5000 to 5000 min./in.	X <sub>A</sub> 1000 Y-30.5 Z15.5	11.2-14
SA4008S	SM compression pad strain, beam 4B	B-E-8	10 s/s	-5000 to 5000 min./in.	X <sub>C</sub> 3 Y-55.3 Z28.5	11.2-14
SA4009S	SM compression pad strain, beam 5A	B-E-9	10 s/s	-5000 to 5000 min./in.	X <sub>A</sub> 1000 Y-24.5 Z-24	11.2-14
SA4010S	SM compression pad strain, beam 5B	B-E-10	10 s/s	-5000 to 5000 min./in.	X <sub>A</sub> 1000 Y-49.5 Z-47	11.2-14
SA4011S	SM compression pad strain, beam 6A	B-E-11	10 s/s	-5000 to 5000 min./in.	X <sub>A</sub> 1000 Y8 Z-33.5	11.2-14
SA4012S	SM compression pad strain, beam 6B	B-E-12	10 s/s	-5000 to 5000 min./in.	X <sub>C</sub> 3 Y14 Z-61.5	11.2-14
Electrical subsystem						
CC0001V	dc voltage main bus A (instrumentation)	A-E-3	10 s/s	22 to 32 V dc	Power control box	--
CC0002V	dc voltage main bus B (instrumentation)	A-E-4	10 s/s	22 to 32 V dc	Power control box	--
CC0003V	dc voltage logic bus A	A-E-36	10 s/s	0 to 36 V dc	LES sequencer	--
CC0004V	dc voltage logic bus B	A-E-37	10 s/s	0 to 36 V dc	LES sequencer	--
CC0005C	Total dc current (instrumentation)	A-E-9	10 s/s	0 to 50 amp	Power control box	--
Launch escape subsystem						
CD0005V	dc voltage LES pyro bus A	A-E-18	10 s/s	0 to 40 V dc	LES sequencer	--
CD0006V	dc voltage LES pyro bus B	A-E-19	10 s/s	0 to 40 V dc	LES sequencer	--
CD0008V	Sequencer start signal A	A-E-23	10 s/s	0 to 36 V dc	LES sequencer	--
CD0009V	Sequencer start signal B	A-E-24	10 s/s	0 to 36 V dc	LES sequencer	--
LD0012P	Pitch-control-motor chamber pressure	A-10	0 to 45 cps	0 to 2000 psia	X <sub>L</sub> 345 Y0 Z-13	11.2-1
LD0013P	Escape-motor chamber pressure	B-11	0 to 45 cps	0 to 2000 psia	X <sub>L</sub> 290 Y0 Z0	11.2-1
CD0021X	Abort initiation, relay close A	A-E-28	10 s/s	Step	LES sequencer	--
CD0022X	Abort initiation, relay close B	A-E-29	10 s/s	Step	LES sequencer	--
CD0023X	CM-SM separation, relay close A	A-E-20	10 s/s	Step	LES sequencer	--
CD0024X	CM-SM separation, relay close B	A-E-20	10 s/s	Step	LES sequencer	--

TABLE 11.2-1.- TEST VEHICLE MEASUREMENT LIST - Continued

Measurement identification	Measurement description	Telemetry link, channel, and segment	Frequency response	Measurement range	Location	Figure
Launch escape subsystem - Continued						
CD0025X	ELS sequencer A start, relay close A	A-E-25	10 s/s	Step	ELS sequencer	--
CD0026X	ELS sequencer A start, relay close B	A-E-25	10 s/s	Step	ELS sequencer	--
CD0027X	ELS sequencer B start, relay close A	A-E-30	10 s/s	Step	ELS sequencer	--
CD0028X	ELS sequencer B start, relay close B	A-E-30	10 s/s	Step	ELS sequencer	--
CD0033X	Tower jettison and separation, relay close A	A-E-22	10 s/s	Step	Tower LFS sequencer	--
CD0034X	Tower jettison and separation, relay close B	A-E-22	10 s/s	Step	Tower LES sequencer	--
CD0116X	Canard A deploy, relay close A	A-E-26	10 s/s	Step	Sequencer	--
CD0117X	Canard A deploy, relay close B	A-E-26	10 s/s	Step	Sequencer	--
CD0118X	Canard B deploy, relay close A	A-E-27	10 s/s	Step	Sequencer	--
CD0119X	Canard B deploy, relay close B	A-E-27	10 s/s	Step	Sequencer	--
CD0150X	Backup abort timer, close A	A-E-31	10 s/s	Step	Sequencer	--
CD0151X	Backup abort timer, close B	A-E-31	10 s/s	Step	Sequencer	--
CD0152X	Abort initiate, relay K20 close A	A-E-29	10 s/s	Step	Sequencer	--
CD0153X	Abort initiate, relay K19 close B	A-E-29	10 s/s	Step	Sequencer	--
CD0154X	Abort enable, GSE system A	A-E-32	10 s/s	Step	Sequencer	--
CD0155X	Abort enable, GSE system B	A-E-32	10 s/s	Step	Sequencer	--
CD0190X	LES pitch control motor fire, relay close A	A-E-21	10 s/s	Step	Tower LES sequencer	--
CD0191X	LES pitch control motor fire, relay close B	A-E-21	10 s/s	Step	Tower LES sequencer	--
CD0230X	Forward heat shield, jettison A	A-E-16	10 s/s	Step	Sequencer	--
CD0231X	Forward heat shield, jettison B	A-E-16	10 s/s	Step	Sequencer	--
1D2070I	LFS motor star point temperature	GSE	-	0 to 160° F	X <sub>L</sub> 260	11.2-1
1D2071I	LFS motor star valley temperature	GSE	-	0 to 160° F	X <sub>L</sub> 260	11.2-1
1D2072I	LES motor temperature	GSE	-	0 to 160° F	X <sub>L</sub> 260	11.2-1
1D2073I	LFS motor temperature	GSE	-	0 to 160° F	X <sub>L</sub> 210	11.2-1
1D2074I	LES motor temperature	GSE	-	0 to 160° F	X <sub>L</sub> 160	11.2-1

TABLE 11.2-1.- TEST VEHICLE MEASUREMENT LIST - Continued

Measurement identification	Measurement description	Telemetry link, channel, and segment	Frequency response	Measurement range	Location	Figure
Launch escape subsystem - Completed						
CE0001X	Drogue deploy, relay close A	A-E-33	10 s/s	Step	ELS sequencer	--
CE0002X	Drogue deploy, relay close B	A-E-33	10 s/s	Step	ELS sequencer	--
CE0003X	Main chute deploy - drogue release, relay A	A-E-34	10 s/s	Step	ELS sequencer	--
CE0004X	Main chute deploy - drogue release, relay B	A-E-34	10 s/s	Step	ELS sequencer	--
CE0009X	Baroswitch locking relay, close A	A-E-35	10 s/s	Step	ELS sequencer	--
CE0010X	Baroswitch locking relay, close B	A-E-35	10 s/s	Step	ELS sequencer	--
CE0014X	Drogue parachute 1 physical monitor	B-E-20	10 s/s	Evert	Drogue mortar 1	--
CE0015X	Drogue parachute 2 physical monitor	B-E-19	10 s/s	Evert	Drogue mortar 2	--
CE0035P	Barometric pressure, static reference	A-E-86	10 s/s	0 to 15 psia	X <sub>C</sub> 81.5 R27.67	11.2-5
Flight technology subsystems						
CK0001R	Pitch rate gyro output	A-3	0 to 10 cps	-150 to 150 deg/sec	X <sub>C</sub> 78 Y0	11.2-5
CK0002R	Yaw rate gyro output	B-3	0 to 10 cps	-150 to 150 deg/sec	X <sub>C</sub> 78 Y0	11.2-5
CK0003R	Roll rate gyro output	B-4	0 to 10 cps	-150 to 150 deg/sec	X <sub>C</sub> 78 Y0	11.2-5
CK00164	Pitch attitude gyro output	B-5	10 s/s	-180 to 180°	X <sub>C</sub> 78 Y0	11.2-5
CK0018H	Yaw attitude gyro output	B-6	10 s/s	-180 to 180°	X <sub>C</sub> 78 Y0	11.2-5
LK0023H	Angle of attack	A-E-71	10 s/s	-40 to 40°	X <sub>L</sub> 399 Y0	11.2-1
LK0024H	Angle of sideslip	A-E-73	10 s/s	-40 to 40°	X <sub>L</sub> 399 Y0	11.2-1
LK0025P	Dynamic pressure	A-E-72	10 s/s	0 to 1250 lb/sq ft	X <sub>L</sub> 399 Y0	11.2-1
CK0034Y	CM interior acoustics	Track 7	20 to 2500 cps	110 to 150 dB	X <sub>C</sub> 50 Y0.5	11.2-5
CK0035Y	CM interior acoustics	Track 14	20 to 2500 cps	100 to 140 dB	X <sub>C</sub> 50 Y0.5	11.2-5
CK0030H	Roll attitude gyro output 1	A-4	10 s/s	-180 to 180°	X <sub>C</sub> 78 Y0	11.2-5
CK0031H	Roll attitude gyro output 2	A-5	10 s/s	-180 to 180°	X <sub>C</sub> 78 Y0	11.2-5
CK0032X	Gyro segment switch 1	A-E-78	10 s/s	Step	X <sub>C</sub> 78 Y0	11.2-5
CK0033X	Gyro segment switch 2	A-E-79	10 s/s	Step	X <sub>C</sub> 78 Y0	11.2-5
LK0120N	Forward heat shield view camera	-	0 to 32 fps	-	LES tower	--
CK0123N	CM rendezvous window view camera	-	0 to 16 fps	-	Left-hand platform	--

TABLE 11.2-1.- TEST VEHICLE MEASUREMENT LIST - Concluded

Measurement identification	Measurement description	Telemetry link, channel, and segment	Frequency response	Measurement range	Location	Figure
Communications and instrumentation subsystems						
CT0001W	Onboard timer	A-8 and B-8	0 to 35 cps	-	CW interior	--
CT0002V	Transponder A trigger	B-E-10	10 s/s	50 to 1000 prf	Transponder A	--
CT0003V	Transponder B trigger	B-E-12	10 s/s	50 to 1000 prf	Transponder B	--
CT0020V	Link A differential PDM (90X10 commutator)	Track B-12	--	--	Telemetry mod bus	--
CT0021V	Link A mixer 2 output	Track 8	--	--	Telemetry mod bus	--
CT0022V	Link B differential PDM (90X10 commutator)	Track 9	--	--	Telemetry mod bus	--
CT0023V	Link B mixer 2 output	Track B-11	--	--	Telemetry mod bus	--
CT0025V	Link A 0-volt reference (90X10 commutator)	A-E-1	10 s/s	0 V dc	Telemetry link A	--
CT0026V	Link A 5-volt reference (90X10 commutator)	A-E-2	10 s/s	5 V dc	Telemetry link A	--
CT0027V	Link A sync A (90X10 commutator)	A-E-89	10 s/s	0 V dc	Telemetry link A	--
CT0028V	Link A sync B (90X10 commutator)	A-E-90	10 s/s	0 V dc	Telemetry link A	--
CT0500V	Link B 0-volt reference (90X10 commutator)	B-E-1	10 s/s	0 V dc	Telemetry link B	--
CT0501V	Link B 5-volt reference (90X10 commutator)	B-E-2	10 s/s	5 V dc	Telemetry link B	--
CT0502V	Link B sync A (90X10 commutator)	B-E-89	10 s/s	0 V dc	Telemetry link B	--
CT0503V	Link B sync B (90X10 commutator)	B-E-90	10 s/s	0 V dc	Telemetry link B	--

TABLE 11.2-II.- LAUNCH VEHICLE MEASUREMENT LIST, AIRBORNE

Measurement identification	Measurement description	Telemetry link, channel, and segment	Frequency response	Measurement range	Location		
					X	Y	Z
BB0001H	Pitch attitude	C-E-23, C-E-53, C-E-83	30 s/s	-60 to 60°	28	-70	0
BB0002H	Yaw attitude	C-E-25, C-E-55, C-E-85	30 s/s	-10 to 10°	28	-70	0
BB0003H	Roll attitude	C-E-24, C-E-54, C-E-84	30 s/s	-10 to 10°	28	-70	0
BB0024V	Instrumentation subsystem voltage	C-E-5	10 s/s	24 to 35 V dc	25	20	-70
BB0025V	Vehicle subsystem voltage	C-E-6	10 s/s	24 to 35 V dc	25	20	-70
BB0027P	Fin 1 actuator hydraulic pressure	C-E-35	10 s/s	0 to 3500 psia	332	70	74
BB0028P	Fin 2 actuator hydraulic pressure	C-E-36	10 s/s	0 to 3500 psia	332	-74	70
BB0029P	Fin 3 actuator hydraulic pressure	C-E-37	10 s/s	0 to 3500 psia	332	-70	-74
BB0030P	Fin 4 actuator hydraulic pressure	C-E-38	10 s/s	0 to 3500 psia	332	74	-70
BB0031V	Quad I command signal	C-10	30 cps	-12 to 12 V dc	30	-52	48
BB0032V	Quad II command signal	C-11	30 cps	-12 to 12 V dc	30	-52	48
BB0033V	Quad III command signal	C-E-8, C-E-26, C-E-44, C-E-62, C-E-80	50 s/s	-12 to 12 V dc	30	-52	48
BB0034V	Quad IV command signal	C-E-9, C-E-27, C-E-45, C-E-63, C-E-81	50 s/s	-12 to 12 V dc	30	-52	48
BB0035R	Roll rate	C-7	30 cps	-10 to 10 deg/sec	32	0	71
BB0036R	Pitch rate	C-8	20 cps	-10 to 10 deg/sec	32	0	71
BB0037R	Yaw rate	C-9	20 cps	-10 to 10 deg/sec	32	0	71
BB0038H	Fin 1 control surface position	C-E-10, C-E-28, C-E-46, C-E-64, C-E-82	50 s/s	-30 to 30°	346	87	95
BB0039H	Fin 2 control surface position	C-E-14, C-E-32, C-E-50, C-E-68, C-E-86	50 s/s	-30 to 30°	346	-97	87
BB0040H	Fin 3 control surface position	C-E-15, C-E-33, C-E-51, C-E-69, C-E-87	50 s/s	-30 to 30°	346	-87	-95

TABLE 11.2-11.- LAUNCH VEHICLE MEASUREMENT LIST, AIRBORNE - Concluded

Measurement identification	Measurement description	Telemetry link, channel, and segment	Frequency response	Measurement range	Location		
					X	Y	Z
BB0041H	Fin 4 control surface position	C-E-16, C-E-34, C-E-52, C-E-70, C-E-88	50 s/s	-30 to 30°	346	95	-87
BB0042X	Launch vehicle lift-off	C-E-11, C-E-56	20 s/s	0 to 5 V dc	355	8	77
BB0043V	Reference battery voltage	C-E-17, C-E-61	20 s/s	4.05 V dc	25	20	-70
BB0044P	Algol 2 chamber pressure	C-E-30, C-E-75	20 s/s	0 to 500 psia	26	2	45
BB0045P	Algol 5 chamber pressure	C-E-31, C-E-36	20 s/s	0 to 500 psia	26	-38	-47
BB0048A	Aft bulkhead acceleration, Y axis	C-14	40 cps	-2 to 2g	302	-74	0
BB0049A	Aft bulkhead acceleration, Z axis	C-15	40 cps	-2 to 2g	302	0	-74
BB0052X	Pitch-up relay 1	C-E-3, C-E-48	20 s/s	0 to 35 V dc	19	70	21
BB0053X	Pitch-up relay 2	C-E-4, C-E-49	20 s/s	0 to 35 V dc	19	-54	50
BB0054X	Abort relay 1	C-E-20, C-E-65	20 s/s	0 to 35 V dc	19	70	21
BB0055X	Abort relay 2	C-E-29, C-E-74	20 s/s	0 to 35 V dc	19	-54	50
BB0057V	Calibration 0-volts	C-E-1	10 s/s	0 V dc	25	20	-70
BB0058V	Calibration 5-volts	C-E-2	10 s/s	5 V dc	25	20	-70
BB0122A	Forward bulkhead acceleration, Y axis	C-12	40 cps	-2 to 2g	12	-74	0
BB0123A	Forward bulkhead acceleration, Z axis	C-13	40 cps	-2 to 2g	12	0	-74
BB0124P	Algol motor 1 chamber pressure	C-E-21, C-E-66	20 s/s	0 to 500 psia	26	41	21
BB0125P	Algol motor 4 chamber pressure	C-E-22, C-E-67	20 s/s	0 to 500 psia	26	2	-24
BB0126X	Second stage ignition relay 1	C-E-12, C-E-57	20 s/s	0 to 35 V dc	19	-71	-17
BB0127X	Second stage ignition relay 2	C-E-13, C-E-58	20 s/s	0 to 35 V dc	19	50	54
BB0128H	Sum pitch attitude and pitch programmer	C-E-40, C-E-60, C-E-73	30 s/s	-10 to 10°	30	-74	10

TABLE 11.2-III.- LAUNCH VEHICLE MEASUREMENT LIST, LANDLINE

Number	Measurement identification	Operating range	Response
1	Algol 1 grain temperature	32 to 100° F	15 samples/hour
2	Algol 2 grain temperature	32 to 100° F	15 samples/hour
3	Algol 4 grain temperature	32 to 100° F	15 samples/hour
4	Algol 5 grain temperature	32 to 100° F	15 samples/hour
5	Algol 1 lower case temperature	32 to 100° F	15 samples/hour
6	Algol 2 lower case temperature	32 to 100° F	15 samples/hour
7	Algol 4 lower case temperature	32 to 100° F	15 samples/hour
8	Algol 5 lower case temperature	32 to 100° F	15 samples/hour
9	Algol 1 upper case temperature	32 to 100° F	15 samples/hour
10	Algol 2 upper case temperature	32 to 100° F	15 samples/hour
11	Algol 4 upper case temperature	32 to 100° F	15 samples/hour
12	Algol 5 upper case temperature	32 to 100° F	15 samples/hour
13	Algol 1 initiator 1, bridgewire 1	0 to 10 amps	50 cps
14	Algol 1 initiator 1, bridgewire 2	0 to 10 amps	50 cps
15	Algol 1 initiator 2, bridgewire 1	0 to 10 amps	50 cps
16	Algol 1 initiator 2, bridgewire 2	0 to 10 amps	50 cps
17	Algol 4 initiator 1, bridgewire 1	0 to 10 amps	50 cps
18	Algol 4 initiator 1, bridgewire 2	0 to 10 amps	50 cps
19	Algol 4 initiator 2, bridgewire 1	0 to 10 amps	50 cps
20	Algol 4 initiator 2, bridgewire 2	0 to 10 amps	50 cps
21	Recruit 3 initiators 1 and 2, bridgewire 1	0 to 11 amps	50 cps
22	Recruit 3 initiators 1 and 2, bridgewire 2	0 to 11 amps	50 cps
23	Recruit 6 initiators 1 and 2, bridgewire 1	0 to 11 amps	50 cps
24	Recruit 6 initiators 1 and 2, bridgewire 2	0 to 11 amps	50 cps
25	Recruit 7 initiators 1 and 2, bridgewire 1	0 to 11 amps	50 cps
26	Recruit 7 initiators 1 and 2, bridgewire 2	0 to 11 amps	50 cps
27	Lift-off signal	0 to 28 V dc	100 cps
28	Ignition timer firing signal	0 to 28 V dc	100 cps
29	Range timing -IRIG	--	--
30	Recruit 8 initiators 1 and 2, bridgewire 1	0 to 11 amps	50 cps
31	Recruit 8 initiators 1 and 2, bridgewire 2	0 to 11 amps	50 cps
32	Recruit 9 initiators 1 and 2, bridgewire 1	0 to 11 amps	50 cps
33	Recruit 9 initiators 1 and 2, bridgewire 2	0 to 11 amps	50 cps

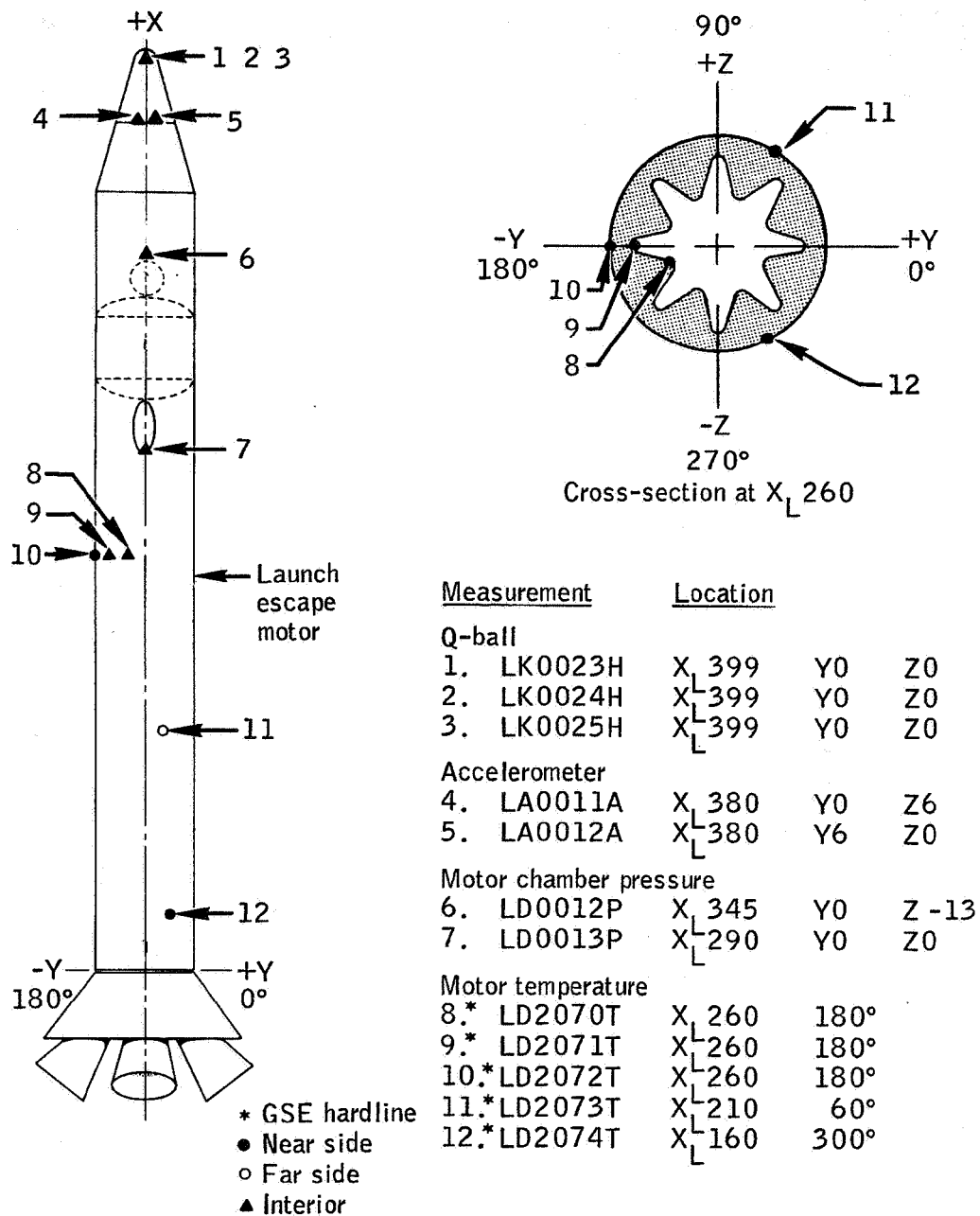


Figure 11.2-1.- LES motor and Q-ball measurement locations, Apollo Mission A-004.



NASA-S-66-3754 APR 15

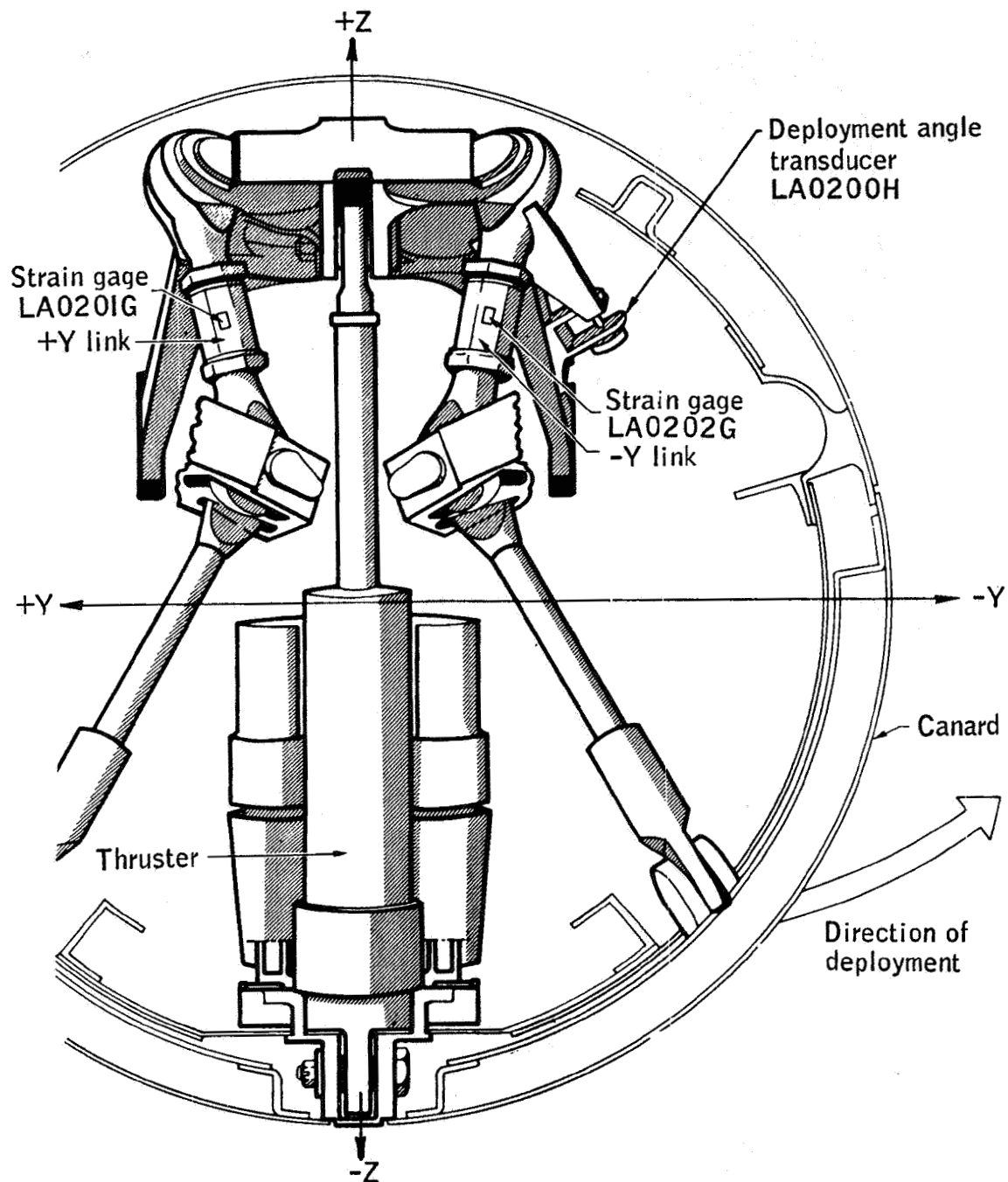
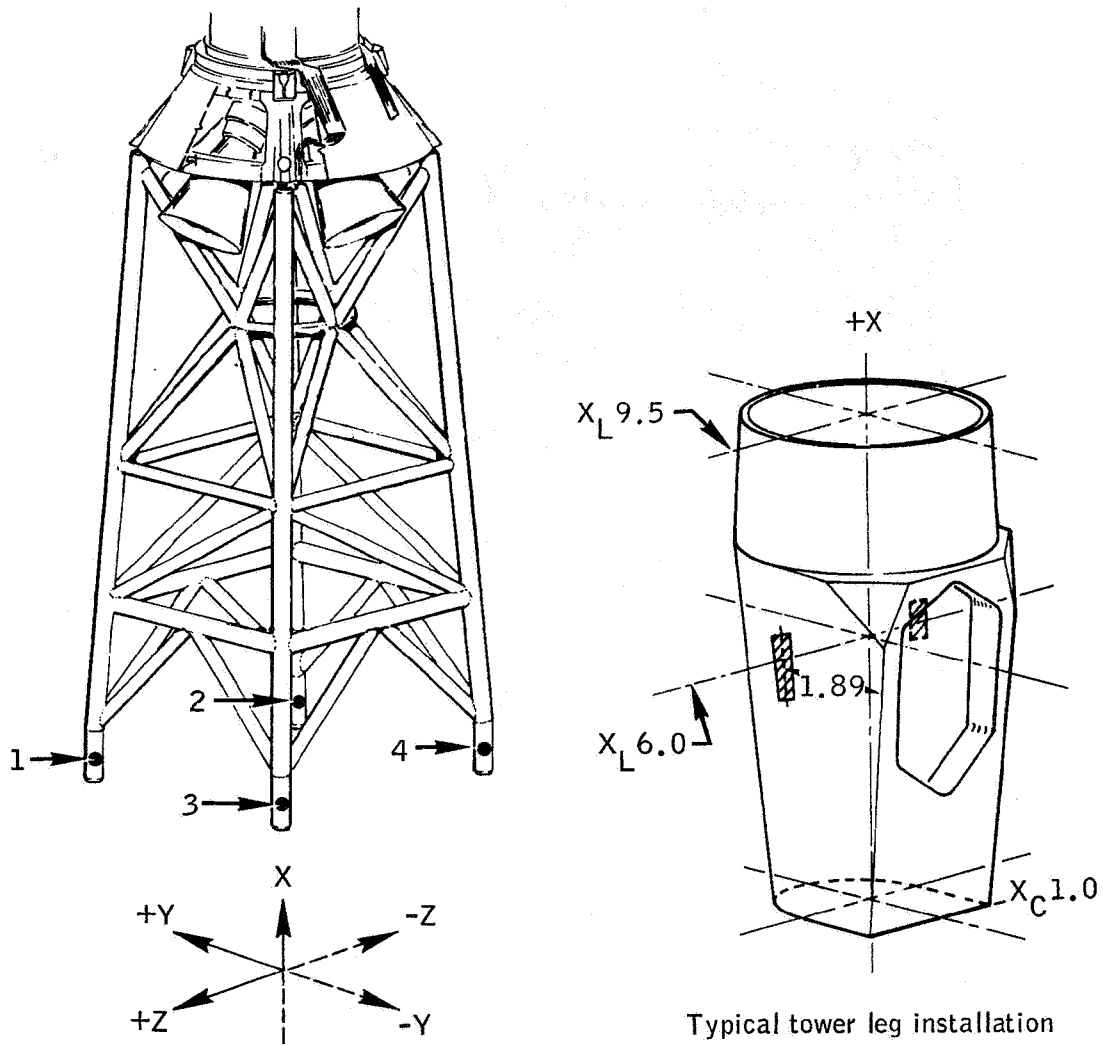


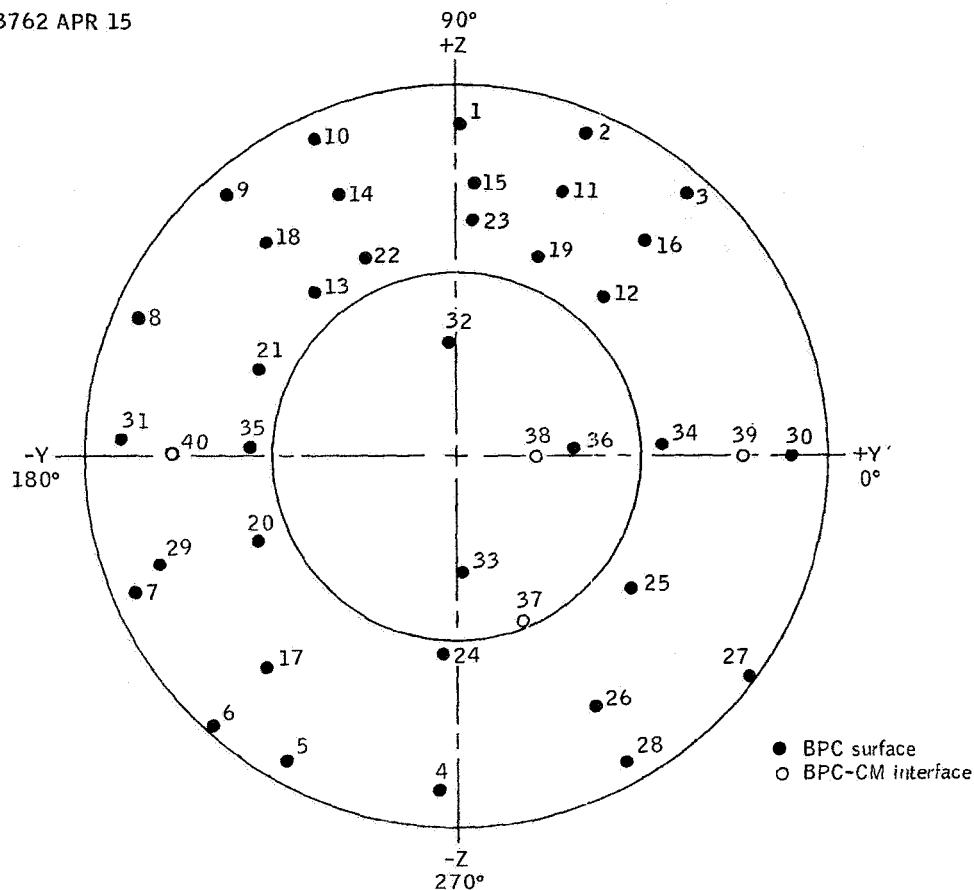
Figure 11.2-2.- Apollo Mission A-004 canard strain and deployment instrumentation.



Measurement	Location		
1. LA0215G	$X_L 5.5$	Y23.4	Z25.3
2. LA0216G	$X_L 5.5$	Y23.4	Z -25.3
3. LA0217G	$X_L 5.5$	Y -23.4	Z25.3
4. LA0218G	$X_L 5.5$	Y -23.4	Z -25.3

Figure 11.2-3.- Launch-escape tower measurement locations, Apollo Mission A-004.

NASA-S-66-3762 APR 15



Measurements	Location	Measurements	Location
BPC surface pressure			
1. CA0228P	X <sub>C</sub> 35 89.5°	22. CA0259P	X <sub>C</sub> 71 114.5°
2. CA0229P	X <sub>C</sub> 30 68.5°	23. CA0260P	X <sub>C</sub> 65 86°
3. CA0230P	X <sub>C</sub> 30 49.25°	24. CA0262P	X <sub>C</sub> 76.7 266°
4. CA0232P	X <sub>C</sub> 34 267°	25. CA0265P	X <sub>C</sub> 71 323°
5. CA0233P	X <sub>C</sub> 30 242°	26. CA0267P	X <sub>C</sub> 50.5 299°
6. CA0234P	X <sub>C</sub> 25.4 228.75°	27. CA0268P	X <sub>C</sub> 25.4 323°
7. CA0235P	X <sub>C</sub> 30 203.5°	28. CA0269P	X <sub>C</sub> 30 299°
8. CA0237P	X <sub>C</sub> 30 156.75°	29. CA0271P	X <sub>C</sub> 40 200°
9. CA0238P	X <sub>C</sub> 30 131.25°	30. CA0272P	X <sub>C</sub> 34 0°
10. CA0239P	X <sub>C</sub> 30 114.5°	31. CA0273P	X <sub>C</sub> 34 177°
11. CA0241P	X <sub>C</sub> 50.5 68.5°	32. CA0274P	X <sub>C</sub> 102 93°
12. CA0242P	X <sub>C</sub> 71 48.084°	33. CA0276P	X <sub>C</sub> 102 273°
13. CA0247P	X <sub>C</sub> 71 131.25°	34. CA0300P	X <sub>C</sub> 74 3.5°
14. CA0248P	X <sub>C</sub> 50.5 114.5°	35. CA0301P	X <sub>C</sub> 74 178.7°
15. CA0249P	X <sub>C</sub> 54 86°	36. CA0302P	X <sub>C</sub> 102 3°
16. CA0250P	X <sub>C</sub> 50.5 49.25°	BPC-CM interface pressure	
17. CA0252P	X <sub>C</sub> 50.5 228.75°	37. CA0309P	X <sub>C</sub> 50.5 90°
18. CA0254P	X <sub>C</sub> 50.5 131.25°	38. CA0310P	X <sub>C</sub> 83.25 292°
19. CA0255P	X <sub>C</sub> 71 68.5°	39. CA0311P	X <sub>C</sub> 50.5 0°
20. CA0257P	X <sub>C</sub> 71 203.5°	40. CA0312P	X <sub>C</sub> 50.5 180°
21. CA0258P	X <sub>C</sub> 71 156.75°		

Figure 11.2-4.- Conical surface pressures, Apollo Mission A-004. (Location of BPC surface and BPC-CM interface pressure measurements)

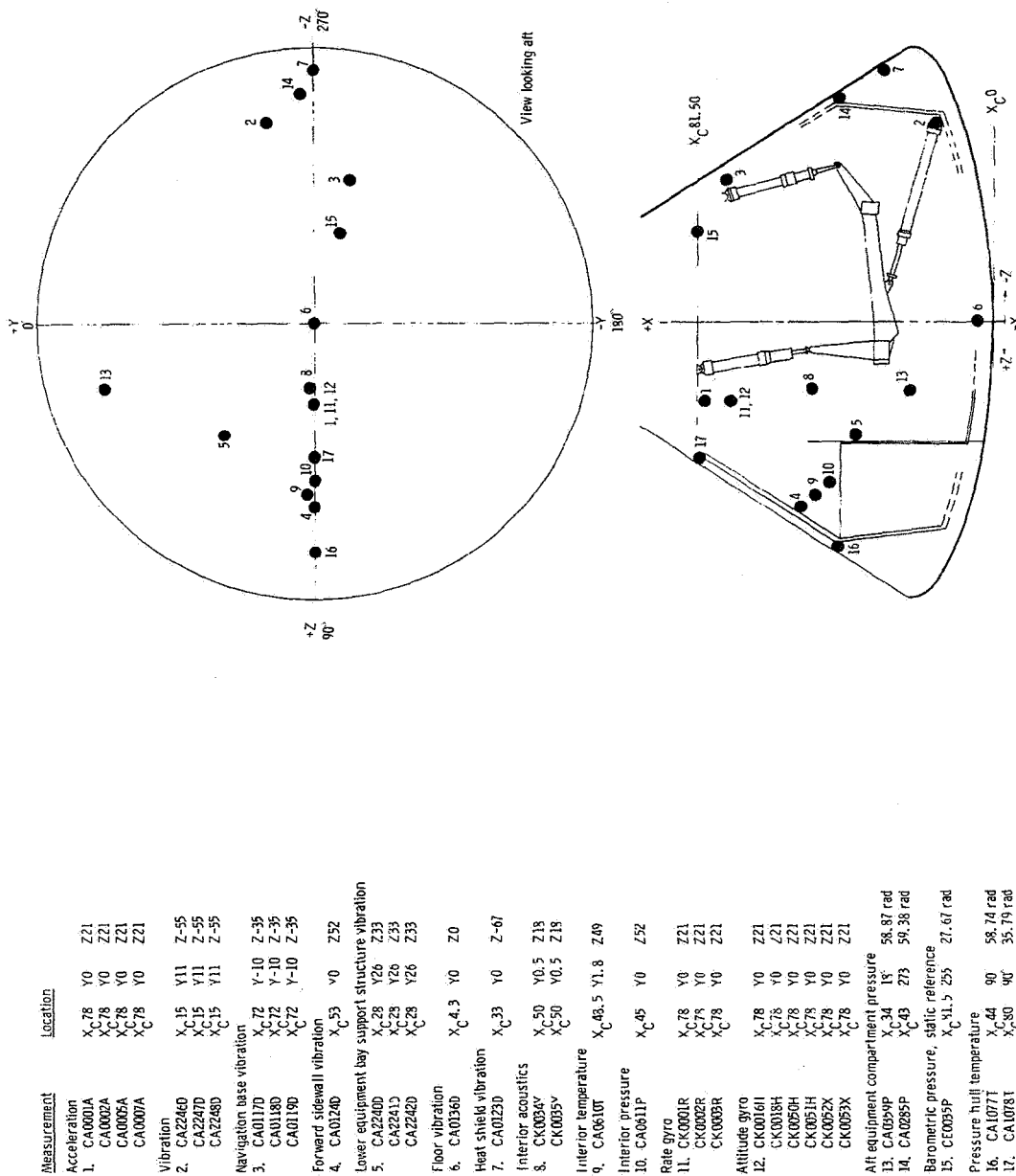


Figure 11.2-5.- Command module structural measurement locations, Apollo Mission A-004.

NASA-S-66-3766 APR 15

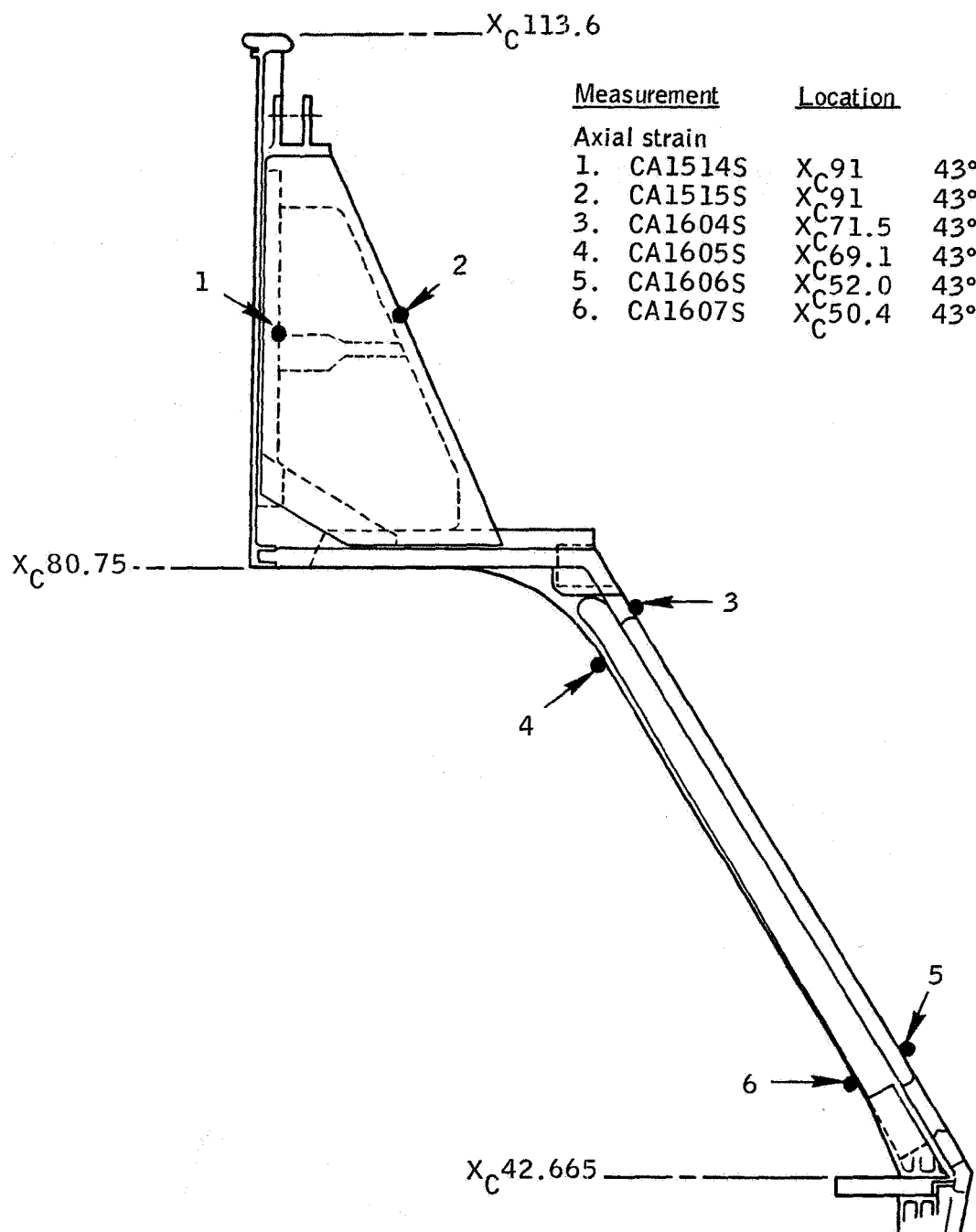


Figure 11.2-6.- Forward sidewall longeron 4 command module inner structure - forward sidewall, Apollo Mission A-004.

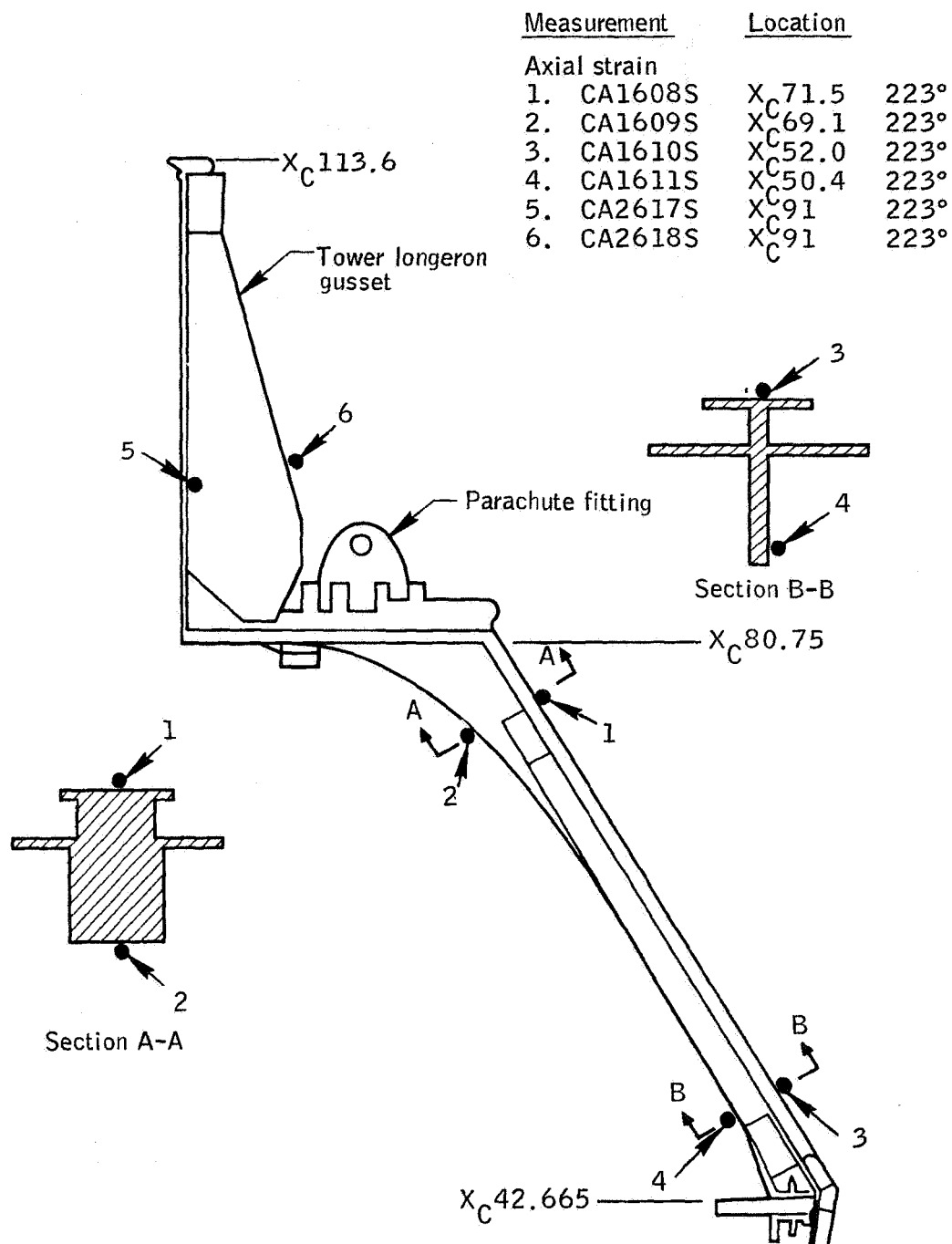


Figure 11.2-7.- Strain gage locations on longeron 8 command module, Apollo Mission A-004.

NASA-S-66-3774 APR 15

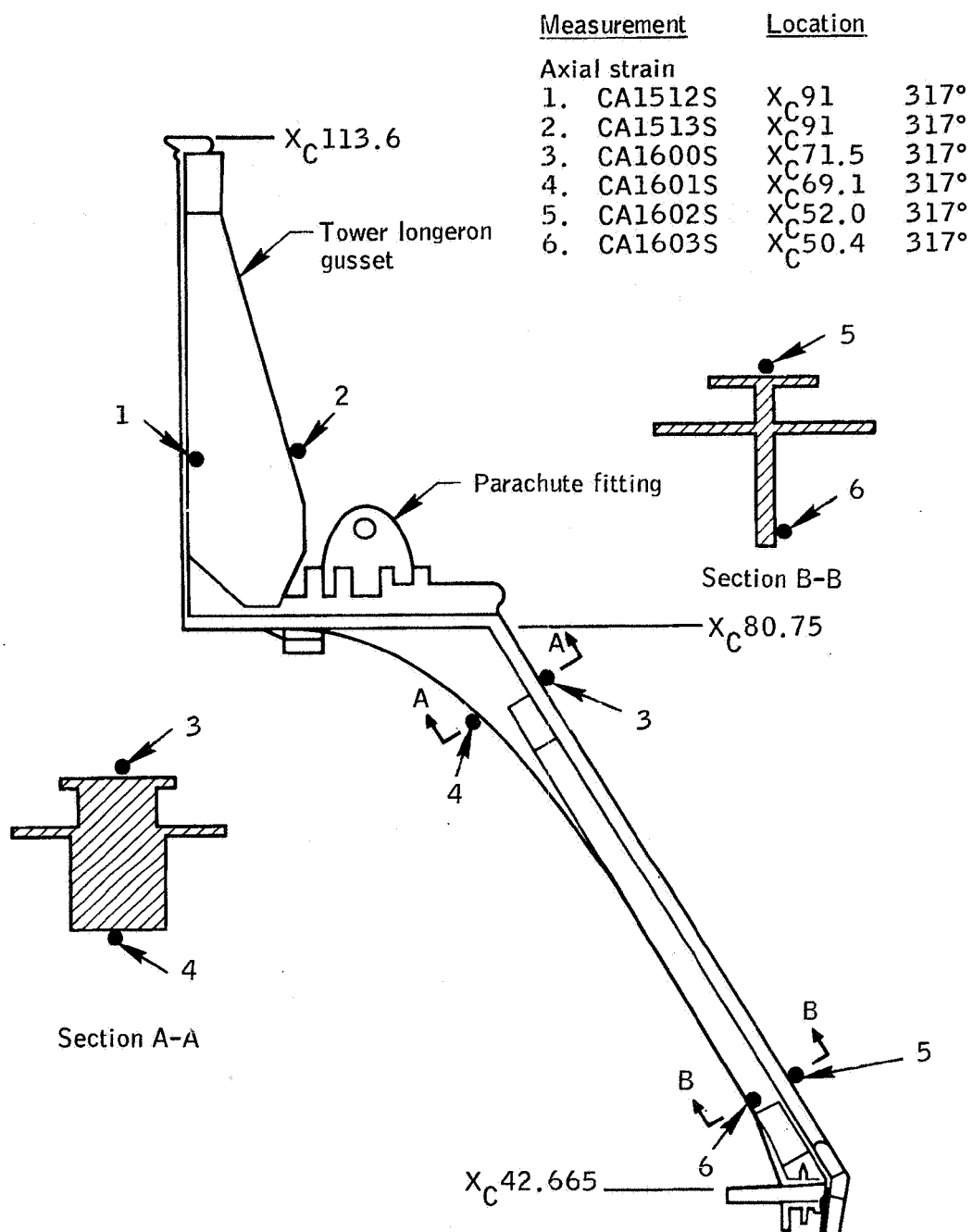


Figure 11.2-8.- Strain gage locations on longeron 2 command module, Apollo Mission A-004.

11-26

NASA-S-66-3778 APR 15

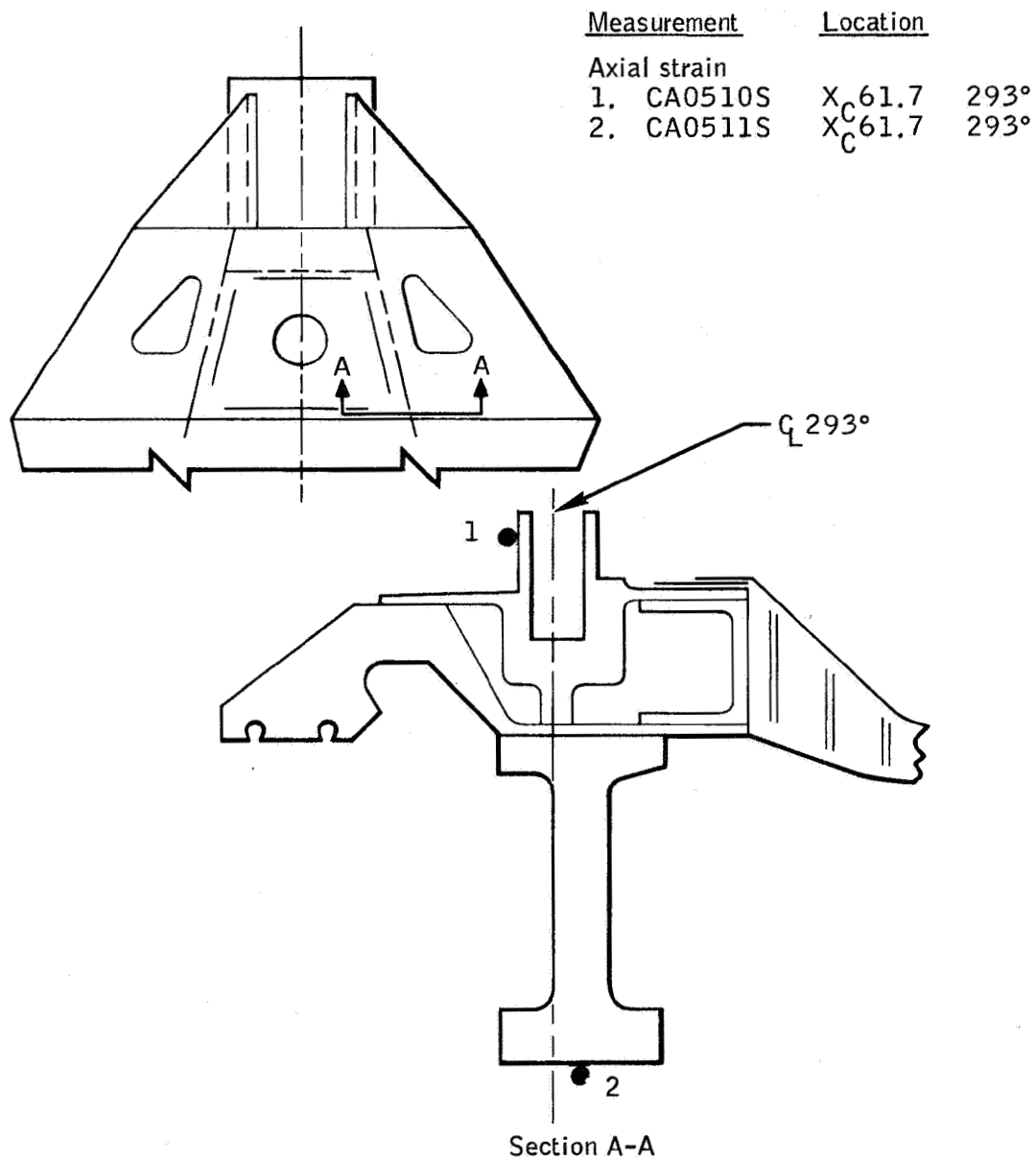
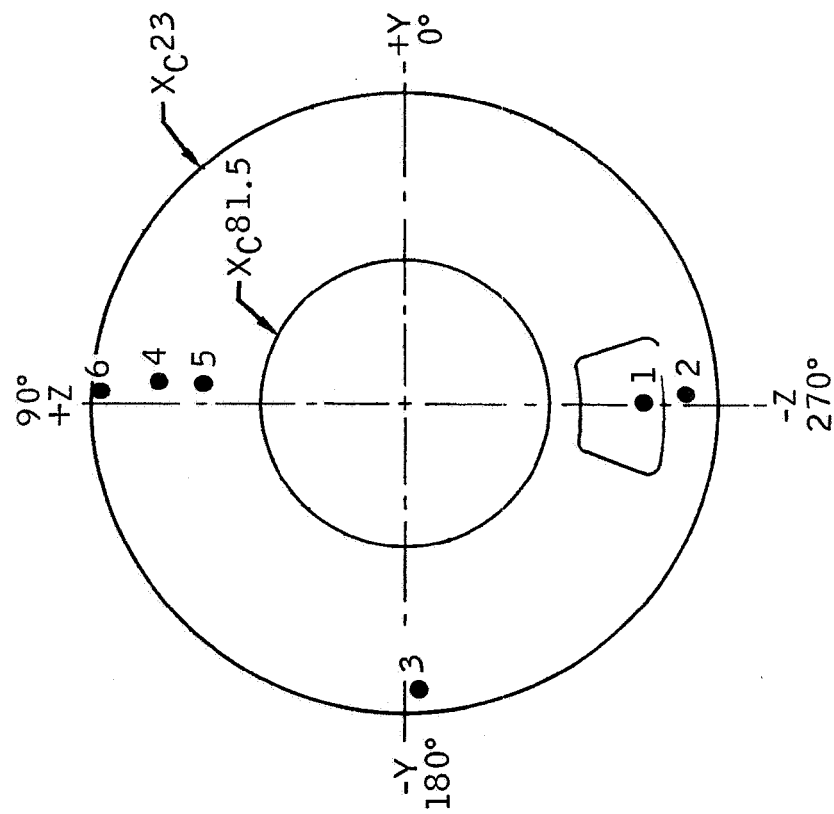


Figure 11.2-9.- Strain gage locations on right-hand beam of main hatch, Apollo Mission A-004.





Measurement	Location
1. CA0574R	X <sub>C</sub> 48 270°
CA0645T	
2. CA0575R	X <sub>C</sub> 34 273°
CA0646T	
3. CA0576R	X <sub>C</sub> 34 183°
CA0647T	
4. CA0577R	X <sub>C</sub> 48 86°
5. CA0578R	X <sub>C</sub> 59 86°
6. CA0579R	X <sub>C</sub> 28 89.5°

Figure 11.2-10.- Command module heat flux measurement locations, Apollo Mission A-004.

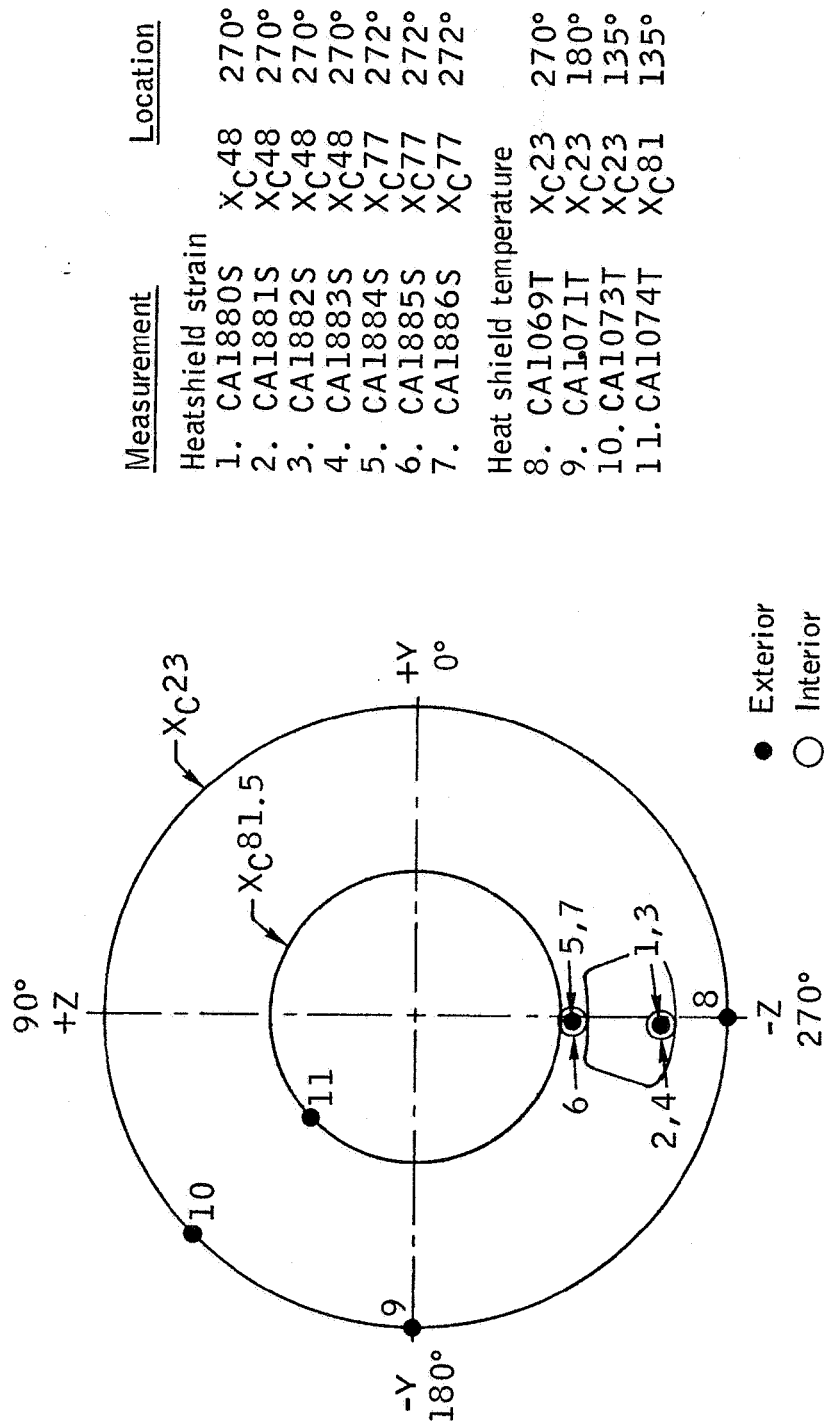


Figure 11.2-11.- Temperature and strain measurements on main heat shield, Apollo Mission A-004.

NASA-S-66-3790 APR 15

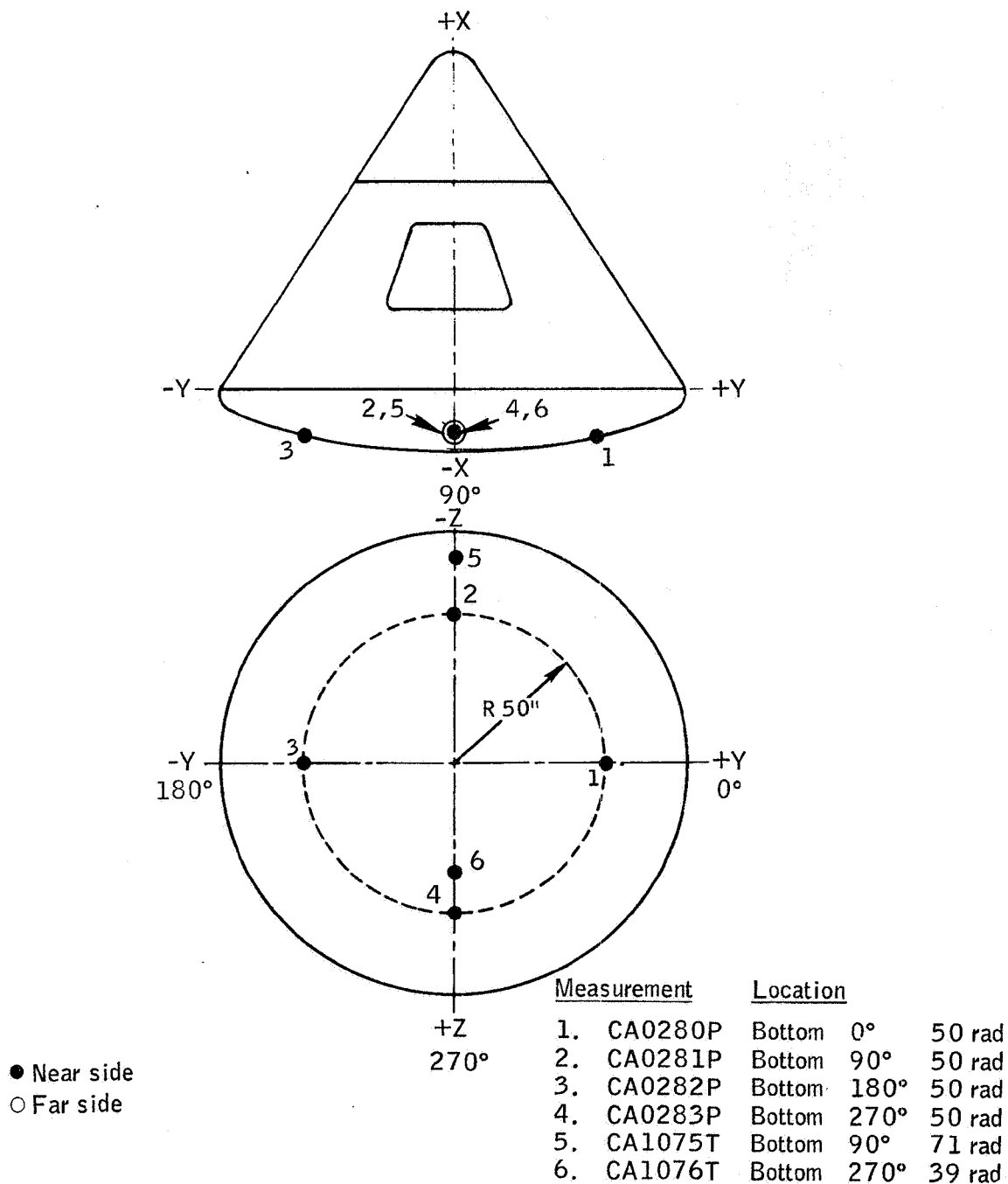
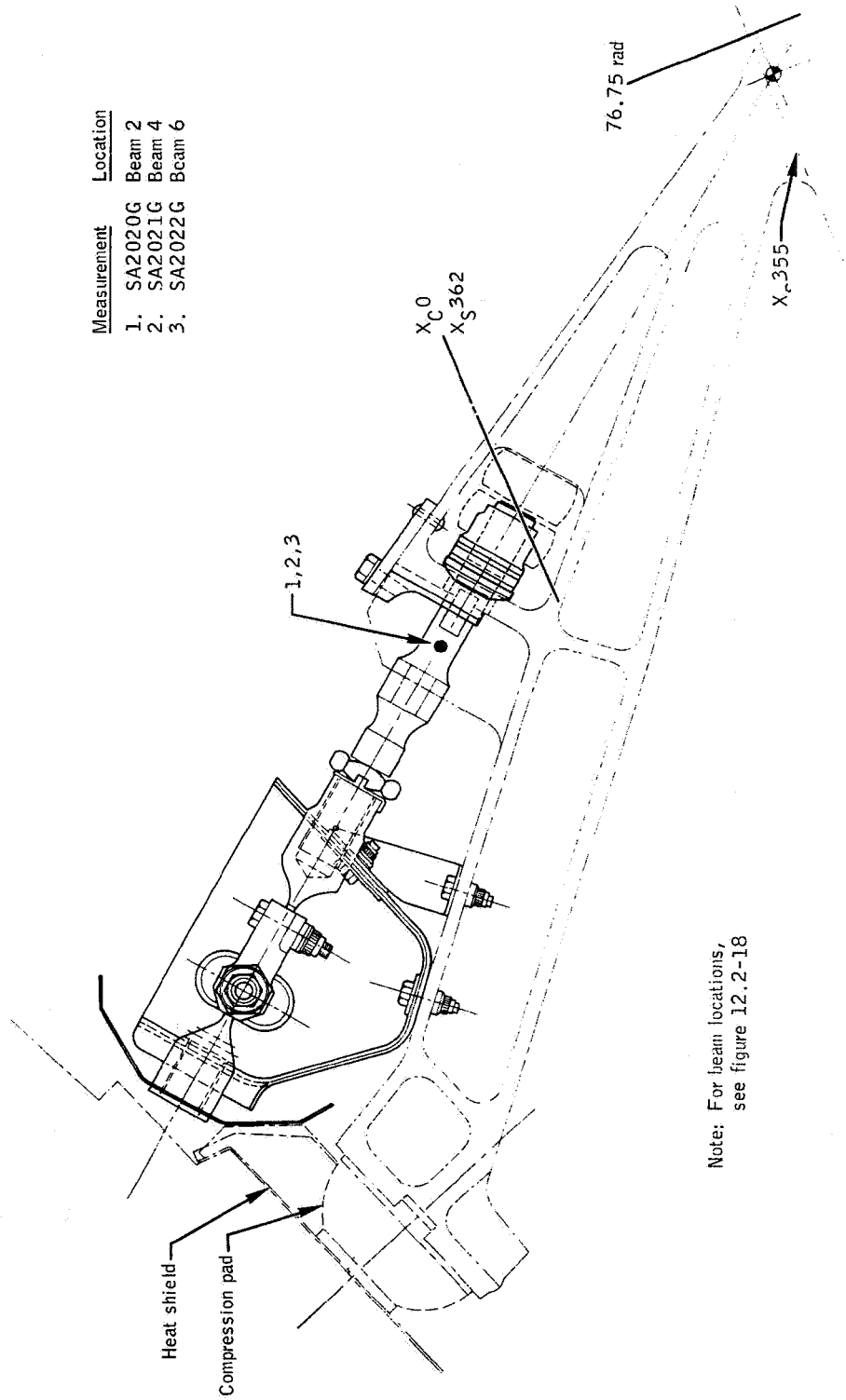


Figure 11.2-12.- Base pressure measurement locations, Apollo Mission A-004.



Measurement	Location
1. SA2020G	Beam 2
2. SA2021G	Beam 4
3. SA2022G	Beam 6

Figure 11.2-13.- Strain gage locations on CM-SM tension-tie bolts 2, 4, and 6, Apollo Mission A-004.

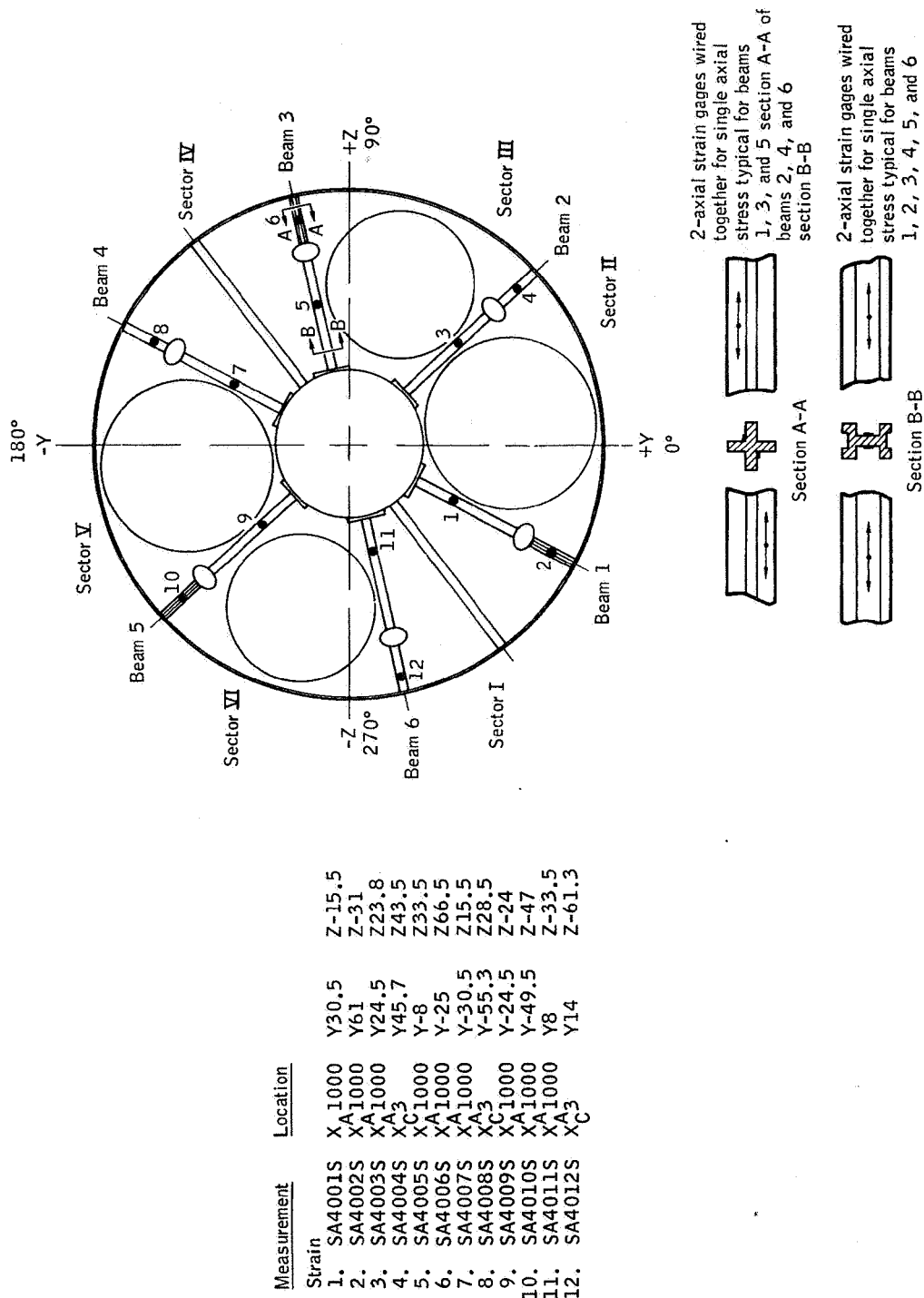


Figure 11.2-14.- Strain gage locations CM-SM compression structure, Apollo Mission A-004.

11-32

NASA-S-66-3802 APR 15

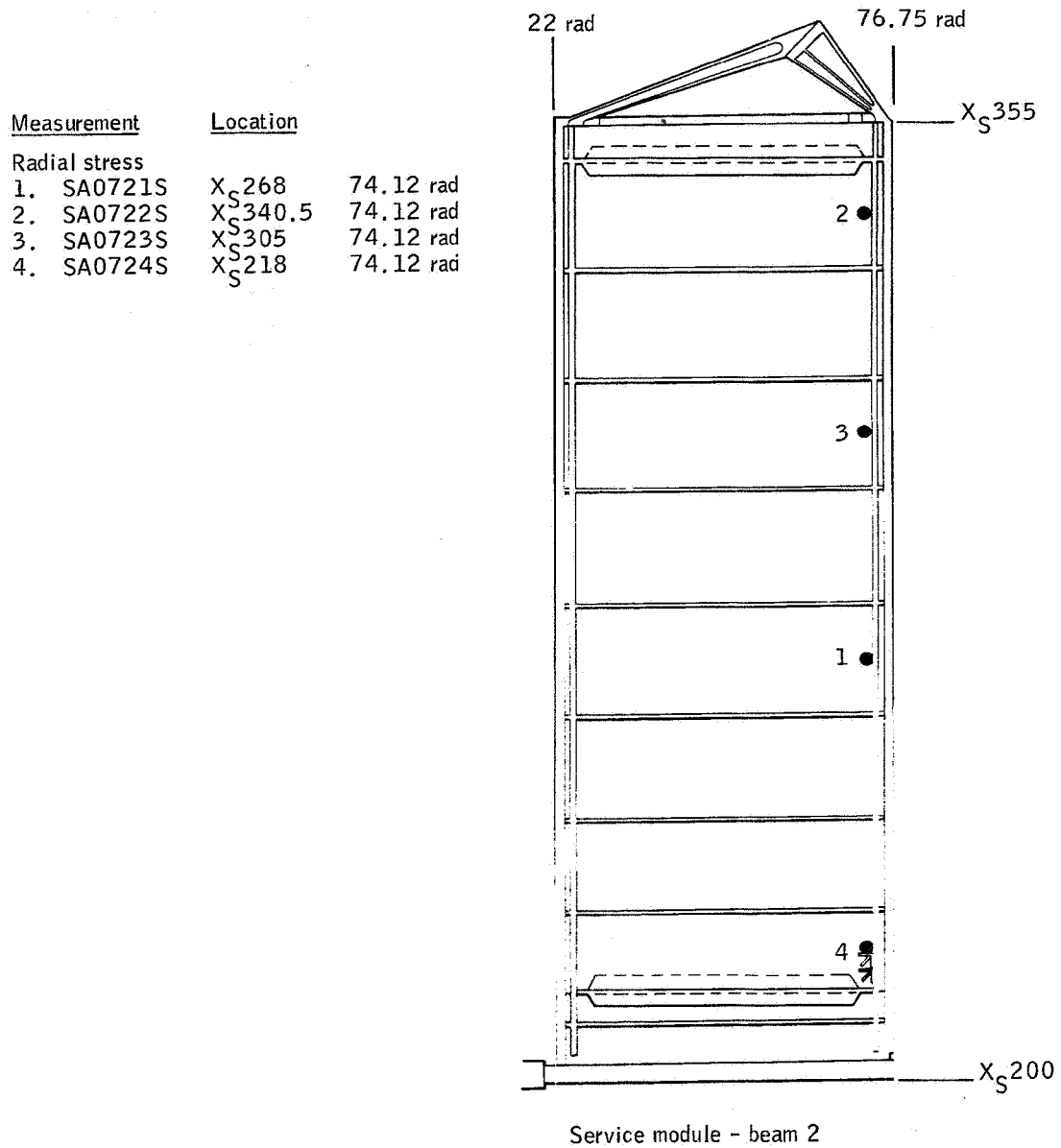


Figure 11.2-15.- Strain gage locations, beam 2, service module, Apollo Mission A-004.

NASA-S-66-3806 APR 15

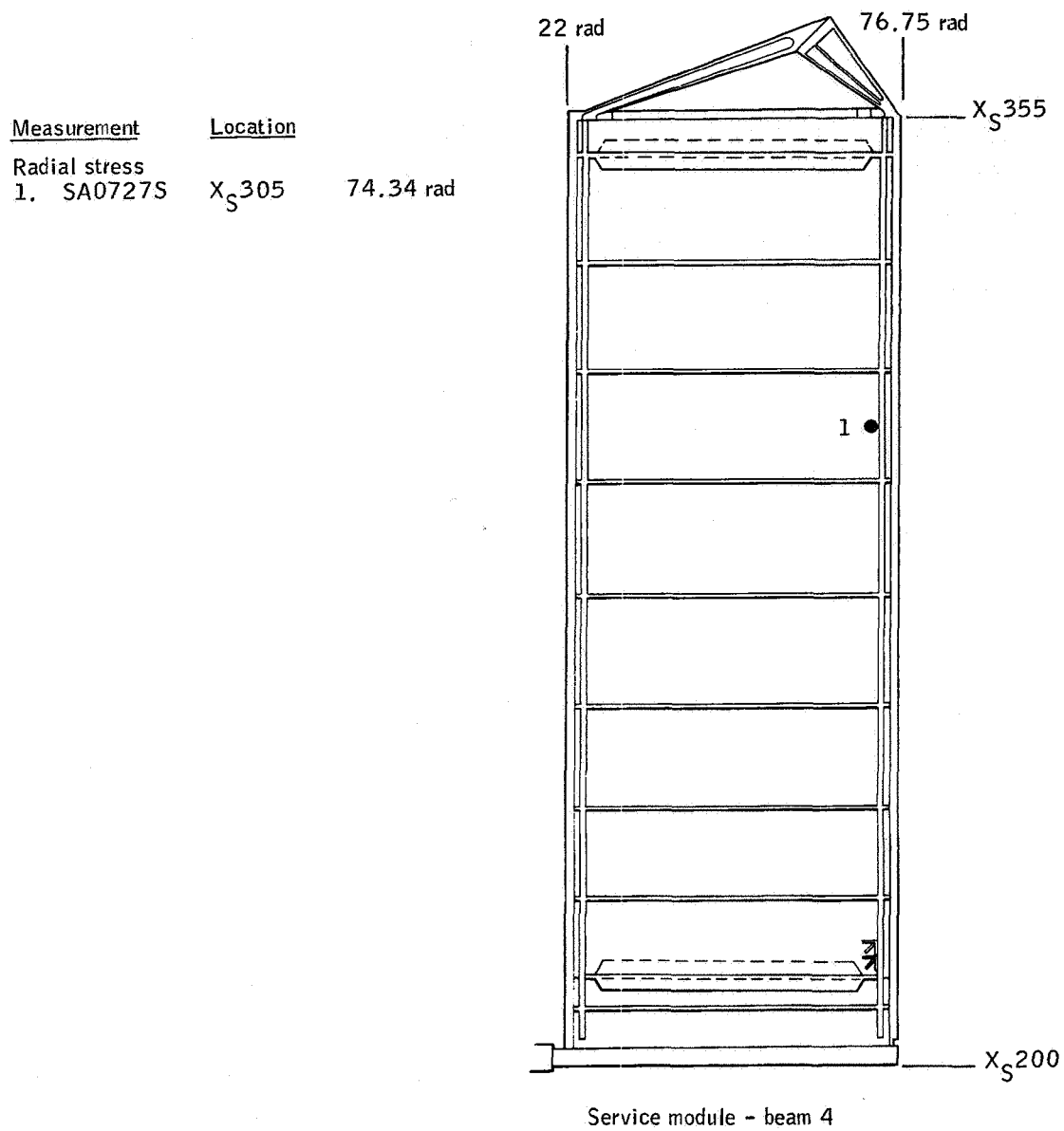


Figure 11.2-16.- Strain gage location, beam 4, service module, Apollo Mission A-004.

Measurement	Location	
Radial stress		
1. SA0725S	X <sub>S</sub> 340.5	74.12 rad
2. SA0726S	X <sub>S</sub> 268	74.12 rad
3. SA0728S	X <sub>S</sub> 305	74.12 rad
Membrane stress		
4. SA0865S	X <sub>S</sub> 218	74.75 rad
5. SA0866S	X <sub>S</sub> 218	74.75 rad
6. SA0867S	X <sub>S</sub> 218	74.75 rad
Bending stress		
7. SA0868S	X <sub>S</sub> 218	74.75 rad
8. SA0869S	X <sub>S</sub> 218	74.75 rad
9. SA0870S	X <sub>S</sub> 218	74.75 rad
Circumferential vibration		
10. SA0994D	X <sub>S</sub> 275	22 rad

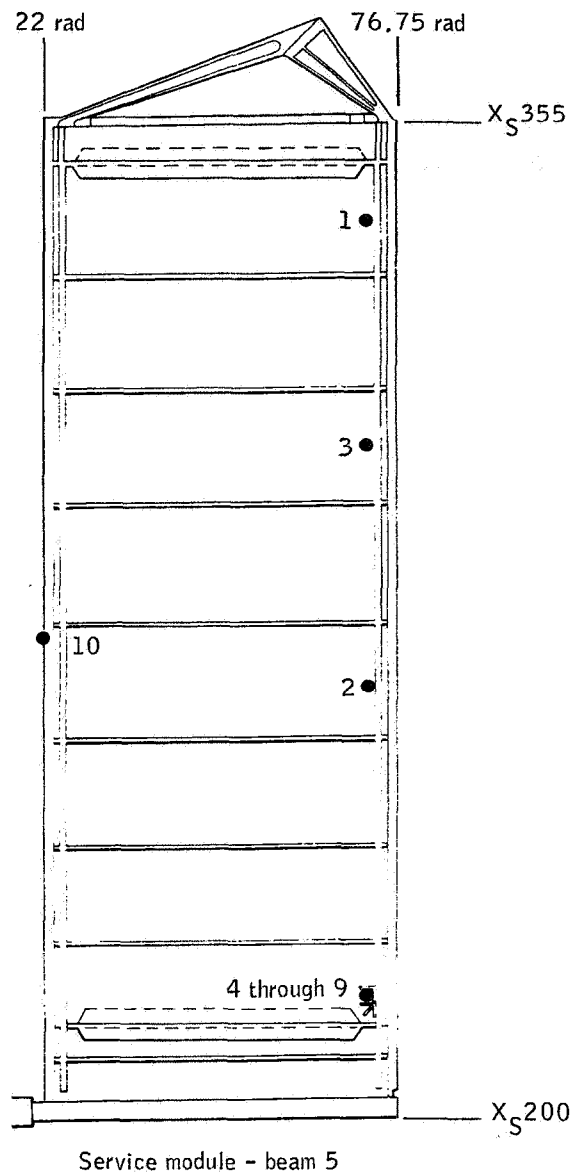


Figure 11.2-17.- Strain gage and vibration measurement location, beam 5, service module, Apollo Mission A-004.



NASA-S-66-3814 APR 15

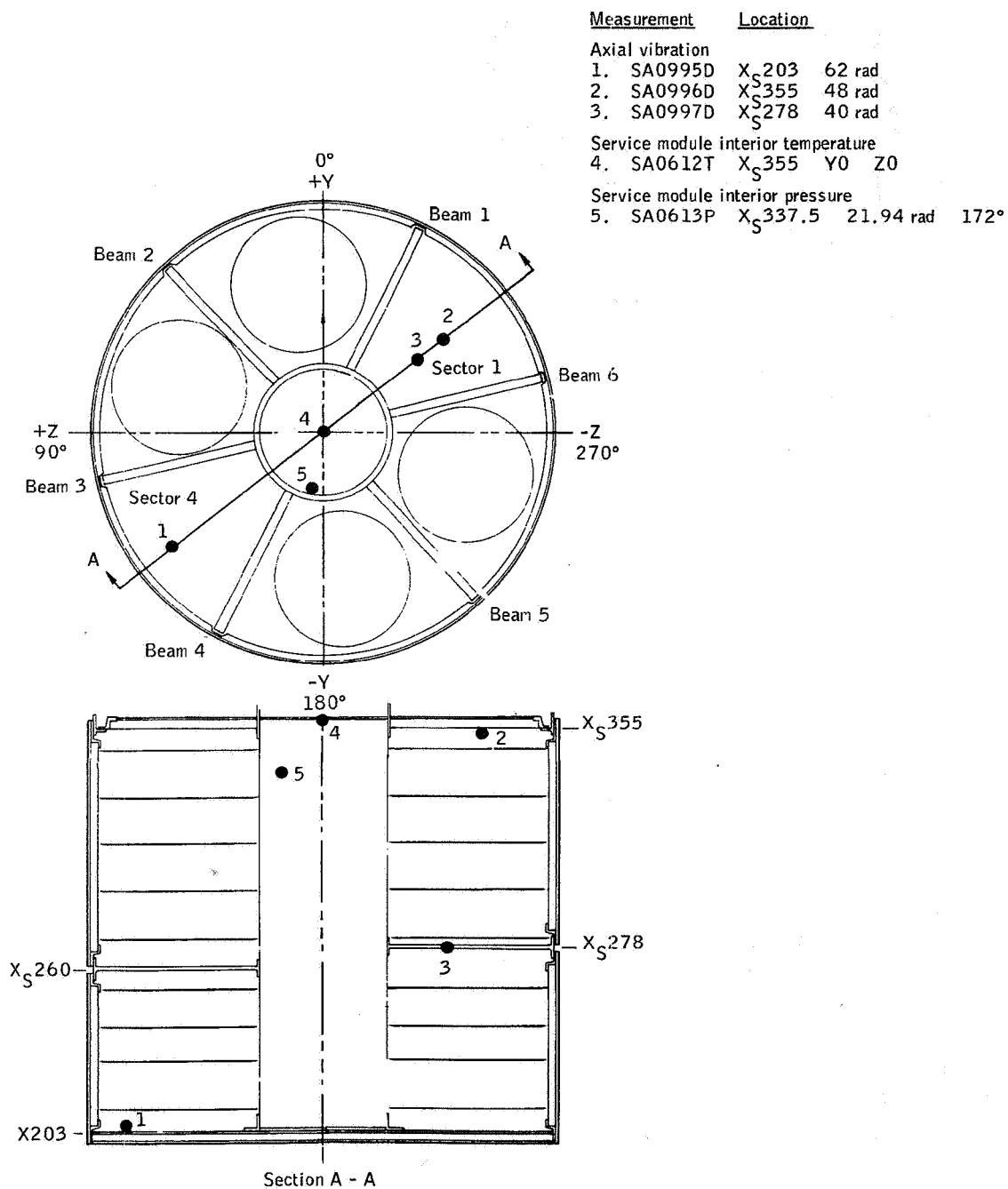


Figure 11.2-18.- Vibration measurements, service module, Apollo Mission A-004.

NASA-S-66-3818 APR 15

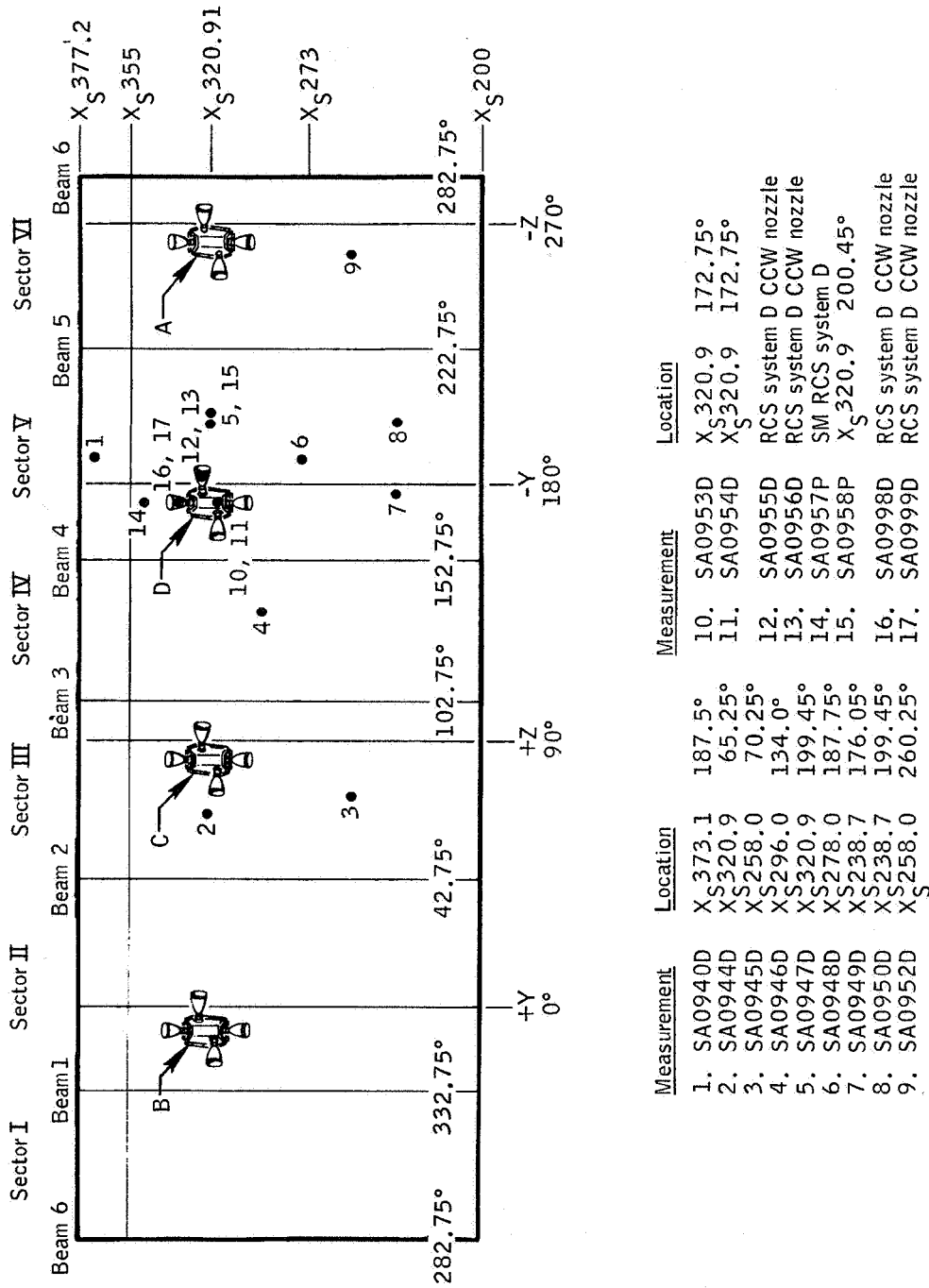
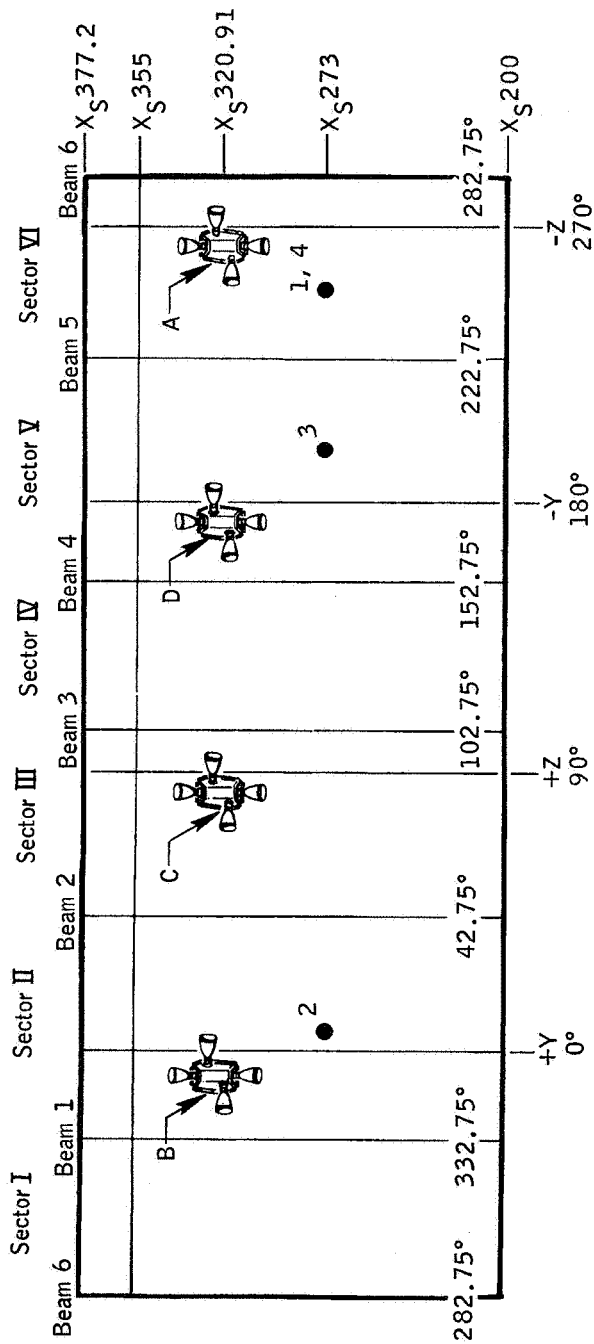


Figure 11.2-19.- Service module vibration and fluctuating pressure measurement locations, Apollo Mission A-004.



Measurement	Location
Strain	
1. SA0936S	X <sub>S</sub> 273 252.75°
SA0937S	X <sub>S</sub> 273 252.75°
SA0938S	X <sub>S</sub> 273 252.75°
SA0939S	X <sub>S</sub> 273 252.75°
Temperature	
2. SA0876T	X <sub>S</sub> 273 7.75° (exterior)
SA0877T	X <sub>S</sub> 273 199.45° (interior)
SA0878T	X <sub>S</sub> 273 199.45° (exterior)
SA0879T	X <sub>S</sub> 273 252.75° (interior)

Figure 11.2-20.- Service module temperature and strain gage locations, Apollo Mission A-004.

## 12.0 REFERENCES

1. Data Processing Planning Office: Flight Data Report for Apollo Mission A-004 (SC-002). NASA Apollo Working Paper 1198, 1966.
2. Staff of North American Aviation: CSM Master End Item Specification (Block I). (Revised Feb. 1965). SID 64-1237 North American Aviation, Inc.
3. Staff of North American Aviation: End Item Specification for SC-002. SID 63-699, North American Aviation, Inc., Feb. 1965.
4. Staff of Manned Spacecraft Center: Postlaunch Report for Apollo Mission A-003 (BP-22). MSC-A-R-65-2, June 28, 1965.
5. Staff of NASA Headquarters: Project Apollo Coordinate System Standard. OMSF Directive SE 008-001-1, June 1965.
6. Staff of General Dynamics/Convair: Launch Vehicle Description Manual, Launch Vehicle 12-51-3, Little Joe II. GD/C-65-145A, General Dynamics/Convair, Sept. 1965.
7. Staff of Manned Spacecraft Center: Apollo Mission Rules - A-004. Nov. 17, 1965.
8. Rother, Melvin R.; and Heetderks, H. Richard: Project Apollo Mission A-004 (AFRM-002) Dispersion Analysis. MSC IN 65-FM-144, Oct. 1965.
9. Staff of North American Aviation: Aerodynamics Data Manual for Project Apollo. SID 64-174A, North American Aviation, Inc., Jan. 1965.
10. Staff of Manned Spacecraft Center: Postlaunch Report for Apollo Mission A-002 (BP-23). MSC-R-A-65-1, Jan. 22, 1965.
11. Staff of Manned Spacecraft Center: Postlaunch Memorandum Report for Apollo Mission PA-2 (BP-23A). MSC-A-R-65-3, July 29, 1965.
12. Staff of Manned Spacecraft Center: Postlaunch Report for Apollo Mission A-102 (BP-15). MSC-R-A-64-3, Oct. 10, 1964.
13. Staff of Manned Spacecraft Center: Postlaunch Report for Apollo Mission A-101 (BP-13). MSC-R-A-64-2, June 18, 1964.

14. Coe, Charles F.; and Kaskey, Arthur J.: The Effects of Nose Bluntness on the Pressure Fluctuations Measured on 15° and 20° Cone - Cylinders at Transonic Speeds. NASA TM X 779, 1963.
15. Staff of North American Aviation: Aerodynamic Noise Measurements on a 0.055-Scale Model of the Apollo/Saturn-1B Launch Vehicle. SID 64-1545, North American Aviation, Inc., Sept. 1964.
16. Coe, Charles F.: Steady and Fluctuating Pressures at Transonic Speeds on Two Space-Vehicle Payload Shapes. NASA TM X 503, 1961.
17. Staff of North American Aviation: Airframe 007 Service Module Environmental Acoustic Test Program. SID 65-1038, North American Aviation, Inc., Aug. 1965.
18. Staff of North American Aviation: Project Apollo Spacecraft 007 Command Module Environment Acoustic Test Program. SID 65-1193, North American Aviation, Inc., Nov. 1965.
19. Staff of North American Aviation: An Investigation of Aerodynamic Noise Measured on a 0.055-Scale Apollo Saturn Vehicle in the NASA Ames 14-foot Transonic and 9 × 7-foot Supersonic Wind Tunnels. SID 63-1480, North American Aviation, Inc., Dec. 1963.
20. Staff of Manned Spacecraft Center: Postlaunch Report for Apollo Mission A-001 (BP-12). MSC-R-A-64-1, May 28, 1964.
21. Staff of Lockheed Aircraft: Airframe 002 Spacecraft Development Flight Instrumentation, Mission A-004. IESD doc. 11-7, Lockheed Aircraft, May 1965.
22. Staff of North American Aviation: Block I CSM Technical Specification. SID 63-313, North American Aviation, Inc., Feb. 1965.

## DISTRIBUTION

<u>Addressee</u>	<u>Number of copies</u>
National Aeronautics and Space Administration Washington, D.C. 20546	
Associate Administrator Office of Manned Space Flight, M	1
Apollo Program Director, MA	1
Flight Operations Director, MAO	1
Program Control Director, MAP	1
Reliability and Quality Assurance Director, MAR	1
Systems Engineering Director, MAS	2
Test Director, MAT	3
MSF Field Center Development Director, MC	1
Deputy Director, Saturn-Apollo Applications, MLD	1
Deputy Director, Mission Operations, MO-1	1
Advanced Manned Missions Program Director, MT	2
National Aeronautics and Space Administration Manned Spacecraft Center 2101 Webster-Seabrook Road Houston, Texas 77058	
Director, AA	1
Deputy Director, AB	1
Special Assistant to the Director, AC	1
Executive Assistant to the Director, AF	1
Chief of Center Medical Programs, AH	1
Office of Patent Counsel, AL3	1

<u>Addressee</u>	<u>Number of copies</u>
Center Medical Office, AM	1
Public Affairs Office, AP	1
Flight Safety Office, AR	2
Assistant Director for Administration, BA	1
Reproduction Services Branch, BF6	1
Forms and Publications Section, BF52	54
Field Test Branch, BH6	1
Security Branch, BM4	1
Technical Information Preparation Branch Records, BM5	4
Technical Information Dissemination Branch, BM6	6
Technical Information Dissemination Branch, BM6 Attention: M. P. McDonough	10
Assistant Director for Flight Crew Operations, CA	1
Astronaut Office, CB	3
Flight Crew Support Division, CF	4
Assistant Director for Engineering and Development, EA	3
Information Systems Division, EB	1
Crew Systems Division, EC	2
Instrumentation and Electronic Systems Division, EE	7
Guidance and Control Division, EG	2
Propulsion and Power Division, EP	3
Structures and Mechanics Division, ES	4
Advanced Spacecraft Technology Division, ET	3

<u>Addressee</u>	<u>Number of copies</u>
Assistant Director for Flight Operations, FA	2
Flight Control Division, FC	4
Landing and Recovery Division, FL	2
Mission Planning and Analysis Division, FM	2
Gemini -- Office of Program Manager, GA	1
Test Operations Manager, GT	1
Apollo -- Office of Manager, PA	3
NASA-RASPO, PB Grumman Aircraft Engineering Corporation Bethpage, L.I., New York 11714	3
NASA-RASPO, PC 12214 Lakewood Blvd. Downey, California 90240	4
Systems Engineering Division, PD	5
LEM Project Engineering and Checkout Division, PE	3
C and SM Project Engineering and Checkout Division, PF	4
Mission Operations Division, PM	5
Program Control Division, PP	1
Reliability, Quality, and Test Division, PR	2
Apollo Analysis and Reporting Team, PM4	50
Resident Liaison Offices	
Goddard Space Flight Center Liaison Office, GSF-L	1
Kennedy Space Center Liaison Office, HALL3	1
Marshall Space Flight Center Resident Liaison Office, RL	1



<u>Addressee</u>	<u>Number of copies</u>
<b>Libraries</b>	
NASA Headquarters Library, USS-10	6
Ames Research Center Library	6
Flight Research Center Library	6
Goddard Space Flight Center Library	2
John F. Kennedy Space Center Library	6
Lewis Research Center Library	6
Marshall Space Flight Center Library	6
NASA Ames Research Center Moffett Field, California 94035 Attention: Director	1
NASA Flight Research Center Post Office Box 273 Edwards, California 93523 Attention: Director	1
NASA Goddard Space Flight Center Greenbelt, Maryland 20771 Attention: Director, 100	1
NASA Langley Research Center Langley Station Hampton, Virginia 23365 Attention: Director, 0.000	1
NASA Lewis Research Center 21000 Brookpark Road Cleveland, Ohio 44135 Attention: Director, 100	1
NASA George C. Marshall Space Flight Center Huntsville, Alabama 35812 Attention: Director, M-DIR	1

<u>Addressee</u>	<u>Number of copies</u>
NASA Electronics Research Center 565 Technology Square Cambridge, Massachusetts 02139	1
NASA MSC-White Sands Test Facility Office of the Manager, RA P. O. Drawer MM Las Cruces, New Mexico 88001	2
John F. Kennedy Space Center, NASA NASA Kennedy Space Center, Florida 32899	6
NASA Marshall Space Flight Center Aero-Astrodynamics Laboratory, R-Aero-F Huntsville, Alabama 35812	3
NASA-RASPO Massachusetts Institute of Technology 75 Cambridge Parkway Cambridge, Massachusetts 02142	2
NASA-RASPO AC Spark Plug Company Milwaukee, Wisconsin 53200	2
North American Aviation, Inc., S&ID Attention: D. M. Cole Systems Engineering, Dept. 692 12214 Lakewood Blvd. Downey, California 90240	3
North American Aviation, Inc., S&ID Attention: Dale D. Myers Apollo Program Manager 12214 Lakewood Blvd. Downey, California 90240	1
Grumman Aircraft Engineering Corp. Bethpage, L. I., New York 11714	4
Arnold Engineering Development Center Attention: General Gossick Arnold Air Force Station, Tennessee 37389	1